Methods in Molecular Biology 1075

Springer Protocols

Stephen W. Paddock *Editor*

Confocal Microscopy

Methods and Protocols

Second Edition

Humana Press

METHODS IN MOLECULAR BIOLOGY™

Series Editor
John M. Walker
School of Life Sciences
University of Hertfordshire
Hatfield, Hertfordshire, AL10 9AB, UK

For further volumes:
http://www.springer.com/series/7651

Confocal Microscopy

Methods and Protocols

Second Edition

Edited by

Stephen W. Paddock

Department of Molecular Biology, University of Wisconsin, Madison, WI, USA

Humana Press

Editor
Stephen W. Paddock
Department of Molecular Biology
University of Wisconsin
Madison, WI, USA

ISSN 1064-3745 ISSN 1940-6029 (electronic)
ISBN 978-1-58829-351-0 ISBN 978-1-60761-847-8 (eBook)
DOI 10.1007/978-1-60761-847-8
Springer New York Heidelberg Dordrecht London

Library of Congress Control Number: 2013947924

Printed on acid-free paper

Humana Press is a brand of Springer
Springer is part of Springer Science+Business Media (www.springer.com)

Preface

Confocal microscopy has become an essential technique in all fields of contemporary biomedical research where a light microscope is required for imaging fixed or living fluorescently labeled cells and tissues. The approach is especially useful in cell biology, developmental biology, neurobiology, and pathology for visualizing the spatial distribution of labeled cells within tissues or the spatial distribution of specific macromolecules within cells.

The field of confocal microscopy has grown exponentially since the publication of the first edition of this book some 10 years ago. While confocal instruments were typically confined to multiuser facilities since they required specialist training and maintenance, the modern instruments have become much more user-friendly and reliable, and are now commonly found in both multiuser microscopy facilities and in individual laboratories.

Before practical confocal microscopes became available to biologists some 30 years ago, fluorescently labeled cells and tissues were imaged using conventional epifluorescence light microscopes. Using these instruments, resolution was compromised by fluorescence from out of the focal plane of interest especially when tissues made up of multiple cell layers such as developing embryos and adult brains were imaged.

In order to attain acceptable resolution in their images at this time, microscopists were forced into all manner of tricks to prepare their specimens for optimal viewing in the microscope. Such techniques include cutting sections of tissues with a microtome, growing cells on a glass coverslip, flattening cells under agar or squashing embryos between a slide and coverslip. While most of these methods produced acceptable images, they ran the risk of introducing artifacts, and as a consequence, the validity of the results could be questioned.

Moreover, the detection of weakly labeled structures was often impossible since long exposure times were necessary to produce an image, and significant photobleaching occurred. Often labeled structures could be observed by eye simply by focusing up and down within the specimen, but it was impossible to document any detailed structural information for further analysis and publication. This was extremely frustrating for the researcher since the exquisite specificity of immunolabeling was lost in the fluorescent haze.

After laser scanning confocal microscopes became commercially available in 1985, the out-of-focus fluorescence was eliminated by the optics of the instrument leaving the in-focus information in the final image. Images produced in this way were reminiscent of those of physically sectioned tissues and were called “optical sections” since light rather than a knife was used to produce them.

The current generation of modern confocal instruments produces optical sections of cells and tissues that are free of out-of-focus fluorescence with reduced chances of artifacts from the techniques of specimen preparation. In addition to imaging fixed specimens, overall improvements to the light efficiency of modern instruments (especially improvements in the sensitivity of the photodetectors) coupled with the introduction and improvement of fluorescent reporter probes over the years has enabled routine imaging of living specimens. Moreover, the measurement of physiological events within cells is now a possibility with faster image acquisition times.

The optical sections collected using the current generation of microscopes are in a digital format, and are easily reproduced on a journal page or a Web site at the exact same resolution and color balance as the data collected by the confocal microscope itself. The images are further processed using various visualization software and analyzed using bioinformatics techniques.

As in the first edition, the second one is aimed primarily, but not exclusively, at the novice user with suggestions for and information about more advanced techniques. The current volume is relatively light on the technical details of the microscopes themselves as these can be found elsewhere, and quickly change as new technology is incorporated into modern confocal systems. As in the previous volume, the aim of the current one is to take the researcher from the benchtop through the imaging process to the journal page for a few protocols.

Emphasis has again been placed on the laser scanning confocal microscope since this instrument continues to be used for most routine applications. There are now many alternatives to the laser scanning confocal microscope for producing optical sections, however. These instruments include the strictly confocal together with instruments such as multiphoton microscopes that have evolved from the confocal approach. These additional methods of collecting optical sections have been listed in our introductory chapter together with some of their applications and possible advantages over the confocal approach.

Protocols for the preparation of tissues from many model organisms including worms, flies, and mice have been included as well as chapters on confocal imaging of living cells, three-dimensional analysis, and the measurement and presentation of confocal images for publication. It is now impossible to include a comprehensive list of protocols in a single volume. Further information on where to obtain additional protocols can be gleaned from Chapter 3 together with the many Web references and links scattered throughout the book.

In addition, we are honored to include an introductory chapter from John White, one of the inventors of the first laser scanning confocal microscopes made available to the biomedical research community in 1985. John epitomizes the spirit of adventure, excitement and cooperation that has largely percolated through the confocal field over the years, and provides us with a flavor of those early years of confocal instrument development and treats us to some of his insight for the future.

Finally, this has been a long project, and has gone through several rounds of revision. We would like to thank all of the authors who have persevered in order to complete their chapters and updates to their chapters in a timely fashion. Finally, we would like to thank our colleagues (past and present) for presenting us with such a variety of stimulating imaging challenges. The series editor, John Walker, has provided expert editorial advice and shown great patience with us. The staff at Humana Press and Springer (and especially Tamara Cabrero) have performed to an extremely high standard of professionalism throughout the project.

Madison, WI, USA

Stephen W. Paddock
Kevin W. Eliceiri

Contents

Contributors

John F. Bertram • *Department of Anatomy and Developmental Biology, Monash University, Clayton, VIC, Australia*

Jeff Boden • *Molecular and Cellular Pharmacology and Vascular Biology Institute, Miller School of Medicine, University of Miami, Miami, FL, USA*

Thomas K. Borg • *Department of Cell and Developmental Biology and Anatomy, School of Medicine, University of South Carolina, Columbia, SC, USA*

Craig R. Brunetti • *Department of Biology, Trent University, Peterborough, ON, Canada*

Tara Bullard • *Department of Cell and Developmental Biology and Anatomy, School of Medicine, University of South Carolina, Columbia, SC, USA*

Robert L. Conhaim • *Department of Surgery, School of Medicine and Public Health, University of Wisconsin, Madison, WI, USA*

Frank Costantini • *Department of Genetics and Development, Columbia University, New York, NY, USA*

Guy Cox • *Australian Centre for Microscopy & Microanalysis, University of Sydney, Sydney, NSW, Australia*

Ian P. Coyle • *IP Coyle Intellectual Property Agency, Fort Lauderdale, FL, USA*

Luise A. Cullen-McEwen • *Department of Anatomy and Developmental Biology, Monash University, Clayton, VIC, Australia*

Zachary C. Cunningham • *National High Magnetic Field Laboratory and Department of Biological Science, The Florida State University, Tallahassee, FL, USA*

Jeffrey Davis • *Department of Cell and Developmental Biology and Anatomy, School of Medicine, University of South Carolina, Columbia, SC, USA*

Michael W. Davidson • *National High Magnetic Field Laboratory and Department of Biological Science, The Florida State University, Tallahassee, FL, USA*

Kevin W. Eliceiri • *Laboratory for Optical and Computational Instrumentation and Laboratory of Molecular Biology, University of Wisconsin, Madison, WI, USA*

Barbara Fasulo • *Molecular and Cellular Biology, University of California, Santa Cruz, CA, USA*

Gabriel Fricout • *Centre de Morphologie Mathématique, Ecole des Mines de Paris, Paris, France*

Kevin J. Frischmann • *Bitplane Inc., Saint Paul, MN, USA*

Andy Golden • *Laboratory of Biochemistry and Genetics, National Institute of Diabetes and Digestive and Kidney Diseases, National Institutes of Health, Bethesda, MD, USA*

Stephen T. Haley • *Beckman Coulter Translational Solutions Business Center, San Diego, CA, USA*

Ian S. Harper • *Department of Anatomy and Developmental Biology, Monash University, Clayton, VIC, Australia*

Kristin L. Hazelwood • *National High Magnetic Field Laboratory and Department of Biological Science, The Florida State University, Tallahassee, FL, USA*

Dennis M. Heisey • *Department of Surgery, School of Medicine and Public Health, University of Wisconsin, Madison, WI, USA*
Karen Hogg • *Imaging and Cytometry Laboratory, Technology Facility, Department of Biology, University of York, York, UK*
Jon Holy • *Department of Anatomy, Microbiology and Pathology, University of Minnesota School of Medicine, Duluth, MN, USA*
Dominique Jeulin • *Centre de Morphologie Mathématique, Ecole des Mines de Paris, Paris, France*
Vazgen Khankaldyyan • *Division of Hematology/Oncology, Department of Pediatrics, Children's Hospital Los Angeles, USC Keck School of Medicine, Los Angeles, CA, USA*
Angela V. Klaus • *Department of Biology, Seton Hall University, South Orange, NJ, USA*
Walter E. Laug • *Division of Hematology/Oncology, Department of Pediatrics, Children's Hospital Los Angeles, USC Keck School of Medicine, Los Angeles, CA, USA*
Glen E. Leverson • *Department of Surgery, School of Medicine and Public Health, University of Wisconsin, Madison, WI, USA*
Yiwen Li • *Bascom Palmer Eye Institute, Miller School of Medicine, University of Miami, Miami, FL, USA*
Richard L. Ludlow • *National High Magnetic Field Laboratory and Department of Biological Science, The Florida State University, Tallahassee, FL, USA*
Joanne Marrison • *Imaging and Cytometry Laboratory, Technology Facility, Department of Biology, University of York, York, UK*
Christopher S. Murphy • *National High Magnetic Field Laboratory and Department of Biological Science, The Florida State University, Tallahassee, FL, USA*
George McNamara • *Analytical Imaging Core, Diabetes Research Institute, Miami Institute for Human Genomics, University of Miami, Miami, FL, USA; UM/Sylvester Comprehensive Cancer Center, Miller School of Medicine, University of Miami, Miami, FL, USA*
Paulo J. Oliveira • *Department of Zoology, University of Coimbra, Coimbra, Portugal*
Anna P. Ozarowska • *National High Magnetic Field Laboratory and Department of Biological Science, The Florida State University, Tallahassee, FL, USA*
Kevin F. O'Connell • *Laboratory of Biochemistry and Genetics, National Institute of Diabetes and Digestive and Kidney Diseases, National Institutes of Health, Bethesda, MD, USA*
Peter O'Toole • *Imaging and Cytometry Laboratory, Technology Facility, Department of Biology, University of York, York, UK*
Stephen W. Paddock • *Howard Hughes Medical Institute, Department of Molecular Biology, University of Wisconsin, Madison, WI, USA*
Matthew J. Parry-Hill • *National High Magnetic Field Laboratory and Department of Biological Science, The Florida State University, Tallahassee, FL, USA*
Edward L. Perkins • *Department of Biomedical Sciences, Mercer University School of Medicine, Savannah, GA, USA*
Robert L. Price • *Department of Cell and Developmental Biology and Anatomy, School of Medicine, University of South Carolina, Columbia, SC, USA*
Adam M. Rainey • *National High Magnetic Field Laboratory and Department of Biological Science, The Florida State University, Tallahassee, FL, USA*
Ericka B. Ramko • *National High Magnetic Field Laboratory and Department of Biological Science, The Florida State University, Tallahassee, FL, USA*
Valerie Schawaroch • *Department of Natural Sciences, Baruch College, New York, NY, USA; Division of Invertebrate Zoology, American Museum of Natural History, New York, NY, USA*

Jerry Sedgewick • *Biomedical Image Processing Lab, University of Minnesota, Minneapolis, MN, USA*
William Sullivan • *Molecular and Cellular Biology, University of California, Santa Cruz, CA, USA*
Louis Terracio • *College of Dentistry, New York University, New York, NY, USA*
Keith Webster • *Molecular and Cellular Pharmacology and Vascular Biology Institute, Miller School of Medicine, University of Miami, Miami, FL, USA*
Rong Wen • *Bascom Palmer Eye Institute, Miller School of Medicine, University of Miami, Miami, FL, USA*
John White • *Laboratory for Optical and Computational Instrumentation and Laboratory of Molecular Biology, University of Wisconsin, Madison, WI, USA*
Anna Yanai • *Division of Hematology/Oncology, Department of Pediatrics, Children's Hospital Los Angeles, USC Keck School of Medicine, Los Angeles, CA, USA*
Richard J. Young • *Department of Anatomy and Developmental Biology, Monash University, Clayton, VIC, Australia*
Timo Zimmermann • *Advanced Light Microscopy Unit, Centre for Genomic Regulation, Barcelona, Spain*
Robert M. Zucker • *Reproductive Toxicology Division, National Health and Environmental Effects Research Laboratory, Office of Research and Development, U.S. Environmental Protection Agency, Research Triangle Park, NC, USA*

Chapter 1

Reflecting on Confocal Microscopy: A Personal Perspective

John White

Abstract

The first practical laser scanning confocal microscopes were introduced to the biomedical community over 30 years ago. Their subsequent development continues to influence the introduction of new methods and applications of optical sectioning microscopy.

Key words Confocal, Laser scanning, Optical section, Fluorescence, Living tissue, Three-dimensional imaging

1 Introduction

The three-dimensional nature of biological structures has presented a fundamental challenge to microscopists over the years. This is because images are often obscured by interfering signals from out-of-focus structures. A traditional approach was to immobilize the specimen by chemical fixation or freezing, and cutting thin sections of it. The sections were then examined sequentially to provide a three-dimensional reconstruction.

In recent years a number of optical sectioning techniques have become available which avoid the necessity to cut sections and thereby open up the possibility of visualizing three-dimensional structures in live specimens. Confocal microscopy is perhaps the most widely used of these techniques. It works by sequentially illuminating a restricted region of the specimen and excluding light that emanates from outside this region (Fig. 1).

In a typical instrument, illumination is restricted to a defined structure within the specimen, such as a single spot, an array of spots, or an array of lines. A spatial filter (in the shape of the illuminated structure) is situated in the imaging path, which acts to block light that emanates from regions away from that which is illuminated. Images are built up by scanning the illuminating structure in tandem with the spatial filter so that the whole two-dimensional field is covered.

Stephen W. Paddock (ed.), *Confocal Microscopy: Methods and Protocols*, Methods in Molecular Biology, vol. 1075,
DOI 10.1007/978-1-60761-847-8_1,

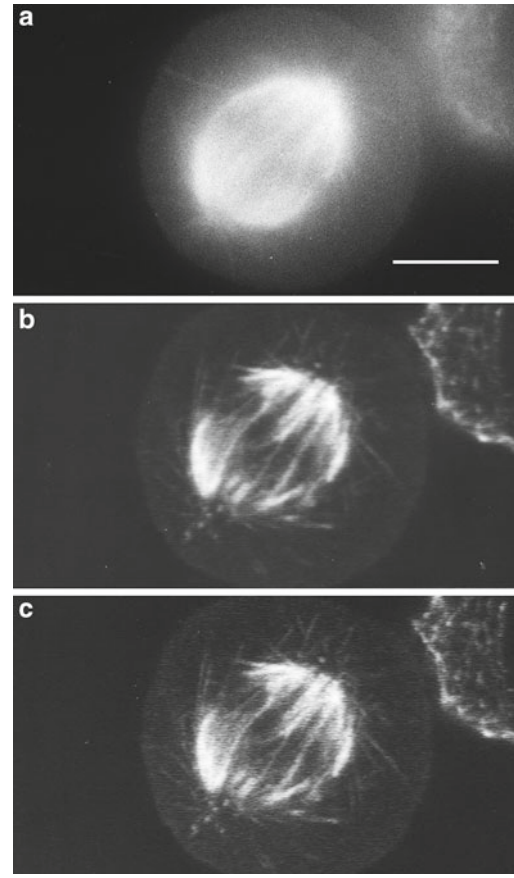

Fig. 1 Confocal microscopy comes of age. Comparison of epifluorescence microscopy and laser scanning confocal imaging of a HeLa cell mitotic spindle labeled using indirect immunofluorescence with anti-tubulin (primary antibody) and a fluorescein labeled secondary antibody. The specimen was imaged using (**a**) conventional epifluorescence light microscopy and (**b**, **c**) using the laser scanning confocal microscope. Note the improved resolution of microtubules in the two confocal images (b) and (c) as compared with the conventional image (a). Image (b) was collected with the pinhole set to a wider aperture than image (c). (Image kindly provided by Brad Amos, University of Cambridge, UK). Scale bar = 5 μm

The basic idea for confocal microscopy was first put forward in a patent by Marvin Minsky in 1957 [1, 2], but it took the development of lasers, microfabrication techniques, and computer image acquisition systems before practical instruments became available to the biomedical community in the late 1980s and early 1990s [3–6].

2 The Laser Scanning Confocal Microscope

The rapid acceptance of confocal microscopy in the late 1980s by the biomedical research community was extraordinary for such a novel and relatively expensive technology. Indeed, the journal Science ran a cartoon of a little girl asking Santa Claus for a laser-scanning microscope for Christmas!

Perhaps the reason for this rapid acceptance was that standard specimen preparation techniques could be used. By far the most common mode of confocal microscopy used by the biomedical community is fluorescence. There are many reasons for this, such as the high signal-to-background ratio of fluorescence, the ability to use multiple labels and the increasing usage of genetically engineered fluorescent proteins [7].

In the early days of using the instruments we used to have conventional fluorescence set up on our confocal microscopes so that people could rapidly switch from conventional to confocal imaging (Fig. 2).

When investigators examined their favorite specimens using the laser scanning confocal microscope for the first time, these instruments became the must-have gadgets of the late 1980s. I remember being thrilled when we first saw images of the microtubule array in the organism that we were studying at the time, the roundworm, *Caenorhabditis elegans* embryos (Fig. 3).

However, on closer examination, the microtubules looked a "bit crinkly", which made us worry about possible optical artifacts with confocal imaging. The problem was soon found out to be due to poor fixation and mounting. Of course, like any microscopy, the quality of the images is dependent on the quality of the specimen. A book such as this, which focuses on methodology and specimen preparation, can be an invaluable practical guide to the investigator who is trying to get the best possible images from his or her specimens in order to push the limits of what is visible.

3 Practical Considerations

The most critical determinant of the image quality in a confocal microscope (sharpness and contrast) is the alignment of the optical system such that the optical mask in the image path is precisely aligned with the illuminated pattern. Early single-point scanning instruments allowed users to laterally align the pin hole relative to the point of illumination manually, and could be set up to give excellent images. Unfortunately, if it was easy to misalign these instruments causing the signal to be lost, so modern instruments tend to limit the amount of adjustments available to the operator. Axial alignment is as important as lateral alignment for obtaining

Fig. 2 The author, John White, photographed in the late 1980s seated at an early version of the MRC 500 laser scanning confocal microscope. In the top panel, John is looking into the eyepieces of the fluorescence microscope in order to find a region of interest for scanning. In the lower image the specimen is being scanned by the laser and the image produced by the confocal microscope is visible on the video monitor. The ability to first locate a region of interest by eye using a conventional wide field epifluorescence microscope, and to subsequently scan the same region in the confocal mode, remains a significant practical advantage of the laser scanning confocal microscope

optimum results. As most instruments use epi-illumination, axial errors generally only arise because of axial chromatic aberration in the optics. This can be a problem when UV excitation is used and/or the fluorophore has a large Stoke's shift. However, this can be overcome if there is an independent adjustment for focus in the excitation illumination pathway.

The ultimate limit on the speed at which fluorescence images can be obtained in a laser-scanning microscope is determined by fluorophore saturation at the point(s) of illumination, caused by ground-state depletion. It is relatively easy to reach fluorophore saturation in single-point scanning microscopes with commonly used fluorophores. When running close to fluorophore saturation, trying to obtain images at a faster rate while retaining signal-to-noise levels by increasing excitation will be futile.

This problem can be overcome by illuminating an extended pattern in the specimen, such as an array of spots or a line, so that

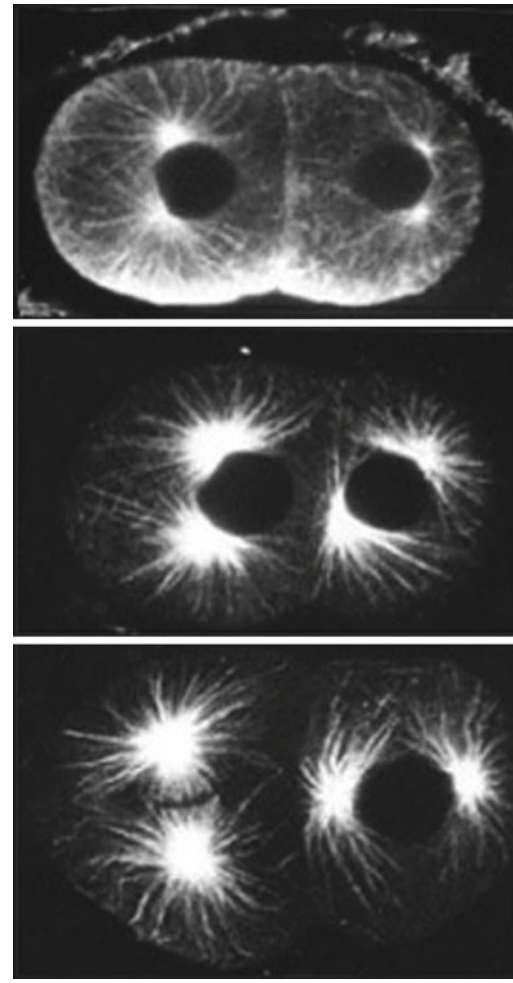

Fig. 3 An early image of a two-cell stage *Caenorhabditis elegans* embryo, fixed and immunofluorescently labeled. Optical sections with the pinhole open and further closed down demonstrate both the improved resolution of the microtubule arrays in these embryos, and the flexibility afforded by the adjustable pinhole for imaging a range of biological specimens with diverse optical properties

fluorescence signals can be increased while keeping below the excitation power density at the point of focus that would induce fluorophore saturation. Confocal microscopes that use multiple or extended focal volumes for illumination (such as the spinning disk systems) have become popular for visualizing dynamic events in living specimens. However, single spot scanning systems will generally give better images in terms of optical sectioning and ultimate resolution, if high image acquisition speeds are not required.

Essentially all confocal microscopes use digital image capture which enables motion or feature detection algorithms to be used for automatic analyses. However, the particular advantage of

confocal, along with other optically sectioning microscopies, is that they also allow unambiguous quantitative measurements of fluorescence emanating from defined regions to be made. This feature enables volumetric maps of fluorophore density to be made thereby facilitating quantitative measurements of label within solid specimens.

4 Future Developments

Although confocal imaging has been extensively used by the biomedical community for only thirty or so years, it is fast becoming a mature technology. However, the technique still has the potential for the development of improved performance and more capabilities. Area detectors for spinning-disk or other high-speed parallel confocal imaging systems are approaching the theoretical limits in sensitivity (i.e., quantum efficiency), but the detectors for single point microscopes still have some way to go in this regard. Perhaps the direction where most new developments will be seen in the foreseeable future is in extracting all the information present in the fluorescence signal.

Microscopes with built-in spectrometers have been available for a few years now and have proved their worth in applications where several fluorophores with overlapping spectra need to be resolved. Fluorescence excited state lifetime is another characteristic of a fluorophore that can be measured. This information can be used both to help identify a fluorophore and also to obtain information on the environment in which it resides by measuring the degree of fluorescence quenching from the concomitant decrease in excited state lifetime.

Bright-field reflection confocal imaging is more difficult to use because of problems with interfering reflections originating from within the optical path of the microscope, but these problems are surmountable, yet the full potential of bright-field confocal imaging has probably not been explored. For example, it is likely that the technique could provide a more economical alternative to optical coherence tomography in some applications.

Currently, there is much interest in using lifetime measurements to estimate fluorescence resonance energy transfer (FRET) interactions because this technique has the potential to provide a direct readout of FRET that is independent of fluorophore concentration. Polarization is another parameter that can be measured and used to obtain useful information on the orientation of the fluorophore. Dynamic measurements of polarization can also be used to measure diffusion rates or estimate homo-FRET interactions. Hopefully, we can look forward in the not-too-distant future to confocal microscopes that can detect most of the fluorescence photons emitted and determine their color and polarization

together with the distribution of lifetimes of the excited state of the fluorescent molecules that emitted them. Then the challenge will be in analyzing these data to determine physiology and cytoarchitecture of living tissue.

References

1. Minsky M (1957) U.S. Patent no. 3013467
2. Minsky M (1988) Memoir on inventing the confocal scanning microscope. Scanning 10: 128–138
3. White JG, Amos WB, Fordham M (1987) An evaluation of confocal versus conventional imaging of biological structures by fluorescence light microscopy. J Cell Biol 105: 41–48
4. White JG, Amos WB (1987) Confocal microscopy comes of age. Nature 328:183–184
5. White JG, Amos WB, Durbin R, Fordham M, (1990) Development of a confocal imaging system for biological epifluorescence application in "Optical Microscopy For Biology". Wiley-Liss Inc, New York, NY, pp 1–18
6. Amos WB, White JG (2003) How the confocal laser scanning microscope entered biological research. Biol Cell 95:335–342
7. Chalfie M, Tu Y, Euskirchen G, Ward WW, Green PDC (1994) Fluorescent protein as a marker for gene expression. Science 263:802–805

Chapter 2

Laser Scanning Confocal Microscopy: History, Applications, and Related Optical Sectioning Techniques

Stephen W. Paddock and Kevin W. Eliceiri

Abstract

Confocal microscopy is an established light microscopical technique for imaging fluorescently labeled specimens with significant three-dimensional structure. Applications of confocal microscopy in the biomedical sciences include the imaging of the spatial distribution of macromolecules in either fixed or living cells, the automated collection of 3D data, the imaging of multiple labeled specimens and the measurement of physiological events in living cells. The laser scanning confocal microscope continues to be chosen for most routine work although a number of instruments have been developed for more specific applications. Significant improvements have been made to all areas of the confocal approach, not only to the instruments themselves, but also to the protocols of specimen preparation, to the analysis, the display, the reproduction, sharing and management of confocal images using bioinformatics techniques.

Key words Confocal, Optical section, Resolution, Laser, Fluorescence, Illumination, Microscopy, Living, Fixed, Digital image, Informatics

1 Introduction

The major application of confocal microscopy in the biomedical sciences is for imaging fixed or living tissues that have usually been labeled with one or more fluorescent probes. When these samples are imaged using a conventional light microscope, the fluorescence in the specimen away from the region of interest interferes with the resolution of structures in focus, especially for those specimens that are thicker than 2 μm.

When compared with the conventional wide field light microscope, the confocal microscope provides an increase in both maximum lateral resolution (0.5 μm vs. 0.25 μm) and maximum axial resolution (1.6 μm vs. 0.7 μm). However, it is the ability of the instrument to eliminate the "out-of-focus" brightness from images collected from thick fluorescently labeled specimens at a range of magnifications that has made it an invaluable instrument for most applications in biomedical imaging (Fig. 1).

Stephen W. Paddock (ed.), *Confocal Microscopy: Methods and Protocols*, Methods in Molecular Biology, vol. 1075,
DOI 10.1007/978-1-60761-847-8_2,

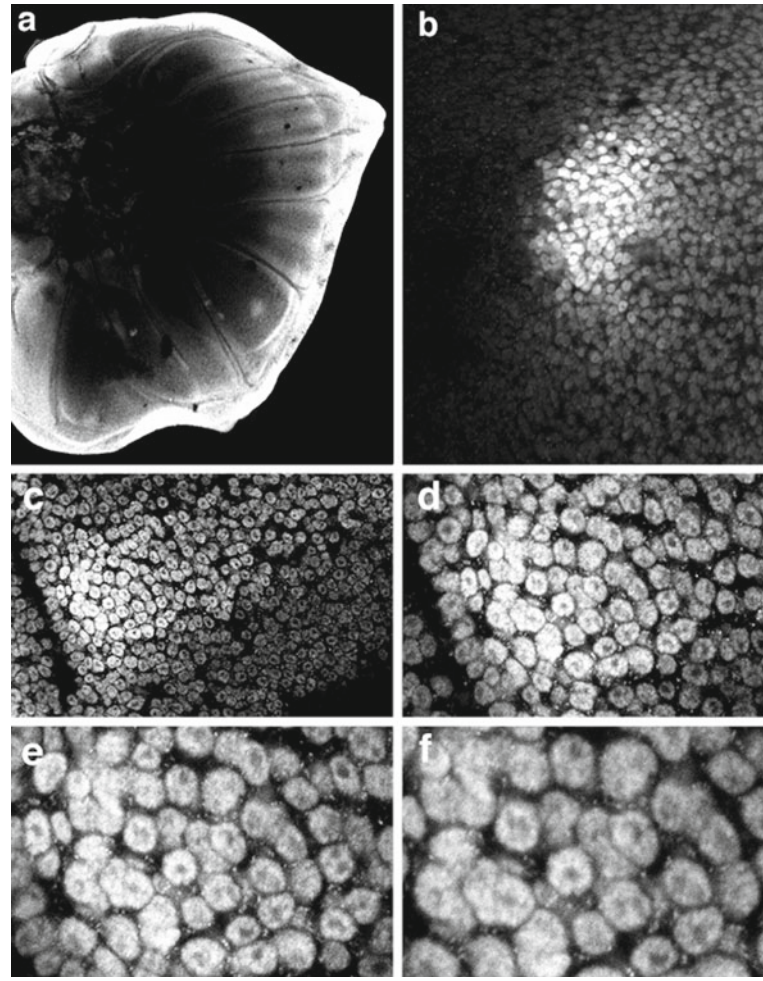

Fig. 1 Examples of Single Optical Sections from the same Specimen. Optical sections can be collected using different objective lenses or using the same lens in combination with the optical zoom function of the LSCM. In this example a fifth instar butterfly wing imaginal disk has been fixed and labeled with *distalless* antibodies and secondary fluorescein-labeled antibodies, and imaged in the LSCM. A single optical section of the entire imaginal disk is imaged using a 4× lens (**a**), whereas a 16× lens is used for improved resolution of an eyespot field (**b**). A 40× lens is required for cellular resolution (in this case resolution of nuclei since distaless is a transcription factor) (**c**). Improved nuclear resolution is achieved by using the optical zoom (**d**–**f**) in conjunction with the 40× objective lens. This strategy is often useful when imaging at high magnifications when switching to a higher power lens will risk losing the field of interest or damaging the specimen

The method of image formation in a confocal microscope is fundamentally different from that in a conventional wide field epifluorescence microscope where the entire specimen is bathed in light from a mercury or xenon source. In contrast, the illumination in a confocal microscope is achieved by scanning one or more

focused beams of light, usually from a laser, across the specimen. Images produced by scanning the specimen in this way are called optical sections [1]. This refers to the noninvasive method of image construction by the instrument, which uses light, rather than a physical method such as a microtome, to section the specimen.

The popularity of the confocal microscope has increased dramatically over the past ten years since the publication of the first edition of this book [2]. This is due in part to the increased number of confocal applications and increased accessibility of the technology and specifically to the introduction of fluorescence reporter techniques that have simplified the imaging of living cells [3].

Confocal technology has been developed to a level where most research institutions and many individual laboratories house one or more confocal instruments. In addition, instruments that produce optical sections for more specific applications continue to be developed as modifications of the confocal design [4, 5]. While the second edition, like the first, is focused on the laser scanning confocal microscope, many of the featured protocols are suitable for use with these new methods of optical sectioning [6, 7].

2 History of Confocal Instrumentation

2.1 Marvin Minsky's Microscope

The development of confocal microscopes was, and continues to be, driven by the desire to image biological events as they occur in vivo. The invention of the confocal microscope is attributed to Marvin Minsky who built a working scanning optical microscope in 1955 with the goal of imaging neural networks in unstained preparations of living brains. Details of Minsky's microscope, and of its development, can be found in his memoir, "On inventing the confocal scanning microscope" [8]. All modern confocal microscopes, by definition, employ the principle of confocal imaging that he patented in 1957 [9], although the term confocal was not introduced in this context until later [10].

In Minsky's original confocal microscope the point source of light is produced by a pinhole placed in front of a zirconium arc source. The point of light is focused by an objective lens into the specimen, and light that passes through it, is focused by a second objective lens at a second pinhole, which has the same focus as the first pinhole. i.e., it is confocal with it. Any light that passes through the second pinhole strikes a low noise photomultiplier, which produces a signal that is directly proportional to the brightness of the light passing through the pinhole. The second pinhole prevents light from above or below the plane of focus from striking the photomultiplier (Fig. 2).

The key to the confocal approach is the elimination of out-of-focus light (sometimes called flare) by scanning a point source of light across the specimen and using a pinhole to eliminate the

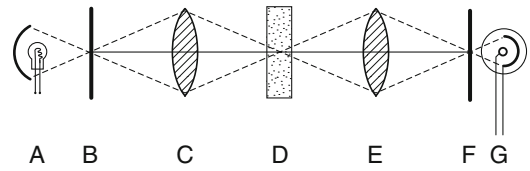

Fig. 2 Schematic of Marvin Minsky's confocal microscope—transmitted light version. A point of light is produced by a zirconium light source (**a**) and a pinhole placed in front of it (**b**). This is focused by an objective lens (**c**) into the specimen (**d**), and light that passes through it, is focused by a second objective lens (**e**) at a second pinhole (**f**), which has the same focus as the first pinhole, i.e., it is confocal with it. Any light that passes through the second pinhole strikes a detector (**g**), which produces a signal that is proportional to the brightness of the light passing through the pinhole. The second pinhole prevents light from above or below the plane of focus from striking the photomultiplier. The image is built up by moving the specimen (**d**) Image drawn by Leanne Olds

out-of-focus light from the detector. Minsky also described a reflected light version of the microscope that used a single objective lens and a dichromatic mirror arrangement (Fig. 3). This arrangement eliminated the considerable problem of aligning the two objective lenses in the transmitted light version since a single objective lens is used for both the excitation and the emission paths. This epi-illuminated design is the basic configuration of most modern confocal systems that are used for fluorescence imaging today.

In order to build an image, the focused spot of light must be scanned across the specimen in some way. In Minsky's original microscope the beam was stationary and the specimen itself was moved on a vibrating stage. This optical arrangement has the advantage of always scanning on the optical axis, which can eliminate any lens defects. However, for biological specimens, movement of the specimen can cause them to wobble, which results in a loss of resolution in the final image.

Finally an image of the specimen has to be recorded. A real image is not formed in Minsky's original microscope but rather the output from the photodetector is translated into an image of the region-of-interest. In Minsky's original design the image was built up on the screen of a military surplus oscilloscope with no facility for hard copy. Minsky admitted that the quality of the final images collected from his microscope was not very impressive. This was most likely due to the inferior quality of the oscilloscope display and sensitivity of the photodetector and not by the lack of resolution achieved with the microscope itself.

The images produced by Minsky's instrument at this time were unremarkable. It is clear that the technology was not available to him in 1955 to fully demonstrate the potential of the confocal approach to the biomedical imaging community. This may have

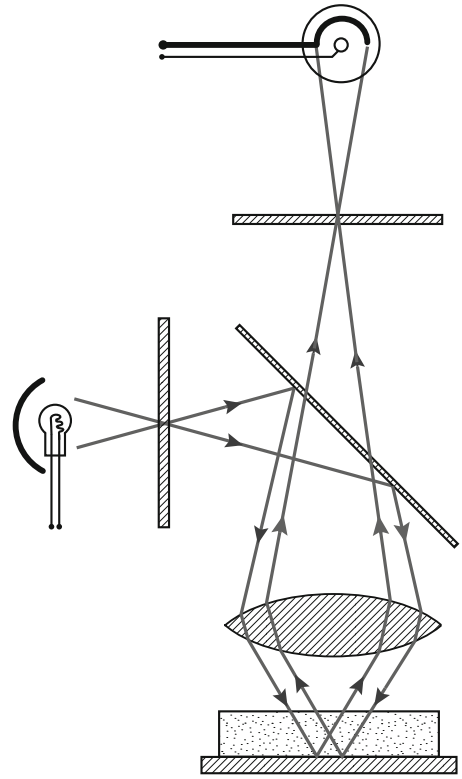

Fig. 3 Schematic of Marvin Minsky's confocal microscope—reflected light version. A zirconium light source (**a**) and a pinhole (**b**) produces a point source of light (**a**). This is reflected by a dichromatic mirror (**c**) and focused by an objective lens (**d**) onto the specimen (**e**). Longer wavelength light is reflected back from the specimen, is subsequently focused by the same objective lens (**d**), passes through the dichromatic mirror (**c**), and focused onto a second pinhole (**f**) in front of the photodetector (**g**). Both source and detector pinholes are confocal with the focused point of light in the specimen. The image is built by moving the specimen (**e**). Image drawn by Leanne Olds

been why confocal microscopy did not immediately catch on. After all, at this time, biologists were used to viewing and photographing their brightly stained and colorful histological tissue sections using light microscopes with excellent optics, and in real color. Confocal imaging of living tissues would have to wait.

2.2 Subsequent Technological Innovation

Several major technological advances that would have benefited Minsky's confocal design have become available to biologists during the years since 1955. These include;

1. Bright and stable laser light sources.
2. Efficiently reflecting mirrors and more precise filters.
3. Improved methods of scanning and electronics for data capture.

4. High quantum efficiency low noise photodetectors.
5. Improved methods of specimen preparation.
6. Fast computers with image processing capabilities.
7. Elegant software solutions for analyzing the images.
8. High-resolution digital displays and color printers.
9. Bioinformatics methods for managing the images.

The introduction of practical confocal microscopes was largely dependent upon the development of efficient methods of scanning the excitation spot within the specimen. Confocal microscopes are typically classified using the method by which the specimens are scanned. Minsky's original design was a stage scanning system driven by a tuning fork arrangement that was rather slow to build an image. It was also extremely difficult to locate a region of interest in the specimen, and even harder to focus, using this system.

The stage scanning confocal microscopes have evolved into instruments that are used traditionally in materials science applications such as the microchip industry. Systems based upon this principle have also been used for screening DNA sequences on microchip arrays.

An alternative to moving the specimen (stage scanning) is to scan the beam across a stationary specimen (beam scanning). This configuration is more practical for imaging biological specimens, and is the basis of those systems that have developed into the current generation of research microscopes.

More details of the technical aspects of confocal microscopes are covered elsewhere [11], but briefly there are two fundamentally different methods of beam scanning; single beam scanning or multiple beam scanning. Single beam scanning continues to be the most commonly used method at this time, and is epitomized by the laser scanning confocal microscope (LSCM). Here the scanning is achieved using computer-controlled galvanometer-driven mirrors to direct a single beam of excitation light across the sample.

The alternative to single beam scanning is to scan the specimen with multiple beams (almost real time). Point-scanning LSCM, when used with high numerical aperture lenses, has an inherent speed limitation in fluorescence. This arises because of a limitation in the amount of light that can be obtained from the small volume of fluorophore contained within the focus of the scanned beam. This can be overcome with parallel or multiple laser excitation approaches. This is most commonly achieved using some form of spinning Nipkow disk; a design adapted from the early days of television transmission. The forerunner of the spinning disk systems was the tandem-scanning microscope (TSM), and subsequent improvements to the design have resulted in instruments that collect acceptable images from fluorescently labeled living specimens. The modern Nipkow or other spinning disk based variants have a

much higher speed potential than conventional LSCMs because the spinning disk based parallelism avoids fluorophore saturation enabling higher levels of excitation to be used. As these systems typically optically reconstruct the image, this allows the use of high sensitivity CCD detectors giving extended red response of great advantage for many of the newly developed fluorophores. Spinning disk based confocal systems have been very popular for applications where close to real time capture is needed such as tracking calcium ion transients in cell environments.

In modern confocal microscopes the image is either built up from the output of a photomultiplier tube or captured using a CCD camera, directly processed in a computer imaging system and then displayed on a high resolution video monitor, and recorded on modern hard copy devices, with spectacular results. Moreover, vastly improved methods of specimen preparation, especially using fluorescent reporters of gene activity, have enabled the realization of Minsky's dream of imaging living neurons in vivo.

2.3 The Laser Scanning Confocal Microscope

The LSCM continues to be the instrument of choice for most routine biomedical research applications, and it is, therefore, most likely to be the instrument first encountered by the novice user. As in the first edition, emphasis has been placed on the LSCM in this edition.

The LSCM is built around a conventional epifluorescence light microscope either in an upright configuration popular with neuroscientists and physiologists or an inverted configuration seen commonly for cell culture and developmental biology applications (Fig. 4).

The conventional light microscope is essential for efficiently finding the region of interest in the specimen by eye before scanning in the confocal mode. This is extremely useful since one of the great strengths of the confocal microscope, i.e., the elimination of out-of-focus information, can make it extremely difficult to locate a region of interest in the specimen in the confocal mode. This configuration is also very stable, especially when mounted on an anti-vibration air table. Any vibration results in a loss of resolution in the image, and can show up in the image as irregular horizontal lines.

The modern LSCM typically uses a laser rather than a lamp for a light source, acousto-optic tunable filters (AOTFs) for selecting specific excitation wavelengths, dichroics for multichannel emission discrimination, sensitive photomultiplier tube detectors (PMTs) and a computer to control the scanning mirrors and to facilitate the collection and display of the images. Modern LSCMs can excite and detect multiple fluorophores simultaneously typically through the use of multiple lasers and multiple detectors for each channel. Images are subsequently stored as digital image files and can be further analyzed using additional software.

In the LSCM, illumination and detection are confined to a single, diffraction-limited, point in the specimen. This point is

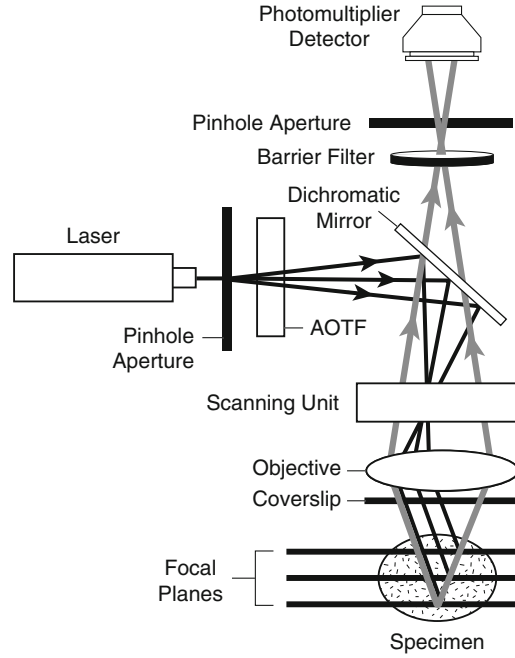

Fig. 4 The main components of a modern laser scanning confocal microscope-reflected light, upright version. Light from one or more lasers passes through a pinhole, attenuated through an AOTF, bounces off a dichromatic mirror, and passes into the scanning unit. A scanned beam enters the back focal plane of the objective lens, which focuses the light at a point in the specimen. Any light coming back from the excitation of a fluorochrome at this point inside the specimen passes back through the objective lens and the scanning unit. Since this light is of longer wavelength than the excitation light, it passes through the dichromatic mirror, is further cleaned up by a barrier filter and it is eventually focused at the second pinhole. Any light that passes through the pinhole strikes a low noise photomultiplier detector, the signal from which subsequently passes to the computer imaging system of the confocal microscope. This configuration is very similar to that of Minsky's reflected light schematic of Fig. 3. Image drawn by Leanne Olds

focused by an objective lens, and scanned across it using some form of scanning device. Points of light from the specimen are detected by a photomultiplier behind a pinhole, and the output from this is built into an image by the computer. Specimens are usually labeled with one or more fluorescent probes (fluorescence mode). Unstained specimens can be viewed using the light reflected back from the specimen (reflected light mode).

One of the more commercially successful LSCMs was designed in the late 1980's at the Medical Research Council laboratories in Cambridge, England by the team of White, Amos, Durbin and Fordham. They set out to tackle a fundamental problem in developmental biology; namely imaging specific macromolecules in fluorescently labeled embryos [12, 13]. They were specifically

interested in imaging microtubules in *C. elegans* embryos. Many of the cells inside developing embryos are impossible to image after the two-cell stage using conventional epifluorescence microscopy because as cell numbers rise, the overall volume of the embryo remains approximately the same, which means that the fluorescence signal increases from the more and more closely packed cells out of the focal plane of interest, and interferes with resolution of those structures in the focal plane of interest.

When he investigated the live cell imaging microscopes available to him in the mid-1980s including early confocal designs, John White discovered that no system existed that would solve his resolution issues caused by the increased signal brightness from the increased cell packing as the embryos developed over time. Technology at this time consisted of the stage scanning instruments, which tended to be impossible to focus and painfully slow to produce images (approximately 10 s for one full frame image that was often out-of-focus), and the multiple beam microscopes, which were difficult to align and the fluorescence images were extremely dim, if not invisible without extremely long exposure times!

The Cambridge team led by John White and Brad Amos designed a LSCM that was suitable for conventional epifluorescence microscopy applications and since evolved into an instrument that has been used in many different biomedical applications over the years [14]. The breakthrough came with the development of more efficient methods of scanning the beam using first a single galvanometer-driven mirror and a spinning polygon mirror design, and subsequently settling upon a dual galvanometer-driven mirror arrangement. It was also necessary to incorporate relatively new computer-based imaging technology and control electronics using a framestore card and analog to digital conversion to coordinate and keep track of the position of the scanning mirrors with the acquisition of the images into the computer. This required the development of software that was reliable and easy to use.

In a landmark paper that captured the attention of the cell biology community because of the vastly improved quality and resolution of the images of a diverse range of familiar specimens, White et al. compared images collected from the same specimens using conventional wide field epifluorescence microscopy and using their LSCM [15]. Rather than physically cutting sections of multicellular embryos their LSCM produced "optical sections" that were thin enough to resolve structures of interest and were free of much of the out-of-focus fluorescence that previously contaminated their images. This technological advance allowed them to follow and record changes in the cytoskeleton in the increasing numbers of cells in early embryos at a higher resolution than using conventional epifluorescence microscopy.

The thickness of the optical section could be adjusted simply by changing the diameter of a pinhole in front of the

photodetector. The image could be zoomed with no loss of resolution simply by decreasing the region of the specimen that was scanned by the mirrors simply by placing the scanned information into the same number of pixels in the image. This imparted a range of magnifications to a single objective lens, and was extremely useful when imaging rare events when changing a lens may have risked losing the region of interest during the experiment (Fig. 1).

This design has proven to be extremely flexible for imaging biological structures as compared with some of the other designs that employed fixed diameter pinholes. This microscope together with several other instruments introduced by others during the same time period, were the forerunners of the sophisticated instruments that are now available to biomedical researchers from several commercial vendors.

The advantage of the LSCM lies within its versatility and large number of applications combined with its relative user-friendliness for producing extremely high quality images from specimens prepared for the light microscope. The first generation LSCMs were tremendously wasteful of photons in comparison to the new microscopes. This meant that photobleaching and photodamage to specimens were often problematic in the older instruments. The early systems tended to work well for brightly labeled and fixed specimens but tended to quickly kill many living specimens unless extreme care was taken to preserve the viability of specimens on the stage of the microscope by limiting the laser power for imaging. Nevertheless the microscopes produced such excellent images of fixed and fluorescently labeled specimens that confocal microscopy was fully embraced by the biological imagers.

Improvements have been, and continue to be, made to all parts of the imaging process. These include more stable lasers, more efficient mirrors, more sensitive photodetectors, electronic filters (AOTFs), improved methods for multichannel collection such as spectral based capture, and improved digital imaging systems. The new instruments have been improved ergonomically so that alignment is much easier to achieve and preserve. Filter combinations are now controlled by software and AOTFs and multiple fluorochromes can be imaged simultaneously with instrumentation for correcting for bleed through and autofluorescence (Fig. 5).

The development and commercial availability of fluorescent probes with improved levels of photostability and specificity for improved localization continues to influence the development of confocal instrumentation. The fluorophores include synthetic fluorochromes, for example, the Alexa dyes and quantum dots and naturally occurring fluorescent proteins, for example the green fluorescent protein (GFP) and its derivatives, for example CFP and YFP. Many of the new fluorescent probes have been designed to

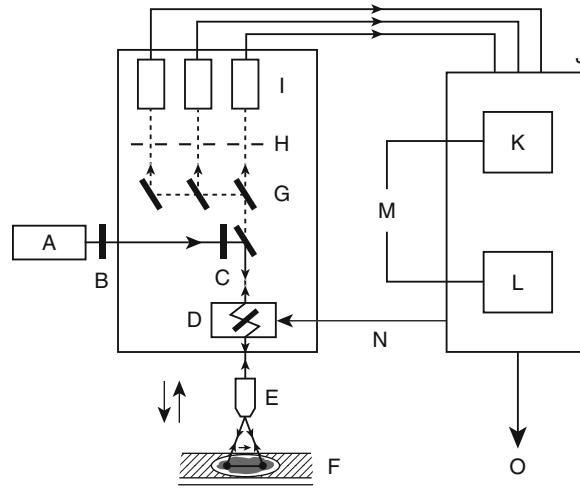

Fig. 5 The information flow in a generic laser scanning confocal microscope. Light from one or more lasers (**a**) passes through a neutral density filter or AOTF (**b**) and an exciter filter or AOTF (**c**) on its way to the scanning unit (**d**). The scanning unit produces a scanned beam at the back focal plane of the objective lens (**e**), which focuses the light at the specimen (**f**). The specimen is scanned in the X and the Y in a raster pattern and in the Z direction by fine focusing (*arrows*). Any fluorescence from the specimen passes back through the objective lens and the scanning unit and is directed via dichromatic mirrors (**g**) to three pinholes (**h**). The pinholes act as spatial filters to block any light from above or below the plane of focus in the specimen. The point of light in the specimen is confocal with the pinhole aperture. This means that only distinct regions of the specimen are sampled. Light that passes through the pinholes strikes the PMT detectors (**i**) and the signal from the PMT is built into an image in the computer (**j**). The image is displayed on the computer screen often as three grayscale images together with a merged color image of the three-grayscale images. The computer synchronizes (**n**) the scanning mirrors (**d**) with the buildup of the image in the computer frame store or memory (**k**). The computer also controls a variety of peripheral devices. For example, the computer controls and correlates movement of a stepper motor connected to the fine focus of the microscope with image acquisition in order to produce a Z-series. Furthermore the computer controls the area of the specimen to be scanned by the scanning unit so that zooming is easily achieved by scanning a smaller region of the specimen. In this way, a range of magnifications is imparted to a single objective lens so that the specimen does not have to be moved when changing magnification. Images are written to the hard disk of the computer or exported to various devices for viewing, hard copy production or archiving (**o**). Final images are produced in the computer by synchronizing input from the scan head with the video card (**m**). Image drawn by Leanne Olds

have their excitation and emission spectra closely matched to the wavelengths delivered by the lasers supplied with most commercial LSCMs (Table 1). The instruments continue to be improved as new technologies from diverse sources are added to the existing LSCM designs.

Table 1
Peak excitation and emission wavelengths of some commonly used fluorophores

Alexa Fluors	350 thru 680	442 thru 702	He–cadmium
Cyanines	489 thru 710	506 thru 805	He–cadmium
DAPI	350	470	He–cadmium
Fluorescein	496	518	Argon ion
GFP	395/475	510	Blue diode
Qdot	350 thru 600	525 thru 655	Blue diode
Rhodamine B	540	625	Green He–Ne
DsRed	558	583	Green He–Ne
X-Rhodamine	580	605	Krypton–argon
TOTO3	642	661	Krypton–argon

3 Confocal Imaging Modes

The value of the LSCM for biomedical imaging is due to the ability of the instrument to both scan and detect a point of light under extremely fine control in the X, the Y and the Z direction within a fluorescently labeled specimen at various time and wavelength resolutions. The basic imaging modes of the instrument will be described.

3.1 Single Optical Sections

The basic output of all confocal microscopes is the optical section. This is a single image of a discrete region of a three dimensional cellular structure with any contribution from fluorescence from above and below the focal plane of interest removed. The resolution and the thickness of the optical section is related to the numerical aperture (NA) of the objective lens chosen for imaging and the diameter of the pinhole in front of the photodetector [16]. Higher NA lenses and narrower pinhole diameters achieve higher resolution images and produce thinner optical sections (Fig. 6).

There is an optimal pinhole setting for each objective lens chosen, which is calculated by the software of the confocal imaging system (after an initial calibration for each objective lens is entered into the software). However, there is a trade-off between the theoretically achievable resolution and the practical constraints imposed by the specimen itself in order to collect an acceptable image.

It is essential to choose the correct objective lens for the specific confocal imaging application (Table 2). Specific objective lenses are available for both high magnification/high resolution imaging and low magnification/high resolution imaging (Fig. 7). While most emphasis has been placed on high resolution and high

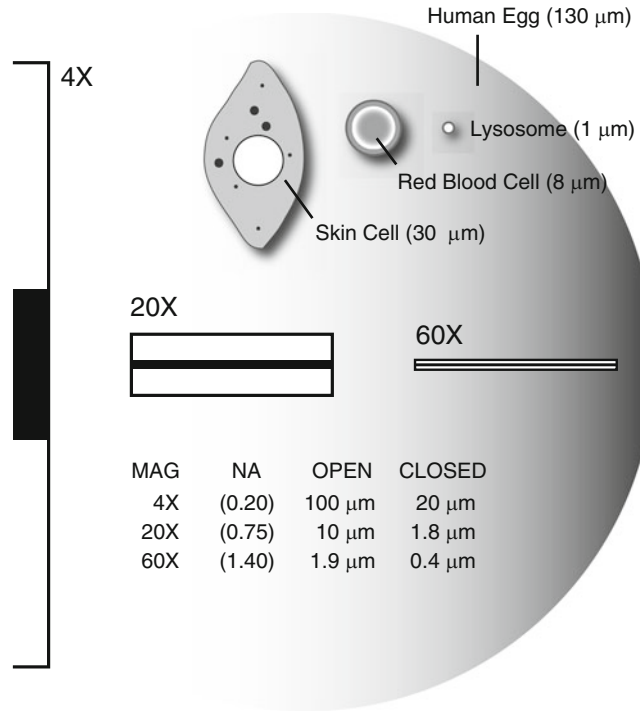

Fig. 6 The thickness of optical sections produced by the LSCM is a function of the numerical aperture of the objective lens chosen for imaging and the diameter of the confocal pinhole. The understanding of the relationship between these two factors is essential for efficient image capture. Some common biological specimens including a human egg, a skin cell, a red blood cell, and a lysosome have been represented in relation to the optical section thicknesses sampled from such biological specimens using a 4× lens, a 20× lens, and a 60× objective lens either with the pinhole open or with the pinhole set at an optimal diameter (filled areas). The maximum theoretical resolution for each lens and for each setting of the pinhole is included in the table. Image drawn by Leanne Olds

Table 2
Properties of microscope objectives for confocal imaging. Objective 1 would be more suited for high resolution imaging of fixed cells, whereas Objective 2 would be better for imaging a living preparation

Property	Objective 1	Objective 2
Design	Plan-apochromat	CF-fluor DL
Magnification	60	20
Numerical aperture	1.4	0.75
Coverslip thickness	170 μm	170 μm
Working distance	170 μm	660 μm
Medium	Oil	Dry
Color correction	Best	Good
Flatness of field	Best	Fair

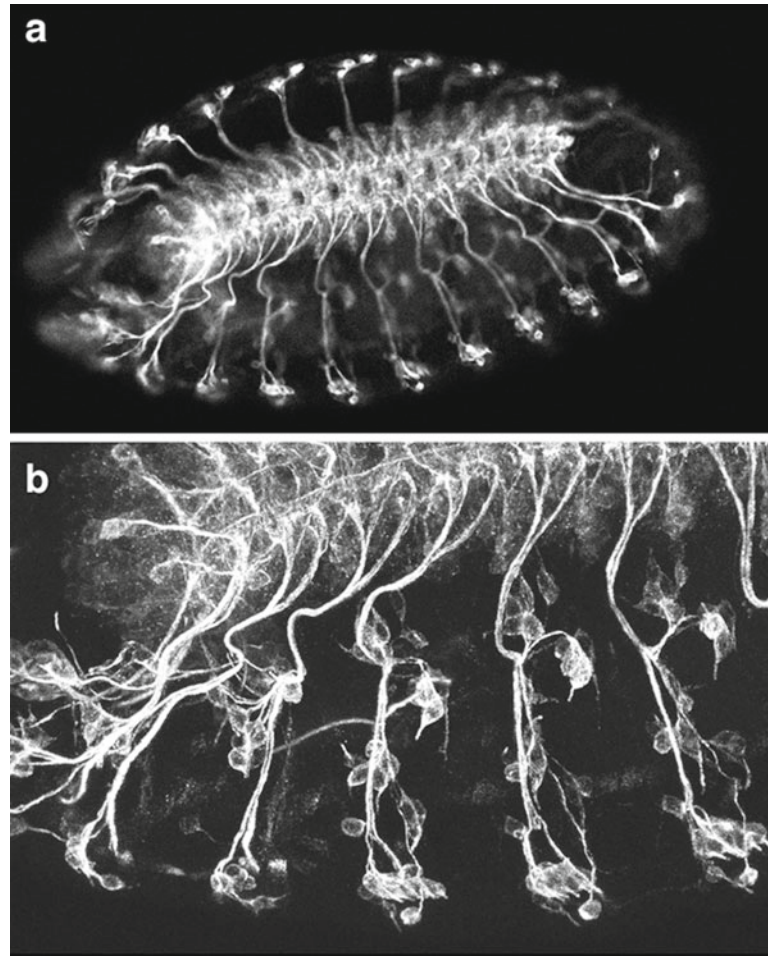

Fig. 7 Optical at the same zoom setting sections of the same specimen produced by two different objective lenses (**a**) 20× NA 0.75 and (**b**) 60× NA 1.4. The specimen is a late stage *Drosophila* embryonic peripheral nervous system labelled with the 22C10 antibody

magnification imaging, low power confocal imaging is also extremely useful in many biomedical applications. In order to attain maximal resolutions at low power it is usually necessary to collect images from several different regions of the specimen with high magnification high numerical aperture (NA) objectives and subsequently "stitch" the images together digitally. This is due to the lack of resolution in conventional low magnification lenses. This is changing however with several recent commercial macroconfocal systems that provide low magnification and relatively high NA. This includes a recent development by Brad Amos and colleagues at the MRC; the "mesolens" produces a full 3D image of large objects (up to 5 mm) such as mouse embryo with cellular detail in a single image.

Using most LSCMs it takes approximately 1 s to scan and collect a single optical section, a frame per second. Several scans are

usually averaged or integrated in order to improve the signal to noise ratio. The time to collect the image of a single optical section depends on the size of the image and the speed of the computer. For example, a typical image of 768 by 512 pixels in size will occupy approximately 0.3 MB. Larger images, e.g., 1,024 × 1,024, will occupy more space and take longer to collect.

An area for speed improvement in LSCMs is the galvo scanning approach. Galvo based systems are driven with a control signal at the rate of several microseconds per pixel, which is often the rate-limiting step in high-speed confocal acquisition. There have been two general strategies for improving the speed. The first has been to use line scanning based approaches where a row of pixels along a single axis of the specimen is collected very quickly and these rows can be then assembled into a image as needed. Line scanning has been proven to be quite useful for tracking dynamic fast phenomena such as calcium sparks but has been proven to be problematic for weak heterogeneous signals that are distributed spatially.

The second has been to explore alternative technologies for directing the beam. Several groups have developed confocals that use acoustical optical deflection (AOD) for beam steering. AOD based confocal designs with their precision and no moving parts allow for highly accurate saw tooth raster scans but typically suffer from poor axial resolution and reduced sensitivity as compared to conventional LSCMs. More recently vendors have developed systems that retain the galvanometer based scanning but rather than using the conventional servo-controlled galvos that are inherently limited to about a frame per second in most configurations are instead using a new class of resonant based galvanometers. These resonant based scanners use vibrational energy to move the mirror and can produce scanning acquisition speeds of up to 30 frames per second.

The value of optimal specimen preparation protocols cannot be overemphasized. There is usually a period of "fine-tuning" the specimen protocol to the constraints imposed by the physical characteristics of the confocal instrument available in order to collect the most information from the specimen in the most efficient way.

3.2 Multiple Wavelength Images

Modern confocal instruments are capable of detecting fluorescence emissions ranging from 400 to 700 nm. This covers a wide range of commonly available fluorescent probes. Spectral imaging systems either via multiple filters in a filter wheel or array of detectors with a spectral grating further aid the detection of probes with overlapping emission spectra and the imaging of more technically challenging specimens that may be compromised by autofluorescence that overlaps the emission wavelength of the probes of interest (Fig. 8). The AOTF is an invaluable aid to imaging multiple wavelength specimens since it affords fine control of both the intensity and the illumination wavelength at a high rate.

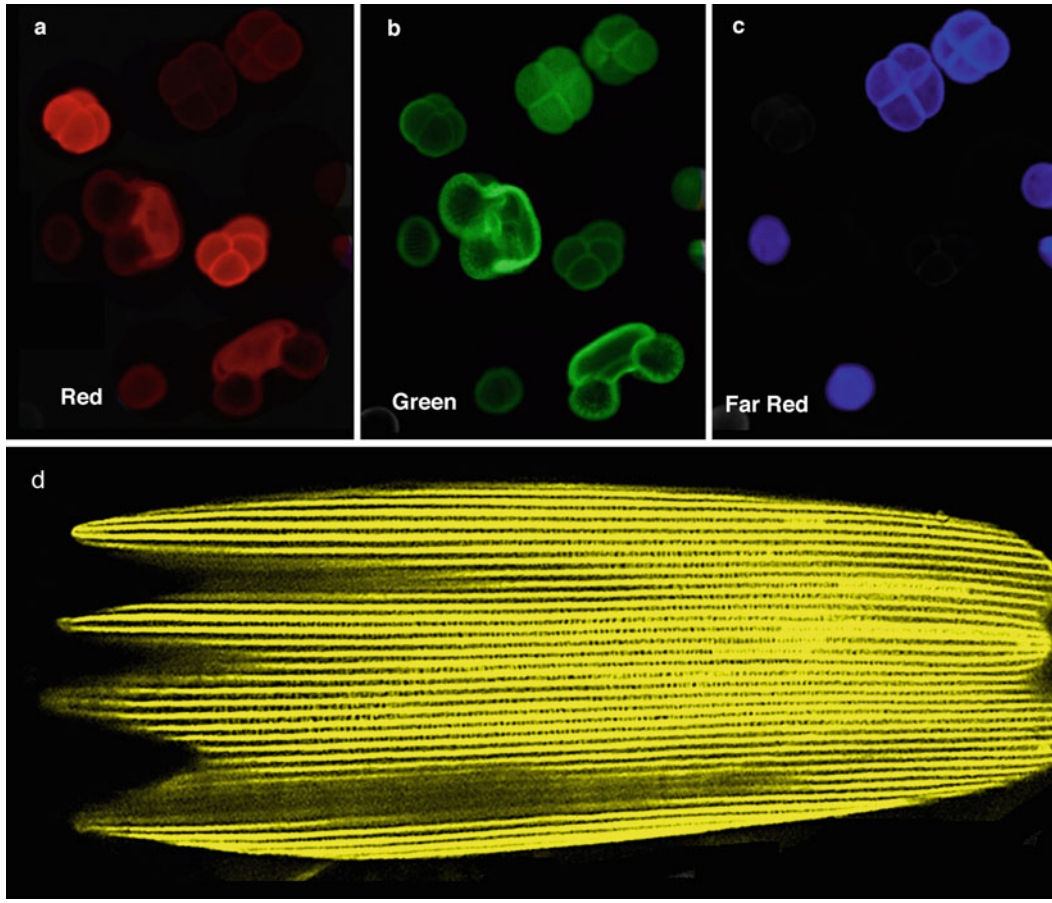

Fig. 8 Example of tissue autofluorescence. Many tissues have endogenous autofluorescence, and it is essential to map the amount of autofluorescence at different excitation wavelengths by imaging an unstained control sample in order to avoid false positive results. It is advisable to make a note of the excitation wavelengths of autofluorescence and the levels of gain and black level required to produce the images. When such autofluorescence is a problem it is best to choose a fluorochrome with an excitation maximum away from the autofluorescence. Autofluorescence can be filtered using a spectral imaging system. Autofluorescence can be an advantage for imaging cell outlines. In this case a sample of pollen grains is imaged in the *red* (**a**), the *green* (**b**) and the far *red* (**c**). Pollen grains from different plants have different autofluorescent characteristics. A single butterfly wing scale exhibits autofluorescence in all three channels (**d**). Such specimens are very convenient test specimens for imaging with the LSCM

Data are collected from either fixed-and-stained samples or living samples in single, double, triple, or multiple wavelength modes [17]. The resulting images will be in register with each other as long as an objective lens that is corrected for chromatic aberration is used and the specimen does not move while all of the emission wavelengths are collected (Fig. 9). Should it be necessary, registration of the images may be restored using digital methods.

Multiple wavelength confocal imaging protocols include those for direct labeling of cellular structures, for example mitochondria, nuclei and stress fibers (cell outlines), immunofluorescence techniques

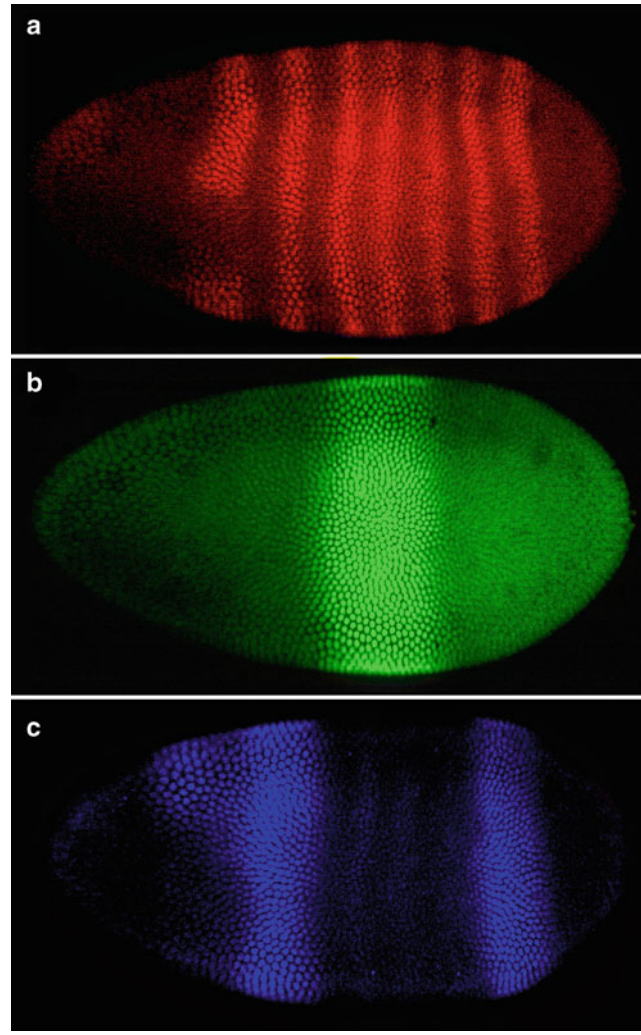

Fig. 9 Single optical sections of a triple labeled *Drosophila* embryo at the cellular blastoderm stage. The three optical sections were collected simultaneously using a single krypton argon laser at three different excitation wavelengths; 488, 568, and 647 nm. The embryo has been labeled for three genes involved with patterning the wing; (**a**) hairy (lissamine rhodamine 572 nm, Emission 590 nm); (**b**) Kruppel (fluorescein 496 nm, Emission 518 nm); and (**c**) giant (cyanine 5 649 nm, Emission 672nm)

(usually fixed specimens), fluorescence *in situ* hybridization (FISH), fluorescent reporter technology, and combinations of these techniques. FISH is used for imaging the distribution of fluorescently labeled DNA and RNA sequences in cells [18].

Specimens prepared by single, double and triple labeling protocols are now relatively routine for most modern confocal imaging systems [19]. The number of different fluorescent probes that can be imaged in a single preparation continues to increase (Fig. 10). Any additional channels will generally require more specialized

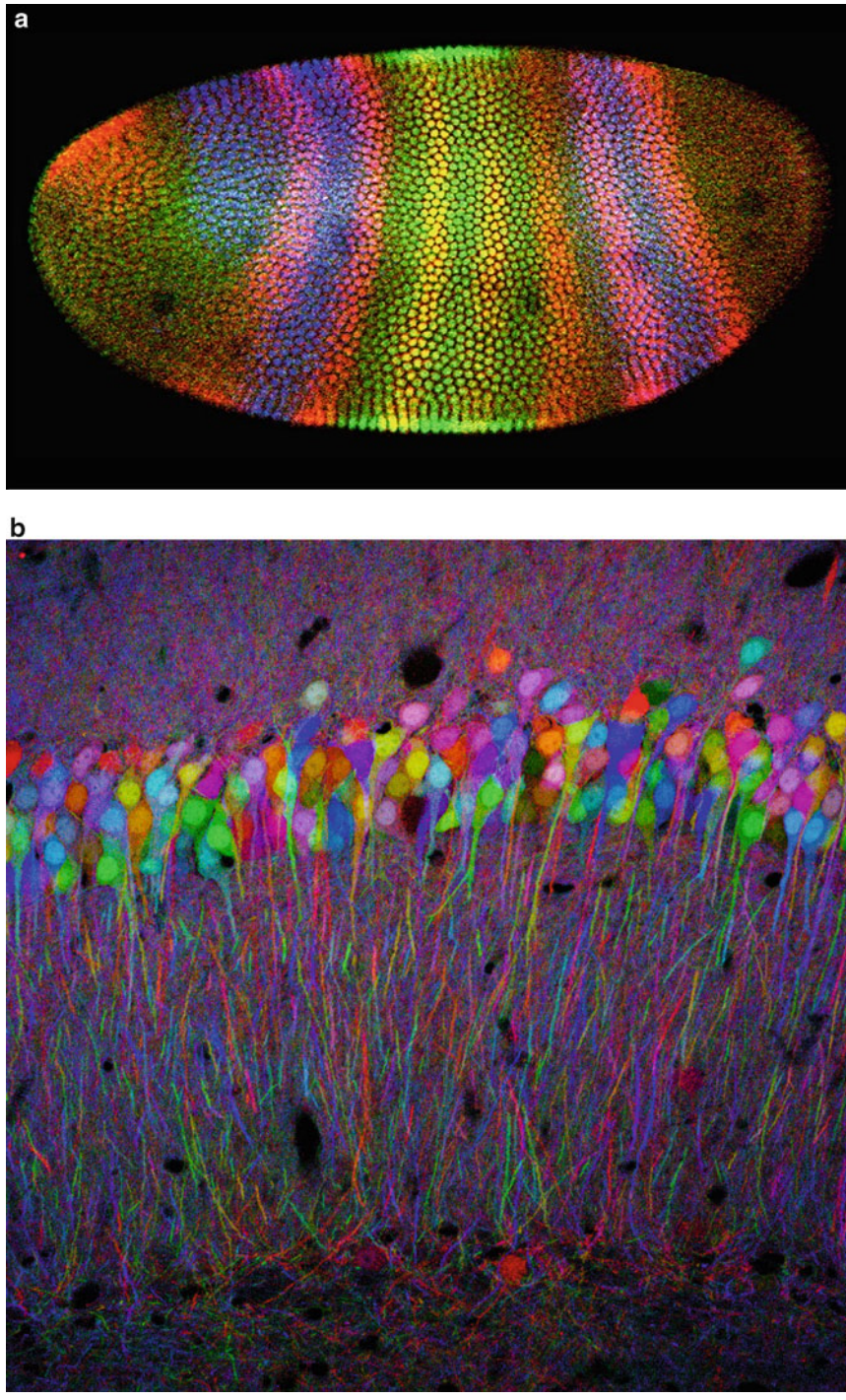

Fig. 10 Multiple Wavelength Imaging. (**a**) Three Color Image of a *Drosophila* embryo. This image was constructed by merging the three grayscale images from Fig. 8 by pasting each image into the *red* (*r*), the *green* (*g*), and the *blue* (*b*) channels of an RGB image using Adobe PhotoShop. Additive color combinations are useful for viewing biological information. For example the two *yellow* hairy stripes in the *blue* Kruppel domain represent nuclei that are expressing the two genes at the same time. Different color combinations for aesthetic and informational purposes can be made simply by rearranging and copying the images to different channels. (**b**) Ninety-nine color image of the hippocampus of a Brainbow transgenic mouse brain. Multiple copies of *red*, *green* and *blue* transgenes are randomly inserted into different cells to give one out of a possible 99 different colors (panel (**b**) *was kindly reproduced with the permission of Dr. Katie Matho and Dr. Jean Livet*)

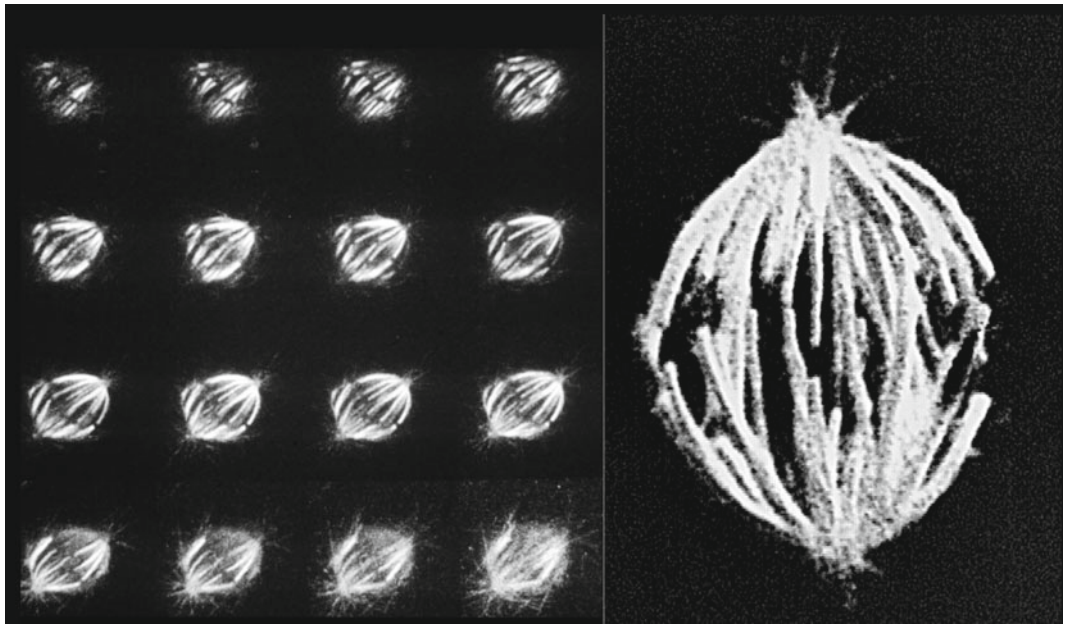

Fig. 11 A Z-series of optical sections collected from a fixed and immunofluorescently labeled mitotic spindle from a HeLa cell. Sixteen optical sections were collected at 0.2 μm intervals from the top of the spindle to the coverslip surface using a 60× NA 1.6 oil immersion objective lens. The optical sections were subsequently processed into a 3D reconstruction

specimen preparation techniques, more specialized imaging protocols and more specialized methods of image presentation and analysis. The current maximum number of colors detected in a single specimen using a standard LSCM is ninety-nine using the "Brainbow" technique where cells are randomly labeled with various combinations and concentrations of different colored fluorescent reporter probes [20].

3.3 Three-Dimensional Imaging

The capacity of confocal instruments to collect optical sections at precisely defined levels in the specimen has facilitated the production of three-dimensional images [21]. This is often necessary in order to glean any information from the images since a single optical section may appear rather abstract and not contain enough information for any meaningful interpretation. For example, single optical sections of fluorescently labeled neurons appear as abstract lines and spots whereas a 3D reconstruction appears as a network.

A Z-series is a sequence of optical sections collected at successive depths from within a specimen (Fig. 11). It is collected by coordinating the movement of the fine focus of the microscope electronically using a stepper motor with image acquisition. This is relatively easily accomplished using a macro program that instructs the LSCM to collect an image, move the focus by a predetermined distance, collect a second image, move the focus and continue until several images at consecutive levels through the region of interest have been collected.

Care must be taken to collect the images at the correct Z-step of the motor in order to calibrate for the actual depth of the specimen in the image. The XY pixel size of the image must match the Z pixel size of the image. This means that there is an optimal Z-step for each objective lens used. This is usually calculated by the confocal acquisition software, which must be calibrated for each objective lens available on the microscope.

The optical sections collected as a Z-series with the LSCM are usually in register with one another (this assumes that the specimen itself does not move during the period of image acquisition) and are output in a digital form. Z-series are ideal for further processing into a 3D representation of the specimen using 3D reconstruction software or volume visualization techniques. The Z-series file is usually processed into a single 3D representation or a movie sequence compiled from different views of the specimen. This appears as a 3D representation rotating or rocking.

Specific parameters of the 3D image such as opacity can be interactively changed in order to reveal structures of interest deep within the specimen. Measurements of length (distance between points in a 3D volume), depth and volume can be made. This approach is used to elucidate the 3D relationships of structures within cells and tissues since it can be conceptually difficult to visualize complex interconnected structures from a 2D montage of 200 or more optical sections.

The series of optical sections from a time-lapse run can also be processed into a 3D representation of the data set so that time is the Z-axis rather than depth. This approach is useful as a method for visualizing physiological changes during development.

A simple method for displaying 3D information is by color-coding optical sections at different depths. This can be achieved by assigning a color (usually red, green or blue) to sequential optical sections collected at various depths within the specimen. The colored images from the Z-series are then merged and colorized using an image manipulation program such as Adobe Photoshop or NIH ImageJ or FIJI. These color based assignments can also be used to colorize different channels based on intensity color maps or look up tables (LUTs) that can be assigned to allow for improved discrimination of different fluorophores or changes in intensity.

3.4 X–Z Imaging

An X–Z section is usually produced by scanning a single line at successive Z depths under the control of the stepper motor (Fig. 12). It is essential to collect the line scans at stepper motor increment that is calibrated to the objective lens chosen so that the resulting pixel size is proportional to the Z-dimension of the specimen. Resolution in the Z dimension (0.7 μm maximum) is not as good as in the X–Y (0.25 μm maximum) and images tend to be a little blurry especially if the Z calibration is not calculated correctly.

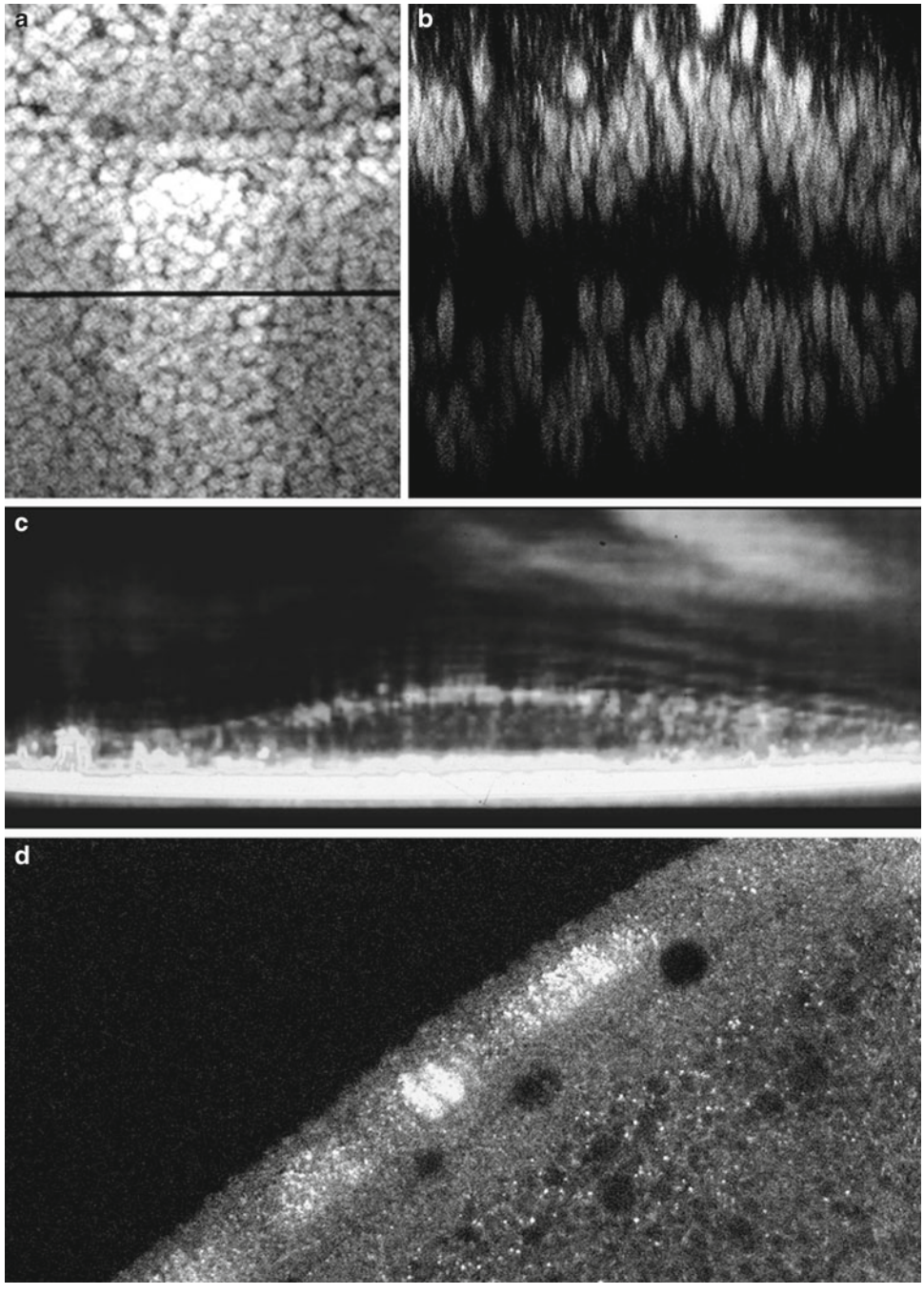

Fig. 12 X–Z imaging; the laser was scanned across a single line at different Z depths-black line in (**a**) and an X–Z image was built up from the line scans in the confocal imaging system (**b**). Note that the butterfly wing epithelium is made up of two epithelial layers, and note that the fluorescence intensity drops off deeper into the specimen This is an artifact caused by attenuation of the signal by the optical properties of the specimen. (**c**) X–Z sectioning in reflected light of an unstained living cell growing on a glass coverslip in tissue culture. The coverslip is visible as a saturated region (*white*) beneath the cell profile. (**d**) Profiles of cells can also be produced by orientation of the specimen in the scanning beam. Here the edge of a *Drosophila* embryo at the cellular blastoderm stage is imaged

An alternative method of producing an X–Z image is to extract the profile from a Z-series of optical sections using a cut plain option in a 3D reconstruction program.

3.5 Live Cell Imaging

Major advancements have been made in the ability to image living cells using confocal microscopy [22]. The photon efficiency of most modern confocal systems has been improved significantly over the early models, and when coupled with high throughput objective lenses and brighter less phototoxic dyes, these improvements have made live cell confocal analysis a practical option. Images are usually collected using a time-lapse mode [23]. Image collection is at pre-selected time intervals, and the images are placed into a single image file, which is usually viewed as a movie (Fig. 13).

Imaging living tissues is perhaps an order of magnitude more difficult than imaging fixed ones using the LSCM [24]. For successful live cell imaging extreme care must be taken to preserve the viability of cells on the stage of the microscope throughout the imaging process (Table 3). Minimal laser powers should be used since harmful levels of light exposure can accumulate over multiple scans, and will eventually cause photo damage to the cells. Cells generally stay healthier for longer time periods when exposed to brief pulses of light. Longer wavelengths (infra-red) of excitatory light are generally less phototoxic than the shorter wavelengths (UV).

Cells from different sources have widely different requirements for imaging in the living state. For example, mammalian cells have more stringent temperature and pH requirements than those from most invertebrate sources. There are a array of microscope incubators available now that can provide precise control of the environment on the microscope stage including control for humidity, $C0_2$ levels and temperature. The choice of the best exposure time for any given tissue is a matter for experimentation with any given experimental set-up. It is necessary to check on the health of the cells after each imaging run. Simple tests might be a comparison with adjacent cells in the same preparation or following the subsequent development of observed cells as compared with a control group of cells after an imaging session. Markers of cell viability are also commercially available that can be used in addition to live dead stains.

New and improved probes for imaging gene expression in living cells continue to be introduced [25, 26]. These reporter probes avoid complicated and potentially harmful methods of loading cells with fluorescent probes by microinjection, chemical or electroporation, since the fluorescent reporter probes are genetically engineered into the cells at the site of protein action.

A commonly used reporter is the green fluorescent protein (GFP). This is used to determine the location, concentration, interactions or the dynamics of target proteins in living cells and tissues [27]. The excitation and emission spectra of enhanced GFP (a genetic

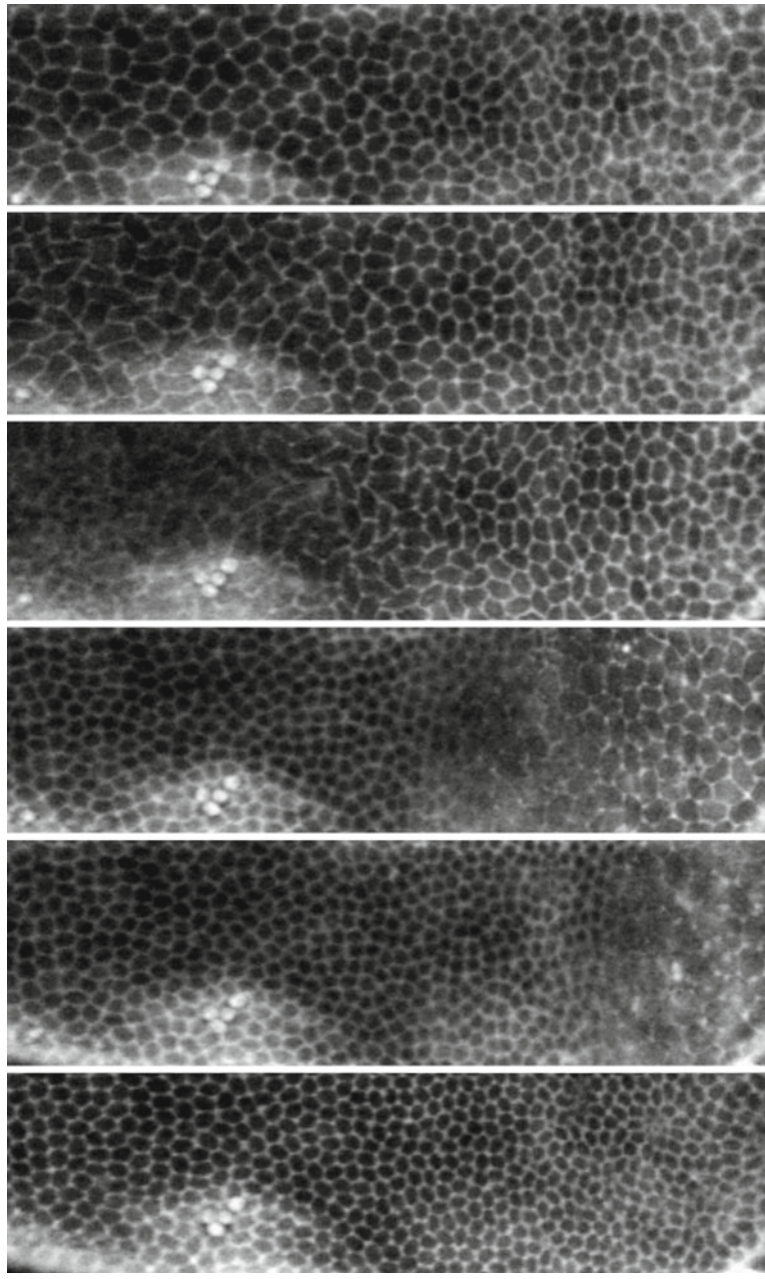

Fig. 13 Time lapse imaging of a living *Drosophila* embryo injected with Calcium green (**a**–**d**). Here Calcium green is used as a marker of cell outlines rather than a calcium indicator dye. A wave of cell divisions (mitotic wave) passing across the embryo is viewed as reduction in cell size and an increase in cell numbers. Image drawn by Leanne Olds

Table 3
Different considerations for imaging fixed and living cell with the LSCM

	Fixed cells	Living cells
Limits of illumination	Fading of fluorophore	Phototoxicity fading of dye
Anti-fade reagent	Phenylenediamine, etc.	NO!!
Mountant	Glycerol ($n = 1.51$)	Water ($n = 1.33$)
Highest NA lens	1.4	1.2
Time per image	Unlimited	Limited by speed of phenomenon; light sensitivity of specimen
Signal averaging	Yes	No
Resolution	Wave optics	Photon statistics

derivative) have maxima at 489 and 508 nm, respectively. This is conveniently close to the excitation maxima and minima of fluorescein so that no modifications are required for the confocal instrumentation when GFP is the chosen reporter. Spectral variants of GFP including blue, yellow and cyan fluorescent proteins and other proteins such as DsRed (from *Discosoma* sp. Red) are now available for multiple wavelength imaging [28]. A new technique, called optogenetics allows the use of light to control behavior [29].

3.6 Multidimensional Imaging

As confocal instrumentation has been improved, the collection of multidimensional images has become more practical (Fig. 14). 4D data sets are Z-series of optical sections collected over time from living preparations [30]. It is important that the phenomenon of interest is not faster than the time it takes to collect each image stack for each time point in the series of images. Multidimensional data sets can be huge and becomes computationally challenging to manage. Extra "dimensions" continue to be added. For example, the collection of multiwavelength images as Z-series over time has been called "5D imaging". Methods are available for the analysis and visualization of multidimensional data [31].

3.7 Reflected Light Imaging

Unstained preparations can be viewed with the LSCM using reflected (backscattered) light imaging [32]. This mode is often overlooked, and can often provide additional information from a specimen with relatively little extra effort (Fig. 15). Reflected light imaging usually requires a different filter combination to be inserted into the scan head. Specimens can be labeled with probes that reflect light such as immunogold or silver grains [33]. Intrinsic proteins such as collagen can also be imaged using this method.

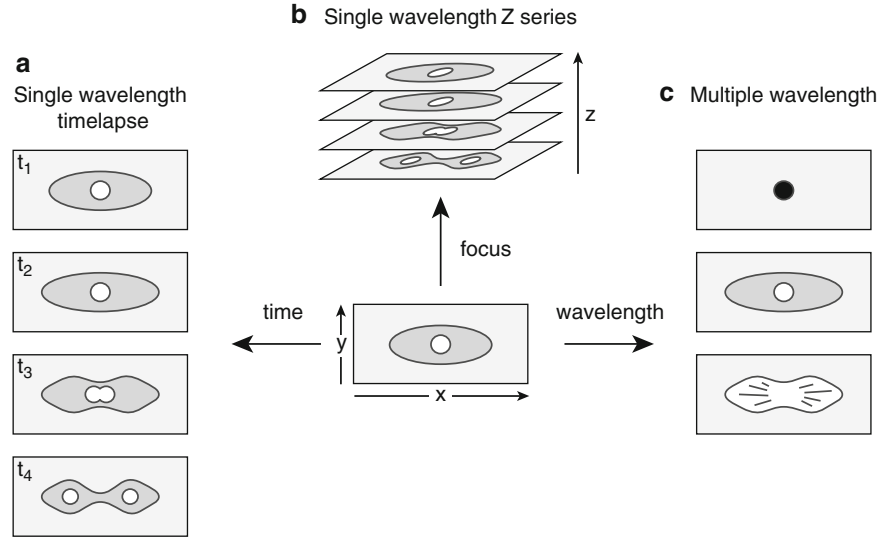

Fig. 14 Multidimensional imaging. (**a**) Single wavelength excitation over time 2D imaging; (**b**) Z-series or single wavelength over depth (3D imaging). The combination of (**a** and **b**) 3D over time is 4D imaging. (**c**) 3D multiple wavelength imaging. Over time is 5D imaging

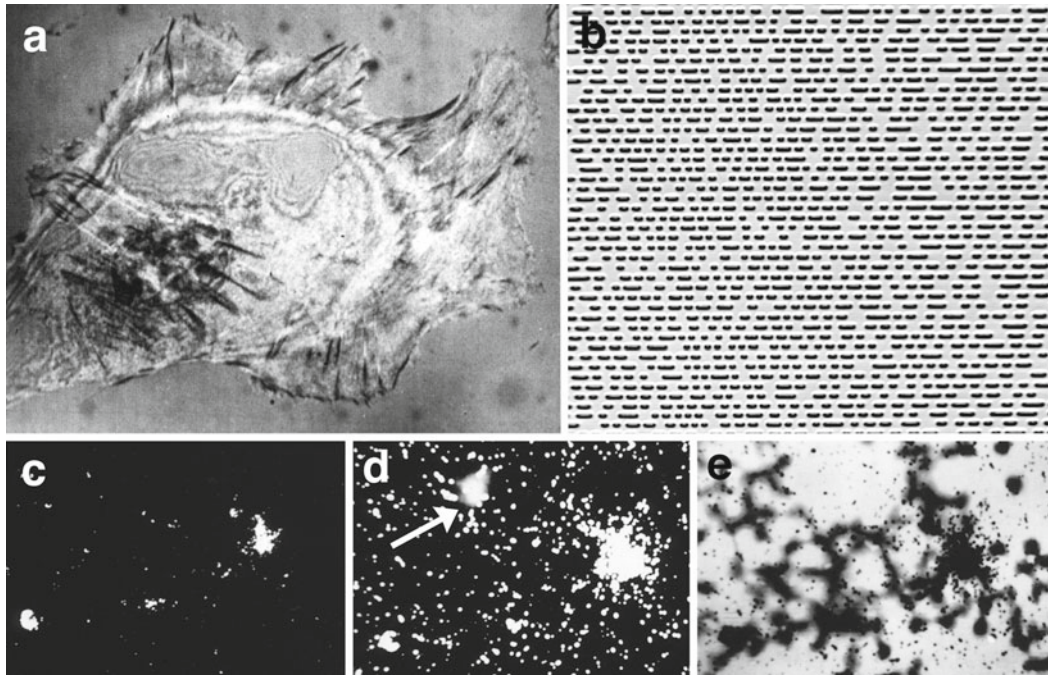

Fig. 15 Reflected light confocal and transmitted light non confocal imaging: (**a**) Reflected light image of an unstained living 3T3 cell focused at the interface of the cell with the coverslip. Such images are similar to those of cell substratum contacts produced by interference reflection microscopy. Here the contacts appear as *black* streaks around the cell periphery. (**b**) Confocal microscopes are used extensively in the materials sciences—here the surface of an audio CD is shown and represents a convenient test specimen. (**c**–**e**) In situ hybridization of HIV infected blood cells. The silver grains are clearly seen in the reflected light confocal image (**c**) and in the transmitted light dark-field image (**d**) and bright-field image (**e**). Note the false positive caused by reflection from a dust particle out of the focal plane of interest. The reflection is visible in the transmitted light dark field image (*arrow* in **d**) but not in the confocal reflected light image (**c**)

Some of the probes tend to attenuate the laser beam, and in some LSCMs there can be a reflection from optical elements in the microscope. The problem can be solved by inserting polarizers into the light path of the LSCM or by electronically zooming away from the artifact, and off the optical axis. The reflection artifact is not present in the slit or multiple beam scanning systems.

3.8 Transmitted Light Imaging

Any form of wide field light microscope image, including bright field, phase contrast, DIC, polarized light or dark field can be collected using the LSCM equipped with a transmitted light detector (Fig. 15). This device collects light that passes through the specimen and through the condenser of the light microscope. It essentially reverses the imaging process by using the objective lens as the condenser and the condenser as the lens. This results in a non-confocal image.

The signal is usually transferred to one of the PMTs in the scan head via a fiber optic. Since the confocal fluorescence images and transmitted light images are collected simultaneously using the same excitation beam image registration is preserved. It is often informative to collect a transmitted, non-confocal image of a specimen and to merge such a transmitted light image with one or more confocal fluorescence images of labeled cells. For example, the spatial and temporal components of the migration of labeled cells (confocal image) within an unlabelled population of cells (non confocal transmitted light image) have been imaged.

An alternative to using a transmitted light detector is to collect an image with a conventional digital video camera attached to a side port of the light microscope.

3.9 Correlative Microscopy

Correlative, or "integrated microscopy", is an approach where images are collected from the same region of a specimen using more than one microscopic technique [34]. The most usual combination of instruments is to use the light microscope to image living cells, and then to take advantage of the improved resolution of transmission electron microscopy to image the same region after fixation.

Confocal microscopy has been used in combination with transmission electron microscopy (TEM) to image the same region of the cell. For example, the distribution of microtubules within fixed tissues has been imaged using the LSCM, and the same region was imaged in the TEM [35]. Here, eosin was used both as a fluorescence marker in the LSCM and as an electron dense marker in the electron microscope. Reflected light confocal imaging and TEM have also been used in correlative microscopy to image focal adhesions in living cells growing on a glass coverslip in culture using the LSCM and the same region at higher resolution using the TEM. Rapid specimen preparation techniques such as high pressure freezing (HPF) that can preserve cellular structure for subsequent observation by high resolution TEM have to proven to be very powerful for correlative experiments.

4 Measurements

Improvements in confocal instrumentation and the development of new fluorescent reporter probes of biological activity have enabled a new level of precision when the confocal microscope is used as a tool for quantitative imaging of biological events within living cells. Most measurements are based on the confocal instrument's ability to accurately record the brightness of and the wavelength emitted from a fluorescent probe within a sample over time at high spatial resolution.

4.1 Intensity

Intensity measurements are made either by using the software provided with the confocal imaging system or a secondary software, for example the public domain ImageJ or FIJI software package. The brightness of the fluorescence from the probe is calibrated to the amount of probe present at any given location in the cell. For example, the concentration of calcium is measured in different regions of living embryos using calcium indicator dyes whose fluorescence intensity is in proportion to the amount of free calcium in the cell. Many probes have been developed for making such measurements in living tissues. Controls are a necessary part of such measurements since photobleaching and dye artifacts during the experiment can obscure the true measurements of physiological levels of calcium inside cells.

4.2 Fluorescence Resonance Energy Transfer (FRET)

The multichannel feature of the LSCM is used for fluorescence resonance energy transfer (FRET) measurements of protein–protein interactions inside cells [36]. FRET occurs between two fluorophores when the emission of the first one (the donor) serves as the excitation source for the second one (the acceptor). FRET only occurs when the donor and the acceptor molecules are extremely close to one another, at a distance of 60 angstroms or less. In this way, sub-resolution molecular measurements are made [37]. For example, the excitation of a cyan fluorescent protein CFP-tagged protein has been used to monitor the emission of a yellow fluorescent protein YFP-tagged protein. YFP fluorescence will only be observed under the excitation conditions of CFP if the proteins are close enough together for excitation. Since this can be monitored over time, FRET has been used to measure direct binding of proteins or protein complexes.

4.3 Fluorescence Lifetime Imaging (FLIM)

Measurement of fluorescence excited-state lifetimes can provide another dimension of information from a fluorophore that is essentially independent of the energy (wavelength) of the emitted photons, and can therefore be used to distinguish photons from different fluorophores that have similar wavelengths [38, 39]. FLIM is a measure of how long an excited fluorophore stays in the excited state before decay. Furthermore changes in the microenvironment

including pH, proximity to other proteins and hydrophobic regions can affect lifetime. Thus lifetime can be used as a noninvasive readout of cellular interactions and microenvironment changes [40].

There are two ways to measure fluorescence lifetime, in frequency or the time domains. Many live cell imaging biologists favor time domain measurements because they can use a specific time domain method, Time Correlated Single Photon Counting (TCSPC) system that minimizes the effects of noise sources such multiplier gain noise in photodetectors. These systems are readily available on many modern confocal microscopes. However, limited photon-counting rates of currently available FLIM systems reduce the dynamic range of measurements and necessitate the use of long exposure times. Further development of FLIM in both the frequency and time domain is underway to allow for faster acquisition.

4.4 Fluorescence Recovery After Photobleaching (FRAP)

This technique uses the high light flux from a laser to locally destroy fluorophores labeling specific macromolecules to create a photobleached zone [41]. The observation and recording of the subsequent movement of undamaged fluorophores into the bleached zone using confocal microscopy gives a measure of molecular mobility.

4.5 Photoactivation

A second technique related to FRAP, photoactivation, uses a probe whose fluorescence can be induced by a flash of short wavelength (UV) light. The method employs "caged" fluorescent probes that are locally activated (uncaged) by a pulse of UV light [42]. More recently, variants of GFP have been expressed in cells and selectively photoactivated. The activated probe is imaged using a longer wavelength of light. Photoactivation has the advantage of a superior signal to noise ratio to FRAP.

5 Alternatives to Confocal Microscopy for Producing Optical Sections

The simplest method of producing optical sections is using a conventional light microscope equipped with differential interference contrast (DIC) optics. This technique is useful for imaging unstained and relatively transparent living specimens, for example sea urchin eggs and embryos. DIC lacks the signal to noise ratio and specificity of the fluorescence technique, however. DIC has been used mainly in the transmitted light function of the LSCM to map specific fluorescence to landmarks in the DIC image.

5.1 Structured Illumination

This technique uses conventional epifluorescence microscopy with a grid structure inserted into the illumination path. Several images are collected with the grid in different positions. Optical sections are subsequently calculated from the images using a computer

program. This is the basis of the ApoTome microscope, which is a relatively inexpensive option for producing optical sections [43].

5.2 Deconvolution

Deconvolution is a computer-based method that calculates and removes the out-of-focus information from an image after a stack of fluorescence images has been collected [44]. The method uses images collected from a conventional epifluorescence microscope equipped with a stepper motor attached to the fine focus control so that images are collected at precisely defined intervals between focal planes in the specimen. This method is used for routine analysis and is especially suited for imaging smaller specimens such as yeast and bacteria where there is insufficient signal for imaging with the LSCM.

5.3 Multiphoton

Multiphoton microscopy uses a scanning system that is identical to that of the LSCM [45, 46]. There is no need for a pinhole, however, because the long wavelength infrared laser only excites at the point of focus, and therefore a pinhole is not necessary (Fig. 16). Fluorophores in the specimen are simultaneously excited by two or three photons to produce excited state transitions that are equivalent to single-photon fluorescence. This is called nonlinear excitation. For example, two and three photon excitation at 900 nm is equivalent to excitation by higher energy photons of 450 and 300 nm, respectively.

Cell viability is generally improved using multiphoton microscopy as compared with confocal microscopy since the excitation wavelengths are in the longer infrared range and the wavelengths utilized are past many of the known UV check-points for biological damage.

Multiphoton microscopy enables penetration 2–3 times deeper into thick specimens than confocal microscopy although this figure is very specimen dependent based on changes in refractive index and scattering properties. This allows investigations on thick living tissue specimens that would not otherwise be possible with conventional imaging techniques [47]. Multiphoton imaging is usually chosen for imaging living cells and tissues both in vitro and in vivo. Multiphoton is also compatible with other nonlinear optical methods such as Second Harmonic Generation (SHG) that can be used to look at intrinsic proteins with a non-centrosymmetric ordered structure such as collagen [48].

5.4 Scanned Light Sheet Microscopy

This method uses a thin sheet of laser light for optical sectioning with an objective lens and CCD camera detector system oriented perpendicular to it (Fig. 16). This technique was developed to improve the penetration of living specimens and enables the imaging of live samples from many different angles at a cellular resolution. The technique has been realized by selective plane illumination microscopy (SPIM) where the specimen itself is rotated in the

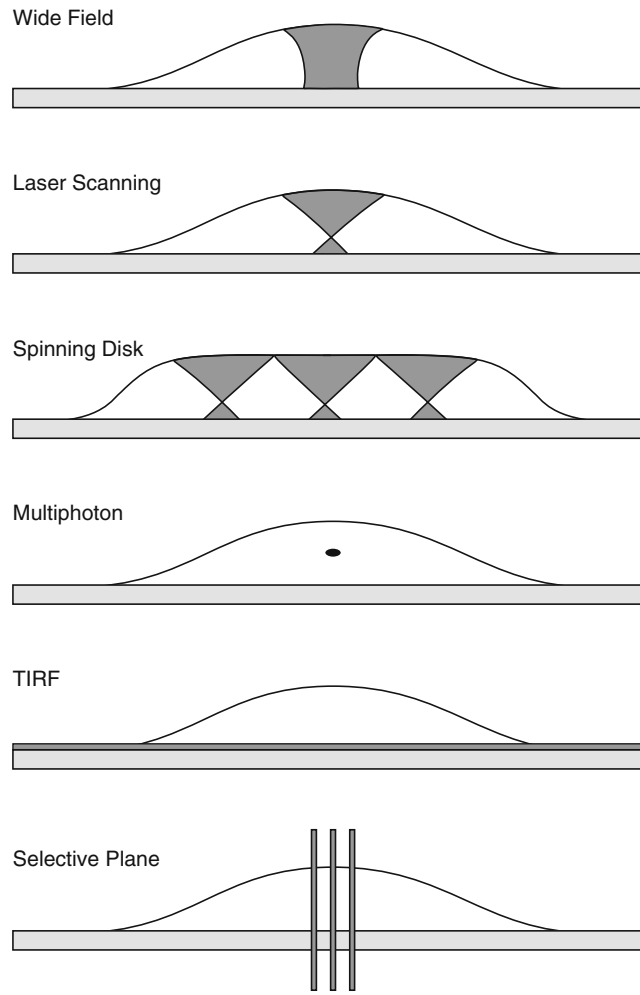

Fig. 16 Illumination profiles in different modes of optical sectioning microscopy. (**a**) Wide field epifluorescence microscopy; (**b**) Laser scanning confocal microscopy; (**c**) Spinning disk confocal microscopy; (**d**) Multiphoton microscopy; (**e**) Total internal reflection (TIRF) microscopy, and (**f**) Selective Plane illumination microscopy. The diagram shows a schematic of a side view of a fluorescently labeled cell on a coverslip. The shaded grey areas in each cell depict the profiles of fluorescent excitation produced by each of the different microscopes. Conventional epifluorescence microscopy (**a**) illuminates throughout the cell. In the laser scanning (**b**) and spinning disk (**c**) confocal microscopes, the fluorescence illumination is throughout the cell but is focused at one (**b**) or multiple (**c**) points in the specimen. In the multiphoton microscope (**d**), excitation only occurs at the point of focus where the light flux is high enough. In TIRF (**e**), a 100 nm thick region of excitation is produced at the glass water interface, and for selective plane illumination (**f**), a plane of laser light is produced that is perpendicular to the axis of viewing, and the specimen itself is moved in this beam. Image drawn by Leanne Olds

beam. Advantages of the technique include low phototoxicity and high acquisition speed. The technique has been used to image every nucleus in zebra fish embryos over 24 hours of development at stunning resolution. Multiphoton SPIM is under development for greater depth penetration [49, 50].

5.5 Total Internal Reflection Fluorescence Microscopy

This technique, usually referred to under the acronym, TIRF, is designed to probe the surface of fluorescently labeled living cells [51]. An evanescent wave is generated by a light beam traveling between two media of differing refractive indices. In practice, an incident laser beam is reflected at a critical angle (total internal reflection) when it encounters the interface between a microscope glass slide and the aqueous medium containing the cells (Fig. 16). Fluorophores within a few nanometers of the surface are excited by the evanescent wave, while those farther away are unaffected. TIRF gives much improved resolution in the Z-axis—TIRF 0.3 μm vs. confocal 0.7 μm vs. wide field fluorescence 1.6 μm.

The technique is commonly employed to investigate the interaction of molecules with surfaces, an area that is of fundamental importance to a wide spectrum of disciplines in cell and molecular biology.

5.6 Super Resolution Methods

Several methods are now challenging the resolution limit of the light microscope [52]. Up until relatively recently, the dogma was that the limit of resolution of the light microscope was dependent on the wavelength of light used, and was fixed at around 150—200 nm. Higher resolutions could only be achieved using electron microscopy, and therefore only fixed specimens were imaged.

New “super resolution” light microscopes are able to achieve resolutions down to 20–30 nm in the lateral dimension and 60–70 nm in the axial direction, and in living cells. Such techniques include fluorescence photoactivation localization microscopy (FPALM) with a resolution of 20–30 nm, stimulation emission depletion microscopy (STED) with a resolution of 30–80 nm, stochastic optical reconstruction microscopy (STORM) with a resolution of 20–30 nm and 3D structured illumination (SIM) with a resolution of 100 nm. These are all exciting improvements for live imaging of sub–cellular structures and are becoming commercially available.

5.7 Optical Projection Tomography

Optical projection tomography (OPT) is useful for imaging specimens that are too big to be imaged using other microscope-based imaging methods, e.g., vertebrate embryos [53]. Here the resolution is better than that achieved using magnetic resonance imaging (MRI) but not as good as confocal microscopy. OPT can take advantage of some of the similar dyes used in confocal microscopy.

5.8 Whole Animal Methods

Various instruments have been designed over the years for imaging cells in living animals [54]. There are two main approaches; mini microscopes that can be mounted on an animal for long term observations or hand-held probes that can be pressed against an animal for immediate diagnostic imaging. This continues to be an area of active research with the development of new lenses for efficient light capture in vivo and fiber based endoscopes that can capture the signal in vivo.

6 The Final Image

Confocal microscopy is routinely used to produce high-resolution images of single, double and triple labeled fluorescent samples. The images are collected as single optical sections (2D imaging), as Z-series (3D imaging), as time-lapse series (2D over time), as Z-series over time (3D over time or 4D imaging), or as multiwavelength, 3D over time (5D imaging). Since the images collected by a confocal instrument are confocal instruments in a digital format, they can be further manipulated using a range of software.

6.1 Recording the Image

Minsky's original microscope suffered from a problem with the final images. The instrument produced a ghostly image on a low-resolution oscilloscope screen. Moreover, it was not possible to record the images in a publication. In contrast, the images produced and published by the Cambridge group from their first LSCM drew the attention of the biological research community to the true potential of confocal microscopy because the final images were so impressive on the journal page.

Most of the confocal images produced at this time were single label grayscale images that were recorded as hard copies by photographing the screen of the computer monitor using a 35 mm camera or using a video printer. Single colors were added digitally using a color look up table (LUT). Color images of double label specimens were produced as red green images, and were again recorded by photographing the screen of the computer using color film in a 35 mm camera.

The current generation of confocal instruments takes advantage of modern methods of digital image display and reproduction so that images produced by the microscope are exactly the same as those delivered to the publisher for reproduction on the printed page and for access on journal Web pages.

Selected images are usually prepared for publication using an intermediary program, for example Adobe PhotoShop or ImageJ or FIJI. Such programs are useful for cropping and arranging images into a plate for publication. Images can be matched for brightness and contrast levels. Most of these manipulations were previously achieved using long hours of skillful chemical manipulation using photographic methods in a darkroom.

Such digital programs are capable of much more, and open up the possibility of unethical image manipulations. Many journals now publish guidelines and best practices for digital image preparations. Some basic practices should be followed, for example always keep all of the original raw data from each experimental run and keep notes of what operations were performed to produce the final published image.

6.2 Presenting the Image

Most of the information contained in a confocal image of a biological specimen is related to the spatial distribution of various macromolecules. Images of different macromolecules are collected at different wavelengths. At the present time images collected at three or four different excitations are routine using the LSCM.

A convenient method for the display of two or three colored images is to use the red, green and blue channels of an RGB color image within PhotoShop where any overlap (colocalization of fluorescent probes) is viewed as a different additive color when the images are colorized and merged into a single three-color image [55].

Several simple applications of this three color merging protocol include the mapping color to depth in Z-series, mapping color to time in a time-lapse series, the production of red/green or red/blue stereo anaglyphs from Z-series and merging confocal and transmitted light images (Fig. 17).

The combination of colors within a three color merged image is important for clearly conveying the biological information collected by the microscope. The true emission colors of two of the most commonly used fluorophores, rhodamine and fluorescein, are, conveniently, red and green, respectively, and overlapping domains of expression are yellow. Also some of the commonly used nuclear dyes that are excited in the near UV, such as Hoechst 33342, emit in the blue. These are the colors observed by eye in a conventional epifluorescence microscope equipped with the appropriate filter sets for simultaneous double label imaging. However, the third channel in a triple-label sample prepared for confocal analysis usually emits in the far red, e.g., Cyanine 5, which is conveniently shown as blue in digital images whereas the real Cyanine 5 emission is often extremely difficult to visualize by eye and not so easily depicted in a digital image. By rearranging the grayscale images, the best combination of colors that conveys the maximum amount of information, and best color balance can be achieved.

Additional images at different wavelengths are theoretically possible given enough lasers and filter combinations. However, many such multiparameter images rapidly become complex and difficult to interpret when more than three of them are colorized and merged unless the images contain many regions of nonoverlapping structures, for example, chromosomes painted with fluorescently labeled DNA probes or individual neurons labeled with specific combinations of dyes.

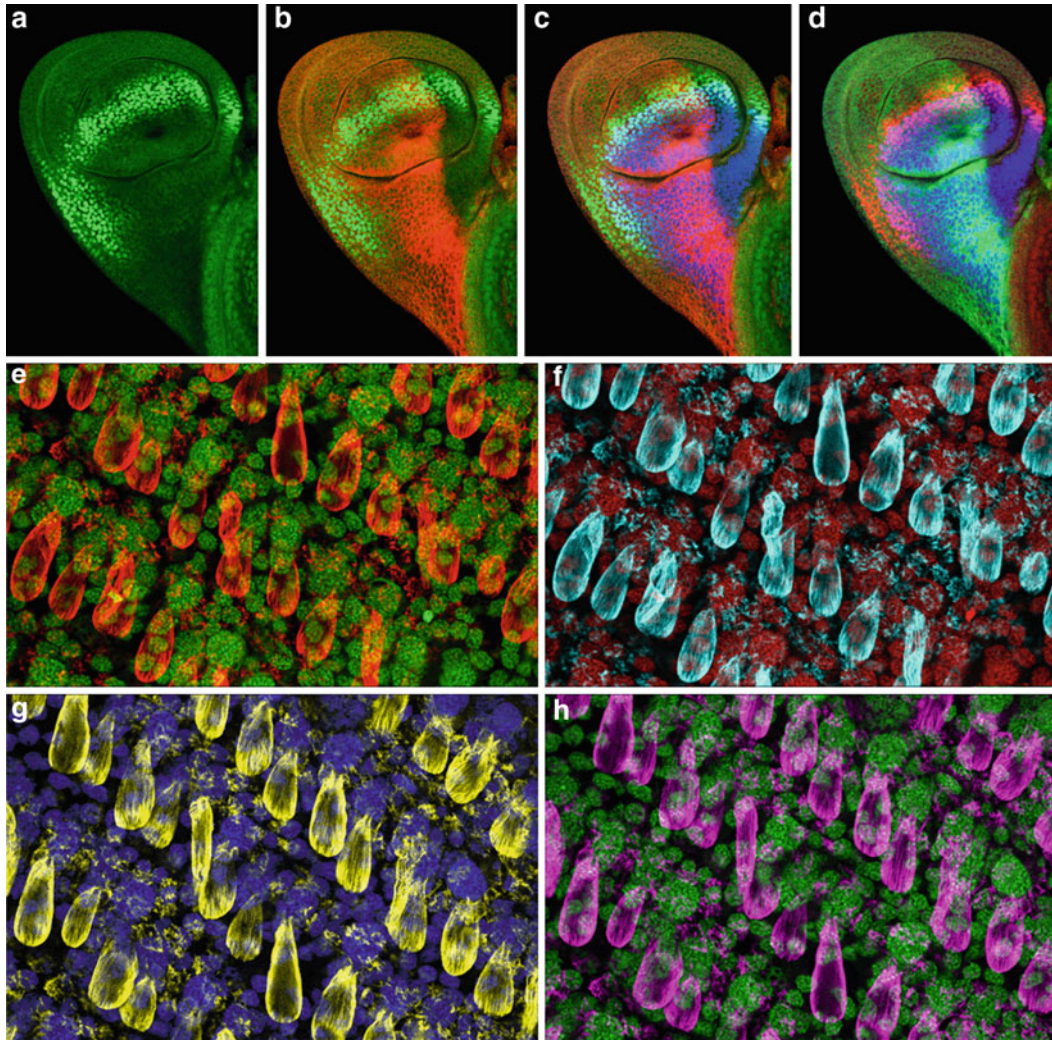

Fig. 17 Image presentation. Using PhotoShop it is a relatively simple task to experiment with various color combinations for optimizing informational quality by rearranging the grayscale images into different *red*, *green,* or *blue* color channels. A single label image is colored *green* (**a**), a double label image is colored *red* and *green* (**b**) and a triple labeled image is colored *red*, *green,* and *blue* in two different color combinations (**c**, **d**) simply by experimenting with cutting and pasting grayscale images. The specimen is a triple labeled third instar *Drosophila* haltere imaginal disk. In addition to displaying the relative distribution of up to three different macromolecules within cells, this method of combining the three images can be used as an alternative to 3D reconstruction for displaying depth information within a specimen (**e**–**h**). Here developing butterfly wing scales are viewed in *red*, *blue*, *yellow,* or *purple* growing out of the pupal wing epithelium colored *green*, *red*, *blue,* or *green*

6.3 Making Movies

The problems of presenting time-lapse series in a publication have been largely solved by the ability to publish QuickTime movie files on the Web pages of various journals or on a dedicated YouTube page. Photoshop also provides a bridge to additional image processing. For example sequences of confocal images of different

stages of development have been manipulated using Photoshop, and subsequently transferred to a commercially available morphing program such as Morpheus, and processed into short animated sequences of development. These sequences can be further edited and compiled using Final Cut Pro, and viewed as a digital movie using QuickTime software directly on the computer or exported to DVD for presentation purposes.

Since all of the images are in a digital form it is relatively easy to export them into presentation software such as PowerPoint and Keynote.

6.4 Image Storage

It is not usually advisable to store image files on the computer hard disk of the confocal microscope for a long period of time or even on a server since space can be limited on a multiuser confocal instrument and also hard disks are notorious for unpredicted crashes especially on computers with multiple users. Many laboratories are now using redundant array based servers (RAID) but even these don't necessarily offer a long-term storage solution and for many labs may be outside their accessibility. It is therefore a good practice to archive image files as quickly as possible after acquiring them. There are several options for archiving image files, including DVD writers and long-term offline redundant hard drive backup. Ideally copies of the most valued files should be stored in at least two different locations.

6.5 Image Informatics

While much emphasis has been placed on the development of specimen preparation techniques and confocal instrumentation for collecting optical sections, the ability to cope with large numbers of images and correspondingly large datasets has been somewhat overlooked in the past [56]. With the increasing use of digital image capture microscopy in the biomedical sciences, it has become a major challenge to locate, view, and interpret large numbers of images collected in a diversity of formats [57].

Many biological research laboratories have a pressing need to archive and annotate vast numbers of images collected by video, laser-scanning microscopy and other photonic-based imaging techniques [58]. Multidimensional images, such as four-dimensional images from multifocal plane time-lapse recordings, or images from spectral and lifetime microscopy, make the challenge even greater. Without careful organization, important research data can be difficult or impossible to find, much less visualize and analyze effectively. This need has spawned the field of "Image Informatics" to develop tools to aid in the management, sharing, visualizing, and the analysis of datasets collected using many different biological imaging platforms with a major emphasis on confocal microscopy [59, 60].

A prominent example of an image informatics platform is the Open Microscopy Environment (OME). OME is a consortium of companies and academics with the mission of developing open

source tools for biological image data management [61]. A unique and important emphasis of OME is the priority it places on having tools that not only can analyze and share the binary image data but the full metadata, which can include instrument, user and experimental information. Unfortunately there are currently over 150 proprietary microscopy formats in use and OME tools like Bio-formats enable the full reading and open sharing of these formats in many programs. As confocal microscopy has become increasingly quantitative and the need and interest to analyze and annotate data from other sources increases, the importance of metadata is only going up. The need for tools like OME to analyze and share the original pixel and metadata information has become more vital.

6.6 Resources

This introductory chapter serves as a primer of confocal microscopy and related optical sectioning techniques and more-detailed information on specific topics can be found in subsequent chapters of this book. The field is huge and continues to grow. Here we provide references to several books and review articles [2, 6, 7, 11, 62–66] together with a list of some of our favorite Web sites (Table 4) as a starting point for gathering more-detailed information and specific protocols.

Table 4
A selection of popular Web sites (active at the time of printing) on all aspects of confocal microscopy from the technical to the artistic

"Microscopy U—The Source for Microscopy Education" http://www.microscopyu.com/
"Molecular Expressions—Exploring the World of Optics and Microscopy" http://www.microscopy.fsu.edu/
"Microscopy Society of America" http://www.msa.microscopy.org
"The Royal Microscopical Society" http://www.rms.org.uk
"The Open Microscopy Environment" http://www.openmicroscopy.org
"ImageJ" http://rsb.info.nih.gov/ij/
"Fiji" http://fiji.sc/Fiji
"Wellcome Trust Microscopy Resource" http://www.well.ox.ac.uk/external-website-links
"Nikon Small World" http://www.nikonsmallworld.com/
"Olympus BioScapes" http://www.olympusbioscapes.com/

References

1. Conchello JA, Lichtman JW (2005) Optical sectioning microscopy. Nat Methods 2: 920–931
2. Paddock SW (1999) Protocols in Confocal Microscopy. Methods Mol Biol 122. Humana Press, Totowa, NJ
3. Chalfie M, Tu Y, Euskirchen G, Ward WW, Prasher DC (1994) Green fluorescent protein as a marker for gene expression. Science 263: 802–805
4. Fraser SE (2003) Crystal gazing in optical microscopy. Nat Biotechnol 21:1272–1273
5. Walter T et al (2010) Visualization of image data from cells to organisms. Nat Methods 7:S26–S41
6. Hibbs AR (2004) Confocal microscopy for biologists. Springer, New York
7. Price R, Jerome WG (2011) Basic confocal microscopy. Springer, New York
8. Minsky M (1988) Memoir on inventing the confocal scanning microscope. Scanning 10:128–138
9. Minsky M (1957) Microscopy apparatus U.S. Patent no. 3013467
10. Brakenhoff GJ, van der Voort HTM, van Spronsen EA, Linnemans WAM, Nanninga N (1985) Three-dimensional chromatin distribution in neuroblastoma nuclei shown by confocal laser scanning laser microscopy. Nature 317: 748–749
11. Pawley JB (2006) Handbook of Biological Confocal Microscopy, 3rd edn. Plenum Press, New York
12. Amos WB, White JG (2003) How the confocal laser scanning microscope entered biological research. Biol Cell 95:335–342
13. White JG, Amos WB (1987) Confocal microscopy comes of age. Nature 328:183–184
14. White JG, Amos WB, Durbin R, Fordham M (1990) Development of a confocal imaging system for biological epifluorescence application in "Optical Microscopy For Biology". Wiley-Liss Inc, New York, NY, pp 1–18
15. White JG, Amos WB, Fordham M (1987) An evaluation of confocal versus conventional imaging of biological structures by fluorescence light microscopy. J Cell Biol 1987(105): 41–48
16. Wilson T (1995) The role of the pinhole in confocal imaging system. Plenum Press, New York, pp 167–182
17. Paddock SW (2002) Confocal imaging of *Drosophila* embryos. In: Matsumoto B (ed) Cell biological applications of confocal microscopy, 2nd edn. Methods Cell Biol 70:355–372
18. Kosman D, Mizutani CM, Lemons D, Cox WG, McGinnis W, Bier E (2004) Multiplex detection of RNA expression in *Drosophila* embryos. Science 305:846
19. Brelje TC, Wessendorf MW, Sorenson RL (1993) Multicolor laser scanning confocal immunofluorescence microscopy: practical applications and limitations. Methods Cell Biol 38:98–177
20. Livet J, Weissman TA, Kang H, Draft RW, Lu J, Bennis RA, Sanes JR, Lichtman JW (2007) Transgenic strategies for combinatorial expression of fluorescent proteins in the nervous system. Nature 450:56–62
21. Murray JM, Appleton PL, Swedlow JR, Waters JC (2007) Evaluating performance in three-dimensional fluorescence microscopy. J Microsc 228:390–405
22. Van Roessel P, Brand A (2002) Imaging into the future: visualizing gene expression and protein interactions with fluorescent proteins. Nat Cell Biol 4:E15–E20
23. Paddock SW (2001) A brief history of time-lapse. Biotechniques 30:283–289
24. Pawley JB (2000) The 39 steps: a cautionary tale of quantitative 3-D fluorescence microscopy. Biotechniques 28:884–887
25. Heim R, Tsien RY (1996) Engineering green fluorescent protein for improved brightness, longer wavelength and fluorescence energy transfer. Curr Biol 6:178–182
26. Shaner NC, Patterson GH, Davidson MW (2007) Advances in fluorescent protein technology. J Cell Sci 120:4247–4260
27. Tsien RY (1998) The green fluorescent protein. Annu Rev Biochem 67:509–544
28. Giepmans BNG, Adams SR, Ellisman MH, Tsien RY (2006) The fluorescent toolbox for assessing protein location and function. Science 312:217–224
29. Fiala A, Suska A, Schulter OM (2010) Optogenetic approaches in neuroscience. Curr Biol 20:R897–R903
30. Mohler WA, White JG (1998) Stereo-4-D reconstruction and animation from living fluorescent specimens. Biotechniques 24:1006–1012
31. Provenzano PP, Eliceiri KW, Keely PJ (2009) Shining new light on 3D cell motility and the metastatic process. Trends Cell Biol 19:638–48
32. Paddock SW (2002) Confocal reflection microscopy; the “other” confocal mode. Biotechniques 32:274–278
33. Paddock SW, Mahoney S, Minshall M, Smith LC, Duvic M, Lewis D (1991) Improved detection of *in situ* hybridisation by laser

scanning confocal microscopy. Biotechniques 11:486–494

34. Gaietta G, Deerinck TJ, Adams SR, Bouwer J, Tour O, Laird DW, Sosinsky GE, Tsien RY, Ellisman MH (2002) Multicolor and electron microscopic imaging of connexin trafficking. Science 296:503–507
35. Deerinck TJ, Martone ME, Lev-Ram V, Green DPL, Tsien RY, Spector DL, Huang S, Ellisman MH (1994) Fluorescence photooxidation with eosin: a method for high-resolution immunolocalisation and in situ hybridisation detection for light and electron microscopy. J Cell Biol 126:901–910
36. Piston DW, Kremers GJ (2007) Fluorescent protein FRET: the good, the bad and the ugly. Trends Biochem Sci 32:407–414
37. Pietraszewska-Bogiel A, Gadella TWJ (2010) FRET microscopy: from principle to routine technology in cell biology. J Microsc 240: 111–118
38. Bastiaens PI, Squire A (1999) Fluorescence lifetime imaging microscopy: spatial resolution of biochemical processes in the cell. Trends Cell Biol 9:48–52
39. Borst JW, Visser AJWG (2010) Fluorescence lifetime imaging microscopy in life sciences. Meas Sci Technol 21:1–21
40. Conklin MW, Provenzano PP, Eliceiri KW, Sullivan R, Keely PJ (2009) Fluorescence lifetime imaging of endogenous fluorophores in histopathology sections reveals differences between normal and tumor epithelium in carcinoma in situ of the breast. Cell Biochem Biophys 53:145–57
41. van Royen ME, Dinant C, Farla P, Trapman J, Houtsmuller AB (2009) FRAP and FRET methods to study nuclear receptors in living cells. Methods Mol Biol 505:69–96
42. Lippincott-Schwartz J, Altan-Bonnet N, Patterson GH (2003) Photobleaching and photoactivation: following protein dynamics in living cells. Nat Cell Biol 2003:S7–14
43. Weigel A, Schild D, Zeug A (2009) Resolution in the ApoTome and the confocal laser scanning microscope: comparison. J BioMed Opt 14. Online article #014023
44. Wallace W, Schaefer LH, Swedlow JR (2001) A workingperson's guide to deconvolution in light microscopy. Biotechniques 5:1076–1080
45. Svoboda K, Yasuda R (2006) Principles of two-photon excitation microscopy and its applications to neuroscience. Neuron 50:823–839
46. Zipfel WR, Williams RM, Webb W (2002) Nonlinear magic: multiphoton microscopy in the biosciences. Nat Biotechnol 21:1369–1377
47. Helmchen F, Denk W (2005) Deep tissue two-photon microscopy. Nat Methods 2:932–919
48. Campagnola PJ, Loew LM (2003) Second-harmonic imaging microscopy for visualizing biomolecular arrays in cells, tissues and organisms. Nat Biotechnol 21:1356–1360
49. Keller PJ, Schmidt AD, Wittbrodt J, Stelzer EHK (2008) Reconstruction of zebrafish early embryonic development by scanned light sheet microscopy. Science 322:1065–1069
50. Keller PJ, Schimdt AD, Santella A, Khairy K, Bao Z, Wittbrodt J, Stelzer EHK (2010) Fast, high-contrast imaging of animal development with scanned light sheet-based structured-illumination microscopy. Nat Methods 7:637–642
51. Axelrod D (2003) Total internal reflection fluorescence microscopy in cell biology. Methods Enzymol 361:1–33
52. Schermelleh L, Heintzmann R, Leonhardt H (2010) A guide to super-resolution fluorescence microscopy. J Cell Biol 190:165–175
53. Sharpe A, Ahlgren U, Perry P, Hill B, Ross a, Hecksher-Sorensen J, Baldock R, Davidson D (2002) Optical projection tomography as a tool for 3D microscopy and gene expression studies. Science 296:541–545
54. St. Croix C, Zipfel WR, Watkins SC (2007) Potential solutions for confocal imaging of living animals. Biotechniques 43:14–19
55. Paddock SW (2001) Channel surfing: creating different colour combinations from multi-label images. Biotechniques 30:756–761
56. Waters JC, Swedlow JR (2007) Interpreting fluorescence microscopy images and measurements. Cell Online 37–42
57. Swedlow JR, Lewis SE, Goldberg IG (2006) Modelling data across labs, genomes, space and time. Nat Cell Biol 8:1190–1194
58. Swedlow JR, Goldberg I, Brauner E, Sorger PK (2003) Informatics and quantitative analysis in biological imaging. Science 300:100–102
59. Peng H (2008) Bioimage informatics: a new era of engineering biology. Bioinformatics 24: 1827–1836
60. Swedlow J.R., Goldberg I.G., Eliceiri K.W., and the OME Consortium (2009) Bioimage informatics for experimental biology. Annu Rev Biophys 38:327–346
61. Linkert M, Rueden CT, Allan C, Burel JM, Moore W, Patterson A, Loranger B, Moore J, Neves C, Macdonald D, Tarkowska A, Sticco C, Hill E, Rossner M, Eliceiri KW, Swedlow JR (2010) Metadata matters: access to image data in the real world. J Cell Biol 189: 777–782

62. Conn PM (2010) Techniques in confocal microscopy (reliable Lab solutions). Academic, New York
63. Goldman RD, Spector DL, Swedlow JR (2009) Live cell imaging: a laboratory manual. Cold Spring Harbor Press, New York
64. Murphy DB, Davidson MW (2012) Fundamentals of light microscopy and electronic imaging. Wiley-Blackwell, Hoboken, NJ
65. Fischer RS, Wu Y, Kanchanawong P, Shroff H, Waterman CM (2011) Microscopy in 3D: a biologist's toolbox. Trends Cell Biol 21: 682–691
66. Swedlow JR (2012) Innovation in biological microscopy: current status and future directions. Bioessays 34:333–340

Chapter 3

Confocal Microscopy on the Internet

Kristin L. Hazelwood, Christopher S. Murphy, Zachary C. Cunningham, Matthew J. Parry-Hill, Richard L. Ludlow, Ericka B. Ramko, Anna P. Ozarowska, Adam M. Rainey, and Michael W. Davidson

Abstract

In a few short years, the Internet (in terms of the World Wide Web) has become a powerful informational resource for the original scientific literature pertaining to biological investigations using the laser scanning confocal microscope. However, there still remains an obvious void in the development of educational Web sites targeted at beginning students and novices in the field. Furthermore, many of the commercial aftermarket manufacturers (for example, those offering live-cell imaging chambers) have Web sites that are not adequately represented in published compilations, and are therefore somewhat difficult to locate. In order to address this issue, several educational sites dedicated to optical microscopy and digital imaging that are being constructed and hosted at The Florida State University are currently turning their attention to the increasing application of confocal microscopy in the biological and materials sciences. The primary focus of this effort is to create new sections on the existing sites that address the important educational issues in confocal microscopy, as well as creating indices of links to both the confocal scientific literature and the Web sites of manufacturers who supply useful accessories.

Key words Confocal microscopy, Internet, Web, HTML, Java, Flash, Interactive tutorials, Digital video, Image processing, Streaming media

1 Introduction

Ten years before the Internet became a practical vehicle for the dissemination of information on an international basis due to the introduction of hypertext transfer protocol (HTTP; 1–3), the first practical laser scanning confocal microscopes were being developed in several laboratories and emerging as a serious instrument for probing the intricacies of biological systems at high resolution [4–8]. Confocal microscopy was becoming more than just a novelty in the early 1980s due to the upswing in applications of widefield fluorescence to investigate cellular architecture and function [9–11]. As immunofluorescence techniques [12, 13], as well as the staining of subcellular structures using synthetic fluorophores [14], became widely practiced in the late 1970s, microscopists grew

Stephen W. Paddock (ed.), *Confocal Microscopy: Methods and Protocols*, Methods in Molecular Biology, vol. 1075,
DOI 10.1007/978-1-60761-847-8_3,

increasingly frustrated with their inability to distinguish or record fine detail in wide-field instruments due to interference by fluorescence emission occurring above and below the focal plane. It therefore comes as no surprise that the introduction of the laser scanning confocal microscope, featuring highly focused beam scanning in a raster pattern across the stationary specimen with the elimination of out-of-focus signal through the application of conjugate pinhole apertures, was immediately embraced by the research community.

The first edition of HTTP was functional for the transfer of hypertext documents, but was unable to support graphics, multimedia (audio and video), or proprietary file formats, such as Microsoft Word or Adobe PostScript. Likewise, the first prototype confocal microscopes were limited in their ability to readily process the potentially large amount of data that could be collected from three-dimensional specimens. In the mid-1980s, desktop computers, which would ultimately, in later years, be widely utilized to control sophisticated confocal microscopes, were still in their infancy with comparatively (by today's standards) slow processor speeds, memory capacity, and operating systems that were limited in their ability to handle graphics. Tasks that are routine on modern confocal microscopes, such as three-dimensional volume rendering, computer control of laser intensity and wavelength, and the creation of video sequences on the fly, were beyond the reach of most computers in the 1980s and early 1990s.

The first commercial confocal microscope prototype was developed by researchers at the Medical Research Council (MRC) Laboratory of Molecular Biology in Cambridge, United Kingdom during the late 1980s [15, 16]. The microscope was accompanied by a powerful software package, entitled SOM (Scanning Optical Microscope), which was amazingly advanced for the period and drew as much attention as the microscope itself. In fact, the software and frame store buffer were so efficient that many investigators ultimately employed them for routine wide-field imaging with conventional cameras. Introduced to the scientific community in 1987 as the Bio-Rad MRC 500, the laser scanning confocal microscope quickly gained widespread recognition in the early 1990s, and was utilized to achieve spectacular results that were previously unattainable with wide-field instruments [17, 18]. During the mid-1990s, as the confocal microscope was becoming a staple of many research programs, the Internet HTTP protocol started to rapidly evolve from a trivial request/response application into a true messaging vehicle capable of transferring a wide spectrum of media formats between localized servers and remote clients. Ultimately, HTTP would become the underlying foundation for electronically linking digitally encoded documents through a virtual international World Wide Web of interconnected computer systems.

By 1997, the Web was burgeoning in popularity due, in no small part, to the introduction of novel software applications, such as Java [19] and Flash [20], and the adaptation of standards for transmission of audio and video multimedia files. During this period, client software (termed "Web browsers") also became increasingly more sophisticated as the competing packages from various manufacturers were incrementally being equipped with the ability to display a larger array of image formats, interface with audio sound systems, and embed specialized "plug-in" modules to enable the control capabilities of emerging interactive (Java and Flash) software. The rapid advances in Internet software development were paralleled by equally dramatic steps in the capability of personal computers to multi-task and handle the continuously increasing hardware demands of video, audio, and other memory-hungry applications. At the turn of the century, a third critical factor in the utility of the Internet, search engine technology, had advanced to the stage where the millions of Web sites being cataloged on a daily basis could be logically categorized and sequentially hyperlinked (ranked) according to a variety of criteria for fast and efficient searches. The final component of the Web explosion from the year 2000 onward was the adoption of widespread home broadband Internet connections; broadband being defined as a connection of 768 kilobits per second (kbps) or higher downstream bandwidth (compared to the 36 kbps downstream bandwidth available over a phone line). In June of 2000, approximately 35 % of American adults had dial-up access to the Internet, with 3 % possessing broadband access. By April 2008, these numbers had shifted to 55 % of adults with broadband access, with a mere 9 % still using dial-up. The massive increase in broadband penetration rates vastly extended the practical reach of Web sites supporting rich content such as the above mentioned streaming video, high quality image galleries, and interactive java and flash applications, and enabled these Web sites to serve as a practical tool accessible outside of major institutions with dedicated Internet connections [21].

Advances in the development of computer hardware and software resources that led to widespread popularization of the Internet during the late 1990s and early twenty-first century also found their way into the evolution of confocal microscopes. These high speed computer systems, which could now be purchased for a couple thousand dollars, enabled the development of increasingly sophisticated software applications for confocal microscopy. New graphical interfaces were developed using Microsoft Foundation Classes [22] and the Visual C++ object-oriented programming language [23], featuring tab-style monitor display for image acquisition and processing, as well as computer control of lasers, photomultipliers, scanning mirrors (pan and zoom), and microscope configuration [24]. The introduction of acousto-optic tunable

filters and modulators [25] enabled fine control of specific region scanning and laser intensity, while advanced protocol control processor software [24] could be programmed through macro command scripts for tight control of sequential scanning and successive recording of events, such as fluorescence resonance energy transfer (FRET), photobleaching recovery techniques (FRAP and FLIP), photoactivation, and time-course studies.

As the Web grew in popularity and became a viable alternative to walk-in libraries, a majority of the relevant scientific publications in fields relating to confocal microscopy began to make their content available on-line in the form of abstracts, HTML documents, and downloadable portable document format (PDF; 26) files that could be viewed in a Web browser and printed locally. These journals are now formally indexed by such services as PubMed (National Center for Biotechnology Information and National Institutes of Health; 27), Chemical Abstracts (American Chemical Society; 28), and PhysicsWeb (Institute of Physics; 29), as well as being informally cataloged by the popular Internet search engines (i.e., Google and Yahoo!; 30, 31) and, to a lesser degree, through the numerous Web sites of researchers in the field [32, 33].

Today, virtually every laboratory involved with confocal microscopy has the potential ability to maintain a site that assists users, the general public, and interested scientists with information relating to equipment, specimens, scheduling, and image galleries, in addition to educational tutorials. Several Web sites [34–44] have been developed by researchers, students, and the microscope manufacturers to specifically address current educational topics in disciplines related to confocal microscopy; however, most of these sites are limited in scope. Unfortunately, exhaustive Web searches have revealed scant educational information other than hyperlinks directly from the search engine return pages to PubMed for the original research articles, which are often difficult to understand for beginning students. To address this issue, the microscopy educational Web sites described in detail below are being populated with information on confocal microscopy in the form of well-illustrated review articles, interactive Java tutorials, image galleries, links to related Web sites, and the original research reports on PubMed, as well as the sister indexing services.

2 Microscopy Educational Web sites

For the past 14 years, the Optical Microscopy Research Group in the National High Magnetic Field Laboratory at The Florida State University (FSU) has been involved in the construction of educational Web sites targeted at undergraduate and graduate students in microscopy. The Molecular Expressions Web site [45], which is the largest product of this effort and hosts approximately 35,000 unique

daily visitors (as determined by Internet Protocol; IP addresses), currently is 9500+ HTML pages in size and contains over 75 digital image galleries featuring a variety of contrast-enhancing techniques, such as phase contrast, fluorescence, darkfield, differential interference contrast (DIC), confocal, Hoffman modulation contrast, and brightfield. The site also offers hundreds of review articles on various topics in optical microscopy [46], which are accompanied by over 500 interactive Java tutorials that enable the visitor to experiment with variables in a manner similar to operating an actual microscope. Included in the many features on this site are an introduction to the physics of light and color, basic principles of the optical microscope, advanced and specialized contrast-enhancing techniques, fluorescence, photomicrography, digital image acquisition and processing, stereomicroscopy, laser scanning confocal microscopy, and a virtual museum of microscopes developed through the ages [47]. Similar Web sites are offered at no charge to the general public by Nikon (MicroscopyU; 48) and Olympus (Microscopy Resource Center; 49). Recently, Olympus has introduced an educational Web site (Olympus FluoView Resource Center; 43) dealing specifically with confocal microscopy.

Among the most useful features of the microscopy educational Web sites is that, unlike printed material, the dynamic nature of HTML enables the ability to continuously modify electronic documents in a timely manner in order to maintain current information. As an example, review articles and interactive tutorials dealing with rapidly expanding fields, such as the technology of diode and diode-pumped solid-state lasers [50, 51], can be easily modified to incorporate new information on these valuable light sources as it becomes available. In addition, Web-based tables and figures, such as the example in Table 1 cataloging the available laser sources for confocal microscopy (which is useful in comparing wavelength profiles during the complex task of matching fluorophore requirements with illumination sources), can be readily modified and maintained to ensure that the latest information is available. Finally, in contrast to the static reference sections of printed scientific publications, HTML listings of literature references can be hyperlinked to the originating journal Web sites or to indexing service databases, such as PubMed [27], which enable researchers and students to conveniently view abstracts and/or download PDF files of the original research reports, news commentaries, and review articles.

3 Laser and Arc-Discharge Lamp Spectral Lines in Wide-Field and Confocal

The compilation of currently available laser sources for confocal microscopy presented in Table 1 is an excellent example of a rapidly evolving research frontier that can greatly benefit from the dynamic nature of the Internet. New semiconductor continuous wave and

Table 1
Microscopy

Source	UV	Violet	Blue	Green	Yellow	Orange	Red	Near-IR
Ar-Ion	351, 364	–	457, 477, 488	514	–	–	–	–
Diode	–	405, 440	–	–	–	–	635, 640	650, 660, 670, 685
DPSS	355	430, 442	457, 473	532	556, 561	593	638	660, 671
He-Cd	325, 354	442	–	–	–	–	–	–
He-Ne	–	–	–	543	594	612	633	–
Kr-Ar	–	–	488	–	568	–	647	676
Kr-Ion	–	–	–	–	–	–	647	676, 752
Mercury	365	405, 436	–	546	579	–	–	–
Xenon	–	–	467	–	–	–	–	–
Mt Hal	365	435	495	520, 545	575	–	625	685

Compilation of the spectral lines from the ultraviolet to the near-infrared portions of the spectrum for useful lasers and arc-discharge lamps in wide-field fluorescence and laser scanning confocal microscopy. Traditional light sources for confocal microscopy are the argon-ion (Ar-Ion), krypton–argon (Kr-Ar), helium–cadmium (He-Cd), and helium–neon (He-Ne) gas lasers, while the new semiconductor lasers that are rapidly finding applications are the diodes and diode-pumped solid state (DPSS) versions. In wide-field fluorescence microscopy, fluorophores can be excited with the predominant spectral lines of the mercury, xenon, and metal halide (Mt Hal) arc-discharge lamps. Due to the rapid advances in semiconductor laser technology, new spectral lines should render this table obsolete within a year

pulsed lasers have been reported at an unprecedented rate over the past couple of years, necessitating periodic updates to this table in order to preserve the timeliness and accuracy of information presented to visitors. Other educational Web site features that require frequent monitoring are listings of Internet resources with hyperlinks to external Web sites that may be of interest to visitors. Typically about 10–15 % of the external links on the combined FSU microscopy educational Web sites require editing on a semi–annual basis due to changes in the URLs.

Addressing topics of interest to science education in the K-12 arena, the breeding ground for future researchers using confocal microscopy techniques, the Web programming team at FSU has developed a site entitled Science, Optics and You [52], which is a microscopy curriculum package being targeted at middle and high school teachers, students, and parents. These activities are designed to promote the asking and answering by students of fundamental questions related to light, color, and optics. The program begins with basic information about lenses, shadows, prisms, light and color, and related topics in optics, leading up to the application of

sophisticated instruments, such as microscopes, binoculars, digital cameras, and telescopes. The goal of Science, Optics and You is for students to acquire the skills with which they can conduct optical and microscopic analysis using entry-level microscopes on a variety of specimens, ultimately resulting in more advanced investigations on research instruments. This program is supported by Web-based student and teacher activities, interactive tutorials, a timeline in optics, and biographies of pioneers in light and optics. In addition, two low-cost microscopes designed for students, the Digital Blue QX3 (and QX5) and the Olympus MIC-D, are thoroughly reviewed, and a short introduction to confocal microscopy techniques is included. Illustrated in Fig. 1 are several interactive Java tutorials that serve as typical examples of the material designed for beginning students on the FSU microscopy and Science, Optics and You educational Web sites.

The interactive Java tutorial featured in Fig. 1a demonstrates the basic fundamentals of the optical astigmatism aberration [53]. Students learn from this tutorial that the aberration is manifested by the off-axis image of a specimen point appearing as a line or ellipse instead of a point. Depending on the angle of the off-axis rays entering the lens, the line image may be oriented in either of two directions, tangentially (meridionally) or sagittally (equatorially). The intensity ratio of the unit image will diminish, with definition, detail, and contrast being lost as the distance from the center is increased. Somewhat more complex in nature, the tutorial illustrated in Fig. 1b demonstrates how a de Sénarmont compensator

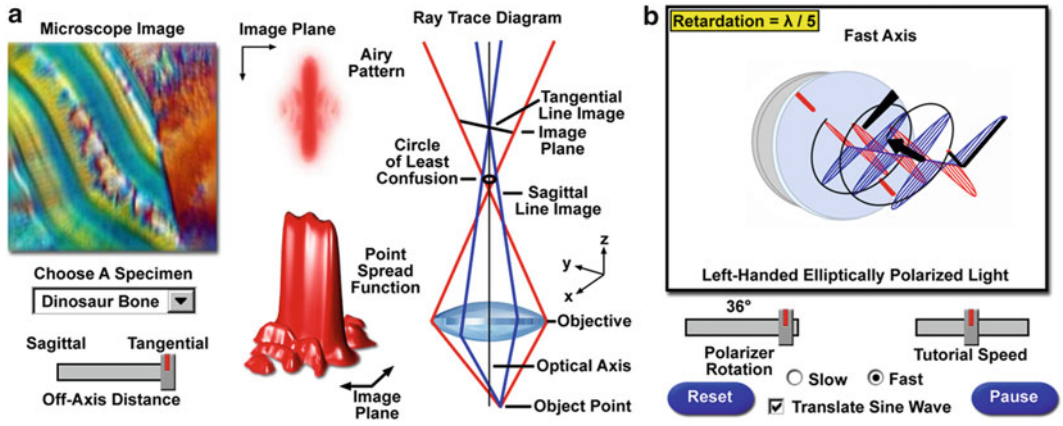

Fig. 1 Interactive Java tutorials based on common optical aberrations (astigmatism) (**a**) and the production of elliptically polarized light by a de Sénarmont compensator (**b**). Visitors to the Web site are able to operate the tutorials using sliders (off-axis distance and polarizer rotation angle), pull-down menus (specimen selection), and radio buttons (slow or fast compensator axis). The wavefront trajectories are dynamically controlled by the sliders in (**b**) and the entire compensator can be rotated using the cursor. Changes to the Airy pattern, point spread function, specimen image, and ray trace diagram (**a**) are continuously updated as the slider position is altered

(implemented by several of the manufacturers in commercial differential interference contrast microscopes) is composed of a linear polarizer combined with a quarter-wavelength retardation plate, and is capable of producing either linear, elliptical, or circularly polarized light, depending upon the orientation of the polarizer vibration axis with respect to the fast and slow axes of the retardation plate. This interactive tutorial explores the relationship between wavefronts emanating from the compensator as the polarizer is rotated through its useful range [54]. Using customized Java class libraries, the tutorial presented in Fig. 1b has been designed to rotate through three-dimensional virtual space using the mouse cursor.

More advanced tutorials [55] on the microscopy educational Web sites are designed to explore complex techniques, such as creation and optical displacement of the wavefront field in differential interference contrast, the origin of specimen contrast using a condenser annulus and phase ring in phase contrast microscopy, the interaction of birefringent materials with linearly and circularly polarized light in optical microscopy, and the effect of condenser numerical aperture in darkfield microscopy. In the fast-paced arena of digital imaging in optical microscopy, a large collection of tutorials [56] is available to teach students how the fundamental tools of digital image processing can be utilized to manipulate, rehabilitate, edit, resize, rotate, and store images captured with an optical microscope (or other digital image recording device). These interactive tutorials each consider a specific algorithm or related series of algorithms that are useful for processing digital images. In addition, review articles on each topic are included for in-depth study in far greater detail.

3.1 Confocal Microscopy Educational Web Sites

The Olympus FluoView Resource Center Web site [43] is primarily focused on delivering educational materials targeting laser scanning confocal microscopy. Included on this site are review articles and interactive Java tutorials on a variety of topics relating to confocal techniques, including basic fluorescence excitation and emission fundamentals, resolution and contrast, spectral bleed-through artifacts, acousto-optic tunable filters, objectives, lasers, photomultipliers, scanning systems, and signal-to-noise considerations. The Web site also contains an exhaustive listing of useful fluorochromes, which is periodically updated as new synthetic probes are reported, as well as an extended glossary of common terms that attempts to simplify the complex nomenclature of fluorescence microscopy and related techniques. A literature section on the site describes the most current books available on confocal microscopy and provides links to the appropriate pages from booksellers on the Internet. Two of the other FSU educational Web sites, Molecular Expressions [45] and Nikon's MicroscopyU [48], also contain extensive information on confocal microscopy, including review

articles, interactive tutorials, digital image galleries and streaming videos of time-lapse image sequences. The following discussion focuses primarily on these three Web sites with references to individual sections.

The broad range of applications available to laser scanning confocal microscopy and discussed on the Olympus FluoView Web site includes a wide variety of studies in neuroanatomy and neurophysiology, as well as morphological studies of a wide spectrum of cells and tissues. In addition, the growing use of new fluorescent proteins is rapidly expanding the number of original research reports coupling these useful tools to modern microscopic investigations. Other applications include fluorescence resonance energy transfer, stem cell research, photobleaching studies, lifetime imaging, multiphoton microscopy, total internal reflection, DNA hybridization, membrane and ion probes, bioluminescent proteins, and epitope tagging. Many of these powerful techniques are described in detail on the Web site while others are the subject of interactive tutorials. A series of specific review articles [57] focuses on a variety of relevant topics, including the colocalization of fluorophores, fluorescent proteins, optical highlighters, epitope tagging, stem cells, resonance energy transfer and photobleaching techniques (FRET and FRAP), multiphoton microscopy, total internal reflection (TIRFM), and in situ hybridization (FISH). The Web site also includes numerous image galleries and links to related resources on the Internet. The hyperlinked resources include manufacturers and distributors of fluorescent filters, digital cameras, antibodies, fluorescent protein vector sources, lasers, specimen chambers, photometric detectors, live-cell imaging supplies, courses and workshops on microscopy, and software for three-dimensional volume rendering.

One of the hallmark interactive tutorials on the FluoView Web site, a Java-powered laser scanning confocal microscope simulator [58], is illustrated in Fig. 2. This tutorial explores multi-laser fluorescence scanning confocal imaging coupled to transmitted DIC with the Olympus FluoView FV1000 microscope software interface as a model. Using a series of selectable prerecorded image stacks for specimens, the tutorial initializes with a randomly selected stack being scanned along the lateral **x**-**y** plane at a modest speed of 20 microseconds per pixel, and the detector channels being set very close to the optimum values with simultaneous scanning in all three channels. Imaging depth in the axial (**z**) direction is adjusted with the z-axis position slider (*see* Fig. 2) according to a range determined by the thickness of each specimen. Upon initialization, each channel corresponding to a fluorophore present in the specimen is activated and labeled with the specific probe being imaged. The transmitted light channel (TD) is turned off by default. Lasers are preassigned (and fixed) to the channels according to the following order: argon-ion (488 nm)—Channel 1; green helium–neon

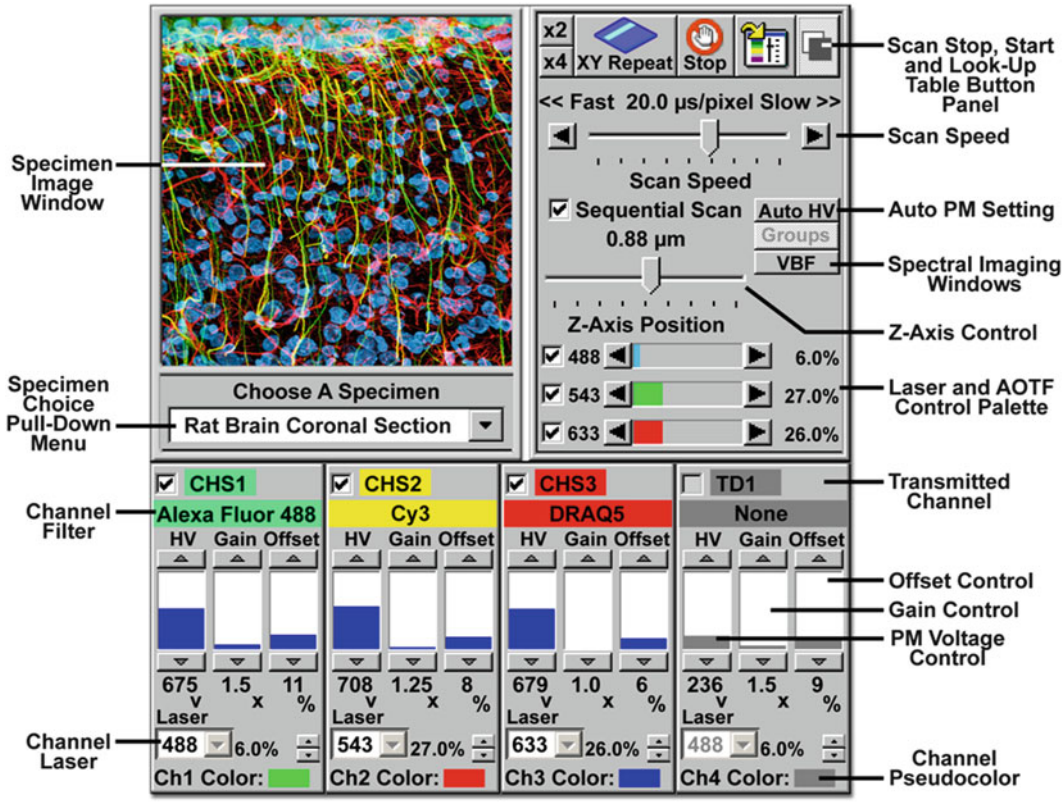

Fig. 2 Laser Scanning Confocal Microscope Simulator interactive tutorial based on the software interface of the Olympus FluoView FV1000 microscope. Specimens in the tutorial were acquired as optical stacks with the FV1000, and image parameters, including intensity, bleed-through, and noise levels, are based on the fluorophore emission spectral profiles. The tutorial is also equipped with a "Help" feature that enables the visitor to right-click on an object in the interface, such as a button, slider, or pull-down menu, to launch a pop-up that describes the function of that control

(543 nm)—Channel 2; and red helium–neon (633 nm)—Channel 3. The TD channel produces transmitted light differential interference contrast images using the argon-ion laser set at 488 nm.

Visitors are able to interact with the confocal microscope simulator tutorial by adjusting the voltage, gain, and offset values for each channel and immediately see the effect on the image. In addition, similar to the actual software, the tutorial is equipped with an automatic photomultiplier high voltage (Auto HV) control that maintains a constant signal level while increasing or decreasing the microscope scan speed. The individual laser intensities are also controllable (through a range of 0–100 %) with sliders and arrow buttons adjacent to each laser activation checkbox (identical with the actual software). Additional features that simulate the microscope software and add a realistic "feel" to the tutorial are the Auto Contrast control for a software best-guess

initial setting of the detector channel levels (typically utilized for pre-scanning a specimen), a look-up table for adjustment of the gamma, intensity, contrast, and pseudocolor for each channel, as well as simulation of rapid specimen scanning.

In order to simulate image acquisition of specimens having strongly overlapping fluorophore emission spectra using the spectral imaging detector channels, the confocal simulator tutorial is equipped with a dialog box illustrating the emission spectra of the selected fluorophores superimposed over the detector slit settings for channels 1 and 2 (the spectral imaging channels). In a manner similar to the microscope software, the tutorial allows users to observe the effects of altering slit size and wavelength range while the simulator is scanning a specimen in order to demonstrate in real-time how increasing or decreasing these variables affects specimen contrast, intensity, and spectral bleed-through. A unique feature of this tutorial is that simulation of bleed-through is based on the degree of overlap between actual fluorophore emission spectral profiles. In our laboratory, students and entry-level technicians are first trained using the confocal microscope simulator software, and must display a minimum level of understanding and expertise before they are deemed qualified to operate the actual microscope.

3.2 Confocal Microscopy: Laser Scanning Systems and Modes Tutorials

Fundamental to a basic understanding of laser scanning confocal microscopy is a working knowledge of the scanning system and the types of modes available to examine specimens and record images in three dimensions. The three basic requirements of a laser scanning confocal microscope system are to bring the laser illumination to a focal point on the specimen, scan a selected area of the surface in a raster pattern, and then gather only the secondary fluorescence that originates from the immediate region being excited by the focused laser beam. During scanning, the focal point size should exhibit even illumination and be maintained as small as possible, two requirements that necessitate the objective rear aperture being completely filled with light throughout the scanning cycle. The interactive tutorial illustrated in Fig. 3a examines how the galvanometer-driven mirrors and optical system of a typical confocal microscope are configured to enable the objective rear aperture to be continuously filled with light during the raster scanning operation [59].

The wide range of laser scanning modes available in the control software of most commercial confocal microscopes (*see* Fig. 3) enables investigators to fine-tune acquisition strategies in order to optimize data collection for three-dimensional imaging, time-lapse analysis, and a host of other specialized applications. Among the common scanning modes featured by most commercial microscopes are point, line, free line, parallel plane, and rectangle scanning over one or more dimensions. The interactive tutorial presented in Fig. 3b reviews various scanning mechanisms in confocal microscopy utilizing a cube-shaped virtual specimen [60].

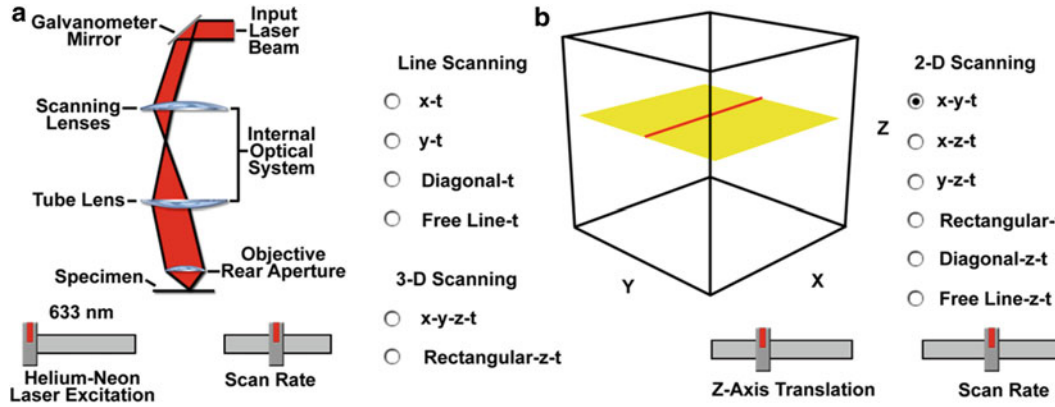

Fig. 3 Interactive Java tutorials describing the basic optical configuration of a typical laser scanning system (**a**) and the most common scanning modes available on commercial instruments (**b**). The scanning system configuration presented in (**a**) features a single galvanometer mirror, scanning lens, tube lens, and uses a single lens element to represent the objective rear aperture. A virtual laser beam incident on the galvanometer is scanned across the specimen surface (only the x-direction is shown in the tutorial). Scanning modes (**b**) are grouped into single line scanning, two-dimensional (2D), and three-dimensional (3D) categories that can be enabled using the appropriate radio button

One of the primary advantages of confocal microscopy is the ability to gather a stack of multiple images from relatively thick specimens through optical sectioning across a selected volume. Traditionally, serial sections are collected by raster scanning the x-y lateral dimensions in selected increments along the microscope optical (z) axis to produce a digital rendition of the specimen volume (3D scanning, x-y-z-t; Fig. 3b). However, in modern commercial instruments, scanning modes are extremely versatile and serial optical sections can also be collected diagonally in horizontal (Rectangular-z-t scanning mode; Fig. 3b) planes or vertically in single slices (x-z-t and y-z-t; 2D scanning in Fig. 3b) to produce profile views of the specimen. Point scanning (not illustrated in the tutorial) allows the instrument to collect data from a single point at any location within the scanning range of the specimen volume. In practice, point scanning enables rapid collection of data that can be utilized to monitor fluorescence emission intensity changes in dynamic settings, such as localized ion concentration investigations in living cells. Line scanning along the x, y, or z axis, or diagonally between axes, provides intensity information across a single set of coordinates in the lateral or axial dimension. This scanning mode is useful for obtaining accurate quantitative information about rapid physiological events, such as calcium waves or sparks. The free line scanning mechanism, available in some commercial configurations, can be used to gather intensity changes over a period of time along the length of a freely drawn line, such as the trace of a neural axon or across a cellular junction.

3.3 Confocal Microscopy: Laser Tutorials

The laser systems commonly employed in point-scanning confocal microscopy are high-intensity monochromatic light sources, emitting one or more spectral lines, which are useful as tools for a variety of techniques including optical trapping, lifetime imaging studies, spinning disk systems, photobleaching recovery, photoactivation and photoconversion, as well as total internal reflection fluorescence [61]. Many of the common lasers used in confocal microscopy are the subject of review articles and interactive tutorials on the Olympus FluoView Resource Center Web site [43, 62]. Among the lasers reviewed on the site are the traditional argon-ion, helium–cadmium, helium–neon, krypton–argon, and the newer diode lasers.

As a distinguished and heavily utilized member of the common and well-explored family of ion lasers, the argon-ion laser [63] operates in the visible and ultraviolet spectral regions by utilizing an ionized species of the noble gas argon. Argon-ion lasers function in continuous wave mode when plasma electrons within the gaseous discharge collide with the excited laser species to produce light. The argon-ion laser is capable of producing approximately 10 wavelengths in the ultraviolet region and up to 25 in the visible region, ranging from 275 to 363.8 nm and 408.9 to 686.1 nm, respectively (*see* Fig. 4a). In the visible light spectral region, the lasers can produce up to 100 W of continuous-wave power with the output concentrated into several strong lines (primarily the 488 and 514.5 nm transitions). The gain bandwidth on each transition is on the order of 2.5 GHz. Argon-ion gas laser discharge tubes have a useful life span ranging between 2,000 and 5,000 h, and operate at gas pressures of approximately 0.1 Torr.

An unfortunate side effect of the high discharge currents and low gas pressure employed by argon-ion lasers is an extremely high plasma electron temperature, which generates a significant amount of heat. In most cases, high power (2 to 100 W) argon-ion

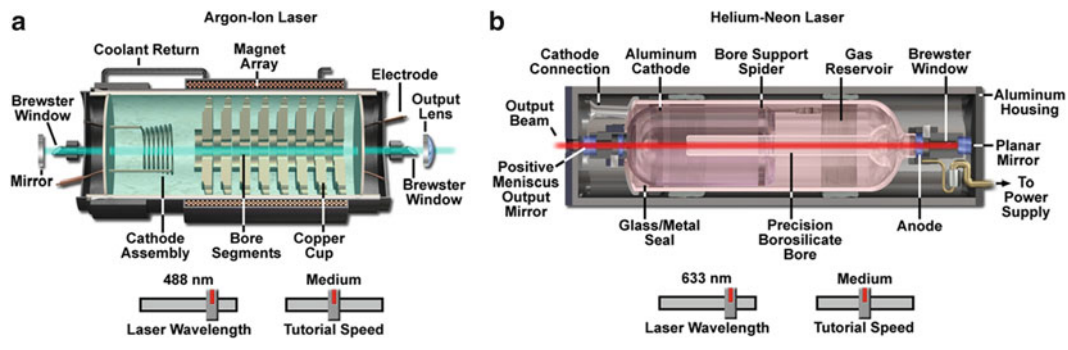

Fig. 4 Animated laser interactive Java tutorials describing the internal anatomy and laser cavity of the two most common lasers used in confocal microscopy. (**a**) Argon-ion gas laser emitting five spectral lines (351, 364, 457, 488, and 514 nm). (**b**) Helium–neon gas laser also emitting five spectral lines (543, 594, 612, 633, and 1,523 nm). The tutorials are both controlled with wavelength and speed sliders

laser systems are water-cooled through an external chiller, but lower power (5–150 mW) models can be cooled with forced air through an efficient fan. Argon-ion lasers utilized in confocal and other fluorescence microscopy techniques are generally of the lower power variety, which produce between 10 and 100 mW of power in TEM(00) mode at 488.0 nm. The laser cavity for these smaller systems is approximately 35–50 cm in length and about 15 cm in diameter, and can be housed in a small cabinet with an integral fan to supply fresh, cool air.

Helium–neon lasers (Fig. 4b) are among the most widely utilized laser systems for a broad range of biomedical and industrial applications, and display a superior Gaussian beam quality that is virtually unrivaled by any laser [64]. These lasers are readily available at relatively low cost, have compact size dimensions, and exhibit a long operating life (often reaching 40,000–50,000 h). The low power requirements, superior beam quality (virtually a pure Gaussian profile), and simple cooling requirements (convection) make helium–neon lasers the choice system for many confocal microscopes. In the past, the application of helium–neon lasers in confocal microscopy was somewhat hampered by the relatively low intensity and red emission wavelength. This difficulty has been overcome in part by the development of new lasers having additional spectral lines. The emission at 633 nm (termed the He-Ne line) of the common helium–neon laser has been supplemented by development of variants having emissions in the green (543 nm), yellow (594 nm), orange (612 nm), and near infrared (1,523 nm) spectral regions. Typical power output values for the 633 nm red spectral line range from 0.5 to 10 mW up to a maximum of about 75 mW. The introduction of semiconductor and diode lasers having spectral lines in similar wavelength regions may ultimately lead to a reduction in the use of helium–neon lasers for confocal microscopy.

3.4 Confocal Microscopy: Photomultiplier Tutorials

In modern wide-field fluorescence and laser scanning confocal optical microscopy, the collection and measurement of secondary emission gathered by the objective can be accomplished by several classes of photosensitive detectors, including photomultipliers, photodiodes, and solid-state charge-coupled devices (CCDs). In confocal microscopy, fluorescence emission is directed through a pinhole aperture positioned near the image plane to exclude light from fluorescent structures located away from the objective focal plane, thus reducing the amount of light available for image formation. As a result, the exceedingly low light levels most often encountered in confocal microscopy necessitate the use of highly sensitive photon detectors that do not require spatial discrimination, but instead respond very quickly with a high level of sensitivity to a continuous flux of varying light intensity [65].

Photomultipliers, which contain a photosensitive surface that captures incident photons and produces a stream of photoelectrons to generate an amplified electric charge, are the popular detector choice in many commercial confocal microscopes. These detectors contain a critical element, termed a photocathode, capable of emitting electrons through the photoelectric effect (the energy of an absorbed photon is transferred to an electron) when exposed to a photon flux. The general anatomy of a photomultiplier consists of a classical vacuum tube [66] in which a glass or quartz window encases the photocathode and a chain of electron multipliers, known as dynodes, followed by an anode to complete the electrical circuit. When the photomultiplier is operating, current flowing between the anode and ground (zero potential) is directly proportional to the photoelectron flux generated by the photocathode when it is exposed to incident photon radiation.

In laser scanning confocal microscopy, the specimen is scanned in a raster pattern by the focused illumination beam, and the resulting fluorescence emission forms a point image that is sequentially detected by a photomultiplier. Most commercial confocal microscopes feature photomultipliers that are limited in dynamic range to 8 bits or 256 gray levels with a wavelength-dependent detection efficiency ranging between 15 and 30 %. Compared to cooled CCD cameras, which typically feature a 10 to 14-bit dynamic range scale and 40–60 % detection efficiency over a wide wavelength range, photomultiplier performance is significantly less. However, in a majority of confocal applications (especially live-cell imaging; 67) fewer than 255 photons per pixel are ever collected, well within the dynamic range of the photomultiplier tube. Furthermore, the excellent linearity of the photomultiplier response and background noise rejection properties renders this detector ideal for confocal microscope applications.

In the side-on photomultiplier tube design, photons impact an internal photocathode and eject electrons from the front face (as opposed to the rear side as in the end-on designs). These ejected photoelectrons have trajectories angled at the first dynode, which in turn emits a larger quantity of electrons angled at the second dynode (and so on). Incident light is detected through the curved side of the envelope in side-on photomultipliers [68]. Due to their high performance ratings and relatively low cost, side-on photomultiplier designs are the most widely used tubes for general photometric applications, such as spectrophotometry, fluorimetry, and laser scanning confocal microscopy.

Channel photomultipliers represent a new head-on monolithic design that incorporates a unique detector having a semitransparent photocathode deposited onto the inner surface of the entrance window. The photomultiplier features similar functionality to conventional units, but with dramatically increased sensitivity and

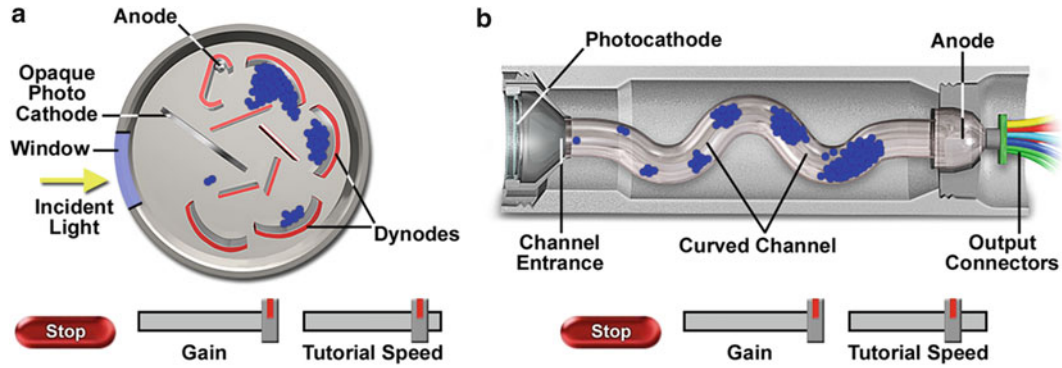

Fig. 5 Animated interactive Java tutorials describing and illustrating the internal anatomy of a side-on (**a**) and channel (**b**) photomultiplier. The tutorials depict cut-away drawings of the photomultiplier tubes with virtual photons, represented by *yellow arrows*, incident on the photocathodes to produce photoelectrons (*blue spheres*). Operation of the tutorial includes a gain slider to increase or decrease the number of electrons created each time an electron collides with the channel, and the tutorial speed slider to regulate the speed of the electrons passing through the photomultiplier. The tutorial can be halted at any point by clicking on the stop button (Color figure online)

high quantum efficiency. Individual photoelectrons released by the photocathode enter a narrow and curved semiconductive channel that serves in place of the traditional dynode chain. Each time an electron impacts an inner wall of the channel, multiple secondary electrons are emitted. The interactive tutorial presented in Fig. 5b explores how electrons are multiplied within the conductive chain of a channel photomultiplier [69].

3.5 Confocal Microscopy: Fluorophore Colocalization Tutorials

Two or more fluorescence emission signals can often overlap in digital images recorded by confocal microscopy due to their close proximity within the specimen. This effect is known as colocalization and usually occurs when fluorescently labeled molecules bind to targets that lie in very close or identical spatial positions. Colocalization is an important concept that students must learn to differentiate from spectral bleed-through. The interactive tutorial described in Fig. 6 explores the quantitative analysis of colocalization in a wide spectrum of specimens [70] that were specifically designed either to demonstrate the phenomenon, or to alternatively provide examples of fluorophore targets that lack any significant degree of colocalization.

Colocalization, in a biological manifestation, is defined by the presence of two or more different molecules residing at the same physical location in a specimen [71, 72]. Within the context of a tissue section, individual cell, or subcellular organelle viewed in the microscope, colocalization may indicate that the molecules are attached to the same receptor, while in the context of digital imaging, the term refers to colors emitted by fluorescent molecules sharing the same pixel in the image. In confocal microscopy, specimens

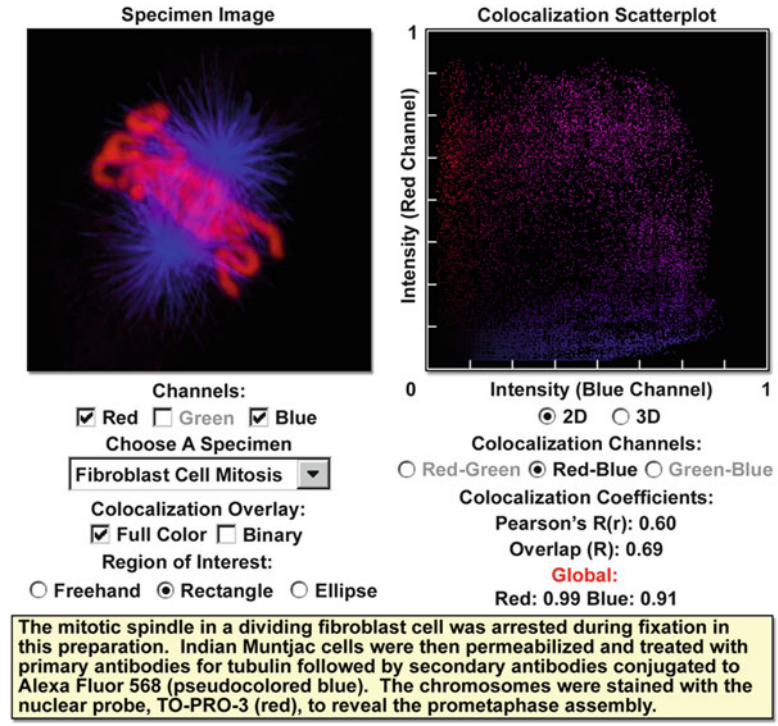

Fig. 6 Colocalization scatterplot analysis interactive tutorial of multiply stained specimens in confocal microscopy. The specimen data collected with the microscope is presented in the specimen image window, while the corresponding scatterplot is graphed in the neighboring window. Plots of the available channel permutations (*Red-Green*, *Red-Blue*, and *Green-Blue*) can be displayed using the Colocalization Channels set of radio buttons. In addition, each channel in the Specimen Image window can be toggled on or off using the checkboxes in the Channels menu. A three-dimensional rendering of the colocalization scatterplot (number of pixels plotted on the *z* axis) can be obtained by activating the 3D radio button. This view can be rotated within the window using the mouse cursor. Colocalization coefficients automatically displayed beneath the scatterplot graph include Pearson's, Overlap, and Global (k1 and k2), as described on the Web site [70]

are recorded as a digital image composed of a multi-dimensional array containing many volume elements termed voxels that represent three-dimensional pixels. The size of a voxel (or detection volume) is determined by the numerical aperture of the objective and the illumination wavelength (which are combined to determine the lateral resolution), as well as the confocal detector pinhole diameter (z-axis resolution). Thus, the colocalization of two fluorescent probes in a specimen, such as Alexa Fluor 488 having green emission and Cy3 with orange-red emission, is represented in the image [73] by pixels containing both red and green color contributions (often producing various shades of orange and yellow).

It is important to note that colocalization does not refer to the likelihood that fluorophores with similar emission spectra will appear in the same pixel set in the composite image. Accurate colocalization analysis is only possible if the fluorescence emission spectra are sufficiently well separated between fluorophores and the correct filter sets (or spectral slit widths) are used during the acquisition sequence. If spectral bleed-through artifacts are present because of a high degree of spectral overlap between the fluorophore emission spectra, or due to the use of incorrect filter combinations or scanning configuration, colocalization measurements will be meaningless. To avoid artifacts, the fluorophores must be carefully matched to the power spectrum of the illumination source (laser lines in confocal microscopy) to obtain the maximum excitation efficiency while still maintaining a useful degree of separation between emission wavelengths. In most cases, the judicious choice of fluorophores for colocalization analysis is paramount in obtaining satisfactory results.

3.6 Confocal Microscopy: Spectral Bleed-Through Tutorials

Bleed-through (often termed crossover or crosstalk) of fluorescence emission, due to the very broad bandwidths and asymmetrical spectral profiles exhibited by many of the common fluorophores, is a fundamental problem that must be addressed in both wide-field and laser scanning confocal fluorescence microscopy. The phenomenon is usually manifested by the emission of one fluorophore being detected in the photomultiplier channel or through the filter combination reserved for a second fluorophore. Bleed-through artifacts often complicate the interpretation of experimental results, particularly if subcellular colocalization of fluorophores is under investigation or quantitative measurements are necessary, such as in resonance energy transfer (FRET) and photobleaching (FRAP) studies. Identification of bleed-through artifacts and their differentiation from colocalization is the subject of several interactive tutorials and review articles on the Olympus FluoView Resource Center Web site [70, 74–76].

The interactive tutorial illustrated in Fig. 7 explores spectral bleed-through [76] in laser scanning confocal microscopy and the mechanisms available to reduce or eliminate the artifact. Fluorescence emission from the specimen is displayed in each of three separate photomultiplier detection channels, labeled Ch1, Ch2, and Ch3, which are positioned in adjacent windows above the tutorial control panel. Upon initialization, the laser output power settings are set to levels that normally exhibit a significant amount of spectral bleed-through from one channel to the next when imaging adequately labeled specimens in order to clearly demonstrate the manifestations to beginning students. The primary exercise of this tutorial is designed to provide instruction and practice on how to control bleed-through by proper adjustment of the laser power, photomultiplier voltage and gain, and the

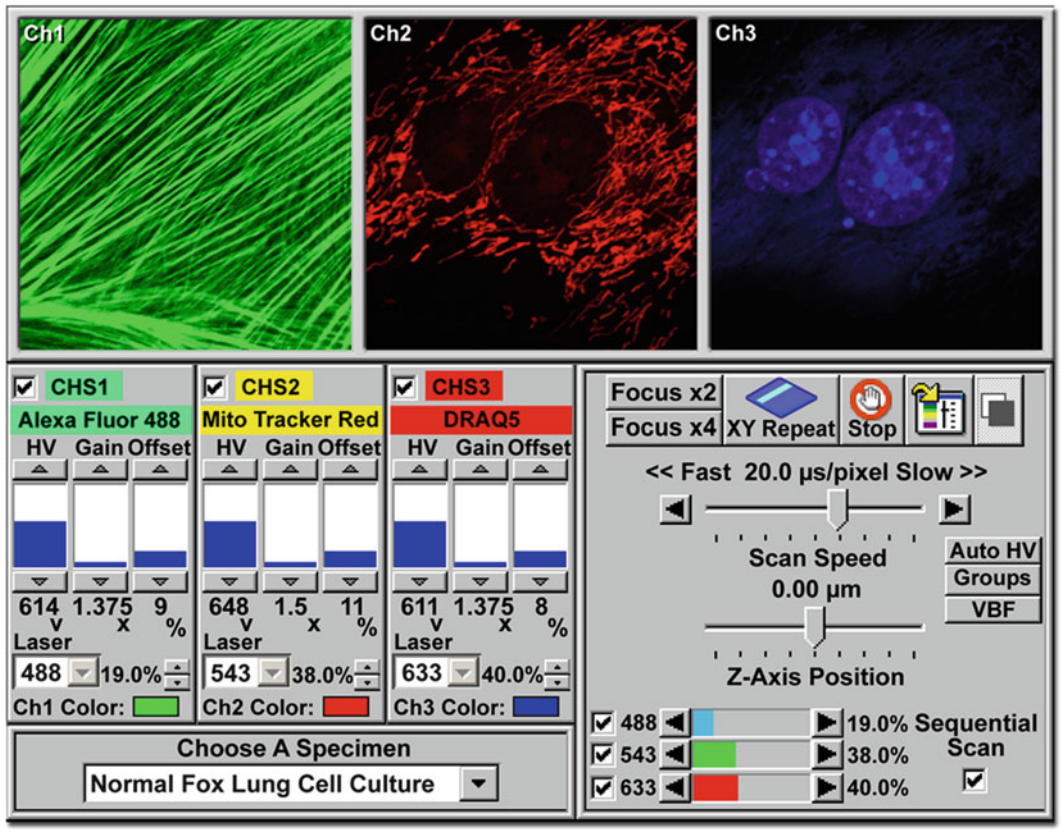

Fig. 7 Interactive Java tutorial designed to demonstrate spectral bleed-through with triple-labeled specimens in confocal microscopy. The tutorial features a similar control panel motif to the confocal microscope simulator tutorial [58], except that each channel is provided with a separate image window to more clearly demonstrate bleed-through artifacts from one channel into another. The sequential scan checkbox, which is not activated by default, can be used to demonstrate the presence and absence of bleed-through

detector entrance slit bandwidths (in spectral imaging instruments) or fluorescence emission barrier filter (Channel 3 in the tutorial) wavelength profile.

In order to operate the tutorial, users can employ the HV, Gain, and Offset sliders for each channel to adjust the signal level and quality by clicking on the arrow buttons at the top and bottom, or anywhere inside the indicator boxes (each containing a gray level bar; *see* Fig. 7). When the channel voltage, gain, and offset values are changed, the level bar is automatically adjusted to show the new value, which is also indicated numerically beneath the indicator box. These values can also be adjusted proportionally, by clicking on the Auto HV button, in order to maintain constant signal levels when increasing or decreasing the scan speed. Laser intensity values for the individual illumination sources can be controlled (through a range of zero to 100 %) with the sliders and arrow buttons adjacent to each laser activation checkbox. The lasers can also be toggled on or off using the appropriate checkbox.

The best fluorophores for confocal or wide-field fluorescence microscopy have absorption maxima that closely match the laser or arc-discharge spectral lines utilized to excite the probe. Choosing fluorophores with the highest quantum yields for the least abundant targets will assist in balancing overall fluorescence emission. In addition, probes with narrow emission spectra may dramatically reduce the problem of bleed-through, but will not eliminate it altogether. The optical filter sets chosen to examine fluorophore emission should be closely matched to the spectral profiles of the probe with regards to bandwidth size and location. Also, interference filter blocking levels often vary by manufacturer and should be checked.

Additional interactive tutorials on the Olympus FluoView Web site relating to bleed-through when imaging synthetic fluorophores and fluorescent proteins include an analysis [77] of fluorescent probe excitation efficiency as a function of laser wavelength (tutorial not illustrated) and a discussion of choosing fluorophore combinations for confocal microscopy (*see* Fig. 8). The fluorophore excitation efficiency tutorial examines why the absorption and fluorescence emission spectral profiles of a fluorophore are two of the most important criteria that must be scrutinized when selecting probes. In addition to the wavelength range of the absorption and emission bands, the molar extinction coefficient for absorption and the quantum yield for fluorescence emission should be considered. At laser excitation levels that do not saturate the fluorophore, fluorescence intensity is directly proportional to the product of the extinction coefficient and the quantum yield. This interactive tutorial examines how these relationships can be utilized to match fluorophores with specific lasers for confocal microscopy.

The tutorial addressing requirements for choosing fluorescent protein and synthetic fluorophore combinations (Fig. 8) addresses the fact that the judicious choice of probes is paramount in obtaining the best target signal while simultaneously minimizing bleed-through artifacts. This interactive tutorial is designed to explore the matching of dual fluorophores with efficient laser excitation lines, calculation of emission spectral overlap values, and determination of the approximate bleed-through level that can be expected as a function of the detection window wavelength profiles.

The Nikon MicroscopyU Web site [48], also being constructed and hosted at FSU, is built around the Molecular Expressions model to act as a sister site, but contains a wealth of exclusive information relating to the microscopy instrumentation, digital cameras, and imaging software developed by Nikon. In addition, MicroscopyU hosts the annual Small World Photomicrography competition [78] and features interactive tutorials and review articles on basic and advanced techniques in optical microscopy. Covered in depth are the principles of resolution, numerical aperture, depth of field, image

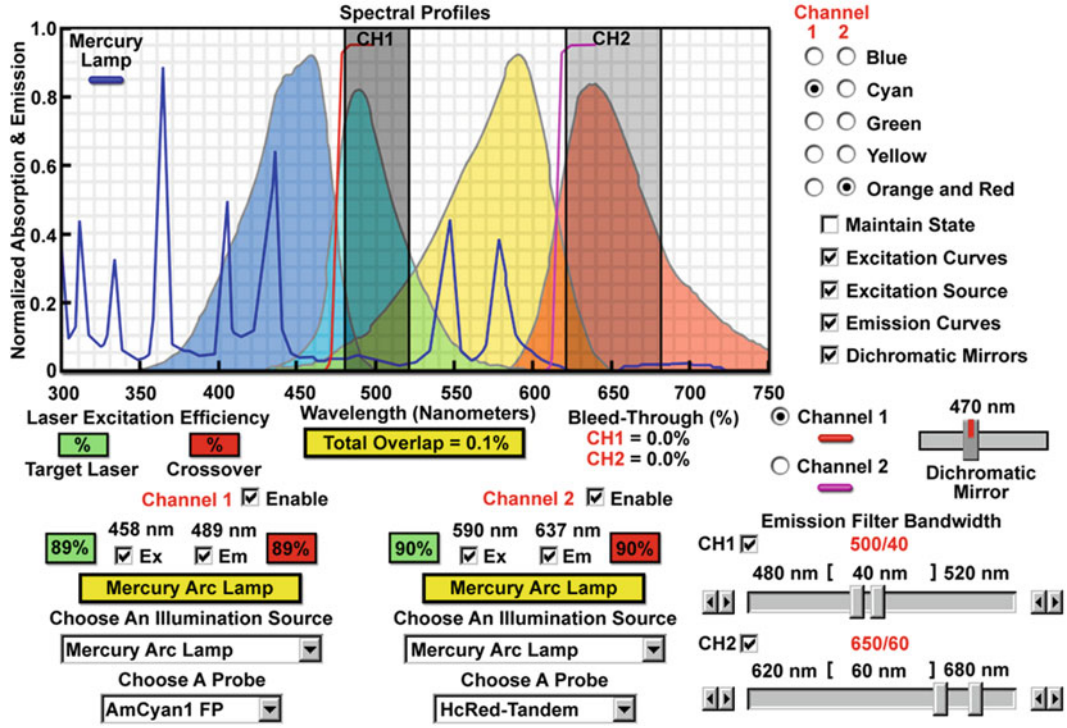

Fig. 8 Interactive Java tutorial designed to aid in determining spectral parameters for imaging two fluorescent proteins or synthetic fluorophores simultaneously. The tutorial initializes with the absorption and fluorescence emission spectral profiles from a useful combination of fluorescent proteins (CFP AmCyan1 and HcRed-Tandem) appearing in the Spectral Profiles window superimposed over the emission spectrum of a mercury arc-discharge lamp. Also included in the window upon initialization are the profiles of dichromatic mirrors appropriate for the fluorophores, as well as the suggested starting points for the Emission Filter Bandwidth profiles. The mouse cursor can be used to vary parameters, such as the width of emission filters, cut-on wavelength of the dichromatic mirrors, or to disable one of the image channels. Radio buttons (*upper right*) are available to choose fluorescent protein emission color classes (*blue*, *cyan*, *green*, *yellow*, *orange*, and *red*). The illumination source can be toggled between arc-discharge lamps and lasers (Color figure online)

brightness, objective working distance, field of view, conjugate planes, and the useful magnification range, as well as comprehensive discussions of the microscope optical train, infinity optical systems, aberrations, and microscope objectives. As is the case with Molecular Expressions, each review article on MicroscopyU is accompanied by one or more interactive tutorials to assist students in assimilating difficult concepts. Several reviews and tutorials featured on MicroscopyU target the basic properties and imaging parameters for fluorescent proteins. In addition, new sections on live-cell imaging are being constructed that discuss how to keep cells alive on the microscope, and cell motility streaming videos with and without fluorescent proteins are being staged for the site.

4 Advanced Imaging Techniques with Fluorescent Proteins

Over the past decade, fluorescent proteins have heralded a new era in cell biology by enabling investigators to apply molecular cloning methods, fusing the fluorophore moiety to a wide variety of protein and enzyme targets, in order to monitor cellular processes in living systems using optical microscopy and related methodology [79–81]. When coupled to recent technical advances in wide-field fluorescence and confocal microscopy, including ultra-fast low light level digital cameras and multitracking laser control systems, the green fluorescent protein and its color-shifted genetic derivatives have demonstrated invaluable service in many thousands of live-cell imaging experiments. Current efforts on the microscopy Web sites discussed above center on developing review articles, image galleries, literature source links, and interactive tutorials targeted at undergraduate-level education in fluorescent protein technology.

Among the most remarkable attributes of the original green fluorescent protein derived from the *Aequorea victoria* jellyfish, as well as the more recently developed palette of color-shifted genetic variants, is that the entire 27 kDa polypeptide structure is essential for the development and maintenance of fluorescence in this very remarkable family of proteins [82]. The principle fluorophore (often termed a chromophore) is a tripeptide consisting of the residues serine, tyrosine, and glycine at positions 65–67 in the sequence. Although this simple amino acid motif is commonly found throughout nature, it does not generally result in fluorescence.

A broad range of fluorescent protein genetic variants have been developed [83] over the past several years that feature fluorescence emission spectral profiles spanning almost the entire visible light spectrum. Mutagenesis efforts on the original jellyfish green fluorescent protein have resulted in new fluorescent probes that range in color from blue to yellow [84], and are some of the most widely used in vivo reporter molecules in biological research. Longer wavelength fluorescent proteins, emitting in the orange and red spectral regions, have been developed from the marine anemone, *Discosoma striata*, and reef corals belonging to the class Anthozoa [85]. Still other species have been mined to produce similar proteins having cyan, green, yellow, orange, and deep red fluorescence emission [79]. Developmental research efforts are ongoing to improve the brightness and stability of fluorescent proteins, thus improving their overall usefulness.

Compared to many traditional synthetic fluorophores, which are often toxic or photoreactive, the use of fluorescent proteins is minimally invasive for living cells, enabling visualization and recording of time-lapse image sequences for extended periods of time. Furthermore, continued advances in genetically fine-tuning the properties of fluorescent protein variants have led to increased

brightness levels, improved photostability, and significantly better expression in mammalian cells [86]. These factors have stimulated and nurtured a wide variety of investigations of protein dynamics and function using fluorescent protein chimeras imaged at low light intensities for many hours to extract valuable information about changes in the steady-state distribution. Unfortunately, time-lapse imaging alone is unable to reveal the kinetic properties of a protein to determine, for example, whether it is undergoing association with other components, freely diffusing, or bound to an immobile scaffold.

The collective photobleaching techniques, including fluorescence recovery after photobleaching (FRAP and the inverse, iFRAP), fluorescence loss in photobleaching (FLIP), and fluorescence localization after photobleaching (FLAP), have been extremely useful when combined with fluorescent proteins to examine protein dynamics in living cells [87–90], as illustrated in Fig. 9. These techniques have enjoyed increasing popularity in the past few years due to the development of laser scanning confocal microscopes equipped with acousto-optic tunable filters (AOTFs) capable of selecting discrete regions of interest that can be selectively bleached with short bursts of high laser power [88]. The various photobleaching techniques are differentiated by the size and location of the bleached region, the required number of bleaching events, and the manner in which recovery of fluorescence

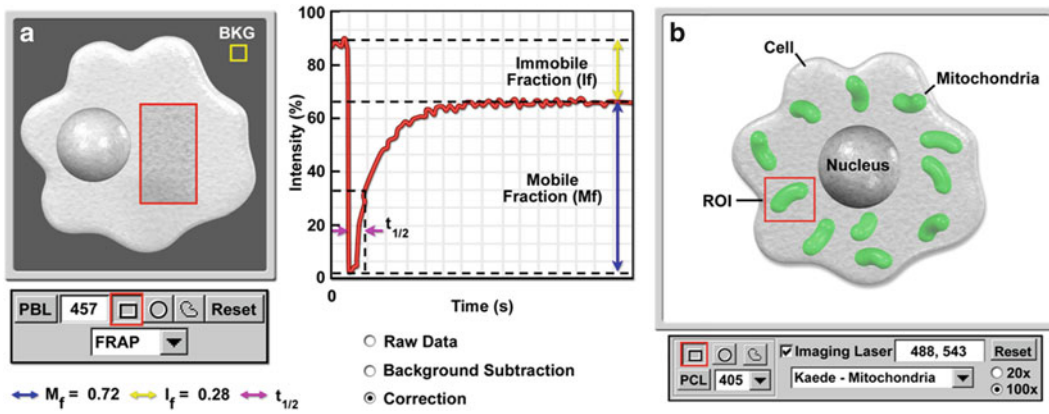

Fig. 9 Interactive Java tutorials exploring the dynamics of photobleaching (**a**) and photoactivation/photoconversion kinetics (**b**) in living cells with fluorescent proteins. In fluorescence recovery after photobleaching (FRAP) studies (**a**), fluorescent molecules in a selected region of interest (ROI) are photobleached and the recovery of fluorescence into the area is monitored as a function of time. Visitors can use the ROI toolbox to select rectangular, oval, or freehand areas, and then click on the photobleach button (PBL) to evoke a simulation of bleaching throughout the region. Recovery of fluorescence and the kinetic parameters are shown in real-time on the accompanying graph. The tutorial demonstrates inverse FRAP, photoactivation, fluorescence loss in photobleaching (FLIP), and spatial techniques. Similar tools are employed for the photoconversion tutorial (**b**), which details individual organelles (i.e., mitochondria) as candidates for photoconversion or photoactivation. Among the proteins featured in this tutorial are Kaede, Eos, Dronpa, KFP, PA-GFP, and PS-CFP

is analyzed. The FSU microscopy educational Web sites examine photobleaching techniques with review articles, interactive Java tutorials (*see* Fig. 9), and streaming videos.

The precise location and nature of the interactions between specific molecular species in living cells is of major interest in many areas of biological research, but investigations are often hampered by the limited resolution of the instruments employed to examine these phenomena. Conventional wide-field fluorescence microscopy enables localization of fluorescently labeled molecules within the optical spatial resolution limits defined by the Rayleigh criterion, approximately 200 nm (0.2 μm). However, in order to understand the physical interactions between protein partners involved in a typical biomolecular process, the relative proximity of the molecules must be determined more precisely than diffraction-limited traditional optical imaging methods permit. The technique of fluorescence resonance energy transfer (FRET), when applied to optical microscopy [91–93], permits determination of the approach between two molecules within several nanometers, a distance sufficiently close for molecular interactions to occur.

One of the major obstacles to the widespread implementation of FRET investigations in living cells has been the lack of suitable methods for labeling specific intracellular targets with the appropriate fluorophores. The recent development of fluorescent proteins possessing a wide array of spectral profiles (from 450 to 650 nm) and the increasing sophistication of protein chimeras (fusions as well as biosensors) has resulted in a number of potential fluorescent protein pairs that are useful in FRET experiments. Several interactive tutorials on the FSU microscopy education Web sites (*see* Fig. 10) have been designed to address this issue and should be useful in enabling investigators to choose fluorescent protein combinations that will properly exhibit FRET characteristics and allow for the maximum dynamic range in order to optimize sensitivity when planning experiments.

5 Tips on Construction of Educational Web Sites

As of the early twenty-first century, basic computer technology has become advanced to the point that almost every scientific research laboratory in the world has at least access to a desktop or laptop personal computer, while many are equipped with a workstation for every student and technician. This fact, coupled with the dramatic expansion in the geographic availability of broadband connections to the Internet over the past several years, has greatly improved the ability of students, researchers, and faculty members to build and host their own Web sites. Even personal desktop computers can now be easily configured with economical Web server software that is capable of handling low to moderate traffic loads

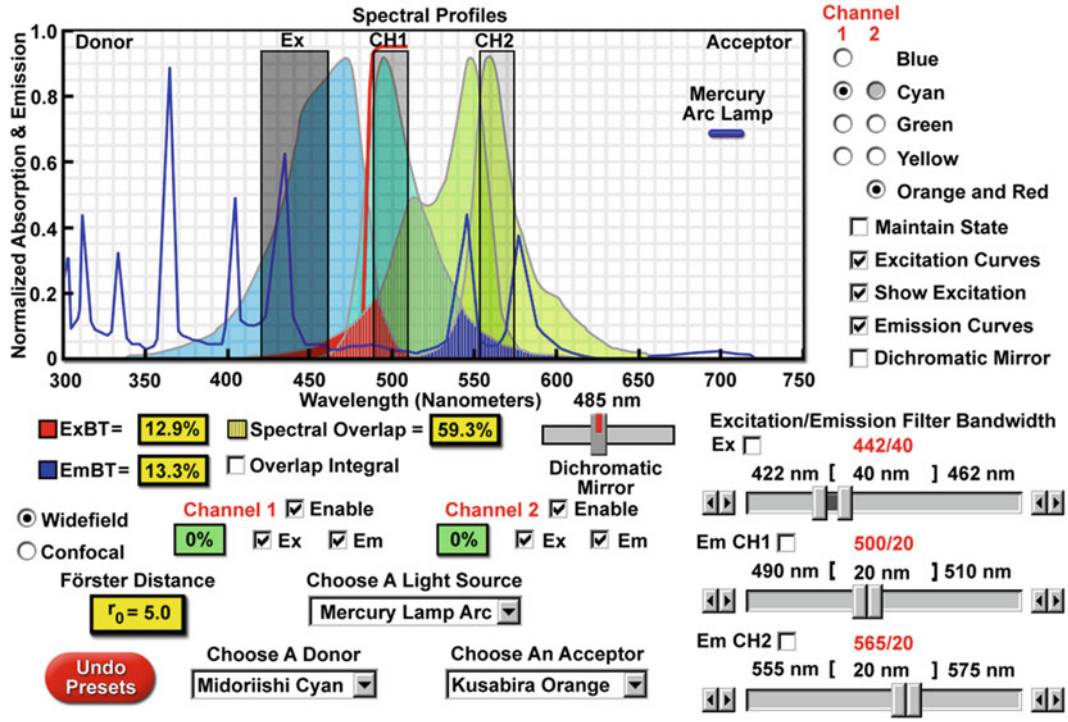

Fig. 10 Interactive Java tutorial examining useful fluorescent pairs for resonance energy transfer (FRET) studies. The tutorial initializes with the normalized absorption and emission spectral profiles of selected fluorophores, appearing in the window superimposed over the emission spectrum of a mercury arc-discharge lamp. Visitors can alter the light source (lasers and arc lamps are available) and use pull-down menus to access additional fluorophores. As new parameters are chosen, several variables, including the excitation and emission bleed-through, spectral overlap, and Förster distance are automatically determined by the tutorial and displayed in the window. In order to determine the optimum filter combination for a specific pair of proteins, the visitor can choose a dichromatic mirror and adjust the excitation filter profile (width and location), as well as the emission filter profiles for the donor and acceptor. To aid in developing usable filter sets, an Apply Presets button can be used to provide suggestions for the initial settings

with ease. The following sections briefly review many of the critical aspects involved with establishing a presence on the Web, including servers, HTML page creation, image compression, construction of interactive tutorials, and preparing digital videos for transmission across the Internet.

5.1 Web Servers

The term "Web server" refers to a software program, usually installed on a fairly robust computer having redundant (failover and backup) hardware features, which responds to an incoming connection from a remote computer (termed the client) and provides a service to the caller. The "service" provided by the server can be delivery of an HTML or PDF document, a digital video stream, Microsoft PowerPoint presentation, or a wide spectrum of other files, images, and electronic documents. Computers can have multiple copies of

server software running simultaneously, each hosting a different Web site, e-mail post office, or file transfer protocol (FTP) server. Like all computers that are connected to the Internet, servers have a unique Internet Protocol (IP) address and usually at least one domain name (and often more than one) for each Web site or other service they are hosting. The most familiar aspect of Web servers is the domain name, which is often referred to as a URL (Uniform Resource Locator) and is unique for every computer on the Internet. For example, the Molecular Expressions Web site communicates with all other computers on the Internet using a single IP address: 146.201.250.172, but can be alternatively, and far more conveniently, located using the domain name http://micro.magnet.fsu.edu or http://microscopy.fsu.edu. The latter domain name is commonly referred to as an alias; Molecular Expressions has 8 aliased domain names that all lead to the same server.

To review how a server computer interacts with a client computer, the first action occurs when the operator of the client computer clicks on a hyperlink embedded in a Web page or types the server domain name into the text input field of a Web browser. Using Molecular Expressions as an example, the operator would type http://www.microscopy.fsu.edu into the browser text field and press the "Enter" key on the keyboard. The browser software initiates a connection to the server by querying a local domain name server (DNS) computer to determine the IP address of the Molecular Expressions server. Once contact has been made between the client and the server using HTTP, the server delivers data to the browser in the form of HTML pages, images, scripts, etc., which are in turn formatted by the browser to be displayed on the monitor. In this manner, the server can simultaneously send files to numerous clients, allowing multiple visitors to view the Web pages at the same time.

Virtually any computer (Windows, Macintosh, or UNIX/Linux) can be a host to a Web server, but many of the available software packages are difficult to properly configure and a personal computer might not have sufficient bandwidth to adequately and reliably deliver pages to a large number of clients. Most departments in colleges and universities host Web services for their faculty members, post-docs, and researchers, often providing drive space for individual pages. There are also a wide range of commercial vendors that offer Web site hosting services at a reasonable cost. For laboratories wishing to invest in server hardware and software to build extensive Web sites, there are considerably more options in terms of the operating system platform and the type and sophistication of the software packages.

Because the Microsoft Windows operating system commands the largest market share of computer software, this platform is naturally the most versatile in terms of available Web server packages to address the needs of individual users. The Apache HTTP server [94]

is one of the oldest and most reliable in general use, is cost-free, features open source code as well as support for a wide spectrum of third-party modules, and can be configured to operate on Windows, Netware, OS/2, UNIX, or Linux servers. For dedicated Windows environments, the Microsoft IIS (Internet Information Server) software [95], which is supplied as a module for all Microsoft server operating systems (i.e., Windows 2003 Server), should probably be the server of choice. IIS is a file and Web application server that can be installed on Windows 2000, 2003, and 2008 Servers. Scaled down versions are available for personal computers running Windows Vista, Windows XP, and Windows 2000. Among the many useful features of IIS is the support for dynamic as well as static Web pages and full connectivity to interface with external data sources such as Microsoft Access and SQL databases. The IIS software supports Active Server Page (ASP) and ASP.NET (the latest runtime development package) technology allowing applications to be embedded in Web pages that modify the content returned to clients.

Additional Web server software packages for Windows computers are BadBlue [96], Savant [97], Essentia [98], PlanetWeb [99], and MiniPortal [100] and a variety of others can be found on the Internet using the search engines. Several of these software programs (Apache and Essentia) have versions compatible with the Linux operating system; however, most commercial versions of Linux, such as RedHat [101], also bundle Web server software with the "enterprise" edition of the operating system. For Macintosh users, the Mac OS X operating system contains a built-in Apache Web server that can easily be configured by relatively inexperienced users. Alternative Macintosh-based Web servers are available from several manufacturers.

5.2 HTML Page Creation

Creating Web pages does not necessarily require a server as the content can be stored on a local drive during the construction process, displayed in a browser to check for errors, and then transferred to the server once the layout is complete. Basic hypertext markup language (HTML) has a very shallow learning curve compared to other computer programming languages, such as Java, Visual C++, or VB .net, and can usually be mastered in a few weeks. An abundance of guides have been published [3, 102, 103] for creating HTML pages using simple text editors (for example, Microsoft Word, Notepad or WordPad), while a variety of both commercial and cost-free HTML editors that have more user-friendly interfaces are widely available. The basic command-line HTML text editors assist in creating code by making it quicker and easier to insert tags and by color-coding the tags to distinguish them from surrounding text. These editors are often cheaper (several are free and distributed on the Internet) than the more sophisticated commercial packages discussed below, and will run on older computers, but they require the user to have some knowledge of the HTML tag library.

More complex HTML creation and editing software, termed WYSIWYG (the acronym for: What You See Is What You Get; typically pronounced "wa-si-wig") editors, typically do not require knowledge of HTML by the user because they automatically generate the code for Web pages as text and graphics are inserted by the "drag-and-drop" method. The content layout in these editors very closely approximates the final Web page as it is displayed in a browser. On the downside, WYSIWYG editors [104] usually produce complicated HTML code that is far more involved than that produced with a simple text editor by often adding tags for layout purposes that are not absolutely necessary. The most popular and advanced WYSIWYG editors are Adobe Dreamweaver [105], Microsoft Visual Studio [106], and Microsoft Expression Web [107]. All three of these software packages are very sophisticated, although Dreamweaver features more support for multimedia content, such as Flash animation and Fireworks rollovers, and Visual Studio is preferred for developing ASP and ASPX pages as well as better integration with databases. Furthermore, the Adobe products are fully integrated with Photoshop and Illustrator, which eases the burden of copying Web page designs to print and vice versa. Microsoft launched a useful WYSIWYG editor termed FrontPage [108] several years ago and still supports the software, although it is far less popular.

Creating Web pages with WYSIWYG editors is probably the best alternative for amateurs who do not want to spend the time necessary to learn the intricacies of HTML. Basic Web page configuration is menu-driven with tasks such as establishing a title, choosing text and background colors, and formatting tables being as simple as preparing an ordinary Microsoft Word document. Adding hyperlinks or anchors is accomplished by highlighting the text to be linked and typing the associated URL in a text box. Button bars or menus are also used to create tables and add bulleted and numbered lists, whereas images and graphics can be inserted in a manner similar to that used by word-processing and page layout software. Once a Web page has been created by the editor, the source code can be checked to determine how HTML tags have been appropriated and edited to add special effects (examining the code is an excellent means to learn HTML). Prior to placing the page on a Web site, WYSIWYG editors provide a "preview" image (much like a print preview) to show how the page will appear.

In the final analysis, the user must ultimately make a selection about how Web pages are to be created, and this should be done prior to attempting to build a Web site. If the target is a simple site that does not need to utilize more advanced design and layout techniques such as Cascading Style Sheets (CSS), then text editors are sufficient. Web sites containing multimedia-rich content, such as interactive tutorials, JavaScript, and connectivity to databases, on the other hand, might benefit from being constructed with

Adobe Dreamweaver. If combining multimedia content with interactive forms and Web-based .ASP applications is desired, then Visual Studio is an excellent choice. One of the most important considerations for any Web site is the quality of content provided to visitors and the navigational aids planted throughout the site. For laboratories that simply want to install digital image galleries of specimens recorded in confocal microscopy, any text or WYSIWYG editor will suffice. However, the more complex Web sites containing tables, digital video files, downloadable reprints in PDF format, instrument time scheduling forms, etc., will require significantly more effort on the part of the Webmaster.

5.3 Editing and Preparing Digital Still Images for the Web

Acquiring single digital images on a confocal or wide-field fluorescence microscope is just the first step down a long pathway if the ultimate target is to prepare the images for display on a Web site. Most of the commercial confocal software packages, as well as those supporting high-end grayscale and color camera systems for wide-field microscopes, are useful for acquisition and often assigning pseudocolors to different channels and merging them together, but most have limited post-acquisition image editing capabilities. A majority of the highly sophisticated third-party commercial instrument control and support software programs, such as Image Pro [109], Slidebook [110], and MetaMorph [111], boast numerous image processing and editing features, but are quite expensive and have steep learning curves. Furthermore, these packages are usually not focused on generating the highest quality, low-resolution graphics needed for the Web and restrict users to only a few output file storage formats, which are generally designed to maintain the spatial resolution and bit-depth of the original image. In order to prepare the high resolution images acquired and processed by the microscope software for display on the Web, relatively low-cost third-party image editors can be of significant benefit.

The images typically generated in confocal microscopy can be of enormous size, presenting problems not only for the storage requirements in terms of disk space, but also in compression and resizing for presentation software (i.e., Microsoft PowerPoint) and for display on the Web. A single-channel image having dimensions of 512×512 pixels, one of the most common sizes for many confocal software packages, requires a minimum storage capacity of 256 Kilobytes (KB), while a three-channel 2048×2048 pixel image (now a routine size on most microscopes) consumes at least 12 Megabytes (MB) of disk space for a single image plane. When this number is multiplied to accommodate a stack of 100 optical sections, the storage requirement blooms to 1.2 Gigabytes (GB). Storage capacities are always increasing; hard drives have doubled in capacity from 1 to 2 Terabytes (TB) between 2007 and 2009, continually shifting the cost per gigabyte of storage lower and lower. However, there is clearly a necessity to explore data

compression mechanisms both for long-term image storage, as well as the preparation of images for transmission over the Internet, where bandwidth limitations are often a far more serious consideration.

The digital images produced by confocal and wide-field fluorescence microscopes using photomultipliers and high-end digital cameras, respectively, are usually stored in the form of pixel arrays known as "bitmaps" in one or more common storage formats [112] that can include: Microsoft bitmap (BMP), tagged image file format (TIF or TIFF), Macintosh bitmap (PICT), the graphics interchange format (GIF), or any of a variety of proprietary file formats (for example the OIB format from Olympus). These file formats are termed "lossless" because none of the image data is discarded during storage in order to maintain the highest possible quality (even though the file may be compressed in some circumstances). A recent addition to this category of lossless file storage formats is PNG (pronounced "ping"; 112), which will usually produce the smallest file sizes of all lossless algorithms and is supported by most Web browsers. For example, a 6 MB image when stored as a TIFF file can be compressed to require slightly over 2.9 MB of disk space as a PNG file, a savings of approximately 50 %. However, this size is still too large for transmission over the Internet, so microscopists must resort to more aggressive compression techniques that are often termed "lossy" due to the fact that some of the image data is discarded during the reduction process. After compression and subsequent decompression of a lossy image for viewing, the compressed image will not retain every aspect of the original and will vary in quality depending upon the amount of data that has been lost. With the best compression algorithms, fortunately, relatively large file size reductions can be achieved without perceptible differences in the image.

The two most common image file formats currently in use on the Web are GIF (lossless if the number of colors is 256 or less) and the Joint Photographic Experts Group standard known as JPEG (lossy). Because the GIF format utilizes a lossless compression mechanism, the file sizes are relatively large for complex images (such as those taken with a microscope), and the algorithm has additional limitations that further restrict its use to simple graphic elements, such as logos and page graphics, which contain only a small number of variable elements [112]. Although the GIF format supports Web-friendly features such as transparency, interlacing, and multiple-image sequences (animated GIFs), the color palette is limited to 256 color levels (8-bit), a severe restriction for the faithful reproduction of full-color images. Often, the lossless compression afforded by the color-limited GIF format appears to the eye as inferior to JPEG even though the latter algorithm discards image data. In contrast, JPEG file compression operates in 24-bit (true) color and the user has full control over the compression level that is being applied to the image (ranging from 1:1 to

over 100:1; 113). Very little degradation is usually observed in JPEG files compressed at ratios between 10:1 and 20:1 for complex images. Unlike GIF, however, JPEG is often not useful for simple graphics that have only a few colors, highly varying levels of contrast, solid borders, or large areas of similar color. Another problem with JPEG compression is that degradation is cumulative upon successive edits of an image.

Digital images destined for the Web should be compressed to yield a file size of less than 100 KB, regardless of the pixel dimensions. Although larger images may appear to load with relatively good speeds in the browser when being tested locally, they usually take a much longer amount of time for visitors who are on the other side of the world. Reducing the file size of a JPEG image to a reasonable level while still maintaining a high level of detail and quality is often a compromise that requires considerable amount of skill and practice on the part of the operator. Too much compression can lead to artifacts while too little compression produces images that are unnecessarily large. Illustrated in Fig. 11 are two of the most common artifacts that occur when JPEG compression ratios are excessively high. The upper panels (a and b) in Fig. 11 depict a grayscale confocal fluorescence image of rat brain neurofilaments labeled with secondary antibodies conjugated to Alexa Fluor 488. The images were compressed at a ratio of 1:10 and 1:100, respectively, using the JPEG algorithm to produce file sizes of 97 and 12 KB. Empty magnification of the images in Fig. 11 has been increased to the point that individual pixels are discernable. Note the smooth transition between pixels in Fig. 11a, but the 8-pixel block artifact resulting from excessive compression that is very evident in Fig. 11b. This effect occurs because the JPEG algorithm breaks the image into blocks of 8×8 pixels [113], with each block being processed through a discrete cosine transformation. At very high compression ratios, the transform is incapable of correctly handling the various frequency components of the image, resulting in the image appearing as a series of seemingly unrelated blocks. A similar effect is obvious in Fig. 11d, which is a DIC-confocal image of a living rabbit kidney cell expressing mCherry fluorescent protein fused to human *beta*-actin. The usually noisy background seen in live-cell imaging (Fig. 11a) exhibits the JPEG block effect at high compression ratios, resulting in a posterization effect (Fig. 11b). In general, grayscale or monochrome images can be compressed to approximately one-fifth of their original size using the JPEG algorithm with no visible loss of quality. Color images, on the other hand, can be compressed to a greater degree because the luminance (brightness values) and chrominance (color values) are treated separately. Regardless of the artifacts incurred by too much compression, JPEG remains the most viable file format for producing images destined for the Web. A wide variety of other factors must be considered when processing digital images [56], but these are beyond the scope of this discussion.

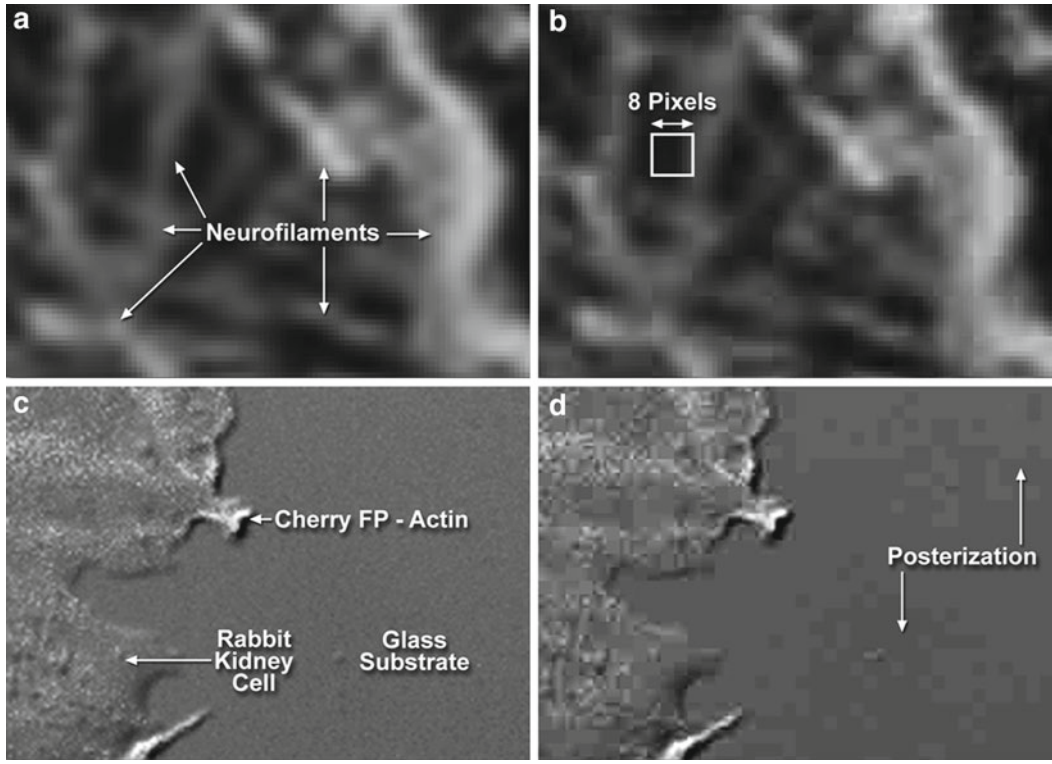

Fig. 11 JPEG compression artifacts in confocal microscopy images for display on the Web. (**a**) and (**b**), rat brain hippocampal thick section labeled with Alexa Fluor 488 to identify neurofilaments and recorded in grayscale using a 40× apochromatic oil-immersion objective at no zoom factor. The image in (**a**) was compressed 10:1 while the image in (**b**) was compressed 100:1. (**c**) and (**d**), a single frame from a time-lapse sequence in live-cell imaging of a rabbit kidney epithelial cell expressing the mCherry fluorescent protein fused to human *beta*-actin. Pixels having high grayscale values represent regions labeled with the protein. The images were compressed at the same ratio as (**a**) and (**b**), respectively. Note the posterization effect in the background (glass substrate) and the severe degradation of features in the living cell at high image compression ratios

Two primary categories of graphics software exist for the creation of images destined for the Internet: pixel-image (bitmap) editors and vector illustration software. For editing and storing grayscale and color images recorded with the microscope, the pixel or bitmap editors (often loosely referred to as "paint" applications) should be seriously considered. Among the popular bitmap editors available, several have proven to be of exceptional use in preparing microscopy images for service on the Web. Adobe Photoshop [114] is one of the more advanced programs, followed closely by CorelDRAW [115], Corel Paint Shop Pro Photo x2 [116], and Corel PhotoImpact x3 [117]. Each of these programs has unique features, but all are capable of nicely processing images gathered on the microscope for maximum compression while still maintaining image integrity. Using Photoshop as an example, images can

easily be saved using the companion plug-in software ImageReady (installed by default; 118) to preview images at varying compression ratios. Thus, a 9.6 MB TIFF image is presented by ImageReady alongside three compressed versions at 314, 157 , and 110 KB having download times calculated at modem speeds by the software (download times are 113, 57, and 40 s, respectively). Alternatively, a single image compressed to a degree selected by the operator can be displayed beside the original to more closely determine whether the algorithm is producing artifacts at the chosen compression ratio. The other competing bitmap software editors have similar features.

Unlike bitmap editors, vector graphics software is designed to create drawings from scratch using lines and curves that are defined, as the name suggests, from vector calculations. Because they consist of points and objects (rather than pixels), vector-based illustrations are not confined to a predetermined size and can be scaled to any dimension without loss of resolution. On the downside, vector images generally do not contain the high degree of detail found in bitmap images (such as photographs) and often have a cartoon-like appearance. The primary commercial packages in this category are Adobe Illustrator [119], CorelDraw [120], Adobe Freehand [121], and Serif DrawPlus [122]. Display of Scalable Vector Graphics (SVG, the format used by vector based graphics packages) images is currently supported by some popular Web browsers including Mozilla Firefox, Opera, and Apple's Safari, however Internet Explorer 8 users must download a third party plug-in to enable support. Vector graphics are primarily utilized to create logos, header graphics, maps, and free-hand drawings. Do not purchase this type of software with the intent of editing bitmap images acquired with the microscope.

5.4 Interactive Tutorials: Java vs. Flash

Web-based tutorials are an excellent mechanism to simplify difficult concepts that benefit from animation in order to provide students with an effective and interactive "hands-on" learning experience, which would otherwise require access to expensive instrumentation or a significant amount of text and illustration. Currently, the best programming options for creating interactive tutorials that will operate in a Web browser are JavaScript, dynamic HTML (A combination of HTML, JavaScript, DOM, and CSS), compiled Java applets, and Flash applications. Other formats, such as digital videos [123], animated GIF image sequences [124], or HTML pages with frames [125, 126] are often useful for instructional purposes, but do not enable the user to interact with and provide feedback to the software.

One of the most useful tools available for building interactivity into Web sites, JavaScript is an object-based scripting programming language based on the concept of prototypes, which does not use classes. Instead, inheritance is accomplished through behavior

reuse by cloning existing objects to serve as prototypes for new objects. JavaScript syntax is similar to that used in the C programming language, but the language is severely limited in its ability to create complex programs that rely heavily on algorithms (such as those necessary for image processing). Rather, JavaScript is excellent for building simple tutorials that tie a roll-over or a clickable button with alternating images for comparison purposes. As an example, demonstration of the image features that vary between a phase contrast and differential interference contrast micrograph of the same specimen could easily be accomplished using JavaScript. Several "virtual" microscopes that have been developed using JavaScript as the underlying foundation are currently available on the Web [127, 128].

Dynamic HTML has also been employed on a limited scale to create interactive Web sites [129] by interweaving static HTML tags with a client-side scripting language, such as JavaScript, coupled to the presentation definition language known as Cascading Style Sheets (CSS) and the Document Object Model (DOM). Cascading style sheets are primarily used to control the presentation of a document written in basic HTML, but the language can be applied to the more advanced Extensible Markup Language (XML) documents as well. For interactive Web sites, style sheets are used to define colors, fonts, layout, and other aspects of the document presentation. The DOM describes how an HTML or XML document is presented in an object-oriented fashion (much like a compiled program) by providing an application programming interface (API) to access and modify content, structure, and style. Because DOM accesses a document in tree form (with parents and children), the entire content is first parsed and stored in memory to enable the dynamic interplay between elements. In general, dynamic HTML is not useful for complex interactive tutorials so relatively little use of this potentially powerful approach has been employed in Web sites other than for applications similar to those featuring JavaScript alone.

In contrast to dynamic HTML and JavaScript, the Java programming language is fully object-oriented (similar to C++) and allows for creation of new data types, such as complex numbers and matrices [19]. The language is excellent for numerical simulations and scientific computing and is now comparable to other seemingly more advanced compiled programming languages. Bestowed with a simpler syntax than C++ and a more robust runtime environment, the Java setting requires the Java Virtual Machine (JVM) to be installed in a Web browser and the Java API for programming [130, 131]. A wide variety of libraries with source code and precompiled binaries (object files) are publicly available to support Java programmers, and the virtual machine supports multi-threading (executing several programs simultaneously). The Java virtual machine is available at no cost for numerous

platforms, including Windows, Linux, UNIX, and Macintosh. For programmers, a plethora of Java compilers are freely available on the Internet, complete with source code, and more sophisticated commercial products can also be purchased. Java has two-dimensional raster graphics capability built into the Applications Programming Interface (API) with interactive three-dimensional graphics available in the newer versions, as well as from third party extensions. Because of the powerful programming capabilities and virtually unlimited possibilities for creative implementation using Java, the language is an excellent choice [43, 45, 46, 48, 132, 133] for the construction of interactive Web sites.

The interactive Java tutorial illustrated in Fig. 12 features a "virtual" microscope that compares the images produced by a laser scanning confocal microscope with those obtained from a wide-field fluorescence instrument [134]. Visitors are able to adjust the focus of both images simultaneously to observe differences between the wide-field and confocal microscopes. Other software controls

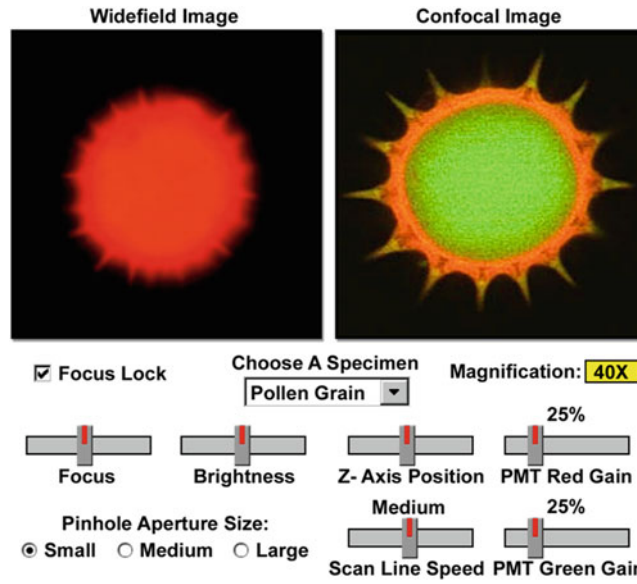

Fig. 12 Java-powered virtual microscope interactive tutorial that compares the images recorded by a wide-field fluorescence microscope with those of a laser scanning confocal instrument. Visitors are able to choose from a palette of ten specimens ranging from plant tissue to animal brain thick sections. The wide-field focus slider is locked to the confocal *z*-axis position slider so that images from the same focal plane are displayed simultaneously. Wide-field images can be adjusted for brightness, while the confocal image intensity is varied using the photomultiplier (PMT) sliders. The virtual confocal pinhole size can be toggled from small to large (arbitrary units) using the radio buttons. Students learn that as the pinhole size is increased, the confocal image appears increasingly similar to the wide-field

in the tutorial enable changing the scan speed, the pinhole aperture size, and the image intensity. Similar Java-powered virtual microscopy tutorials on the Molecular Expressions Web site target phase contrast, differential interference contrast, Rheinberg illumination, Hoffman modulation contrast, reflected light confocal microscopy, and fluorescence microscopy.

A growing alternative to the power of Java, the Adobe Flash [20] Studio authoring software is perhaps the most widely implemented resource for the creation of interactive educational Web sites targeted at microscopy [135–138]. The Flash client-side software, which is compatible with all Web browser versions, is available at no cost from the Adobe Web site [139], but Flash application software development requires purchasing the "Flash Professional" construction package from Adobe [140] and third-party extensions (available on the Internet) can be very expensive. Flash is programmed with a scripting language known as Actionscript. The first implementation (Actionscript 1) is similar to JavaScript, and is not a fully fledged programming language. However, the far more advanced second and third versions (Actionscript 2 and3) are a formal and highly structured object-oriented programming language that is loaded with specialized functions, many of which are similar to those present in Java. Actionscript 2 and later allows for robust interactive application development, but similar to other sophisticated object-oriented languages, requires a significant degree of computer programming experience.

One of the most versatile features of Flash is the advanced multimedia power afforded by the platform, which has many classes designed for this purpose. Among the capabilities of Flash that are specifically targeted to multimedia are two-dimensional vector graphics animation and bitmap support (in the latest versions) to manipulate pixel-based images. Flash is also one of the platforms of choice for high quality video service at high compression rates. In addition, video can easily be merged with other content in Flash and the streaming server software available from Adobe can support the high-definition television (HDTV) standard. As of Flash Player 10.0, support for hardware accelerated graphics is included, accelerating playback of HD video and allowing manipulation of 3d graphics that would not be possible on the CPU alone.

The choice of programming technology utilized to construct interactive Web sites will be largely determined by the level of expertise held by the developer, as well as the amount of time available to learn new programming languages. For simple Web sites, dynamic HTML and JavaScript will usually suffice, especially when mixed together with creatively animated GIF sequences and video. More advanced Webmasters may choose to develop interactive sites based on Java or Flash. In the past, the learning curve on Java programming was much steeper than that for Flash, but the two

are beginning to merge with respect to power and complexity. Because of the widespread popularity of Flash over Java, the former platform is probably the safest avenue for long-term stability with regard to backwards compatibility and potential longevity in support from the parent corporations.

5.5 Preparing Digital Video for the Web

Because of the inherent time-lapse capabilities and ease of creating large axial (z) image stacks containing up to 100 or more optical sections from a single specimen field, the confocal microscope is the ideal tool with which to create digital video sequences that explore a wide range of biological phenomena and structure. Recognizing this fact, the manufacturers of every available commercial instrument have incorporated the necessary features to assist the user in producing videos (i.e., movies) with the native software. In most cases, the confocal software is able to capture image sequences that are saved as successively numbered individual files (such as JPEG or TIFF) or bundled together using proprietary file formats (OIB for Olympus, LSM and PIC for Zeiss/Bio-Rad, etc.). The latter formats can usually be exported by the microscope software into common file types that are compatible with third-party image editors and video production software.

Once a sequence of images (for example, a time-lapse series) has been gathered with a confocal or wide-field microscope, the native software can be employed to assemble the image sequence into a digital video file that is usually not compressed. In order to prepare a video for delivery in a presentation or over the Web, it should first be compressed by one of several available techniques to reduce bandwidth and ensure smooth playback with client software known as a "media player" [141]. Digital video files are composed in video editing software, then both compressed (and decompressed for playback) using a dedicated software program known as a "codec", a term that is abridged from the fusion of the functions: coder and decoder [142]. Digital video streams may be contained in many file types (AVI, MPEG, etc., as discussed below), and each file type can contain video encoded with a variety of codecs. Fortunately, these codecs are usually contained in the operating system software or are available cost-free on the Internet. Encoding videos makes heavy demands on the CPU of a computer, with the main memory (RAM) and I/O subsystem (hard disks) also playing a critical role. Fortunately, video encoding scales almost linearly with additional processor power, so for optimal performance a multi-(4 or more) core CPU should be used in conjunction with the highest performing hard drive possible. Without an appropriately powerful processor and capable I/O, artifacts such as frame dropping, temporal and spatial aliasing, compression errors, and other potential problems can occur during composition and encoding of videos.

Before investing the time to prepare a large number of digital video files for service on the Internet, the Webmaster should first decide on the compression format (in terms of file type and the required video editing software), and then choose between the two video server hosting schemes that are available. A standard HTTP Web server can be used to deliver video files through a mechanism referred to as "http streaming" or "progressive download" that simply downloads the video file to a client computer. Video data is transferred using HTTP, which is not the most efficient method for fast delivery of large files. For example, a video file encoded at 250 Kbps (kilobits per second) is sent from the server to the client as quickly as possible and may appear to be "streaming" since playback begins almost immediately when enough of the data is downloaded. However, bandwidth restrictions too often come into play, and the HTTP-delivered video can hang as the client media player drops frames or automatically pauses the video in order to collect more of the file. When choosing this method to deliver confocal microscope video sequences, the Webmaster must carefully match the video compression ratio with the estimated bandwidth of the client computers. In general, and to the detriment of the images, very high levels of compression are necessary to ensure smooth playback.

The second, and far more advanced, mechanism to deliver digital video over the Internet is to implement "streaming server" software that is specifically designed to accept client requests for video files [143]. A streaming server operates by first opening a connection to the client media player to determine the optimum transfer rate (bandwidth) and communicates with the client as the video is being downloaded to reduce errors. In effect, two pipelines are simultaneously open between the server and client: one of the streaming video and the other for control messages back and forth to ensure that delivery speed is adjusted to changing network connections as the video is played. The control messages also inform the server of client actions such as play, pause, stop, and seek. Because the streaming server sends video data only when requested by the client (and at the maximum possible rate), the software allows precise control over the number of streams allowed by the available bandwidth. Unlike the case for video delivered by HTTP, however, many of the standard format streaming video files are discarded immediately after display and cannot be replayed without downloading (streaming) the file again. Several newer video formats permit local caching (i.e., Windows Media) that allow the client to save files for off-line viewing. Unfortunately, slower Internet connections (for example, a 56 Kbps modem) require specialized encoding of streaming video at much lower quality. In the final analysis, the choice of video server is determined by the amount of control desired and the type of files that will be made available to clients. Very short videos (a few to tens of

seconds) will not entail the expense and configuration problems associated with streaming video servers, whereas files that play for more than a few minutes benefit from streaming. Clients can also be given the option to download the entire video file for playback at a later date.

Dealing with digital video can easily appear to be overwhelming when trying to sort through the large number of both codecs and file formats involved, as well as the interaction between file format and codec. Each digital video file format (AVI, MPEG, MP4, MKV, MOV, FLV, WMV, and others) is a container capable of holding a video and audio stream encoded with one of many commonly available codecs(DivX, MPEG 1–4, WMV, H.264, etc). Each file type also supports different video related features such as chapters, subtitles, menus, and attached metadata tags. The fact that a single file type is capable of containing multiple forms of encoded video can easily be a cause for confusion; A PC may have codecs installed enabling it to play some of the video streams capable of being contained in an AVI file, but be lacking codecs required to play others.

The most common digital video file types are AVI (Audio Video Interleave; 144) by Microsoft, MPEG (Moving Picture Experts Group; 145) an industry standard, QuickTime by Apple [146], Real by RealNetworks [147], and Flash Video [148] by Adobe. Because of the popularity of the Microsoft Windows operating system platform, AVI is one of the most common digital video formats, although also one of the most dated. AVI files, which are usually much larger in size than the other formats (even with compression), can be formatted with highly varying levels of compression (or even without) to fine-tune the file size. AVI is most commonly used for capturing, editing, and working with uncompressed video, before encoding it in to another, more suitable compressed format. Although the AVI standard can be hosted on a simple HTTP Web server for purposes of downloading and viewing, and the format is capable of delivering higher quality video than most streaming video codecs, AVI video files are not able to be streamed. Still, the AVI container is an excellent choice for capturing, processing, and archiving high-quality video content and has become the default standard format for a majority of the microscopy software packages that process digital video.

Perhaps the most universally accepted digital video format is MPEG (format of choice for DVDs), whose compression and file designs are based on the “bitrate” (a term referring to the quantity of storage space that is consumed by each second of video) concept. The amount of information loss that occurs during MPEG video compression is dependent upon the selected bitrate [145]. MPEG has evolved over the years into several versions ranging from MPEG-1 to MPEG-4 (the latest) that sport increasingly enhanced features. The first two versions provide considerable

economy with regards to file size while still maintaining high video image quality, but are unable to support streaming. However, similar to the AVI format, MPEG-1 and MPEG-2 digital videos can be downloaded (without playback) through a Web browser to the client computer for local viewing. Unlike its previous versions, the MPEG-4 standard supports streaming video.

The operating system manufacturers, Microsoft and Apple, both supply proprietary video formats that are optimized for their platforms. QuickTime is the Apple version, which is very popular and has gained widespread acceptance [146]. A large variety of compression codecs are available for the QuickTime format, but the most sophisticated is Apple's version of the MPEG-4 codec. QuickTime is capable of delivering streaming video, with optimum performance being delivered by the Apple streaming software packaged with the Macintosh OS-X server. Windows Media is a bitrate-based compression file format developed by Microsoft to support a variety of encoding schemes. Like QuickTime, Windows Media supports streaming through the proprietary MMS (Microsoft Media Server; 149) protocol, which attempts to negotiate the optimum delivery conditions for each client.

Aftermarket digital video file formats and specifications have also been developed by Real Networks and Adobe. The Real System [147] is a combination player system and streaming video delivery server (named Helix) that can be hosted on Windows, Linux, and UNIX servers. In addition, the Helix server is designed to also deliver Windows Media, QuickTime, MP3, and MPEG-4 streaming videos. The playback software, RealPlayer, which is cost-free, is available for Windows, Macintosh, Linux, UNIX, and mobile devices. The latest entry into the streaming video field is Flash Video from Adobe [148]. Flash video can be embedded within standard SWF files, downloaded progressively, or streamed from a Flash Media Server.

A number of affordable software packages designed for assembling and editing video sequences are commercially available or can be obtained without cost on the Internet. However, the best performance is usually obtained from the commercial versions that are produced by the major software manufacturers. Adobe Premiere Pro [150] and Apple Final Cut Pro [151] are two of the best values and most popular editors for the Windows and Macintosh platforms, respectively. Both programs feature extended editing and timeline capabilities, special effects creation, incorporation of audio, color correction, multiple file format support, compression algorithms, text capabilities, and media management tools. Additional software that should be considered is Sony Vegas, Apple iMovie [152], Windows Movie Maker [153], and video authoring tools from Adobe [148] and Real Networks [147]. The

art and science of editing digital videos is beyond the scope of this review, but the reader is referred to the many excellent texts listed in the discussion.

6 Additional Internet Resources

The barrage of new techniques and ideas for active research in confocal microscopy is continually discussed by almost 2,000 scientists who subscribe to the confocal email listserver located at the University of Minnesota in Minneapolis [154]. Registered users of the listserver are placed on a mailing list to receive pertinent messages from other investigators and students about a wide variety of topics pertinent to confocal microscopy. Among the recent topics discussed on the listserver are autofluorescence, live-cell imaging chambers, damage to cells in photobleaching experiments, spectral imaging, and announcements of confocal workshops and courses. The listserver message archive is searchable and dates back to November, 1991.

Another useful program is the Open Microscopy Environment (OME), which is being developed as an informatics solution for the storage and analysis of optical microscope image data [155, 156]. Collaborators on the OME system include academic laboratories as well as commercial hardware and software imaging vendors, with all source code being made available under the GNU library general public license. A tutorial demonstrating the system is available on the Web site [155]. The programmers at OME have developed standardized file formats for the exchange of image data and database schema to seamlessly integrate effectively with commercial software packages.

7 Conclusions

Taking advantage of the dynamic nature of the World Wide Web, the microscopy educational Web site initiative at The Florida State University has resulted in the production of several interactive sites targeted at entry-level and advanced students in biology, chemistry, and physics. In addition to hundreds of review articles on all aspects of optical microscopy, the Web sites contain image galleries, streaming videos, interactive Java tutorials, listings of Internet resources, and reference sections with links to the original research documents. As the attention of the development team is refocused on topics related to confocal microscopy, new sections will emerge on the FSU microscopy Web sites that are targeted at educational tutorials and review articles in the rapidly evolving arena in fluorescence microscopy.

Acknowledgments

This work was supported in part by contracts with Nikon USA, Inc., Olympus America Inc., and Olympus Corporation (Tokyo), who also supplied instrumentation, and with funds generated by licensing images through The Florida State University Research Foundation. Web site construction and imaging were conducted at the National High Magnetic Field Laboratory, supported by Cooperative Agreement (DMR-0084173) and the State of Florida. The authors wish to also thank their many industrial partners who have supplied equipment and expertise: Nikon USA (Anna Scordato, Stanley Schwartz, Stephen Ross, Joseph LoBiondo, Eric Flem, Chris Brandmaier, and Deborah O. Robbins), Olympus America (Ian Kirk, Monica Mahler, Brad Burklow, Kimberly Wicklund, William K. Fester, George E. Steares, Nicolas George, Christopher Higgins, Kenji Matsuba, Esther Ahrent, Rainer Wegerhoff, John Crenshaw, and Mortimer Abramowitz), QImaging (John Bogan and David Barnes), Omega Optical, Inc. (Dan Osborne), Hunt Optics and Imaging (John Marchlenski and Andrew Hunt), Hamamatsu Photonics, Inc. (Butch Moomaw), Semrock, Inc. (Turan Erdogan), Invitrogen Molecular Probes (Michael O'Grady and Iain Johnson), and Covance, Inc. (Poonam Kaul).

References

1. Berners-Lee T, Fischetti M (1999) Weaving the Web: the original design and ultimate destiny of the World Wide Web by its inventor. Harper, San Francisco, CA, p 226
2. Cailliau R, Gillies J (2000) How the Web was born: the story of the World Wide Web. Oxford University Press, Oxford, p 372
3. Castro E (2006) HTML, XHTML, and CSS (Visual Quickstart Guide), 6th edn. Peachpit Press, Berkeley, CA, p 456
4. Brakenhoff GJ, Blom P, Barends P (1979) Confocal scanning light microscopy with high aperture immersion lenses. J Microsc 117:219–232
5. Sheppard CJR, Wilson T (1982) The image of a single point in microscopes of large numerical aperture. Proc R Soc Lond Phy Sci A379:145–158
6. Wilson T, Sheppard CJR (1984) Theory and practice of scanning optical microscopy. Academic, New York, p 213 (first book on confocal microscopy)
7. Brakenhoff GJ, van der Voort HTM, van Sprousen EA, Linnemans WAM, Nanninga N (1985) Three-dimensional chromatin distribution in neuroblastoma nuclei shown by confocal scanning laser microscopy. Nature 317:748–749
8. Wilke V (1985) Optical scanning microscopy—the laser scan microscope. Scanning 7:88–96
9. Tsien RY, Rink TJ, Poenie M (1985) Measurement of cytosolic free calcium in individual small cells using fluorescence microscopy with dual excitation wavelengths. Cell Calcium 6:145–157
10. Taylor DL, Waggoner AS, Murphy RF, Lanni F, Birge RR (1986) Applications of fluorescence in the biomedical sciences. Alan R. Liss, Inc., New York, p 639
11. Ploem JS, Tanke HJ (1986) Introduction to fluorescence microscopy. Oxford University Press, New York, p 56
12. Kilmartin JB, Wright B, Milstein C (1982) Rat monoclonal antitubulin antibodies derived by using a new nonsecreting rat cell line. JCell biol 93:576–582
13. Lazarides E, Weber K (1974) Actin antibody: the specific visualization of actin filaments in non-muscle cells. Proc Natl Acad Sci U S A 71:2268–2272
14. Titus JA, Haugland RP, Sharrow SO, Segal DM (1982) Texas Red, a hydrophilic, red-emitting

fluorophore for use with fluorescein in dual parameter flow microfluorometric and fluorescence microscopic studies. J Immunol Methods 50:193–204
15. Amos WB, White JG (2003) How the confocal laser scanning microscope entered biological research. Biol Cell 95:335–342
16. White JG, Amos WB, Fordham M (1987) An evaluation of confocal versus conventional imaging of biological structures by fluorescence light microscopy. JCell Biol 105:41–48
17. Matsumoto B (1993) Cell biological applications of confocal microscopy. Academic, New York, p 380
18. Pawley JB (2006) Handbook of biological confocal microscopy, 3rd edn. Springer Science + Business Media, LLC, New York, p 985
19. Flanagan D (2005) Java in a Nutshell, 5th edn. O'Reilly Media, Sebastopol, CA, p 1252
20. Green T, Chilcott JL (2005) Macromedia flash professional 8: training from the source. Macromedia Press, San Francisco, CA, p 512
21. Horrigan J (2008) Home Broadband Adoption 2008, Pew Internet & American Life Project. http://www.pewinternet.org/~/media/Files/Reports/2008/PIP_Broadband_2008.pdf, Washington, DC
22. Bugg KE (1999) Building better interfaces with Microsoft foundation classes. John Wiley and Sons, New York, p 268
23. Kruglinski D, Wingo S, Shepherd G (1998) Programming Microsoft Visual C++. Microsoft Press, Seattle, WA, p 1153
24. Hibbs AR (2004) Confocal microscopy for biologists. Kluwer Academic, New York, p 467
25. Fellers TJ, Davidson MW (2004) Acousto-Optic Tunable Filters, Olympus FluoView Resource Center. http://www.olympusconfocal.com/theory/aotfintro.html, National High Magnetic Field Laboratory, The Florida State University, Tallahassee
26. Marin J, Shaffer J (2007) The PDF print production guide, 3rd edn. PIA/GFTFPress, Sewickley, PA, p 290
27. National Center for Biotechnology Information, National Library of Medicine, National Institutes of Health (2007) PubMed. http://www.ncbi.nlm.nih.gov/, Washington, DC
28. Chemical Abstracts Indexing Service, American Chemical Society (2007) http://www.cas.org/, Columbus, Ohio
29. PhysicsWeb, Institute of Physics (2007) http://physicsweb.org/, London, United Kingdom
30. Google, Inc. (2007) http://www.google.com/, Mountain View, California
31. Yahoo!, Inc. (2007) http://www.yahoo.com/, Sunnyvale, California
32. Cromey DW (2007) Confocal Microscopy, Southwest Environmental Health Science Center. http://swehsc.pharmacy.arizona.edu/exppath/micro/confocal.html, University of Arizona, Tucson
33. Gould J (2007) The Confocal Microscopy List. http://www.microscopy-online.com/confocal.shtml, NanoTEM, Scottsdale, Arizona
34. Robinson JP (2007) Purdue University Cytometry Laboratories. http://www.cyto.purdue.edu/, Purdue University, West Lafayette, Indiana
35. White JG et al (2007) Confocal Imaging, Laboratory for Optical and Computational Instrumentation. http://www.loci.wisc.edu/index.html, University of Wisconsin, Madison
36. Hall E, Hall W (2007) Confocal Laser Scanning Microscopy, Cytometry Lab. http://www.wehi.edu.au/cytometry/confocalHome.html, The Walter and Eliza Hall Institute of Medical Research, Melbourne, Australia
37. Rezai N (2004) Confocal Microscopy—A Visual Slide of the Cellular World, The Science Creative Quarterly, Issue 3, September 2007-April 2008. http://www.scq.ubc.ca/confocal-microscopy-a-visual-slice-of-the-cellular-world/, University of British Columbia, Vancouver, Canada
38. Aebi U, Engel A (2007) From Bones to Atoms. http://www.mih.unibas.ch/Booklet/Booklet96/Booklet96.html, M. E. Müller-Institute for Microscopy Biozentrum, Basel, Switzerland
39. Wolverton C (2002) Confocal Microscope. http://confocal.owu.edu, Ohio Wesleyan University, Delaware, Ohio
40. Flem E et al (2007) Nikon Confocal Microscopes. http://www.nikoninstruments.com/Products/Microscope-Systems/Confocal-Microscopes, Nikon USA, Inc., Melville, New York
41. Webmaster et al (2007) Leica Confocal Microscopes. http://www.leica-microsystems.com/, Leica Microsystems AG, Wetzlar, Germany
42. Webmaster et al (2007) PerkinElmer Live Cell Solutions. http://las.perkinelmer.com/Imaging/default.htm, PerkinElmer Inc., Boston, Massachusetts
43. Davidson MW et al (2007) Olympus FluoView Resource Center. http://www.olympusconfocal.com/, National High Magnetic Field Laboratory, The Florida State University, Tallahassee

44. Webmaster et al (2007) Laser Scanning Microscopes. http://www.zeiss.com/, Carl Zeiss Inc., Göttingen, Germany
45. Davidson MW et al (2007) Molecular Expressions. http://www.microscopy.fsu.edu/, National High Magnetic Field Laboratory, The Florida State University, Tallahassee
46. Abramowitz M, Keller E, Spring KR, Murphy DB, Parry-Hill MJ, Swedlow J, Lippincott-Schwartz J, Patterson G, Piston DW, Davidson MW (2007) The Molecular Expressions Microscopy Primer. http://www.microscopy.fsu.edu/primer/, National High Magnetic Field Laboratory, The Florida State University, Tallahassee
47. Davidson MW et al (2002) The Molecular Expressions Museum of Microscopy. http://www.microscopy.fsu.edu/primer/museum/, National High Magnetic Field Laboratory, The Florida State University, Tallahassee
48. Schwartz S, Ross S, Spring KR, Fellers TJ, Parry-Hill MJ, Murphy DB, Lippincott-Schwartz J, Patterson G, Piston DW, Davidson MW (2007) Nikon MicroscopyU. http://www.microscopyu.com/, National High Magnetic Field Laboratory, The Florida State University, Tallahassee
49. Abramowitz M, Fester WK, Fellers TJ, Spring KR, Parry-Hill MJ, Murphy DB, Davidson MW (2007) The Olympus Microscopy Resource Center. http://www.olympusmicro.com/, National High Magnetic Field Laboratory, The Florida State University, Tallahassee
50. Deguil N, Mottay E, Salin F, Legros P, Choquet D (2004) Novel diode-pumped infrared tunable laser system for multi-photon microscopy. Microsc Res Tech 63:23–26
51. Girkin JM, McConnell G (2005) Advances in laser sources for confocal and multiphoton microscopy. Microsc Res Tech 67:8–14
52. Dixon PJ, Neaves SH, Parry-Hill MJ, Davidson MW (2002) Science, Optics, and You. http://www.microscopy.fsu.edu/optics/, National High Magnetic Field Laboratory, The Florida State University, Tallahassee
53. Keller HE, Spring KR, Parry-Hill MJ, Davidson MW (2000) Astigmatism Optical Aberration. http://www.microscopy.fsu.edu/primer/java/aberrations/astigmatism/index.html, National High Magnetic Field Laboratory, The Florida State University, Tallahassee
54. Hinsch J, Parry-Hill MJ, Davidson MW (2005) de Sénarmont Compensators. http://www.microscopy.fsu.edu/primer/java/dic/desenarmont/index.html, National High Magnetic Field Laboratory, The Florida State University, Tallahassee
55. Abramowitz M, Parry-Hill MJ, Davidson MW (2005) Specialized Microscopy Techniques: Interactive Java Tutorials. http://www.microscopy.fsu.edu/primer/techniques/technojava.html, National High Magnetic Field Laboratory, The Florida State University, Tallahassee
56. Spring KR, Russ JC, Parry-Hill MJ, Fellers TJ, Davidson MW (2007) Basic Concepts in Digital Image Processing. http://www.microscopy.fsu.edu/primer/digitalimaging/javaindex.html, National High Magnetic Field Laboratory, The Florida State University, Tallahassee
57. Davidson MW et al (2005) Applications in Confocal Microscopy, Olympus FluoView Resource Center. http://www.olympusconfocal.com/applications/index.html, National High Magnetic Field Laboratory, The Florida State University, Tallahassee
58. Shand SH, Watkins SC, Matsuba K, Parry-Hill MJ, Claxton NS, Davidson MW (2004) Laser Scanning Confocal Microscope Simulator, Olympus FluoView Resource Center. http://www.olympusconfocal.com/java/confocalsimulator/index.html, National High Magnetic Field Laboratory, The Florida State University, Tallahassee
59. Fellers TJ, Parry-Hill MJ, Davidson MW (2004) Scanning System Basics, Olympus FluoView Resource Center. http://www.olympusconfocal.com/java/aperturescanner/index.html, National High Magnetic Field Laboratory, The Florida State University, Tallahassee
60. Fellers TJ, Parry-Hill MJ, Davidson MW (2004) Laser Confocal Microscopy Scanning Modes, Olympus FluoView Resource Center. http://www.olympusconfocal.com/java/scanningmodes/index.html, National High Magnetic Field Laboratory, The Florida State University, Tallahassee
61. Gratton E, vandeVen MJ (1995) Laser sources for confocal microscopy. In: Pawley JB (ed) Handbook of biological confocal microscopy. Plenum Press, New York, pp 69–98
62. Fellers TJ, Parry-Hill MJ, Davidson MW (2007) Interactive Java Tutorials, Olympus FluoView Resource Center. http://www.olympusconfocal.com/java/index.html, National High Magnetic Field Laboratory, The Florida State University, Tallahassee
63. Parry-Hill MJ, Davidson MW (2004) Argon-Ion Lasers, Olympus FluoView Resource Center. http://www.olympusconfocal.com/java/argonionlaser/index.html, National

High Magnetic Field Laboratory, The Florida State University, Tallahassee
64. Parry-Hill MJ, Davidson MW (2004) Helium-Neon Lasers, Olympus FluoView Resource Center. http://www.olympusconfocal.com/java/henelasers/index.html, National High Magnetic Field Laboratory, The Florida State University, Tallahassee
65. Spring KR, Inoué S (1997) Video microscopy: the fundamentals, 2nd edn. Plenum Press, New York, p 741
66. Carter DR (1989) The photomultiplier handbook. Burle Industries, Inc., Lancaster, PA, p 180
67. Patterson GH, Knobel SM, Sharif WD, Kain SR, Piston DW (1997) Use of the green fluorescent protein and its mutants in quantitative fluorescence microscopy. Biophys J 73:2782–2790
68. Parry-Hill MJ, Davidson MW (2003) Side-On Photomultipliers, Olympus FluoView Resource Center. http://www.olympusconfocal.com/java/sideonpmt/index.html, National High Magnetic Field Laboratory, The Florida State University, Tallahassee
69. Parry-Hill MJ, Davidson MW (2003) Channel Photomultipliers, Olympus FluoView Resource Center. http://www.olympusconfocal.com/java/channelpmt/index.html, National High Magnetic Field Laboratory, The Florida State University, Tallahassee
70. Casavan W, Gaidoukevitch Y, Parry-Hill MJ, Claxton NS, Davidson MW (2005) Colocalization of Fluorophores in Confocal Microscopy, Olympus FluoView Resource Center. http://www.olympusconfocal.com/java/colocalization/index.html, National High Magnetic Field Laboratory, The Florida State University, Tallahassee
71. Smallcombe A (2001) Multicolor imaging: the important question of co-localization. Biotechniques 30:1240–1244
72. Demandolx D, Davoust J (1997) Multicolor analysis and local image correlation in confocal microscopy. J Microsc 185:21–36
73. Kumar RK, Chapple CC, Hunter N (1999) Improved double immunofluorescence for confocal laser scanning microscopy. J Histochem Cytochem 47:1213–1217
74. Murphy DB, Piston DW, Shand SH, Watkins SC, Davidson MW (2005) Spectral Bleed-Through Artifacts in Confocal Microscopy, Olympus FluoView Resource Center. http://www.olympusconfocal.com/theory/bleedthrough.html, National High Magnetic Field Laboratory, The Florida State University, Tallahassee
75. Casavan W, Gaidoukevitch Y, Murphy DB, Claxton NS, Davidson MW (2005) Colocalization of Fluorophores in Confocal Microscopy, Olympus FluoView Resource Center. http://www.olympusconfocal.com/applications/colocalization.html, National High Magnetic Field Laboratory, The Florida State University, Tallahassee
76. Shand SH, Watkins SC, Matsuba K, Parry-Hill MJ, Claxton NS, Davidson MW (2005) Spectral Bleed-Through (Crossover) in Confocal Microscopy, Olympus FluoView Resource Center. http://www.olympusconfocal.com/java/crossoversimulator/index.html, National High Magnetic Field Laboratory, The Florida State University, Tallahassee
77. Piston DW, Tille S, Parry-Hill MJ, Davidson MW (2005) Choosing Fluorophore Combinations for Confocal Microscopy. http://www.olympusconfocal.com/java/dualprobes/index.html, National High Magnetic Field Laboratory, The Florida State University, Tallahassee
78. Flem E, Davidson MW (2007) The Nikon Small World International Photomicrography Competition. http://www.microscopyu.com/smallworld/, National High Magnetic Field Laboratory, The Florida State University, Tallahassee
79. Shaner NC, Steinbach PA, Tsien RY (2005) A guide to choosing fluorescent proteins. Nat Methods 2:905–909
80. Chudakov DM, Lukyanov S, Lukyanov KA (2005) Fluorescent proteins as a toolkit for *in vivo* imaging. Trends in Biotechnology **23** (in press)
81. Miyawaki A, Nagai T, Mizuno H (2005) Engineering fluorescent proteins. Adv Biochem Eng Biotechnol 95:1–15
82. Rizzo MA, Piston DW (2005) Fluorescent protein tracking and detection. In: Goldman RD, Spector DL (eds) Live cell imaging: a laboratory manual. Cold Spring Harbor Laboratory Press, Cold Spring Harbor, NY, pp 3–23
83. Verkhusha VV, Lukyanov KA (2004) The molecular properties and applications of Anthozoa fluorescent proteins and chromoproteins. Nat Biotechnol 22:289–296
84. Tsien RY (1998) The green fluorescent protein. Annu Rev Biochem 67:509–544
85. Matz MV, Fradkov AF, Labas YA, Savitsky AP, Zaraisky AG, Markelov ML, Lukyanov SA (1999) Fluorescent proteins from nonbioluminescent Anthozoa species. Nat Biotechnol 12:969–973
86. Zhang J, Campbell RE, Ting AY, Tsien RY (2002) Creating new fluorescent probes for

cell biology. Nat Rev Mol Cell Biol 3:906–918
87. Lippincott-Schwartz J, Altan-Bonnet N, Patterson G H (2003) Photobleaching and photoactivation: following protein dynamics in living cells. Nat Cell Biol Suppl 5:S7–S14
88. Rabut G, Ellenberg J (2005) Photobleaching techniques to study mobility and molecular dynamics of proteins in live cells: FRAP, iFRAP, and FLIP. In: Goldman RD, Spector DL (eds) Live cell imaging: a laboratory manual. Cold Spring Harbor Laboratory Press, Cold Spring Harbor, NY, pp 101–126
89. Phair RD, Misteli T (2001) Kinetic modeling approaches to *in vivo* imaging. Nat Rev Mol Cell Biol 2:898–907
90. Dunn GA, Dobbie IM, Monypenny J, Holt MR, Zicha D (2002) Fluorescence localization after photobleaching (FLAP): a new method for studying protein dynamics in living cells. J Microsc 205:109–112
91. Periasamy A, Day RN (2005) Molecular Imaging: FRET Microscopy and Spectroscopy. Oxford University Press, New York, p 312
92. Berney C, Danuser G (2003) FRET or no FRET: a quantitative comparison. Biophys J 84:3992–4010
93. Harpur AG, Wouters FS, Bastiaens PIH (2001) Imaging FRET between spectrally similar GFP molecules in single cells. Nat Biotechnol 19:67–169
94. Behlendorf B, Fielding RT, Hartill R, Robinson D, Skolnick C, Terbush R, Thau RS, Wilson A (2007) Apache HTTP Server Project. http://httpd.apache.org, The Apache Software Foundation
95. Microsoft Development Team (2007) Internet Information Server. http://www.microsoft.com, Microsoft Corporation, Redmond, Washington
96. BadBlue Development Team (2007) BadBlue Personal and Enterprise Business Web Servers. http://www.badblue.com, Working Resources Inc., Atlanta, Georgia
97. Savant Development Team (2007) Savant Web Server. http://savant.sourceforge.net/, Open Source Technology Group, Mountain View, California
98. Essentia Development Team (2007) Essential Web Server, Cyber Outlet, Enterprise Java Application Server. http://www.essencomp.com/, The Essen Group, Bombay, India
99. PlanetWeb Development Team (2007) Simple Server. http://www.planetdns.net/, PlanetDNS, Inc., Sarnia, Canada
100. MiniPortal Development Team (2007) MiniPortal Web Server. http://www.instant-servers.com/. InstantServers, Inc., Mountain View, California
101. Red Hat Development Team (2007) Enterprise Linux. http://www.redhat.com/, Red Hat, Inc., Raleigh, North Carolina
102. Castro E (2002) HTML for the World Wide Web with XHTML and CSS: Visual Quick Start Guide, 5th edn. Peachpit Press, Berkeley, CA, p 480
103. Musciano C, Kennedy B, Loukides M (2004) HTML: the definitive guide. O'Reilly Media, Sebastopol, CA, p 576
104. Google Directory (2007) WYSIWYG HTML Editors. http://directory.google.com/Top/Computers/Software/Internet/Authoring/HTML/, Mountain View, California
105. Page KA (2006) Macromedia Dreamweaver 8: training from the source. Macromedia Press, San Francisco, CA, p 608
106. Randolph N, Gardner D (2008) Professional Visual Studio 2008. Wrox Press, Hoboken, NJ, p 1032
107. Hester N (2007) Microsoft Expression Web (Visual QuickStart Guide). Peachpit Press, Berkeley, CA, p 256
108. Colligan P, Cheshire J (2003) Special edition: using Office Microsoft FrontPage 2003. Que Publishing, Pearson Education, Indianapolis, IN, p 992
109. Software Development Team (2007) Image-Pro Plus 6.2. http://www.mediacy.com, MediaCybernetics, Silver Spring, Maryland
110. Software Development Team (2007) SlideBook 5.0. http://www.intelligent-imaging.com, Intelligent Imaging Innovations, Denver Colorado
111. Software Development Team (2007) MetaMorph 7.5. http://www.moleculardevices.com/home.html, Molecular Devices Corporation, Sunnyvale, California
112. Miano J (1999) Compressed image file formats: JPEG, PNG, GIF, XBM, BMP. Addison-Wesley Professional, New York, p 288
113. Pennebaker WB, Mitchell J (1993) JPEG still image compression standard. Van Nostrand Rheinhold, New York, p 650
114. Team AC (2007) Adobe Photoshop CS3 classroom in a book. Pearson Education, Adobe Press, Berkeley, CA, p 496
115. Bouton GD (2008) CorelDRAW: the official guide. McGraw-Hill Osborne Media, San Francisco, CA, p 892
116. Nichols R (2003) Paint shop Pro 8: the guide to creating professional images. Focal Press, Elsevier, New York, p 288
117. Meadhra M, Celeste AL (2002) PhotoImpact 7: the official guide. McGraw-Hill, New York, p 512
118. Staples T (2003) Adobe Photoshop CS/ImageReady CS for the Web: hands-on training. Peachpit Press, Berkeley, CA, p 840

119. Team AC (2005) Adobe illustrator CS2 classroom in a book. Adobe Press, Pearson Education, Berkeley, CA, p 472
120. Bain S (2004) CorelDRAW 12: the official guide. McGraw-Hill Osborne Media, New York, p 696
121. Schulze P (2003) Macromedia FreeHand MX: training from the source. Macromedia Press, Berkeley, CA, p 350
122. Software Design Team (2007) Serif DrawPlus X3. http://www.serif.com/drawplus/drawplus/, Serif, Inc., Amherst, New Hampshire
123. Zaluzec NJ (2001) MicroScape: The Virtual Laboratory. http://www.microscopy.com/MicroScape/MicroScape.html, The Microscopy Society of America
124. Schmidt M (2006) The Scanning Tunneling Microscope: What it is and how it works. http://www.iap.tuwien.ac.at/www/surface/STM_Gallery/stm_schematic.html, Institute for General Physics, Vienna University of Technology, Austria
125. Swan J (2003) The Virtual Microscope. http://webanatomy.net/microscope/microscope.htm, Online Anatomy and Physics Resources, University of New Mexico, Albuquerque
126. Benfer D, Cohen BJ, Kutzer B (2003) Virtual Microscope: Histology Slides for Human Anatomy. http://www.dccc.edu/departments/biology/virtuals/virtualmicroscope/VMPage/very1st.htm, Delaware County Community College, Media, Pennsylvania
127. Kunkel D (2005) Virtual Scanning Electron Microscope. http://education.denniskunkel.com/, Dennis Kunkel Microscopy, Inc., Honolulu, Hawaii
128. Fontelo P, DiNino E, Johansen K, Khan A, Ackerman M (2005) Virtual Microscopy: Potential applications in medical education and telemedicine in countries with developing economies, Proceedings of the 38th Hawaii International Conference on System Sciences, 1–7.
129. Fryer C (2000) Development of a virtual laboratory in a World Wide Web system using JavaScript and dynamic HTML. http://www.cebe.heacademy.ac.uk/learning/habitat/HABITAT7/lab.pdf, the ATLAS Project, University of Derby
130. Horstmann C, Cornell G (2004) Core Java 2, volume 1: fundamentals, 7th edn. Prentice Hall, New York, p 784
131. Schildt H (2004) Java: the complete reference, 6th edn. McGraw-Hill Osborne Media, New York, p 1000
132. MicroBrightField Development Team (2007) Web Enabled Virtual Microscope Demonstration. http://www.neuroinformatica.com/, MBF Bioscience, Williston, Vermont
133. Goldman MV, et al (2004) Physics 2000. http://www.colorado.edu/physics/2000/index.pl, University of Colorado, Boulder
134. Murray JM, Spring KR, Johnson I, Metcalfe WK, Lerant A. Riddle KA, Bass HW, Fajer P, Cusma AM, Parry-Hill MJ, Davidson MW (2001) Laser Scanning Confocal Microscopy. http://www.microscopy.fsu.edu/primer/virtual/confocal/index.html, Molecular Expressions, National High Magnetic Field Laboratory, The Florida State University, Tallahassee
135. Edwards DJ (2001) The Virtual Microscope. http://met.open.ac.uk/vms/vms.html, Department of Earth Sciences and Multimedia Enabling Technologies Group, The Open University, Milton Keynes, United Kingdom
136. Donald RL, Cahill MC (2007) DiscoverySchool.com, The Virtual Electron Microscope. http://school.discoveryeducation.com/lessonplans/activities/electronmicroscope/, Discovery Education, Discovery Communications, Inc.
137. Ketcham B (2004) Microscopy Pre-Lab Activities: Virtual Microscope. http://www.udel.edu/Biology/ketcham/microscope/, Department of Biology, University of Delaware, Newark
138. Purchon ND (2001) The Virtual Microscope. http://www.purchon.com/biology/palisade.htm, Gondar Design Science, Shepton Mallet, United Kingdom
139. Product Development Team (2007) Macromedia (Adobe) Flash CS3 Software Kit. http://www.adobe.com/products/flash/, Macromedia, Inc., San Francisco, California
140. Webmaster et al (2007) http://www.adobe.com, Adobe Systems Inc., San Jose, California
141. Ozer J (2003) PC magazine guide to digital video. John Wiley and Sons, New York, p 472
142. Richardson I (2002) Video codec design: developing image and video compression systems. John Wiley and Sons, New York, p 328
143. Austerberry D (2002) Technology of video and audio streaming. Focal Press, Elsevier, New York, p 352
144. Birney B, Gill T (2003) Microsoft windows media resource Kit. Microsoft Press, Redmond, WA, p 512
145. Haskell BG, Puri A, Netravali AN (1996) Digital video: an introduction to MPEG-2. Springer, New York, p 775
146. Farrell J (2002) Digital movies with QuickTime Pro. Charles River Media, Hingham, MA, p 362
147. Product Development Team (2007) Real Player. http://service.real.com/business

products/, RealNetworks, Inc., Seattle, Washington
148. Reinhardt R (2006) Macromedia flash video: training from the source. Macromedia Press, San Francisco, CA, p 304
149. McEvoy S (2003) Fundamentals of programming the Microsoft windows media platform. Microsoft Press, Redmond, WA, p 448
150. Geduld M (2004) Premiere Pro editing workshop. CMP Books, Gilroy, CA, p 384
151. Weynand D (2005) Apple Pro training series: final Cut Pro 5. Peachpit Press, Berkeley, CA, p 656
152. Pogue D (2005) IMovie HD and iDVD 5: the missing manual. O'Reilly Media, Inc., Sebastopol, CA, p 528
153. Ozer J (2005) Microsoft windows movie maker 2: visual QuickStart guide. Peachpit Press, Berkeley, CA, p 392
154. Webmaster et al (2007) Confocal Listserver. http://lists.umn.edu/cgi-bin/wa?A0=confocal-microscopy, University of Minnesota, Minneapolis, Minnesota
155. Swedlow J, Sorger P, Goldberg I, White J, Eils R (2007) Open Microscopy Environment. http://www.openmicroscopy.org/, Massachusetts Institute of Technology, Cambridge, Massachusetts
156. Swedlow J, Goldberg I, Brauner E, Sorger PK (2003) Informatics and quantitative analysis in biological imaging. Science 300: 100–102

Chapter 4

Using Photoshop with Images Created by a Confocal System

Jerry Sedgewick

Abstract

Many pure colors and grayscales tones that result from confocal imaging are not reproducible to output devices, such as printing presses, laptop projectors, and laser jet printers. Part of the difficulty in predicting the colors and tones that will reproduce lies in both the computer display, and in the display of unreproducible colors chosen for fluorophores. The use of a grayscale display for confocal channels and a LUT display to show saturated (clipped) tonal values aids visualization in the former instance and image integrity in the latter. Computer monitors used for post-processing in order to conform the image to the output device can be placed in darkened rooms, and the gamma for the display can be set to create darker shadow regions, and to control the display of color. These conditions aid in visualization of images so that blacks are set to grayer values that are more amenable to faithful reproduction. Preferences can be set in Photoshop for consistent display of colors, along with other settings to optimize use of memory. The Info window is opened so that tonal information can be shown via readouts. Images that are saved as indexed color are converted to grayscale or RGB Color, 16-bit is converted to 8-bit when desired, and colorized images from confocal software is returned to grayscale and re-colorized according to presented methods so that reproducible colors are made. Images may also be sharpened and noise may be reduced, or more than one image layered to show colocalization according to specific methods. Images are then converted to CMYK (Cyan, Magenta, Yellow and Black) for consequent assignment of pigment percentages for printing presses. Changes to single images and multiple images from image stacks are automated for efficient and consistent image processing changes. Some additional changes are done to those images destined for 3D visualization to better separate regions of interest from background. Files are returned to image stacks, saved and then printed to best reveal colors, contrast, details and features.

Key words Colorizing, Image processing, Gamma, CMYK, Colocalization, Image mode, Vector, Banding, Rasterization, Gaussian, Median, Sampling, Quantization, Dialogue box, Palette, Saturation, Midtone, Compressed, Conformance, Profile

1 Introduction

The post-processing of confocal images has become a necessary practice for nearly every researcher using these devices. Except for those researchers who need to retain optical intensity of image features for subsequent measurement, and those who must show comparative optical intensities of two or more experimental

Stephen W. Paddock (ed.), *Confocal Microscopy: Methods and Protocols*, Methods in Molecular Biology, vol. 1075,
DOI 10.1007/978-1-60761-847-8_4,

conditions, confocal images simply do not contain color and grayscale values always amenable to output and these must be changed (1–3). These outputs include printing presses; inkjet (including wide format for posters), laserjet, thermal, dye sublimation, or photographic (such as the Fujix 3000) printers; LCD projection at meetings; screen displays for collaborators and other members within a work group, other software applications such as Word, Acrobat, and PowerPoint; or for 3D reconstruction software. For that reason, conformance of images to output is necessary in order to avoid obscuring important features, and to retain the look of the original without a loss in resolution along the way [4].

Clearly, in this discussion, it should be self-evident that local enhancement of the image be avoided (as was once done by dodging and burning when using photographic enlargers in a darkroom). Post-processing should only be applied to the entire image and, in the same way, to its experimentally related images. Outlining a feature in order to increase or decrease its optical intensity to the exclusion of other features, along with the inclusion of features (by cutting and pasting) that were not present in the original image, violates ethical practices [5]. The only arguable exception would include the elimination of artifact for 3D visualizations, as these obstruct the view of more important features.

Finally, the methods and procedures that follow provide the means to create a generic, "target" image. The thought is to balance every image so that it is ready for publication. From those images, then, subtle brightness changes can be made, or printing dimensions (and, possibly, image resolutions) can be set for other outputs, if that is deemed necessary. That approach is followed to simplify the imaging workflow, and to ensure that a standard is followed in workgroups. Most importantly, however, is that the final image will nearly always contain correct grayscale and color values—and reveal important features—no matter what the output.

2 Correct Colors

The operative word here is "correct." Monitor to monitor variation (even when two monitors are the same make and model), will necessarily lead to differences in the rendition of color and contrast. For that reason, calibration tools can be bought for the monitor to more exactingly view color and contrast. These tools are relatively inexpensive at less than $200.00 (US), available at professional photography supply stores. Even when every monitor in a workgroup is not calibrated, a "proofing" monitor is best set aside for that purpose in a windowless room with dim, ambient lighting [6]. Not every Liquid Crystal Display, flat screen monitor is made alike. Most use Twisted Nematic (TN) technology as the cheapest alternative. TN technology results in poor displays (more at

quickphotoshop.com). A better monitor can be paired with an inkjet or dye sublimation printer for making printed proofs as examples for how an image would reproduce when published. Protocol for making proofs can be found at http://www.quickphotoshop.com.

3 Good Images Before Photoshop

3.1 Viewing Images on the Confocal System

The design of confocal instruments always moves in the direction of making these easier to use. Part of that process includes colorizing images in order to view fluorochromes for easy identification. To clearly differentiate fluorochromes, three primary colors are typically used: green, red and blue. These are often used not only for display of the representative images on the computer screen, but software is also included to save what is a colorized image. In that manner, the object of making the confocal easier to use is fulfilled: the user can clearly view the different fluorochromes by color and these can be saved in color.

Yet, colorized displays can lead to poor decisions in regard to setting brightness levels, and unfortunate conclusions when interpreting the images. The color blue, for example, can be far more difficult to see, and that can lead to a user arbitrarily amplifying the signal beyond the dynamic range of the instrument. If a fourth display on the confocal system shows the combination of these three primary in a single window, the problem can then compound. The combination of pure red and green produces the color yellow, which appears bright; combinations of blue with red or green produce magenta or cyan, both dimmer than yellow and more uncertain when the two colors do not occur at equal intensities. Thus, any combination of colors with that of blue can again be interpreted poorly, and arbitrary adjustment of brightness is the natural tendency for users.

To make the setting of gain and black level on a computer similar among fluorochromes no matter what the color, the better option is to remove color altogether and view each fluorochrome as grayscale. Color images on a computer screen may look pretty, but the look also serves to confuse the eye. Images are best viewed in grayscale on the computer screen in order to make better decisions in regard to grayscale values (notwithstanding the use of LUT overlays to show saturation in the white and black ends of the dynamic range), and interpreting levels of fluorescence compared to background.

3.2 Use LUT Overlays in Order to Stay Within Detector's Dynamic Range

Manufacturers of confocal equipment provide several LUTs for visualization, one of which displays colors in order to alert the user to "clipped" values. Clipped values include pixels that are at or greater than the dynamic range of the instrument, measured as a pure black at one end of the scale (pixel value of 0), and pure white

at the other end (pixel value of 255 on an 8-bit scale, 4,095 at 12-bits and 65,535 at 16-bits). On an Olympus confocal system, a red overlay indicates clipped white values and a blue overlay indicates black, clipped values. Confocal settings must be changed in order to bring significant values within the dynamic range of the instrument (artifacts can be regarded as outside the range). Do not always adjust to remove all of the color overlay, however: randomly occurring spots of green or red are often a result of noise generated by the photomultiplier tube (PMT) and amplifier. When frame averaging is employed, these significantly brighter pixels become dimmer and fall into the dynamic range of the instrument.

By remaining within the dynamic range of the instrument, the darkest and whitest values will not contain untextured and featureless image information. In that way, all the image information is available later when post processing in Photoshop. The image may appear darker than what is desired, or the brighter features may not appear bright enough against the background, but, in either case, the image information lies in the digital file. If at all possible—when it does not interfere with the operation of confocal acquisition software (check with the manufacturer)—this monitor is calibrated.

4 Viewing Images in Photoshop

After the image is acquired within the dynamic range of the confocal instrument, then images can be edited in Photoshop. The first problem is, again, seeing the correct colors. Though the monitor may have been calibrated, the display of color jumps through yet another hoop: the display of color depends on its source and its destination. Taking the latter, the destination is assumed by Photoshop (in its default settings) to be within the limited range of colors used on the Web.

As far as the source of the colors, Photoshop can be alerted by the manufacturer of a color profile (tagged image) or not (untagged). Because confocal instruments produce untagged colors, the concern lies only with the destination of the image.

The act of displaying source and destination colors while in Photoshop is referred to as “Color Management.” The decision about how to view the colors while in Photoshop comprises the color editing space. So three possible categories of color are available for color management: the source colors, the editing color “space,” and the destination colors. Also included, are settings for grayscale press reproduction. These are all set in the “Color Settings” dialog box within Photoshop (Edit > Color Settings for Windows or for Macintosh OSX). What follows is a guide to decisions made in the “Color Settings” dialog box specific to confocal and fluorescence imaging for different working spaces (Fig. 1):

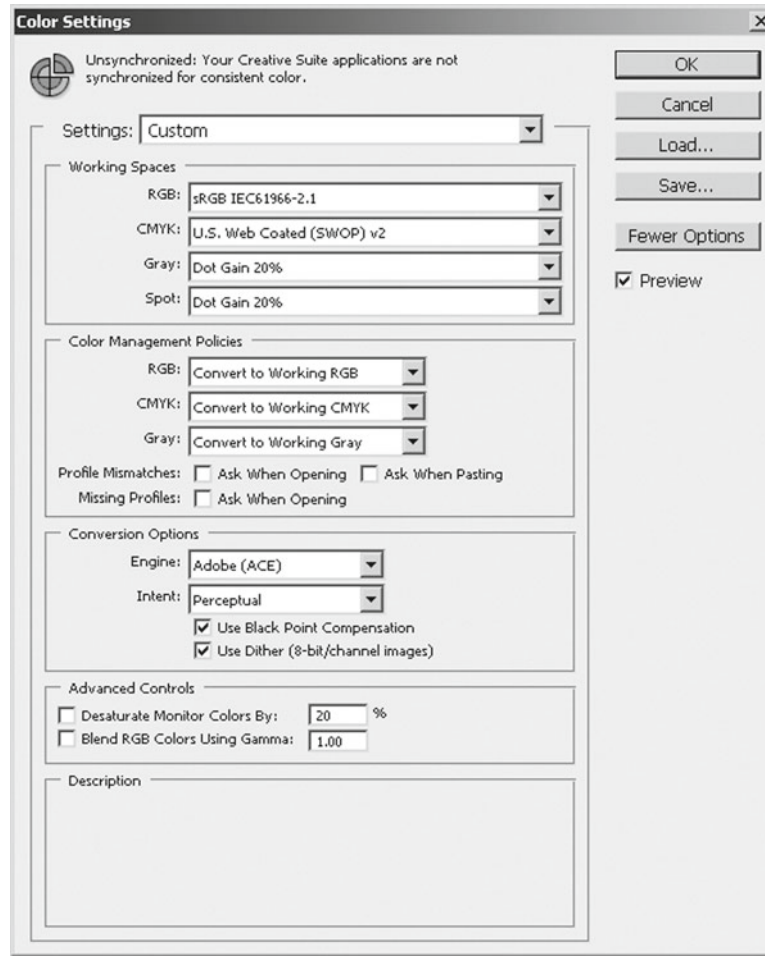

Fig. 1 Color settings dialogue box: working space is left at the default setting of sRGB IEC61966-2.1. The device independent, generic printing press settings depends upon the publisher's country: here it is set to the USA. Color Management is turned off in this instance, but, when desiring to know the color space of the original file, these are turned on. Conversion Options appear when checking Advanced. The intent is set to Perceptual, what appears to be a good result for CMYK conversion of confocal images

4.1 RGB

Keep the default "sRGB IEC61966-2.1" (sRGB) setting. This is not generally the approach recommended by Photoshop experts, unless the colors are specifically destined for uploading to the Web [7]. In fluorescence microscopy, the colors are pure (saturated) and generally outside the range for printing press capabilities. In environmental photography, these saturated colors rarely exist, and so the approach is to see as many colors as possible, what would be result from choosing either Adobe RGB 1998 or ProPhoto Color for the color editing space. Color conversion, in particular to publication (though useful for other outputs, such as

posters), is determined more accurately while retaining tonal ranges (when done correctly), when the default setting is retained (sRBG).

4.2 CMYK

Change this to the press that applies to the country in which a publication will be printed. For the USA, the recommended setting is "U.S. Web Coated (SWOP) v2". In Europe and Japan it is "Euroscale Coated v2" and "Japan Standard v2," respectively. Japan and Europe's standard includes a dot gain that is less than in the USA, thus allowing for darker blacks to be printed along a greater range of colors. The difference is most notable for hard to publish colors, such as green. When colors are converted from the primary colors for light (red, green and blue) to the primaries for the printing press (Cyan, Magenta, Yellow, with the addition of a blacK channel: CMYK) the colors are set according to respective printing press conventions, or standards.

4.3 Gray

Set this the same as the monitor at Dot Gain 20 % as a default standard, unless author's guidelines for particular journals state otherwise.

4.4 Spot

Dot Gain of 20 %. Generally, this is not used by scientists, as it addresses situations in which a specified color of ink is designated for printing on areas (spots) of a printed material.

4.5 Color Management Policies

Generally, these are set to "Convert to Working …" When set to that policy, any image that opens, whether it comes with a profile or not, is treated as though it is in the current working (editing) space (sRGB).

4.5.1 For RGB, CMYK, and Gray

4.5.2 Profile Mismatches

Generally, this, too, is unchecked, along with Ask When Pasting and Ask When Opening. Those who are more familiar with Color Management will want to be alerted, and these users will want the boxes left checked.

4.5.3 Advanced or More Options

Click on the Advanced checkbox (pre-CS) or on More Options (CS versions) to show Conversion Options. Set this engine to Adobe (ACE) for what is considered the best conversion engine for changing modes from RGB Color to CMYK Color and to LAB Color. Set the intent to Perceptual, when wishing to have colors that are converted to CMYK to have the same perceptual brightness levels. Uncheck Use Dither if images will be measured, because conversions will fill in colors to create smooth gradients. However, if images are for visualization, then consider leaving this box checked. Leave other settings at the defaults.

Other Photoshop settings, if not already determined, are listed below:

5 Photoshop Preferences

5.1 Memory

The use of computer hard disk memory should also be set. Photoshop requires ~3 times the hard disk space than the size of any single image file. That is required to complete many functions in Photoshop, as well as for clipboard space.

Under Edit > Preferences choose Plug-Ins and Scratch Disks (newer versions call this Performance). If more than one hard disk, or a partitioned drive exists, set the 1st, 2nd, etc., respectively, to the disk that has the greatest amount of free space, the next largest, and so on.

5.2 Transparency and Gamut, Display and Cursors

The following changes in Photoshop settings are based upon personal preference.

If the checkerboard pattern of squares that appears in images when working in Photoshop is confusing or annoying, under Transparency Settings set Grid Size to None.

If the diameter of Brush settings is desired so that the diameter of its size can be viewed (versus a crosshair), under Display and Cursors, choose Brush Size.

6 Photoshop Troubleshooting

Once preferences are set, if unfamiliar with Photoshop, some possible user troubles may interfere with completion of methods discussed in this chapter. While this chapter does not cover all possible troubles in Photoshop, the following are pointed out because of the frequency of their occurrence:

The "prohibited" symbol appears (red circle with diagonal line) or many options in the menus are grayed out:

1. The image mode is incorrect. Change the mode from Indexed Color to RGB Color or Grayscale, depending on the final destination for the image.
2. The image is 16-bit (versus 8-bit) and the version of Photoshop is pre-CS. Change from 16-bit to 8-bit, but only if the version is pre-CS. Photoshop CS versions are optimized for image processing 16-bit images. These images are better processed at the greater bit depth to allow for what is called "headroom." In other words, the 16-bit image contains more gray values that can be eliminated, something that occurs at every step of image processing because of rounding errors for the greater glory of revealed features and output-corrected tones and colors.
3. The text or symbol layer is selected. If the image is layered, such as what is done in Photoshop automatically when creating text and symbols, the layer may not be an image layer.

Note that the text and symbol layers are vector layers. These are not a collection of so many pixels (like images); instead, these are libraries from which printer drivers determine shapes. The conversion of a vector file to so many pixels is a process called rasterization. At that point, both text and symbols act like images insofar as these become a collection of pixels, and these display on the monitor much like these will print when viewed at about 100 % (the only real test of how text will print at this point lies in printing the images to an ink jet, photographic or dye sublimation printer: NOT a laser printer, as this may introduce artifacts into the lettering).

The prompt that reads as follows: "Warning: No pixels are more than 50 % selected. The selection edges will not be visible." If that warning appears as a prompt, it means that a selection has been drawn too small, and probably by accident. It is easy, especially when first using Photoshop, to accidentally drag the mouse while on a selection tool (such as the marquee tool in the upper left of the Photoshop toolbox). If this warning appears, deselect the selection under Select > Deselect, or use the keyboard: Control/Command Key + D.

7 The Most Important Window in Photoshop: Info Palette (Fig. 2)

In order to determine effects upon images on an objective basis while referring to numeric readouts, a palette is opened for viewing at all times. This palette is not opened by default, and so it is opened by choosing it under Window in the menu (Window > Info).

All of the pixels that make up the image contain tonal values assigned to each pixel. These can be viewed along several different units of measurement: for purposes of confining the units of measurement to a single scale (thus making these easier to recall) these are displayed as RGB Color, 8-bit (0–255 discrete tonal levels). This reading can be selected for grayscale images (as opposed to the default unit of measurement in K:, or "percent of ink deposited were it printed to paper") so that these values remain uniform across all types of images. For color images, the 8-bit values are read for each channel: an RGB Color image contains three channels: red, green and blue. Note that 16-bit values can also be chosen as the unit of measurement, but readouts are, confusingly, in the 15-bit range (0–32,768) as a result of carryover from earlier Photoshop programs (these values are not the intrinsic values of the image, however). Thus, readouts in 16-bit values are not referred to in methods.

The small eyedropper tool in the Info box can be clicked on to reveal a drop down list. Choose RGB Color from this box (or RGB Color, 8-bit in CS versions).

This box has the added advantage of displaying values at specific positions on the image, up to a total of four. These are called

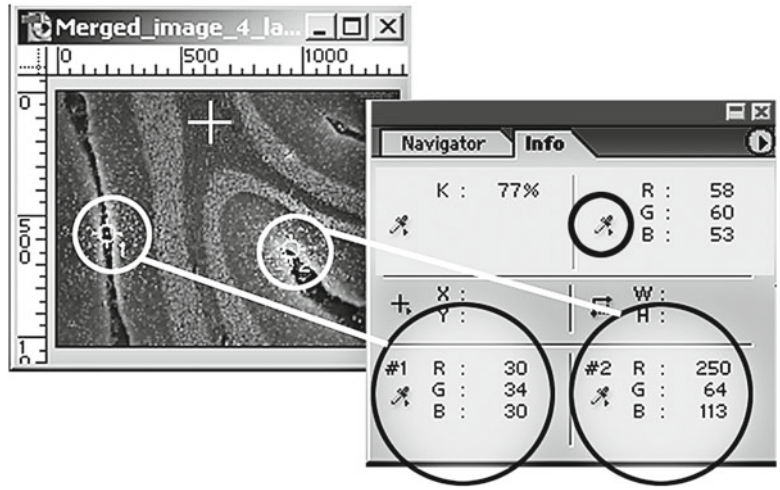

Fig. 2 Using sampling eyedropper tool and info box: (from *right* to *left*) First image shows two sampling tool markers on the darkest and the brightest positions (determined visually and iteratively by checking values in the Info box while moving cursor over the image, and then clicking at these positions with the sampling eyedropper tool). The second image shows placeholders taken by sampling positions in the Info box, labeled #1 and #2. Typical readouts are shown: the first readout, which takes the upper left position in the Info box is set to Grayscale and this indicates the percentage of ink laid on paper were the image to be printed (values from 0 to 100 %). The second readout is set to 8-bit, RGB Color so that 0–255 tonal values are shown. By clicking on the circled eyedropper tool, units of measurement for readout values can be changed by choosing from a drop down list

sampling points or markers, and these are purposefully created at desired positions on your image, typically at the whitest significant point of your image and at the blackest point. Values at those positions can be then be tracked while making contrast, brightness, and, possibly, gamma adjustments.

To prepare to mark these points, do as follows:

1. Click on the eyedropper tool in the toolbar or type the letter "I."
2. On the options bar, below the menu, click on arrowhead adjacent to Sample Size. Choose 3 × 3 Average for most images and 5 × 5 Average if the image is excessively noisy (grainy). The idea is to sample an average of several pixels rather than only one, as a single pixel would be less likely to garner a representative value.

To sample an area of the image, do the following (*see* Fig. 3):

1. Click on the eyedropper tool in the toolbar or type the letter "I." Choose the Sample Eyedropper tool, or hold down the Shift key with the standard eyedropper.

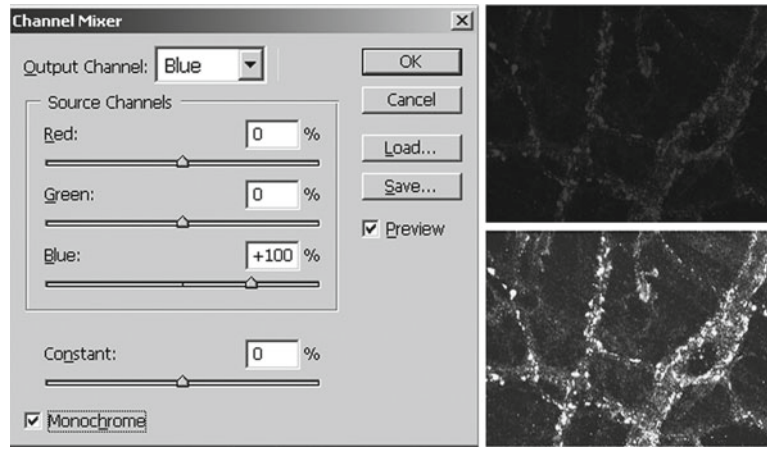

Fig. 3 Channel Mixer dialogue box and example image: Top, darker, blue colored image on right shows the image were it simply converted to Grayscale using Image > Mode > Grayscale: note the loss of brightness. The image on the right below the darker image and the dialogue box settings to the left show the grayscale image converted first by using Channel Mixer and then converted to grayscale using Image > Mode > Grayscale. Note the retention of brightness values. Image courtesy of Martin Wessendorf, Ph.D.

2. Click on desired part of the image. That will nearly always mean the brightest significant (non-artifact) point(s) on the image, and the darkest point(s). The Info box will expand to display pixel values at these locations and a marker will be left that is visible, but will not print.
3. To remove sampling marks, either click Clear button on submenu when the eyedropper tool is active, or hold down the control/command key and click and drag marker off the image area.

8 Working with Images in Photoshop

Here are typical steps that are required in Photoshop when working with fluorescent images:

8.1 Opening Image: Indexed Color to Grayscale or RGB Color

Many confocal images from older systems are saved as indexed color with 256 levels of gray or color assigned to the image. Before subsequent methods can be used, the image must be converted to Grayscale or RGB Color, depending on the final intent.

Under Image > Mode, choose Grayscale or RGB Color.

8.2 Converting 16-Bit to 8-Bit

As mentioned above, it is always best to preserve 16-bit depth of a potential 65,536 gray values (though images could have been

rescaled to 16-bit from 10-, 12- and 14-bit ranges). Keep images at 16-bit, if possible, when using Photoshop CS and greater when working on the image. When the image is readied for output, or when using pre-CS versions of Photoshop, convert the image from 16- to 8-bits/channel:

Under Image > Mode, choose 8-Bits/Channel.

8.3 Resetting Colorized Single Fluorescent Images to Grayscale

If an image from confocal software is saved as a colorized image (versus an image with levels of gray), the result will be an image that is impossible to publish without a loss of brightness in the highlights, a shift in color and a general dimming of the image. Of the three primary colors used for colorizing (red, green and blue), only the color red contains the greatest possibility for matching what is seen on the computer screen to output. That is because the range of hues (gamut) of available colors for light (RGB) do not always overlap with the range of colors available for printing with pigments (CMYK) at desired intensities. Even when colors are simply displayed on a computer screen, the color green dominates as brightest, red appears dimmer than green and blue is often so dim that it is hard to see detail.

It follows, then, that a colorized image saved from confocal software must be altered in color so that it can conform to output and be viewed correctly on the monitor. That saved image may be re-colorized by choosing from a panel of colors in certain software packages in order to get a better fit for output, or it can be returned to a grayscale image and then colorized again in Photoshop.

Note that the colorized image cannot be returned to grayscale by simply changing the mode in Photoshop to grayscale. A change in mode to grayscale is heavily weighted by the green channel (versus the red or blue channels). Because of that, red and blue images will lose their inherent brightness levels! These images must be changed to grayscale using Channel Mixer in Photoshop. This is critical for those wishing to measure optical intensity values from colorized confocal images.

8.4 Channel Mixer Procedure: Returning a Colorized Image to Grayscale to Preserve Brightness (Fig. 3)

1. Under Image > Adjust(ments), choose Channel Mixer.
2. Check the Monochrome box. The Output Channel indicator will change to Gray, indicating a grayscale image.
3. In the Channel Mixer dialogue box, choose the output channel that matches the colorized image (if the image is red, choose Red). Be sure the appropriate source channel is at 100 % (if the output channel is Red, the Source Channels should be at Red: 100 %, Green: 0 % and Blue: 0 %).

Please note that if the Channel Mixer selection is grayed out and unavailable for selecting, then your image is, very likely, saved as indexed color or 16-Bits/Channel (in pre-CS versions). Change according to directions listed above.

8.5 Colorizing Grayscale Images

If images are saved with grayscale values (versus color), or if colorized images have been made into grayscale using the previous method, these can be colorized or re-colorized in Photoshop for the best rendition of color values for output. Three methods are presented.

The first method, called the Channel Assignment Method, has the advantage of predictable and repeatable assignment of color to grayscale values, much like what is done in confocal software. The channel assignment method also produces a saturated red and green suited to the visualization of colocalization with the color yellow. Its advantage lies in producing images destined for quantization of color values, and for colocalization. The downside to this method, however, is that these color values do not reproduce well when output for presentation purposes, and one only replicates many irreproducible colors of confocal software.

The second method, called the Levels Colorizing Method, is best suited for creating colors fit for output. At the same time, the colors can also be used to visualize colocalization, since these hues of the popular red/green combination of colors will also produce yellow. These can be set according to the provided table to the tastes of the researcher, with the idea that fluorochromes are not necessarily viewed by the color of their correct emission, anyway (CY3, for example, emits in yellow, but is often visualized and presented as red).

A third method is often presented in Photoshop manuals as the preferred way to colorize. That is done by using the Hue and Saturation function under Image > Adjust(ments). In that dialogue box, Colorize can be checked and a color can be selected by moving the Hue slider to the user's preference. The Saturation slider is typically set to the greatest saturation. The procedure works, but, for many confocal images in which values exist at or near 255 on an 8-bit scale, the highlights are not colored at all unless the Lightness slider is used to darken the entire image. Furthermore, luminance values in the dominant color channel no longer read on a linear scale because colors from all three channels are re-assigned. Finally, the colors are not as saturated: these do not have the look associated with a colorized, confocal image. For all these reasons, this method is not described in detail.

Either method can be made into an automated or semi-automated action in Photoshop to save time and to create consistence among all members of individual labs. *See* Subheading 11.

8.6 Channel Method for Colorizing Images

Photoshop requires three channels when colorizing is desired. If only one color is desired from one image, then two duplicate, "dummy" images have to be created to substitute for the other two channels. The dummy images are completely black images. All images need to be the same dimensions in pixels across and down (x and y).

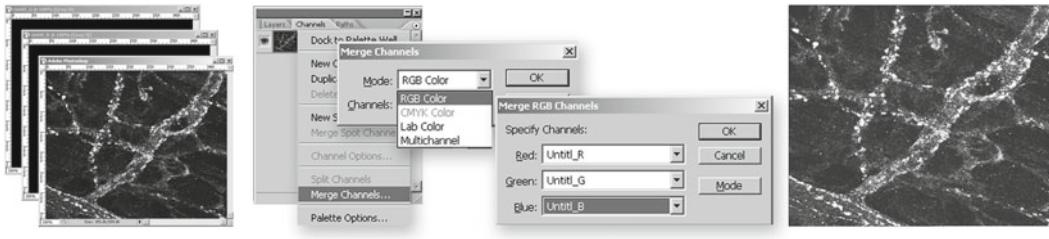

Fig. 4 Channels method for colorizing grayscale images: (from *left* to *right*) (1) A single, grayscale image is duplicated twice to create additional "dummy" images. These dummy images are then filled with *black* (Select > Select All, then Edit > Fill: choose Black). (2) In the Channels box, the *top*, *right arrowhead* is clicked to reveal a drop down list: Merge Channels is chosen. (3) RGB Color is then chosen from a drop down list from the first of two prompts. (4) Images are placed into desired channels. (5) A colorized image results

Otherwise, selections in the Channels dialogue box will be grayed out and unavailable (*see* Fig. 4).

1. Open first image from Photoshop. Under Image, select Duplicate. Select Duplicate again to make a third image.
2. On two out of three images you have made, select the entire image and fill with black according to the following: Under Select, choose Select All (or control/command + A). Under Edit select Fill. In the Fill dialogue box, click on arrowhead adjacent to Use. From drop down list, choose Black.
3. Under Window > Show Channels or Channels. In the Channels dialogue box, click on upper, right arrowhead to reveal drop down list. From that list, choose Merge Channels.

A prompt appears entitled Merge Channels. Click arrowhead next to Mode to reveal drop down list. Choose RGB color.

A second prompt appears entitled Merge RGB Channels. Enter non-black image into color desired. Be sure to also place black images into dummy channels, then click okay.

This protocol, once completed, cannot be undone. This method can also be used for merging (overlaying) up to three colors. In that instance, the 2nd and/or 3rd images represent the other colors you wish to create and then merge.

8.7 Levels Colorizing Method

The Levels method works similarly to the Channels method insofar as the two unwanted color channels are minimized and the desired channel remains. The unwanted channels, however, are not made completely black: instead, varying degrees of color from the other two channels then combine with the desired color to make a third hue that is fit for output and improved display (Figs. 5 and 6).

1. Open desired grayscale image from Photoshop. Under Image > Mode select RGB Color in order to include two more channels.

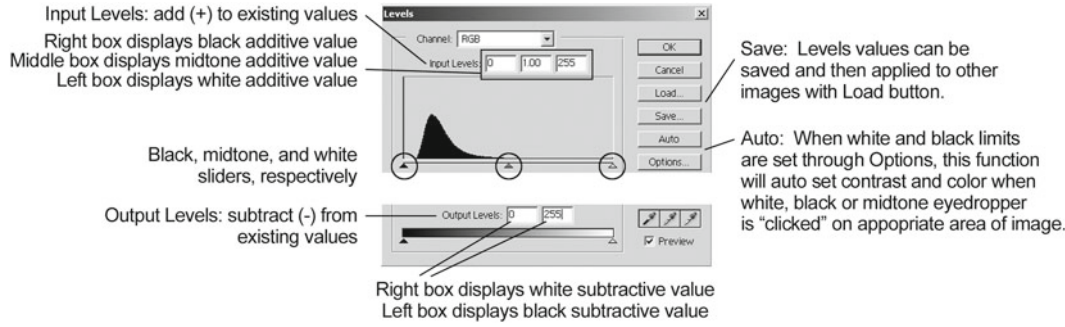

Fig. 5 Levels box and more important features

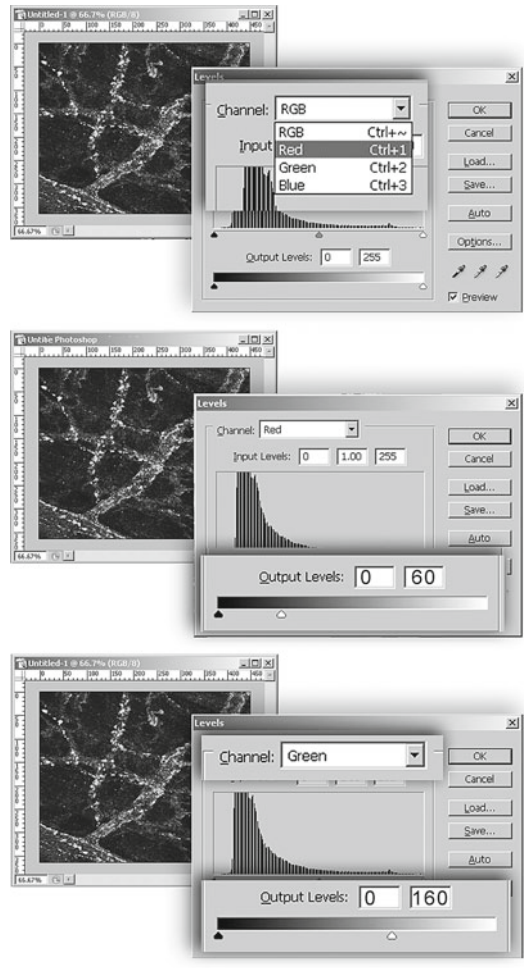

Fig. 6 Levels method for colorizing grayscale images: (*top to bottom*). (1) The "unwanted" colors in appropriate channels are chosen, in this instance the colors red and green (the grayscale image is first made into an RGB Color image: Image > Mode > RGB Color). (2) According to values included in Table 1, a value of 60 is entered into the *right box* of the Output Levels for Red. (3) A value of 160 is entered into the *right box* of the Output Levels for Green. A more cyan shifted blue results, a bright and easy to distinguish color that conforms readily to outputs

Table 1
Setting red, green, blue channels in levels to colorize images

Color desired	Red output value	Green output value	Blue output value	Shade of color
Green	110	255	160	Bluer green
Green	160	255	140	Yellower green
Red	255	40	50	Red
Red	255	120	50	Oranger red
Blue	60	160	255	Cyan blue

2. Under Image > Adjust select Levels. In the Levels dialogue box, click on the arrowhead adjacent to Channel to reveal drop down list. Select one of the two color channels NOT desired as the final color (e.g., if you wish to make a red-colorized image, select the green or blue channels).
3. Type in value in the Output Levels box (the box to the right at the bottom: these values that reflect the position of the output white slider) according to Table 1.

These values may not work effortlessly with every image when converting to CMYK color mode, but the likelihood is greater, especially with the blue and red values.

8.8 Reducing Noise

Once images are colorized, grainy or "snowy" images can be corrected to varying degrees in Photoshop, but often at the loss of some detail. When possible, it is best to average frames when acquiring images to avoid having to reduce noise in post-processing. If that cannot be done, then a Reduce Noise filter can be applied in CS versions of Photoshop, or a median filter in earlier versions (Filter > Noise > Median).

The better means for noise removal, however, is through the use of plugins to Photoshop. Two companies make noise removal software that is superior to noise reduction found not only in Photoshop, but in many scientific software programs. These include Neat Image and Noise Ninja. The cost for these plug in and stand alone programs are less than $50.00 (US). Procedures for noise reduction in these software plugins and links to the Web sites are provided on the quick Photoshop Web page: http://www.quickphotoshop.com.

Here is the method for reducing noise in Photoshop with the Noise Reduction, or Median filters:

1. In the Layers palette, make a new layer for application of the noise filter: Layer > Duplicate Layer.
2. Change View of the image to 100 % by using zoom tool or by using keystrokes: Control/Command + 0 (zero).

3. Reduce Noise Filter: Filter > Noise > Reduce Noise. In the Reduce Noise dialog box, set the Strength to 7–10 with other settings at 0. Determine the noise reduction visually. A certain noise level will introduce blurring, something less will not reduce noise to satisfactory levels. Attempt to find a mid point.
4. Median Filter: Filter > Noise > Median. Move the slider in the Median dialogue box to the right to reduce noise level. Usually a level of 1–3 is sufficient.
5. Double click on the noise-reduced layer. A "Layer Style" dialog box appears. In the "Blend if" part of the dialog box, adjust both the black slider (left) and white slider (right) in "This Layer" to the center until the noise reduction effect is eliminated. Then back off from the slider position until the noise reduction is re-introduced. This will limit the noise reduction to discrete tonal levels.

8.9 Conforming Images in Photoshop to Output

Often details close to background and small bright details (such as bacteria) need to be amplified in order to make these readily apparent. First time users of Photoshop tend to gravitate to the Brightness/Contrast function, but this method applies a linear transformation of pixel values, so that if one pixel is brightened by ten grayscale values, then approximately the same additive value is applied to every pixel in the image (rounding errors and black compensation excluded).

It is far better to change values within the image by adjusting these within two major pixel value ranges of the image: the dark or shadow areas, and the brighter areas. Adjustments to those areas are typically done using Curves or Levels (for this chapter, the use of Curves is shown).

The adjustments are made, again, so that the image can conform to outputs. That requires the black or dark values in images be within the range of publication to coated paper, sometimes less dark than what might be desired by those in research. As stated previously, it must also be limited in the highest significant white values for publishing purposes (for most purposes at an RGB, 8-bit value of 240 maximum in the red, green, or blue colors).

A two-step workflow can also be used in which one set of images is saved for all but publication purposes, and a second set is made to be destined for publication when that is desired. The idea behind this workflow involves saving files in the Photoshop format, the TIFF format (with layers left unchecked in later versions of Photoshop; in earlier versions, if layers are made, the image will have to be flattened: Under Layer > Flatten Image), and the JPEG format for inclusion in Microsoft products and the Web. File formats then serve as reminders: a Photoshop image retains the original's grayscale values (unless converted from 16- to 8-bit) and it can be reviewed when a collaborator or advisor is displeased; a

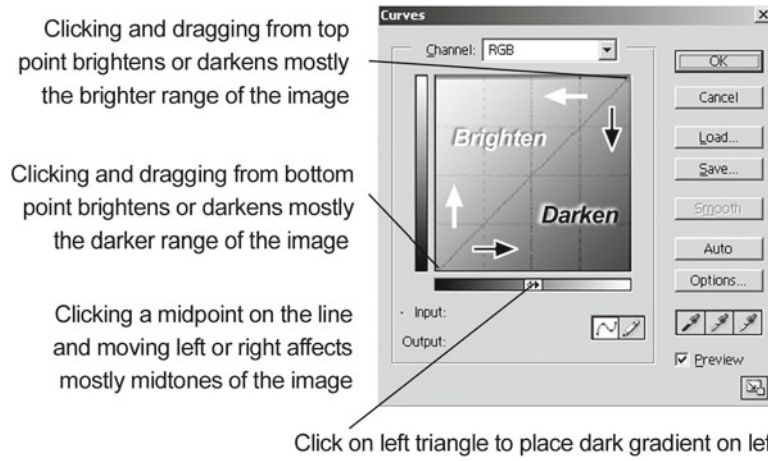

Fig. 7 General explanation for the use of Curves (Image > Adjust(ments) > Curves)

TIFF file is a full resolution file with adjustments applied and it can withstand minimal editing; and a JPEG file is a compressed file in which some data has been lost, and this should be saved over if re-editing the TIFF or Photoshop file. To conserve shared hard disk space, CDs or DVDs can be made.

The following method assumes saving as three different formats. It also assumes that values in Table 1 have been used to colorize images. Adjustments are described using Curves (*see* Figs. 7 and 8):

1. Open colorized image. Use Sample Eyedropper Tool and select from the toolbar. Mark points on the image that correspond to background (darkest black), and the brightest significant part of the image.
2. Under Image > Adjust(ments) > choose Curves. In the Curves dialogue box, adjust as follows (*see* Table 2).
   (a) Click on bottom point of line and move it along the horizontal axis (to the left) or along the vertical axis until the black background value reads 20 for the dominant color channel. When looking at values in the Info Box, the numbers to the right of the slash are the current values, to the left the former values. For the Curves box, be sure that the black gradient is at the left side of the box so that black values are adjusted by moving the bottom of the line and white values are affected by moving the top of the line.
   (b) Click on the top part of the line and move line either along the horizontal or vertical axis until the value in the dominant color reads 240. If, by chance, the brightest position of the image was not sampled, then the image may become too bright, and the adjustment will have to be done visually.

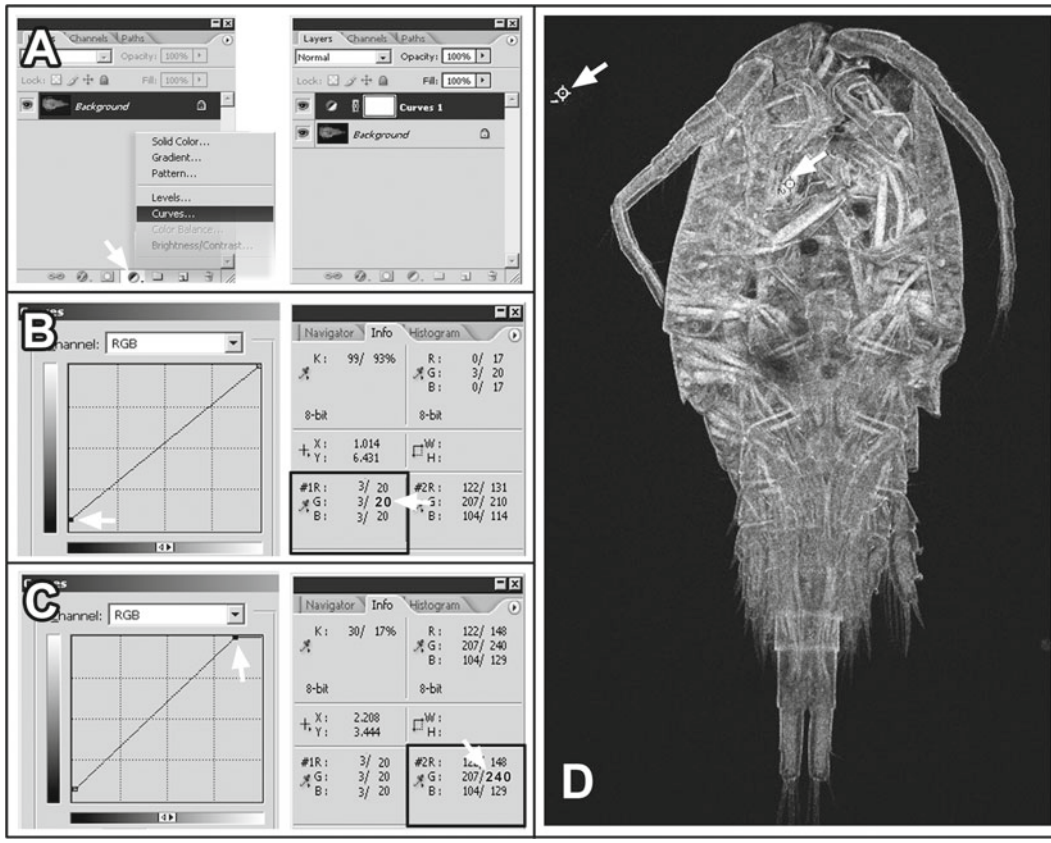

Fig. 8 Setting white and black levels: *Arrow* in panel (**a**) shows the location of the Adjustment Layer in the Layers box, chosen in this instance so that adjustments do not irretrievably change values in the image (though originals should always be archived to media so that original values can be retrieved), and so that the layer can be discarded, if deemed necessary. Panel (**b**) shows the adjustment of Curves to create a minimum value of 20 in the red, green, or blue channel, or 92 % for the *K* value, both shown on the right side of a slash. The sampling position for the black level is shown on panel (**d**) in the *upper, left corner*. Panel (**c**) shows the curves adjustment to place the significant white values from the second sampling position shown in (**d**) at 240 maximum in the red, green, or blue channel, or 6 % for the *K* value. White and black levels can be found in Table 2

Table 2
RGB Color, Grayscale and CMYK Color readouts from the Info Palette for Max and Min output tonal values

	Darkest black	Brightest significant sample
RGB color	Max value = 20	Max value = 240
Grayscale	*K*: value = 92 %	*K*: value = 6 %
CMYK color	Cyan = 75 Magenta = 40 Yellow = 40 Black = 10	Cyan = 5 Magenta = 3 Yellow = 3 Black = 0

If the sampling point contained clipped values and reads out at 255 in the dominant color, then the image may darken overall, but keep the clipped values at 240.

(c) Save the Curves adjustments so that these can be applied to images taken at the same session. The same Curves adjustments must absolutely be applied to related images using different fluorochromes!

(d) Save the file as a Photoshop file with layers, a TIFF file without layers, and as a JPEG, (choosing a Maximum setting when prompted, or less than that for Web images).

(e) Create an action so that these Curves can be applied to all images in a directory using the Batch command (*see* Subheadings 11 and 12).

(f) Gamma (Fig. 9). Once the upper and lower limits are set, then the relationship of tones can be altered. Figure 9 shows several examples of tonal changes that will brighten discrete tonal ranges without affecting white or black limits. Note that some publications may require that gamma alterations be reported.

8.10 Merging More Than One Image/ Colocalization

More than one image can be merged so that the maximum (brightest) colors appear when stacked over each other. The Channels method described above can be used to accomplish merging by assigning grayscale images to appropriate red, green and blue color channels.

The Channel method is limited, however, to three channels; and users do not have control over opacities in each of the three images. That is important, because green appears brighter than red or blue, and that color will dominate when visualizing. Also, in the event of misregistration, the images cannot be easily realigned.

A method which lends itself to greater control places each of the colorized images into separate layers stacked one above the other. These layers can be made into varying levels of opacity, as well, using a global opacity slider. The red-colorized image is used as the background layer because the green and blue layers tend to appear brighter, if the color of blue was shifted to cyan according to Table 1 (*see* Fig. 10 for explanation of Layers box):

1. If available, open red-colorized image to be used as the background, or bottom layer. Otherwise, if no red-colorized image is used, open the blue-colorized image. The green image is often best left as the top layer as it appears brightest.
2. Duplicate the image to avoid saving over the original (Image > Duplicate). Close the original image (File > Close).
3. Open other images. For each image, select all (Select > All or Cntrl/Cmd + A), copy (Edit > Copy or Cntrl/Cmd + C) and close

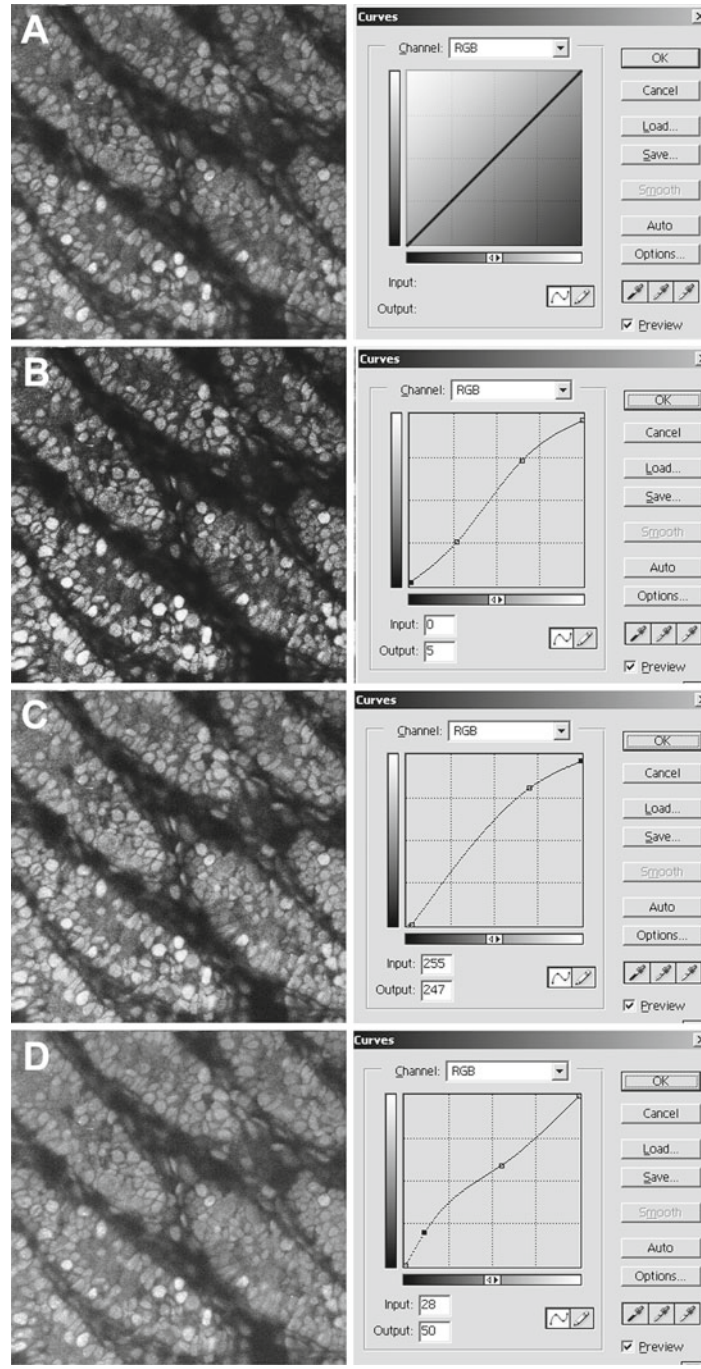

Fig. 9 Setting gamma values: panel (**a**) shows the original and unadjusted image. The *S* curve in panel (**b**) shows a midtone modification to increase contrast by darkening the darker areas in the image and brightening lighter areas. An increase in the brighter portion of the image is done for panel (**c**), increasing mostly the midtone to brighter values. Panel (**d**) shows a brightening of darker values to reveal features closer to background values. Images are not representative of the midtone adjustments shown: additional midtone adjustment was done to emphasize differences for publication purposes

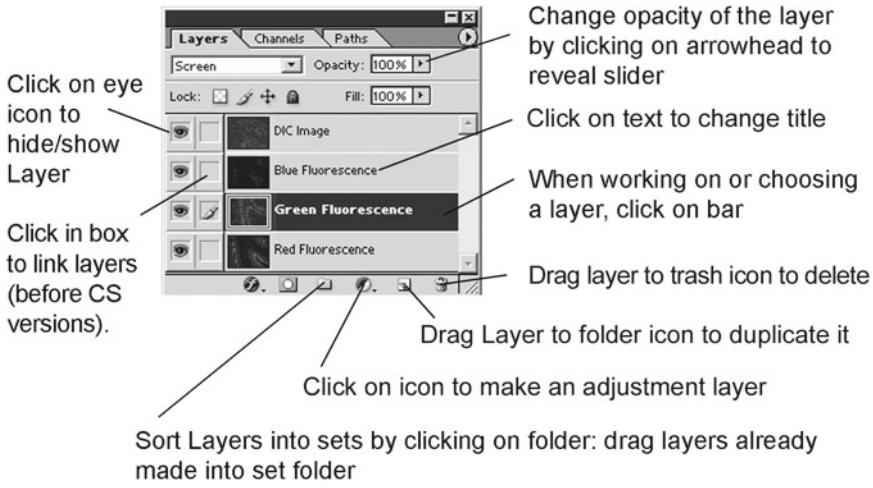

Fig. 10 Important features in the Layers box

the image without saving it (File > Close, choose No when prompted to save; or Cntrl.Cmd + W). Then choose the red-colorized image (or the target image) and paste (Edit > Paste or Cntrl/Cmd + V).

4. The target image will be "covered" by subsequent images, each occupying a separate layer. To reveal maximum amounts from two or more layers, choose Lighten from the Layers dialogue drop down list (click on arrowhead at the top, left of the Layers dialogue box and choose Lighten). Layers are compared and the brightest value for each red, green and blue channel results at each pixel position.
5. Choose the layer taken by the green, colorized image (by clicking on the non-text part of that layer). If necessary, use the opacity slider to reduce its opacity to ~85–90 %. Make the adjustment visually. The opacities of other layers can also be adjusted visually. Look for a blend of colors in the midtone values represented by non-specific tissue, if that appears in the image.
6. If an increase in brightness or darkness from a layer is deemed necessary, then it is easiest to simply click on that image layer in the Layers Box, then adjust (under Image > Adjust(ments) > Curves).
7. Save the image.

This procedure can be made into an action and then applied to image files in several folders. If each series of colorized images are saved to separate folders, then a Batch automation can not only colorize respective images, but it can also take those images and place these in layers above the red-colorized image.

9 CMYK Output

Scientific journals are increasingly requesting CMYK images; though, at present, alternate ways to submit are often provided. However, when submitting RGB Color images to journals (versus CMYK) authors run the risk of having an art department at a print shop balance the color so that it reproduces well as pigments on paper. While those who do that kind of work for a living should be expected to balance color, the reality is that these people generally have little to no experience with the kinds of pure colors used in science, and countless examples of darkened, flat highlights can be found in major journals: much of what is published hardly resembles the RGB colors and intensities of the original. As a result, for best reproduction, a scientist may desire balancing colors for CMYK output on his/her own.

The idea behind CMYK conversion is to make the image better than how it appeared in RGB Color. While that may seem impossible because the range of colors used when blending pigments (CMYK) is somewhat more limited and different than the colors of light (RGB), the conversion can be improved in appearance. That is primarily done by increasing the level of black in the background after conversion to CMYK., and through recommended sharpening methods in this chapter. At the same time, it must be remembered that LCD screen appearance may not adequately show contrast levels when published, or when projected: black levels are generally a darker gray, leading to an overall low contrast appearance. The goal is to make the images look more elegant than graphic.

9.1 Converting RGB Color to CMYK

Be sure Color Settings are set appropriately to the correct press.

1. Images may first be checked to see if these will convert to CMYK without becoming flat and losing highlights. This is done by turning on Gamut Warning (View > Gamut Warning: *see* Fig. 11). A gray, colorized overlay will appear wherever the image is deemed unprintable. Use that to provide some idea about offending colors. Alternatively, Under View, select Proof Colors. The image will display as CMYK colors, but remain in RGB color space. If highlights become darker and muddy in appearance, then the color is too saturated and the background is often too dark.
2. To create CMYK reproducible colors, make sure, first of all, that the darkest background value is 20 and the brightest value is 240. Often the conversion improves when the darkest background values are increased even higher, to a value of 30. Place sampling points on the black background, open Curves (Image > Adjust(m ents) > Curves) and increase the background value to 30.
3. Next, with the gamut warning activated, open Hue and Saturation and reduce the saturation of the color. Do that by moving the

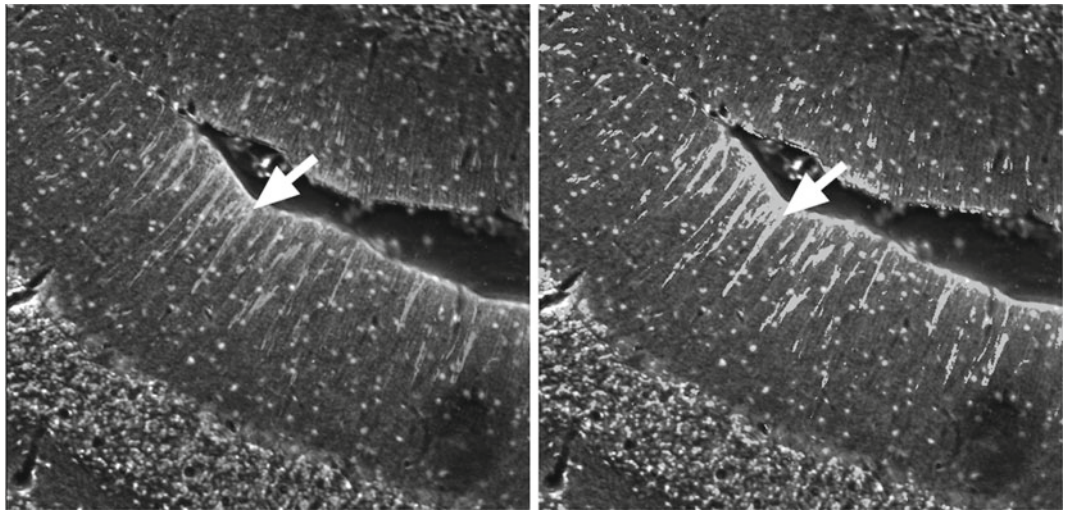

Fig. 11 Gamut warning: image on the *left* shows original image; on the *right* the same image with *gray overlay* showing areas in which colors do not match up with the output device. This overlay can be activated by using Gamut Warning (View > Gamut Warning)

saturation slider in the Hue and Saturation dialog box to the left until the gray overlay disappears. At this point, the image will look low in contrast, but that will be corrected in later steps.

4. Convert the image to CMYK: Image > Mode > CMYK.
5. Open Curves to increase the black level: Image > Adjust (ments) > Curves. Click on the Channel drop down list and select the K (black) channel. Increase the black level until the sampling point readout in the Info box reads 98–100 %.
6. Open Hue and Saturation: Image > Adjust(ments) > Hue and Saturation. Increase the saturation slider as far as possible while maintaining separation of the brightest values. Alternatively, if the intensity of the color is most important, increase saturation to 90–100 % and decrease lightness until brightest values become as intensely colored as other values.
7. Contrast can now be increased by using the Sharpening method.

10 Increasing Sharpness (Fig. 12)

Normally a sharpening filter is not applied until after the image has been properly set for its darkest black and brightest significant white. For confocal images, however, some liberties may be taken with sharpening that will also affect the grayscale levels by creating brighter whites and deeper blacks (more contrast). The filter that provides varying degrees, along with other effects, is called Unsharp Mask.

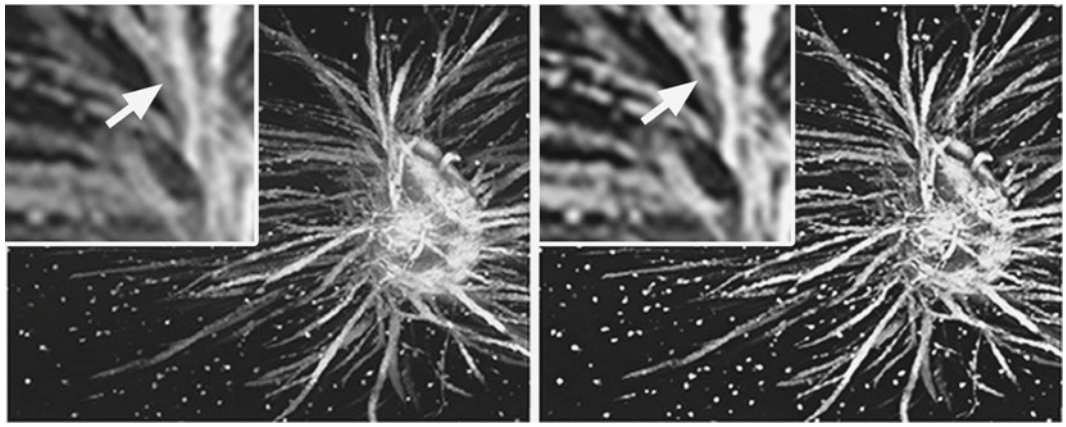

Fig. 12 Results of Unsharp Mask with Radius set at high values: image on the *left* shows original image and detail before applying unsharp mask to the lightness channel in LAB Color. Image on the *right* shows the image and detail after applying Unsharp Mask at an Amount of 100, a Radius of 20, and a Threshold of 3. Note the increase in darkness near edges of features and the general increase in contrast over the entire image. The bold use of the Radius slider might be more useful for some outputs, such as on-screen projection at meetings, but not for others, such as publication purposes

Unsharp Mask works by introducing a darker band along edges of the image where neighboring pixels differ in grayscale value. Because the human eye is drawn to areas of contrast such as at edges, the appearance of a sharp delineation at these locations fool the eye into believing the entire image is focused. The same effect can be obtained by making a high contrast copy of the image so that edge values are pure black and other values pure white, placing that image behind the original, and then allowing only the black portion from the high contrast image to appear through the original.

Within the Unsharp Mask dialogue box lie three sliders. The Amount slider determines the degree of sharpening applied to the image. The Radius slider determines how many pixels out from the edge the banding will occur. The threshold slider determines how different a pixel must be from the surrounding area before it is considered an edge pixel.

The steps are as follows:

1. Change View of the image to 100 % by using zoom tool or by using keystrokes: Control/Command + 0 (zero).
2. Under Filter > Sharpen, select Unsharp Mask. Start by setting the Amount to 100 %, the Radius to 3, and the Threshold to no more than 3 (the lower the threshold, the greater the number of edge pixels that are found). Start by altering the Amount value until the image can be sharpened as much as possible without the amplification of noise. Iteratively change the Amount to find the right balance. If the image contains small features or fibers that need to be amplified in order to increase that detail, increase the Radius so that the dark banding at the

edges increases in darkness to separate brighter signal from background. Iteratively decrease the Amount and increase Radius until the features are amplified with a modest increase in noise. Or, increase until details are best revealed.

11 Making Actions (Macros) in Photoshop to Apply to All Images Within One or Several Folders (Fig. 13)

Actions in Photoshop can be made by simply recording a series of steps in the Actions dialogue box. The actions are organized within the Actions dialogue box under Sets. Those steps can then be applied to one or several files within folders and subfolders by using the Batch function (File > Automate > Batch).

1. Open image to be worked on. Open Actions dialogue box (Window > Actions or Show Actions).
2. Click upper, right arrowhead to reveal drop down list. Choose New Set. Provide name for the Set and click OK.

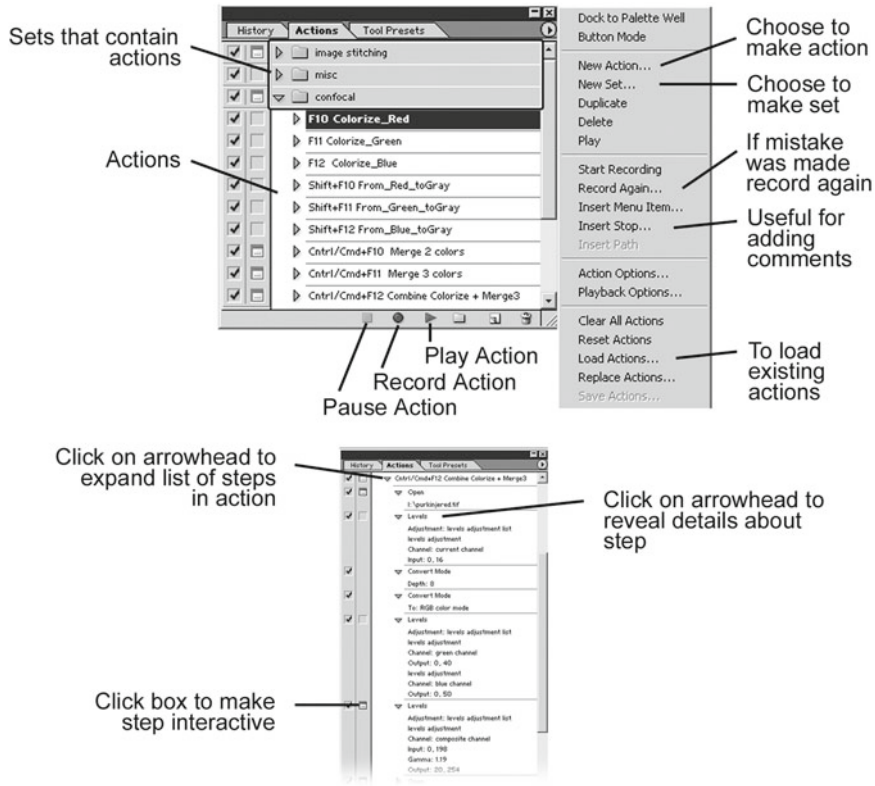

Fig. 13 Actions box and example of steps in an action: important features of the actions dialogue box appear in the *top image*. The *bottom image* shows an expanded view of steps in an action with important features indicated

3. Again, click on arrowhead to reveal drop down list. Choose New Action. Name the action according to its function.
4. Once the action is named, then every step taken thereafter is recorded. Carefully complete steps: if you make a mistake and use the Edit > Undo function, the Undo may not be recorded under certain circumstances, and it may be best to start over, or work around the error.

If a step was missed, this can be recorded later (by clicking on the red, record button). When finished click the black, square button, and then click and drag that step into the correct position so that it is in the correct sequence. When finished with recording steps, click on black box at bottom of actions dialogue box to stop the recording.

Click on a box next to the step in the action to make interactive. In that instance, steps in the action will automatically take place until the interactive step. At that point, the actions stop to allow you to interactively set values (such as brightness levels) manually for each image to which the action is applied. Because of image to image differences, this can be a valuable aid.

12 Batch Processing Entire Directories (Fig. 14)

To apply this action to several files within a folder and subfolders, a routine can be used called Batch.

1. Open the Batch dialogue box (File > Automate > Batch):
2. In the Batch dialogue box, make sure the correct set and action are listed at the top. If not, click on arrowheads to reveal drop down lists and choose the correct set and action:
3. For Source, click on adjacent arrowhead to reveal drop down list and choose folder.
4. Click on Choose button below Source and browse to the correct file folder of images to which action will be applied.
5. Under the Choose button, three functions can be checked. The first prompt asks if you wish to override the "open" command in the action. If, as part of your series of steps when creating your action, you also opened a file at the beginning (not following the directions above for step 1: opening the image first, then starting the action), then you will want to check this box. Otherwise, the batch function will keep opening the image file you specified in your action. The second prompt asks if you wish to include subfolders. Check if you want actions applied to image files within subfolders as well. The third asks about suppressing color warnings. If you followed the steps at the beginning of these methods to turn

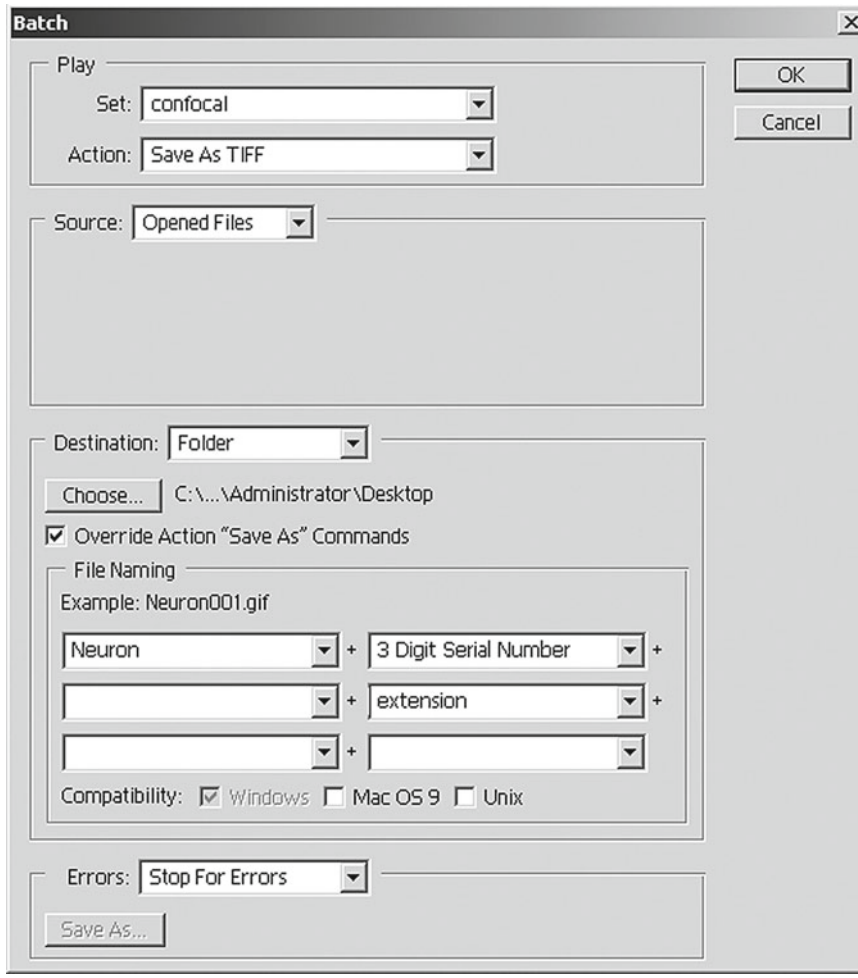

Fig. 14 Batch dialogue box: this batch automation uses a Set entitled "confocal" and an action entitled "Save as TIFF." The Source is more often a directory that is chosen, but, in this instance, files were opened in Photoshop and each of these opened files were slated to be made from layered, Photoshop files into non-layered, TIFF files. A Destination folder was chosen and "Override Action 'Save As' Commands" was checked so that filenames would follow the File Naming protocol

off prompts for color warnings in Color Settings, then this box need not be checked. If you have not, then you will want to check this box so that you do not have to respond to a prompt each time Photoshop responds to color space problems. The better solution would be to suppress the warnings in Color Settings as recommended.

The Destination button is normally set to Save and Close. Then the 2nd Choose button can be clicked to place the saved files into another folder so that existing files are not saved over (so that original is not altered and to preserve the original files in case the action does not work as planned).

Under this Choose button lies the option to Override Save as command. If checked, the batch will use only the save function you have included as a step in the actions file.

Click okay. If, after the Batch starts to run, you receive a prompt warning about not being able to complete a function, very likely the file worked on has a mode problem (maybe it is indexed color or 16-bit) or it is in a format that Photoshop cannot read (maybe a BioRad .PIC file) or it is in layers and the wrong layer is chosen. In that instance, double check images in the directory of interest to make sure the mode, format or layer is correct. You may want to flatten layered images, another procedure that can be made into an action and automated with the Batch command.

13 Working with Image Stacks in Photoshop

Even with the newest version of Photoshop (CS6 extended), no means have been provided to open confocal image stacks. However, that does not preclude the use of Photoshop. The confocal stack can be saved as an AVI file, and then opened in Photoshop to place each image on a layer (more about this method can be found in "Scientific Imaging with Photoshop CS3: Methods, Measurement and Output"). However, layers do not always provide an efficient means for altering numerous files: instead, it is often faster to create automated actions and apply changes to each image that comprises a confocal image stack. In order to do that, the confocal image stack needs to be separated into individual TIFF or JPEG files. That can be accomplished with proprietary software, or with Image J (downloadable freeware from NIH: http://rsb.info.nih.gov/ij/download.html)

13.1 Making Separate TIFF Files from a Confocal Stack

Start by making separate folders for each confocal stack. Within these folders, make folders for each fluorophore. Name the folders so that the order in which files are worked on can be tracked according to a scheme of 001, 002 and so on. For example, the confocal stack named astrocytes_slide1 would be placed in its own file folder named "001 astrocytes_slide001." Within that folder, each of the fluorophores that were used in this experiment would have folders named 001DAPI astrocytes_slide001, 002FITC astrocytes_slide001, 003CY5 astrocytes_slide001, and so on. This kind of naming protocol helps immensely when creating automated actions that will be applied to innumerable TIFF files.

1. Open ImageJ or scientific software made for confocal imaging. Open the confocal image stack.
2. Find the means for splitting a confocal stack into individual TIFF files. In ImageJ that is found under File > Save As > Image Sequence. That function will automatically split

each of the *z*-planes in the stack into individual TIFF or JPEG files.

Once the TIFF or JPEG files are separated from the stack, several procedures can be implemented:

13.2 Reducing Noise

Noise can be removed before a 3D reconstruction is made if no means for filtering exists in 3D software.

1. Open file from the middle of the confocal stack in which salient features are sure to appear.
2. Open Actions dialogue box (Window > Actions or Show Actions). Create a new action within your set and name it.
3. Use appropriate noise reduction tool at settings that work best.
4. Click okay. Then click on the black button at the bottom of the actions box to end the recording.
5. Close the opened image without saving.
6. Run a batch on all TIFF images in a directory using this action (File > Automate > Batch).

13.3 Adjusting Contrast for 3D Reconstruction

3D reconstruction software provides tools for adjusting contrast, gamma and brightness. There may be times, however, when those tools are difficult to use, or when interactivity is limited.

Making an action for these adjustments is relatively straightforward.

1. Open an image file, generally from the middle of the confocal stack, in which contrast and brightness changes need to be altered.
2. Open the actions dialogue box or select it. Make a new action and name the action.
3. Open either Levels or Curves to make adjustments to the image so that, when subsequently thresholded in a 3D imaging program, areas of interest appear sans background and artifacts. Do not increase brightness to the degree that white areas lose details: better to increase brightness by bending the line in Curves to brighten features without losing details; and/or increase black level (contrast). Often these adjustments are dramatic in order to completely blacken background to leave only features with brighter signal.
4. Stop recording by clicking on black, square box at bottom of the Actions dialogue box. Then click on the box adjacent to the Levels or Curves step to make it interactive, if changes will be different at each z-section. If not, then go on to the next step.
5. Apply the action to all files in a directory using the Batch command (File > Automate > Batch).

13.4 Returning Separated TIFF Files to an Image Stack

Commercial scientific software, 3D reconstruction programs and ImageJ can return a series of TIFF files to an image stack. The following contains directions for doing so in ImageJ.

1. Import the TIFF files into ImageJ (File > Import > Image Sequence).
2. Enter appropriate values into the dialogue box that appears, keeping in mind that large file sizes may cause ImageJ to stop functioning, so you may consider checking boxes for opening files at one-half size and as grayscale. Note: that processing may take several minutes.
3. Save as TIFF stack (File > Save As > TIFF).

3D software may find information about how the confocal stack was collected in the header (such as laser used, pinhole size, dimensions of the images, and so on). The header includes lines of text included with the image files. Those lines of text are removed during the process of working in Photoshop. It is possible that this information may have to be included manually in the 3D software.

14 Saving Files Processed in Photoshop

Except for saving files as TIFF stacks, something that cannot be done in Photoshop as of this writing, consider saving all files in more than one format. While this may eat up hard disk space, the advantage of doing so lies in the various ends to which files may be used. If the file needs to be edited later, it is advantageous to save it in a form in which it contains layers for easy editing as a Photoshop (PSD) file. If the file needs to be included in a Microsoft product or for the Web, then it is best saved as a JPEG so that the file size is small and the program can "handle" it. If the file is to be sent to a publication, then it needs to be in the TIFF format; and, possibly, a CMYK TIFF file.

Saving files as an automated function makes it more efficient to not only accomplish saving, but it ensures that the three mentioned formats are created. Furthermore, if every file is duplicated as a JPEG, then browsing for files goes much faster with these smaller file sizes.

In the CS versions of Photoshop, a script has been included for saving in these three formats. Under File > Scripts choose Image Processor and set appropriate values.

In earlier versions of Photoshop make an action to accomplish the same end as follows:

1. Open a PSD formatted file. If the file does not contain layers, simply select all (control/command + A), copy (control/command + C), make new file (control/command + N), and paste into the new file (control/command + V).

2. Make an action by choosing New Action from the drop down list in the Actions dialogue box. Name the action. It may be useful to also assign a keystroke so that the keystroke can be used later to activate this action.
3. Start by saving the file (File > Save As) in the Photoshop format to a directory (the directory can be changed when it is used later on). It might be useful to create a directory entitled "Photoshop formatted files."
4. Next Flatten Layers (Layers > Flatten Image).
5. Now save the file (File > Save As) to a TIFF formatted file. Make sure nothing is checked (such as Alpha Channels or Layers: an indication that the file was not flattened). Save to a directory. It might be useful to name this directory "TIFF formatted files." A second dialogue box appears. Make sure the file is uncompressed (because it may be unreadable in other programs).
6. Save the file again (File > Save As), only this time as a JPEG file to a directory. Choose the level of compression. Remember that any JPEG compression throws away data, and so the Maximum setting may be desired. However, if the destination of the JPEG is the Web, or if computer administrators require small files, you can choose a greater compression (High or Low) to save disk space. Again, it may be useful to name this directory "JPEG formatted files."
7. Click on the black, square button at the bottom of the Actions dialogue box to stop the recording.
8. Make all the save steps interactive by clicking on the box adjacent to each save step. When this action is run later on, a prompt appears for naming the file and choosing its directory.

15 Conclusion

White level, black level, gamma and other changes to image files nearly always need to be made to bring images in conformance with various outputs. In order to create these changes, computer screens must be calibrated to similar points within work groups in dim lighting and Photoshop's preferences must be set correctly and in common. Working with confocal manufacturer's colorized images will rarely produce an image generically fit to output devices and software applications (including the Web), and so changes to the black and white levels, gamma and hues must be done, especially with the hue that is blue to purple-blue. Sometimes these images need to be returned to grayscale in order to re-colorize, and other times these will have to be adjusted by using Hue and Saturation with a gamut overlay, most often when images are already merged and original files cannot be located. Files can then

be saved in three formats: psd, JPEG, and TIFF for output, and then printed appropriately for color matching to what is seen on the computer screen. Confocal stacks can be made more suitable for 3D reconstruction and visualization by dividing confocal stacks into separate TIFF files, one for each z-plane. These can be altered in several ways, and then re-combined into a TIFF stack using commercial scientific software, ImageJ or FUJI. Many of these multiple step methods can be made into actions, so that these can be applied to entire directories when also using a batch command. Thus, Photoshop can be made far more efficient and less cumbersome for users.

References

1. Sedgewick, J (2008) Scientific Imaging with Photoshop: Methods, Measurement and Output. New Riders Press, Berkeley, CA (Visual Data and Ethics, p. 5–9)
2. Fraser B, Murphy C, Bunting F (2005) Real world color management, 2nd edn. Peachpit Press, Berkeley, CA (Computers and Color, p. 51–78)
3. Margulis D, Professional Photoshop: The Classic Guide to Color Correction, 4th edn., Wiley, Hoboken, NJ (Preflight: How can we make this image better? p. 3–8)
4. Sedgewick, Et al., (Conformance, p. 35–40)
5. Cromey D (2010) Avoiding Twisted Pixels: Ethical Guidelines for the Appropriate Use and Manipulation of Scientific Digital Images. Springer Science+Business Media, Philadelphia, PA
6. Fraser, et al. (Building Display Profiles p. 125–146)
7. Margulis, et al. (RGB: Freedom is Slavery 268–270)

Chapter 5

Clearing Up the Signal: Spectral Imaging and Linear Unmixing in Fluorescence Microscopy

Timo Zimmermann, Joanne Marrison, Karen Hogg, and Peter O'Toole

Abstract

The ongoing progress in fluorescence labeling and in microscope instrumentation allows the generation and the imaging of complex biological samples that contain increasing numbers of fluorophores. For the correct quantitative analysis of datasets with multiple fluorescence channels, it is essential that the signals of the different fluorophores are reliably separated. Due to the width of fluorescence spectra, this cannot always be achieved using the fluorescence filters in the microscope. In such cases spectral imaging of the fluorescence data and subsequent linear unmixing allows the separation even of highly overlapping fluorophores into pure signals. In this chapter, the problems of fluorescence cross talk are defined, the concept of spectral imaging and separation by linear unmixing is described, and an overview of the microscope types suitable for spectral imaging are given.

Key words Spectral imaging, Linear unmixing, Image analysis, Fluorescence cross talk, Multichannel imaging

1 Introduction

The introduction of fluorescent dyes for microscopy and their combination with immunochemistry provided important stimuli for light microscopy after decades of relative stagnation in regard to new developments. The possibility to exclusively visualize highly specific intracellular structures in distinctive colors against a dark background has changed our visual perception as well as our understanding of cellular mechanisms. The replacement of photographic film by highly sensitive monochromatic CCD cameras that generate digital images that can be easily merged into dramatic multicolor images helped to establish fluorescence light microscopy as the method of choice for cell biological imaging. Fluorescence imaging was also ideally suited for a groundbreaking new technology, confocal microscopy, which emerged as a powerful tool for biological imaging at the end of the 1980s and allowed the generation of highly resolved three-dimensional datasets of

Stephen W. Paddock (ed.), *Confocal Microscopy: Methods and Protocols*, Methods in Molecular Biology, vol. 1075,
DOI 10.1007/978-1-60761-847-8_5,

biological samples. The cloning of genes for autocatalytic fluorescent proteins in the middle of the 1990s allowed the observation of living structures in fluorescence with unprecedented ease and revolutionized the field of in vivo imaging, as acknowledged in the 2008 Nobel Prize for Chemistry awarded to O. Shimomura, M. Chalfie, and R. Tsien.

These days, the availability of an elaborate palette of fluorescent dyes extending even beyond the visible spectrum, an almost equally well-distributed range of fluorescent proteins and instruments capable of simultaneously acquiring dozens of spectral image channels provide us with an unprecedented richness in labeling possibilities [1–4]. This however also highlights inherent limitations in the specificity of fluorescence signals. Even though commonly used fluorophores seem to possess very distinct color signatures to the eye of the observer, their true spectral distributions are wide and significantly overlapping with the spectra of other fluorescent dyes. Some combinations of fluorophores, as well as a higher number of labels within one sample, will result in signals that cannot reliably be separated. Incomplete separation however makes quantitative analysis or the study of localization impossible.

Recently the analysis of spectral datasets and the signal separation by linear unmixing to overcome these problems have become widely used. Spectral imaging was initially used for spectral karyotyping [5] and subsequently combined with linear unmixing for immunohistochemistry [6]. It generated much interest after being applied to two-photon microscopy [7] and subsequently to confocal microscopy [8].

In this chapter we are going to define the problems inherent in fluorophore cross talk and cross-excitation and we are going to highlight the instrumentation and the processing methods that allow the reliable separation of multiple fluorescence signals.

2 Fluorescence Cross Talk and Cross-Excitation

Fluorescence at the molecular level consists of the ability of a molecule to absorb the energy of a photon and to subsequently reemit a photon of less energy. Only photons within a certain energy range can be absorbed and the fluorescence emission can only happen within a second defined energy range. The wavelength of a photon is inversely proportional to its energy level, so that this relation can also be described inside the color spectrum of light, with longer (i.e., “red”) wavelengths corresponding to lower energy levels. The difference between the wavelength at which a fluorophore is most efficiently excited and the wavelength at which most emission photons are generated is referred to as the Stokes’ shift. In reality fluorescence phenomena are far from monochromatic. The wavelength maxima are embedded in much wider excitation and

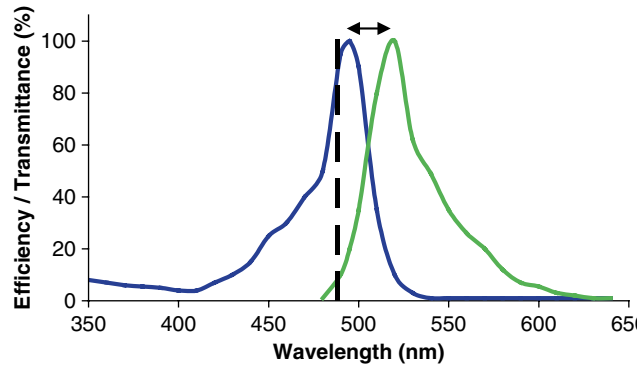

Fig. 1 Excitation profile (*blue line*) and emission profile (*green line*) of Fluorescein isothiocyanate (FITC) excited with a 488 nm argon laser (*broken line*). Stokes shift is illustrated by the *double arrow*. The long slopes of the excitation spectrum to the blue and of the emission spectrum to the red are clearly visible

emission spectra which represent the efficiency of excitation at a certain wavelength and for the emission side the likeliness of a photon being generated at a certain wavelength. Most fluorophores have near mirror image symmetry between their excitation and emission spectra, with the excitation spectra extending to significantly shorter wavelengths than the excitation maximum and with emission wavelengths tailing far to the red of the emission maximum (Fig. 1). Even for fluorophores with fairly defined spectra, each spectrum can cover around 100 nm, meaning that, inside our spectrum of visible light from 350 to 700 nm, most fluorophores are excitable or detectable over a significant range [9].

Fluorophore cross talk can be defined as the overlap of the emission spectra of two different fluorophores. In practice it means that, depending on the spectral region chosen for detection, the signal will consist of contributions from both fluorophores if both are excited at the same time (Fig. 2). Fluorophore cross-excitation describes the phenomenon of simultaneous excitation of two fluorophores due to the fact that at the excitation maximum of one of them, the other can often be excited with significant efficiency. Sometimes, both phenomena are jointly referred to as fluorophore cross talk, but for a more thorough understanding, it is useful to separate them. Another frequently used term is bleed-through.

Specificity problems in samples with several fluorescence stains may be compounded by the fact that, depending on their efficiency in absorbing and also in emitting photons, some fluorophores are significantly brighter than others. Combinations of “dim” and “bright” fluorophores may cause problems in reliably identifying the signals of the “dim” dyes. The same problem can arise even if both fluorophores are equally bright, but their relative concentrations in the sample are significantly different.

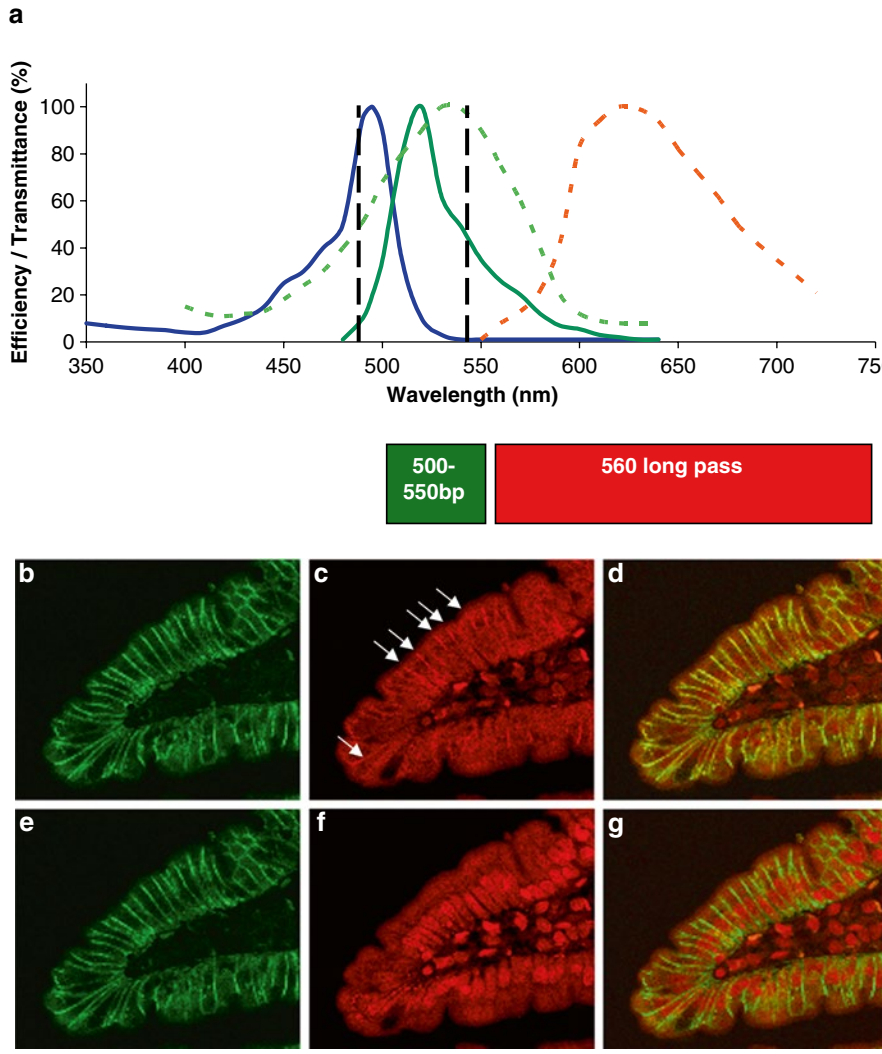

Fig. 2 (**a**) Excitation and emission spectra of FITC (*solid lines*) and propidium iodide (*broken lines*) showing the laser lines at 488 nm and 543 nm (*black*). The emission filter sets routinely used are shown below the spectra and the level of FITC emission which bleeds through into the red channel during simultaneous data collection using a 560 long pass emission filter is blocked in red. (**b**–**g**) Confocal images of a gut section labeled with anti-glucose transporter 5 and a secondary FITC antibody (*green*) and the nuclear stain propidium iodide (*red*). (**b**)–(**d**) are imaged simultaneously and (**e**)–(**g**) are imaged sequentially. FITC emission is shown in *green* (**b**, **e**, 488 nm excitation, 505–550 band pass emission) and propidium iodide emission is shown in *red* (**c**, **f**, 543 nm excitation, 560 long pass emission), (**d**, **g**) Composite images of the green and red channels. The bleed through of FITC emission into the red channel during simultaneous collection is highlighted by the *arrows* in (**c**) and consequently alters the color of the *green* localization in (**d**)

Methods to insure a reliable identification of the fluorescence signals in a sample containing several labels are therefore a fundamental requirement for the analysis of fluorescence microscopy images.

Even though the wide spectra of fluorophores are indeed prone to problems of cross talk and cross-excitation, specific recognition of fluorescence microscopy signals has been successfully

achieved for most standard applications. The use of properly configured fluorescence filtersets, i.e., the ensemble of excitation filter, dichroic mirror, and emission filter, achieves a reliable separation of the signals of the most commonly used fluorophore combinations. This separation is possible because the characteristics of most fluorophore spectra are the following:

- Excitation spectrum: Long tail to the shorter ("blue") wavelengths, rapid drop after the excitation maximum.
- Emission spectrum: Rapid rise to the emission maximum, long tail to the longer "red" wavelengths.

In a pair of two partially overlapping fluorophores A and B (with fluorophore B having spectra more shifted to the red relative to fluorophore A), B is thus likely to get cross-excited at the excitation maximum of A. However, in the shorter wavelengths of A's emission spectrum, there will be no contribution from B, as fluorophore B only starts emitting shortly before its own emission maximum. Fluorophore A can therefore be separated reliably from B through the use of a band-pass emission filter that collects fluorescence only from that part of A's emission spectrum that does not overlap with B's emission. In fluorophore B's emission range, especially around its own emission maximum, there will be significant overlap with emission from fluorophore A. However, as fluorophore A's excitation spectrum drops rapidly after its excitation maximum, B can be excited at its own excitation maximum without any simultaneous excitation of A. Emission overlap thus becomes irrelevant as A is not emitting and B can be imaged specifically by using an excitation band-pass filter that does not overlap with A's excitation spectrum.

This is the most commonly used solution for the imaging of standard fluorophore combinations in fluorescence microscopy. It is robust and its main disadvantage, the incomplete collection of fluorescence emission due to the use of band-pass emission filters, can be minimized by the choice of fluorophores that are bright and that are spectrally as separated as possible.

This solution becomes less applicable under several conditions:

1. In the presence of higher numbers of fluorophores.
2. In the presence of fluorophores that are not matched to existing filtersets.
3. In time-limited (and exposure-limited) situations like in vivo imaging.

Karyotyping using multicolor fluorescent in situ hybridization (FisH) probes is a good example of the first case. To reliably identify all chromosomes, a high number of fluorescence signatures are needed. Specificity for such samples was initially achieved through the use of highly restrictive filter combinations, at the cost of signal efficiency [10, 11].

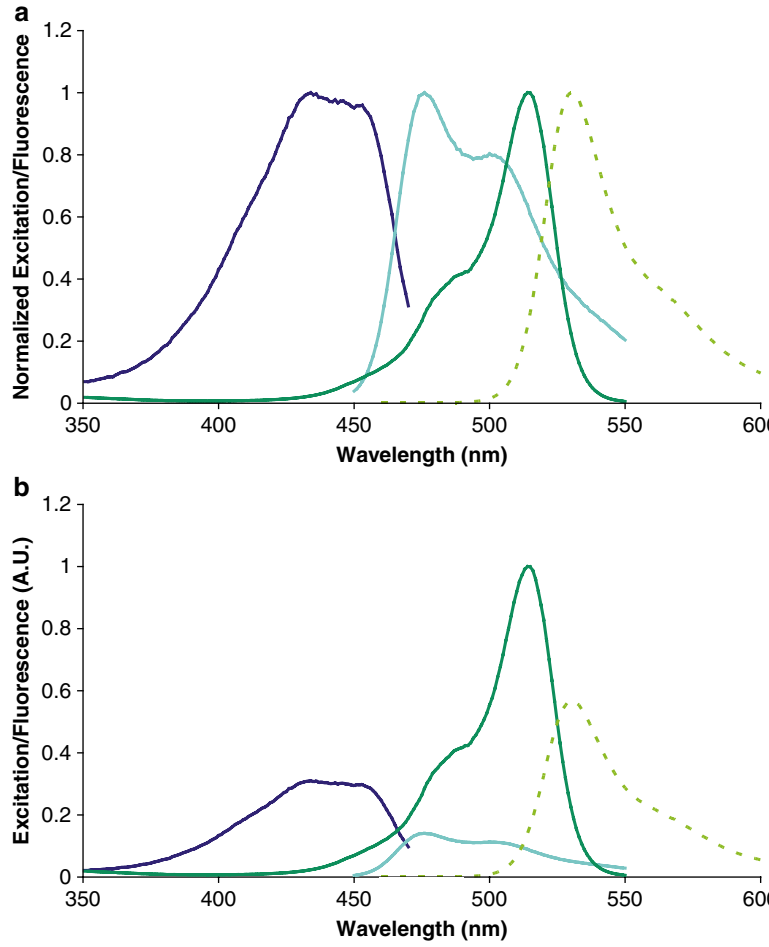

Fig. 3 Excitation and emission spectra of two frequently combined fluorescent proteins, Enhanced Cyan Fluorescent Protein (ECFP, excitation: *blue*, emission: *cyan*) and Enhanced Yellow Fluorescent Protein (EYFP, excitation: *green*, emission: *yellow*). The normalized spectra (**a**) show the significant amount of overlap of the ECFP emission with the EYFP emission. Without normalization (**b**) it becomes clear that EYFP is the significantly brighter fluorophore due to its higher absorption and emission efficiency. YFP can also be excited with light suitable for ECFP excitation, and can provide a significant fluorescence signal that overlaps with the second half of the ECFP emission, so that a band-pass filter is needed to insure specific detection

The second case can be encountered when dealing with genetically encoded protein-tags. The currently available fluorescent proteins offer a wide spectral distribution [1, 2, 12], but their spectra are often not matched to existing filter combinations and due to their complex properties (brightness, pH stability, oligomerization) they can not readily be "mixed and matched" solely on their spectral properties. Viable combinations often present significant problems with fluorophore cross talk (Fig. 3).

The use of specific filtersets for multichannel fluorescence imaging normally requires sequential acquisition of the different channels. The more channels there are to be acquired, the longer the whole acquisition process takes. During in vivo experiments, the observed process may be so fast that the next image of a time-series already needs to be taken when the acquisition of all channels is not even finished. Also, a living sample may change even while the different fluorescence channels are being recorded, so that the information in the channels is not completely matched.

Confocal microscopes generally have more than one fluorescence detection channel and therefore could be used for more time-efficient parallel acquisition of several channels. If the aim is however to separate fluorescence signals clearly into detection channels confocals can be operated in sequential imaging modes with the same problem of accumulating acquisition times. Simultaneous excitation of several dyes would immediately lead to problems with fluorophore cross talk and it is normally avoided by offering the possibility of imaging modes like "multitracking," "sequential imaging," etc.

The cases described above make it clear that standard fluorescence imaging approaches cannot provide solutions for some of the current experimental requirements of biological imaging.

Recent instrument developments and the implementation of image processing approaches originally established in remote sensing do however provide solutions, allowing the clear separation even of highly overlapping fluorescence signals.

3 The Concept of Spectral Imaging and Linear Unmixing

In remote sensing, multiband images taken by satellites represent the same geographical region in distinct spectral channels of the visible and also the invisible (and radar) spectrum. The signals of different types of vegetation and geological formations show a characteristic spectral distribution and are in this aspect similar to the emission spectra of fluorophores.

For the analysis of such multiband images, approaches have been developed that allow a clear assignment of distinct spectral signatures to specific ground features, even though such signatures are not specific for one image channel, but distributed over many image channels (called image bands) and significantly overlapping with one another [13, 14]. In the last years some of the analysis methods established in remote sensing for multiband data have also been applied for multichannel fluorescence microscopy datasets [7, 8].

Three approaches were tested for the analysis of fluorescence microscopy data:

- Supervised classification analysis.
- Primary component analysis.
- Linear unmixing.

The first two methods are classification-based. Such classification approaches have been used for some time in spectral karyotyping using multicolor FisH [5] where the labeled chromosomes have only one characteristic signature. Classification techniques do however not work for colocalized fluorophore signals such as can be found in tissues or cells. It has been shown that the third method, linear unmixing, is the one best suited to analyze mixed contributions to a pixel, as would be the case for colocalizing labels [6–8].

4 Linear Unmixing

Fluorescence signals can be described as a linear mixture of contributions coming from the fluorophores present in the observed volume. The concentration of the fluorophores in the observed spot determines their contribution to the total signal. If one looks only at parts of the total signal that would correspond to different fluorescence image channels, the relative contribution of the fluorophores to a channel will vary according to the distribution of their emission spectra, even though the concentration of the fluorophore is the same for all channels.

As a linear equation the contribution of fluorophores to an image channel can be expressed in the following way:

$$S(\lambda) = A_1 \times \mathrm{Fluo1}(\lambda) + A_2 \times \mathrm{Fluo2}(\lambda) + A_3 \times \mathrm{Fluo3}(\lambda)\ldots \quad (1)$$

where S represents the total detected signal for every channel λ, Fluo$X(\lambda)$ represents the spectral contribution of the fluorophores to every channel, and A_x represents the abundances (i.e., concentrations) of the fluorophores in the measured spot.

More generally, this can be expressed as:

$$S(\lambda) = \sum A_i \times R_i(\lambda) \quad (2)$$

or

$$S = A \times R \quad (3)$$

where R represents the reference emission spectra of the fluorophores [8].

If the reference spectra R for all contributing fluorophores are known, the abundances A can be calculated from the measured signal S. The process through which this can be achieved is called linear unmixing. It calculates the contribution values that most closely

match the detected signals in the channels. A least square fitting approach minimizes the square difference between the calculated and measured values with the following set of differential equations:

$$\frac{\partial \sum_j \left\{ S(\lambda_j) - \sum_i A_i R_i(\lambda_j) \right\}^2}{\partial A_i} = 0 \tag{4}$$

where j represents the number of detection channels and i the number of fluorophores.

The linear equations are usually solved with the singular value decomposition (SVD) method [6, 15], so that after the calculation of the weighing matrix (A), clear representations of the separated fluorophores can be created. The separated fluorophore signals can then be displayed as distinct image channels without contributions from any other label in the sample. The intensity distribution of the signals in each position is preserved as the total signal is redistributed into the specific fluorescence channels, but not altered. It can therefore be analyzed quantitatively.

5 Requirements for the Linear Unmixing of Spectral Datasets

5.1 Reference Spectra

To be able to calculate the fluorophore contributions, linear unmixing requires knowledge of the reference spectra for the fluorophores present in the sample (Fig. 4). For maximum accuracy, such reference spectra are best taken from samples containing only the fluorophore of interest. They can also be taken from mixed samples, if specific regions only contain the signal of interest, but this contains a risk of introducing contaminating contributions from other fluorophores.

For instruments with one detector, or with several detectors that are spectrally calibrated to each other, reference spectra can be saved in a spectral database and can be reused whenever needed. Reference spectra normally have to be taken under exactly the same detection conditions as the sample so if the spectral information is sampled by several detectors which have independent settings from each other (e.g., for gain or the spectral detection range) the reference spectra have to be acquired for every session. The characteristics and strengths of different instrument designs will be discussed in a later section of the chapter.

5.2 Channel Number

For a successful separation of overlapping signals, the number of spectral detection channels has to be equal to, or greater than the number of fluorophores present in the sample. Only then can the linear equations that represent the channels be solved for all the unknowns (i.e., fluorophore contributions). In the case of fewer channels than fluorophores, the equation system is *underdetermined* and a unique solution of the equations is therefore not possible.

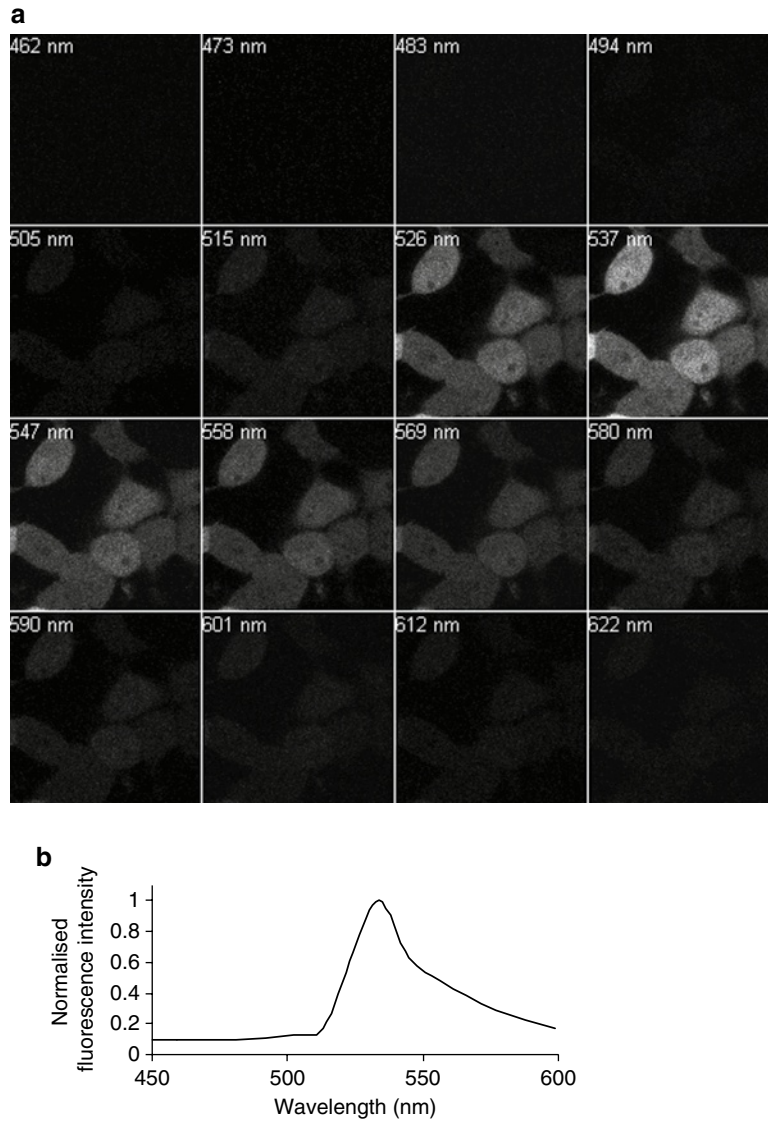

Fig. 4 Gallery of 16 YFP emission images spanning 456–628 nm in bins of 10.7 nm of 293T cells transfected with a plasmid expressing YFP transiently throughout the cell. YFP was excited using a 514 nm laser with a HFT 458/514 main dichroic, and a Plan-Apochromat 63×/1.4 oil DIC objective. The wavelength data on each image represents the center point of each 10.7 nm bin. A spectral curve for YFP emission (**b**) covering the range of the wavelength scan can be generated from the proportions of YFP fluorescence in the 16 bins

6 Related Methods to Linear Unmixing

The separation of fluorescence microscopy spectral datasets can also be achieved with methods other than linear unmixing. In very simple cases, like unidirectional bleed-through of one channel into the other, a simple subtraction of the known contribution to the second

channel can be used to separate the signals (subtractive compensation). This approach is for example used in simple variants of FRET measurements by sensitized emission [16] and in some of the first methods for simultaneous fluorescent protein detection [17].

In approaches like Automatic Dye Separation [18], Automatic Component Extraction (ACE) and Blind Source Separation [19], spectral separation can be achieved without the knowledge of reference spectra. Such approaches are especially useful for spectral data that are acquired with several detectors that are not spectrally calibrated to each other as they avoid the need to take a new set of references whenever settings are modified. An important requirement for this approach however is the presence in the dataset of significant amounts of "pure" areas containing the signature of only one of the fluorophores of interest. This information is necessary for the extraction of robust reference spectra and in cases of too abundantly co-localized fluorescence signals these methods fail.

7 Microscopes for Spectral Imaging

Spectral imaging for subsequent linear unmixing can in principle be performed on any fluorescence microscope that is capable of generating a multichannel image [20–22].

In the last years there have however been many technical developments in microscopy that specifically provide greater spectral flexibility and that are especially suited for spectral data analysis. A short overview of different instrument solutions shall therefore be given (*see* also Table 1).

Table 1
Overview of different commercial microscope setups for spectral imaging

Acquisition mode	Overdetermined ($N_c \gg N_f$)	Determined ($N_c \approx N_f$)
Parallel	Zeiss LSM 710/780 (N_c: 32–34)[a] Nikon A1 (N_c: 32)	Leica SP5/SP8-AOBS[a] Olympus FluoView 1000[a] Zeiss LSM 710 (N_c: 3)[a] Beamsplitter setups Confocal microscopes
**Sequential	Leica SP5/SP8-AOBS[a] Leica SPE Olympus FluoView 1000[a] Zeiss LSM 710/780 (N_c: 3)[a] Zeiss LSM 700 SpectraCube (FTS) Nuance (LCTF detection) Optical Insights Spectral-DV	Widefield microscopes w. filterwheels/ filtercubes

N_c number of detection channels, N_f number of fluorophores
[a]Configuration with 32 channel PMT array
**Sequential: λ-series into a single detector. Parallel: multiple detectors (2–5)

7.1 Confocal Microscopy

The importance of spectral flexibility beyond what is possible through the use of filterwheel combinations is illustrated by the fact that all current high-end confocals of the major confocal microscope providers contain solutions for spectral imaging. It is important to understand in this context that the term "spectral confocal microscope" describes a design that offers spectral flexibility for the detection and therefore an easy way of generating spectral datasets. Linear unmixing is however a data-processing step and its implementation inside the microscope software varies significantly between different companies. Some offer for example spectral separation during the acquisition and others only as a postprocessing step.

Spectral single beam scanning confocal microscopes separate the information contained in the de-scanned emission light into its spectral components by using either a prism (Leica confocal microscopes) or a diffractive grating (Zeiss, Nikon, Olympus confocal microscopes) or a blazed holographic grating (Zeiss 710). The spectral detection flexibility is then given either by projecting the entire spectrum on a fixed array of 32 photomultiplier tubes (PMTs) (Zeiss, Nikon) or by reflecting the light on fewer and separate PMTs whose spectral detection range is controlled by blocking sliders in front of the PMTs and where unused spectral information is passed on to the next PMT in the optical arrangement (Leica, Olympus).

In the case of the 32 element PMT arrays, the information is directly available as a spectrum of up to 32 points with a spectral resolution of approx. 9–11 nm (Fig. 4). The signals of two or four PMT elements can also be "binned" into a single channel to increase the collected signal per channel at the cost of spectral resolution (reduced to ~20–40 nm). To emulate the effect of a band-pass filter, virtual channels can be created by collecting all the information inside a spectral detector by combining the information of all PMT elements that cover that range.

If the information is sampled onto separate PMTs with variable slits in front of them, the main function for the spectral PMTs is to offer the possibility to freely optimize the band-pass characteristics of all detection channels. The spectral information consists of significantly fewer channels and the appearance of the spectrum may be altered by different bandwidths and gain settings of the detectors, but the channels can also be used for linear unmixing. On confocal microscopes of this design type, the spectrometer appearance of PMT array signals can be emulated by sequentially modifying the detection range of a single PMT by shifting the slit in front of it. This allows the readout of very defined spectra, but it can only be done in sequence, not instantaneously.

The advantage of PMT arrays lies in their defined spectral calibration which permits the use of existing libraries of reference spectra for linear unmixing. The advantage of separate detectors is the flexibility in their ranges and gain settings that can accommodate strong intensity peaks in parts of the spectrum without saturating the signal.

As the beam containing the fluorescence information needs to be dispersed into its spectral components for the different PMT detectors, all spectral detection systems can only work with a single confocal pinhole in front of the dispersive element and not with multiple pinholes in front of the individual detectors. As the thickness of an optical section is wavelength-dependent, this should be taken in consideration when working over a big range of the spectrum. Normally, however, spectral imaging has its use in the separation of closely spaced, overlapping signals that are not strongly affected by this consideration.

Although most current "spectral" confocal microscopes are based on a prism or grating as the dispersive element, a recent design by Zeiss also deserves mention as it provides some spectral flexibility in a different way. In the LSM 710 confocal microscope, a variable secondary dichroic (VSD) beamsplitter allows to choose the separation wavelength between the two available detection channels freely. This is not the same as the completely free spectral definition of detection channels possible in fully "spectral" confocals, but it allows an optimization of the channel properties that serves as a good basis for subsequent unmixing. Also, sequential spectral series can be acquired in a similar way to the one mentioned above for single PMTs.

Dedicated spectral imaging solutions also exist for widefield microscopy. These special solutions either provide multiple channels at the same time in the form of split images or they allow the sequential detection of the spectral information.

One of the first methods to generate spectral microscopy data uses an interferometer coupled to a microscope for Fourier Transform Spectroscopy (FTS). This technique was used initially for spectral karyotyping [5] and subsequently in conjunction with linear unmixing for the separation of seven fluorescence signals in a fixed tissue section [6].

The DualView series of imagesplitters (Optical Insights) offers two- and four-channel solutions where images corresponding to different regions of the spectrum are projected onto different areas of the camera CCD chip. Using the same camera to simultaneously image two or four images inevitably causes a corresponding loss in spatial resolution. Therefore other solutions exist that project two spectral images on different cameras. This requires an acquisition set-up that can simultaneously read out multiple cameras. The Spectral DualView uses a grating to generate true spectral information along a line of the image field. A two-dimensional spectral image is then generated sequentially by moving the sample line by line through the detection area.

The Nuance Multispectral Imaging System (Cambridge Research & Instrumentation, Inc.) uses a Liquid Crystal Tunable Filter (LCTF) in front of the camera to sequentially generate a series of spectral images of fluorescence or transmission signals that can then be separated into their contributions.

Spectral separation can also be achieved using the different distributions of the excitation spectra of fluorophores. Using different excitation wavelengths and detecting with a wide emission window to efficiently collect the signals generates image channels that can be processed easily with the same procedures as data with different emission channels [22]. Accordingly spectral separation can be achieved by tuning the wavelength of a two-photon light-source and thus generating "excitation fingerprint" datasets that are then used for unmixing. For confocal imaging, the recently introduced white-light lasers in conjunction with freely definable acousto-optical beam splitter (AOBS) configurations also allow the full use of the excitation spectra for spectral analysis and imaging.

The combination of different excitation and emission settings for unmixing significantly increases the number of information-bearing channels even on systems with only few changeable components on the excitation and emission side [22, 23]. Incorporating excitation variations also significantly helps with blind spectral decomposition approaches that work without predefined reference spectra [19, 23].

8 Method Limitations and Optimization Approaches

As with any methodology, spectral imaging and linear unmixing is affected by different parameters that need to be optimized for the best possible results. The amount of overlap of the contributing spectra influences how reliably different signals can be distinguished. Datasets with a strong spectral overlap will be more affected by noise on the image data. This may result in noisy image channels or in the incomplete separation of different fluorophores. In such cases the signal to noise ratio needs to be improved by averaging or longer integration. In detection systems that allow the definition of the spectral channels by the user, the channels should be configured to detect the maximum difference between the spectra, as this directly influences the separation of the data [22, 24]. If the fluorophores in the sample can be chosen during the sample preparation, the combinations that provide the most difference should be favored rather than relying on the ability of the unmixing software post-acquisition.

For linear unmixing of a spectral dataset, all contributing spectra have to be defined correctly. The absence of a contributing spectrum, or the use of incorrect spectra can cause mis-assignments of the signals that will lead to a misrepresentation of the fluorophore distributions in the image. If there is an autofluorescent background, it has to be considered as an extra fluorophore, otherwise it will lead to false results. The quality of an unmixed spectral dataset can in some software packages be assessed by visualizing the residual values after unmixing, i.e., the difference between the

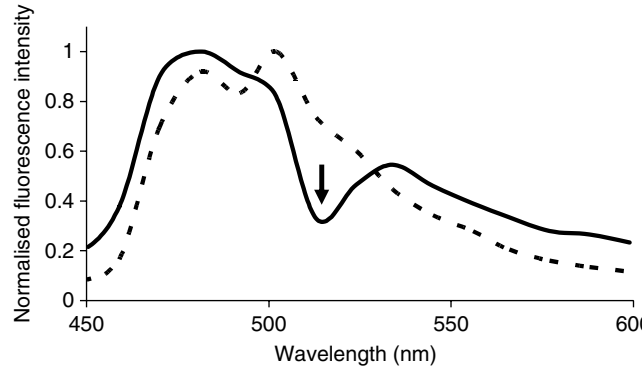

Fig. 5 Spectral profiles of CFP emission generated from similar wavelength scans to those in Fig. 4a. The profile generated using 458 nm laser excitation and a HFT458 nm main dichroic is shown with a *broken line* whilst the equivalent profile using a HFT458/514 nm main dichroic is shown in a *solid line* and illustrates the drop in fluorescence intensity at 514 nm as the HFT458/514 main dichroic reflects this wavelength (*arrow*)

calculated fit and the data values. Significant amounts of residuals indicate a separation problem due to noise or spectral overlap or due to wrong or incomplete spectral information.

It is very important to take into account that the change of optical components like the beamsplitter will significantly affect the apparent detected spectra. The replacement of a single dichroic with a double dichroic can completely alter the spectra due to the additional dip in transmission and will therefore require the collection of its own set of reference spectra (Fig. 5). These problems are alleviated in confocal microscopes by the use of Acousto-Optical Beamsplitters (AOBS, Leica) that only deflect the selected excitation laser wavelengths and by the use of high incidence beamsplitters (Zeiss, Nikon) that also have very steep and defined reflection characteristics.

Depending on the optimization functions incorporated in the unmixing routines, the number of spectra selected as potential contributors may also affect the outcome. Generally only the spectra present in the sample should be selected for the unmixing step. To improve the results, unmixing routines can use non-negativity constraints (i.e., there can be no negative fluorophore contribution to a signal) and iterative end-member ejections (i.e., the removal of spectra with no or negative contributions to the pixel from the calculation and the repetition of the unmixing step with fewer spectra) [25].

The number of channels into which a spectral dataset is split may also affect the quality of the separated result. Since the prerequisite for spectral separation is that the number of channels equals or exceeds the number of fluorophores in the sample, an equal

number of channels is in principle sufficient. The advantage is that signals are stronger since they are collected into fewer channels and that less signal-independent detector noise is accumulated [22, 24]. On the down-side, the effect of channel positioning for optimal separation is stronger when collecting fewer channels. A significantly over-sampled signal (as is acquired by 32 channel PMT array detectors) is less prone to optimization effects by the position of the channels. Additionally, the signal on PMT array detectors can be configured to be collected into fewer and wider bins by combining the input of several neighboring PMTs.

9 Applications for Spectral Imaging

9.1 Multilabeling

As the linear unmixing of spectral imaging data provides signal specificity its main applications are experiments that contain multiple signals like multi-fluorophore Fluorescence in situ Hybridization (FisH) as used in spectral karyotyping [5] or the simultaneous staining of multiple tissue markers [6].

9.2 Autofluorescence Removal

Sample autofluorescence is a persistent problem of fluorescence microscopy when working in tissues, especially in plants [26, 27]. It often has a wide distribution and can therefore not be separated from the signals of interest through the use of band-pass filters. Also, in signal strength it may completely mask a weakly expressed fluorescent protein [28]. It can however in many cases be spectrally defined and then treated as an additional signal in the unmixing process. This allows for an efficient removal of the autofluorescence signal from the image channels, which only then can be utilized for quantitative colocalization studies [29].

9.3 Time-Lapse Imaging

Since time limitations are not relevant in fixed samples, the problems of fluorophore overlap are generally caused by the high number of fluorophore signals that cannot be separated reliably even by sequential imaging of the channels. Due to the time constraints in in vivo imaging significant overlap problems can already be encountered with significantly fewer fluorophores due to simultaneous imaging or if the choice of fluorescent tags is limited to pairs that have very similar spectral characteristics, as is the case for many fluorescent proteins [30], Fig. 6.

9.4 Fluorescence Resonance Energy Transfer

Fluorescence Resonance Energy Transfer (FRET) is a powerful tool for molecular interaction studies and generally involves the use of a matched pair of fluorophores (FRET pair) respectively as donor and acceptor of the transferred energy. A prerequisite for the pairing of two fluorophores for FRET is significant spectral overlap between the emission spectrum of the donor and the excitation spectrum of the acceptor. For many FRET pairs this required

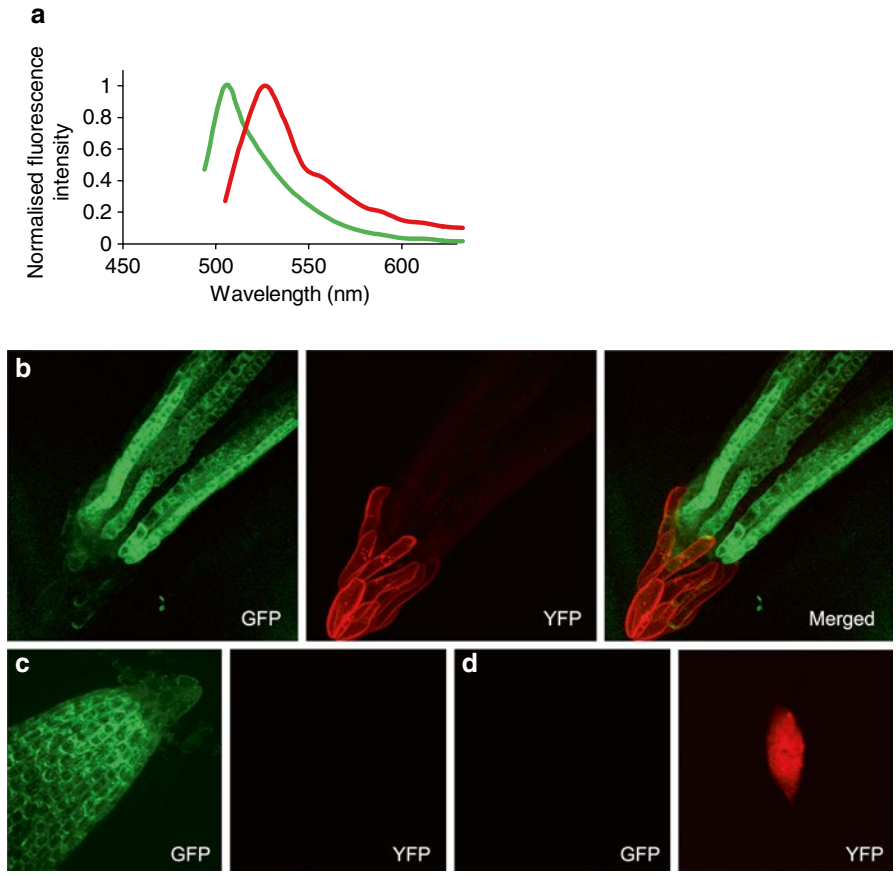

Fig. 6 GFP (*green*) and YFP (*red*) emission spectral profiles taken from wavelength scans of an *Arabidopsis thaliana* mGFP5 enhancer-trap line and a histone-YFP transformed *Arabidopsis thaliana* seedling root respectively (**a**). GFP and YFP were excited using a 488 nm laser with a HFT488 main dichroic. The wavelength scans covered 490–630 nm in bins of 10.7 nm using a plan-Apochromat 63×/1.4 oil objective. A wavelength scan of an *Arabidopsis thaliana* seedling root can be spectrally unmixed to reveal GFP (*green*) and YFP (*red*) expression (**b**) using the curves shown in (**a**). The mean wavelength images in (**b**) were captured in three dimensions (*x*, *y*, *z*) and are shown as 3D projections of the spectrally separated fluorochromes. To verify the spectral separation a wavelength scan of an *Arabidopsis thaliana* mGFP5 enhancer-trap seedling was unmixed using the GFP and YFP spectral curves (**c**) and correct assignment of the GFP fluorescence (*green*) to the GFP channel is shown (YFP channel is *blank*). Also a wavelength scan of an *Arabidopsis thaliana* seedling transformed with histone-YFP was unmixed using the GFP and YFP spectral curves (**d**) and correct assignment of the YFP fluorescence (*red*) to the YFP channel is shown (GFP channel is *blank*)

spectral proximity leads as well to significant problems in fluorophore cross talk and cross-excitation that make a quantitative analysis problematic. Spectral imaging and linear unmixing methods have in the last years been used to correct for the channel contaminations in acceptor photobleaching methods [28, 31–34], Fig. 7, as well as in methods for the detection of ratiometric signals and sensitized emission [35–38]. It is especially important for FRET

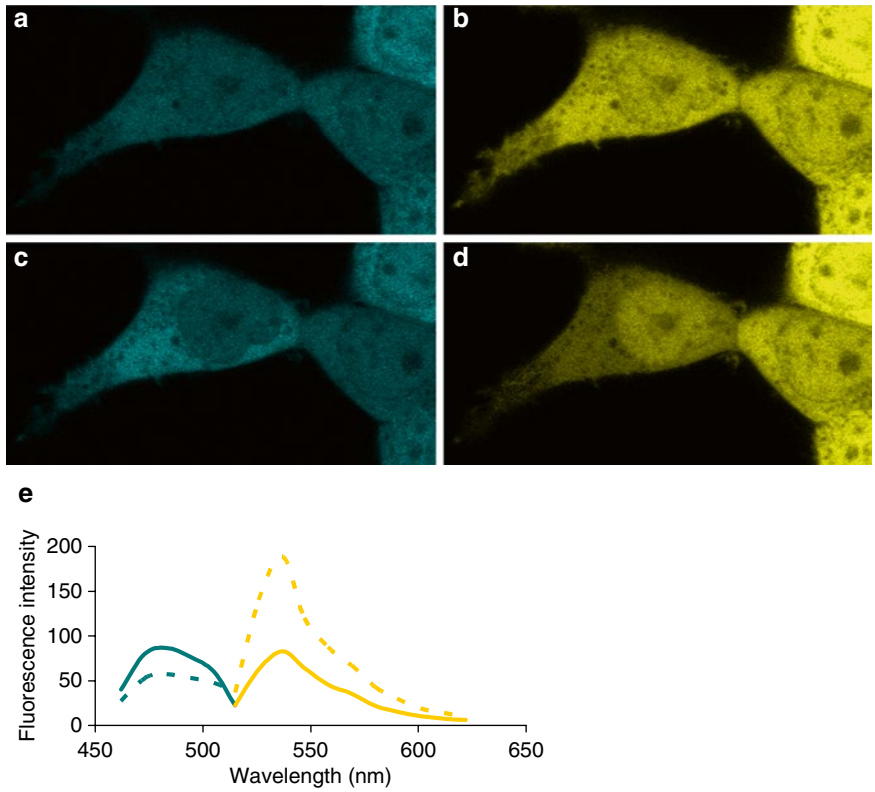

Fig. 7 293T cells transfected with a plasmid expressing tandem linked CFP and YFP. CFP and YFP were excited with 458 nm and 514 nm lasers respectively using a HFT458/514 main dichroic and plan-apochromat 63×/1.4 oil DIC objective. A wavelength scan was taken between 456 and 628 nm in bins of 10.7 nm. Data were spectrally unmixed using curves similar to those shown in Figs. 5.4b and 5.5. Images of unmixed CFP and YFP prior to acceptor (YFP) photo bleaching are shown in (**a**, **b**) and after acceptor photo bleaching in (**c**, **d**). The cytoplasmic bleach region is outlined in (**b**). After bleaching YFP using the 514 nm laser at 100 % transmission the intensity of the YFP in the cytoplasm decreases (**d**, **e** *broken yellow line* cf. *solid yellow line*) and the intensity of the CFP increases (**c**, **e** *broken blue line* cf. *solid blue line*)

pairs with high efficiency that unfortunately coincides with poor separation [33, 39].

The possibility to combine multiple markers and probes for multiparameter imaging [40, 41] increases the need for reliable signal separation. This has been demonstrated by the use of two fluorescent protein-based FRET pairs that can be excited by a single excitation wavelength and whose FRET interactions can be resolved by linear unmixing [38].

10 Conclusions

Commercially available spectral imaging and linear unmixing software has solved the problems of spectral bleed through encountered in multicolor confocal laser scanning as well as in widefield

microscopy. The user can capitalize on the increased numbers of fluorochromes available, use them simultaneously in a single experiment and be confident that mixed fluorescent samples are separated cleanly and clearly into their respective detection channels. Spectral unmixing can bring increased sensitivity over conventional optical filter systems because the entire emission spectra is collected and it also has the advantage of allowing fluorochromes whose spectra do not fit with conventional optical filters to be used.

Spectral unmixing can not only be used to identify and remove the interference from autofluorescence, which is especially problematic in plants, but also to analyze the autofluorescence spectra and study the development of the underlying molecules in situ. Spectrally separated autofluorescence can also be used as a "background" image for the sample on which to superimpose the specific probe fluorescence. Users can also verify their fluorescent signal by checking the spectra obtained from their sample with well documented, previously published spectra and identify any spectral shifts due to different cellular environments. Furthermore, spectral imaging enhances the visualization of molecular interactions or conformational changes detected by FRET and increases the number of FRET pairs available to include the more spectrally overlapping high efficiency FRET pairs. All of the above advances are possible in 4 dimensions (x, y, z, t) with the added benefit of multicolor analysis allowing dynamic live cell imaging of multiple fast cellular processes.

References

1. Lippincott-Schwartz J, Patterson GH (2003) Development and use of fluorescent protein markers in living cells. Science 300(5616):87–91
2. Miyawaki A, Sawano A, Kogure T (2003) Lighting up cells: labelling proteins with fluorophores. Nat Cell Biol Suppl 5(9):S1–S7
3. Hu CD, Kerppola TK (2003) Simultaneous visualization of multiple protein interactions in living cells using multicolor fluorescence complementation analysis. Nat Biotechnol 21(5): 539–545
4. Zhang J et al (2002) Creating new fluorescent probes for cell biology. Nat Rev Mol Cell Biol 3(12):906–918
5. Schrock E et al (1996) Multicolor spectral karyotyping of human chromosomes. Science 273(5274):494–497
6. Tsurui H et al (2000) Seven-color fluorescence imaging of tissue samples based on Fourier spectroscopy and singular value decomposition. J Histochem Cytochem 48(5):653–662
7. Lansford R, Bearman G, Fraser SE (2001) Resolution of multiple green fluorescent protein color variants and dyes using two-photon microscopy and imaging spectroscopy. J Biomed Opt 6(3):311–318
8. Dickinson ME et al (2001) Multi-spectral imaging and linear unmixing add a whole new dimension to laser scanning fluorescence microscopy. Biotechniques 31(6):1272, 1274–6, 1278
9. Lichtman JW, Conchello JA (2005) Fluorescence microscopy. Nat Methods 2(12):910–919
10. Speicher MR, Gwyn Ballard S, Ward DC (1996) Karyotyping human chromosomes by combinatorial multi-fluor FISH. Nat Genet 12(4):368–375
11. Garini Y et al (1999) Signal to noise analysis of multiple color fluorescence imaging microscopy. Cytometry 35(3):214–226
12. Shaner NC, Steinbach PA, Tsien RY (2005) A guide to choosing fluorescent proteins. Nat Methods 2(12):905–909
13. Landgrebe D (2002) Hyperspectral image data analysis as a high dimensional signal processing problem. IEEE Sig Proc Mag 19(1):17–28
14. Keshawa N, Mustard JF (2002) Spectral unmixing. IEEE Sig Proc Mag 19(1):44–57

15. Hiraoka Y, Shimi T, Haraguchi T (2002) Multispectral imaging fluorescence microscopy for living cells. Cell Struct Funct 27(5): 367–374
16. Wouters FS, Verveer PJ, Bastiaens PIH (2001) Imaging biochemistry inside cells. Trends Cell Biol 11:203–211
17. Zimmermann T, Siegert F (1998) Simultaneous detection of two GFP spectral mutants during in vivo confocal microscopy of migrating Dictyostelium cells. Biotechniques 24(3): 458–461
18. Olschewski F (2002) Living colors. Imaging & Microscopy 4(2):22–24
19. Neher RA et al (2009) Blind source separation techniques for the decomposition of multiply labeled fluorescence images. Biophys J 96(9): 3791–3800
20. Castleman KR (1993) Color compensation for digitized FISH images. Bioimaging 1:159–165
21. Castleman KR (1994) Digital image color compensation with unequal integration periods. Bioimaging 2:160–162
22. Zimmermann T, Rietdorf J, Pepperkok R (2003) Spectral imaging and its applications in live cell microscopy. FEBS Lett 246:87–92
23. Shirakawa H, Miyazaki S (2004) Blind spectral decomposition of single-cell fluorescence by parallel factor analysis. Biophys J 86(3):1739–1752
24. Zimmermann T (2005) Spectral imaging and linear unmixing in light microscopy, 95th edn. Advances in biochemical engineering/biotechnology. pp 245–265
25. Zimmermann T (2005) Spectral imaging techniques for fluorescence microscopy. In: Stephens D (ed) Cell imaging. Scion Publishing Limited, Oxfordshire, pp 95–118
26. Rost FWD (1995) Autofluorescence in plants, fungi and bacteria. In: Rost FWD (ed) Fluorescence microscopy. Cambridge University Press, New York, pp 16–39
27. Berg RH (2004) Evaluation of spectral imaging for plant cell analysis. J Microsc 214(Pt 2): 174–181
28. O'Toole PJ et al (2004) Use of spectral unmixing and FRET to study GFP and nile red in *Nicotiana bethamiana* leaf epidermal cells. Imag Microsc 6(2):28–29
29. Nadrigny F et al (2006) Detecting fluorescent protein expression and co-localisation on single secretory vesicles with linear spectral unmixing. Eur Biophys J 35(6):533–547
30. Lenz JC et al (2002) Ca2+-controlled competitive diacylglycerol binding of protein kinase C isoenzymes in living cells. J Cell Biol 159(2): 291–302
31. Gu Y et al (2004) Quantitative fluorescence resonance energy transfer (FRET) measurement with acceptor photobleaching and spectral unmixing. J Microsc 215(Pt 2):162–173
32. Sturmey RG, O'Toole PJ, Leese HJ (2006) Fluorescence resonance energy transfer analysis of mitochondrial:lipid association in the porcine oocyte. Reproduction 132(6):829–837
33. Dinant C et al (2008) Fluorescence resonance energy transfer of GFP and YFP by spectral imaging and quantitative acceptor photobleaching. J Microsc 231(Pt 1):97–104
34. Amiri H, Schultz G, Schaefer M (2003) FRET-based analysis of TRPC subunit stoichiometry. Cell Calcium 33(5–6):463–470
35. Thaler C, Vogel SS (2006) Quantitative linear unmixing of CFP and YFP from spectral images acquired with two-photon excitation. Cytometry A 69(8):904–911
36. Domingo B et al (2007) Imaging FRET standards by steady-state fluorescence and lifetime methods. Microsc Res Tech 70(12): 1010–1021
37. Megias D et al (2009) Novel lambda FRET spectral confocal microscopy imaging method. Microsc Res Tech 72(1):1–11
38. Tomosugi W et al (2009) An ultramarine fluorescent protein with increased photostability and pH insensitivity. Nat Methods 6(5): 351–353
39. Zimmermann T et al (2002) Spectral imaging and linear un-mixing enables improved FRET efficiency with a novel GFP2-YFP FRET pair. FEBS Lett 531(2):245–249
40. Schultz C et al (2005) Multiparameter imaging for the analysis of intracellular signaling. Chembiochem 6(8):1323–1330
41. Piljic A, Schultz C (2008) Simultaneous recording of multiple cellular events by FRET. ACS Chem Biol 3(3):156–160

Chapter 6

Low Magnification Confocal Microscopy of Tumor Angiogenesis

George McNamara, Anna Yanai, Vazgen Khankaldyyan, Walter E. Laug, Jeff Boden, Keith Webster, Yiwen Li, and Rong Wen

Abstract

Blood vessels are critical to normal mammalian development, tissue repair, and growth and treatment of cancer. Mouse research models enable mechanistic studies of blood vessels. We detail how to perfuse mice with fluorescent tomato lectin or the lipophilic fluorophore DiI. We provide details on how to image fluorescently labeled blood vessels.

Key words Blood vessels, Angiogenesis, Fluorescent lectin, DiI, Confocal microscope

1 Introduction

Inhibiting tumor growth with anti-angiogenic therapies has received much interest because of the work by Judah Folkman [1]. Blood vessels, and blood flow, can now be visualized in vivo at depths to ~1 mm in mouse tissues using intravital microscopy with expensive multiphoton excitation laser microscopes (*see* refs. 2–6). Not having a multiphoton excitation laser, and because our tumors were implanted several millimeters deep in mouse brains, we have adopted an alternative approach of quantifying tumor growth by in vivo bioluminescence and MicroMRI imaging, and then performing visible and near-infrared confocal microscopic imaging of tumors in hemi-sectioned mouse brains. We were inspired to use a 10× objective lens for this project, by the work of R.M. Zucker with low-magnification confocal microscopy of mouse and rat fetuses [7–9]. We used fluorescent tomato lectin for our work, but note that Debbage and colleagues have obtained excellent staining of blood vessels, both by perfusion and in tissue sections, using any of several other lectins [10–12].

Stephen W. Paddock (ed.), *Confocal Microscopy: Methods and Protocols*, Methods in Molecular Biology, vol. 1075,
DOI 10.1007/978-1-60761-847-8_6,

2 Materials

Female athymic nude mice (nu/nu, albino outbred stock from NCI), 6–8 weeks of age (Harlan, Indianapolis, IN).

U87MG human glioblastoma cell line (ATCC, Manassas, VA).

hrLuc-DsRed2-sr39tk HSV TK tribrid gene (Ray et al. [20]; S.S. Gambhir, pers. comm.).

RPMI with 10 % FBS in 5 % CO_2 (GIBCO™ Invitrogen Corp., Carlsbad, CA).

Fluorescein-conjugated tomato lectin (Vector Laboratories, Burlingame, CA).

Biotin-conjugated tomato lectin (Vector Laboratories, Burlingame, CA).

Alexa Fluor® 647-streptavidin (Molecular Probes, Inc., Eugene, OR).

Glass bottom culture dishes, P35G-0-14-C or P35GC-1.5-14-C (Mattek Corp., Ashland, MA).

Leica TCS SP1 confocal microscope optics mounted on a Leica DMIRBE inverted microscope; LCS and LCS Lite confocal microscope acquisition and analysis software (Leica Microsystems, Exton, PA and Heidelberg, Germany). 2009 (U Miami): Leica SP5 spectral confocal DMI6000 inverted microscope or Zeiss LSM510/UV confocal Axiovert 200M inverted microscope.

Antigen Unmasking Solution (Vector Laboratories, Burlingame, CA).

Anti-PECAM-1 (M-20) (Santa Cruz Biotechnology, Santa Cruz, CA).

Anti-Smooth Muscle Actin Clone 1A4 (DakoCytomation, Carpenteria, CA).

Cy3-conjugated AffiniPure Donkey Anti-Goat IgG (Jackson ImmunoResearch Laboratories, Inc., West Grove, PA).

Fluorescein (FITC)-conjugated AffiniPure Donkey Anti-Rabbit IgG (Jackson ImmunoResearch Laboratories, Inc., West Grove, PA).

Purified rat anti-mouse CD31 (PECAM-1) monoclonal antibody (BD Pharmingen, San Diego, CA).

Biotinylated anti-rat IgG (VECTOR Laboratories, Burlingame, CA).

Hoechst 33342, H3570 (Invitrogen/Molecular Probes), 10 mg/mL stock solution, diluted to 100 μg/mL in distilled H_2O, used at 0.1 μg/mL (live cell experiments) or 10 mg/mL in PBS (hemi-sectioned brain nuclear labeling).

Leica Microsystems (Bannockburn, IL) DMRXA fluorescence microscope (*see* text for additional details).

Pathscan Enabler III (in 2008 version IV) (Meyer Instrument, Houston, TX).

Polaroid SprintScan 4000+ (Polaroid Corp., Cambridge, MA).

MetaMorph Imaging System 6.25 (Universal Imaging Corp., Downingtown, PA).

Adobe Photoshop CS (Adobe Systems Inc., San Jose, CA).

3 Methods

The methods described below outline animal injection, sacrifice, brain confocal imaging, and immunofluorescent analysis of tissue sections. The tribrid reporter gene is described in Ray et al. [20],. Details of other methods can be found in other publications [13, 14, 19, 21–26]. Athymic nude (nu/nu) immunocompromised female mice, 6–8 weeks of age (Harlan, Indianapolis, IN), are used as the recipients of human tumor cells.

3.1 Tribrid Reporter Gene

A multipurpose reporter gene was introduced into the U87MG glioblastoma cell line by lentivirus transduction [22]. The hrLuc-RFP-TK tribrid gene [20, 27], courtesy of Sam Gambhir, UCLA (now at Stanford University), is a triple fusion of human codon-optimized *Renilla* luciferase (hrLuc), DsRed2 red fluorescent protein (RFP) (BD Clontech) and mutant sr39tk herpes simplex virus type 1 thymidine kinase (TK) (Ray et al. [20] for the precursor Rluc-sr39tk hybrid gene fusion article). Note that Ray et al. [20] report on an improved tribrid vector that replaces the DsRed2 RFP with a monomeric DsRed derivative (mRFP1, Campbell et al. [28]) and R.Y. Tsien's lab has made spectral and brightness improvements to mRFP1 in their fruity fluorescent protein series of papers [29, 30].

Rluc enables whole animal in vivo bioluminescence imaging with a Xenogen 3D IVIS® imaging system for quantitation of tumor cell mass following native coelenterazine injection (collaboration with Mike Rosol and Maya Otto-Duessel, CHLA). In this and related studies, tumor size was also estimated by T1- or T2-weighted or contrast enhanced (tumor tissue edema) MicroMRI using either a custom mouse coil on a clinical MRI machine (GE Medical Systems 1.5 Tesla MRI) or on a 7 Tesla Bruker MicroMRI (collaboration with Rex Moats, Harvey Pollack and Maya Otto-Duessel, CHLA). MRI cross-section area correlates well with histology area [22, 31].

The DsRed2 red fluorescent protein (RFP) enables whole mount confocal microscopy and fluorescence stereomicroscope (Leica MZ FL III) of split brains, fluorescence microscopy of tissue sections by DsRed2 fluorescence or anti-DsRed immunofluorescence or immunohistochemistry with a compound microscope

(Leica DM RXA), and flow cytometry (BD Biosciences FACSCalibur) of trypsinized brain. The tumor cells are labeled with the tribrid hrLuc-RFP-TK fusion triple reporter because we wanted to reserve the more sensitive firefly luciferase (Fluc) in vivo reporter for therapeutic stem cell tracking [22, 29, 32, 33].

The TK gene product uses a ganciclovir substrate, which the herpes simplex virus mutant sr39tk thymidine kinase converts to a toxic product, and as a PET reporter (MicroPET collaboration with Xiaoyuan (Shawn) Chen, USC PET Imaging Science Center).

3.2 Intracranial Xenograft Tumor Implantation

Mice were orthotopically injected with 10^5 U87 glioblastoma cells. Mice were anesthetized using ketamine (Ketajet 100 mg/kg) and xylazine (Xyla-ject 10 mg/kg) and 1×10^5 U87 MG glioblastoma cells in 1 μL of serum free medium were inoculated in 20 min stereotactically in the defined location of the caudate/putamen (0.5 mm anterior to the bregma, 2.0 mm lateral to the midline) using a 10 μL Hamilton syringe (Reno, NA) advanced to a depth of 3.3 mm from the cortical surface. The slow rate of 100,000 cells in 1 μL in 20 min was necessary for the tumor cells to remain deep in the brain tissue. Rapid infusion, or rapid drawback of the injection needle, can result in the tumor cells becoming dispersed along the needle track and rapid growth along the track and along the surface of the mouse brain (S. Yamada, V. Khankaldyyan, W. Laug, R. Moats, I. Gonzalez-Gomez, unpublished MicroMRI and histology data). A full stereotaxis rig maximizes consistency of the xenograft model (M. Rosol, M. Jensen, pers. comm.).

3.3 Tomato Lectin Intravital Labeling of Blood Vessels (Vascular Casting)

We used either 1 mg/mL fluorescein (isothiocyanate) conjugated tomato (*Lycopersicon esculentum*) lectin (Vector Laboratories), or Alexa Fluor®-streptavidin (Molecular Probes) mixed immediately before use with biotin-conjugated tomato lectin (Vector Laboratories). Tumor-bearing mice were anesthetized and injected by cardiac puncture using a 28 gauge needle with 200 μL of fluorescent tomato lectin in PBS. Two minutes later, the mice were perfused with PBS intracardially to flush out red blood cells. Best results are obtained after maximally flushing out the red blood cells. An alternative to PBS perfusion (not used in the current work) is freshly prepared 4 % paraformaldehyde in PBS. This has the advantage of making the tumor tissue stiffer for hemi-sectioning, but has the disadvantage of increasing tissue auto-fluorescence, greatly increasing red blood cell auto-fluorescence, and disruption of some antigenic epitopes used for later immunofluorescence or immunohistochemistry. An alternative to cardiac puncture is tail vein injection. For lectin staining of brain microvessels, we obtained more consistent labeling with cardiac puncture. We have on occasion harvested other organs (liver, spleen, kidney/adrenal gland, lungs) from mice in this study (A. Yanai and V. Khankaldyyan) or from neuroblastoma orthotopic implantation or tail vein injection

metastasis models (Chantrain et al. [34]; Y. DeClerck, C. Chantrain, K. Bajou, L. Sarte, S. Jodele, pers. comm.) after cardiac or tail vein injections. Cardiac puncture has a clear advantage for brain microvessel labeling, due to the "straight shot" from the aorta to the carotid arteries and brain blood vessels. Tail vein injection works somewhat better for the other organs, for those mice that have good tail veins and available injection sites following repetitive injections of chemotherapies or bioluminescent substrates. The neuroblastoma group has also evaluated Texas Red®-streptavidin tomato lectin for microvessel imaging with similar performance to those reported here (DeClerck et al. and McNamara, unpublished). Animal protocols were performed with CHLA animal care committee and biosafety committee approval. We anticipate future experiments that will obtain similar or superior data with fluorescent nanocrystals (aka quantum dots), i.e., QD655-streptavidin and/or QD705 streptavidin (Quantum Dot Corp., http://www.qdots.com) or Evitag720-streptavidin (Evident Technologies, http://www.evidenttech.com), as has been published for blood (Larson et al. [3]) and lymph node (Kim et al. [35]) imaging in live animals [35].

3.4 Brain Excision and Hemi-sectioning

For confocal imaging, brains were excised and sectioned in half (horizontal section). Horizontal sectioning was chosen because the U87MG-tribrid gene transfected human glioblastoma tumor cells were orthotopically injected in the middle of the mouse brain [21, 22, 26, 31]. The hemi-section was made with a scalpel, the cut being from the olfactory bulb to cerebellum, approximately bisecting the orthotopic implanted tumor. This is the same plane as one of the axes of the MicroMRI 3D scans [31], and is also used for histological sections by fluorescence immunohistochemistry and standard immunohistochemistry with either light microscopy (*see* below) or 35 mm film/Pathscan microscope slide scanner and image analysis [21, 34]. The brain halves were placed in cold PBS on ice, transported to the confocal microscope, transferred to a uncoated #0 or #1.5 coverglass 35 mm glass bottom dish (P35G-0-14-C, or P35GC-1.5-14-C, Mattek Corp., http://www.glassbottomdishes.com/gbcustomerpriceweb.pdf). Following confocal imaging, the brain hemi-sections were put back on ice, transported back to the wet lab, fixed, sectioned and then individual sections were processed for H&E histology, immunofluorescence and immunohistochemistry. In collaboration with Dr. Christine Brown, Renate Starr and Professor Michael Jensen, we have imaged Hoechst 33342 dye nuclear counterstaining of hemi-sectioned mouse brains, at the Light Microscopy Core of City of Hope National Medical Center. Brain nuclei were imaged on a Zeiss LSM 510 NLO confocal/multiphoton microscope in PBS with Hoechst 33342 at 10 μg/mL for 15 min, transferred to an imaging dish with PBS, and imaged using 750 nm, ~80 MHz,

~100 femtosecond pulses with a Zeiss 10×/0.5 NA lens. On the same microscope we have performed live cell experiments with Hoechst 33342 at 0.1 μg/mL in bicarbonate free, phenol red free, tissue culture medium. This concentration was chosen because higher concentrations of Hoechst are known to inhibit normal cell behavior [37]. When using Hoechst dyes, it is important to dilute the 10 mg/mL stock solution 100-fold in water because diluting in PBS results in formation of dye precipitates.

3.5 Confocal Microscopy

Details of the CHLA confocal microscope hardware can be found in the Appendix. The Leica SP1 confocal spectrophotometry hardware has been described [38, 39]. This and other spectral confocal microscopes is also available [40], where the CHLA system is system L4.

Most Images were acquired with Leica TCS SP1 confocal optics, equipped with air-cooled Argon ion (457, 476, 488, and 514 nm laser lines, ~2 mW power at 488 nm at the specimen plane), air-cooled Krypton ion laser (568 nm, ~2 mW power) and HeNe laser (633 nm, ~2 mW) mounted on a Leica DM IRBE inverted fluorescence microscope. The Argon and Krypton ion lasers operational lifetime is low if run at full power (maximum power knob setting of 4 o'clock on laser front panel); we routinely operated both at 12 o'clock power settings (mW power shown above for 100 % AOTF settings); when idle, the laser power was set to the minimum (knob setting 8 o'clock). Laser power was attenuated with the Leica SP1 AOTF. The Leica confocal microscope is maintained under an annual service contract with the manufacturer (Leica Microsystems, Exton, PA). In addition to an annual preventive maintenance visit by the manufacturer's field service engineer, the image core manager performs periodic performance tests and arranges service visits as needed (testing details available from GM). Confocal system performance data, during the time period of image acquisition for this study, was published as system L4 [40].

Three reflection/fluorescence and one transmitted light (through the condenser) photomultiplier tubes (PMTs) are present on our SP1 confocal microscope. For fluorescence, the PMT offset were adjusted such that a positive intensity value was read out even with no light reaching the detector. Typical PMT gains were in the 700–900 settings range (maximum 1,250). A Leica RSP500 or TD488/568/633 triple dichroic mirror was used in the scanhead to reflect laser excitation to the microscope and pass emission photons to the PMTs. The SP1 optical head uses a prism spectral dispersion element with wavelength selection slits in front of each PMT. The SP1 is controlled from Leica LCS 2.5 on a Pentium 400 MHz computer. Confocal images were acquired with no filter cube in place. The Leica DM IRBE microscope stand is equipped Leica A, I3 and N2.1 longpass filter cubes, for DAPI,

fluorescein/GFP/Alexa488, Cy3/DsRed, respectively, excited with a 50 W Hg lamp for visual inspection (a 100 W Hg voltage stabilized lamp would be a better choice for standard microscopy, since the Leica 50 W Hg lamp flickers). Information on filter cubes can be found in Ploem and Walter [41]. We occasionally acquired brightfield or Nomarski differential interference contrast (DIC) images with the laser line(s) from the objective lens and specimen being detected through the microscope condenser and a transmitted light path PMT that was positioned adjacent to the microscope transmitted light path, and switchable with a Leica knob. The transmitted light images were not confocal because that light path does not include a pinhole to reject out of focus light; the transmitted light images were in register with the confocal fluorescence. The laser illumination transmitted light DIC images do exhibit optical sectioning because of the intrinsic characteristics of DIC, but the images are not particularly good as the Leica optics exhibit significant shading, the contrast range of the 8-bit images are small, and the thickness of the hemi-sectioned mouse brains scatter much of the light.

Most brain images were acquired with a Leica 10×/0.40 NA HC Plan Apo Ph1 dry objective lens (Leica SP1 confocal microscope). Some images were acquired with a 10×/0.4 NA HC Plan Apo IMM lens, using water immersion, without significant improvement in image quality. We have tested a Leica N Plan 5×/0.12 NA, N Plan 2.5×/0.07 NA, and Plan Fluotar 1.3/0.04 NA objective lenses, for the unfixed hemi-sectioned brain application, but have been whelmed by the fluorescence brightness and contrast. These lenses may perform better using completely transparent, low-scattering, tissue with bright fluorescent markers, such as Zucker's 1:1 benzyl benzoate–benzyl alcohol (BABB) clearing solution [8] or methyl salicylate clearing solution of brains perfused with red fluorescent latex vascular casts (S. Yamada, CHLA). BABB or methyl salicylate clearing of brain tissue requires ~1 week time after transfer to absolute ethanol, and leaves the tissue fragile with respect to later handling. By contrast, our unfixed brain hemi-section imaging adds a few hours delay between the time the mouse is sacrificed and when the tissue is ready for histological processing.

The confocal pinhole size was routinely set to either 1.0 or 1.5 Airy units when using the 10×/0.40 NA dry objective lens. At 1.0 Airy units, this lens has a theoretical XY resolution of 488 nm and Z resolution of 2,630 nm, with a working distance of 2,200 μm. (The deepest into a fluorescent specimen we have ever imaged was 836 μm with a methyl salicylate cleared red fluorescent latex mouse brain vascular cast.) Opening the pinhole from 1.0 to 1.5 Airy units results in the collection of more photons from the specimen from a thicker optical section. The image capture settings were

1,000×1,000 μm field of view (512×512 pixels), medium scan speed, 2 or 3 Kalman frame averaging. A Z step size of 2 μm (slightly oversampling in Z) was used to make the XY and Z pixel dimensions equal as a convenience for later image analysis and display ("orthogonal dimensions"). Our Leica SP1 confocal microscope is equipped with a Leica high speed, high resolution galvonometer based focus motor ("galvo-Z"). The galvo-Z enables high speed XZ scanning (at appropriate zoom) at the same speed as standard XY image scanning. The galvo-Z has a step size of ~0.040 μm, range of 160 μm and a mass limit of 90 g. For the purposes of this study, we used the Leica DMIRBE microscope internal focus motor, which has a nominal step size of ~0.100 μm.

Basic Leica SP1 microscope operations are described in a Web document by John Runions at the Haseloff lab (http://www.plantsci.cam.ac.uk/Haseloff/JohnRunions/Confocal_instructions/Confocal_instructions(old)/Confocal.pdf). The Haseloff SP1 system is on an upright microscope and uses different lasers than the CHLA system.

Mouse skin blood vessels were imaged by sacrificing the mouse pinching the skin and cutting the skin scissors. For this work, an approximately 25 mm piece of skin (with white hair), was imaged in a 25 mm Mattek glass bottom dish (P35G-1.5-20-C, http://www.glassbottomdishes.com) with a thin layer of PBS to improve optical contact to the coverglass. Tile scans were acquired with a Leica SP5/DMI6000 inverted confocal microscope (University of Miami). DiI perfused mouse skin blood vessels were acquired with a 561 nm laser, 10×/0.4 NA objective lens, 512×512 pixel images with 8×6 tile scan Z-series of 21 planes using 10 μm step size (200 μm thick). Non-confocal RGB transmitted light tile scans were acquired on the Leica SP5 microscope using 458, 561 and 633 nm laser lines for blue, green and red channels, respectively, using three scan track sequential frame mode (3× longer time than a single scan track). Because hemoglobin is the major absorbing molecule, in the red blood cells of the mouse that did not perfuse with DiI, we could have used any of the laser lines between 458 and 561 nm for the blue and green channels by applying a cyan lookup table, plus the 633 nm laser line for the red channel. This would have reduced scan time by one third (e.g., 90 min to 60 min for a 21 plane Z-series, 8×6 tile scan). For anyone performing transmitted light laser scanning diaminobenzidine and hematoxylin (DAB&H) tissue section slides, we recommend either the 405 or 458 nm laser line for DAB (blue channel) and 633 nm laser line for hematoxylin (green and red channels). Transmitted light laser scanning of hematoxylin and eosin (H&E) slides can performed with transmitted light 633 nm for hematoxylin, and either 488, 496, or 514 nm for eosin, with confocal fluorescence (520–560 nm) and/or non-confocal transmitted light detection (green and blue channel).

3.6 Immunofluorescence and Histological Processing of Tissue Sections

After brains were removed, bisected through the tumor, and imaged on the confocal microscope, they were processed, half for paraffin embedding (Zinc Fixative followed by 10 % formalin fixation) and half for frozen sections (4 % paraformaldehyde followed by 16 h in 30 % sucrose). Tissue for frozen sections were snap frozen in OCT embedding medium and maintained at –80 °C until sectioned. Hematoxylin and eosin stained sections were examined to note extent of tumor growth.

Immunofluorescence for CD31 and αSMA was performed on Zinc fixed paraffin-embedded sections. Five micrometer sections were mounted on Superfrost/Plus glass slides. After baking at 60 °C overnight, the slides were deparaffinized in xylene and rehydrated. For antigen retrieval, sections were boiled 12 min in Antigen Unmasking Solution (Vector Laboratories, Burlingame, CA). The sections were stained using anti-PECAM-1 (M-20) (Santa Cruz Biotechnology, Santa Cruz, CA) 1:100 and/or anti-Smooth Muscle Actin Clone 1A4 (DakoCytomation) 1:100 and incubated overnight at 4 °C. The secondary antibodies: Cy3-conjugated AffiniPure Donkey Anti-Goat IgG (Jackson ImmunoResearch Laboratories, Inc., West Grove, PA) (1:200) and Fluorescein (FITC)-conjugated AffiniPure Donkey Anti-Rabbit IgG (Jackson ImmunoResearch Laboratories, Inc., West Grove, PA) (1:200). Frozen sections were stained with purified rat anti-mouse CD31 (PECAM-1) monoclonal antibody (BD Pharmingen) 1:75 Biotinylated anti-rat IgG (VECTOR Laboratories, Burlingame, CA).

3.7 Immunofluorescence Microscopy of Tissue Sections

Tissue immunofluorescence images were acquired with a Leica Microsystems (Bannockburn, IL) DMRXA fluorescence microscope, Sutter Instrument Company (Novato, CA) LS 300 Xenon arc lamp with 1 m liquid light guide, Life Imaging Services (Reinach, Switzerland) LLG-DMRXA quartz lens coupler, Chroma Technology Corp. (Rockingham, VT) HQ filter sets for fluorescein (set 41001), Cy3 (41007a), and Cy5.5 (41022). The microscope was also equipped with a 61000v2 DAPI/Ffluorescein/Cy3 triple pass filter set for viewing specimens by eye, and was equipped with additional filter sets for other applications. The DMRXA was equipped with a Leica optovar with 1× (lensless), 1.25× and 1.6× magnifications. Images were acquired using 100 % light to an Applied Spectral Imaging Inc. (Carlsbad, CA) SKY™ SD-300/VDS-1300 spectral imager, 12-bit digital CCD camera, using EasyFISH software. The camera was usually binned 2×2 to improve the signal to noise ratio, and decrease image exposure time, of the fluorescence images. All images were saved in 16-bit/channel quantitative EasyFISH file format, and in standard 24-bit TIFF format. For microvessel density measurements, slides were scanned at low power (HC Plan 10×/0.4 lens) to identify areas of highest vascularity. Ten to 20 high-powered (HC Plan 20×/0.7 lens)

fields were then selected randomly within these areas, and microvessel densities were calculated based on the number of CD31/biotinylated tomato lectin positive structures. Microvessel counting was performed by multiple blinded observers in conjunction with a pathologist. A pericyte-positive vessel was defined as a CD31-positive vessel surrounded by at least one cell staining positive for α SMA.

For whole-section tumor area quantitation, H&E or immunohistology slides were acquired with a Pathscan adapter (Meyer Instruments) on a Polaroid SprintScan 4000Plus 35 mm slide scanner [23, 42]. *See* ref. 21 for examples of Pathscanned U87MG orthotopic tumor implantation model mouse brain tissue sections.

3.8 LCSLite Software for Viewing Leica Confocal Microscope Datasets

Leica Microsystems generously granted us permission to include the LCSLite software on the book CD (also available for free download from ftp://ftp.llt.de/softlib/LCSLite/ and the newer Leica LAS AF Lite is available for free download at ftp://ftp.llt.de/softlib/LAS_AF_Lite/). LCSLite operates in Microsoft Windows. The oldest version of LCSLite, v2.0.0871, runs under Windows NT, 2000 and XP. The newer 2.50.1347a and 2.61.1537 only run on Windows NT and XP. Windows Administrator privileges are required for installation. For best results, install on a computer with a dual monitor display and identical monitors. After running LCSLite (or LCS if you are a Leica confocal customer), by default the two channels in the demonstration datasets will open as green and red. Right clicking on the image window will bring up a menu from which you can turn on the LUT control. Clicking on the LUT slider allows you to change to gray or other lookup table color schemes. We recommend grayscale. Positioning the cursor over a LUT slider (but not clicking) results in thumbs being displayed along the top and bottom of the LUT—these allow you to adjust the contrast of a LUT channel. We suggest pulling the upper thumb down to increase the brightness of the DsRed2 channel. The overlay button can be used to display the combined colors.

Leica confocal microscope images are saved in tagged image file format (TIFF) with Z-plane and channel information as part of the filename. For our demonstration datasets, channel 0 (ch00) is PMT1 (fluorescein) and channel 1 (ch01) is DsRed2. Individual TIFF files can be opened in Adobe Photoshop CS, NIH Image, ImageJ, MetaMorph and other image analysis software packages. For ImageJ, we recommend the MBF ImageJ bundle (http://www.macbiophotonics.ca/downloads.htm). For MetaMorph 6.25, we typically copy each channel set to its own subfolder, then use the Image Browser to open each channel as a separate stack. Some images were processed with Adobe Photoshop CS or MetaMorph 6.25 for publications.

3.9 Perfusion with DiI

The DiI labeling method [13] can also be applied to visualize blood vessels in the lungs or other tissues with the following procedure. An animal is killed by CO_2 overdose or sodium phenobarbital overdose (120 mg/kg, i.p) and then placed on a perfusion stage, positioned on its back. The trachea is exposed and cannulated with a blunt needle of #21-G. Cardiac perfusion is carried out as described (Li et al. [13]), but starts from the right ventricle instead of the left one and drains by cutting the descending aorta instead of the right atrium. The DiI solution is 3 mL with 30 μl of DiI stock solution. After perfusion, lungs are fixed with 4 % paraformaldehyde through the #21-G needle by connecting it to a small reservoir through a line under 20 mm H_2O intrapulmonary pressure (by raising the reservoir to 20 mm above the animal level) for 5–10 min. The lungs then are removed and submerged in 4 % paraformldehyde for 1 h. Tissue can be viewed directly under a fluorescence microscope to examine the surface vasculature. Thick vibratome sections (100 μm) are recommended to view vasculatures deeper than 100 μm from the tissue surface.

If perfusion fails with either tomato lectin or DiI, you can obtain useful information by transmitted light imaging, using hemoglobin absorption of the red blood cells, as your primary contrast. This is described in Subheading 3.5. The images will not be confocal optical sections, but you can still obtain useful information. We have successfully used RGB transmitted light mode Z-series tile scanning to acquire 200 μm thick Z-series from excised mouse skin.

When perfusing sacrificed mice, we encourage harvesting additional tissues and sharing them with colleagues interested in specific organs or tissues. You can contact your veterinarian about tissue sharing.

4 Results

Fluorescent labeled tomato lectin perfused blood vessels and DsRed2 fluorescent protein expressing tumor cells in hemisectioned mouse brains are readily visible by eye with a 10× objective lens and appropriate optics. The orthotopically implanted U87MG-DsRed2 human glioblastoma cell line tumors were typically imaged when 1–4 mm diameter. Foreknowledge of size was based on MicroMRI, Xenogen in vivo imaging data, and/or growth curves of the tumor model. Fluorescein-tomato lectin perfused blood vessels appear neon green to the eye when viewed through a Leica I3 (longpass green fluorescence) filter set; the DsRed2 tumor mass is opaque orange and the surrounding brain tissue is weakly green fluorescent. With the N2.1 filter set, DsRed2 tumors are bright orange-red, Texas Red-streptavidin–biotin-tomato lectin

appears red (and is used with nonfluorescent tumors); Alexa Fluor® 647-streptavidin–biotin-tomato lectin vessels are crimson-red, normal brain tissue is dimmer orange. For tissue sections we often stain nuclei with both DAPI and To-Pro-3 since our confocal microscope does not have a UV laser for DAPI excitation; the former fluorophore is blue-white with the Leica A UV excitation/visible longpass emission filter set while To-Pro-3 is crimson-red with the N2.1 set and can be imaged by the confocal optics with the 568 and/or 633 nm laser lines; likewise, LysoTracker Red can be imaged with either the I3 or N2.1 filter sets and with 568 or 488 nm laser excitation. In the future, there may be value in perfusing vessels with both fluorescent-tomato lectin and cell permeable counterstains such as DAPI or Hoechst 33342/33258, SYTO dyes, LysoTracker, etc.

Choice of laser line(s), laser power(s), confocal beamsplitter (i.e., RSP500 vs. TD488/568/633), pinhole size, detector settings, and Z-step size, and Z-range (Z-series depth range) need to be optimized for each specimen type. If necessary, sequential scanning, i.e., with the Ar488 laser line with RSP500 beamsplitter (or RSP525, which often works better for green dyes), followed by HeNe633 with TD488/561/633 for NIR imaging, can be used. Sequential scanning may optimize fluorophore excitation and collection of emission photons but trades off by requiring longer exposure times. On the SP1 this is somewhat mitigated by keeping the spectral detection band passes the same, using PMT1 for short wavelength and PMT2 or 3 for long wavelength. With our visible light confocal microscope, fluorescent tomato lectin and DsRed2 tumor cell masses, freshly excised mouse brains that had been perfused to flush most of the red blood cells, could be imaged to a depth of between 100 and 150 μm. Other organs, i.e., liver, spleen, kidney, could be usefully imaged to a maximum depth of 60–100 μm. Two confocal microscope datasets of ex vivo brain tumor cells orthotopically implanted in a mouse brain are included with the book CD, along with the Leica LCSLite confocal software image viewer. The datasets were consecutive Z-series of 258 and 178 μm with 1 mm × 1 mm field of view. The Leica SP1/DMIRBE settings were: pinhole 1.0, Argon ion 488 nm laser line was used (12 o'clock laser power knob, 69 % AOTF), RSP500 reflection shortpass dichroic beamsplitter, PMT gains ~780, PMT1 wavelength range 502–537 nm, and PMT2 range 579–710 nm. The Leica LCS confocal acquisition software (not the free LCSLite software) includes cytofluorogram and spectral deconvolution processing options. We opted not to use these, but instead to use a relatively narrow PMT1 virtual band pass of 35 nm to acquire the fluorescein-tomato lectin images, and a well separated PMT2 band pass of 130 nm for the DsRed2 fluorescence.

The accompanying DVD has a confocal dataset and the free Leica LCS Lite visualization software. The g60m07 top 01 data is

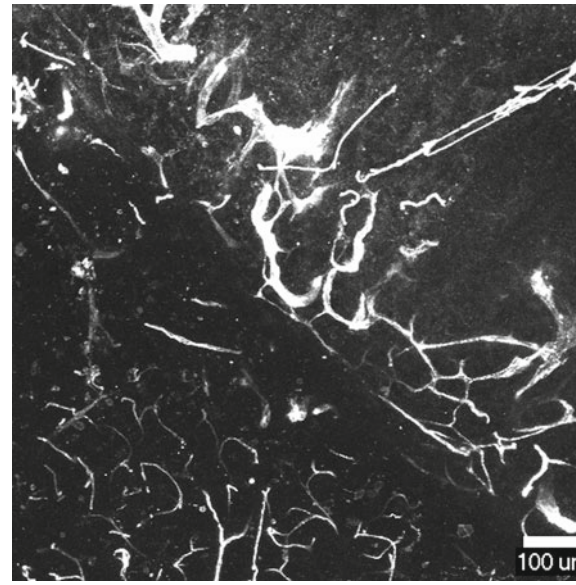

Fig. 1 Fluorescein tomato lectin in vivo labeling of blood vessels in human glioblastoma orthotopic implantation model. Maximum projection image of 1,000 × 1,000 × 253 μm volume Z-series (same volume as Fig. 2). Z-series starts from just inside the cut surface of a hemi-sectioned mouse brain. 100 μm scale bar

a 258 μm Z-series, with maximum projections of fluorescein tomato lectin of blood vessels (Fig. 1) and DsRed2 fluorescence of human U87MG glioblastoma cells expressing hrLuc-RFP-TK tribrid fusion proteins (Fig. 2). Color overlays of maximum, average and triple view orthogonal projections, plus the entire Z series is on the CD. The CD also includes a movie (AVI format) of each channel, plus color overlay of the Z-series (false colored for better visualization) and a 360 rotating view. For comparison with classic histology, a Pathscan histology slide scan is also on the CD.

DiI perfusion of the lungs is describe in Methods (Subheading 3.9) and is adapted from [13]. DiI (lowest purity Sigma-Aldrich product) is less expensive than fluorescent tomato lectin. DiI is a member of a family of lipophilic carbocyanine fluorophores that are available in other excitation and/or emission colors: DiA, DiO, DiI, DiD, and DiR. The Di_ family have relatively broad excitation and emission spectra compared to many immunofluorescence fluorophores, e.g., Alexa Fluor 488 or Cy3, or to quantum dots, such as eFluor 605NC (eBiosciences, licensed from Evident Technologies) or QD625 (Invitrogen/Molecular Probes). The Di_ family is also characterized by different lipid lengths, which result in preferential localization to plasma membrane or mitochondria and endoplasmic reticulum. At University of Miami,

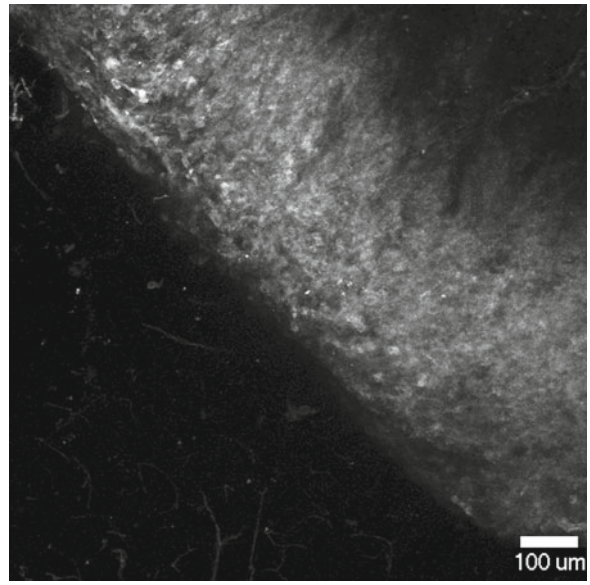

Fig. 2 DsRed2 red fluorescent protein expression detected in hrLuc-RFP-TK tribrid gene fusion vector transfected human glioblastoma cells previously orthotopically injected into a mouse brain. Maximum projection image of 1,000 × 1,000 × 253 μm volume Z-series (same volume as Fig. 1). Z-series starts from just inside the cut surface of a hemi-sectioned mouse brain. 100 μm scale bar

we now use DiI nearly exclusively for blood vessel painting. We have not (yet) done so, but expect to be able to combine DiI blood vessel painting with immunofluorescence by using digitonin as a tissue permeabilizing agent—instead of Triton X-100 or saponin—based on the results of Matsubayashi et al. [43].

Fluorescent lectin or DiI endothelial cell labeling can also be combined with DNA counterstaining, either in vivo [44] or by immersing the tissue in a DNA binding dye solution ex vivo, as briefly described in Subheading 3.4.

If a mouse fails to perfuse, you can use the absorption contrast of hemoglobin in red blood cells to acquire single field of view or tile scan single images or Z-series. The images will not be confocal, but you can still resolve multiple focal planes. The tissue needs to be transparent enough to get the light through (inquisitive users can also try reflection confocal mode). We illustrate this in supplemental data *RGBZZZ (if the editors want the data set or sets)* where we used 458, 561, and 633 nm sequential scan tracks for blue, green, and red, respectively, for XY stage tile scanning with 200 μm Z-series (90 min scan). Because hemoglobin absorbs in both the blue and green, we could have decreased total scan time (to 60 min) by using 458 or 488 nm laser line for both the blue and green channel (cyan lookup table).

5 Discussion

Having been impressed by the success of R.M. Zucker in low-magnification confocal microscopy [7, 8], we decided to evaluate tumor microvessels labeling by 10× magnification confocal microscopy. Prior to the current method with unfixed hemisectioned brain tissue, we had previously established that we could image by confocal microscopy over 800 μm deep into hemisectioned mouse brains by using a bright red fluorescent latex vascular cast (S. Yamada and authors). However, the disadvantages of the vascular cast method, including 1 week tissue clearing time, fragility of cleared tissue, potential loss of antigenicity, and concern as to whether the latex penetrated all blood vessels before hardening, led us to rapid fluorescent-tomato lectin imaging in unfixed tissue. In unfixed mouse brain, we can image fluorescent cells and structures from the hemi-sectioned surface to 80–150 μm deep in DsRed2 expressing tumor masses and >150 μm deep in normal brain tissue. With Alexa Fluor® 647-streptavidin–biotinylated tomato lectin we have >200 μm depth is not unusual, though it is unnecessary for our project. The greater depth afforded by Alexa Fluor® 647 vs. fluorescein is more likely due to the increased tissue penetration of far red 647 nm (or 568 nm) excitation and near infra-red (650–800 nm) fluorescence emission, because longer wavelength light scatters less and is typically absorbed less, rather than the number of fluorophores per lectin molecule for the dye–streptavidin–lectin compared to dye–lectin.

Debbage et al. [10–12] evaluated many different fluorescent lectins. They obtained excellent results with several, though oddly did not evaluate tomato lectin conjugates. Microscopic blood vessel imaging has been achieved with many probes and techniques, including classic histology, immunohistochemistry, fluorescence conventional, confocal and multi-photon microscopies (*see* Introduction—a full review is beyond the scope of this article). One of the simplest—and has the virtue of being applicable to human specimens—is to simply immerse a formalin fixed biopsy or tissue block in dilute eosin, which results in bright fluorescent red blood cells and vessel structures in high magnification 100 μm thick confocal microscope data sets [45]. The importance of labeling and visualizing endothelial cells in context was highlighted by Chi et al. [46], who found, by mRNA expression microarray analysis, tremendous diversity of endothelial cells from microvasculature, macrovasculature and by organ and tissue.

Multimodal imaging synergies of longitudinal in vivo bioluminescent, fluorescent, and radiographic (MicroMRI, MicroCT, Volumetric CT, MicroSPECT, MicroPET, plain film X-ray) results in more information per subject than conventional sacrifice at each time point pathology methods. With longitudinal cancer therapy

studies, small numbers of mice can be selected at well chosen time points, labeled intravitally with blood vessel markers, such as the fluorescent tomato lectin used here, sacrificed, and the organs of interest imaged post vivo. The organs can then be examined further by conventional histology, immunohistochemistry, immunofluorescence, and in situ hybridization. Quantitation of tumor blood vessels using radiographic or light microscopic datasets has not been standardized. Pathologists and tumor biologists have shown great interest in histology quantitation of tumor blood vessels, but there is no consensus method [47]. Confocal fluorescence microscopes can image to depths of 100 μm, but are less expensive and more widely available to researchers than are multi-photon excitation microscopes which have maximal depth penetration of 500–1,000 μm [3, 48]. Hillman and Moore [49] invented a method, dynamic contrast enhancement (DyCE) to use differences in blood perfusion rates to segment organs and tumors in live mice, to assist in identifying the anatomical location(s) of molecular imaging agents such as near infrared fluorophore conjugated antibodies or firefly luciferase (DyCE is now available at http://www.cri-inc.com/products/dyce.asp). Simon [50] reported that what is now called selective plane illumination microscopy (SPIM) can be used to acquire single focus plane or an extended focus image using lateral sheet illumination. *See* ref. 51 for update on current uses of SPIM.

We anticipate further improvements as luciferase substrates are optimized for in vivo imaging (Promega's EnduRen™ for Renilla luciferase), transgenic mice with specific cells expression of fluorescent proteins [6, 52], fluorescent proteins whose photophysics are optimized for deep tissue microscopy (i.e., long wavelength fruity mRFP1 derivatives [30, 53]), and luciferase-fluorescent protein fusion proteins are optimized for both bioluminescent resonance energy transfer and emission from animals and deep tissues [20, 27, 28]. These improvements will be useful for both macroscopic imaging, i.e., using the Xenogen IVIS instrument with hrLuc-optimized red fluorescent protein fusions to maximize BRET in vivo imaging, and the optimized red fluorescent protein fusion for confocal microscopy. We are especially looking forward to a high efficiency BRET fusion of effLuc [15] with an mRNA (lack of) secondary structure and codon optimized version of mKate2 [54]. We also note that Rabinovich et al. [15] have developed improved *Gaussia* luciferase and *Renilla* luciferase, that may serve as useful BRET donors for fluorescent proteins in vitro and in vivo, for example replacing the RLuc8 donor in mOrange-RLuc8 [55] with erLuc8 (Rabinovich pers comm.), and fully optimizing mOrange.

Fluorescent tomato lectin labeled blood vessels serve as excellent landmarks for confocal/multiphoton imaging of thick tissue. These are complemented by labeling specific cell populations with fluorescent proteins and labeling all nuclei with Hoechst 33342 or

other DNA staining dyes. The simplicity of our approach involves minimal fixation and processing of the mouse brain for imaging, and is compatible with further processing of the tissue for histology, immunohistochemistry and in situ hybridization.

Since moving to University of Miami, we have switched to the less expensive DiI perfusion method described briefly here [13, 36]. We have obtained excellent confocal Z-series with both many tissues, including tumor masses, heart and trachea (M. Jawad, pers comm.), retina (Y.L. and R.W.), muscle and skin (M. Jawad, pers. comm., J.B. and K.W.), and brain [36]. DiI has broad absorption and emission spectra, so you will see DiI blood vessels with standard GFP filter sets when searching by eye. The DiI bleedthrough into the GFP confocal fluorescence channel can be reduced by careful selection of emission filter (e.g., BP505-530 instead of BP505-550 or LP505) or using a spectral confocal microscope such as Leica SP1, SP2, or SP5 or Zeiss LSM710 (GFP and DiI are often bright enough that even a Zeiss LSM510META detector can separate these two fluorophores).

DiI has broad excitation and emission spectra. DiI at standard [13] concentration is much brighter than EGFP+ cells. This is both bad and good. Bad because DiI is excitable at 488 nm and has some fluorescence in the standard EGFP green emission channel of 500–530 nm. Good because it is unnecessary to use multitrack mode when imaging EGFP and DiI: use 488 nm excitation and two emission channels, such as 500–530 nm for EGFP and 550–650 nm for DiI. Crosstalk of DiI into the green channel can be corrected by subtraction (ex. EGFP = "green" – ["red"/scaler], where scaler is a scaling factor), or by spectral unmixing software in the acquisition or analysis software. Note that for quantitative correction the user needs to avoid detector saturation. The software may also need to account for different detector gain settings for the green and red channels (PMTs are intrinsically linear with respect to photons in to data out—for any single gain setting).

For deep tissue imaging of blood vessels DiI also excites well by multiphoton excitation fluorescence microscopy.

DiI blood vessel labeling should be combined with recent huge improvements in luciferase technology [15–18], that go beyond what Gambhir and colleagues had previously achieved. Rabinovich et al. [15] have generated improved firefly, *Renilla* and *Gaussia* luciferases (eFFLuc, eRLuc8, eGLuc). Mezzanotte et al. [16] reported on thermostable firefly luciferase (the same labs have also worked on improving the related click beetle luciferases). Saito et al. [17] fused Venus yellow fluorescence protein to RLuc8 to produce efficient bioluminescence energy transfer (BRET). Nagai et al. [18] have improved Venus-RLuc8 even further, taking advantage of efficient BRET to improve the quantum yield per coelenterazine substrate oxidation from 0.05 for RLuc8 to 0.70 for their SuperStar fusion construct. Neither Mezzanotte nor Saito and

Nagai et al. have taken advantage of optimizations of Rabinovich et al. [15], suggesting that further improvements are possible. An additional benefit of fusing Venus to RLuc8 is that this construct includes a fluorescent protein for in vivo and ex vivo imaging confocal and multiphoton excitation fluorescence microscopy. Venus YFP is also compatible with STED fluorescence nanoscopy (http://www.mpibpc.mpg.de/groups/hell/STED_Dyes.html) should SuperStar be fused to a specific protein or organelle targeting sequence.

DiI, as well as other in vivo blood vessel labeling methods (fluorescent tomato lectin, dextran) is compatible with new "living window" models—including real time in vivo immunophenotyping [22], to facilitate maximizing quantitative data from longitudinal in vivo studies of tumor growth and angiogenesis.

Acknowledgments

GM thanks Bob Zucker (US EPA, Research Triangle Park, NC) for low power inspiration and discussions, and Thomas D. Coates (CHLA) for direction. We thank Shinya Yamada (CHLA and Tokai University Hachioji Hospital, Tokyo, Japan) for the latex vascular cast method. We thank Clark Thom and Klaus Schreck (Leica Microsystems, Exton, PA) for confocal on-site service, Kolja Wawrowsky (Cedars-Sinai Medical Center Los Angeles, formerly with Leica) for confocal training, Frank Lie, Scott Young, Rob Dunakin, David Zemo, Bob Vogel, and Chris Kier for confocal technical and application support. We are grateful to Bob Vogel and Martin Hoppe of Leica Microsystems for permission to include LCS Lite software with the Paddock 2.0 book CD-ROM. LCS Lite is available for free download from the Leica Microsystems Web site and from Leica salespeople and dealers. Experiments involving multiphoton excitation of Hoechst 33342 were conducted on a Zeiss LSM 510 META NLO microscope at the Light Microscopy Core of City of Hope National Medical Center (http://www.cityofhope.org/LMC/LSM510.asp), in collaboration with Dr. Christine Brown, Renate Starr and Prof. Michael Jensen.

We are grateful to Sam Gambhir for providing the tribrid hrLuc-DsRed2-TK reporter gene construct prior to publication (Ray et al. [20]). We thank Denise Petersen, Karen Pepper, and Don Kohn, CHLA Gene Vector Core, for inserting the tribrid reporter gene into the lentivirus vector and transducing U87MG cells. We thank Dr. Ignacio Gonzalez for histology slide preparation and tissue diagnoses. Our thanks to Ignacio Gonzalez, Dr. Rex Moats, Dr. Mike Rosol, Maya Otto-Duessel, and Dr. Shawn Chen, for discussions.

This work was supported by grants from the National Institutes of Health (CA 82989 to W.E. Laug), the T.J. Martell Foundation (New York) (to W.E. Laug), and an U.S. HRSA capital equipment grant (to Y. DeClerck). Confocal and standard fluorescence microscopy was performed in the Congressman Julian Dixon Cellular Imaging Facility of Children's Hospital Los Angeles. Hoechst 33342 multiphoton imaging at City of Hope National Medical Center was done in collaboration with Dr. Christine Brown, and Renate Starr, and was funded by NIH grants to Professor Michael Jensen.

The University of Miami Leica SP5 and MP-NDD4/SP5/FCS/FLIM confocal microscopes were purchased with funds from the Diabetes Research Institute Foundation. Rong Wen and Yiwen Li are supported by the National Eye Institute and Bascom Palmer Eye Institute.

Appendix

Instrumentation

Few publications provide complete specifications on the instrumentation used. Each confocal microscope is built from specialty parts, many of whose performance vary between units. It is unlikely that any two confocal microscopes perform identically on all tests—*see* Lerner and Zucker [40] for examples. It is unlikely that the same confocal microscope performs identically on the same tests performed on sequential days, weeks, months or years. The intensity of the laser lines change over time (seconds and hours) and intensity changes can be confounded by focus drift of the microscope stage and/or warping of the specimen. In this appendix we list many of the components present in the Leica SP1 confocal DMIRBE inverted microscope that was delivered to CHLA in March 2000 and since upgraded with several new components. We recognize that in 2013 the SP1 is a discontinued model, but think a detailed explanation will help the reader. A major difference between the SP1 and the newer SP2 and SP5 models is that the latter have an acousto-optical beam splitter (AOBS) that replaces the primary laser dichroic beamsplitter(s) for most visible light lasers (the 405 nm and multiphoton laser do not use the AOBS). A correctly calibrated AOBS should enable collection of fluorescence emission from as close as 5 nm of the laser line. The laser light rejection from the emission light path can be disabled for reflection mode imaging.

The Leica SP1 confocal microscope has three lasers, with the Krypton ion laser having been replaced by diode-pumped solid-state (DPSS) laser in November 2004 (Table 1). The photomultiplier tubes (PMTs) in the SP1 are integrated with individual spectrophotometer-style scanning slits (Calloway [38], Tauer and Hils [39]) and the performance depends on correct alignment of the assembly (Table 2). High resolution spectral scanning (5 nm slits, 1 nm

Table 1
Lasers

Laser type	Manufacturer	Model	Wave-lengths	Power (mW)	Maximum power (10× lens output)
Arion ion (Ar)	Uniphase	Ar-2211-65MLQYV	457 476 488 514	65	– – 2.85 –
Krypton ion (Kr)	Melles Griot	Omnichrome series 43, model 643R-LICA-B02	568	20	2.14
Diode-pumped solid-state microchip (DPSS)	Melles Griot	85 YCA 010	561	10	
Helium-Neon (HeNe)	Uniphase	1300 series	633	2	

Uniphase is now JDS Uniphase (http://www.jdsu.com). Power is the manufacturer's rating (laser head output, all laser lines). Maximum power is measured at the microscope specimen at full power with the TD488/568/633 beamsplitter, through the 10×/0.30 dry lens, 10× zoom, Coherent power meter model FM part #33-0506 with "visible detector" (Leica field service engineer kit). The Ar and Kr lasers are only operated at full power (4 o'clock) for this test—the laser knob is set to the 12 o'clock position for standard use. The DPSS and HeNe use on/off switch so their power is only controlled with the SP1 AOTF "neutral density" attenuation control. The original Kr laser and power supply (installed 3/2000) died and was replaced under service contract (12/2001) and retired (11/2004) in favor of the DPSS 561 nm laser

Table 2
Photomultiplier tubes

PMT	Model	Type/grade	Remarks	Range (nm)	Peak (nm)
1	R6358	LMA/UV	Low dark current	185–830	530
2	R6357	MA/UV high	High sensitivity	185–900	450
3	R6357	MA/UV high	High sensitivity	185–900	450
Trans	R6350	Sb-Cs/UV	UV to visible, general purpose	185–650	340

PMT1, 2, and 3 are assemblies of a photomultiplier tube integrated with virtual band-pass sliders of the SP1 scanhead confocal spectrophotometer. The detection efficiency depends on the PMT detector and the double slider slit being aligned correctly. PMT photocathode quantum efficiency curves were published by Zipfel et al. [56]. For simultaneous imaging of fluorescein and DsRed2, PMT1 is ch00 and either PMT2 or PMT3 is ch01. Choice of second PMT is made on the basis of whether the PMT2 assembly (tube plus virtual band-pass unit) is operating correctly (for example, in 12/2004, the unit produced readings of +40 nm for a Nanofilm reflection slide laser spectral scanning test. The assembly was replaced under service contract and performed acceptably)

step size, 200 steps, i.e., from 450 to 650 nm) of either the tungsten-halogen transmitted light source or laser lines reflected from a Nanofilm or Leica mirror slide, have revealed problems at different times with PMT assemblies (fixed with a service visit).

For a core facility where many different specimens are imaged, i.e., fluorescein-tomato lectin blood vessels and DsRed2 fluorescent

protein tumor cell masses, CFP→YFP FRET, and Cy5.5-RGD peptide labeled cells, having a large selection of filter sets on hand for viewing specimens *by eye* is crucial (Table 3). Compared to the price of the confocal microscope (~$360,000) and annual service contract (~$17,000), filter sets at <$1,000 each are inexpensive compared to the entire system. Our filter sets are shared between the Leica SP1 confocal DMIRBE microscope (four cube positions, three filter cubes used plus one empty position for confocal scanning) and a Leica DMRXA/RF8 microscope with eight filter cubes. To maximize compatibility, our Leica MZFLIII motorized fluorescence stereomicroscope has many matched filter sets (the MZFLIII uses a plastic slider with one exciter and two emission filters, and a mirror to reflect Leica Xe 75 W light to the specimen).

The confocal scanhead uses an acousto-optical tunable filter (AOTF) as a wavelength selective neutral density control. The AOTF gives much finer and reproducible control over laser power than do the knobs on the Ar and Kr lasers (the DPSS and HeNe lasers do not have knobs, only on/off switches). The AOTF enables adjusting laser power independently for each of the six laser lines in ~0.4 % steps, from 0 to 100 %. The actual output depends on the laser power knob. The Ar457 line power fluctuates over time, at any knob setting, and tends to be low at low knob power settings.

The Leica SP1 scanhead has five beamsplitters (Table 4) for directing the laser light from the AOTF neutral density unit to the objective lens and specimen, and then back from the objective lens to the prism spectral dispersion element and PMT slits/tube assemblies. Our SP1 has a triple dichroic, TD488/568/633, three reflection shortpass (RSP465, RSP500, RSP525) and one reflection/transmission (RT30/70) beamsplitters. The numbers indicate appropriate laser lines (TD filter), approximate 50 % reflection wavelength (RSPs), or approximate reflection/transmission performance (RT). The choice of 30 % reflection (laser light to the specimen) and 70 % transmission (specimen reflection and/or fluorescence emission) is a trade-off of wanting to excite the specimen with as much light as possible, but even more importantly, collecting as much (in focus) light as possible. If the SP1 had much more powerful lasers, it might make more sense to use a RT10/90 (resulting in $0.1 \times 0.9 = 0.09$ total throughput, but crucially, 90 % of the emitted light), than our RT30/70 ($0.3 \times 0.7 = 0.21$ total throughput, 70 % of the emitted light) (Table 4). The scanhead beamsplitter numbers do not tell the whole story. For any given laser line, fluorophore(s), specimen (autofluorescence), and PMT assembly spectral band pass (especially if out of whack), a particular confocal beamsplitter may be found empirically to outperform another. In particular, we sometimes find the 488 nm laser line and RSP525 beamsplitter often outperforms the RSP500 beamsplitter for fluorescein imaging. *See* Table 5 for objective lenses.

Table 3
Microscope filter sets for visual imaging

Manufacturer	Filter cube	Part number	Excitation	Dichroic	Emission	Typical fluorophores
Leica	A	513824	BP 340–380	400	LP425	DAPI
Leica	I3	513828	BP450–490	510	LP515	Fluorescein, EGFP
Leica	N2.1	513832	BP515–560	580	LP590	Cy3, DsRed
Chroma	HQ Cy5.5	41022	HQ665/45×	Q695LP	HQ725/50 m	Cy5.5, To-Pro-3
Chroma	HQ Cy3	41007a	HQ545/30×	Q570LP	HQ610/75 m	Cy3
Chroma	HQ Fluorescein	41001	HQ480/40×	Q505LP	HQ535/50 m	Fluorescein, EGFP
Chroma	DAPI	31000	D360/40×	400DCLP	D460/50 m	DAPI
Chroma	DAPI/Green/Red	61000v2				Triple
Chroma (ASI)	SKY	SKYv3				Green, orange, red, Cy5, Cy5.5
Chroma	CFP	31044v2	D436/20×	455DCLP	D480/40 m	Cyan Fluorescent Protein, autofluorescence (DAPI, fluorescein, Cy3 slides)
Chroma	YFP	41028	HQ500/20×	Q515LP	HQ535/30 m	Yellow Fluorescent Protein
Chroma	CFP→YFP FRET	31052	D436/20×	455DCLP	D535/30 m	Cyan→Yellow FP FRET
Chroma	Rex	Custom	E650SP	700DCXR	RG715	Cy7
Chroma	Qdot/Evitag LPES	Custom	E460spuvV2	475DCXRU	HQ480LP (w/AR)	QDots, Evitags
Chroma	Custom IGS	Custom	E550spuv+21003Pol	20/80 beamsplitter (Chroma 21008)	E450LP+21003Pol	Immunogold staining, DIC analyzer, polarized fluorescence

Data from Leica Microsystems and Chroma Technology product literature. *See* Ploem [58] and Reichman [59] for information on filter cubes and filters, respectively. The above cubes are interchangeable between the Leica SP1 confocal DMIRBE and Leica DMRXA/RF-8 microscopes. The CHLA Image Core has identical filter sets, for most of the above sets, for a Leica MZFLIII stereomicroscope (excitation and emission filter slider). Confocal imaging is performed with no filter set in the microscope. Non-confocal fluorescence images can be acquired using the epi-illumination arc lamp and any of the filter sets with wide open detection pinhole. This is an inefficient method because spot scanning is used with wide-field illumination, but is useful for localizing DAPI stained nuclei on a visible-lasers only system. Transmitted light RGB images can be acquired with sequential imaging of the 457 nm (blue), 568 nm (yellow-green), and 633 nm (red) lasers with the RT30/70 scanhead beamsplitter and the transmitted light PMT detector. Spectral data for most of the filters and dyes discussed can be found at http://works.bepress.com/gmcnamara/9/ [57]

Table 4
Scanhead beamsplitters

Scanhead beamsplitter	Excitation laser line(s)	Fluorophore(s)
TD488/568/633	488, 568, 633	488: Fluorescein, Alexa Fluor 488, EGFP 568: Cy3, DsRed 633: To-Pro-3, Alexa Fluor 647, Cy5, Cy5.5
RSP465	457	CFP, CFP → YFP FRET, SYTO40, SYTO45
RSP500	488 (457, 476)	Fluorescein, Alexa Fluor 488, EGFP
RSP525	514 (457, 476, 488)	Fluorescein, Alexa Fluor 488, EGFP, YFP
RT30/70	Any	Any

Note: The confocal microscope can also be operated in reflection mode, with the PMT assembly band pass set to match the laser line, i.e., 486–490 nm band pass for the 488 nm Ar laser line. All of the dichroic filters can reflect some laser light and transmit the laser light and some (a little or a lot) of any emission wavelength. Spending a few moments to evaluate all combinations is advised. Published fluorescent dye spectra (ex. http://www.spectra.arizona.edu/ and http://www.invitrogen.com/site/us/en/home/Products-and-Services/Applications/Cell-Analysis/Labeling-Chemistry/Fluorescence-SpectraViewer.html) are useful but not definitive

Table 5
Confocal microscope objective lenses

Leica lens	10×/0.30	20×/0.40	40×/1.25–0.7	63×	10×/0.4
Markings	HC Plan Fluotar Ph1	N Plan Corr	HCX Plan Apo	1.4 NA	HC Pl Apo
Immersion	Dry	Dry	Oil	Oil	IMM (water, glycerol, oil)

Condenser lens: 0.9 NA, with condenser numerical aperture control and field aperture. Transmitted path has two filters above the condenser. One is a neutral density filter. The other is a polarizer. The polarizer enables Nomarski differential interference contrast (DIC) imaging both by eye (lamp to this polarizer to Wollaston prism in condenser to specimen to A/C/E Wollaston prism in microscope, to polarizer slider in base) and by confocal (opposite light path to the above, *with the exception that* the polarizer in the base is left *out* of the light path, since the laser light is polarized)
In 2005 one of us (G.M.) moved to City of Hope National Medical Center

Web Sites

Chroma Technology Corp	http://www.chroma.com
Chroma Handbook	http://www.chroma.com/sites/default/files/uploads/files/HandbookofOpticalFilters_0.pdf
Mattek Corp.	http://www.mattek.com and http://www.glass-bottom-dishes.com
Leica SP manual	http://www.leica-microsystems.com/products/confocalmicroscopes/details/product/leica-tcs-sp2/downloads/

(continued)

(continued)

Leica Microsystems	http://www.leica-microsystems.com
Leica Microsystems confocal microscopes	http://www.confocal-microscopy.com or http://www.llt.de
Meyer Instruments—Pathscan adapter	http://www.meyerinst.com/html/oem/pseiii/default.htm
Krogh 1920 Nobel lecture	http://www.nobel.se/medicine/laureates/1920/krogh-lecture.html.
Uniphase is JDS Uniphase	http://www.jdsu.com/
Melles Griot	http://www.mellesgriot.com/
Nanofilm	http://www.nanofilm.com

CD Image Files

LCSLite200871.exe	Leica LCS Lite 2.0.871 (Windows NT, 2000, XP)
LCSLite2051347a.exe	Leica LCS Lite 2.5.1347a (Windows NT and XP only)
LCSLite2611537.exe	Leica LCS Lite 2.61.1537 (Windows NT and XP only)

Note: All versions of LCS Lite require Administrator privileges to install on a Windows PC. LCS Lite is the free, limited capabilities version of the LCS (Leica Confocal Software) used for acquisition. Leica confocal download sit is ftp://ftp.llt.de/softlib. LCS Lite is available for download from ftp://ftp.llt.de/softlib/LCSLite/ (2.6.1, dated 12/09/2004 is final version). Leica LAS AF Lite is available at ftp://ftp.llt.de/softlib/LAS_AF_Lite/ (version 2.1.0 is dated 5/29/2009).

McNamara 2005 Figure 1 max green channel FTL.tif	Digital Fig. 1. Fluorescein tomato lectin maximum projection of 1,000 × 1,000 × 253 μm volume
McNamara 2005 Figure 2 max red DsRed RFP.tif	Digital Fig. 2. DsRed2 red fluorescent protein transfected glioblastoma cells maximum projection of 1,000 × 1,000 × 253 μm volume
McNamara 2005 G60M07 H&E pathscan image 4,000 dpi.tif	Histology image of hematoxylin and eosin (H&E) tissue section from the brain previously imaged in Figs. 1 and 2, acquired using Pathscan Enabler™ with Polaroid SprintScan 4000+ 35 mm slide scanner. 4,000 dpi is 6.35 μm pixel size
G60m07 top 01 (folder)	Confocal dataset used for Figs. 1 and 2
G60m07 top 02 (folder)	Confocal dataset from a different part of the same mouse brain and tumor as used in G60m07 top 01

References

1. Hlatky L, Hahnfeldt P, Folkman J (2002) Clinical application of antiangiogenic therapy: microvessel density, what it does and doesn't tell us. J Natl Cancer Inst 94:883–893
2. Abdul-Karim MA, Al-Kofahi K, Brown EB, Jain RK, Roysam B (2003) Automated tracing and change analysis of angiogenic vasculature from in vivo multiphoton confocal image time series. Microvasc Res 66:113–125
3. Larson DR, Zipfel WR, Williams RM, Clark SW, Bruchez MP, Wise FW, Webb WW (2003) Water-soluble quantum dots for multiphoton fluorescence imaging *in vivo*. Science 300: 1434–1436
4. Yoder EJ, Kleinfeld D (2002) Cortical imaging through the intact mouse skull using two-photon excitation laser scanning microscopy. Microsc Res Tech 56:304–305
5. Angiogenesis Workshop (2003) Intravital microscopy and live cell imaging in angiogenic research. Angiogenesis 5:281–338
6. Gerber SA, Moran JP, Frelinger JG, Frelinger JA, Fenton BM, Lord EM (2003) Mechanism of IL-12 mediated alterations in tumour blood vessel morphology: analysis using whole-tissue mounts. Br J Cancer 88:1453–1461
7. Zucker RM, Hunter S, Rogers JM (1998) Confocal laser scanning microscopy of apoptosis in organogenesis-stage mouse embryos. Cytometry 33:348–354
8. Zucker RM, Hunter ES 3rd, Rogers JM (1999) Apoptosis and morphology in mouse embryos by confocal laser scanning microscopy. Methods 18:473–480
9. Price OT, Lau C, Zucker RM (2003) Quantitative fluorescence of 5-FU-treated fetal rat limbs using confocal laser scanning microscopy and Lysotracker Red. Cytometry 53A: 9–21
10. Debbage PL, Solder E, Seidl S, Hutzler P, Hugl B, Ofner D, Kreczy A (2001) Intravital lectin perfusion analysis of vascular permeability in human micro- and macro-blood vessels. Histochem Cell Biol 116:349–359
11. Debbage PL, Seidl S, Kreczy A, Hutzler P, Pavelka M, Lukas P (2000) Vascular permeability and hyperpermeability in a murine adenocarcinoma after fractionated radiotherapy: an ultrastructural tracer study. Histochem Cell Biol 114:259–275
12. Debbage PL, Griebel J, Ried M, Gneiting T, DeVries A, Hutzler P (1998) Lectin intravital perfusion studies in tumor-bearing mice: micrometer-resolution, wide-area mapping of microvascular labeling, distinguishing efficiently and inefficiently perfused microregions in the tumor. J Histochem Cytochem 46: 627–639
13. Li Y, Song Y, Zhao L, Gaidosh G, Laties AM, Wen R (2008) Direct labeling and visualization of blood vessels with lipophilic carbocyanine dye DiI. Nat Protoc 3:1703–1708
14. Li Y, Huang D, Xia X, Wang Z, Luo L, Wen R (2011) CCR3 and choroidal neovascularization. PLoS One 6:e17106
15. Rabinovich BA, Ye Y, Etto T, Chen JQ, Levitsky HI, Overwijk WW, Cooper LJ, Gelovani J, Hwu P (2008) Visualizing fewer than 10 mouse T cells with an enhanced firefly luciferase in immunocompetent mouse models of cancer. Proc Natl Acad Sci USA 105: 14342–14346
16. Mezzanotte L, Fazzina R, Michelini E, Tonelli R, Pession A, Branchini B, Roda A (2010) In vivo bioluminescence imaging of murine xenograft cancer models with a red-shifted thermostable luciferase. Mol Imaging Biol 12: 406–414
17. Saito K, Hatsugai N, Horikawa K, Kobayashi K, Matsu-Ura T, Mikoshiba K, Nagai T (2010) Auto-luminescent genetically-encoded ratiometric indicator for real-time Ca2+ imaging at the single cell level. PLoS One 5:e9935
18. Nagai T, Chang Y-F, Saito K, Horikawa K, Matsuda T (2011) High performance genetically-encoded auto-luminescent Ca2+ indicators, SuperBRACs. Focus on Microscopy 220. http://www.focusonmicroscopy.org/2011/program.html
19. Abdulreda MH, Faleo G, Molano RD, Lopez-Cabezas M, Molina J, Tan Y, Echeverria OA, Zahr-Akrawi E, Rodriguez-Diaz R, Edlund PK, Leibiger I, Bayer AL, Perez V, Ricordi C, Caicedo A, Pileggi A, Berggren PO (2011) High-resolution, noninvasive longitudinal live imaging of immune responses. Proc Natl Acad Sci USA 108:12863–12868
20. Ray P, De A, Min JJ, Tsien RY, Gambhir SS (2004) Imaging tri-fusion multimodality reporter gene expression in living subjects. Cancer Res 64:1323–1330
21. Avramis IA, Christodoulopoulos G, Suzuki A, Laug WE, Gonzalez-Gomez I, McNamara G, Sausville EA, Avramis VI (2002) *In vitro* and *in vivo* evaluations of the tyrosine kinase inhibitor NSC 680410 against human leukemia and glioblastoma cell lines. Cancer Chemother Pharmacol 50:479–489

22. Burgos JS, Rosol M, Moats RA, Khankaldyyan V, Kohn DB, Nelson MD Jr, Laug WE (2003) Time course of bioluminescent signal in orthotopic and heterotopic brain tumors in nude mice. Biotechniques 34:1184–1188
23. Chantrain CF, DeClerck YA, Groshen S, McNamara G (2003) Computerized quantification of tissue vascularization using high-resolution slide scanning of whole tumor sections. J Histochem Cytochem 51:151–158
24. Moats RA, Velan-Mullan S, Jacobs R, Gonzalez-Gomez I, Dubowitz DJ, Taga T, Khankaldyyan V, Schultz L, Fraser S, Nelson MD, Laug WE (2003) Micro-MRI at 11.7 T of a murine brain tumor model using delayed contrast enhancement. Mol Imaging 2:150–158
25. Yamada S, Khankaldyyan V, Bu X, Suzuki A, Gonzalez-Gomez I, Takahashi K, McComb JG, Laug WE (2004) A method to accurately inject tumor cells into the caudate/putamen nuclei of the mouse brain. Tokai J Exp Clin Med 29:167–173
26. Mouchess ML, Sohara Y, Nelson MD Jr, DeCLerck YA, Moats RA (2006) Multimodal imaging analysis of tumor progression and bone resorption in a murine cancer model. J Comput Assist Tomogr 30:525–534
27. Ray P, Tsien R, Gambhir SS (2007) Construction and validation of improved triple fusion reporter gene vectors for molecular imaging of living subjects. Cancer Res 67:3085–3093
28. Campbell RE, Tour O, Palmer AE, Steinbach PA, Baird GS, Zacharias DA, Tsien RY (2002) A monomeric red fluorescent protein. Proc Natl Acad Sci USA 99:7877–7882
29. Wang L, Jackson WC, Steinbach PA, Tsien RY (2004) Evolution of new nonantibody proteins via iterative somatic hypermutation. Proc Natl Acad Sci USA 101:16745–16749
30. Shaner NC, Lin MZ, McKeown MR, Steinbach PA, Hazelwood KL, Davidson MW, Tsien RY (2008) Improving the photostability of bright monomeric orange and red fluorescent proteins. Nat Methods 5:545–551
31. Moats R, Ma LQ, Wajed R, Sugiura Y, Lazaryev A, Tyszka M, Jacobs R, Fraser S, Nelson MD Jr, DeClerck YA (2001) Magnetic resonance imaging for the evaluation of a novel metastatic orthotopic model of human neuroblastoma in immunodeficient mice. Clin Exp Metastasis 18:455–461
32. Greer LF 3rd, Szalay AA (2002) Imaging of light emission from the expression of luciferases in living cells and organisms: a review. Luminescence 17:43–74
33. Bhaumik S, Gambhir SS (2002) Optical imaging of Renilla luciferase reporter gene expression in living mice. Proc Natl Acad Sci USA 99:377–382
34. Chantrain CF, Shimada H, Jodele S, Groshen S, Ye W, Shalinsky DR, Werb Z, Coussens LM, DeClerck YA (2004) Stromal matrix metalloproteinase-9 regulates the vascular architecture in neuroblastoma by promoting pericyte recruitment. Cancer Res 64:1675–1686
35. Kim S, Lim YT, Soltesz EG, De Grand AM, Lee J, Nakayama A, Parker JA, Mihaljevic T, Laurence RG, Dor DM, Cohn LH, Bawendi MG, Frangioni JV (2004) Near-infrared fluorescent type II quantum dots for sentinel lymph node mapping. Nat Biotechnol 22(93–9):7
36. Defazio RA, Levy S, Morales CL, Levy RV, Dave KR, Lin HW, Abaffy T, Watson BD, Perez-Pinzon MA, Ohanna V (2011) A protocol for characterizing the impact of collateral flow after distal middle cerebral artery occlusion. Transl Stroke Res 2:112–127
37. Idziorek T, Estaquier J, De Bels F, Ameisen JC (1995) YOPRO-1 permits cytofluorometric analysis of programmed cell death (apoptosis) without interfering with cell viability. J Immunol Methods 185:249–258
38. Calloway CB (2000) A confocal microscope with spectrophotometric detection. Leica Microsystems CDR 4:4–14
39. Tauer U, Hils O (2000) Confocal spectrophotometry. Leica Microsystems CDR 4:15–27
40. Lerner JM, Zucker RM (2004) Calibration and validation of confocal spectral imaging systems. Cytometry 62A:8–34
41. Ploem JS, Walter F (2001) Multi-wavelength epi-illumination in fluorescence microscopy. Leica Microsystems CDR 5:1–15
42. Montague PR, Meyer M, Folberg R (1995) Technique for the digital imaging of histopathologic preparations of eyes for research and publication. Ophthalmology 102:1248–1251
43. Matsubayashi Y, Iwai L, Kawasaki H (2008) Fluorescent double-labeling with carbocyanine neuronal tracing and immunohistochemistry using a cholesterol-specific detergent digitonin. J Neurosci Methods 174:71–81
44. Arribas SM, Daly CJ, McGrath IC (1999) Measurements of vascular remodeling by confocal microscopy. Methods Enzymol 307: 246–273
45. Jirkovska M, Kubinova L, Krekule I, Hach P (1998) Spatial arrangement of fetal placental capillaries in terminal villi: a study using confocal microscopy. Anat Embryol (Berlin) 197: 263–272
46. Chi JT, Chang HY, Haraldsen G, Jahnsen FL, Troyanskaya OG, Chang DS, Wang Z, Rockson SG, van de Rijn M, Botstein D, Brown PO

(2003) Endothelial cell diversity revealed by global expression profiling. Proc Natl Acad Sci USA 100:10623–10628

47. Fox SB, Harris AL (2004) Histological quantitation of tumour angiogenesis. APMIS 112: 413–430
48. Tozer GM, Ameer-Beg SM, Baker J, Barber PR, Hill SA, Hodgkiss RJ, Locke R, Prise VE, Wilson I, Vojnovic B (2005) Intravital imaging of tumour vascular networks using multi-photon fluorescence microscopy. Adv Drug Deliv Rev 57:135–152
49. Hillman EM, Moore A (2007) All-optical anatomical co-registration for molecular imaging of small animals using dynamic contrast. Nat Photon 1:526–530
50. Simon W (1965) Photomicrography of deep fields. Rev Sci Instrum 36:1654–1655
51. Huisken J, Stainier DY (2009) Selective plane illumination microscopy techniques in developmental biology. Development 136: 1963–1975
52. Forde A, Constien R, Grone H-J, Hammerling G, Arnold B (2002) Temporal Cre-mediated recombination exclusively in endothelial cells using Tie2 regulatory elements. Genesis 33: 191–197
53. Wang X, Rosol M, Ge S, Peterson D, McNamara G, Pollack H, Kohn DB, Nelson MD, Crooks GM (2003) Dynamic tracking of human hematopoietic stem cell engraftment using in vivo bioluminescence imaging. Blood 102:3478–3482
54. Shcherbo D, Murphy CS, Ermakova GV, Solovieva EA, Chepurnykh TV, Shcheglov AS, Verkhusha VV, Pletnev VZ, Hazelwood KL, Roche PM, Lukyanov S, Zaraisky AG, Davidson MW, Chudakov DM (2009) Far-red fluorescent tags for protein imaging in living tissues. Biochem J 418:567–574
55. De A, Ray P, Loening AM, Gambhir SS (2009) BRET3: a red-shifted bioluminescence resonance energy transfer (BRET)-based integrated platform for imaging protein-protein interactions from single live cells and living animals. FASEB J 23(8):2702–2709
56. Zipfel WR, Williams RM, Webb WW (2003) Nonlinear magic: multiphoton microscopy in the biosciences. Nat Biotechnol 21:1369–1377
57. McNamara G, Gupta A, Reynaert J, Coates TD, Boswell C (2006) Spectral imaging microscopy web sites and data. Cytometry A 69:863–871
58. Ploem JS (1971) A study of filters and light sources in immunofluorescence microscopy. Ann N Y Acad Sci 177:414–429
59. Reichman J (2000) Handbook of Optical Filters for Fluorescence Microscopy. Chroma Technology, Brattleboro, VT, USA. p 40

Chapter 7

Confocal Imaging of Butterfly Tissue

Craig R. Brunetti

Abstract

To understand the molecular events responsible for morphological change requires the ability to examine gene expression in a wide range of organisms in addition to model systems to determine how the differences in gene expression correlate with phenotypic differences. There are approximately 12,000 species of butterflies, most, with distinct patterns on their wings. The most important tool for studying gene expression in butterflies is confocal imaging of butterfly tissue by indirect immunofluorescence using either cross-reactive antibodies from closely related species such as *Drosophila* or developing butterfly-specific antibodies. In this report, we describe how indirect immunofluorescence protocols can be used to visualize protein expression patterns on the butterfly wing imaginal disc and butterfly embryo.

Key words Butterfly wing imaginal disc staining, Confocal microscopy, Butterfly embryo staining, Indirect immunofluorescence, Lepidoptera

1 Introduction

The study of morphological evolution involves the fusion of two distinct disciplines: evolution and developmental biology (evo-devo). Evo-devo seeks to understand how evolutionary change can occur through alterations in gene expression that results in phenotypic alterations. The bulk of the genetic and gene expression data in developmental biology has focused on model systems such as *Drosophila melanogaster*, *Caenorhabditis elegans*, and *Mus musculus*. However, to understand the molecular events responsible for morphological change requires the ability to examine gene expression in a wide range of organisms in addition to model systems to determine how the differences in gene expression correlate with phenotypic differences. The major hurdle facing evo-devo is therefore the ability to develop techniques and methodology to examine gene expression in non-model organisms.

There are approximately 12,000 species of butterflies, most, with distinct patterns on their wings. In fact, even butterflies that are very closely related can have dramatically differing wing patterns [1].

Stephen W. Paddock (ed.), *Confocal Microscopy: Methods and Protocols*, Methods in Molecular Biology, vol. 1075,
DOI 10.1007/978-1-60761-847-8_7,

Therefore, butterfly wings represent an important model system to study how patterns are created and how these patterning systems are altered in differing species. Since butterflies represent a non-model system, there are limited tools available to study gene expression.

Probably the most important tool for studying gene expression in butterflies is confocal imaging of butterfly tissue by indirect immunofluorescence using either cross-reactive antibodies from closely related species such as *Drosophila* or developing butterfly-specific antibodies [2–5]. Indirect immunofluorescence protocols from *Drosophila* have been adapted to work on butterfly tissue [2]; however, a number of differences between *Drosophila* and butterflies require significant modification of the protocol. First, a thin cellular layer called the peripodial membrane that must be removed prior to confocal imaging of the tissue surrounds butterfly pupal tissue. Secondly, staining of butterfly embryos requires dissection of the embryo out of the egg. Finally, butterfly tissue can be quite large encompassing multiple objective fields on a microscope. Imaging such large tissue samples poses unique challenges when analyzed by confocal microscopy including how to examine expression patterns of genes in large tissue while maximizing the fluorescent signal and retaining a high level of resolution of the tissue. The best method for doing this is to image the large tissue sample by acquiring multiple confocal images using a high power objective. Using readily available computer software such as Adobe Photoshop (Adobe Systems Incorporated, San Jose, CA), the multiple confocal images can be reassembled to generate the entire tissue section to provide a detailed image of the expression pattern of genes throughout the tissue.

To demonstrate how gene expression patterns can be monitored in a non-model system such as butterflies, indirect immunofluorescence will be carried out on butterfly wing discs and embryo tissue using antibodies against Distal-less (Dll) [2], engrailed/invected (en), and cubitus interruptus (Ci) [4].

2 Materials

1. 50 % bleach.
2. PBS: 137 mM NaCl, 2.7 mM KCl, 10 mM Na_2HPO_4, 2 mM KH_2PO_4.
3. Embryo fix buffer: 0.1 M Pipes, pH 6.9, 1 mM EGTA, pH 6.9, 2 mM $MgSO_4$, 9 % formaldehyde at 4 °C.
4. Heptane.
5. Methanol at 4 °C.
6. Ethanol washes: 25 %, 50 %, 75 % ethanol diluted in water at 4 °C.

7. Wing disc fix buffer: 0.1 M PIPES, pH 6.9, 1 mM EGTA, pH 6.9, 1 % Triton X-100, 2 mM $MgSO_4$, 1 % formaldehyde.
8. Block buffer: 50 mM Tris, pH 6.8, 150 mM NaCl, 0.5 % NP40, 5 mg/ml BSA.
9. Wash buffer: 50 mM Tris, pH 6.8, 150 mM NaCl, 0.5 % NP40, 1 mg/ml BSA.
10. Vectashield (Vector Laboratories Inc., Burlingame, CA).
11. Goat anti-rabbit Cy5 (Jackson ImmunoResearch Laboratories, West Grove, PA).
12. Goat anti-mouse FITC (Jackson ImmunoResearch Laboratories, West Grove, PA).
13. Goat anti-rat Cy3 (Jackson ImmunoResearch Laboratories, West Grove, PA).
14. Dissecting microscope.
15. PBT buffer: 0.1 % Tween 20 in PBS.

3 Methods

The methods outlined below will describe the preparation and fixation of butterfly embryo (1) and wing disc (2) tissue. The tissue will then be stained by indirect immunofluorescence (3) (protocol modified from Brakefield et al., 1996), and the stained tissue will be analyzed using multiple confocal images (4) that will be reassembled to visualize the entire tissue (5).

3.1 Butterfly Embryo Fixation Protocol

1. Butterfly eggs are collected at various times after deposition and placed in glass scintillation vials.
2. The eggs are covered with a 50 % bleach solution and incubated at room temperature for 2 min.
3. Remove the bleach solution using a Pasteur pipette.
4. Wash the eggs five times with PBS.
5. Completely cover the eggs with embryo fix buffer and overlay with a layer of heptane. Incubate at 4 °C for 30 min, shaking occasionally.
6. Remove the bottom layer of embryo fix buffer, leaving the heptane layer and add 5 ml of methanol. Gently shake the eggs for 15 min.
7. Remove the heptane/methanol solution and wash the eggs three times with methanol (*see* **Note 1**).
8. Rehydrate the eggs by washing in 75 % ethanol followed by a 50 % ethanol wash and finally a 25 % ethanol wash.
9. Rinse eggs four times in PBS at 4 °C.

10. Transfer the eggs out of the scintillation vial and into a small dish containing PBS that can be worked with under a dissecting microscope.
11. To remove the embryo from the egg, gently grasp the outer membrane of the egg with two pairs of forceps relatively close together. Slowly pull the egg apart to release the embryo (*see* **Note 2**).

3.2 Butterfly Wing Disc Fixation Protocol

Butterfly wing discs can either be isolated from the larval (caterpillar) (Subheading 3.2.1) or pupal stages (Subheading 3.2.2) and subsequently fixed (Subheading 3.2.3).

3.2.1 Isolation of Larval Wing Discs

1. Anesthetize the butterfly larva by placing in water for 10–20 min
2. Place the anesthetized larva in a dissecting tray containing cold PBS. Place pins in an "X"-like pattern near the anterior and posterior end of the larva to hold it in place.
3. The butterfly larval wing discs are located on the lateral wall of the caterpillar in the second and third thoracic segments (the segments containing the second and third pair of larval legs, *see* Fig. 1a) (*see* **Note 3**). Remove the wing disc using a pair of forceps to grasp the lateral cuticle and pull upwards. Using surgical scissors, cut the cuticle. The wing disc should be visible. Using forceps and scissors, remove the wing disc from the larva and place in cold PBS.

3.2.2 Isolation of Pupal Wing Tissue

The pupal wing tissue is located beneath the pupal case (*see* Fig. 1b). Within the first 24 h after pupation, the forewing disc will be tightly associated with the pupal cuticle, while the hind wing

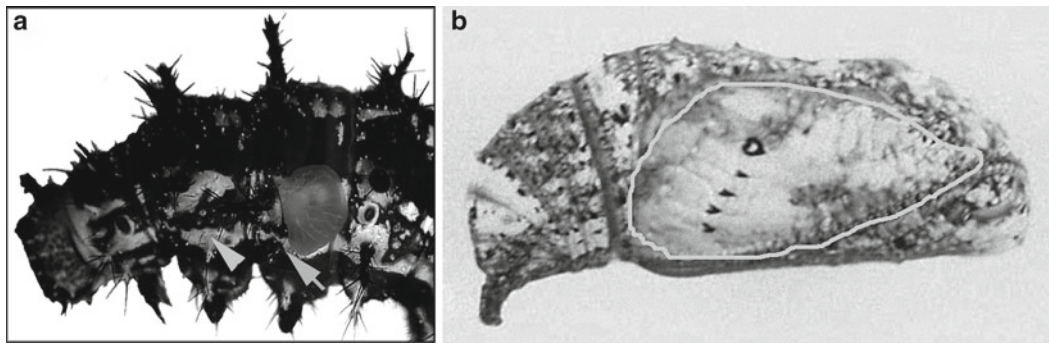

Fig. 1 *Junonia coenia* fifth instar wing discs lie underthe second (forewing—*white arrowhead)* and third (hindwing—*white arrow)*thoracic segments (**a**). An incision has been made to expose the hind wingdisc. In the pupal stage (**b**), the forewing tissue creates part of thepupal cuticle. Therefore, the location of the forewing tissue can be preciselylocated based on the morphological features of the pupal cuticle (outlined in *white*)

disc lies below the forewing disc. Twenty-four hours after pupation, the forewing disc will be easily separable from the pupal cuticle. To isolate the pupal wing tissue:

1. Transfer a pupal case to a dissecting tray containing ice cold PBS and place a pin through the anterior and posterior of the pupal case to hold the pupa in place.
2. Using scissors, cut around the edge of the pupal cuticle containing the forewing disc (*see* Fig. 1b). The forewing will either remain attached to the pupal cuticle or will lie within the open pupal case.
3. Using scissors, carefully excise the forewing and hind wing tissue and transfer to a staining dish containing ice cold PBS (*see* **Note 4**).

3.2.3 Fixation of Butterfly Wing Disc Tissue

1. Transfer the larval or pupal wing tissue to a small dish containing wing disc fix buffer. Incubate the tissue for 30 min on ice.
2. Rinse the wing discs three times for 5 min each time with ice cold PBS.

3.3 Indirect Immunofluorescence of Butterfly Embryos and Wing Disc Tissue

1. Place fixed wing discs (Subheading 3.2.3) or fixed embryos (Subheading 3.1) in 1 ml of block buffer for 1–2 h at 4 °C.
2. Remove the block buffer and incubate the butterfly tissue for 18–24 h at 4 °C with 300 μl of the following primary antibodies diluted in block buffer: mouse anti-engrailed/invected 4F11 at 1:5 dilution [6], rabbit anti-distal-less 1:100 dilution [2], and rat anti-Ci 1:25 dilution [4].
3. Remove the primary antibodies and wash the tissue four times for 5 min each, with 1 ml of wash buffer at 4 °C.
4. The butterfly tissue is incubated for 2 h at 4 °C with 300 μl of secondary antibodies donkey anti-rabbit Cy5, donkey anti-mouse FITC, and donkey anti-rat Cy3 diluted 1–200 in wash buffer.
5. Wash tissue four times 5 min each wash with 1 ml of wash buffer at 4 °C.
6. Place discs or embryos in Vectashield and mount on glass slide with coverslip.

3.4 Confocal Imaging

To examine the indirect immunofluorescence staining in large tissue while maximizing the fluorescent signal and retaining a high level of resolution requires acquisition of multiple confocal images. To image the tissue,

1. Using a fluorescent microscope, scan the image quickly to avoid photobleaching using the 5× objective lens to determine the overall fluorescent patterns on the tissue.

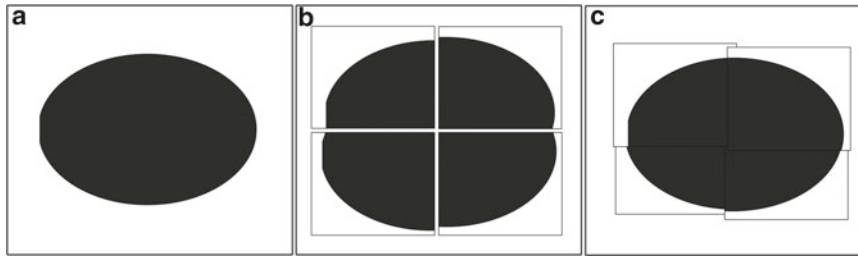

Fig. 2 A schematic showing confocal imaging of a large tissue sample. The original sample (**a**) is too large to be imaged under a single objective field. Thus, multiple overlapping confocal images are obtained (**b**). These images are subsequently reassembled to generate a single confocal image detailing the entire tissue sample

2. Once the fluorescent details of the total tissue have been determined, switch to the 10× objective lens and begin to scan the image using the confocal system.
3. Move to the areas of the tissue where fluorescent signals are present and using the focus adjustment, insure that the target area is in focus.
4. Move the objective lens to the top-left corner of the tissue specimen and collect a confocal image.
5. Move objective lens to the right until the field of view partially overlaps with the previously collected image (*see* **Note 5**) (*see* Fig. 2). Acquire a second confocal image (*see* **Note 6**).
6. Continue collecting confocal images in this manner until the end of the tissue specimen is reached (*see* Fig. 2).

3.5 Assembling Images in Photoshop

Once the confocal images have been acquired, it is time to assemble the final image representing the entire tissue. Assembly of the final image:

1. Open all the confocal images in Adobe Photoshop as individual layers.
2. Using the <NEW> function, open up a new window with a resolution of 300 pixels/in and a window size appropriate for the number of confocal images to be assembled (*see* **Note 7**).
3. Copy and paste each of the individual confocal images into the newly created window. Be sure that each confocal image occupies a different layer (*see* Figs. 2b and 3a) (*see* **Note 8**).
4. Arrange the confocal images in their approximate place in the window, i.e., the first image captured of the top left of the tissue should be put in the top-left corner of the Photoshop window. The second image captured should be placed just to the right of the first image (*see* Fig. 3b).
5. Once all the images are arranged in order, it is time to begin piecing the individual images together. There will be some

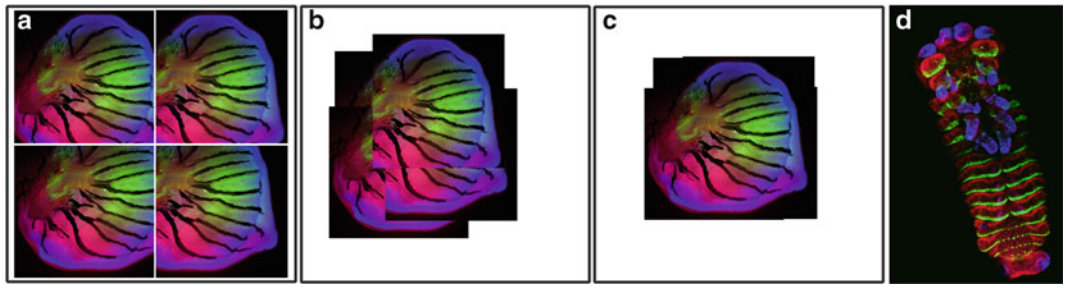

Fig. 3 Confocal imaging of *Junonia coenia* fifth instar wing disc (**a**–**c**) and embryo (**d**). Embryos (**d**) and wing discs (**a**–**c**) were stained for Distal-less (*blue*), engrailed/invected (*green*), and cubitus interruptus (*red*). Multiple confocal images covering the entire wing disc tissue were collected and opened in Adobe Photoshop software package (**a**). The images were then carefully repositioned to reconstruct the original wing disc (**b**, **c**). A similar approach was taken to reconstruct a *J. coenia* embryo (**d**)

level of photobleaching on the samples. For instance, the area of overlap between two confocal images will most likely be fainter than the rest of the image due to the fact that the overlapped section will have been imaged twice. Therefore, the confocal image that was acquired first should be in a higher Photoshop layer than the image captured second to hide the photobleached section.

6. Once the image has been fully assembled, the image layers can be flattened into a single layer and the image is publication ready (*see* Figs. 2c and 3c, d).

4 Notes

1. If the eggs are to be saved for future use, they can be stored at this stage. Remove all methanol and replace with a 100 % ethanol solution. The eggs can be stored at −20 °C for several weeks.
2. The embryo may have bits of yolk attached which will not affect the indirect immunofluorescence protocol.
3. We have successfully isolated and stained butterfly wing disc material from second through fifth instar larva. However, we have been unable to isolate wing discs from first instar larva and butterfly embryos.
4. It is often best to transfer pupal wing tissue between solutions using a flat metal spatula. The pupal wing tissue are fragile and very sticky and can clump together to produce a small ball of tissue that is difficult to unravel unless care is taken when transferring out of the dissecting tray into the staining dish.
5. The current image must overlap partially with the previous image so that the complete image can be reassembled without gaps.

6. It is important not to adjust any of the settings of the confocal during the entire acquisition process. Otherwise, it will be extremely difficult to compile the individual confocal images back into the full-sized image.
7. Often times a 5 in. by 5 in. window is a good place to begin. You can always increase the window size using the <CANVAS SIZE> function under the <IMAGE> menu. If the window ends up being too large, it is possible to use the CROP tool to reduce the window size.
8. It is possible to have up to 99 layers in a single graphic image.

References

1. Nijhout HF (1991) The development and evolution of butterfly wing patterns. Smithsonian Institution Press, Washington, DC
2. Brakefield PM, Gates J, Keys D, Kesbeke F, Wijngaarden P, Monteiro A, French V, Carroll SB (1996) Development, plasticity and evolution of butterfly eyespot patterns. Nature 384:236–242
3. Brunetti CR, Selegue JE, Monteiro A, French V, Brakefield PM, Carroll SB (2001) The generation and diversification of butterfly eyespot color patterns. Curr Biol 11:1578–1585
4. Carroll SB, Gates J, Keys DN, Paddock SW, Panganiban GE, Selegue JE, Williams JA (1994) Pattern formation and eyespot determination in butterfly wings. Science 265:109–114
5. Keys DN, Lewis DL, Selegue JE, Pearson BJ, Goodrich LV, Johnson RL, Gates J, Scott MP, Carroll SB (1999) Recruitment of a hedgehog regulatory circuit in butterfly eyespot evolution. Science 283:532–534
6. Reed RD, Serfas MS (2004) Butterfly wing pattern evolution is associated with changes in a Notch/Distal-less temporal pattern formation process. Curr Biol 14: 1159–1166
7. Patel NH, Martin-Blanco E, Coleman KG, Poole SJ, Ellis MC, Kornberg TB, Goodman CS (1989) Expression of engrailed proteins in arthropod, annelids, and chordates. Cell 58:955–968

Chapter 8

Confocal Microscopy of Cardiac Myocytes

Robert L. Price, Stephen T. Haley, Tara Bullard, Jeffrey Davis, Thomas K. Borg, and Louis Terracio

Abstract

Detailed methods are provided for the preparation and confocal imaging of cardiac myocyte development and differentiation. Examples include protocols for the analysis of cultured myocytes as well as vibratome sections of hearts from embryonic and adult tissue. Techniques include routine labeling of F-actin with phalloidin as well as multiple labeling protocols for colocalization studies and cell volume analysis.

Key words Cardiac myocyte, Cardiovascular, Confocal microscopy, Image analysis

1 Introduction

The heart is a dynamic tissue comprised of a number of cell types that are continually remodeled in response to a variety of mechanical and chemical factors during development, normal cardiac contraction, and disease. The majority of the heart is comprised of two primary cell types, myocytes and fibroblasts, and others such as endothelial and smooth muscle cells that are associated with the coronary vasculature. Cardiac myocytes represent the bulk of the heart mass, and the majority of this chapter will present techniques we have used to image these cells by confocal microscopy.

The high-resolution, high-contrast, and three-dimensional imaging capabilities of confocal microscopy provide an exceptional technique to investigate the changes that occur in the structure of myocytes during developmental and pathological processes. In the following pages, we will present several protocols that we have used to examine how cultured and in vivo cardiac myocytes respond to the variety of signaling events to which they are continually exposed. For the most part, the techniques presented could also be used to image any of the cell types present in the heart by modifying the probes used.

Stephen W. Paddock (ed.), *Confocal Microscopy: Methods and Protocols*, Methods in Molecular Biology, vol. 1075,
DOI 10.1007/978-1-60761-847-8_8,

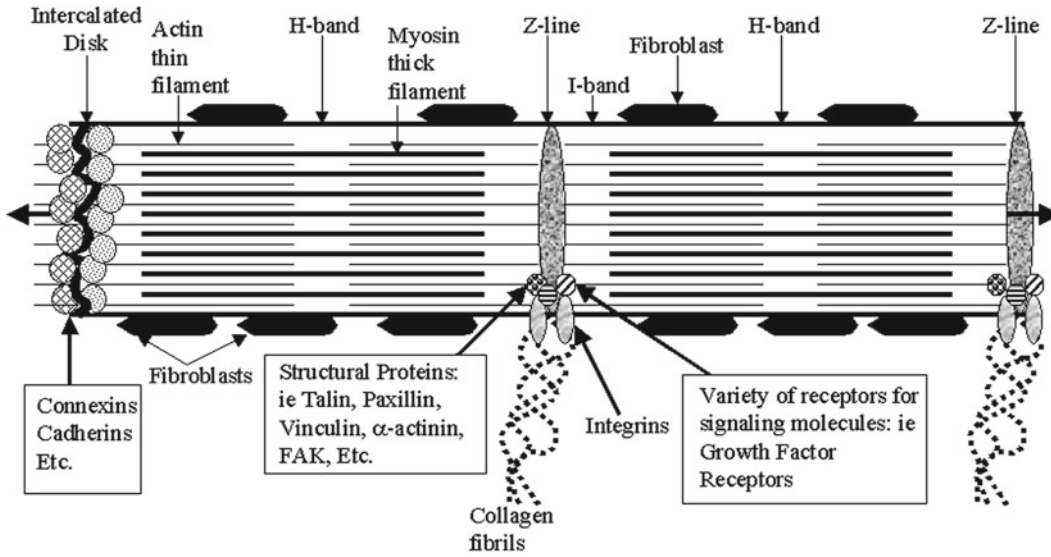

Fig. 1 Diagram of a cardiac myocyte showing many of the major structural features that are commonly examined by confocal microscopy. When stained with a fluorochrome conjugated to phalloidin, the areas with F-actin thin filaments are labeled. The H bands, which lack F-actin, remain unstained resulting in the characteristic striated appearance of myocytes stained with phalloidin

1.1 Phalloidin Staining

Before detailing specific protocols, it is appropriate to discuss phalloidin staining and its role in the study of cardiac myocytes. Phalloidin is from the poisonous mushroom (Amanita) and binds specifically to filamentous or F-actin, which is a primary component of the contractile apparatus of cardiac myocytes. By conjugating a fluorochrome to phalloidin, it is possible to obtain a highly specific and clean stain that can provide information about the architecture of the myocytes. At the concentrations commonly used for staining (typically a 1:20 up to a 1:100 dilution of purchased stock or 0.33–0.066 μM dilution), the fluorescence obtained from phalloidin is linearly related to F-actin concentrations with little or no binding to non-sarcomeric or G-actin making it suitable for quantitation of F-actin [1, 2].

Figure 1 shows a generalized diagram of cardiac myocyte structure and the location of the F-actin thin filaments in the sarcomeres. Note that in the region of the H band, there is no F-actin present. If myocytes are stained with a fluorochrome-conjugated phalloidin, these areas will be unstained while areas with F-actin will be stained. This staining pattern results in the characteristic banding pattern observed when cardiac myocytes are stained with phalloidin. When not limited by the number of available channels, it is our practice to routinely perform a phalloidin stain to outline the structure of the myocytes. We then use the other available channels for staining of other cell types and proteins associated with the myocytes (Fig. 2).

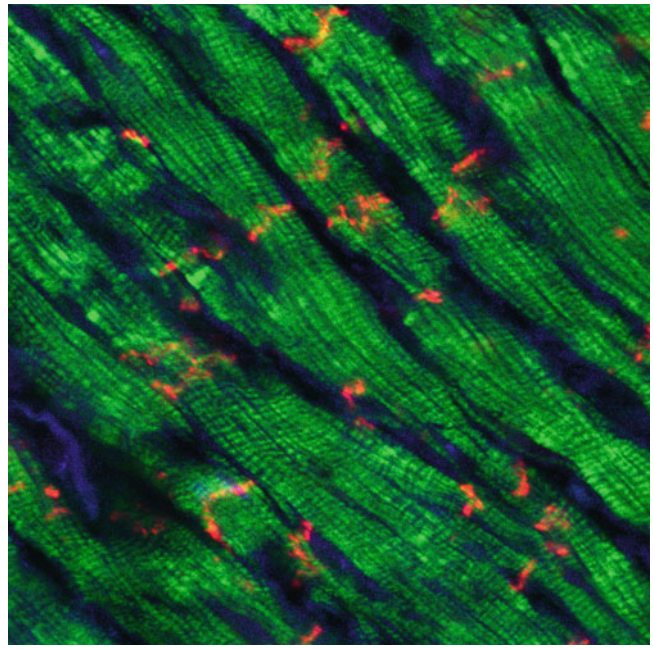

Fig. 2 A single optical section through a vibratome section of an adult mouse heart that has been triple labeled for F-actin with Alexa-488 phalloidin (*green*), connexin 43 which is a component of intercalated disks (*red*), and discoidin domain receptor 2 (*blue*) which is a stain for fibroblasts

1.2 Cardiac Myocyte Structure

Early in mammalian development, the heart is a straight tube that undergoes a complex looping process that results in the four-chambered adult heart. During this looping process and subsequent maturation of the heart, cardiac myocytes are exposed to significant changes in mechanical force related to myocyte contraction and an increase in blood pressure [3]. In addition a number of chemical mediators, such as growth factors and hormones, affect cell division and differentiation during this time frame [4, 5]. These various stimuli induce significant changes in myocyte phenotype that results in initially round, undifferentiated cells becoming spindle shaped with a well-developed and architecturally complex structure (Fig. 3a, b).

Following birth the normal beating of the adult heart and flow of blood past the cells of the heart also exposes the myocytes to a constantly changing environment to which they often respond by structural remodeling. In addition to changes associated with the normal development and function of the heart, a number of pathologies also result in phenotypic changes in myocyte structure and their surrounding extracellular matrix [6–8]. Many of these pathological changes result in myocyte hypertrophy and disruption of the architecture of the contractile components of the cell that may

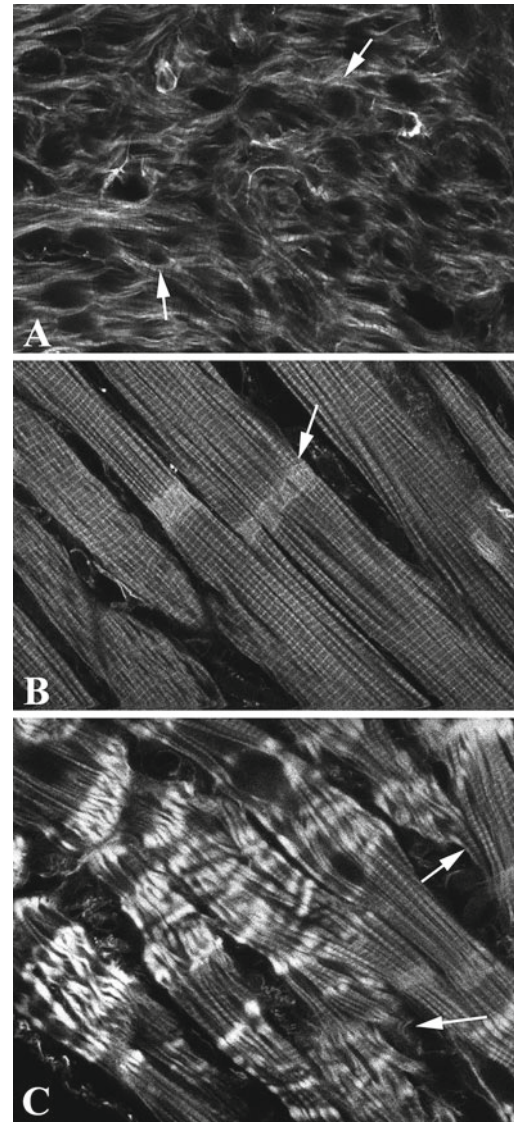

Fig. 3 Single optical sections of an embryonic day 13.5 mouse heart (**a**), the left ventricle of a normal adult heart (**b**), and the left ventricle of a hypertrophied heart entering the transition to heart failure (**c**). All sections were stained with rhodamine phalloidin. *Arrows* in (**a**) indicate developing myofibrils on the edges of rounded myocytes. The *arrow* in (**b**) indicates an intercalated disk from a normal adult myocyte. The *arrow* in (**c**) indicates branching of myofibrils associated with severe cardiac hypertrophy and changes in the distribution and organization of intercalated disks

lead to severe cardiac dysfunction and death. Although transmission electron microscopy is necessary to image many of the minute structural changes that occur, others are readily imaged by confocal microscopy (Fig. 3c).

2 Materials

The materials and methods we use are dependent upon whether cultured myocytes, whole embryos, or sections of heart are being processed. Protocols for each of these types of sample will be presented. Unless otherwise stated, reagents can be purchased from Sigma (St. Louis, MO). All images were collected with a BioRad MRC1024ES confocal microscope equipped with an argon/krypton laser on a Nikon E800 platform.

2.1 Standard Buffers, Fixatives, Fluorochromes, and Mounting Media

1. HEPES with 2 mM $CaCl_2$ (GIBCO, Carlsbad, CA) (*see* **Note 1**).
2. Phosphate buffered saline (PBS):

   1,000 ml deionized water.

   7.2 g NaCl.

   1.43 g Na_2HPO_4.

   0.43 g KH_2PO_4.

   0.02 % sodium azide may also be added to prevent bacterial growth.

   A 5× stock solution can also be prepared by using 200 ml of water rather than 1,000 ml.

   25 mM KCl.
3. Fixatives: Our fixative of choice is 2–4 % paraformaldehyde prepared in PBS at a pH of 7.2–7.4. To prepare 100 ml of paraformaldehyde, add 4 g of paraformaldehyde powder to 100 ml of PBS and gradually heat to 60 °C under a fume hood. To clear the solution, slowly add drops of 1 N NaOH while stirring. Do not allow the temperature of the solution to exceed 65 °C. The final pH can be adjusted with NaOH or HCl if necessary.

   If antibody efficiency is not optimum with aldehyde fixation, an alternative fixative for cell culture protocols is methanol used at 4 °C. However, phalloidin staining is poor when methanol fixation is used.
4. Washing buffer: 0.1 M glycine in PBS to block free aldehyde groups. If intracellular components are being stained, 0.1 % Triton X-100 may also be added to permeabilize cell membranes.
5. Blocking buffer: 1 % BSA (IgG- and protease-free) in PBS to block nonspecific staining. If background problems exist, 5 % normal serum from the host of the secondary antibody may be added to the blocking buffer. For example, if the secondary antibody was made in a donkey, use 5 % normal donkey serum as an additional blocking agent.
6. Phalloidin conjugated to fluorochrome of choice (Molecular Probes, Eugene, OR).

7. Primary and fluorochrome-conjugated secondary antibodies diluted to desired concentrations in PBS-1% BSA blocking buffer. Antibodies should be centrifuged at 4 °C to remove particulate matter.
8. Mounting media: 2.5 g DABCO (1,4-diazabicyclo[2.2.2] octane) dissolved in 25 ml of PBS and mixed with 75 ml of glycerine. Store at 4 °C. DABCO/PBS/glycerine remains fluid and specimens mounted with this mixture are routinely sealed with fingernail polish and stored in the dark at 4 °C. Gloves must be used when handling DABCO solutions (*see* **Notes 2** and **3**).

2.2 Additional Solutions for Processing Cultured Cardiac Myocytes

1. Nifedipine (*see* **Note 4**): Nifedipine should be made fresh for each use. Mix 52 mg of nifedipine in 10 ml of 70 % ethanol, vortex, and use at a concentration of 1 μl per ml of cell culture media.
2. CMFDA: To determine changes in cell volume, myocytes can be loaded with CellTracker™ Green 5-chloromethylfluorescein diacetate (Molecular Probes, Eugene, Oregon) diluted in DMSO to produce a 20 mM stock solution. Stock can be stored at −20 °C.

2.3 Additional Solutions for Processing Embryonic Hearts

Solutions and protocols for processing embryonic hearts depend on the age and size of the embryos. For our purposes, rat embryos less than embryonic day 9.5 and mouse embryos less than embryonic day 10.5 are processed intact. After these time points, embryos are too large and the tissue too dense for imaging through the entire heart. To image internal structures such as developing ventricular trabeculae and cardiac valves of older embryos we typically vibratome section the embryo. If three-dimensional reconstructions are necessary, the added thickness of vibratome sections is often preferred over cryo- or paraffin-embedded sections (*see* **Note 5**). For embryos between embryonic days 10–15, entire embryos are embedded in 13 % acrylamide to provide support for the embryo while sectioning. For older embryos, the thorax region is isolated and embedded in acrylamide.

2.3.1 Imaging of Entire Embryo Without Sectioning

Bovine testicular hyaluronidase—1,500 units/ml.

2.3.2 Imaging of Embryos with Vibratome Sectioning

30 % acrylamide stock (mix 30 g electrophoresis grade acrylamide and 0.8 g bisacrylamide cross-linker in 100 ml distilled water).

PBS.

10 % tetramethylethylenediamine (TEMED) stock.

2 % ammonium persulfate.

Tissue-embedding molds.

3 Methods

The following methods have been selected because they are representative of the techniques used in our laboratory. Some variation in the basic techniques does exist dependent upon the antibodies used. However, the protocols presented can serve as starting points for additional studies. Procedures for the culture of cardiac myocytes [9, 10] and whole embryo culture [2–4] have been published elsewhere and will not be covered here.

3.1 Protocols for Processing Cultured Cardiac Myocytes

The protocols described below cover three basic types of experiments we perform: routine staining with double and triple fluorochromes, experiments in which the differentiation of the contractile apparatus is followed, and experiments in which changes in cell volume are tracked over time in response to a variety of perturbation techniques.

3.1.1 Routine Staining Protocols

1. Obtain cell cultures and rinse the cell culture media away with several quick washes of PBS at 37 °C. Immediately fix myocytes in 2 % paraformaldehyde in PBS (pH 7.2) for a minimum of 1 h at room temperature or overnight at 4 °C.
2. Rinse the fixative off with several quick washes of PBS.
3. If cells have been cultured in large Petri dishes or on a slide, outline the area of interest with a PAP pen (Electron Microscopy Sciences) to create a small well for staining. This will minimize the amount of expensive antibodies required for staining. If cells have been cultured on coverslips or small Petri dishes, use just enough fluid to cover the cells. To prevent drying, a moist chamber can be created by placing the cultures in a plastic container such as Tupperware with several moist towels or a thin layer of water in the bottom of the container. Enough buffer or staining solution must be used to prevent drying of samples.
4. Permeabilize myocytes by incubating at room temperature in three changes of PBS with 0.1 M glycine and 0.1 % Triton X-100 for 15 min per change. Cultures should be gently agitated during this and subsequent steps.
5. Rinse cells in two changes of PBS with 1 % BSA for 10 min per change.
6. Add blocking PBS buffer containing 1 % BSA and 5 % normal serum for 30 min.
7. Add enough primary antibody (i.e., 1.5 ml per 35 mm culture dish) diluted to the appropriate concentration in the above blocking buffer and incubate for 1 h at 37 °C or overnight at 4 °C.
8. Rinse three times at 10 min each in blocking buffer.

9. Incubate in fluorochrome-conjugated secondary antibody at 37 °C for 1 h or 4 °C overnight. Keep dishes covered with foil to prevent fading of fluorochrome.
10. Rinse and repeat for staining with additional antibodies. If no additional antibodies are used, rinse and incubate in 1:100 phalloidin-conjugated fluorochrome at 37 °C for 1 h or overnight at 4 °C.
11. Rinse three times at 10 min each in PBS.
12. Mount sample in PBS/glycerine/DABCO solution.
13. Coverslip and seal the coverslip with fingernail polish.

3.1.2 Myofibrillar Differentiation Protocols

1. Obtain cells on day 3 of culture. This time period in culture ensures that cells are healthy and they should be spontaneously contracting.
2. Remove the culture media and replace with fresh media containing 1 μl of nifedipine stock solution per ml of culture media.
3. Replace with fresh media containing nifedipine at 6, 24, and 48 h. At 72 h replace the nifedipine-containing media with fresh media that does not contain nifedipine. The new media should contain the experimental factor (i.e., drugs, growth factors, viral vectors). At each preset time point during the experiment, fix a control culture and the required number of dishes.
4. Stain, rinse, and mount slides as described above.

Figure 4 shows images collected from cardiac myocytes that have been treated with nifedipine as described above and infected with an adenovirus that expresses GFP and overexpresses the platelet-derived growth factor receptor α (PDGFRα). The GFP expression ensures that we are examining cells that overexpress the receptor of interest and allows us to test the hypothesis that overexpression of the PDGFRα results in an increase in the rate of myofibril assembly. Similar experiments can be performed to test a number of factors expressed in the myocytes or added to the culture media.

3.1.3 Cell Volume (CMFDA) Protocols

1. Obtain cells at the predetermined experimental time point.
2. Warm the CMFDA stock to 37 °C and thoroughly mix 5 μl of CMFDA per 2 ml of cell culture media.
3. Replace the normal cell culture media with media containing the CMFDA and incubate cells at 37 °C for 30 min.
4. Replace the culture media containing the CMFDA with normal culture media and incubate for an additional 30 min at 37 °C.
5. Remove the culture media and fix in 2 % paraformaldehyde for a minimum of 1 h at room temperature.

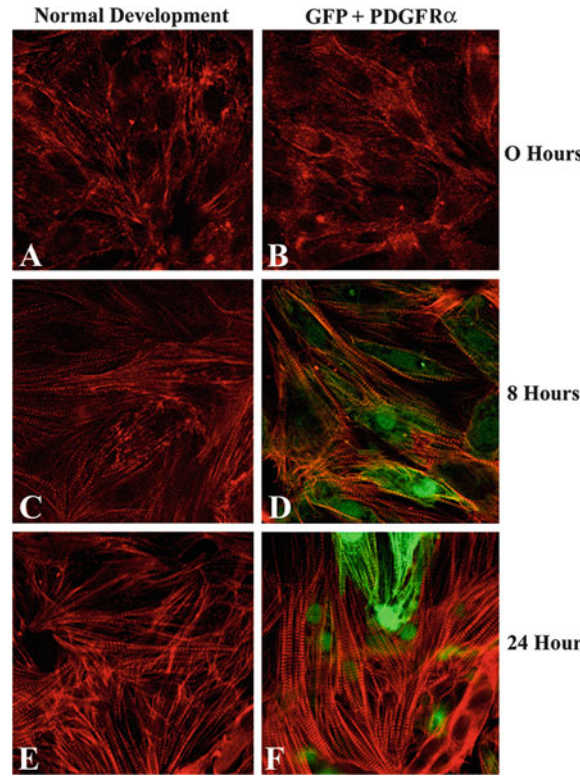

Fig. 4 Single optical sections of control cells (**a**, **c**, and **e**) and cells that have been infected with an adenovirus that expresses GFP and overexpresses the PDGFRα (**b**, **d**, and **f**) at 0, 8, and 24 h following infection. In cells that overexpress the PDGFRα, the rate of myofibril assembly is accelerated. Correlative physiological data showing that the rate of myocyte contraction and synchronicity of the beating pattern not presented here also show that myofibrillar function is improved in the experimental cultures

6. Rinse in PBS with 0.1 M glycine. No further staining is necessary.
7. Mount specimen in PBS/glycerine/DABCO and seal coverslip with fingernail polish.
8. CMFDA should fill the cytoplasm of the cells and excite with a 488-laser line. Select the optimum z-thickness for the objective being used so that overlap or gaps between optical sections of a Z-series will be minimal. For our system, we routinely use a 40× objective with an NA of 1.2 and a Z-thickness of 1 μm for each section.
9. We also set the working conditions of the confocal system so that all pixels within the cell boundaries have a value above a threshold of 50, so automated determination of the area of each image in the Z-series is readily accomplished in image analysis programs such as Image-Pro Plus (Media Cybernetics,

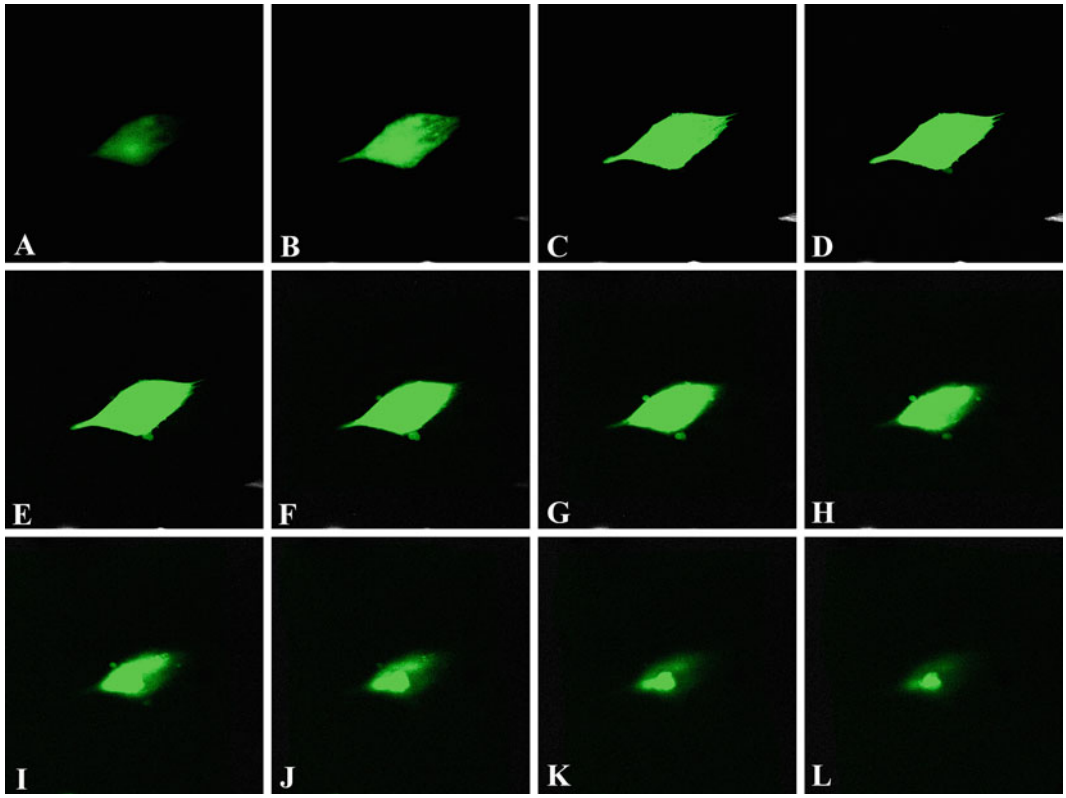

Fig. 5 Optical sections from a Z-series collected at 1 μm intervals through a cardiac myocyte that had been incubated in CMFDA. Images were collected from the substrate surface of the cell where signal is first detected (**a**) through its apex (**l**). By adding the area of each optical section, an estimate of the total cell volume can be obtained to detect the effects of a variety of treatments on cell growth

Silver Spring, MD). A good estimate of total cell volume can then easily be determined by adding the areas of each optical section (Fig. 5). Examples of data collected and analyzed by this technique can be found in reference [11].

3.1.4 Preparation and Imaging of Whole Embryos

It is often possible to collect images through the entire depth of a small embryonic heart as discussed above. For rat and mouse embryos that are small enough:

1. Rinse the embryo for 1–2 min in HEPES buffer containing 2 mM $CaCl_2$ to relax the heart.
2. Fix the embryo for 1–2 h at room temperature or overnight at 4 °C in 4 % paraformaldehyde prepared in PBS.
3. Wash in PBS containing 0.1 % Triton X-100 and 1,500 units/ml of testicular hyaluronidase for two changes of 45 min each to permeabilize the pericardium and myocardial membranes.
4. Rinse in three changes of PBS/BSA for 15 min each.

5. Stain as above for cardiac myocytes. It may be necessary to increase staining times to 2–3 h at room temperature or up to 24 h at 4 °C for adequate penetration of primary and secondary antibodies.
6. Mount with PBS/glycerine/DABCO mix in depression slides or use supports such as the CoverWell imaging chamber gaskets (Molecular Probes, Eugene, OR) to raise the coverslip. This will prevent compression of the embryo and alteration of its three-dimensional structure. To support the coverslip, we often use small pieces of capillary tubes, fragments of coverslips, or imaging chamber supports that are available in various thicknesses from Molecular Probes (Eugene, Oregon) or Electron Microscopy Sciences (Fort Washington, PA). Avoid the use of mounting media that polymerize as this may cause excessive shrinkage of soft embryonic tissues (*see* **Note 6**).

3.1.5 Protocols for Vibratome Sections of Larger Embryos

1. Relax the embryos in HEPES containing 2 mM $CaCl_2$ or PBS containing 25–50 mM KCl.
2. Fix overnight at 4 °C in 4 % paraformaldehyde prepared in PBS.
3. Prepare a working solution of acrylamide by mixing the following: 4 ml of 30 % acrylamide stock, 155 μl of TEMED, 3 ml of 3× PBS, and 1.85 ml of distilled water
4. Place the sample in a tissue-embedding mold commonly used for paraffin embedding of tissue.
5. Add enough acrylamide to cover the sample.
6. From the corner of the mold, add 2–3 drops of freshly prepared 2 % ammonium persulfate for each 0.5 ml of acrylamide.
7. Gently and rapidly mix the ammonium persulfate and acrylamide taking care to not add air bubbles to the mix
8. Rapidly orient the tissue. Polymerization of the acrylamide will occur in less than 1 min. The rapid polymerization results in the specimen being encased in the acrylamide gel with little or no penetration into the tissue.
9. Before polymerization is complete, place a coverslip over the top of the mold to create a flat surface.
10. Refrigerate for approximately 1 h.
11. Remove the acrylamide from the mold, invert, and superglue the flat surface to a vibratome specimen holder. If necessary, specimens can be stored in PBS at 4 °C prior to sectioning.
12. Trim away excess acrylamide and mount specimen holder in vibratome.
13. Fill the specimen tray with ice water and allow the specimen to cool for several minutes prior to cutting.

14. Cut sections at desired thickness which is usually between 50 and 200 μm depending on the age of the embryo. As the heart develops and myofibrils, as well as other proteins, are added, the tissue becomes more dense, and it becomes increasingly difficult to obtain sufficient penetration of the laser and recovery of signal without distortion from sections thicker than 50 μm.
15. Stain sections as described above for cell cultures. It may be necessary to extend staining times for adequate penetration of some antibodies into the vibratomed tissue.
16. Mount stained sections with PBS/glycerine/DABCO solution. As with whole embryos, compression of sections and mounting media that polymerizes should be avoided.
17. Collect images in the Z-axis with an appropriate Z-step [12, 13] and project with software associated with the confocal or with an ancillary program. For the creation of AVI movies, we usually project and assemble images in VoxBlast (VayTek, Inc., Fairfield, Iowa).

Figure 6a, b, and the associated movies on the CD, shows 50 μm Z-series projections collected from phalloidin-stained vibratome sections of similar regions of the developing hearts of two mice. Images in Fig. 6a, b are of the projected Z-series from each animal showing the outer surface of the developing heart. By the creation of rotating data sets as shown on the CD, information on the outer as well as the luminal surface of the hearts can be imaged. The differences in the thickness of the compact zone of the myocardium and the increased intensity of the phalloidin staining become much more obvious when rotated 180° on the CD, so the luminal surfaces are imaged.

Although differences in the F-actin staining patterns and intensity of staining are apparent in the hearts, it is often desirable to quantitate these differences. Since, as noted above, the fluorescence obtained from phalloidin is linearly related to F-actin concentrations, if images are collected with identical working conditions on the confocal microscope, it should be possible to determine differences in F-actin concentrations in various regions of the heart following treatment [1, 2]. One way we have attempted to do this is to place a 5×5 mask over the entire image and to determine average pixel intensities along the lines of the masks as shown in Fig. 6c, d. Statistical analyses can then be performed on the images to support the qualitative observations that exposure to platelet-derived growth factor affects myofibril development in the developing heart.

3.1.6 Adult Hearts

1. Anesthetize the animal, remove the heart, and place it in a Petri dish with PBS containing 25 mM KCl for 1–2 min to wash out the blood and relax the myocytes. Gently massaging the walls of the ventricles will improve the removal of red blood cells that often autofluoresce.

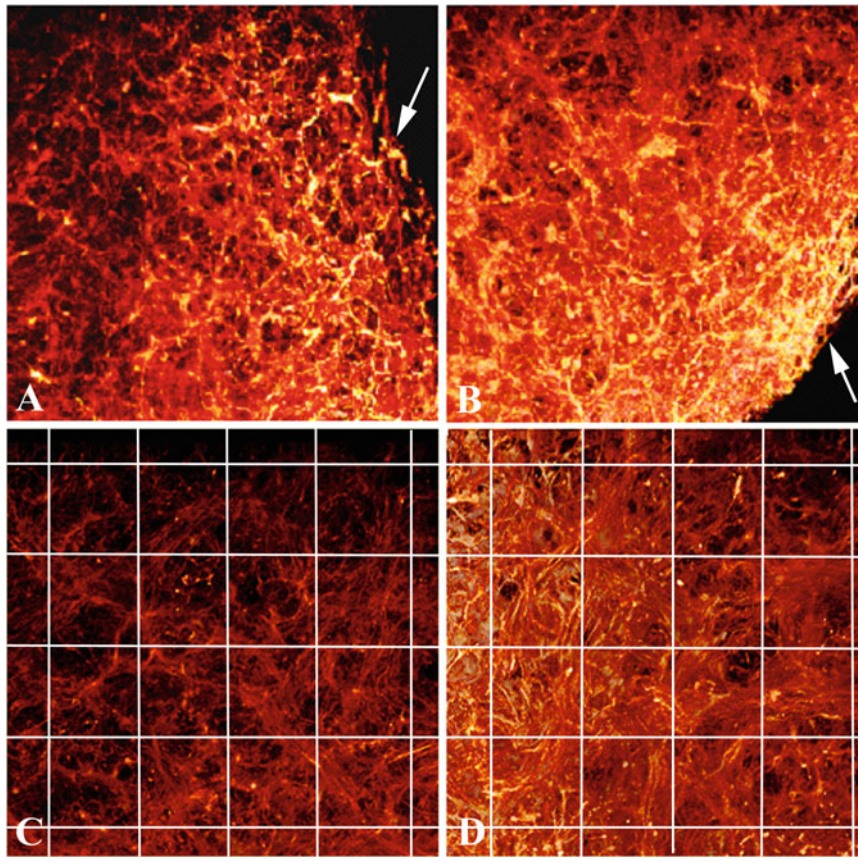

Fig. 6 Projected Z-series (50 μm at 1 μm Z-steps) of hearts from control (**a** and **c**) and whole embryo cultured embryos (**b** and **d**) that had 50 ng/ml of PDGF BB ligand added to the culture media (*see* ref. 2 for experimental details). Movies of figure (**a**) and (**b**) are also shown on the CD and illustrate the advantages of these types of data sets when analyzing various surfaces of organs. In the printed figures in (**a**) and (**b**), the outside surfaces of the developing compact zone of the myocardium of the left ventricles are shown (*arrows*). In the movies, the data sets can be rotated to show the differences in the structure of the outer and inner zones of the compact zone and the effect of the added PDGF BB on the development of the ventricles. To quantitate these types of qualitative observations, we have placed a 5×5 grid over identically processed and collected images from control (**b**) and experimental (**d**) data sets to determine differences in pixel intensities along the lines

2. Fix the heart in 4 % paraformaldehyde in PBS containing 25 mM KCl overnight at 4 °C.
3. Rinse in several changes of PBS containing 0.1 M glycine and 1% BSA.
4. As above for embryonic hearts, we routinely vibratome section adult hearts rather than using paraffin or cryo-sections. Adult hearts following fixation are usually rigid and can be vibratomed at 25–50 μm without acrylamide embedding. However, if sections do collapse, a small amount of acrylamide can be polymerized inside the ventricles to maintain the shape of the sections as they are cut.

5. Staining and imaging of vibratome sections from adult hearts should be carried out as described above for sections of embryonic hearts.

4 Notes

1. If cardiac myocytes are directly exposed to fixatives such as paraformaldehyde, they often hyper-contract which may affect measurements and the normal orientation of the cells. If this is a problem, 2 mM $CaCl_2$ or 25 mM KCl may be added to a rinse buffer prior to and during the addition of the fixative.
2. Fingernail polish: Care should be taken when sealing coverslips with fingernail polish. While it is an excellent choice for sealing coverslips, it does take some time for it to dry. If sufficient time is not allowed, some polish may be transferred to the objective. If this happens, we have been successful in removing polish with a very small amount of acetone, but great care is necessary as this may damage lens coatings and the glue holding the lens in place. You may wish to contact the manufacturer of the lens before attempting to remove polish by this method.
3. DABCO is a carcinogen and protective gloves should be worn during handling.
4. It is often desirable to synchronize the state of myofibrillar differentiation for all myocytes in an experiment and to then follow the reassembly of the contractile apparatus in response to experimental variables. Nifedipine is a calcium channel blocker that inhibits myocyte contraction. The addition of nifedipine to the culture media for a period of 48–72 h stops cell contraction and results in the breakdown of the myofibrillar apparatus. When fresh culture media without nifedipine are added, myofibrils will begin to reassemble over the course of 36–48 h. The rate of reassembly is accelerated in response to a number of conditions, and the state of reassembly can be tracked over time by fixing cultures at set times and imaging by confocal microscopy.
5. For confocal microscopy we routinely use vibratome sections rather than cryo- or paraffin sections. The use of vibratome sections rather than paraffin sections has several advantages. They are quicker to prepare since there is no embedding procedure, it is not necessary to dehydrate the sections which can cause significant shrinkage and disruption of the three-dimensional architecture, they are not subjected to harsh chemicals such as xylene or heat that may diminish antibody staining, and samples can be cut into thicker slices by vibratoming which is advantageous for three-dimensional reconstructions. Cryosections have many of these advantages in that they can be

processed without the use of harsh chemicals or heat, but the thickness of sections is limited when compared to vibratome sections.

6. Alternatively dipping lenses may be used. This will provide less aberration as deeper optical sections are imaged, but the cost of a complete set of dipping lenses for the various magnifications that images may be collected at is prohibitive for some laboratories.

Acknowledgements

We would like to thank Anna and Alex McFadden for their help with staining some of the samples. Portions of this work were supported by NIH grants HD35253, HL58893, and HL42249 and an American Heart Predoctoral Fellowship for T. Bullard.

References

1. Huang ZJ, Haugland RP, You WM, Haugland RP (1992) Phallotoxin and actin binding assay by fluorescent enhancement. Anal Biochem 1:199–204
2. Price RL, Haley ST, Bullard TA, Goldsmith EC, Simpson DG, Thielen TE, Yost MJ, Terracio L (2003) Effects of platelet-derived growth factor-AA and -BB on embryonic cardiac development. Anat Rec 272A:424–433
3. Price RL, Chintanowonges C, Shiraishi I, Borg TK, Terracio L (1996) Local and regional variations in myofibrillar patterns in looping rat hearts. Anat Rec 245:83–93
4. Price RL, Carver W, Simpson DG, Fu L, Zhao J, Borg TK, Terracio L (1997) The effects of angiotensin II and specific angiotensin receptor blockers on embryonic cardiac development and looping patterns. Dev Biol 192:572–584
5. Evans HJ, Sweet JK, Price RL, Yost M, Goodwin RL (2003) A novel 3-D culture system for the study of cardiac myocyte development. Am J Physiol Heart Circ Physiol 285:H570–H578
6. Yan X, Price RL, Nakayama M, Ito K, Schuldt A, Manning AJ, Sanbe A, Borg TK, Robbins J, Lorell BH (2003) Ventricular-specific expression of angiotensin II type 2 receptor causes dilated cardiomyopathy and heart failure in transgenic mice. Am J Physiol Heart Circ Physiol 285(5):H2179–H2187
7. Ehler E, Horowits R, Zuppinger C, Price RL, Perriard E, Leu M, Caroni P, Sussman M, Eppenberger HM, Perriard JC (2001) Alterations at the intercalated disk associated with dilated cardiomyopathy in two mouse models. J Cell Biol 153:763–772
8. Ding B, Price RL, Goldsmith EC, Borg TK, Yan X, Douglas PS, Ma L, Weinberg EO, Thielen T, Bartunek J, Lorell BH (2000) Left ventricular hypertrophy in ascending aortic stenosis mice: anoikis and the progression to early failure. Circulation 101:2854–2862
9. Borg TK, Rubin K, Lundgren E, Borg K, Obrink B (1984) Recognition of extracellular matrix components by neonatal and adult cardiac myocytes. Dev Biol 104:86–96
10. Simpson DG, Sharp W, Terracio L, Price RL, Borg TK, Samarel AM (1996) Mechanical regulation of cardiac myocyte protein turnover and myofibrillar structure. Am J Physiol 270:C1075–C1087
11. Price RL, Potts JD, Thielen TE, Borg TK, Terracio L (2001) Growth factor regulation of embryonic, fetal and neonatal cardiac development. In: Tomanek RJ, Runyan R (eds) Formation of the heart and its regulation. Springer, NY, pp 171–199
12. Paddock SW (1998) An introduction to confocal imaging. In: Paddock SW (ed) Confocal microscopy: methods and protocols, vol 122, Methods in Mol Biol. Humana, Totowa, NJ, pp 1–34
13. Pawley JB (1955) Handbook of biological confocal microscopy. Plenum, New York

Chapter 9

Confocal Imaging of Fluorescently Labeled Proteins in the *Drosophila* Larval Neuromuscular Junction

Ian P. Coyle

Abstract

The *Drosophila* larval neuromuscular junction (NMJ) consists of a presynaptic motor neuron terminal and a postsynaptic muscle cell that offer an accessible and popular model system for the analysis of synaptic growth and function. I describe techniques for visualizing fluorescently labeled proteins within dissected, formaldehyde-fixed second to third instar larval NMJs. In addition, I present two strategies using confocal microscopy to solve a particular problem in NMJ analysis: distinguishing fluorescence in the presynaptic nerve terminal from that in the adjacent postsynaptic muscle cell. This problem arises from the fact that the membrane of the muscle cell envelops the motor neuron terminal with a convoluted process called the subsynaptic reticulum, obscuring the boundary between muscle and nerve. A first strategy entails taking thin optical sections through synaptic boutons to capture a cross section of the nerve terminal, and a second strategy involves visualizing epitope-tagged isoforms of particular proteins that have been transgenically expressed in either the nerve or the muscle.

Key words *Drosophila* neuromuscular junction, Periactive zone, Synaptic bouton, Subsynaptic reticulum, Epitope tag, Nervous wreck, Pak

1 Introduction

Extensive molecular analyses of synaptic growth and function have been performed at the larval neuromuscular junctions (NMJs) of *Drosophila melanogaster* [1–4]. This system is popular because many of the synaptic proteins present within *Drosophila* NMJs have homologs in the vertebrate CNS and because the motor axons of third instar larvae form large, accessible contacts on the surfaces of the body wall muscles. Fluorescence immunocytochemistry combined with confocal microscopy make it possible to visualize the subcellular localization of synaptic proteins at ~0.2 μm horizontal resolution in the NMJs of fixed, eviscerated larvae. Moreover, confocal microscopy is being used for live imaging of nerve growth and synaptic vesicle dynamics in either dissected or undissected larvae, discussed elsewhere [5–8]. These studies are

Stephen W. Paddock (ed.), *Confocal Microscopy: Methods and Protocols*, Methods in Molecular Biology, vol. 1075,
DOI 10.1007/978-1-60761-847-8_9,

enhanced by the genetic tractability of *Drosophila*, because epitope- or reporter-tagged chimeras can be expressed specifically in the presynaptic neuron, the postsynaptic muscle cell, or both. This not only facilitates labeling of subcellular compartments in nerve terminals but also permits visualizing the localization of putative synaptic proteins when specific antisera are not available.

High-resolution confocal analysis of the larval NMJ has helped identify discrete functional domains within synapses. For example, numerous cell signaling molecules that regulate NMJ growth, such as Fasciclin II (FasII) or nervous wreck (Nwk), are found in a network of doughnut-like rings around active zones, collectively called the "periactive zone" within the presynaptic nerve terminal [9–11]. In contrast, "active zones," which contain the proteins necessary for neurotransmitter release, such as voltage-gated calcium channels [12, 13], are clustered in a counterpattern of distinct puncta. Such subcellular organization indicates that the factors involved in exocytosis, endocytosis, and cytoskeletal dynamics are grouped in distinct microdomains [14–16]. These observations not only help illustrate synaptic architecture but also make it possible to infer the functions of novel synaptic proteins based on their subcellular localization.

Despite the relatively detailed resolution that has been achieved through confocal analysis at the *Drosophila* NMJ, a caveat arises when attempting to visualize the subcellular localization of proteins that are expressed both pre- and postsynaptically, such as actin and many cytoskeleton-associated proteins. This problem stems from the fact that the presynaptic nerve terminal is enveloped by a convoluted extension of the muscle membrane called the subsynaptic reticulum (SSR) [17]. If a protein were expressed in the SSR, its signal may obscure the presence and distribution of the same protein expressed in the underlying nerve. Taking thin optical sections through the nerve terminal can delimit the presynaptic cytosol in some cases. However, if the protein were membrane associated, the presynaptic and postsynaptic complement may be situated as close as 20 nm apart, below the resolution of confocal light microscopy. In such instances, epitope (i.e., HA or c-Myc) or reporter (i.e., GFP) tags can assist the analysis because chimeric proteins incorporating such tags can be expressed exclusively within nerves or muscle cells using the UAS-GAL4 system and subsequently visualized using fluorescent antibodies directed against the tag or via autofluorescence of the tag itself.

2 Materials

2.1 Larval Dissection and Fixation

1. Larvae at second or third instar stage. Younger animals (first instars and embryos) are difficult to dissect and are generally analyzed by whole mount techniques [18, 19].

2. Calcium-free saline (128 mM NaCl, 2 mM KCl, 4 mM $MgCl_2$-$6H_2O$, 35.5 mM sucrose, 5 mM HEPES, 1 mM EGTA).
3. Insect dissecting chambers [19] and pins. Dissections can also be performed using insect pins in Falcon 35 mm Petri dishes coated with Sylgard resin.
4. Forceps and small scissors or scalpel.
5. Dissection microscope.
6. 4 % paraformaldehyde fixative (PFA) in phosphate buffered saline, pH 7.4.
   (a) Mix 20 ml of 0.5 M dibasic sodium phosphate (Na_2HPO_4) and 80 ml ddH_2O in a 200 ml beaker
   (b) Add 8 g paraformaldehyde (Sigma) and ~200 mg NaOH or two pellets (Mallinckrodt).
   (c) Seal beaker with paraffin and mix well on a hot plate in a flow hood at ~75 °C for 15 min. Avoid boiling, which generates formic acid.
   (d) Separately, mix 20 ml 0.5 M monobasic sodium phosphate (NaH_2PO_4) with 80 ml ddH20.
   (e) After 15 min, the formaldehyde solution becomes nearly translucent. Add all 100 ml of the monobasic sodium phosphate dilution. Verify that solution is ~pH 7.4 using litmus strips (MCB reagents).
   (f) Add 2 ml of 50 mM EGTA (0.5 μM final concentration).
   (g) Gravity filter with Whatman filter paper. The fixative is usable for up to 3 weeks if refrigerated.

2.2 Larval Staining

1. PBTX (1× PBS, 0.1 % Triton X-100). *See* **Note 1** about alternatives to Triton X-100 detergent.
2. Blocking solution (PBTX, 3 % bovine serum albumen); optional.
3. Microscope slides, glass coverslips, Vectashield mounting medium (Vector laboratories), and nail polish.
4. Primary antisera (*see* Table 1).
5. Secondary antisera conjugated to fluorophores. For example, goat anti-rat IgG-conjugated Alexa-568 (Molecular Probes).

2.3 Imaging

Images were acquired with a Bio-Rad MRC 1024 laser scanning confocal apparatus mounted on a Nikon microscope. Images were processed in image J (free from NIH at http://rsb.info.nih.gov/ij/) and Photoshop (Adobe).

Table 1
Antisera for NMJ markers

Pattern	Reagent (source)	Final dilution
All insect nerves	Anti-HRP (Molecular Probes)	1:200
Muscle cells	Fluorophore-conjugated phalloidin (Molecular Probes)	1:6
Periactive zone	Anti-Nwk, rat [11] Anti-fasciclin II, mouse (Hybridoma Bank[a] #1D4) Anti-DAP160, rabbit [20]	1:500 1:100 1:200
Postsynaptic density (PSD)	Anti-Pak, rabbit [21] Anti-GluR2[b], mouse (Hybridoma Bank[a], #8B4D2)	1:2,000 1:100
Subsynaptic reticulum (SSR)	Anti-Dlg, rabbit [22] Anti-Spectrin, mouse [23]	1:1,000 1:25
Epitope tags	Anti-GFP, rabbit (Molecular Probes) Anti-HA 3 F10, rat (Roche Applied Science) Anti-Myc 9E10, mouse (Roche Applied Science)	1:1,500 1:10 1:10

[a]Monoclonal antiserum obtained from the developmental studies Hybridoma Bank (*see* **Note 2**)
[b]Must use an acid fixative such as Bouin's (*see* **Note 3**), not formaldehyde

3 Methods

3.1 Larval Dissection and Fixation

1. Dissection. Place a larva in the dissection chamber. Under a dissecting scope, pin larva at the anterior and posterior ends with dorsal surface up. Bathe in calcium-free saline, which will inhibit muscle contraction upon incision. Cut along dorsal midline from pin to pin and remove tissue (i.e., gut, salivary glands, fat bodies, and gonads; *see* **Note 4**), leaving brain intact and avoiding damage to the ventral surface. Using pins, secure the edges of the cuticle on both sides near the head and tail, so it lays flat with its interior surface exposed. The nerves and muscles are attached to this surface. For a detailed protocol, *see* ref. 19.
2. Fixation. Pipette out the calcium-free saline and quickly replace with 4 % PFA. Incubate on a gently rotating platform (~50 RPM) for 15–60 min (precise time required varies with different antibodies/epitopes).
3. Washes. Unpin the larva and transfer to a watch glass or small volume (<1 ml) tube using forceps. Wash three times for 15 min each with PBTX or a phosphate buffer that contains a detergent compatible with your antisera.

3.2 Larval Staining

Each primary antiserum must be used at an empirically determined concentration, with monoclonals generally requiring a higher titer than polyclonals (*see* Table 1). Fluorophore-conjugated

secondary antibodies are commonly applied at a final concentration of 1:200. Use small incubation volumes to conserve precious antisera.

1. (Optional) Block 30 min in blocking solution at room temperature with gentle agitation (~50 RPM on a flat rotator).
2. Incubate the larvae in PBTX or fresh blocking solution for 2 h at room temperature with the appropriate concentration(s) of primary antisera. I prefer to incubate in ~100 μl PBTX in a watch glass covered with a glass slide at 4 °C overnight and then for 1 h at room temp on the rocker at 50 RPM. 1 ml Eppendorfs may be used instead of a watch glass. In any case, make sure the vessel is covered to prevent evaporation.
3. Wash three times for 15 min each in PBTX.
4. Repeat **step 2** with secondary antisera. From this point onward, keep samples protected from light, which will attenuate the fluorophores.
5. Wash four times for 15 min each in PBTX.
6. Mounting. Transfer larvae to a glass slide with forceps so that the interior surface faces up. It may be necessary to gently unfold the edges of the cuticle using forceps to get it flat. Wick away excess PBTX using a Kimwipe (twist a corner into a wick and hold it next to the larva on the slide for 2 s) and cover the prep with a small drop of Vectashield mounting medium. Add a cover slip, gently pressing it straight downwards to flatten the larva without crushing it or shearing it. Wipe away excess Vectashield and seal the edges of the coverslip completely with nail polish.
7. Store mounted preps at 4 °C in the dark to preserve fluorophores.

3.3 Imaging Part I: Identifying Functionally Distinct Subcellular Domains in the NMJ

Each abdominal hemisegment of a *Drosophila* larva contains ~30 muscle cells innervated by ~40 motor neurons [3]. In each neuromuscular junction (NMJ), presynaptic sites of neurotransmitter release (synapses) are clustered within distinct spherical "boutons" that form in the motor axon terminal (Fig. 1a, d). Postsynaptically, the muscle cell surrounds these synaptic boutons with complex lamellae, called the subsynaptic reticulum (SSR). The SSR can be visualized using antisera to discs large (Dlg) (Fig. 1b, e), which is a PDZ domain containing scaffold protein [24].

Within synaptic boutons, each individual synapse contains a specialized scaffold that organizes the machinery of neurotransmitter release, identifiable via electron microscopy as a characteristic "t-bar" structure, sometimes called an "active zone" [17]. Across the synaptic cleft from each active zone, membrane-associated scaffolds in the muscle cell, enriched with ligand-gated ion channels

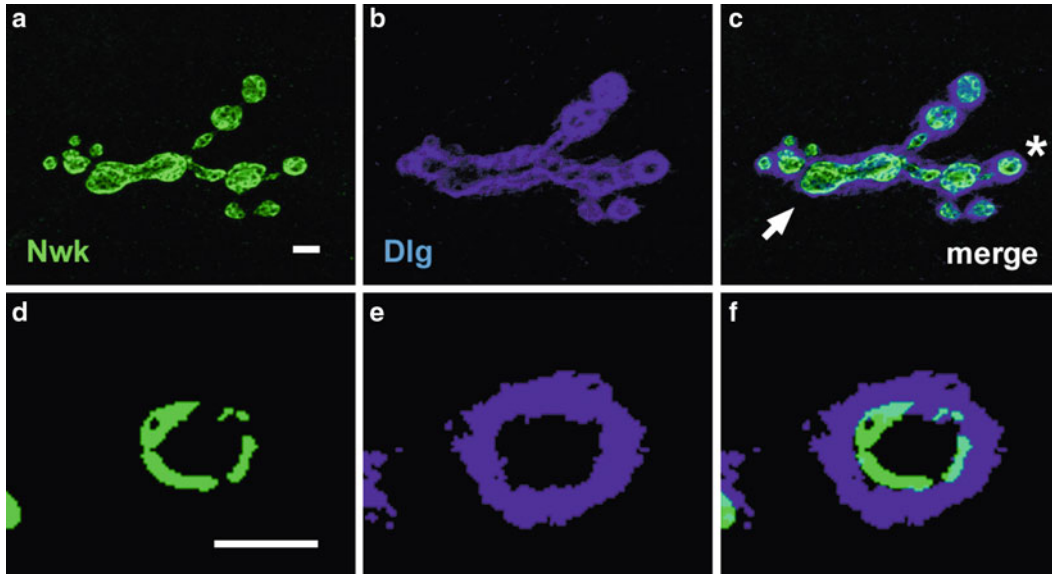

Fig. 1 An NMJ from muscle 4 on segment A2 of a third instar larva stained with anti-Nwk and anti-Dlg to illustrate the major pre- and postsynaptic compartments of the nerve terminal. Panels (**a**–**c**) are derived from a Z-projection of 20 optical sections. The motor axon terminal forms spherical synaptic boutons (**a**) which are surrounded by the subsynaptic reticulum (SSR) (**b**) of the muscle cell. The proximal portion of the motor axon (not labeled) intersects the bouton-enriched region at the position marked by an *arrow*. Except for the SSR, the muscle cell is not labeled. A single bouton, marked by the *asterisk*, is shown at a higher magnification in (**d**–**f**). In (**d**–**f**), a single optical section approximately 0.5 μm in depth cross sections the bouton. Nwk (**d**) lines the inner surface of the bouton membrane in the discontinuous pattern characteristic of the periactive zone. Dlg (**e**) is enriched in the SSR of the muscle cell that envelops the bouton. There is a distinct boundary between the pre- and postsynaptic proteins (**f**) (scale bars = 5 μm)

and cytoskeletal regulators, appear as an electron-dense signature termed the "postsynaptic density" (PSD). Antisera specific for Pak, a postsynaptic kinase, is an excellent marker of PSDs [9].

Many presynaptic growth regulators and endocytic proteins are organized in a domain adjacent to but distinct from active zones. Appearing as doughnut-like rings surrounding each active zone, the periactive zone is a quasi-continuous boundary around sites of neurotransmitter exocytosis that marks a crucial interface between the processes of signal transduction and cytoskeletal dynamics (Fig. 2a) [9]. Nervous wreck is an SH3 adaptor protein that yields a particularly robust signal in the periactive zone [11].

1. *Identifying the NMJ* (Fig. 1a–c). The boutons in a given NMJ rarely lie in one smooth plane. Therefore, the most attractive images will be made from a stack of confocal sections collected as a Z-series and compounded into a Z-projection (using software such as Image J from NIH or AxioVision from Zeiss). Figure 1a–c consists of 20 optical sections, each a composite averaged according to the Kalman algorithm, acquired at a

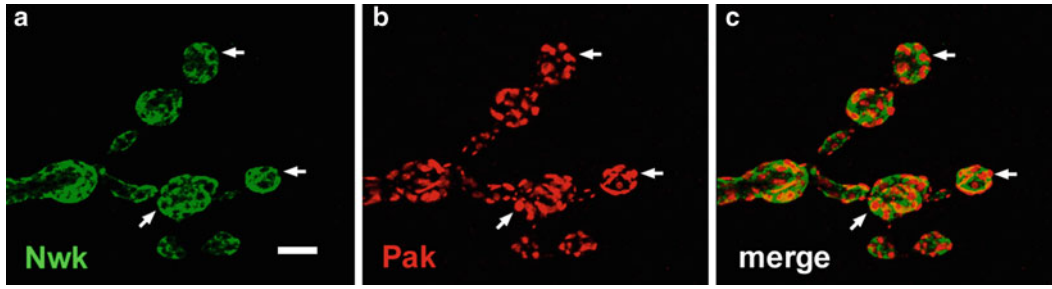

Fig. 2 An NMJ on muscle 4 stained with Nwk and Pak to illustrate the relationship between the periactive zone and active zones/postsynaptic densities. Nwk marks the periactive zone (**a**), a partially continuous network of cytoskeletal and endocytic proteins that surround each punctate active zone, marked by Pak (**b**). *Arrows* mark instances where the relationship is particularly clear. Note that there is virtually no overlap between the Nwk and Pak signals in the merged image (**c**). (scale bars = 5 μm)

Z-step of 0.25 μm. The precise settings are iris 2.2, objective magnification 40×, optical zoom 3.0, laser power 9 % (Nwk) and 20 % (Dlg), gain 1,229 (Nwk) and 1,384 (Dlg), and Kalman $N = 7$.

2. *Cross sections* (Fig. 1d–f). The average diameter of a bouton is ~5 μm. Using a confocal microscope with the iris set near the minimum (*see* **Note 5**), it is feasible to capture optical sections ~0.5 μm thick that represent thin cross sections through the center of synaptic boutons at 40–60× magnification. The optimal iris setting is reached when a hollow, circular outline of a bouton or row of boutons is observed with no background or foreground fluorescence appearing to curve towards the bouton lumen at the upper or lower depths of the field of view. Large boutons with well-preserved spherical boundaries are rare but can be found if one scans many NMJs in different larval segments. Moreover, some antisera or antigens do not yield signals with sufficient intensity to produce an informative image in a thin section (anti-Nwk, anti-HRP, and anti-Dlg are the best I have encountered).

   The settings in Fig. 1, panels d–f, are iris 2.2, objective magnification 60×, optical zoom 3.0, laser power 9 % (Nwk) and 20 % (Dlg), gain 1,345 (Nwk) and 1,399 (Dlg), and Kalman $N = 6$. The image in panels d–f was modified in the following ways. First, in Image J, the "smooth" function was applied to both the Nwk and Dlg channels. Next, in Photoshop, the "threshold" value (under the "image" menu) was reduced 35 % for the Dlg channel and 50 % for the Nwk channel.

3. *The relationship between the periactive and active zone* (Fig. 2). Antisera that stain either active zones or the PSD will generate a punctate pattern complementary to that of the periactive zone and can be used to label the basic functional domains in

synaptic terminals. This relationship is especially clear when NMJs are double labeled with anti-Nwk and anti-Pak.

The settings in Fig. 2 are iris 2.2, objective magnification 60×, optical zoom 3.0, laser power 9 % (Nwk) and 4 % (Pak), gain 1,345 (Nwk) and 1,250 (Pak), Kalman $N = 6$, 20 optical sections, and Z-step = 0.25 μm.

3.4 Imaging Part II: Characterizing the Pre- Versus Postsynaptic Expression Patterns of Epitope- or Reporter-Tagged Proteins

The UAS-GAL4 system is commonly used in *Drosophila* to express transgenes in a tissue-specific manner [25, 26]. It comprises two elements. First is a *Drosophila* "driver" line carrying the yeast transcription factor, GAL4, inserted near to and under the control of a known endogenous promoter. Second is a Drosophila "UAS" line carrying a separate transgenic construct in which a certain open reading frame is linked to the target sequence of GAL4, the Upstream *A*ctivating *S*equence transcription initiator. When the two lines are crossed together, progeny inheriting both elements will express the sequence linked to the UAS element specifically in those cells and at those developmental stages where the GAL4-linked promoter is active. A variety of UAS and GAL4 lines can be obtained from specific laboratories as well as the Flybase stock center (www.fruitfly.org). Custom UAS lines are commonly made by cloning a sequence of interest into the pUAST vector [27] and transforming *Drosophila* via transposition into germline cells. A conventional neuron-specific driver is elav-Gal4, and a strong muscle-specific driver is MHC-Gal4.

Importantly, the *subcellular* localization of the UAS-linked transgene product is determined after transcription and translation according to its structure, not by any feature of the GAL4 driver. The GAL4-UAS system is commonly used for transformation rescue of mutant phenotypes, so it is well established that the protein products of UAS-transgenes can function and localize normally in many cases. Therefore, the subcellular localization of an uncharacterized protein for which antiserum does not exist can be ascertained by expressing it as a fusion protein with an epitope tag and subsequently staining for the tag. HA, GFP, and Myc tags generally do not inhibit protein function, so long as they do not interrupt conserved motifs.

Figure three illustrates an NMJ from a larvae carrying UAS-GFP::actin and elav-Gal4. If actin itself had been labeled (e.g., with fluorescently conjugated phalloidin), the nerve would be invisible due to massive signal from the muscle cell behind it (personal observation; *see* **Notes 6** and **7**). Instead, GFP::actin can be visualized via the fluorescence of GFP alone or, in this case, via anti-GFP antiserum (*see* **Notes 8** and **9**).

The settings for Fig. 3 are iris 2.2, objective magnification 60×, optical zoom 2.0, laser power 2.5 % (GFP) and 9 % (Nwk), gain 1,125 (GFP) and 1,307 (Nwk), Kalman $N = 5$, 20 optical sections, and Z-step = 0.25 μm.

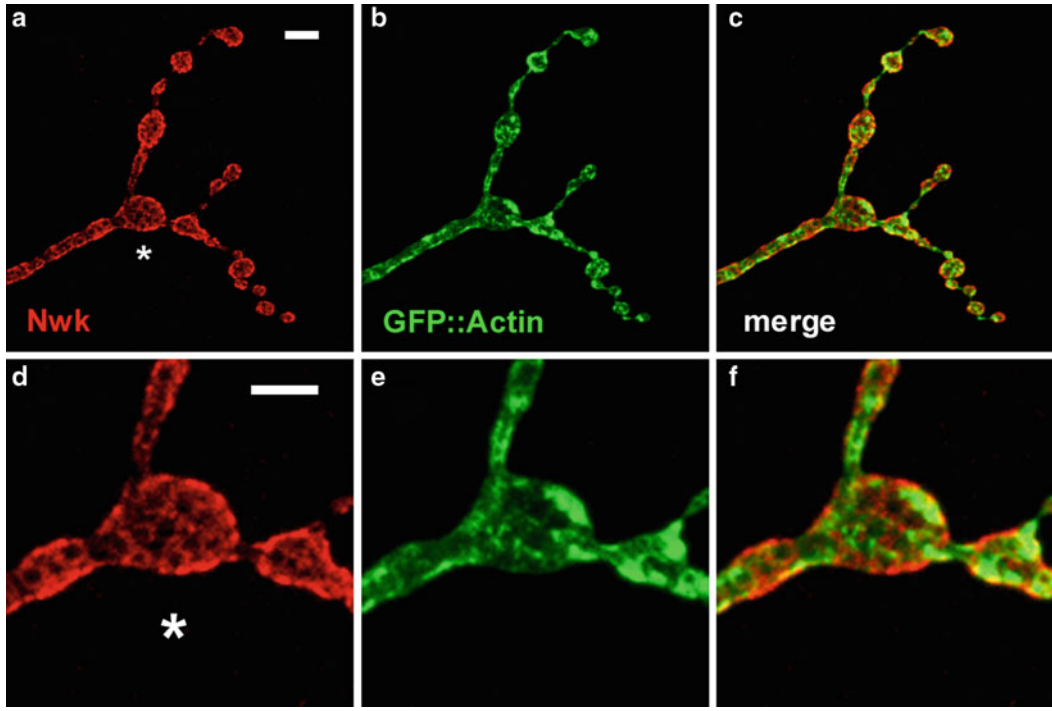

Fig. 3 A Z-projection depicting an NMJ from muscle 4 of an elaV-GAL4; UAS-GFP::actin larva. Nwk highlights the periactive zone (**a**), while GFP::actin, stained with anti-GFP antiserum, is visible in a partially overlapping pattern (**b**) and (**c**). The muscle and SSR are not labeled, emphasizing that the GAL4-UAS system produces cell-specific expression of transgenes. The region marked by the *asterisk* is digitally enlarged in (**d**–**f**). GFP::actin colocalizes with Nwk in the periactive zone but also encroaches into active zones, sometimes forming bright puncta that may represent transient signal transduction or growth events

4 Notes

1. Alternative detergents may be used in the uncommon case where Triton X-100 adversely affects your antiserum. I have experimented with Tween 20; however, it did not fully permeabilize boutons at 0.2 % concentration, yielding incomplete antibody penetration into the nerve and higher background signal. Saponin and SDS are two detergents occasionally used for milder and harsher membrane extraction, respectively. A good summary of fixation and permeabilization principles is available from the Imaging Technology Group at http://www.itg.uiuc.edu/.
2. A library of monoclonal antisera, searchable by target protein or epitope, is available from the Developmental Studies Hybridoma Bank maintained by the University of Iowa at http://www.uiowa.edu/~dshbwww/.

3. Bouin's fixative (10.5 ml): 2.5 ml formalin, 7.5 ml saturated picric acid, 0.5 ml acetic acid. Fix 5–20 min.
4. Gonads can be identified by the third instar stage, so larvae can be sexed if it is necessary to discern genotype [28].
5. The iris or pinhole size is proportional to optical section thickness along the *z*-axis, which is also affected by the numerical aperture of the objective lens and the wavelength of light illuminating the sample. In the past, it was difficult to calculate optical section thickness, but an iris setting of 1.0–2.0 represents the minimum section thickness on the typical rig. The most recent software from Zeiss, AxioVision, calculates section thickness automatically. Keep in mind that in order to view sections of identical thickness using two different wavelengths, iris size may need to be set differently on each channel.
6. The overwhelming background signal encountered when the NMJ is stained with phalloidin results from actin that is concentrated in the Z-bands of the muscle cell. However, muscle nuclei do not contain significant F-actin, and therefore boutons that happen to contact the muscle surface directly above a nucleus may be clearly observed after phalloidin labeling. I used this trick to visualize the general distribution of F-actin around synaptic boutons [11].
7. The lumen of boutons can be labeled with antiserum to synaptotagmin (Syt) [29] or cysteine string protein (CSP) [30], which are regulators of exocytosis located on synaptic vesicles. Counting Syt- or CSP-labeled boutons is a common method for quantifying and comparing synaptic growth phenotypes among mutants [10, 31, 32]. Monoclonal anti-Syt is also available from the Developmental Studies Hybridoma Bank (clone# 3H2 2D7).
8. When visualizing epitope tags, do not use FLAG tags in *Drosophila*, as all anti-FLAG antisera recognize *Drosophila* tissues (nerves and nuclei) and will produce unacceptable background staining.
9. When staining using anti-GFP antisera, always use a secondary antibody conjugated to a fluorophore that emits in the green spectra (such as Alexa 488) because there will be some residual GFP fluorescence in fixed tissues which will otherwise interfere with the green channel. The same logic applies for RFP and potentially other autofluorescent reporters.

Acknowledgments

I am indebted to Barry Ganetzky, Troy Littleton, Tim Fergestad, and Young Ho Koh for teaching me the methodology of *Drosophila* molecular biology and confocal microscopy. I thank Steve Paddock

and Sean Carroll for generously providing time, expertise, and a confocal microscope. This work was supported by NIH grant NS15390 to B. Ganetzky.

References

1. Johansen J, Halpern ME, Johansen KM, Keshishian H (1989) Stereotypic morphology of glutamatergic synapses on identified muscle cells of Drosophila larvae. J Neurosci 9(2):710–725
2. Hoang B, Chiba A (2001) Single-cell analysis of Drosophila larval neuromuscular synapses. Dev Biol 229(1):55–70
3. Chiba A (1999) Early development of the Drosophila neuromuscular junction: a model for studying neuronal networks in development. Int Rev Neurobiol 43:1–24
4. Koh YH, Gramates LS, Budnik V (2000) Drosophila larval neuromuscular junction: molecular components and mechanisms underlying synaptic plasticity. Microsc Res Tech 49(1):14–25
5. Kuromi H, Kidokoro Y (1998) Two distinct pools of synaptic vesicles in single presynaptic boutons in a temperature-sensitive Drosophila mutant, shibire. Neuron 20(5):917–925
6. Umbach JA, Saitoe M, Kidokoro Y, Gundersen CB (1998) Attenuated influx of calcium ions at nerve endings of csp and shibire mutant Drosophila. J Neurosci 18(9):3233–3240
7. Zito K, Parnas D, Fetter RD, Isacoff EY, Goodman CS (1999) Watching a synapse grow: noninvasive confocal imaging of synaptic growth in Drosophila. Neuron 22(4): 719–729
8. Poskanzer KE, Marek KW, Sweeney ST, Davis GW (2003) Synaptotagmin I is necessary for compensatory synaptic vesicle endocytosis in vivo. Nature 426(6966):559–563
9. Sone M, Suzuki E, Hoshino M, Hou D, Kuromi H, Fukata M, Kuroda S, Kaibuchi K, Nabeshima Y, Hama C (2000) Synaptic development is controlled in the periactive zones of Drosophila synapses. Development 127(19):4157–4168
10. Wan HI, DiAntonio A, Fetter RD, Bergstrom K, Strauss R, Goodman CS (2000) Highwire regulates synaptic growth in Drosophila. Neuron 26(2):313–329
11. Coyle IP, Koh YH, Lee WC, Slind J, Fergestad T, Littleton JT, Ganetzky B (2004) Nervous wreck, an SH3 adaptor protein that interacts with Wsp, regulates synaptic growth in Drosophila. Neuron 41(4):521–534
12. Kawasaki F, Zou B, Xu X, Ordway RW (2004) Active zone localization of presynaptic calcium channels encoded by the cacophony locus of Drosophila. J Neurosci 24(1):282–285
13. Zhai RG, Bellen HJ (2004) The architecture of the active zone in the presynaptic nerve terminal. Physiology (Bethesda) 19:262–270
14. Winckler B, Mellman I (1999) Neuronal polarity: controlling the sorting and diffusion of membrane components. Neuron 23(4): 637–640
15. Roos J, Kelly RB (1999) The endocytic machinery in nerve terminals surrounds sites of exocytosis. Curr Biol 9(23):1411–1414
16. Fergestad T, Broadie K (2001) Interaction of stoned and synaptotagmin in synaptic vesicle endocytosis. J Neurosci 21(4):1218–1227
17. Atwood HL, Govind CK, Wu CF (1993) Differential ultrastructure of synaptic terminals on ventral longitudinal abdominal muscles in Drosophila larvae. J Neurobiol 24(8): 1008–1024
18. Ashburner M (1989) Drosophila. Cold Spring Harbor Laboratory, Cold Spring Harbor, NY
19. Sullivan W, Ashburner M, Hawley RS (2000) Drosophila protocols, vol xiv. Cold Spring Harbor Laboratory Press, Cold Spring Harbor, NY, p 697
20. Marie B, Sweeney ST, Poskanzer KE, Roos J, Kelly RB, Davis GW (2004) Dap160/intersectin scaffolds the periactive zone to achieve high-fidelity endocytosis and normal synaptic growth. Neuron 43(2):207–219
21. Harden N, Lee J, Loh HY, Ong YM, Tan I, Leung T, Manser E, Lim L (1996) A Drosophila homolog of the Rac- and Cdc42-activated serine/threonine kinase PAK is a potential focal adhesion and focal complex protein that colocalizes with dynamic actin structures. Mol Cell Biol 16(5):1896–1908
22. Woods DF, Wu JW, Bryant PJ (1997) Localization of proteins to the apico-lateral junctions of Drosophila epithelia. Dev Genet 20(2):111–118
23. Dubreuil RR, Maddux PB, Grushko TA, MacVicar GR (1997) Segregation of two spectrin isoforms: polarized membrane-binding sites direct polarized membrane skeleton assembly. Mol Biol Cell 8(10):1933–1942
24. Budnik V, Koh YH, Guan B, Hartmann B, Hough C, Woods D, Gorczyca M (1996) Regulation of synapse structure and function by the Drosophila tumor suppressor gene dlg. Neuron 17(4):627–640
25. Phelps CB, Brand AH (1998) Ectopic gene expression in Drosophila using GAL4 system. Methods 14(4):367–379

26. McGuire SE, Roman G, Davis RL (2004) Gene expression systems in Drosophila: a synthesis of time and space. Trends Genet 20(8):384–391
27. Brand AH, Perrimon N (1993) Targeted gene expression as a means of altering cell fates and generating dominant phenotypes. Development 118(2):401–415
28. Campos-Ortega JA, Hartenstein V (1997) The embryonic development of *Drosophila melanogaster*, vol xvii, 2nd edn. Springer, Berlin, p 405
29. Littleton JT, Bellen HJ, Perin MS (1993) Expression of synaptotagmin in Drosophila reveals transport and localization of synaptic vesicles to the synapse. Development 118(4): 1077–1088
30. Zinsmaier KE, Hofbauer A, Heimbeck G, Pflugfelder GO, Buchner S, Buchner E (1990) A cysteine-string protein is expressed in retina and brain of Drosophila. J Neurogenet 7(1):15–29
31. Schuster CM, Davis GW, Fetter RD, Goodman CS (1996) Genetic dissection of structural and functional components of synaptic plasticity. I. Fasciclin II controls synaptic stabilization and growth. Neuron 17(4):641–654
32. DiAntonio A, Haghighi AP, Portman SL, Lee JD, Amaranto AM, Goodman CS (2001) Ubiquitination-dependent mechanisms regulate synaptic growth and function. Nature 412(6845):449–452

Chapter 10

Confocal Imaging and Three-Dimensional Visualization of Thick Autofluorescent Specimens

Angela V. Klaus, Valerie Schawaroch, and Kevin J. Frischmann

Abstract

Three-dimensional (3-D) rendering methods (maximum intensity projection, alpha blending, and isosurface rendering) are described for the visualization of thick, autofluorescent, arthropod cuticular structures (e.g., *Drosophila melanogaster* external genitalic structures) imaged by confocal laser scanning microscopy (CLSM). Additionally, specimen mounting and data collection strategies for thick specimens are described. Axial aberration artifacts are discussed in the context of these methods because of the critical roles they play in the quality of final 3-D images.

Key words Confocal microscopy, Spherical aberration, Drosophila, Maximum intensity projection, Volume rendering, Surface rendering, Three-dimensional reconstruction, Volume visualization, Axial aberration

1 Introduction

Confocal imaging offers the ability to produce three-dimensional (3-D) data sets of fluorescent biological specimens. This capability is made possible through the use of a pinhole aperture placed in front of the signal detector which blocks out-of-focus light from inclusion in the final image. The pinhole allows only light from each focal plane in a 3-D object to be collected; this process is called "optical sectioning." If imaging conditions are properly optimized, data sets obtained by optical sectioning can be reconstructed into accurate, 3-D representations of the original specimen.

For some biological materials, the natural endogenous fluorescent signal (autofluorescence) can be exploited in order to determine the overall morphology of a 3-D object. In confocal microscopy, the autofluorescent signal is usually a source of unwanted background which detracts from visualizing the signal of interest. However, for some specimens, such as pollen grains [1] and arthropod cuticular structures [2–5], the autofluorescent signal is a useful source of morphological information.

Stephen W. Paddock (ed.), *Confocal Microscopy: Methods and Protocols*, Methods in Molecular Biology, vol. 1075,
DOI 10.1007/978-1-60761-847-8_10,

1.1 Aberration Artifacts

In order to produce a 3-D reconstruction of a structure which accurately represents the original specimen along the *x*, *y*, and *z* axes, particular attention must be paid to specimen mounting and imaging conditions. This is especially true if the investigator wishes to accurately represent dimensions along the z-axis (axial direction). Artifacts arising from suboptimal mounting and imaging conditions can distort 3-D confocal data sets of thick (~10 μm or more) specimens. Axial artifacts in 3-D data sets arise from two main imaging conditions: (1) refractive index mismatch in the optical setup and (2) increased imaging depth as the illuminating spot penetrates further into a specimen in order to collect deeper optical sections. These conditions, in turn, can result in (1) distortion (compression or elongation) of structures along the *z*-axis (Fig. 2a) and (2) data loss from deeper optical slices (Fig. 2c–f). Spherical aberration of the illuminating spot and scattering/absorption of excitation photons are the major physical causes of axial aberration artifacts in thick specimens [3, 6, 7].

As mentioned above, artifact minimization can be achieved by optimizing specimen mounting and imaging conditions. In order to minimize axial distortion (elongation or compression), refractive index (RI) mismatch between the mounting medium and the immersion medium must be avoided. However, for the issue of increased penetration depth in thick specimens, it is not possible to completely eliminate data loss. Our approach to the latter problem has been to mount thick specimens between two coverslips and image the structures of interest from both sides by flipping the mount (Figs. 1 and 2c–f). Other possible approaches to the problem of data loss include software-controlled attenuation correction either during data collection (*see* **Note 1**) or specialized computational compensation methods performed on acquired data sets [8, 9]. Additionally, volumes collected from each side of a thick specimen can be aligned and reconstructed into a single volume [4].

1.2 Volume Visualization

The depth dimension of 3-D confocal data sets can be viewed in a number of ways. Confocal optical sections can be viewed either individually by successively slicing through a volume or simultaneously as a sequenced array of x, y images with volume depth indicated for each slice. These techniques are extremely useful, but they can be insufficient when an overall picture of the 3-D volume is needed.

Common 3-D rendering techniques for confocal data visualization include volume and isosurface rendering. Advantages of these methods include the ability to (1) produce lighting and shading effects which improve perception of depth and texture, (2) vary opacity settings in order to visualize internal structures, (3) enhance surface textures, and (4) create models that can be rotated interactively (or made into movies) for visualization of the spatial interrelationship of structures from all viewing angles. In instances

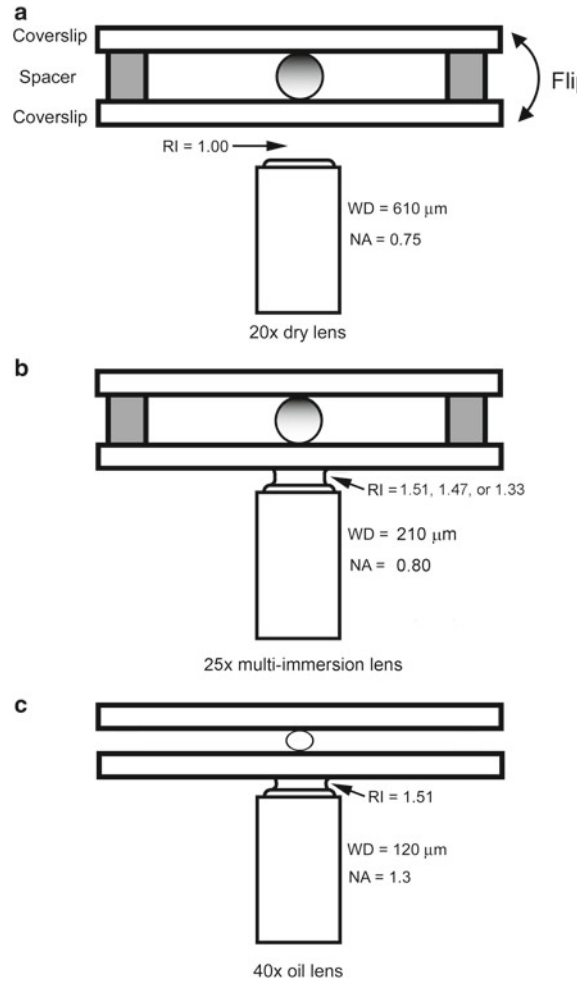

Fig. 1 Side views of mounting method and imaging setup for various sized specimens imaged on an inverted microscope. Lens selection will vary according to what objectives are available to the investigator. (**a**) 20× dry objective lens. Very thick specimens can be accommodated because of the long working distance (610 μm) of the lens. However, the large refractive index mismatch between the immersion medium (air; 1.00) and the mounting medium (e.g., 1.51 for euparal or 1.47 for glycerin jelly) will cause severe artifacts including axial compression and data loss. Increased penetration depth inherent to imaging thick specimens is also a major contributor to data loss from optical sections farthest from the sources of illumination and detection. Spacers are used with larger structures to avoid crushing. (**b**) 25× multi-immersion lens. This lens is equipped with a correction collar which enables the use of variable immersion media (oil, glycerin, or water). The working distance of the lens (210 μm) allows for imaging of intermediate thickness specimens with reduced spherical aberration due to the ability to match refractive indices. The gradient shown within the specimen in *panels A* and *B* represent data loss as a function of penetration depth. (**c**) 40× oil immersion lens. This lens has a short working distance (120 μm) and is therefore suitable for smaller structures. Specimens that are naturally flattened do not require the use of spacers. If specimens are mounted in a medium with an RI close to that of oil, the match in refractive index and the shallow sample depth will minimize axial artifacts. Both the lateral and the axial resolution improve when the numerical aperture (NA) of the lens increases

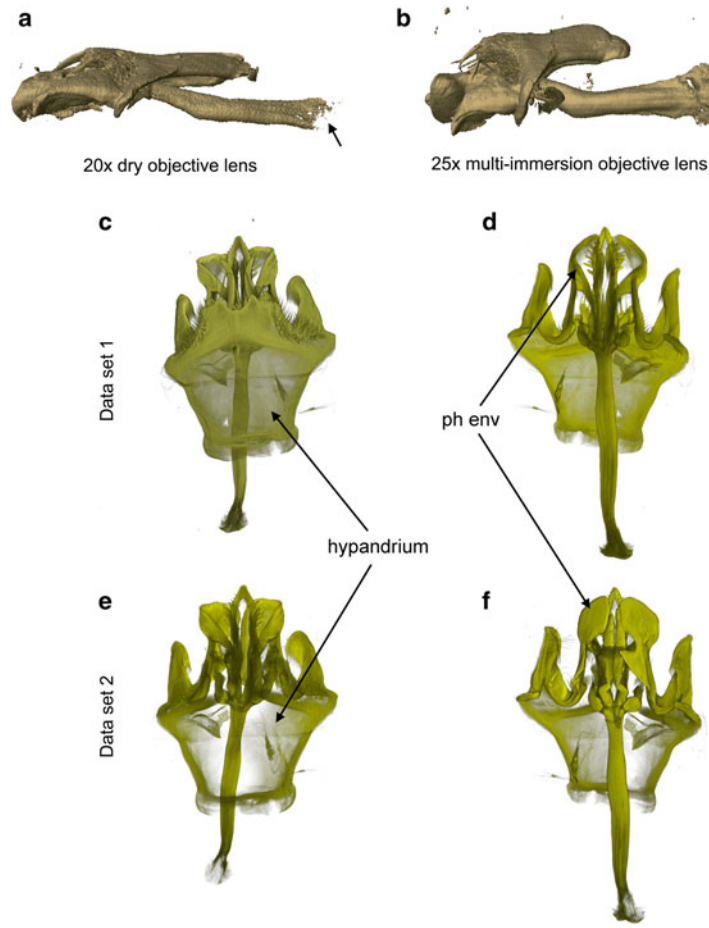

Fig. 2 Axial (*z*-axis) aberration artifacts in a thick autofluorescent specimen. The specimen shown in all panels is the phallic structure from *D. melanogaster* and measures approximately 100–150 μm in thickness as determined by scanning electron microscopy measurements (*see* ref. 3). (**a**) This specimen was mounted in glycerin jelly (RI ~ 1.47) and imaged with a dry objective lens (RI of air = 1.00); therefore, the refractive index mismatch was severe. Note that the tip of the aedeagal apodeme (*arrow*) was lost during image processing. (**b**) This specimen was mounted in euparal medium (RI when dry ~1.52) and imaged with oil as an immersion medium (RI = 1.51) using the multi-immersion lens described in Fig. 1b. Note the severe compression of the data set in (**a**) vs. (**b**). (**c**, **d**) These images depict one complete data set that has been volume rendered as viewed from the side of specimen closest to (panel **c**) and farthest from (panel **d**) the sources of illumination and detection (laser and photomultiplier tube [PMT], respectively). (**e**, **f**) The structure shown in panels **c** and **d** was imaged again after flipping the mount. In this example, (**f**) is now the side of specimen closest to the laser and PMT, and (**e**) is the farthest away. Panels (**c**) and (**e**) both depict the "shield side" of the hypandrium; a comparison of the two renderings clearly shows a significant loss of data in (**e**). Likewise, a comparison of panels (**d**) and (**f**), which depict the other side of the specimen, shows significant data loss in panel (**d**) as judged by the partial loss of the phallic envelope (ph env). Panels **a** and **b** were rendered using the surface rendering function in the Surpass module in Imaris; panels (**c**–**f**) were rendered using the blend function in Surpass

where imaging conditions are optimized (i.e., aberration free or very nearly so), it is possible to use advanced 3-D visualization techniques to create accurate representations of the original object along all axes (*x*, *y*, and *z*).

This chapter describes the mounting, imaging, and 3-D visualization techniques that we have used with great success for confocal imaging of thick autofluorescent insect cuticular structures.

2 Materials

2.1 Obtaining Specimens

Drosophila melanogaster (wild type) can be ordered from a variety of sources: (1) scientific supply houses which distribute live materials such as Carolina Biological Supply Co. (www.carolina.com) and Ward's Natural Science Supply company (www.wardsci.com) and (2) *Drosophila* stock centers such as the Bloomington *Drosophila* Stock Center at Indiana University at Bloomington Indiana for mutant animals (http://flystocks.bio.indiana.edu/) and the UC San Diego *Drosophila* Species Stock Center (https://stockcenter.ucsd.edu/info/welcome.php). A complete listing of stock centers can be found on Flybase (http://flybase.org).

2.2 Coverslips for Mounting and Spacing

Fisher Scientific brand cover glass No. 1.5 (0.16–0.19 mm nominal thickness), 22 × 50 mm (Fisher scientific catalog # 12544D).

2.2.1 Top and Bottom Glass

2.2.2 Spacers

Use spacers as needed when mounting thick, deformable specimens. Whole coverslips or broken fragments can be used to create spacers. The thickness of the spacers can be varied by using coverslips of different thicknesses (see below).

1. No. 0 (0.10 mm nominal thickness) (Fisher catalog # NC9115219).
2. No. 1 (0.13–0.17 mm nominal thickness) (Fisher catalog number 12542B).
3. No. 1.5 (0.16–0.19 mm nominal thickness) (Fisher catalog number 12541B).

2.3 Chemicals

1. Euparal (Bioquip Products, #6372A).
2. Glycerin (Ward's #945 V7206 or Fisher #S74606).
3. Gelatin (Sigma #G-1890, Type A from porcine skin).
4. KOH.
5. 70 % Ethanol.
6. Glacial acetic acid.

2.4 Clearing and Mounting Media

2.4.1 Clearing Medium (for Soft Tissue Removal)

To make a 10 % (w/v) KOH solution, dissolve 10 g KOH pellets in 100 ml distilled or deionized water. To make 10 % glacial acetic acid, add 10 ml of glacial acetic acid to 90 ml of distilled or deionized water. Mix gently.

2.4.2 Glycerin Jelly Mounting Medium

Dissolve 1 g of gelatin in 17 ml of boiling distilled or deionized water. Remove the solution from heat and mix by swirling (this minimizes bubbles or foam). Add 17 ml of glycerin and mix by swirling, making sure that all the gelatin has dissolved.

2.4.3 Euparal Mounting Medium

This medium comes prepared and ready for use from the manufacturer.

3 Methods

Specimens were mounted between glass coverslips in euparal (permanent mountant) or glycerin jelly (nonpermanent mountant) and imaged on a Zeiss LSM 510 confocal laser scanning microscope (CLSM).

3.1 Specimen Preparation

3.1.1 Step I: Initial/Gross Dissection of Male Genitalia and Removal of Soft Tissue

Dried museum insect specimens mounted on points or pins must be relaxed or softened in a relaxing chamber (*see* **Note 2**) prior to dissection. After approximately 2 days, the insect should be pliable, not brittle. Remove the posterior half of the abdomen using iridectomy scissors. For insects stored in 70 % ethanol (or recently sacrificed), use forceps and/or pins to pull off the posterior half of the abdomen. Clear (or remove) the soft tissue by placing the posterior half of the abdomen in a 0.6 ml Eppendorf containing 10 % KOH solution (*see* **Note 3**). Place the tube in a heated water bath (70 °C) for 1.5–2.5 h.

3.1.2 Step II: Arrest the Clearing Process

The clearing of the tissue by KOH is curtailed either by (a) placing the specimen in 10 % glacial acetic acid solution to neutralize the specimen tissues (as used in the euparal based procedure) or (b) by moving the specimen through a series of washes in water followed by ethanol (*see* **Note 4**).

3.1.3 Step III: Dissect Out the Structure of Interest and Remove Any Ancillary Material

This final dissection with disarticulation prior to mounting is performed in a more viscous medium (a) clove oil for the euparal-based procedure and (b) glycerin for the glycerin jelly-based procedure.

3.2 Specimen Mounting

Instead of using the traditional glass slide and coverslip, specimens are mounted between two coverslips (Fig. 1). This allows for image capture from both sides of the specimen in order to compensate for data loss from deeper optical slices (Fig. 2c–f).

Specimens are mounted between two rectangular 22 × 50 mm coverslips (*see* **Note 5**), and pieces of coverslip placed to either side of specimen serve as spacers between the rectangular coverslips (*see* Fig. 1 and **Note 6**). Spacers are necessary to prevent crushing and subsequent loss of the 3-D nature of the specimen. Spacers are "glued" to the outer rectangular coverslip using a thin layer of mounting media. Whenever possible, the smallest spacer size should be used to make the thinnest possible mount without compressing the specimen. For insect cuticular structures, we have had good results with specimens mounted in either euparal or in glycerin jelly (*see* Subheading 3.1). Euparal mounts need to cure in a 70 °C oven for at least 2–3 days. Glycerin jelly mounts should be allowed to solidify at room temperature for 1 day under the pressure of a flat weight.

3.3 Confocal Imaging

In our previous studies of glycerin jelly and euparal-mounted insect cuticular structures [2, 3], we detected little or no photo bleaching; therefore, confocal imaging is greatly simplified for these specimens because of the ability to use very slow scan speeds, full laser intensity, and line averaging (*see* **Note 7**).

3.3.1 Scan Speed, Laser Intensity, and Averaging

3.3.2 Choice of Objective Lens

The choice of objective lens is critical for most imaging projects and relies on a number of factors including numerical aperture and working distance (for a detailed overview, *see* ref. 1). For imaging insect structures, we are generally guided by sample thickness in our choice of objective lens. As shown in Fig. 1, longer working distance lenses are used for imaging thicker structures.

3.4 Image Processing and Volume Visualization

Generally, we have found that no single program meets all our processing and visualization needs; therefore, we use a combination of freeware, confocal manufacturer, and stand-alone commercial software packages to view, process, and render 3-D data sets. In our lab, we currently use Image J (http://rsb.info.nih.gov/ij/), the projection module in the Zeiss LSM Image Browser, (www.zeiss.com), and Imaris by Bitplane, Inc. (http://www.bitplane.com/). Many other programs are available, and the method used for 3-D visualization will vary according the needs of the research project. Described below are the processing and 3-D visualization strategies we use for confocal data sets generated from thick autofluorescent cuticular structures.

3.4.1 Image Processing: Background Removal, Filtering, and Contrast Adjustments

The image-processing steps used to prepare our confocal data sets after acquisition for improved visualization are, in order, (1) set a minimum intensity threshold so that background values do not obscure the data of interest, (2) apply a contrast stretch so the darkest parts of interesting structures are near black and the brightest parts are maximally bright (this step may not be required for all data sets), and (3) apply a smoothing filter to reduce noise.

In general, confocal images are inherently noisy, so smoothing is usually needed for optimum results. Commonly employed smoothing methods are Gaussian or median filtering. These filters use "convolution kernels" to replace the value of each voxel with a new value that is computed using the intensities of the surrounding voxels, thus reducing local intensity variations (noise). The size of the kernel or "voxel neighborhood" is specified by the user as a filter width, which is given in number of voxels or as a distance. While a larger filter width tends to provide greater noise reduction, one must be conservative, because details smaller than the filter width are usually lost. Deconvolution can also reduce noise without this loss of resolution; however, in the current work, a 3-D Gaussian filter (combined with line averaging during data acquisition) was the chosen approach for noise reduction.

Image processing and visualization times, in general, can be reduced if the 3-D data set is initially cropped to only include the object and omit extraneous field of view. This often significantly reduces the CPU time for all remaining functions.

3.4.2 Visualization of 3-D Volumes

Three methods of volume visualization are routinely used for analyzing and presenting morphological details of autofluorescent cuticular structures: (1) maximum intensity projection, (2) alpha blending, and (3) isosurface rendering.

Maximum intensity projection (MIP) is an extremely useful technique as it is easy to perform and requires minimal computing power. MIP allows for rapid initial visualization of results and can be used exclusively for final rendering if only a limited number of viewing angles are required to represent the structure(s) of interest. When the number of pixel rows or columns in each confocal slice is far greater than the number of slices (as is usually the case), MIP rendering of the x, z or y, z "side views" usually gives a poor quality image. MIP does not necessarily provide accurate depth cues in a still image. Bright internal structures can be perceived as nearer if they overlay or obscure the faint (truly near) portions in the specimen or object (Fig. 3). Therefore, accurate depth perception in a MIP requires animation or stereo rendering [10]. A notable illustration of this "depthless" property is seen when a MIP rendering is viewed from opposite sides of the data set; the images will be identical but will appear as mirror images. For creating maximum intensity projections, we have found Image J and the Zeiss LSM Image Browser (both available as freeware) to be capable software packages for this simpler approach to rendering a 3-D volume. Additionally, the Zeiss LSM Image Browser has the capability of rendering a MIP image in combination with a more advanced blending function (see below), which often allows for improved MIP visualization (Fig. 3)

Alpha blending is typically referred to simply as "blend" mode in volume rendering software. In typical color images, each pixel

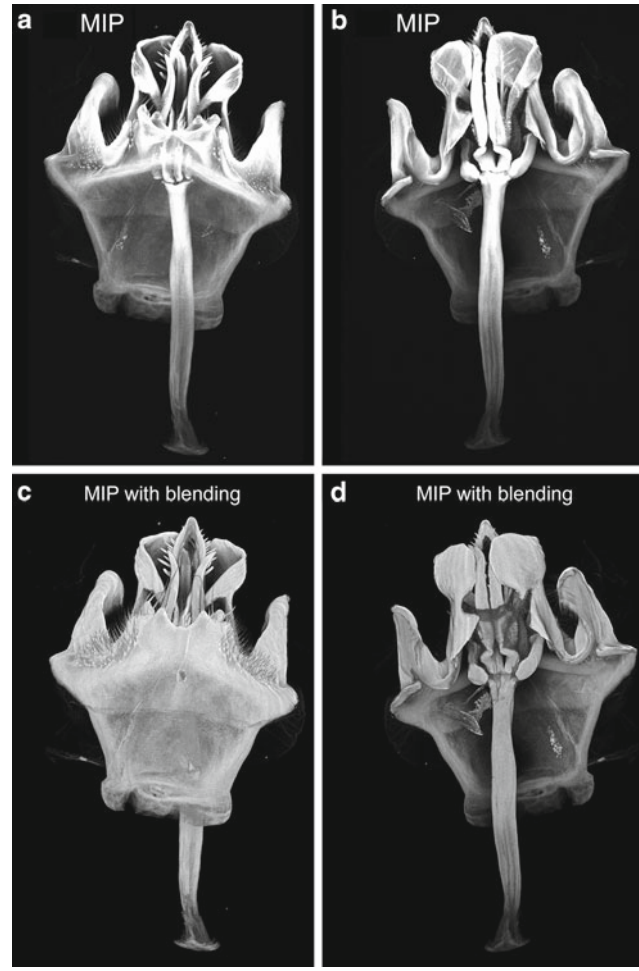

Fig. 3 Maximum projection intensity (MIP) and MIP with blending. (**a**, **b**) Pure maximum intensity projection images. The algorithm used for MIP identifies the most intense value along a given line-of-site and uses that intensity as the pixel value in a two-dimensional projection image. For some types of data sets, such as those shown in panels (**a**) and (**b**), this method of volume rendering can be misleading if the most intense values appear in the middle of the data set. (**c**, **d**) Maximum intensity projection with alpha blending. This method combines MIP with alpha blending functions. The top-down views shown here are similar to those obtained with pure alpha blending (*see* Fig. 2c–f). All panels were rendered with the freeware version of the Zeiss LSM Image Browser

holds a value for each of the red, green, and blue (RGB) color channels. Those three values are combined to determine the color at that pixel. The concept of a fourth "alpha" or transparency channel was introduced to allow control over the blending of multiple overlaid images in a way that shows the front-to-back order [11]. When alpha blending is used for 3-D volume rendering, the voxels that are nearer the viewer are always visible. One can, however,

adjust the transparency so that the degree of opacity can be controlled to either hide or reveal any structure that lies underneath. Therefore, unlike MIP, the alpha blending method of volume rendering conveys accurate depth information even in a non-stereo still image. Because the lower intensity voxels fade from pure color gradually toward black, a lighter background is often used to increase visibility of lower intensities (this is in contrast to MIP images which are rendered on a black background). MIP images generally require very little adjustment, while blending usually requires multiple cycles of contrast and opacity adjustment in order to arrive at the ideal image. We have found that software, which uses 3-D graphics acceleration hardware (such as Imaris), is the best choice when using blending. When graphics acceleration is used, instant or near-instant feedback is obtained, making it simpler to see how adjustments will affect the final rendering. Another very useful advanced volume rendering technique is ray tracing. We have not used ray tracing extensively for the visualization of insect cuticular structures; however, a description of the technique can be found in **Note 8**.

Unlike the previously mentioned rendering methods, isosurfaces are not generally referred to as "volume rendering" because they do not attempt to represent the entire data volume as a 3-D matrix of discrete sampling points. While so-called volume rendering approaches do tend to hide a great many of those sampling points (typically those points of low intensity), isosurface rendering essentially discards most of the information that does not fall near a single intensity. Instead of placing the surface at the center of each voxel that exactly matches the chosen intensity (which would usually create significant artifacts), the position of this iso-value (or "threshold" as it is referred to in most software) within the data volume is computed by an interpolation algorithm known as "marching cubes" [12]. Isosurfaces are desirable when one wishes to represent the structure of interest with a distinctly solid appearance (Fig. 4).

4 Notes

1. Some confocal manufacturers may have an attenuation correction function available in their data acquisition software.
2. To relax (soften) a dried insect specimen requires placing the dried insect in a controlled humid environment. A relaxing chamber can be purchased from scientific supply company or built by filling a desiccant chamber with water instead of desiccant. Pinned insects are placed on foam tray in the chamber above the water.
3. "Clear" means to selectively degrade the tissue. Softer tissue is destroyed early in the early in the process (i.e., short-term

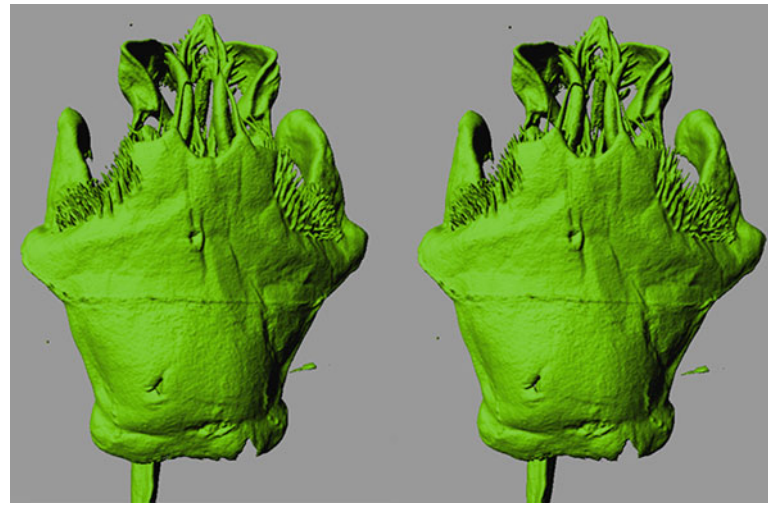

Fig. 4 Isosurface rendering of the *D. melanogaster* hypandrium, shown as a stereopair. These images were created using the surface rendering function in the Surpass module in Imaris

exposure). Usually clearing is done only long enough to remove soft tissue. The degree of tissue destruction depends upon the length of time the specimen remains in the clearing solution. Clearing can be performed at room temperature or hastened by heating (e.g., 17 h at room temperature equals approximately 2.5 h of heating at 70 °C).

4. Wells (depressions/concavities) within a spot plate contain either water or 70 % ethanol. The dissected specimen is placed in distilled water for 5–15 min to remove KOH. The specimen is then transferred to 70 % ethanol for 5–15 min and transferred again to a 70 % ethanol wash. Ethanol treatment partially dehydrates the specimen before placement in glycerin.
5. Most objective lenses are designed to work optimally with a No. 1.5 cover slip (170 μm nominal thickness).
6. Spacers are constructed using square coverslips (Nos. 0–1.5). A single spacer (or combination of spacers) is broken in half, and each half is placed to either side of the specimen. The required thickness of the spacer can be determined by trial and error using the dissecting liquid (clove oil or glycerin) or can be measured along the z-axis using a micrometer.
7. A Zeiss LSM 510 confocal laser scanning microscope (CLSM) equipped with an Axiovert 100 M inverted microscope was used for our investigations. A helium/neon (HeNe) laser (543 nm) set on full power was used for excitation, and a long pass 560 nm filter was used for detection. The collection

settings were chosen to maximize quality within the constraints of computer memory capacity and time required for image collection. These aspects will need to be optimized for each investigator. Image frames were collected at an image resolution of 1024×1024 pixels. Eight-bit data were collected at a dwell time of 12.80 μs/pixel, and line averaging was set to 2. The pinhole was set to 1.00 airy units. The gray scale was set so that only a few saturated pixels (red) were visible in the slice within the specimen that had the most intense fluorescence and black (offset) corresponded to a setting that just eliminated blue pixels on the monitor. During image acquisition, one typically strives to avoid clipping of the dynamic range (avoid having any pixel intensities at the minimum or maximum possible values). This means that in a properly acquired image, (1) the background is not at zero and (2) the brightest structures are not seen as bright and contrasted as they could be made to appear. After the data set is acquired, it is simpler to determine the baseline and maximal intensities for the structures of interest, and these are used to set thresholds to hide less important data (e.g., background), which is followed by stretching the remaining intensity range to improve contrast.

8. Ray tracing is a term that seems to vary in definition, but it can generally be said that *conceptually* the goal is to calculate how a light ray (or typically multiple rays) is affected by interaction with one or more objects before it reaches (or does not reach) the eye of the viewer. This calculation is used to determine the color and intensity of each pixel in the resulting image. Ray tracing has all the advantages of alpha blending and more, save acceleration by graphics hardware. This advanced rendering approach can be used to show shadowing effects, which even further enhance the perception of relative depths and heights in the data set beyond what is seen with a basic alpha blending approach. There are even more adjustments to make, such as the number of lights, the color and intensity of the light(s), as well as object transparency and contrast, but the results can be quite dramatic. With a more advanced software package (such as Imaris), one may have the ability to pre-calculate ray tracings from multiple viewing angles and thereby take advantage of 3-D graphics acceleration hardware to interactively rotate, pan, and zoom in three dimensions.

Acknowledgments

VS acknowledges the generous support for this work from a National Science Foundation award (DEB0075360), two PSC-CUNY awards (60052-34-35 and 67621-00-36), and a Eugene

M. Lang Junior Faculty Research Fellowship. VS also wishes to thank Dean Myrna Chase of the Weisman School of Arts and Sciences of Baruch College for reassigned time.

References

1. Paddock SW (1999) An introduction to confocal imaging. In: Paddock SW (ed) Confocal microscopy: methods and protocols. Humana Press, Totowa, NJ, pp 1–34
2. Schawaroch V, Grimaldi D, Klaus AV (2005) Focusing on morphology: applications and implications of confocal laser scanning microscopy (Diptera: Campichoetidae, Camillidae, and Drosophilidae). Proc Entomol Soc Wash 107:323–335
3. Klaus AV, Kulasekera VL, Schawaroch V (2003) Three-dimensional visualization of insect morphology using confocal laser scanning microscopy. J Microsc 212:107–121
4. Zill S, Frazier SF, Neef D, Quimby L, Carney M, Dicaprio R, Thuma J, Norton M (2000) Three-dimensional graphic reconstruction of the insect exoskeleton through confocal imaging of endogenous fluorescence. Microsc Res Tech 48:367–384
5. Galassi DMP, De Laurentis P, Giammatteo M (1998) Integumental morphology in copepods: assessment by confocal laser scanning microscopy (CLSM). Fragmenta Entomologica (Roma) 30:79–92
6. Diaspro A, Federici F, Robello M (2002) Influence of refractive-index mismatch in high-resolution three-dimensional confocal microscopy. Appl Optics 41:685–690
7. de Grauw CJ, Frederix PLTM, Gerritsen HC (2002) Aberrations and penetration in in-depth confocal and two-photon microscopy. In: Diaspro A (ed) Confocal and two-photon microscopy: foundations, applications, and advances. Wiley-Liss, New York, NY, pp 153–169
8. Can A, Al-Kofahi O, Lasek S, Szarowski DH, Turner JN, Roysam B (2003) Attenuation correction in confocal laser microscopes: a novel two-view approach. J Microsc 211:67–79
9. Wu H-X, Ji L (2005) Fully automated intensity compensation for confocal microscope images. J Microsc 220:9–19
10. Schroeder W, Martin K, Lorensen B (1998) The visualization toolkit, 2nd edn. Prentice Hall, Upper Saddle River, NJ
11. Porter T, Duff T (1984) Compositing digital images. Comput Graph 18:253–259
12. Lorensen W, Cline H (1987) Marching cubes: a high resolution 3d surface reconstruction algorithm. Comput Graph 21:163–169

Chapter 11

Vital Imaging of Multicellular Spheroids

Paulo J. Oliveira, Edward L. Perkins, and Jon Holy

Abstract

Cell behavior is significantly different in two-dimensional and three-dimensional culture conditions, and a number of methods have been developed to establish and study three-dimensional cellular arrays in vitro. When grown under nonadherent conditions, many types of cells form structures called multicellular spheroids (MCSs), which have been popular models to study cell behavior in a three-dimensional environment. The histoarchitecture of MCSs derived from malignant cells resembles that of tumors, and there is rapidly increasing interest in using these structures to more accurately understand the dynamics of cancer cells in situ, including their responses to chemotherapeutics. Confocal microscopy is an extremely useful method to investigate cell behavior in MCSs due to its ability to more clearly image fluorescent probes at some depth in three-dimensional structures. This chapter describes some basic approaches toward visualizing a variety of fluorescent probes in MCSs.

Key words Multicellular spheroid, Vital imaging, Fluorescent labeling, Mitochondria, Nuclei

1 Introduction

An intriguing approach toward assessing cell function by microscopical methods is the use of multicellular spheroids (MCSs) as experimental material. Although individual cells in monolayer culture generally yield the best resolution and clearest imaging, their behavior can be quite different from that of cells existing in their normal milieu, namely, surrounded by other cells and/or extracellular matrix. MCSs can be used to strike a balance between studying cell behavior under more natural conditions while allowing for a significantly better level of imaging that is achievable with an actual tissue or organ. MCSs have been constructed from untransformed cells in order to study tissue organization and function in vitro as well as from transformed cell lines in order to study malignant cell behavior in a more tumor-like setting [1–3]. This chapter deals solely with the use of transformed cell lines to study cell behavior in living MCSs treated with various vital imaging probes.

Stephen W. Paddock (ed.), *Confocal Microscopy: Methods and Protocols*, Methods in Molecular Biology, vol. 1075,
DOI 10.1007/978-1-60761-847-8_11,

Similar to in situ solid tumors, MCSs derived from transformed cell lines display structural heterogeneity and exhibit a range of microenvironments with respect to oxygen, glucose, pH, and other gradients. A primary difference between the two reflects the vascularization of in situ tumors, but in both cases, gradients of diffusible material are dominant factors in the establishment of functionally distinct regions. In general, all of the cells in smaller MCSs may remain viable, but larger MCSs characteristically consist of an outer shell of proliferating cells, an intermediate layer of quiescent cells, and a core of moribund or dead cells [4, 5]. This architecture is usually presumed to reflect a low internal oxygen pressure, but the actual mechanisms influencing survival, growth, and death in an MCS appear to be more complex [3].

The behavior of cells in MCSs is usually quite different than that of the same cell line grown as an adherent monolayer. Notably, MCSs commonly exhibit increased resistance to anticancer agents compared to monolayer cultures [6–9]. This effect has been termed multicellular-mediated resistance [10] and arises from multiple mechanisms. For example, the expression of integrins, cadherins, cyclin-dependent kinase inhibitors, and other proteins can all be altered in three-dimensional cultures of MCSs compared to their monolayer counterparts [9, 11–14]. Furthermore, mathematical modeling studies indicate that drug penetration is a critical feature of the increased resistance of MCSs to chemotherapeutic treatment [15] and the expression of P-glycoprotein can influence the distribution of cell-permeant xenobiotic compounds within MCSs [16–18]. Together, these observations have led to compelling arguments for the superiority of MCSs over monolayer cultures for in vitro drug testing [3, 19, 20]. Germain to this chapter, MCSs ranging from a few dozen to many hundreds of cells in size are also ideal platforms to showcase the advantages of confocal microscopy over routine epifluorescence microscopy in imaging thicker specimens and multicellular aggregates.

2 Materials

2.1 Cell Lines and Culture Conditions

Most of our studies have so far been conducted using various human and mouse cancer cell lines because of the ease in maintaining continuous cultures for experimental material. Some cell lines readily form well-organized MCSs when maintained in suspension, whereas others are not suitable in that lack of adhesion to a surface triggers a type of cell death termed *anoikis*. In addition, some cell lines simply do not adhere well enough to each other in suspension to form a well-organized MCS (e.g., PC-3 prostate cancer cells and H9c2 myoblasts). In some cell lines such as MCF-7 breast cancer cells, MCS formation is sensitive to specific culture conditions [3], and the best approach for a particular cell line can

either be suggested from the literature or derived empirically. Overall, the form, function, ontogeny, senescence, and death of MCSs are composite reflections of both the cell line and the culture conditions.

One of the most straightforward approaches to producing MCSs is to simply culture dispersed cells in suspension; MCSs can subsequently form either from an aggregation of suspended cells, by the cohesion of daughter cells from a mitotically active founder cell(s) or a combination of both processes. A number of different methods to keep cells in suspension during MCS formation have been described and include the use of spinner flasks, roller tubes, plating cells on bacteriological-grade culture dishes, or adding a cell suspension to a dish that has been coated with agarose to prevent attachment. We normally use bacteriological-grade dishes to establish MCSs in static cultures, which give acceptable results for most of the cell lines we commonly use (*see* **Note 1**). We have adapted most of the cell lines we use in our laboratory to a standard cell culture medium consisting of Dulbecco's modification of Eagle's medium (DMEM; GIBCO Biologicals, Grand Island, N.Y.), 1 mM sodium pyruvate, and 7.5 % Fetal Clone III (FCIII; HyClone, Logan, UT).

2.2 Fluorescent Probes

Three different examples of vital imaging approaches using MCSs are discussed here, namely, (a) imaging cell viability and nuclear and mitochondrial dynamics using calcein-AM, Hoechst dyes, and tetramethylrhodamine methyl ester (TMRM); (b) imaging the uptake and distribution of certain drugs that are intrinsically fluorescent; and (c) using cells transfected with fluorescent reporter constructs to seed MCSs. If the experiment only requires a relatively short imaging period (e.g., 10 min or less), fluorescent probes can be added directly to the medium used to culture MCSs. However, most media intended for use in a CO_2 incubator soon become excessively basic when kept outside of the incubator, as occurs, for example, during time-lapse studies on the stage of a confocal microscope. For these experiments, the media can be modified to maintain a neutral pH outside of an incubator (*see* **Note 2**).

1. Tetramethylrhodamine methyl ester (TMRM; catalog no. T668, Molecular Probes, Eugene, OR): A mitochondrial membrane potential-sensitive probe. TMRM predominantly labels polarized mitochondria (i.e., mitochondria with transmembrane electric potentials generated by respiration) a bright red color. A primary stock solution of 10 mg/ml is prepared by diluting the contents of a 25 mg vial with 2.5 ml dimethyl sulfoxide (DMSO). The resulting solution will have a deep red color and should be divided into small aliquots and kept frozen and protected from light (*see* **Note 3**).

When needed for experiments, a working stock solution is prepared by diluting the primary stock 1:100 in culture medium lacking serum (e.g., add 1 μl of 10 mg/ml TMRM to 99 μl DMEM). Add 1.5 μl of working stock/ml of cell culture medium (containing MCSs) and incubate for about 1 h in a cell culture incubator prior to imaging. The working solution can be stored in a freezer and thawed when needed; it can withstand a few freeze-thaw cycles over about 7–10 days. TMRM can be used to assess differences in the morphology of functional mitochondrial as well as the magnitude of the mitochondrial transmembrane electric potential (*see* **Note 4**). Depending on the experimental conditions and probe concentration, TMRM can be used in a "self-quenching mode," where a decrease in membrane potential will initially result in increased TMRM fluorescence or in the "non-quenching" mode, where a decreased mitochondrial membrane potential will result in decreased probe fluorescence [21, 22]. The ideal concentration for visualizing mitochondria in MCSs made from different cell lines can be empirically determined; a final concentration of between 100 and 200 nM has worked well for all of the cell lines we have examined to date.

2. Calcein-AM (catalog no. C1430, Molecular Probes): An esterase substrate that living cells hydrolyze to yield calcein, a membrane impermeant, polyanionic fluorescein derivative. A stock solution of 10 mM is prepared by diluting the contents of a 1 mg vial with 100 μl DMSO. The resulting solution is colorless and should be divided into small aliquots and stored as described for TMRM. When needed for experiments, a working solution should be prepared by performing a 1:10 dilution in culture medium lacking serum (e.g., add 10 μl of 10 mM calcein-AM to 90 μl DMEM). 2.5 μl/ml of the working stock is added to culture media containing MCSs for about 1 h prior to imaging. Calcein-AM begins to be hydrolyzed once diluted in aqueous solution, so it is best to make up just the amount of working stock required for each experiment (*see* **Note 3**). This is a useful probe to assess cell morphology and viability, as calcein is retained in living cells upon cleavage of the acetoxymethylester moiety by cellular esterases [23].

3. Hoechst (bisBenzamide): A DNA intercalator that inserts into A-T rich regions of chromatin and labels nuclei blue. A stock solution of Hoechst 33342 (Catalog no. B 2261, Sigma Chemical Co., St. Louis, MO) of 1 mg/ml is made in water and stored in the dark at 4 °C. Other varieties of Hoechst are available, but 33342 is reported to penetrate living cells somewhat more readily than, for example, 33258. Hoechst is a suspected mutagen, and the use of gloves when handling is advised.

4. Sanguinarine: A benzophenanthridine alkaloid that binds to C-G rich regions of DNA. A number of studies have focused on the ability of sanguinarine to induce malignant cell death by triggering apoptosis [24–26]. Sanguinarine has been reported to induce a bimodal pattern of cell death, with lower concentrations triggering caspase activation and apoptosis, and higher concentrations causing oncosis, or "blistering cell death" in the absence of caspase activation [26, 27]. Sanguinarine can be visualized with a blue Krypton-Argon laser (488 nm excitation line) in conjunction with either a green 515/30 nm band pass filter or a red 605/75 band pass filter (*see* **Note 5**), and previous studies showed that sanguinarine rapidly accumulates within the nucleus [28]. A 50 mM stock solution of sanguinarine (sanguinarine chloride, catalog no. S 5890, Sigma) is made in DMSO, aliquoted into small volumes, and stored in the freezer. A working stock solution of 500 μM is made by diluting the 50 mM stock 1:100 in serum-free culture medium just before use and 2–40 μl/ml added to make final concentrations of between 1 and 20 μM, depending on the experiment. The 50 mM stock solution in DMSO can be freeze-thawed a number of times and is stable for a few weeks.
5. Spectral variants of green fluorescent protein and DsRed: Since the development of green fluorescent protein (GFP) as a reporter molecule, a number of improvements have been made in the use of GFP and related molecules for cell and molecular biological studies. Newer versions of these probes have been engineered to be more photostable, less self-aggregating, and more tolerant of N-terminal fusions [29]. For the work shown in this chapter, we used the plasmid phrGFP-1 expressing the humanized Vitality hrGFP *Renilla reniforms* green fluorescent protein from the CMV promoter (Stratagene Inc., La Jolla, CA) and the plasmid pcDNAtdTomato (tdTomato open reading frame was a generous gift from Dr. Roger Tsien, University of California at San Diego and is commercially available from Clontech Laboratories, Inc., Mountain View, CA). This vector expresses the tdTomato fluorescent protein, a modified DsRed *Discosoma sp.* tandem-dimer fluorescent protein.

3 Methods

3.1 Construction of MCSs

We routinely make MCSs from P19 mouse embryonal carcinoma cells, K1735-M2 mouse melanoma cells, and LNCaP human prostate cancer cells. The easiest approach for these cell lines is to maintain them as monolayers in tissue culture-grade dishes and to use cells to seed MCSs during passaging using routine phosphate-buffered saline (PBS)/EDTA (ethylenediaminetetraacetic acid)-trypsin protocols.

For example, we use the following steps to construct MCSs from these cell lines:

1. Trypsinize cultures when they are between 50 and 75 % confluency; count cells using a trypan blue solution and hemocytometer by standard methods.
2. Adjust cell density to about 5×10^4/ml in fresh media (e.g., DMEM/7.5 % FCIII) and add to a bacteriological-grade ("nonsticky") Petri dish. A single 60 mm diameter dish will yield enough MCSs for a small number of vital imaging experiments; cultures can easily be scaled up (e.g., multiple 100 mm diameter dishes can be seeded).
3. Incubate cells for a few days in a regular CO_2 incubator at 37 °C. During the first few days, MCSs are small and composed of healthy, viable cells. By 5 or 6 days, they are much larger and begin to contain a core of dead and dying cells, surrounded by a layer of living cells. For vital labeling and imaging, a number of the MCSs are removed from the bacteriological plates and transferred to a suitable labeling/imaging chamber (see below), and the remainder returned to the incubator. At this time, MCSs can be size-selected if desired, using a low-power inverted or dissecting microscope.
4. MCSs can be maintained in the bacteriological plates for quite a few days with periodic aspiration and replacement of the culture media. We simply remove old media with a sterile Pasteur pipette connected to a vacuum source; a few MCSs are lost during this procedure, but most can be left in the dish if one is reasonably careful during aspiration (they are visible and can be avoided). MCSs continually grow and change while cultured, so MCSs of the same age should be used for comparison purposes across experiments.

3.2 Fluorescent Labeling of Living MCSs

The first step is to remove the desired number of spheroids from the bacteriological-grade dishes and transfer them to an appropriate imaging chamber. Because our confocal unit is mounted on an inverted microscope, we routinely use glass-bottom 30 mm diameter culture dishes from Mat-Tek (Ashland, MA) for this purpose. For example, add 2.4 ml media (e.g., DMEM/7.5 % FCIII) to a 30 mm diameter dish and then transfer 100 μl media containing MCSs from the bacteriological dish. MCSs are usually easily visualized by the naked eye, and we simply use a micropipette and a sterile tip to remove them from the bacteriological plate.

1. For studies of cell viability and mitochondrial morphology, we use a cocktail of Hoechst, TMRM, and calcein-AM. While swirling the medium in a glass-bottom dish containing MCSs, add 5 μl/ml Hoechst 33342 (1 mg/ml stock), 1.5 μl/ml diluted TMRM stock (100 μg/ml in DMEM), and 2.5 μl/ml

diluted calcein-AM stock (1 mM in DMEM). Replace the dish in a CO_2 incubator for about 1 h prior to imaging. Under these conditions, the fluorescent probes penetrate and can be visualized to a depth of about 20 μM (Figs. 1, 2, and 3).

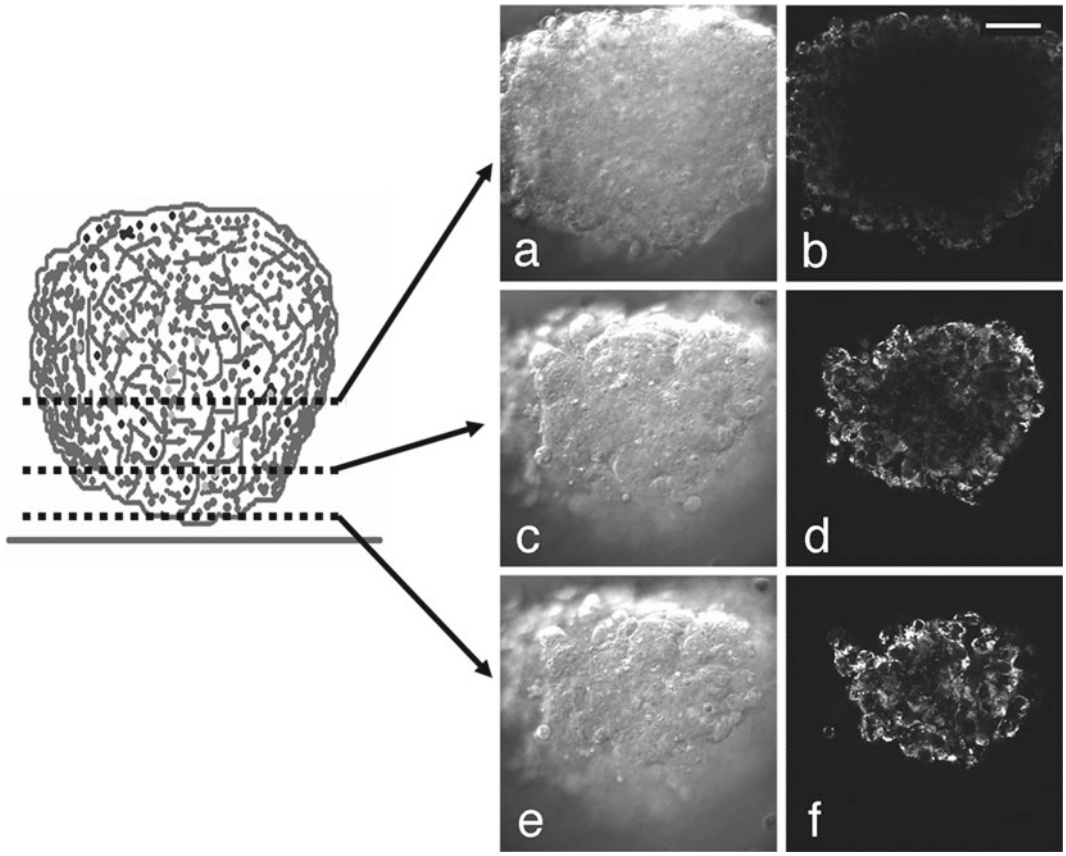

Fig. 1 Schematic diagram of an MCS in a glass-bottom culture dish. The *bottom line* denotes the glass coverslip of the culture dish; the *dotted lines* represent three optical sections at increasing depths into the MCS. With an inverted microscope, the first optical sections lie where the MCS rests on the coverslip. This spheroid surface yields the clearest and most strongly fluorescing images because of the proximity to the objective lens (which is positioned below the coverslip). (**a**, **b**) Optical section taken approximately 15 μm deep to the surface of a P19 MCS; (**c**, **d**) Optical section taken 5 μm deep to the MCS surface; (**e**, **f**) Optical section taken 1 μm deep to MCS surface. (**a**, **c**, and **e**) show DIC images, and (**b**, **d,** and **f**) show the corresponding TMRM signal of the same optical sections using confocal optics. The same settings were used to collect these fluorescent images to demonstrate the distinct falloff in signal intensity that occurs with increasing depth into the MCS. The reduction in fluorescence intensity is due to absorption of both excitation and emission wavelengths by cells as deeper regions of the MCS are imaged. In addition, central regions of the MCS appear dark due to the limited penetration of TMRM. Different fluorescent probes display different abilities to penetrate and label cells of an MCS over time, but many can only be clearly imaged within a peripheral shell about 10–20 μm in thickness. (**a**–**f**) are the same magnification; the scale bar in (**b**) represents 40 μm

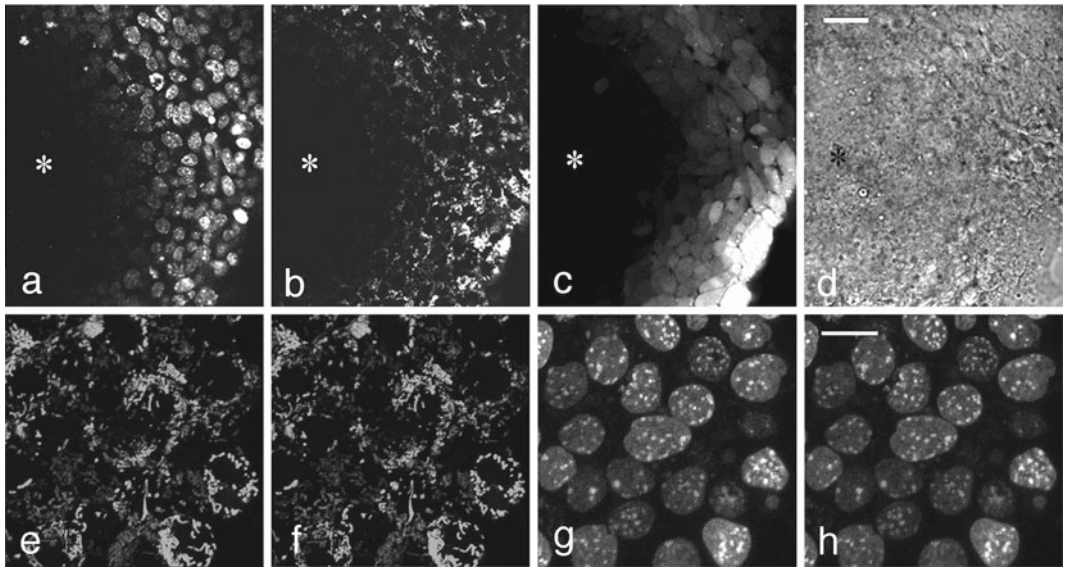

Fig. 2 (**a**–**d**) Single optical section approximately 10 μm from the surface of a P19 MCS triple-labeled with Hoechst (**a**), TMRM (**b**), and calcein-AM (**c**). The same focal plane is shown by DIC microscopy in (**d**). Note that the lack of penetration of the probes into the center of the spheroid (*asterisk*) results in a dark, unlabeled interior. (**a**–**d)** are the same magnification; the scale bar in (**d**) represents 30 μm. (**e**–**h**) Two stereo pairs of TMRM and Hoechst fluorescence from cells in a P19 MCS. TMRM mitochondrial fluorescence is shown in (**e**, **f**), and the Hoechst nuclear fluorescence of the same field of view is shown in (**g**, **h**). Stereo pairs were made by rotating z-stacks containing 15 optical sections taken at 1 μM steps by 9°. The scale bar in (**h**) indicates 5 μm

2. Sanguinarine: Depending on the experiment, we add 2–40 μl of the diluted 500 μM stock solution/ml of culture media (final concentration, 1–20 μM). One can remove different dishes at sequential timepoints or set up time-lapse acquisitions to study the uptake and distribution of sanguinarine (samples labeled with sanguinarine display a rise and fall in nuclear fluorescence with increasing incubation times). To ensure that a fluorescent signal of useful intensity is gathered over the span of time-lapse studies, we preincubate extra dishes with the desired concentration of sanguinarine for 2–3 h prior to beginning an experiment and use this dish to establish illumination and collection conditions that result in a good imaging signal. A new dish containing MCSs is then placed on the microscope stage, the time-lapse acquisition sequence started, and the same concentration of sanguinarine carefully added to the dish (Fig 4).
3. Engineering hrGFP- and tdTomato-expressing P19 cells: P19 cells are seeded into a 24-well dish and grown to about 50 % confluence. Individual wells are then transfected with either the plasmid phrGFP-1 or the plasmid pcDNAtdTomato.

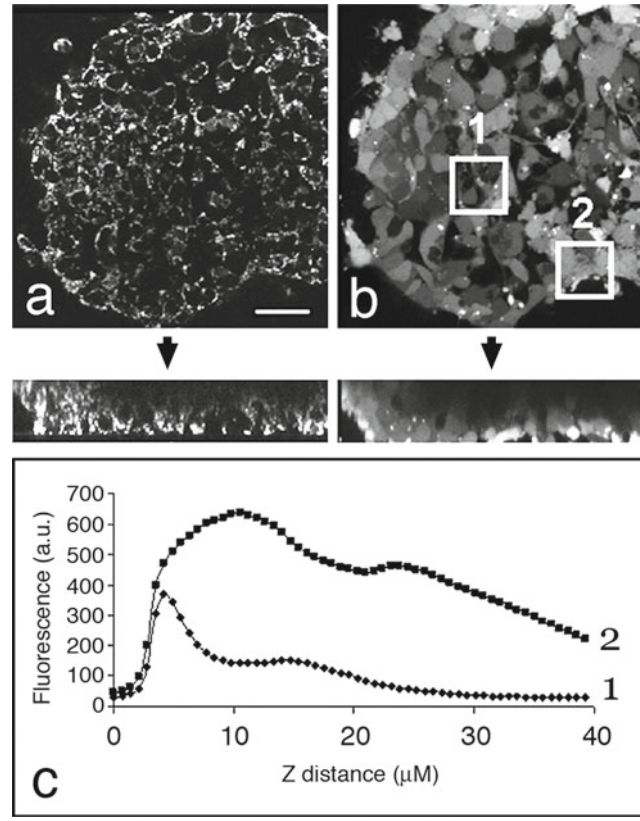

Fig. 3 Z-series of optical sections taken through a P19 MCS, showing attenuation of fluorescence signal with increasing depth. Strong TMRM (**a**) and calcein (**b**) signals are present in optical sections close to the MCS surface. Below these images are shown reconstructions of 40 optical sections taken at 1 μm steps from the surface of the MCS and rotated 90° (the coverslip would be at the bottom of these reconstructions). Notice the loss of fluorescence intensity in the middle of the spheroid and as the laser scans deeper in the specimen. The scale bar in (**a**) represents 35 μm. Two regions of interest were selected to span radial (1) and tangential (2) planes of the spheroid in the *z*-axis. The microscope software was used to measure the average fluorescence intensity of the calcein signal within these regions throughout the stack of 40 optical sections and is plotted in (**c**). The calcein fluorescence along the radial plane (1) decreases more rapidly than along the edge of the MCS (2), which primarily reflects the limited penetration of probe into the sample

For both transfections, 500 ng of each vector is added to each well, and plasmid delivery performed using Lipofectamine Plus (Invitrogen, Inc., La Jolla, CA) according to the manufacturer's instructions. Forty-eight hours post-transfection, P19 cells are trypsinized for the production of MCSs. Using these methods, we usually achieve about 10–20 % transfection efficiency, with the transfected cells exhibiting a continuum of fluorescence intensity (from very dim to very bright).

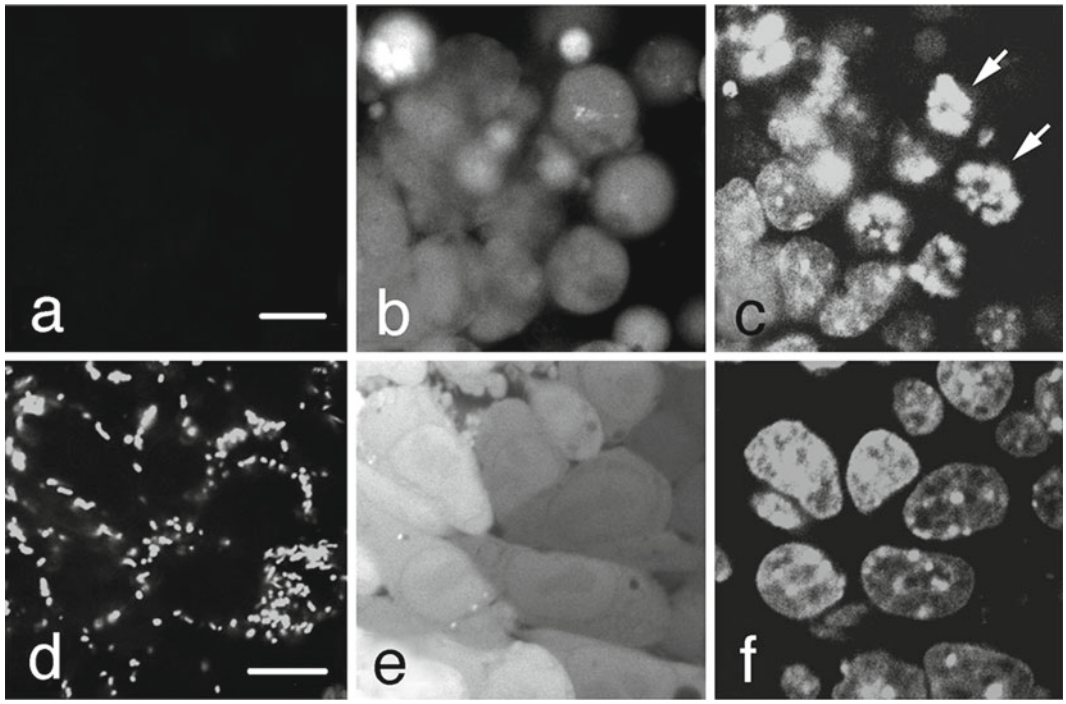

Fig. 4 Effect of FCCP on P19 MCSs. (**a**–**c**) MCS treated with 10 μM FCCP for 40 min, showing TMRM (**a**), calcein-AM (**b**), and Hoechst (**c**) labeling. Note the complete loss of mitochondrial TMRM signal in (**a**) (compare with the control MCS shown in **d**–**f**). In addition, cells are rounding up (**b**), and chromatin is condensing (*arrows* in **c**), which suggests that FCCP has triggered apoptosis in these cells. However, the persistence of the calcein signal indicates that these cells still possess an intact plasma membrane and the loss of TMRM signal is not due to loss of membrane integrity. (**d**–**f**) Control MCS labeled at the same time as that shown in (**a**–**c**), showing normal patterns of TMRM (**d**), calcein (**e**), and Hoechst (**f**) labeling. Scale bars in (**a**) and (**d**) indicate 10 μm

MCSs can be made solely from hrGFP or tdTomato expressing cells or can be constructed from a mix of cells from each transfection. Because cell number is more limiting when using cells from a 1 ml well (of a 24-well plate) to seed MCSs, we use agarose-coated 24 well plates instead of bacteriological-grade dishes to receive the cells, thereby concentrating the cells and insuring that most seeded cells end up in MCSs. Approximately 5 x 10^4 transfected cells in 1 ml of culture media are added to agarose-coated wells and replaced into the CO_2 incubator for another 48 h. MCSs are then removed with a sterile pipette tip and placed into glass-bottom dishes for confocal microscopy (Fig. 5, *see* **Note 2**). MCSs can be counterstained with Hoechst as described above prior to examination, if desired.

3.3 Confocal Microscopy

For the studies described in this chapter, we used a Nikon C1 laser-scanning confocal unit mounted on a Nikon TE2000 inverted microscope. It is a three-laser system and includes a Coherent

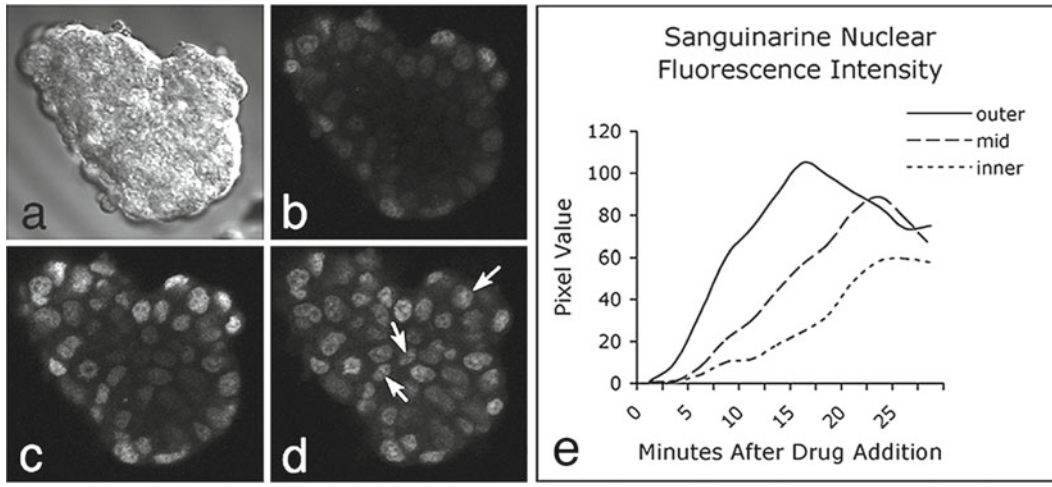

Fig. 5 Time-lapse sequence of an LNCaP MCS incubated in sanguinarine, showing nuclear uptake of this fluorescent compound. (**a**) DIC optics of MCS. (**b**–**d**) Three frames from a time-lapse movie, with the focal plane set at approximately in the middle of the spheroid. (**b**) 5 min after addition of 20 μM sanguinarine (the field was completely dark prior to sanguinarine addition); (**c**) 15 min after addition of sanguinarine; (**d**) 25 min after addition of sanguinarine. The inherent fluorescence characteristics of sanguinarine allow its nuclear transport and DNA binding to be visualized in living cells. Note the progressive increase in fluorescence intensity over time from the periphery to the central regions of the MCS, illustrating the penetration of this compound through the MCS. The *arrows* in (**d**) identify three nuclei representing peripheral (close to the surface), midpoint, and centrally located cells; measurements of the fluorescence intensity of these nuclei were measured over the time-course of this experiment and are shown in (**e**)

VioFlame solid-state laser (20 mW at 405 nm), a Spectra Physics Krypton-Argon Model 163C polarized laser (40 mW at 488 nm), and a Melles Griot green HeNe-polarized laser (1 mW at 543 nm). The filters used in conjunction with the photomultiplier tubes (PMTs) include a 480 nm dichroic long pass, with a 450/35 nm band pass for the blue channel (PMT 1), and a 545 nm dichroic long pass, with a 515/30 nm band pass for the green channel (PMT 3) and a 605/75 band pass for the red channel (PMT 2). The objective lenses we most commonly use for MCS vital imaging studies include a Nikon 60× XA/1.4 Plan Apo oil immersion lens and a Nikon 40×/0.60 Plan Fluor ELWD Ph2 phase contrast lens. For time-lapse and extended imaging studies, the use of a warming device and/or a CO_2 incubation system is desirable. However, many experiments can be conducted using glass-bottom dishes freshly removed from an incubator. Useful information can also be obtained with certain experiments conducted at room temperature, using DMEM-L15 media (*see* **Note 2**).

To image the specimens, place the glass-bottom dish on the stage of the confocal microscope and adjust the settings to obtain an acceptable signal. Because living MCSs are being viewed, one of the primary considerations is to avoid damaging or killing cells

with the lasers. A number of approaches are useful for minimizing irradiation damage to MCSs. Selection of MCSs and finding the focal planes of interest can initially be pursued using bright-field optics (i.e., without laser illumination). Also, less desirable MCSs can be used to adjust the image quality to avoid unnecessary bleaching or damaging the best areas of interest. Laser settings themselves are set to minimize exposure time in the following ways: (a) neutral density filters are placed in the laser path to attenuate laser intensity (we routinely use both ND4 and ND8 filters), (b) pixel dwell time is set to a short value (we use a 6 μs dwell time), and (c) the lowest resolution and fastest scan rate are used to find areas of interest and compose the image prior to taking a slower scan, higher-resolution picture. PMT gain is adjusted so that the fluorescence signal lies completely within the range of gray scale values and is not saturating (most types of confocal microscopes have software features that assist the user in avoiding overexposing the image). Although the specific fluorescent compound used will determine which laser should be used to excite the probe, adjunct differential contrast (DIC) or phase contrast images can be obtained using any laser. However, our experience suggests that the Krypton-Argon (Spectra Physics 163C) and green HeNe lasers are much better than the VioFlame laser for obtaining these types of bright-field images.

Collecting a series of optical sections through the *z*-axis or collecting a series of time-lapse images results in significantly higher levels of laser exposure. For both of these approaches, irradiation time can be reduced by avoiding the collection of averaged images from multiple laser passes. In both instances, the impact of the resulting higher noise level is mitigated by the fact that multiple images are used for the final display (i.e., either a rotating projection of optical sections or a time-lapse movie). Practically, one of the most important allies in obtaining the best images with the least amount of laser damage is familiarity with the microscope hardware and software. Experienced operators can more rapidly establish appropriate settings for an imaging experiment, and the less the specimen is scanned prior to image collection, the longer the specimen will remain viable.

4 Notes

1. Depending on the cell line, some cells may adhere to the bacteriological-grade Petri dish. In fact, with some cell lines, most of the cells will be adhered to the plate as either individually attached cells or as large cell aggregates (partial spheroids), with the minority of cells residing in free-floating MCSs. If this becomes problematic, the yield of free-floating MCSs can be

increased by culturing these cells over a layer of 1 % agarose in serum-free culture media. For example, add 0.2 g of DNA-grade agarose to 2 ml of DMEM, microwave until molten, and pour to cover the bottom of a 60 mm diameter plastic Petri dish (or pour a thin layer in each well of a multiwell plate). Chill briefly in a refrigerator to gel the agarose, rewarm in an incubator, and then add a cell suspension to the dish.

2. The pH of many types of media will become quite basic after just a few minutes outside of the incubator. To avoid this, brief imaging sessions can be attempted or an additional buffer added (e.g., 50 mM HEPES, pH 7.0). Alternatively, we have found that a 1:1 mixture of DMEM and Liebovitz's L15 medium maintains a neutral pH in the absence of CO_2 and is well suited to maintain cells for many hours outside of an incubator. Therefore, for studies where imaging sessions longer than about 10 min are required, we routinely add MCSs to glass-bottom dishes containing this media mix (also containing 5–10 % FCIII) prior to fluorescent probe addition/incubation and imaging.
3. Many fluorescent probes are somewhat sensitive to light, and some are rapidly hydrolyzed in aqueous solutions. Therefore, we handle all probes in reduced light and minimize the amount of time working stocks are thawed and at room temperature. Where hydrolysis is of concern (e.g., calcein-AM), we make the working stock solution fresh for each experiment and discard the unused portion. Most probes can withstand at least a few minutes under regular room lights, but if photolysis appears to be a problem, lamps containing yellow light bulbs (e.g., 60 W "bug lights") can be used in the tissue culture hood during drugging.
4. Carbonyl cyanide *p*-trifluoromethoxyphenylhydrazone (FCCP, Sigma) can be used as a mitochondrial uncoupler to dissipate mitochondrial membrane potential [30, 31]. FCCP is a good control to assess if the TMRM signal is entirely mitochondrial in origin. After an incubation of 30–40 min with 10 μM FCCP, around 95 % of the mitochondrial TMRM signal should disappear; in most cases, the cytosol should now present a faint red color due to the exit of TMRM from mitochondria (Fig. 6). After more extensive periods of incubation, most of the cytosolic TMRM signal will ultimately fade.
5. With our system, sanguinarine is excited with a Krypton-Argon laser but can be detected using either PMT 3 (which utilizes a 545 nm dichroic long pass filter with a 515/30 nm band pass for the green channel) or PMT 2 (which uses the same dichroic with a 605/75 band pass for the red channel). The most sensitive imaging results from using PMT 2 or the red channel.

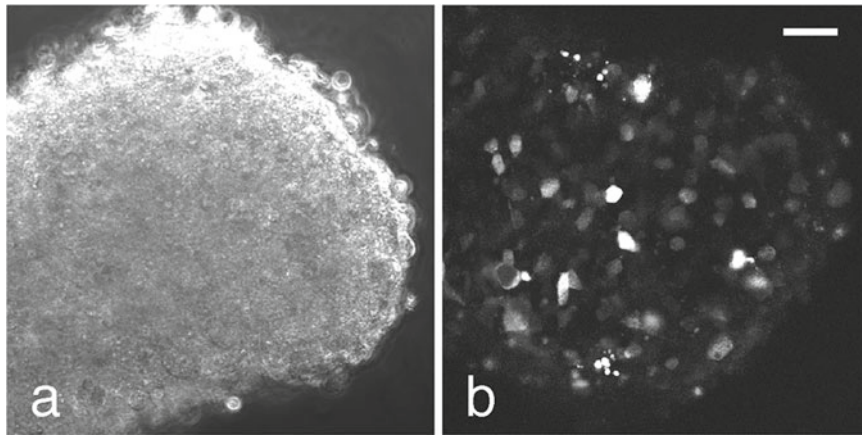

Fig. 6 P19 MCS constructed from cells transiently transfected with hrGFP and tdTomato expression vectors. In this experiment, transfection efficiency was estimated to be about 10–20 %; monolayer cultures were trypsinized 48 h after transfection, and the cells from hrGFP-transfected and tdTomato-transfected wells combined in an agarose-coated well and cultured for another 48 h. MCSs were transferred to glass-bottom Petri dishes in a 1:1 mixture of DMEM-L15 medium containing 5 % FBS and directly imaged. The fluorescent cells appear to be suspended in an empty spherical space, which is actually occupied by non-transfected, non-fluorescent cells. Left micrograph (a) is a brightfield image of the same field of view shown by fluorescence in (b). Scale bar in (**b**) indicates 50 μM

References

1. Kunz-Schughart LA (1999) Multicellular tumor spheroids: intermediates between monolayer culture and in vivo tumor. Cell Biol Int 23(3):157–161
2. Mueller-Klieser W (1987) Multicellular spheroids. A review on cellular aggregates in cancer research. J Cancer Res Clin Oncol 113(2): 101–122
3. Mueller-Klieser W (2000) Tumor biology and experimental therapeutics. Crit Rev Oncol Hematol 36(2–3):123–139
4. Kunz-Schughart LA, Kreutz M, Knuechel R (1998) Multicellular spheroids: a three-dimensional in vitro culture system to study tumour biology. Int J Exp Pathol 79(1):1–23
5. Mueller-Klieser W (1997) Three-dimensional cell cultures: from molecular mechanisms to clinical applications. Am J Physiol 273(4 Pt 1):C1109–C1123
6. Kobayashi H et al (1993) Acquired multicellular-mediated resistance to alkylating agents in cancer. Proc Natl Acad Sci U S A 90(8):3294–3298
7. Olive PL, Banath JP, Evans HH (1993) Cell killing and DNA damage by etoposide in Chinese hamster V79 monolayers and spheroids: influence of growth kinetics, growth environment and DNA packaging. Br J Cancer 67(3):522–530
8. Olive PL, Durand RE (1994) Drug and radiation resistance in spheroids: cell contact and kinetics. Cancer Metastasis Rev 13(2):121–138
9. Sakata K et al (1994) Resistance to verapamil sensitization of multidrug-resistant cells grown as multicellular spheroids. Int J Cancer 59(2):282–286
10. Graham CH et al (1994) Rapid acquisition of multicellular drug resistance after a single exposure of mammary tumor cells to antitumor alkylating agents. J Natl Cancer Inst 86(13): 975–982
11. LaRue KE, Bradbury EM, Freyer JP (1998) Differential regulation of cyclin-dependent kinase inhibitors in monolayer and spheroid cultures of tumorigenic and nontumorigenic fibroblasts. Cancer Res 58(6):1305–1314
12. Timmins NE et al (2004) Identification of three gene candidates for multicellular resistance in colon carcinoma. Cytotechnology 46(1):9–18
13. Gaedtke L et al (2007) Proteomic analysis reveals differences in protein expression in spheroid versus monolayer cultures of low-passage colon carcinoma cells. J Proteome Res 6(11):4111–4118
14. Grun B et al (2009) Three-dimensional in vitro cell biology models of ovarian and endometrial cancer. Cell Prolif 42(2):219–228

15. Ward JP, King JR (2003) Mathematical modelling of drug transport in tumour multicell spheroids and monolayer cultures. Math Biosci 181(2):177–207
16. Martin C et al (2003) The expression of P-glycoprotein does influence the distribution of novel fluorescent compounds in solid tumour models. Br J Cancer 89(8):1581–1589
17. Wartenberg M et al (1998) Development of an intrinsic P-glycoprotein-mediated doxorubicin resistance in quiescent cell layers of large, multicellular prostate tumor spheroids. Int J Cancer 75(6):855–863
18. Xing H et al (2007) Knock-down of P-glycoprotein reverses taxol resistance in ovarian cancer multicellular spheroids. Oncol Rep 17(1):117–122
19. Friedrich J et al (2009) Spheroid-based drug screen: considerations and practical approach. Nat Protoc 4(3):309–324
20. Durand RE, Olive PL (2001) Resistance of tumor cells to chemo- and radiotherapy modulated by the three-dimensional architecture of solid tumors and spheroids. Methods Cell Biol 64:211–233
21. Scaduto RC Jr, Grotyohann LW (1999) Measurement of mitochondrial membrane potential using fluorescent rhodamine derivatives. Biophys J 76(1 Pt 1):469–477
22. Guo X et al (2001) Proteomic characterization of early-stage differentiation of mouse embryonic stem cells into neural cells induced by all-trans retinoic acid in vitro. Electrophoresis 22(14):3067–3075
23. Lemasters JJ et al (1999) Confocal microscopy of the mitochondrial permeability transition in necrotic and apoptotic cell death. Biochem Soc Symp 66:205–222
24. Adhami VM et al (2003) Activation of prodeath Bcl-2 family proteins and mitochondrial apoptosis pathway by sanguinarine in immortalized human HaCaT keratinocytes. Clin Cancer Res 9(8):3176–3182
25. Adhami VM et al (2004) Sanguinarine causes cell cycle blockade and apoptosis of human prostate carcinoma cells via modulation of cyclin kinase inhibitor-cyclin-cyclin-dependent kinase machinery. Mol Cancer Ther 3(8): 933–940
26. Ding Z et al (2002) The alkaloid sanguinarine is effective against multidrug resistance in human cervical cells via bimodal cell death. Biochem Pharmacol 63(8):1415–1421
27. Weerasinghe P, Hallock S, Liepins A (2001) Bax, Bcl-2, and NF-kappaB expression in sanguinarine induced bimodal cell death. Exp Mol Pathol 71(1):89–98
28. Slaninova I et al (2001) Interaction of benzo[c] phenanthridine and protoberberine alkaloids with animal and yeast cells. Cell Biol Toxicol 17(1):51–63
29. Shaner NC et al (2004) Improved monomeric red, orange and yellow fluorescent proteins derived from Discosoma sp. red fluorescent protein. Nat Biotechnol 22(12):1567–1572
30. Collins TJ et al (2000) Inositol 1,4,5-trisphosphate-induced Ca^{2+} release is inhibited by mitochondrial depolarization. Biochem J 347(Pt 2):593–600
31. Slater EC (1967) Application of inhibitors and uncouplers for a study of oxidative phosphorylation. Meth Enzymol X:48–57

Chapter 12

Live Confocal Analysis of Mutant- and Drug-Treated *Drosophila* Embryos

Barbara Fasulo and William Sullivan

Abstract

The model organism *Drosophila melanogaster* is particularly well suited for live image analysis. The availability of GFP transgenic flies and a wide array of fluorescent probes, in conjunction with laser scanning confocal microscopy, allow us to image multiple aspects of the cell cycle simultaneously. Confocal microscopy provides the sensitivity and resolution to observe the dynamics of specific cellular events in real time. For example, GFP-histone and rhodamine-labeled tubulin enable one to follow specific nuclear and cytoskeletal events including nuclear envelope formation, nuclear envelope breakdown, spindle formation, centrosome duplication, separation and migration, chromosomes condensation, and segregation. This analysis permits a detailed morphological and temporal description of nuclear and cytoskeletal events in normal or drug-injected embryos.

Key words *Drosophila*, Microinjection, Drugs

1 Introduction

Advances in fluorescent microscopy and the development of sensitive highly specific fluorescent probes have considerably advanced our ability to observe subcellular events in living organisms. Laser scanning confocal microscopy provides the sensitivity and resolution to observe the dynamics of specific cellular events in real time. GFP technology and other technologies have provided the community of cell biologists with a wealth of fluorescent probes to follow countless cellular events. These techniques have proven especially powerful in producing detailed analysis of mutant phenotypes.

The model organism *Drosophila melanogaster* is particularly well suited for live image analysis. In *Drosophila*, the events of early embryogenesis have been characterized in detail using both fixed and live analysis [1–4]. The initial nuclear divisions are rapid (10–20 min long), synchronous, and syncytial. The first seven rounds of nuclear division occur in the interior of the embryo.

Stephen W. Paddock (ed.), *Confocal Microscopy: Methods and Protocols*, Methods in Molecular Biology, vol. 1075,
DOI 10.1007/978-1-60761-847-8_12,

During nuclear cycles 8 through 10, the majority of the nuclei migrate to the cortex where they undergo four more rounds of division before cellularizing during a prolonged interphase of nuclear cycle 14. These divisions alternate between M and S with highly abbreviated G1 and G2 phases. Importantly, these cell cycles are regulated in the same fashion as more conventional cell cycles. In spite of many statements to the contrary, these cycles possess robust S-phase, DNA damage, and mitotic cell cycle checkpoints [5–8]. A unique feature of these cycles is that they do not require zygotic transcription and do not undergo apoptosis [9]. As will be described below, this is advantageous because the posttranslational effects of drugs and inhibitors on the cell cycle can be readily determined. Finally, multiple rounds of nuclear divisions can be imaged on a single focal plane, as the cortical divisions occur in a monolayer [7, 10].

The availability of GFP transgenic flies and a wide array of fluorescent probes, in conjunction with confocal microscopy, allow us to image multiple aspects of the cell cycle simultaneously. For example, GFP-histone and rhodamine-labeled tubulin enable one to follow specific nuclear and cytoskeletal events including nuclear envelope formation, nuclear envelope breakdown, spindle formation, centrosome duplication, separation and migration, chromosomes condensation, and segregation. Figure 1 illustrates the power of this approach. Panel A shows nuclear envelope formation (NEF), which occurs at the end of telophase and is characterized by the exclusion of tubulin (in red) from the nuclei (in green). As shown in panel B, the appearance of bright histone-GFP dots in the nuclei marks the initiation of chromosome condensation (ICC). Following ICC, the chromosomes become more condensed and pull away from the nuclear envelope, thus defining a second distinct phase of chromosomes condensation (CC2). Nuclear envelope breakdown (NEB) marks the beginning of prophase. The entrance of monomeric tubulin in the nuclear space characterizes this stage (D). Entrance into metaphase is marked by the formation of a bipolar spindle, decrease in asters, and alignment of condensed chromosomes on the metaphase plate (Panel E). In panel F, elongation of the metaphase spindle, in addition to segregation of chromosomes, indicates the initiation of anaphase (IA). Equally important to the analysis of the morphological events is that the abbreviated cycles enable one to precisely time the interval between each event. Another important attribute of analyzing the cortical syncytial cycles is that it is possible to inject inhibitors at precisely timed stages of the cell cycle. For example, if we want to time the S-phase in a colchicine-injected embryo, it is necessary to inject the drug after anaphase when chromosomes have already separated, and there is no risk of activation of the spindle checkpoint. This analysis permits a detailed morphological and temporal description of nuclear and cytoskeletal events in normal or in

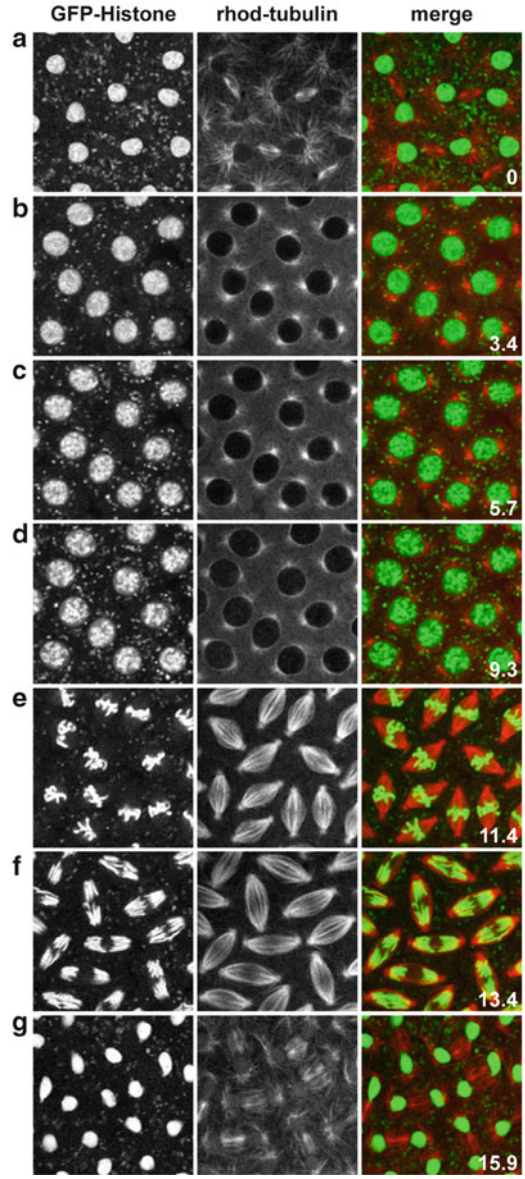

Fig. 1 Images of nuclear and cytoskeletal events of a syncytial *Drosophila* embryo bearing the histone-GFP construct and injected with fluorescently labeled tubulin

drug-treated embryos. It is even possible to identify drugs that, when injected into the embryo, do not show any visible phenotype but do alter the relative timing of cell cycle events.

2 Materials

2.1 Embryo Preparation

1. Mechanical needle puller (Model P-30, Sutter Instrument Co.).
2. Injection apparatus.

3. 75 mm capillary tubing with an outer and inner diameter of 1.21 and 0.90 mm, respectively (Drummond Scientific Broomall, PA cat. no. N-51 A).
4. Atoxic clay mount in a Petri dish.
5. 10 µl syringe (Hamilton).
6. Microscope slides (Fisher).
7. 22×50 mm^2 coverslips (Fisher).
8. 22×22 mm^2 coverslips (Fisher).
9. Tape (Fisher).
10. Dissecting forceps (Dumont # 5).
11. Halocarbon oil (Series 77, CAS no. 9002-83-9, Halocarbon Products Corp.).
12. Heptane (EM Science).
13. Double-stick tape (3 M).
14. Refrigerated microcentrifuge.
15. Drierite granular desiccant.
16. Lids from 35×10-mm disposable plastic tissue culture dishes (Falcon).
17. Plastic "flies collection" bottles (Applied Scientific).

2.2 Visualization and Drug Treatment

1. Inverted microscope with confocal imaging system.
2. Fluorescently labeled tubulin: Molecular Probes (Eugene, OR), or Cytoskeleton, stored at –80 °C in 2 µl aliquots of 20 µg each.
3. GFP-Histone fly stock kindly provided by Robert Saint.

3 Methods

3.1 Preparation of Glue

To allow the embryos to remain stably attached to the cover slip during the period of observation, prepare a concentrated embryo adhesive: 10 ml of heptane are added to a 50 ml conical tube containing 12 in. of double-stick tape, and the tube is allowed to rotate overnight. The resulting solution is aliquoted in 1.5 ml microcentrifuge tubes and then centrifuged at 14,000 rpm ($15{,}800 \times g$) for 10–15 min to remove the particulate matter. The clear solution is then transferred to a tightly closed container to avoid evaporation. To make a working solution, the concentrated glue should be diluted roughly five times with heptane.

3.2 Preparation of Needles

Draw out several needles with a mechanical needle puller. Examine the tip of each needle under a dissecting microscope. It should be

smooth and should come to a sharp unbroken tip. Store the needles upon a clay mount in a Petri dish as shown in Fig. 2 and keep them at 4 °C.

3.3 Needle Slide Preparation

Using a drop of the embryo adhesive, attach a 22 × 22 mm^2 cover slip to the left or right side of the 22 × 50 mm^2 cover slip's surface (Fig. 3). Store it in a place protected from dust. This will be used to break the needle tip.

3.4 Embryo Slide Preparation

Attach a 22 × 50 cover slip to a slide with a piece of tape. Then attach a piece of double-stick tape to one end of the slide. Pour a strip of embryo adhesive along the short axis and in the center of the slide (Fig. 4). For convenience, it is useful to mark the position of the glue with a marker. Several of these slides can be prepared in advance and stored in a place protected from dust.

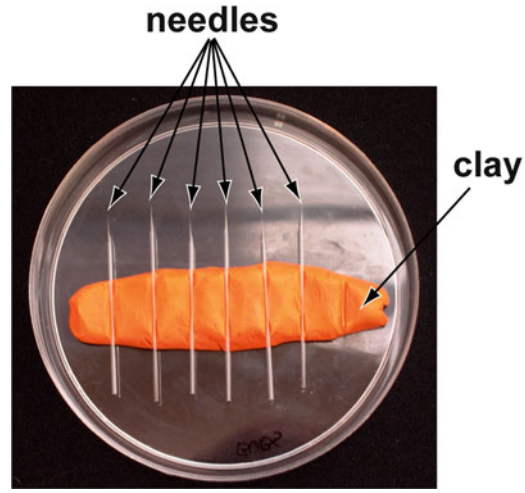

Fig. 2 Petri dish with clay to store injection needles

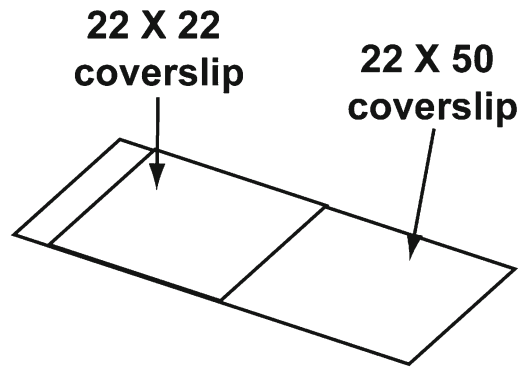

Fig. 3 Needle preparation slide to break the tip of the needle

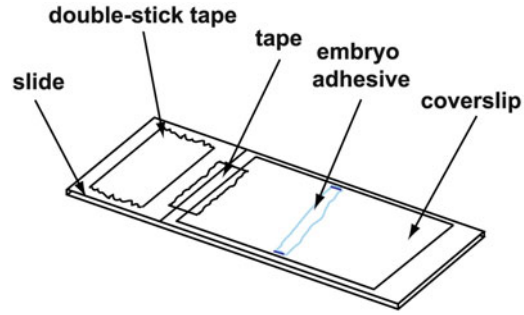

Fig. 4 Embryo slide to dechorionate and align the embryos

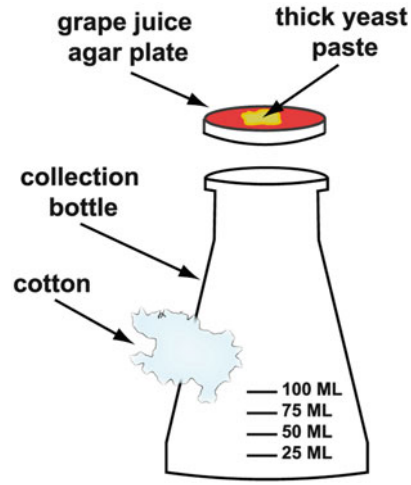

Fig. 5 Collection bottle capped with a grape juice agar plate for embryo collections

3.5 Collecting Embryos

One day before the in vivo analysis, place 100–200 adult *Drosophila* flies (equal numbers of males and females) in a collection bottle (Fig. 5) made from a 6-ounce plastic bottle. On one side of the bottle, make a hole and plug it with cotton to let the flies breathe. Spread a little yeast paste in the middle of a grape juice agar plate and use the plate to close the collection bottle. Invert the bottle and place it at 25 °C overnight. The following day, discard the old grape juice agar plate and replace it with a new one. In order to collect staged embryos, from cycles 10 to 13, let the flies lay for 1 h. The grape juice plate is then removed, protected, and aged for another hour. Usually the first hour of collection is discarded.

3.6 Needle Filling and Breaking

While the embryos age, thaw a 2 μl aliquot of rhodamine-labeled tubulin on ice and centrifuge it for 3–5 min at 14,000 rpm (15,800 × *g*) in a refrigerated microcentrifuge. This procedure, pellets denatured or aggregated protein and diminishes the chance of clogging the needle. Immediately after centrifugation, draw up the labeled protein with a pre-cooled Hamilton syringe, avoiding

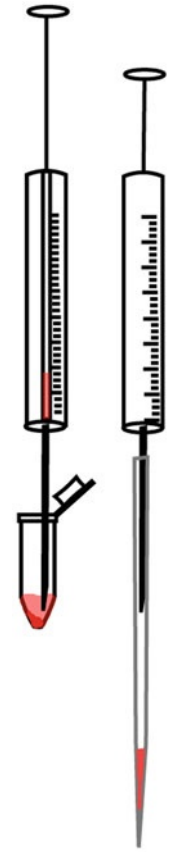

Fig. 6 Hamilton syringe filled with rhodamine-labeled tubulin after centrifugation

the pellet (Fig. 6). Use this syringe to fill as many cold needles as possible with the labeled protein.

To prepare the needles with the drug, choose the appropriate dilution and follow the same procedure as above.

To break the needles, take the needle preparation slide and add a small amount of Halocarbon oil on the edge of 22×22 mm^2 cover slip (Fig. 7). Place the slide on the stage of a microscope with a 10–20× objective. Mount the needle in the microinjection apparatus and apply gentle pressure. Direct the tip of the needle towards the edge of the cover slip covered with the Halocarbon oil and break the tip by maintaining pressure. A break is promptly identified by a bubble of fluid released from the tip of the needle into the oil. Given that the syncytial embryonic nucleus has a diameter of 5 μm, try to generate a small hole, approximately 3–5 μm in diameter. Immediately after breaking the needles, store them upon clay mount in a Petri dish and keep them on ice, protected from the light. A rhodamine-labeled tubulin needle can be used for up to 2 days if kept rigorously on ice and at 4 °C over night.

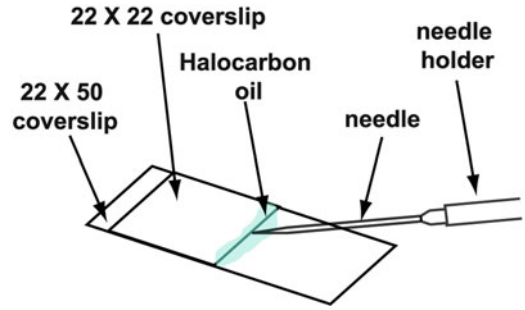

Fig. 7 Needle preparation slide with Halocarbon oil covering the edge needed to break the needle

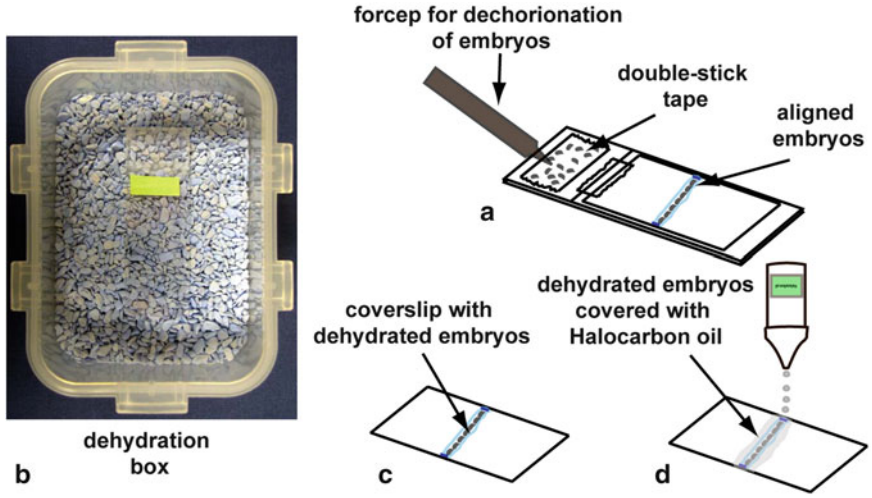

Fig. 8 Steps of preparation before embryos injection

3.7 Dechorionation of Embryos

Transfer some embryos from the aged collection onto the double-stick tape on the embryo slide. Roll the embryos on the double-stick tape to dechorionate them and align them on the film of glue (Fig. 8a). This should be done as quickly as possible to avoid excessive dehydration. In order to prevent the flow of cytoplasm when the embryos are injected, the slide is placed in a dehydration chamber for 4–10 min (Fig. 8b). The time of dehydration depends on the day-to-day variation in temperature and humidity. The dehydration chamber consists of a Tupperware box containing drierite granular desiccant. Once the embryos are dehydrated (Fig. 8c), they are covered with a film of Halocarbon oil to prevent further dehydration (Fig. 8d). The cover slip with the aligned embryos is then removed from the slide and is placed on the microscope stage for injection.

3.8 Tools Needed for Injection

To perform the microscopy, we use an inverted photoscope (DMIRB; Leitz) equipped with a laser confocal imaging system (TCS SP2, Leica confocal software, version 2.6.1).

To set the microscope for injection, a micromanipulator and a microinjector are required. The microinjector we use consists of a 20 ml syringe connected via a rubber tube to a needle holder (Fig. 9).

The micromanipulator is a Narishige Joystick Micromanipulator model MN-151. As shown in Fig. 10, this allows the needle to be moved along the three axes—*x*, *y*, *z*—by micro-movements with the knobs (arrowheads in the picture).

3.9 Setting the Microscope

For the acquisition of images, we select a specific set of acquisition parameters. We set a two-channel recording for the two fluorescent dyes FITC and TRITC. The FITC channel is used to visualize GFP-Histone, and the TRITC channel is used for rhodamine tubulin. To observe the needle and embryo simultaneously during injection, the 20× microscope objective is more appropriate. To record the data stack we are interested in, we select the time-scan mode xyt and 512 width and 512 height as scan format. We configure a time series with intervals no longer than 20 s.

3.10 Injecting the Embryo

After the embryos have been dehydrated and covered with Halocarbon oil, the 50 × 22 cover slip is placed on the microscope stage (Fig. 11). After examining the entire row of aligned embryos, only those with cells at the posterior pole (the nascent germline) are injected. The presence of pole cells indicates that the somatic nuclei have or will shortly reach the surface. To inject drugs, we

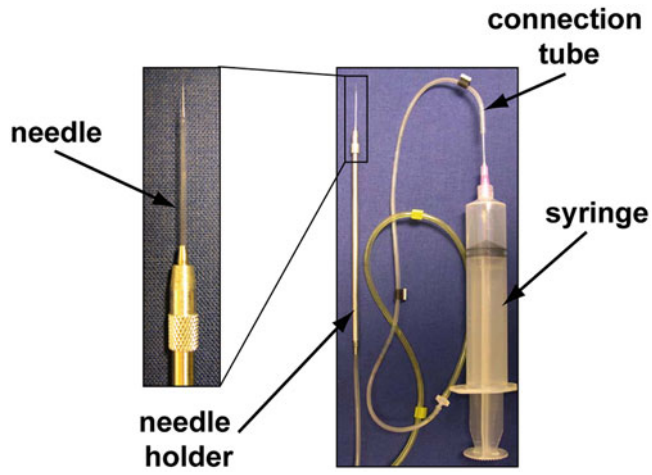

Fig. 9 Microinjector consisting of a 20 ml syringe and a needle holder

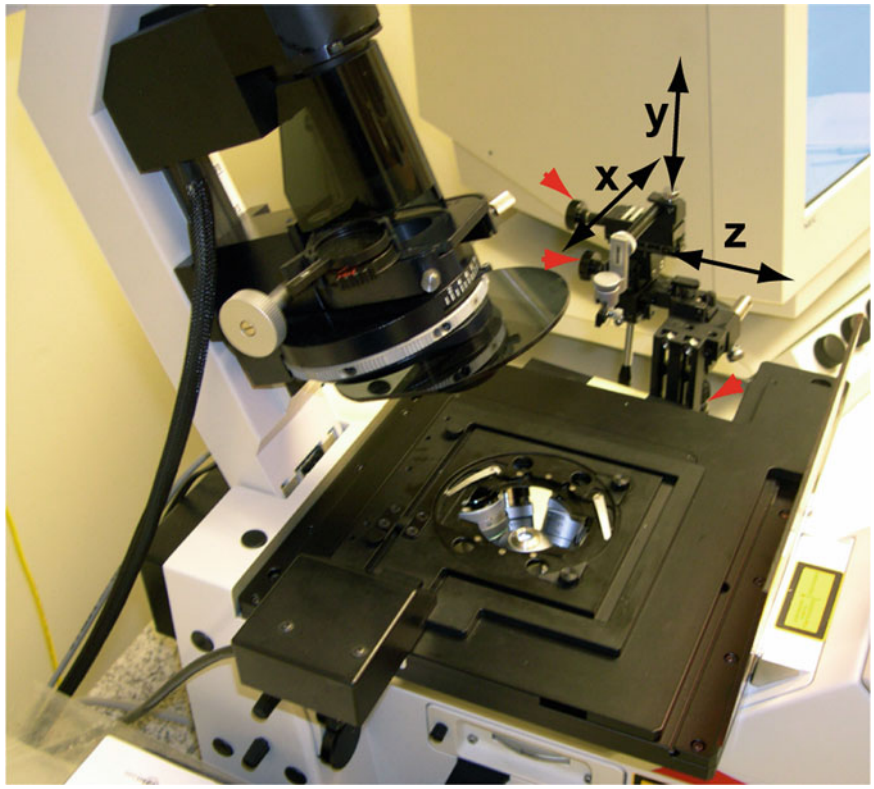

Fig. 10 Micromanipulator to direct the needle along the three axes

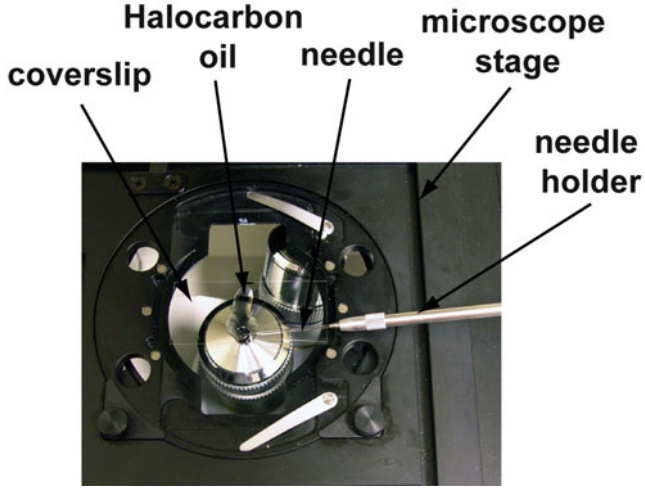

Fig. 11 Microscope stage with embryos aligned on coverslip

select embryos at cell cycle 12. By setting the acquisition parameters in continuous scan mode, it is possible to find the embryos at the right cell cycle by observing the density of nuclei on the surface. Furthermore, the continuous mode allows us to optimize image quality, because we can modify the scan parameters and check the results directly in the image while the embryo is being scanned. With bleach-sensitive specimens, it is advisable to restrict the use of the continuous scan function to short-time intervals. Subjecting the embryo to the laser's continuous light can damage it photochemically.

Once the right embryo has been visualized, the broken needle containing rhodamine tubulin is removed from the Petri dish on ice and is placed in the needle holder. This should be done just before injection to avoid deterioration of the dye. The needle holder is then blocked on the micromanipulator. Immediately prior to injection, it is advisable to check whether the rhodamine tubulin-containing needle has clogged. If so, exchange it with another previously prepared needle.

After the embryo is in focus, the tip of the needle is focused on the same plane and is slowly moved towards its surface, as shown in Fig. 12a. Then the microscope stage with the cover slip is moved towards the needle, and the tip of the needle is allowed to penetrate the embryo (Fig. 12b), just below its surface. During injection, we try to avoid the release of the dye between the vitelline and the plasma membranes. If the embryo is well dehydrated, the dye will be taken up without having to apply pressure with the syringe (Fig. 12b). If the embryo is not sufficiently dehydrated, the embryo will "bleed" cytoplasm and injected material, as shown in Fig. 12c, d. The injected rhodamine tubulin is immediately visible in the interior of the embryo but will take almost a cycle before it is uniformly distributed. Do not inject excess amounts of rhodamine tubulin if a second injection is still to be performed in the same embryo, as the embryo cannot withstand large quantities of liquid. Remove the needle with rhodamine tubulin and place it on ice as soon as the embryo has been injected.

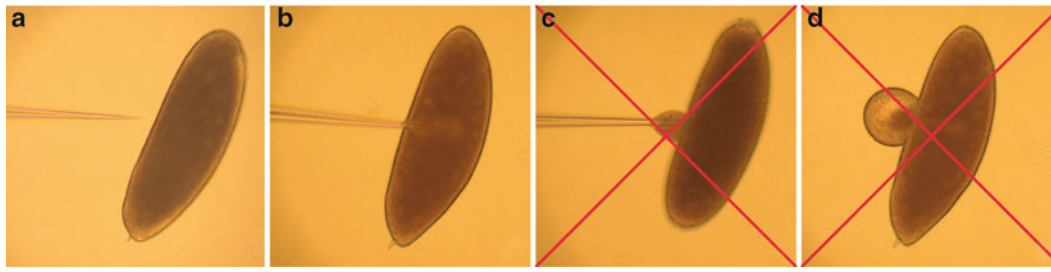

Fig. 12 Correct embryo dehydration avoids cytoplasm "bleeding"

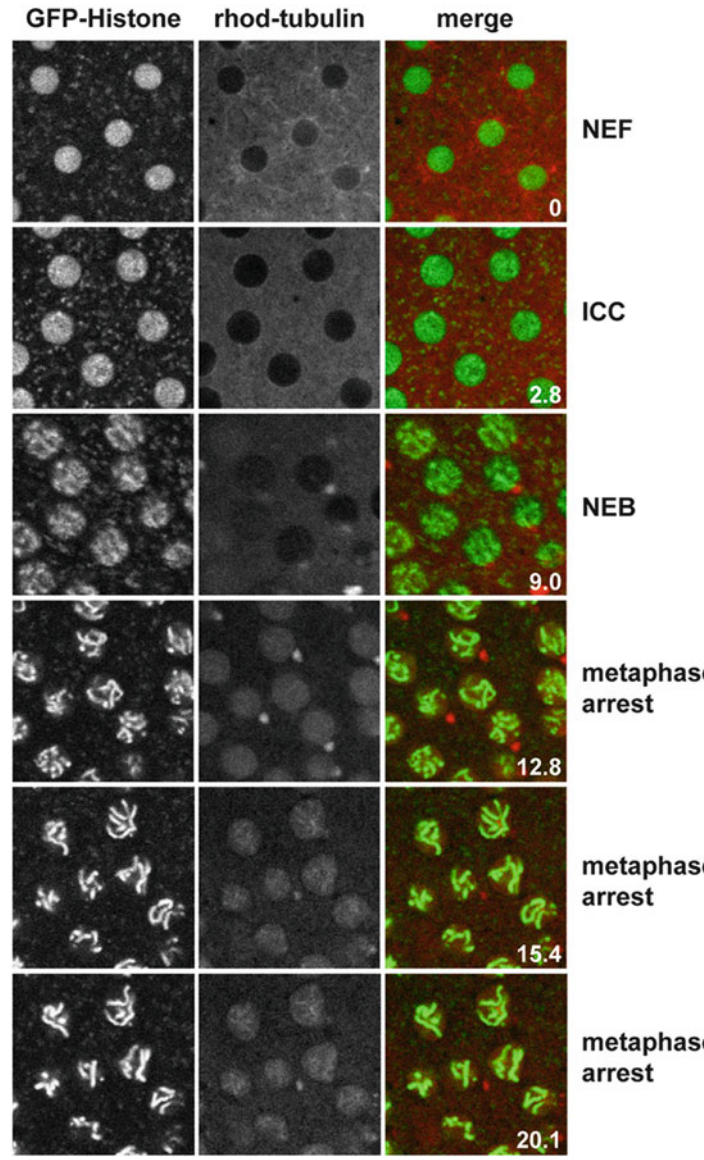

Fig. 13 Embryo injected with the microtubule depolymerizer colchicine

By following the dynamics of rhodamine tubulin on the monitor, it is possible to determine the appropriate time for drug injection. It is important, however, to avoid extended use of the continuous mode, in order to limit photobleaching of the rhodamine signal. If the aim is to inhibit DNA replication by injection of aphidicolin, choose to inject immediately after nuclear envelope formation, prior to the initiation of DNA replication. Alternatively, if one is interested in examining the effects of the microtubule inhibitor colchicine on interphase events, it is necessary to inject the

drug after anaphase when chromosomes have already separated to avoid activation of the spindle checkpoint. When injecting the drug, it is advisable to use the same hole created when injecting rhodamine tubulin. The pressure applied trying to make a second hole may otherwise allow the cytoplasm to exit through the first hole.

3.11 Imaging the Injected Embryo

In continuous mode, prior to filming the embryo, define the acquisition parameters to optimize image quality: the exact z-position within the embryo, the amplification factor of the selected detector (for GFP or rhodamine), the diameter of the detection pinhole, and the zoom factor. If the acquisition is three dimensional (3D series), define the upper and lower limit of the data set to be acquired and the number of optical sections. Next, begin scanning to create the image series. During this process, it is advisable to monitor the GFP-Histone and rhodamine-tubulin signals. Photobleaching may weaken the signals, and they should therefore be adjusted accordingly. Figure 13 shows an example of an embryo injected with the microtubule depolymerizer colchicine, a drug known to activate the spindle assembly checkpoint. Time is shown in minutes on the right side of each picture.

3.12 Saving Data

Individual images can be saved as TIFF files, and movies can be saved as AVI movies.

References

1. Minden JS et al (1989) Direct cell lineage analysis in *Drosophila melanogaster* by time-lapse, three-dimensional optical microscopy of living embryos. J Cell Biol 109(2):505–516
2. Kellogg DR, Mitchison TJ, Alberts BM (1988) Behaviour of microtubules and actin filaments in living Drosophila embryos. Development 103(4):675–686
3. Debec A et al (1996) Live analysis of free centrosomes in normal and aphidicolin-treated Drosophila embryos. J Cell Biol 134(1): 103–115
4. Foe VE, Alberts BM (1983) Studies of nuclear and cytoplasmic behaviour during the five mitotic cycles that precede gastrulation in Drosophila embryogenesis. J Cell Sci 61: 31–70
5. Song YH (2005) Drosophila melanogaster: a model for the study of DNA damage checkpoint response. Mol Cells 19(2):167–179
6. Yu KR, Saint RB, Sullivan W (2000) The Grapes checkpoint coordinates nuclear envelope breakdown and chromosome condensation. Nat Cell Biol 2(9):609–615
7. Sullivan W et al (1993) Delays in anaphase initiation occur in individual nuclei of the syncytial Drosophila embryo. Mol Biol Cell 4(9): 885–896
8. Yu KR, Duronio RJ, Sullivan W (1998) Cell cycle checkpoints: safe passage through mitosis. In: Mechanisms of cell division: frontiers in biology. Oxford University Press, Oxford
9. Saint R, Patterson B (1993) Zygotic transcription and cell proliferation during Drosophila embryogenesis. Genetica 90(2–3):157–163
10. Valdes-Perez RE, Minden JS (1995) Drosophila melanogaster syncytial nuclear divisions are patterned: time-lapse images, hypothesis and computational evidence. J Theor Biol 175(4): 525–532

Chapter 13

Confocal Imaging of the Microtubule Cytoskeleton in *C. elegans* Embryos and Germ Cells

Kevin F. O'Connell and Andy Golden

Abstract

The microtubule cytoskeleton plays important roles in a number of cellular processes including cell division, establishing and maintaining cell architecture and polarity, and intracellular trafficking. The identification and characterization of factors required for the proper functioning of the microtubule cytoskeleton have been aided by approaches that combine sensitive and rapid methods for high-resolution optical imaging, such as confocal microscopy, with the powerful genetics available in model organisms. Here we present methods for confocal imaging of live and fixed tissues of the nematode *C. elegans*, a model organism that has been employed with great success to study the microtubule cytoskeleton and its roles in cell division and cell polarity.

Key words Microtubules, Centrosomes, *C. elegans*, Immunofluorescence, GFP

1 Introduction

Microtubules are linear polymers composed of alpha- and beta-tubulin and possess a defined polarity: a highly dynamic plus end and a less dynamic minus end. Within dividing cells, the microtubule cytoskeleton is in a constant state of flux as it is organized and reorganized to fulfill different purposes. Key to regulating the organization of the microtubule cytoskeleton is the centrosome [1], a non-membrane-bound organelle that nucleates the formation of microtubules such that minus ends are proximal to the centrosome and plus ends distal, leading to the formation of microtubule arrays of uniform polarity. Through the action of microtubule-based motor proteins, these arrays can promote the directed movement of cellular constituents to specific regions of the cell or be organized into a mitotic spindle for the segregation of chromosomes.

Analysis of the behavior and composition of the microtubule cytoskeleton has been aided by the application of confocal microscopy [2]. In combination with a model genetic organism, this imaging technique can be used to study the role of individual genes

Stephen W. Paddock (ed.), *Confocal Microscopy: Methods and Protocols*, Methods in Molecular Biology, vol. 1075,
DOI 10.1007/978-1-60761-847-8_13,

in controlling various aspects of microtubule behavior. The nematode *Caenorhabditis elegans* is one such model system that has been used to great advantage to identify genes with microtubule-related functions [3–5]. In the germ cells and embryos of this organism, powerful forward (mutation) and reverse (RNAi) genetic methodologies can be combined with confocal imaging to probe gene function. The large cells of the early embryo have been the preferred tissue for cytological studies. In these cells, robust microtubule arrays, including meiotic and mitotic spindles, are assembled and disassembled according to a rigid developmental plan. This reproducible behavior of the microtubule cytoskeleton allows investigators to readily identify mutations that have even subtle effects on centrosome or microtubule function. Cells of the oocyte and sperm lineages are also amenable to this combined genetic and cytological approach and can be used to study how the microtubule cytoskeleton is specialized to function during oogenesis and spermatogenesis. In this review, we present confocal imaging methods for studying the centrosome and microtubule cytoskeleton in *C. elegans* embryos and germ cells. Although we present these methods as optimized for the imaging of centrosomes and microtubules, they are applicable to the study of many other intracellular components.

2 Materials

1. Superfrost slides (Fisher Scientific; Catalog No. 12-550-15).
2. 24 mm × 50 mm cover glasses (Fisher Scientific; Catalog No. 12-545-88).
3. Tungsten carbide pencil (Fisher Scientific; Catalog No. 13-378).
4. Poly-L-lysine solution (Sigma; Catalog No. P 8920).
5. M9 Buffer (1 L) KH_2PO_4 (3.0 g), Na_2HPO_4 (6.0 g), NaCl (5.0 g), 1 M $MgSO_4$ (1.0 ml). Mix all but $MgSO_4$. Adjust volume to 999 ml and autoclave. When cooled add sterile 1 M $MgSO_4$.
6. Anti-α-tubulin monoclonal antibody DM1A (Sigma; Catalog No. T 9026).
7. 10× PBS (1 L) KH_2PO_4 (2.4 g), Na_2HPO_4 (14.4 g), NaCl (80.0 g), KCl (2.0 g). Dissolve in 800 ml distilled deionized water. Adjust pH to 7.2, bring volume to 1 L, and autoclave.
8. PBSBT (0.1 L) Add 10 ml 10× PBS and 0.5 ml Tween 20 to 89.5 ml distilled deionized water. Mix well then add 0.5 g bovine serum albumin (Fraction V). Gently stir the solution

until the BSA dissolves. Once made, PBSBT can be stored at 4 °C for 1–2 months.

9. Alexa Fluorescently labeled secondary antibodies (Molecular Probes).
10. Vectashield Mounting Medium (Vector Laboratories; Catalog No. H-1000).
11. TOTO-3 iodide (Molecular Probes; Catalog No. T-3604).
12. OliGreen (Molecular Probes; Catalog No. O-7582).
13. 37 % Paraformaldehyde (Electron Microscopy Sciences; Catalog No. 15686).
14. 10 % Paraformaldehyde Fixing Solution (10 ml) 37 % paraformaldehyde (2.7 ml), 1 M PIPES, pH 6.7 (1.2 ml). Add components to 6.1 ml water and mix.
15. 16 % Paraformaldehyde (Electron Microscopy Sciences; Catalog No. 15710).
16. Modified Seydoux and Dunn Fixative (0.1 L) 10× PBS (10 ml), 1 M HEPES pH 6.9 (8 ml), 1 M $MgSO_4$ (0.16 ml), 0.1 M EGTA (0.8 ml), fresh 16 % paraformaldehyde (10 ml). Bring volume to 100 ml with water.
17. Concavity slides (PGC Scientifics; Catalog No. 60-5500-16).
18. 6 mm × 50 mm disposable glass culture tubes (Fisher Scientific; Catalog No. 14-958-A).
19. Gonad buffer (1 L) NaCl (3.5 g), KCl (2.4 g), $Na_2HPO_4{\cdot}7H_2O$ (0.8 g), 1 M $MgCl_2$ (2 ml), 1 M $CaCl_2$ (2 ml), 1 M HEPES pH 7.2 (5 ml), 20 % Glucose (10 ml). Add HEPES, NaCl, KCl, and $Na_2HPO_4{\cdot}7H_2O$ to 900 ml water and dissolve thoroughly. Add glucose and mix thoroughly. Add $MgCl_2$ and $CaCl_2$ dropwise to avoid precipitation. Adjust pH if necessary and bring to 1 L with distilled deionized water. Sterilize by filtration.
20. Silicone grease (Fisher Scientific; Catalog No. 14-635-5D).
21. Egg buffer (1 L) NaCl (6.9 g), KCl (3.58 g), 1 M $MgCl_2$ (2 ml), 1 M $CaCl_2$ (2 ml), 1 M HEPES pH 7.4 (5 ml). Dissolve NaCl and KCl in 800 ml distilled deionized water then add HEPES, $MgCl_2$, and $CaCl_2$. Adjust pH if necessary and bring to 1 L with water. Autoclave.
22. Agarose in egg buffer (0.1 L). Add 3 g agarose to 100 ml egg buffer. Heat in a microwave oven until dissolved. Aliquot 4–5 ml per 15 ml disposable polypropylene tube and store at 4 °C.
23. Lab tape (Daigger; Catalog No. TX14831).
24. Mouth pipet (Sigma; Catalog No. A-5177).

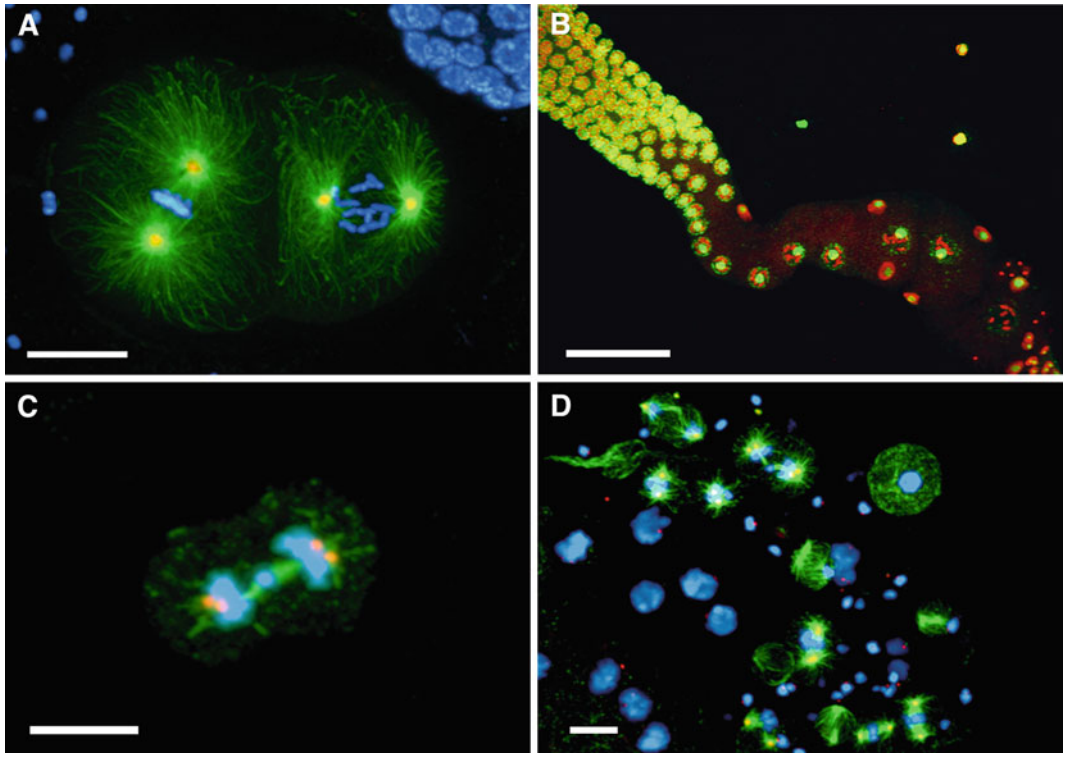

Fig. 1 Confocal images of embryos and germ cells. (**a**) A two-cell embryo stained for microtubules (*green*), SPD-2, a centrosome marker (*red*), and DNA (*blue*). The SPD-2 staining appears *yellow* due to overlap with microtubules. (**b**) An adult gonad stained with anti-NOP1 antibody (*green*) to reveal the nucleolus and TOTO-3 (*red*) to show DNA. Nuclei in pachytene of meiotic prophase are to the *left* and oocytes in diakinesis to the *right*. (**c**) A primary spermatocyte undergoing meiosis and (**d**) a field of male germ cells stained for microtubules, SPD-2, and DNA. Bars in **a** and **b**, 10 μm. Bars in (**c**) and (**d**), 5 μm

3 Methods

3.1 Fixation and Staining of Embryos

All protocols for preparing *C. elegans* for immunofluorescence microscopy include a step to permeabilize the specimen to the fixatives, antibodies, and dyes that are typically used. In intact animals, embryos are protected by a chitinous eggshell and vitelline membrane, and gonads by the cuticle. The eggshell, like the cuticle, is impenetrable by most chemicals and is dealt with in one of two ways. Below we present our version of the popular freeze-crack method in which the eggshell is mechanically disrupted [6, 7]. Embryos are sandwiched between a glass slide and cover glass that is quickly frozen before being snapped apart. There are many permutations of this method, but we find that the protocol below is easy to perform, is highly reproducible, and gives excellent results (Fig. 1a). Alternatively, the eggshell can be removed with alkaline hypochlorite and the embryos stained in suspension [8].

This method, which typically requires a large number of animals, is not suitable for the youngest embryos but does avoid mechanical damage to the specimen.

3.1.1 Preparation of Slides

1. Using a tungsten carbide pencil, etch a circle ~15 mm in diameter on the underside of each Superfrost Plus slide to be used (*see* **Note 1**). The circle will mark the area of the slide containing the specimen.
2. Turn the slides over and pipet 10 μl of poly-L-lysine solution onto the surface of the slide (*see* **Note 2**).
3. Using a back-and-forth motion, spread the liquid over the surface with the edge of a glass cover slip. After 5–6 strokes, move to the next slide and do the same. Return repeatedly to each slide re-spreading the liquid until it stays spread and begins to dry.
4. Leave the slides face up on the bench to finish drying.

3.1.2 Freeze-Cracking

Embryos stain optimally when they are released from the body of the hermaphrodite. This can be accomplished by dissecting gravid hermaphrodites directly on the glass slide (*see* **Note 3**).

1. Draw 18–20 μl of M9 buffer into a micropipette tip.
2. Dispense approximately two thirds of this in the center of the inscribed circle on the glass slide leaving the rest in the pipet tip.
3. Using a stereomicroscope, pick hermaphrodites into the drop of M9. To avoid background staining, minimize the amount of bacteria carried over into the M9 buffer. Do not spend more than a few minutes transferring animals as the buffer will evaporate significantly.
4. Use the edge of a 21-gauge hypodermic needle to cut hermaphrodites in half at the vulva. A well-placed cut will release most of the embryos from the uterus.
5. Pipet the remaining M9 buffer onto a 24 mm × 50 mm cover glass. Invert the cover glass and turn it so that the long axes of the cover glass and slide are perpendicular. Keeping the cover glass horizontal, gently place it straight down on top of the dissected worms.
6. Leave the glass sandwich on the bench for 30s to allow the embryos and gonads to adhere to the slide.
7. Place the glass sandwich on the horizontal surface of a potato masher and gently lower the slide into a Dewar flask of liquid nitrogen (*see* **Note 4**). The slide should remain immersed until the liquid nitrogen stops boiling. At this point, the slide can be stored in the liquid nitrogen while you prepare any additional slides.

8. Using forceps, carefully draw the slides from the liquid nitrogen one by one and immediately remove the cover glass by holding the slide while flicking the overhanging edge of the cover glass with your finger. Immediately proceed to fixation.

3.1.3 Fixation Methods

Methanol is the most common fixative, yields a well-preserved microtubule cytoskeleton, and is compatible with a large number of centrosomal antigens.

Methanol Fixation

1. Immediately after freeze-cracking, submerge the slide in 100 % methanol at room temperature (*see* **Note 5**).
2. Leave slide submerged for 2–5 min (*see* **Note 6**).

Formaldehyde/Methanol Fixation Protocol 1

1. Immediately after dissecting worms, add an equal volume of 10 % Paraformaldehyde Fixing Solution to the specimen.
2. Cover specimen with a 24 mm × 50 mm cover glass and leave for 5 min.
3. Process the samples by freeze-cracking (**steps 7** and **8** Subheading 3.1.2) followed by methanol fixation (Subheading 3.1.3.1).

Formaldehyde/Methanol Fixation Protocol 2

This fixation protocol was published by Seydoux and Dunn [9] and later modified by J. Schumacher (personal communication). It works well with a wide variety of antibodies.

1. Immediately after freeze-cracking, submerge slides in –20 °C methanol for 10 s to 1 min.
2. Postfix for 15 min at room temperature in modified Seydoux and Dunn Fixative (*see* **Note 7**).

3.1.4 Staining and Mounting

During the staining process, slides are kept in a humidity chamber to avoid evaporation of antibody solutions during lengthy incubations (*see* **Note 8**).

1. When fixation is complete, transfer the slides to the humidity chamber and pipet 200 µl of blocking solution (PBSBT) onto the specimen. Watch the slide for a minute or so to make sure that the PBSBT stays in contact with the specimen.
2. Allow the slide to incubate for 20–30 min at room temperature.
3. While the slides are incubating, prepare working dilutions of the primary antibodies using PBSBT as the diluent (*see* **Note 9**). For labeling microtubules, monoclonal antibody DM1A can be used at a 1:1000 dilution (*see* **Note 10**).
4. After blocking is complete, turn the slide on its long edge to allow the liquid to run off onto a paper towel. Touch the edge of the slide to the paper towel to wick away liquid but do not

allow any contact between the paper towel and the specimen as embryos will be lost.

5. Place the slide back in the humidity chamber and add 50–200 μl of the primary antibody solution.
6. Allow the antibody to bind the specimen for either 2 h at room temperature or overnight at 4 °C. If choosing the longer overnight incubation, cover the specimen with a ~2.0 × 2.5 cm piece of Parafilm. This will hold the antibody solution in place by capillary action.
7. Blot off the primary antibody solution and wash the slide with 200 μl of PBSBT three times for 10 min each at room temperature.
8. During the last wash, dilute the secondary antibodies in PBSBT. After the last wash, cover each specimen with 200 μl of secondary antibody solution.
9. Incubate 1–2 h at room temperature.
10. Wash three times as before. To stain the sample for DNA, OliGreen, TOTO-3, or another appropriate reagent can be added to the second wash (*see* **Note 11**).
11. Add 8 μl of Vectashield mounting medium to an 18 mm × 18 mm cover glass and set aside. Blot the last wash off the slide and using a tissue, carefully wipe off excess buffer from areas immediately surrounding the specimen. Invert the cover glass and gently lay it down on top of the specimen, allowing the mounting medium to spread across the sample evenly. Being careful not to move the cover glass, tack the corners down with nail polish. Allow a few minutes to dry and then completely seal all edges with nail polish.

3.2 Fixation and Staining of Gonads

The germ line of the *C. elegans* hermaphrodite has often been the subject of studies relating to cell cycle regulation, differentiation, and development [10]. Its most striking characteristic is its linear arrangement of nuclei undergoing the transition from mitosis to meiosis. At the distal end, a population of stem cell nuclei undergoes mitosis. As these nuclei move proximally, they exit mitosis, enter meiosis, and finally differentiate into oocytes. Genes that play a role in the cell cycle—including those that regulate the microtubule cytoskeleton—can often be readily identified because they perturb this invariant arrangement of germ cell nuclei. Like the embryo, the hermaphrodite germ line is susceptible to RNAi and has a large size. Thus confocal imaging of mutant or RNAi-treated gonads can be very informative with regard to gene function. In many instances, suitable staining of gonads is obtained with the freeze-crack method used for embryos (Subheading 3.1.2). However, it is often imperative that the cytoarchitecture be as well preserved as possible. Below are two protocols to stain extruded

whole gonads (Fig. 1b). One is a modification of the dissection method described above where animals are dissected and fixed on slides. The other protocol is carried out entirely in concavity slides and test tubes, and thus the animals are stained in suspension.

3.2.1 Tissue Extrusion on Slides

1. Prepare slides as in Subheading 3.1.1.
2. Pick hermaphrodites into a drop of water in a concavity slide to clean away from bacteria. Or pick first to non-seeded plate to rid them of bacteria.
3. Add a 10–15-μl drop of egg buffer to the circled area of a prepared slide.
4. Transfer 10–20 animals from the concavity slide to the drop of egg buffer by scooping them with your pick. This is easier than it sounds.
5. While viewing through a stereomicroscope, quickly nick adult animals just below the pharynx or just above the anus with a new 27-gauge needle. Hold the needle in place until gonad arms pop out. Animals will thrash around. Even animals nicked in the wrong place will often extrude at least one gonad arm.
6. Cover the dissected animals with a 24 mm × 50 mm cover glass, placing it so that its long axis is perpendicular to that of the slide. The weight of the cover glass will help to extrude the gonad arms.
7. Freeze crack, fix, and stain (Subheadings 3.1.2–3.1.4) (*see* **Note 12**).

3.2.2 Tissue Extrusion in Suspension

Dissection

1. Pick adult animals to a drop of M9 or egg buffer in a concavity slide.
2. Quickly cut the worms with a hypodermic needle either just below the pharynx or at the anus. This process must be relatively fast (<3 min) so that proteins do not become modified (i.e., dephosphorylated) (*see* **Note 13**).

Fixation

1. Immediately after the dissections, add fresh 16 % paraformaldehyde so that final concentration in the concavity slide is 3 %.
2. With a glass pipet, transfer animals to disposable glass culture tubes and parafilm the tubes.
3. Allow gonads to fix for 1 h at room temperature or overnight at 4 °C. Try to get the gonads that are not attached to any carcasses—these often stain best.

Staining

1. Allow animals and free gonads to settle to bottom of tubes or gently spin them in a microfuge for 30 s.
2. Gently aspirate fixative with drawn out glass pipet. Be careful not to remove any animals or gonads.

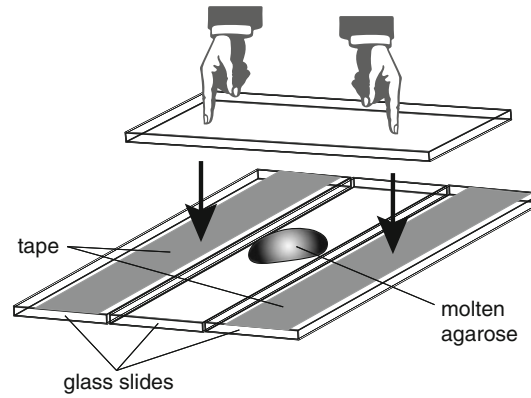

Fig. 2 Casting an agarose pad for live-mount imaging of a *C. elegans* embryo. Two glass slides, each with a single layer of laboratory tape, are laid on either side of a third slide. A drop of molten agarose in egg buffer is applied to the central slide, and a fourth slide is set on top. Gentle pressure is applied to the edges of the top slide as shown. Immediately before use, the top and bottom slide are pried apart, and the slide to which the pad sticks is laid face up on the bench

3. Wash animals and gonads 3–4 times in 50–100 µl of PBSBT.
4. Block in PBSBT for 0.5–1.5 h at room temperature.
5. Dilute primary antibody in PBSBT. After removing the blocking solution, add 100–250 µl of the primary antibody solution to each tube. Parafilm each tube and mix by gentle agitation (*see* **Note 14**). Incubate for 4 h at room temperature or overnight at 4 °C.
6. Wash gonads as before 3–4 times.
7. Incubate gonads with 100–250 µl of secondary antibodies diluted in PBSBT. Parafilm tubes, wrap in foil, and mix by gentle agitation for 2 h at room temperature or overnight at 4 °C.
8. Wash gonads as before 3–4 times. DNA can be stained by adding a dye such as TOTO-3 or DAPI in the next to last wash (*see* **Note 15**).
9. Prepare a mounting slide with 2 % agarose (in M9 buffer or water) solution (Subheading 3.5 and Fig. 2).
10. Add 10–15-µl Vectashield mounting medium to specimens and mouth pipet them to the agarose pad.
11. Using a needle or eyelash pick, arrange specimens so that gonad is away from carcass.
12. Trim agarose pad, add cover glass, and seal with nail polish as described (Subheading 3.1.4) (*see* **Note 16**).

3.3 Fixation and Staining of Sperm

Spermatogenesis in *C. elegans* is similar to that of other organisms [11]. A primary spermatocyte undergoes two successive meiotic divisions to form a spermatid, which subsequently differentiates

into a sperm. In *C. elegans* as in other species, the male—but not female—meiotic spindles are organized by canonical centrosomes [12]. Thus, analysis of spermatogenesis offers the potential to learn how centrosome replication and function might be regulated differently during meiosis and mitosis.

While confocal microscopy is not performed on male meiotic tissue as routinely as it is on embryos or hermaphrodite gonads, the methodology is relatively straightforward. All cellular intermediates of the male meiotic program can be dissected away from the gonad where they can be processed for confocal imaging (Fig. 1c, d).

1. Prepare Superfrost Plus slides (Subheading 3.1.1). Using a grease gun (*see* **Note 17**), apply four very small dots of silicone grease onto a 24 mm × 50 mm cover glass. The dots should be spaced ~18 mm apart at the corners of an imaginary square. Set aside.
2. Pick males into an 11-μl drop of gonad buffer (*see* **Note 18**) on the slide and cut just behind the pharynx with a hypodermic needle.
3. With the slide on the bench top, invert the cover glass and set it down on the glass slide so that the long axes of the cover glass and slide are perpendicular. The grease should be sandwiched between the slide and cover glass. Using fingers apply pressure downward on the cover glass until the worms appear clear. The grease, which will spread as pressure is applied, helps to avoid crushing the specimen.
4. Freeze slide in liquid nitrogen.
5. Flick off the cover glass and submerge slide in 100 % room-temperature methanol for 5 min.
6. Place slide face up in humidity chamber.
7. Immediately add 200-μl PBSBT and incubate at room temperature for 30 min.
8. Follow the antibody-staining protocol (Subheading 3.1.4).

3.4 Imaging of Fixed Specimens

Imaging of centrosomes and microtubules in fixed *C. elegans* embryos and germ line cells is done using standard confocal procedures [6]. On our spinning disk confocal microscope, we routinely use a 100× objective for embryos and male germ cells and a 40× objective for gonads. Because the microtubule cytoskeleton extends throughout the entire volume of embryos and most germ cells, z-series can provide important spatial information that is missed when viewing a single focal plane. When performing a z-series, we typically space optical slices 0.2 to 0.5 μm apart.

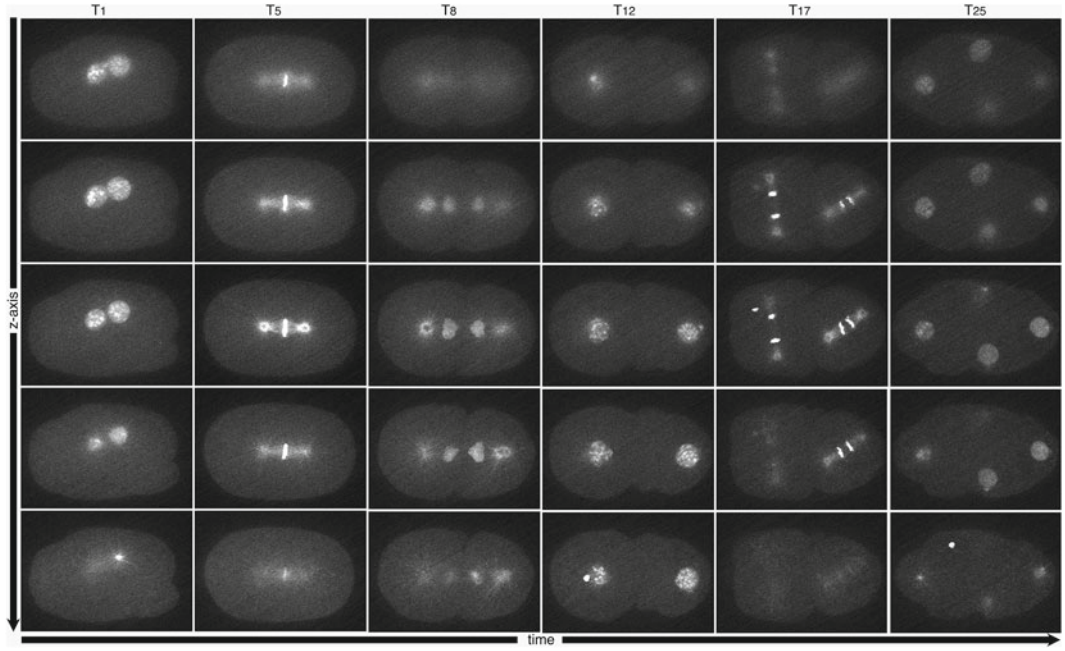

Fig. 3 A temporal progression of individual z-series from a four-dimensional data set. A spinning disk confocal microscope was used to record early development of a *C. elegans* embryo expressing GFP-histone and GFP-alpha-tubulin. Eight optical sections, spaced 2 μm apart, were collected every 90 s. Each column displays the six central focal planes at the indicated time points

3.5 Imaging of Live Specimens

Analysis of the dynamic behavior of centrosomes and microtubules in live specimens can be achieved in *C. elegans* through the combined use of GFP tagging and spinning disk confocal microscopy (Fig. 3). Embryos, at nearly all stages of development, can be isolated from mothers and cultured in vitro. Under the appropriate conditions, even very young embryos will undergo normal development while being intensively imaged (*see* **Note 19**).

To ensure a favorable orientation, embryos are slightly flattened when mounted for live imaging. This is achieved by gently sandwiching the embryo between a buffer-equilibrated agarose pad and a cover glass [13].

1. To cast an agarose pad, apply a single strip of lab tape to each of two glass slides. With their taped sides facing up, position the two slides on either side of a third glass slide (Fig. 2). Add a drop of molten agarose in egg buffer to the center slide and immediately place a fourth slide on top of and perpendicular to the slide containing the agarose. Press down on the ends of the top slide and set aside. Cast in this way, the thickness of the agarose pad will approximate that of the tape.
2. Under a stereomicroscope, dissect hermaphrodites to obtain young embryos. Pick two to three gravid hermaphrodites into

a drop of egg buffer on an 18 mm × 18 mm cover glass. Using a hypodermic needle, cut the animals in half to release the embryos.

3. Pry the two slides holding the agarose pad apart.
4. Hold the slide with the agarose pad over the drop of egg buffer, such that the pad is facing down. Gently lower the slide until the pad contacts the drop of egg buffer. The buffer should immediately spread out drawing the cover glass onto the pad by capillary action.
5. If needed, carefully trim the agarose pad so that it is about the size of the cover glass. Using a small paintbrush dipped in molten petroleum jelly, seal the edges of the cover glass to prevent the specimen from drying out.
6. Immediately proceed with imaging (*see* **Note 19**).

4 Notes

1. An alternative to using the precoated Superfrost slides is to coat your own slides as previously described [6].
2. Because Superfrost slides are precoated, addition of poly-L-lysine is not absolutely necessary. However, we do find that this step improves retention of embryos.
3. In addition to embryos, dissection of hermaphrodites in the manner outlined will yield single gonad arms and smaller fragments that will adhere to the slide and stain. For some purposes, this method of staining gonads will suffice. Alternatively, to better preserve morphology, whole gonads can be extruded from worms and stained in suspension (Subheading 3.2).
4. In many freeze-crack protocols, slides are frozen by laying them on a metal block that has been pre-chilled on dry ice. If performed correctly, this method yields a well-preserved microtubule cytoskeleton. However, because microtubules are cold and pressure sensitive (exactly the conditions embryos are subject to during freeze-cracking), freezing needs to be performed as rapidly as possible to avoid microtubule loss. For this reason, we prefer freezing slides by submersion in liquid nitrogen.
5. Some older fixation protocols perform the methanol fixation at –20° and follow this with a 5-min post-fixation step in cold acetone [6]. We have found that at least with *C. elegans*, the acetone step is unnecessary. However, when performing immunofluorescence on other species of nematodes such as *Acrobeloides*, treatment with acetone is necessary [14]. We have also found that methanol fixation works better for embryos at room temperature. Cold fixation often results in

significant shrinkage of embryos that often results in bending of long microtubules.

6. Lengthier fixation times in methanol have been found to result in loss of some centriolar antigens (S. Leidel and P Gonczy, pers comm.).
7. For reproducibility, it is best to make this fixative fresh each time using a new vial of 16 % paraformaldehyde.
8. Our humidity chambers consist of a plastic box with a sealable lid. Two pieces of Whatman paper are wetted with water and placed on the bottom of the box. On top of this, we lay one or two flat plastic rectangular inserts from a disposable pipet tip box to serve as a dry pedestal on which the slides are laid face up.
9. Some older protocols employ different solutions for blocking and for antibody incubations and washing. We have found this to be unnecessary, as use of PBSBT throughout gives identical results.
10. Primary Antibodies
    (a) If direct immunofluorescence is an option, FITC-conjugated DM1A (Sigma; Catalog No. F2168) produces excellent results [15].
    (b) When testing a new antibody, it is often wise to co-stain with an antibody that you know works to confirm that your freeze crack and fixation worked. A number of commercially available antibodies raised against non-nematode antigens have proven quite cross-reactive with the corresponding *C. elegans* protein and may serve as useful controls when staining specimens. Those antibodies are the following:

Antibody name	Catalog #	Antigen	Supplier
MAb 414	MMS-120P	Nuclear pore complex	Covance
MAPK-YT	M8159	Activated MAPK	Sigma
MCA-38F3	MCA-38F3	NOP1	EnCor Biotech
Anti-pH3 (ser10)	06-570	Phosphohistone H3	Upstate Biotech
MAb C4	691001	Actin	MP Biomedicals

11. Selection of the appropriate DNA dye will depend upon the fluorophore-conjugated secondary antibodies that are used. The krypton/argon lasers that power many confocal systems

produce output maxima at wavelengths of 488, 568, and 647 nm, allowing simultaneous detection of fluorescein, rhodamine, and Cy5, respectively. OliGreen, which excites at 488 nm, is used at a final dilution of 1:8,000. A stock solution is prepared by diluting the concentrated dye 1:8 in DMSO and storing at –20 °C in aliquots. Just before each use, the stock is diluted 1:1,000 in wash buffer. TOTO-3 iodide excites at 642 nm, can be detected in the Cy5 channel, and is used at a dilution of 1:4,000. A stock solution is prepared by diluting the concentrated dye 1:4 in DMSO and storing at –20 °C in aliquots. Just before each use, the stock is diluted 1:1,000 in wash buffer. Molecular Probes also offers BOBO-3 iodide (Catalog No. B3586), which excites in the rhodamine channel. Before final dilution, make sure dye/DMSO solutions are completely thawed and well mixed.

12. In contrast to embryos, gonads seem to stain best after overnight fixation in methanol at –20 °C.
13. Animals may be anesthetized to facilitate dissection. This can be accomplished by including 0.5 mM levamisole or 0.01–0.05 % sodium azide in the dissection buffer.
14. For gentle agitation, we prefer to use an Adams Nutator (Fisher Scientific; Catalog No. 14-062).
15. Alternatively, one can use Vectashield mounting medium that contains DAPI (Vector Laboratories; Catalog No. H-1200). However, DAPI cannot be imaged by confocal systems that use a krypton/argon laser.
16. Mounting Gonads
    (a) It is best to examine specimens within 24 h. Otherwise, leave the specimens in the last wash until you are ready to mount and view them.
    (b) Alternatively, the gonads may be mounted directly on a glass slide without the use of an agarose pad.
17. To make a grease gun, backfill a 5 ml syringe with silicone grease and reattach the plunger. Attach an 18-gauge hypodermic needle to the syringe and snip off most of the length of the needle with wire cutters. Keep the needle capped when not in use.
18. Sperm medium [16] or M9 buffer may be used in place of gonad buffer.
19. Live cell imaging:
    (a) For imaging live specimens, we use a PerkinElmer Ultraview LCI spinning disk system. Embryos are imaged with a 100× (NA 1.4) Plan Apo objective lens, a 488/10 nm band pass excitation filter, and a 500 nm long pass emission filter.

(b) Centrosomes are small organelles, and in the large volume of the *C. elegans* embryo, they exhibit dramatic movements. For these reasons, embryonic centrosomes can be a challenge to image if just one focal plane is being recorded. Thus, when possible, we use a multifocal plane time-lapse (four-dimensional) approach. At every time point, we record 5–10 focal planes, each separated by ~2 μm. Due to the effects of photoxicity of the specimen and bleaching of the GFP fluorophore, there is a limit to the number of images that can obtained from a single specimen. Thus, if you increase the number of focal planes to be acquired, you must offset this by decreasing the number of time points sampled.

(c) In utero imaging of embryos during ovulation or meiosis, adults need to be anesthetized: pick young adult hermaphrodites into a 200-μl drop of M9 buffer containing 0.1 % tricaine and 0.01 % tetramisole in a concavity slide. Let the animals incubate for 15–30 min. Worms should become completely immobile and should stay immobile for 1–2 h. Remove animals from anesthetic and transfer to an agarose pad for viewing.

Acknowledgments

We thank Jill Schumacher for sharing her modification of the Seydoux and Dunn protocol, Mary Kosinski and Michael Miller for their modifications of the gonad suspension method, Penny Sadler for her sperm squash protocol, and Catherine Kemp, Murali Addepalli, and Anna Burrows for critically evaluating the manuscript.

References

1. (2004) Centrosomes in Development and Disease. Edited by Erich A. Nigg copyright 2004 Wiley-VCH Verlag GmbH &Co. KGaA, Weinheim ISBN 3-527-30980-2
2. Gard DL, Cha BJ, Schroeder MM (1995) Confocal immunofluorescence microscopy of microtubules, microtubule-associated proteins, and microtubule-organizing centers during amphibian oogenesis and early development. Curr Top Dev Biol 31:383–431
3. Bowerman B (2001) Cytokinesis in the *C. elegans* embryo: regulating contractile forces and a late role for the central spindle. Cell Struct Funct 26:603–607
4. Goldstein B (2000) Embryonic polarity: a role for microtubules. Curr Biol 10:R820–R822
5. Gonczy P (2002) Mechanisms of spindle positioning: focus on flies and worms. Trends Cell Biol 12:332–339
6. Crittenden SL, Kimble J (1999) Confocal methods for *Caenorhabditis elegans*. Methods Mol Biol 122:141–151
7. Miller DM, Shakes DC (1995) Immunofluorescence microscopy. Methods Cell Biol 48:365–394
8. Aroian RV, Field C, Pruliere G, Kenyon C, Alberts BM (1997) Isolation of actin-associated

proteins from *Caenorhabditis elegans* oocytes and their localization in the early embryo. EMBO J 16:1541–1549

9. Seydoux G, Dunn MA (1997) Transcriptionally repressed germ cells lack a subpopulation of phosphorylated RNA polymerase II in early embryos of *Caenorhabditis elegans* and *Drosophila melanogaster*. Development 124: 2191–2201
10. Schedl T (1997) Developmental genetics of the germ line. In: Riddle DL, Blumenthal T, Meyer BJ, Priess JR (eds) *C. elegans* II. Cold Spring Harbor Laboratory Press, Plainview, NY, pp 241–269
11. L'Hernault SW (1997) Spermatogenesis. In: Riddle DL, Blumenthal T, Meyer BJ, Priess JR (eds) C. ELEGANS II. Cold Spring Harbor Laboratory Press, Plainview, NY, pp 271–294
12. Albertson DG, Thomson JN (1993) Segregation of holocentric chromosomes at meiosis in the nematode, *Caenorhabditis elegans*. Chromosome Res 1:15–26
13. Verbrugghe KJ, White JG (2007) Cortical centralspindlin and G alpha have parallel roles in furrow initiation in early *C. elegans* embryos. J Cell Biol 120:1772–1778
14. O'Connell KF, Maxwell KN, White JG (2000) The spd-2 gene is required for polarization of the anteroposterior axis and formation of the sperm asters in the Caenorhabditis elegans zygote. Dev Biol 222:55–70
15. Golden A, Sadler PL, Wallenfang MR, Schumacher JM, Hamill DR, Bates G, Bowerman B, Seydoux G, Shakes DC (2000) Metaphase to anaphase (mat) transition-defective mutants in Caenorhabditis elegans. J Cell Biol 151:1469–1482
16. L'Hernault SW, Roberts TM (1995) Cell biology of nematode sperm. Methods Cell Biol 48:273–301

Chapter 14

Measurement in the Confocal Microscope

Guy Cox

Abstract

All measurements require that the microscope must be aligned as accurately as possible, and the gain (or PMT voltage) and black level must be set to avoid any overflow or underflow. Measuring surface profiles and relative depths is straightforward and can be carried out to a higher accuracy than the depth resolution of the microscopes, even though the actual images may look poor. Measuring the thickness of objects which are labeled throughout is less accurate. Length and 2D area measurements are common image analysis problems and easily carried out with image analysis software. Volume measurements are conceptually equally simple but require manual techniques or 3D analysis software. 3D surface area measurements require specialist software, or can be carried out with stereological techniques. Fluorescence intensity measurements require careful calibration. For ratiometric measurements filters and/or laser lines should be chosen to optimize the response and calibration should be done in conditions as close as possible to the experimental ones. FLIM allows exploration of the chemical environment, and multiple labelling even where spectra overlap. When the hardware is available it is also usually the method of choice for measuring FRET, which can measure molecular interactions in the nanometer range. Without FLIM hardware, either intensity measurements with correction for bleed-through and cross talk or acceptor bleaching are the most popular methods of measuring FRET.

Key words Alignment, Contrast, Depth measurement, Thickness measurement, Length measurement, Area measurement, Volume measurement, Fluorescence measurement, Stereology, Ratiometry, FLIM, FRET

1 Prerequisites

1.1 Alignment

Accurate alignment of the microscope is vital for most measurements. Many of the more complex modern microscopes do not provide any alignments accessible to the user but even so regular checks to be sure that the system is functioning properly are essential. Many of the alignments described below are not user adjustable on the current generation of high-end systems but that does not make it any the less essential to check them. Experience shows that the service engineer may not always know best.

If the focussed spot is not aligned precisely on the pinhole the image will not be at its brightest when it is in true focus. This is guaranteed to destroy the accuracy of any measurement, particularly

Stephen W. Paddock (ed.), *Confocal Microscopy: Methods and Protocols*, Methods in Molecular Biology, vol. 1075,
DOI 10.1007/978-1-60761-847-8_14,

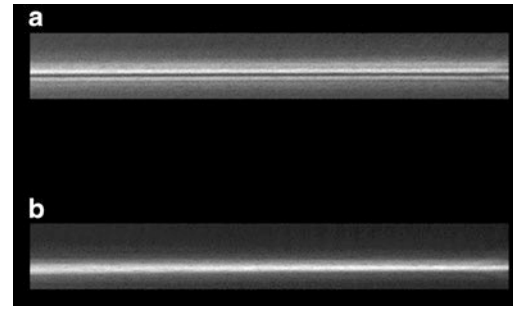

Fig. 1 Confocal reflection images of a mirrored coverslip. (**a**) XZ image with the pinhole misaligned. Note how the reflective surface appears artifactually as a *double line*. (**b**) With the pinhole aligned correctly the surface appears as a *single line*

measurements of depth and intensity. A mirror coverslip (*see* **Note 1**) is a very useful test specimen for this. To check the pinhole alignment with a mirror coverslip take a vertical (X–Z) section of the coverslip with the pinhole fully closed—misalignment will show as a double image of the reflective surface (Fig. 1). The actual alignment is best carried out with a brightly fluorescent sample, adjusting the pinhole for maximum signal, but the mirror slide is the most sensitive test. Carry out the alignment with the pinhole fully closed (or the smallest pinhole selected) for greatest accuracy. Then select the best size—between 0.7 and 1 times the airy disk diameter—for the objective being used.

The axis of the scan must pivot around the back focal plane of the objective lens. If this is not so vignetting will occur—the edges of the image will be dimmer than the center. This will affect some measurements more than others, but it will have most importance where structures are being segmented out by grey values. Some manufacturers provide a tool to check this in the form of a prism (upright microscopes) or a diffuser (inverted microscopes) which fits in the objective position. If not, just remove an objective and place a piece of paper or card on the stage. *Do not use any reflective object such as a mirror or even a glass slide.*

The circular patch of laser light should appear stationary. If it is not, the appropriate adjustment must be made. On older or simpler microscopes this may be accessible to the user—on the now-discontinued Biorad systems, for example, the height of the transfer lens between microscope and confocal head is adjusted by a screw collar. On more modern or sophisticated systems a service call will be required. After this adjustment the confocal and conventional optical systems may need readjustment to make them parfocal so that both the confocal image and that seen through the eyepiece are in focus. (This is worth doing purely as a matter of convenience, but it could also affect the magnification if it was severely out.) Again taking the Biorad as an example, the confocal head is moved towards or away from the microscope port to make both

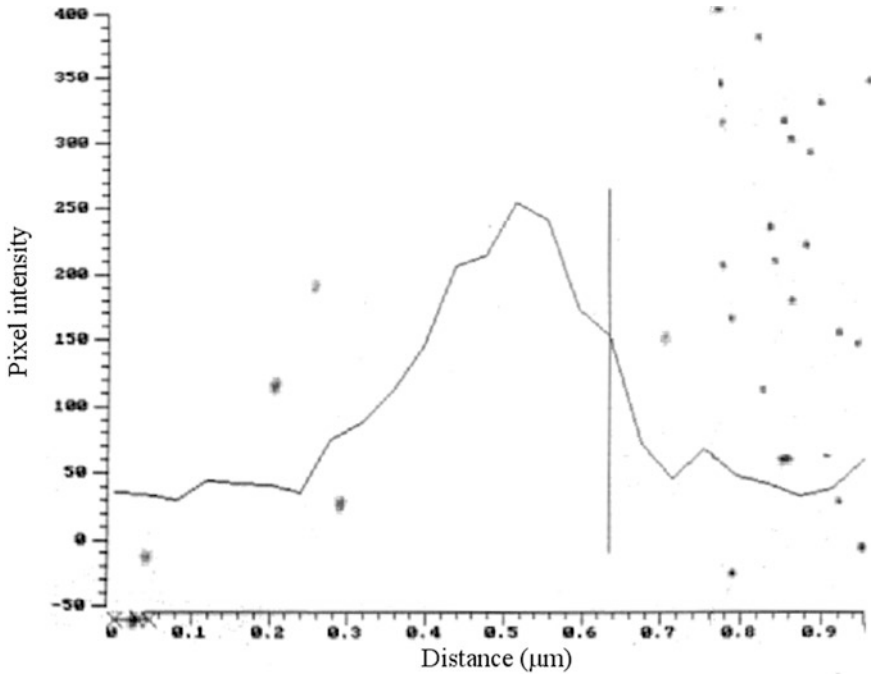

Fig. 2 Line profile across a 100 nm fluorescent bead, taken using a ×63, NA 1.4 oil immersion lens. The width of the curve, taken half-way between the maximum and minimum values, gives the resolution of the system. To obtain a meaningful value the peak must not reach saturation intensity (256) and the background has to be above 0

sets of optics parfocal—and once again more complex systems will need a visit from the technician.

The field of view of the confocal optics should be centered on the optical view. It is inconvenient if it is not, and although measurements will not be affected, resolution might be as all lenses perform at their best in the center of the field of view. The illumination should be even across the confocal image. A piece of fluorescent plastic is a good test specimen for this—the filter manufacturer Chroma (Brattleboro, Vt, USA) supply uniformly fluorescent plastic microscope slides in several colors, which are ideal for this. Some microscopes are notably uneven at their lowest zoom settings—in this case it is better to use a higher zoom.

1.2 Contrast

The requirements for obtaining accurate measurements in the confocal microscope are not necessarily compatible with the best image quality as judged by eye. First, it is essential, when making any measurements of intensity or resolution, that the mean background intensity nowhere goes to zero. While this is not so essential for measurements of position or depth, it is still advisable since otherwise the resolution, and hence the possible error, cannot be estimated (Fig. 2). In most cases the background level needs to be the dark current from the photomultiplier, since background fluorescence in the tissue may

vary from sample to sample. Therefore the first step should be to remove the sample from the microscope and adjust the black level until a (just) nonzero value is present across the entire field of view. The resulting background will probably be higher than would be chosen for visual impact, but it is easy to rescale the image for publication and impossible to recover information that has been lost. Never use automatic gain or black level control when making measurements.

It is even more important, for any sort of measurement, that the intensity at any point in the image never exceeds the maximum which the system can record. Most modern confocals will acquire and store 12-bit images (maximum value 4,095 counts) but in many cases they default to 8-bit images, in which case the maximum recordable intensity is 255. This is all too easy to exceed, and it is very important to set the gain of the amplifier or the PMT voltage to a value at which even your brightest sample will not saturate the image. If the intensity values saturate at any point in an object then its true intensity cannot be measured, and neither can its position laterally or in depth. Always select the 12-bit option when possible.

1.3 Summary

Before you start, the microscope must be aligned as accurately as possible, and the gain (or PMT voltage) and black level must be set to avoid any overflow or underflow.

2 Depth and Thickness Measurement

Confocal microscopes are commonly used for making measurements in depth—something which conventional microscopes, whether light or electron, cannot easily do. Their major rivals in this field are scanning probe (atomic force) microscopes and interferometric microscopes, both of which offer superior accuracy to confocal microscopes but can only measure surfaces. In the confocal microscope various types of measurement are possible, with varying degrees of accuracy. The relative heights of various parts of a single surface can be measured with considerable precision, whereas measurements of vertical depths and spacings within a three-dimensional solid or liquid are constrained to some extent by the resolution of the system, which is unlikely to exceed 0.5 μm in the axial direction. Since axial resolution is related to the *square* of the numerical aperture, it is absolutely essential to use the highest NA objective which is capable of covering the desired area.

Common to all depth measurements is the need to take account of the refractive indexes of the specimen and of the medium in which it is mounted (which should be the same if possible). If specimen, mountant, and the medium between sample and lens are all equivalent in refractive index, the displacement of

the slide or the objective will give the actual depth difference and no correction is needed. This applies whatever the actual refractive index is.

Examples are as follows:

1. Sample mounted in permanent mountant, under a coverslip, viewed with an oil immersion lens (refractive index (n) = ~1.5 throughout).
2. Surface sample, such as a tooth, bone, or pollen grain viewed in reflection mode, in air (n = 1 throughout).
3. Living sample, viewed in water, using a water-immersion lens, with or without a coverslip (n = ~1.3).

In each case the lens must be optically corrected for the medium. In (1) it is obvious that an oil-immersion lens is needed, while in (2) the objective must be corrected for use without a coverslip (the prefix epi- is often used). In (3) the lens must not only be designed for water immersion, but it will also specify whether or not a coverslip is required. (The coverslip will only affect the optical correction, not the measurement since it will introduce an equal apparent displacement to all levels of the sample.) A lens which is not matched to the medium will give a very poor image because of spherical aberration (SA), which can only be corrected for a single working distance and optical medium. The effects of SA increase as the *cube* of the NA, and since we saw above that a high NA lens is required for good depth resolution it follows that a refractive index mismatch can severely reduce resolution both laterally and in depth. In some circumstances it can actually give incorrect depth measurements [1].

Conventional "dry" (non-immersion) objectives for biological use are intended for use with a coverslip, and with the specimen beneath mounted in a medium of refractive index ~1.5. The distance from the top of the coverslip to the sample should be 0.17 mm, and this figure will be marked on the lens. Provided that this distance is, overall, approximately correct, reasonably well-corrected images can be obtained over a distance of several microns, but relative depth measurements must be corrected for the difference between the refractive index of the medium around the lens and the medium containing the sample. Figure 3 shows why this is so. Rays of light from the object are refracted away from the normal as they leave the coverslip, according to Snell's law of refraction. They therefore appear to emanate from the point indicated by the dotted lines. The correct measurement will be given by multiplying the apparent measurement by the refractive index of the mountant (1.5) over that of air (1)—in other words the correct figure will be 1.5 times the measured value.

Samples mounted in water should not, in theory, be measured with a dry lens but in the real world we may want to do this. The image will be reasonable about 0.2 mm below the upper surface

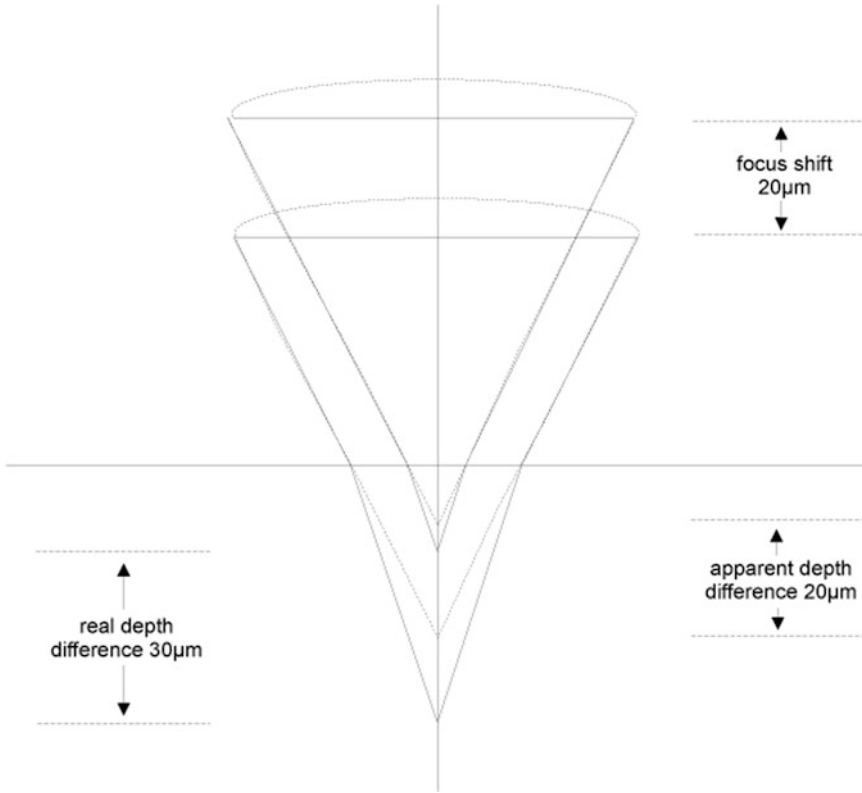

Fig. 3 The relationship between real and measured depth when using a dry lens with a permanently mounted sample

of the coverslip, and the measured depth should be corrected by multiplying by 1.3, the refractive index of water. Nevertheless a water immersion lens is strongly preferable—as well as not needing any correction, the image will be aberration free. Measuring depth or thickness in aqueous media under oil immersion should not be attempted—while a passable image can be obtained immediately below the coverslip the image quality deteriorates so rapidly with depth that measurements could not be trusted [2].

The software built into the microscope should make these apparent depth corrections automatically, so that reconstructions and depth measurements will be correct. But the standard software is often limited in functionality, and when using third-party programs such as Image J or one of the commercial analysis systems it is important to ensure that these corrections are made.

2.1 Measuring Heights on a Surface

Variations of height in a single plane surface can be measured with considerable accuracy in the confocal microscope; this is very commonly done in the engineering sciences but also has applications in biology. A line profile can be taken by making a vertical (X–Z)

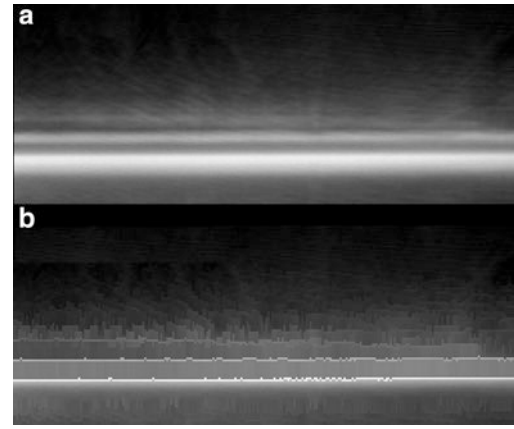

Fig. 4 X–Z section through a sample consisting of a 3 μm layer of SiO_2 on a silicon substrate. Over the oxide is a thin layer of oil (not normally a recommended practice but deliberate in this case!). In the original image (**a**) although the actual position of the surface of each layer is actually the brightest part this is not apparent to the unaided eye, and accurate measurements of layer thickness would seem impossible. After only five iterations of an erosion (thinning) algorithm, which preserves the peak intensity, the actual position of each surface (to the nearest pixel) is clearly visible

section of the surface, or an overall view can be had by collecting a series of optical sections. The accuracy to which a surface can be located considerably exceeds the vertical resolution of the microscope (resolution being the vertical distance between two objects which can be distinguished from each other). The spacing between planes (or lines in an X–Z section) should therefore be as fine as is compatible with a reasonable size for the resultant file.

The resulting dataset, viewed as an X–Z section or a side view in a 3D reconstruction, will generally look very disappointing at first glance. The plane surface will be stretched or smeared in depth—possibly to the extent that measurement seems impossible (Fig. 4a) [3]. However a line intensity profile through the surface will show that there is in fact a strong maximum at the actual location of the surface. This can be used directly as the basis for measurement, or various image processing techniques can be used. Thinning or erosion algorithms can produce a single-pixel wide line indicating the profile of the surface to the nearest depth step (Fig. 4b). Some systems include this feature as part of their standard software, but in other cases third-party software will be needed. Free software is available which will not only extract a surface in this way but also carry out hyperbolic interpolation to give sub-pixel accuracy (*see* **Note 2**). Another alternative is to create a height-coded image, which is effectively a contour-colored map of the surface, plotting the depth of the brightest pixel as the intensity in the output image.

2.2 Thickness Measurements

When measuring the thickness of a cell or a similar structure the simplest approach is again to take an XZ section, or multiple XZ sections. Where the boundary of the object is stained (for example where a cell is bounded by a labeled membrane or wall) the brightest pixel can again be taken as an indicator of the true position of the surface. The depth (with any necessary correction for refractive index) can then be measured from a line profile.

If the object to be measured is stained or labeled throughout its thickness the problem of determining the true edge of the structure is more complex. The best general approximation is to take the halfway point between the background level and the peak intensity. This will be reasonably valid provided that there is no refractive index difference between the object and the surrounding medium.

2.3 Summary

Refractive index effects must always be borne in mind when making this class of measurement. Measuring surface profiles and relative depths is straightforward and can be carried out to a higher accuracy than the depth resolution of the microscopes, even though the actual images may look poor. Measuring the thickness of objects which are labeled throughout is less accurate.

3 Length, Area, and Volume Measurement

Most confocal microscopes have a wide range of image analysis facilities built into their software. However no two offer the same features, and in many cases some features are quite expensive options which therefore may or may not be present on any individual microscope. Therefore some of the measurement protocols outlined in this section will require third-party software and some will not; the aim is to make the methods clear so that the user can select appropriate tools for the task. Almost all can be done in the popular freeware package Image J for which many plug-ins have been supplied by the user community, though commercial packages may be more user friendly.

3.1 Two-Dimensional Measurements

There is little here that is specific to the confocal microscope. Since the image is already in digital form these measurements are simple to do, and most microscopes include software permitting segmentation of single or multiple grayscale ranges for simple area measurement, and line cursors for measurements of straight-line lengths. More sophisticated measurements will require the files to be exported to specialist image analysis software.

3.2 Surface Area and Volume

Volume measurement from a confocal dataset is straightforward, since a count of the voxels in the volume of interest (with appropriate corrections for scaling in the vertical dimension) is all that is required.

Sometimes thresholding by intensity is enough to separate out the required object or objects, if the staining is sufficiently specific. In more complex situations "seeding" can be a valuable tool. This involves identifying a voxel within the desired volume and then setting intensity thresholds to segment out the required volume, spreading outward from the seed so that only the specified object is selected. This will give a numerical result very simply so long as intensity does not become significantly attenuated with depth. Some programs provide correction for depth attenuation, and so long as suitable fiduciary markers are present to validate the correction this can be extremely useful. Such markers can be structures for which it is reasonable to assume that staining is depth independent (such as expressible fluorescent protein markers) or fluorescent beads which are introduced into the sample. If these conditions cannot be met it may be preferable to segment out the structure of interest in the individual layers and measure each one. Naturally refractive index considerations for determining the true depth will still apply.

Surface area is less simple since a count of voxels making up the surface is *not* a measure of the actual area. The software must fit a surface to the 3D object and then measure it—a computationally intensive task but easily within the power of modern computers. Nevertheless, since statistical significance will often require many examples to be measured, there will be cases where a stereological approach (below) is more appropriate.

3.2.1 Stereological Approaches for Cases Where the Volume of Interest Is Not Fully Contained Within the Confocal Dataset

Measurements made on a random sample of sections can provide very accurate estimates of surface area and volume and this is often a more appropriate approach to determining these parameters in many biological systems. Textbooks on stereology offer a bewildering array of solutions which may well be necessary in difficult cases but two very simple formulae will be useful in a wide range of cases [4].

These are as follows:

1. $V_V = A_A$
   In other words, the volume of a structure or a compartment, per unit volume(V_V), is the same as the measured area of that component in a section, per unit area (A_A). The area of interest is segmented out, either by grey level, gradient changes or as a last resort by drawing, and its area (and that of the full image) is measured. This will (after measuring a suitable number of images) give an accurate estimate of the volume of the structure of interest.
2. $S_V = (4/\pi) L_A$.
   This tells us that by measuring the length of intercept of a membrane (or other surface) per unit area of section (L_A), and multiplying it by $4/\pi$, or ~1.27, we can estimate the surface area of the membrane present in a unit volume (S_V).

Both these measurements depend on the structure being oriented randomly in relation to the plane of sectioning. Provided that this assumption holds, confocal microscopes are excellent tools for stereology, since the need for physical sectioning is removed and fluorescent probes enable cells or organelles to be identified with high specificity and contrast. However, if the structure has a particular orientation in the specimen you must section in a range of random directions, and in that case sometimes conventional sectioning and wide-field microscopy will be more appropriate. It is essential to sample the section so as to include all parts equally—picking views which contain the structure you are measuring will **not** give the correct result. Usually it is best, to avoid any unconscious bias, to sample the specimen in a grid pattern, taking images at a series of predetermined coordinate points in *x*, *y*, and *z*.

3.3 Summary

Length and 2D area measurements are common image analysis problems and easily carried out with image analysis software. Volume measurements are conceptually equally simple but require manual techniques or 3D analysis software. 3D surface area measurements require specialist software but are often better carried out with stereological techniques.

4 Fluorescence Intensity Measurements

Making relative intensity measurements is relatively simple, while making absolute measurements is absolutely impossible.

Within its limitations the confocal microscope is probably the most accurate tool available for measuring intensity within a defined voxel space, but we need to be clear what this implies. If we want to measure the total fluorescence of an organelle—for example to determine the DNA content of a nucleus—this measurement is of little use, and wide-field fluorescence or flow cytometry are more likely to be useful tools.

The major problem we face in making fluorescence measurements is bleaching of the fluorochrome—this is likely to be at least as significant a factor as instrumental parameters [5]. Second to this is the problem of attenuation with depth in the sample which is very hard to quantify since it will be a mixture of absorption, scattering, and aberration of the beam and hence very dependent on local properties of the sample. As we shall see, these problems can be minimized by using measures that are independent of intensity, such as ratios or fluorescence lifetime.

4.1 Linearity Calibration

Photomultiplier tubes (PMTs) are quite reasonably linear through the major part of their range, though they are poor at very low gain (bias voltage)—rarely a problem when measuring fluorescence—and

they are often noisy at maximum gain. Nevertheless, if we want to quantify, for example, the increase in fluorescence following a stimulus it is a good idea to check the linearity of the response. This can be done with a fluorescent plastic sample, as mentioned above, but ideally should be done with a solution of a fluorescent dye to avoid bleaching. Adjust the laser intensity using the acousto-optic tunable filter (AOTF) or neutral density (ND) filters (whichever is used on your microscope) and plot the image intensity against laser power. Both AOTFs and NDs are normally accurate, but this can easily be checked with a laser power meter, which should be part of the troubleshooting kit in any confocal lab. You do need to take care that the fluorescence does not saturate (all available molecules in the excited state) at the higher intensities. This can be assessed by using more than one concentration of your fluorochrome solution, which will have the fringe benefit of showing whether measured intensity is linear with concentration (which it should be except at very high concentrations).

Ideally this should be done with more than one emission wavelength, though it is reasonable to expect that the detector will be equally linear at all wavelengths even though it is not equally sensitive.

4.2 Measurement

The black level should still be at the "no sample" setting established in 1.2. Insert the brightest sample you will wish to measure (highest concentration, poststimulus, or whatever) and (quickly so that bleaching is avoided) set the gain to keep the maximum intensity comfortably below saturation. From now on the PMT voltage and black level controls must not be touched. For safety's sake write down the values, or save them in a "method" file if your microscope has this facility.

There are three measurements you will normally need to make. Since there will always be background fluorescence in tissues, you must measure an unlabeled sample to quantify this. Then you need to measure a labeled negative control as well as your various experimental treatments. The relative differences in the amounts by which the fluorescence in the control and experimental samples exceed the background fluorescence of the unlabeled sample, corrected if necessary for nonlinearity in the detection, will be a reasonable measure of the differences in fluorescence resulting from the experimental treatments.

4.3 Ratio Imaging

Many fluorochromes can be used to measure pH, calcium, or other ion concentrations, since the wavelength of their emission or excitation peak (or both) will change with the concentration of the ion in question. Examples of curves for both emission-ratioing and excitation-ratioing dyes are shown in Fig. 5. It will be clear from these that since all curves are distinct, *in principle* measurements of intensity at any two wavelengths could be used to determine which

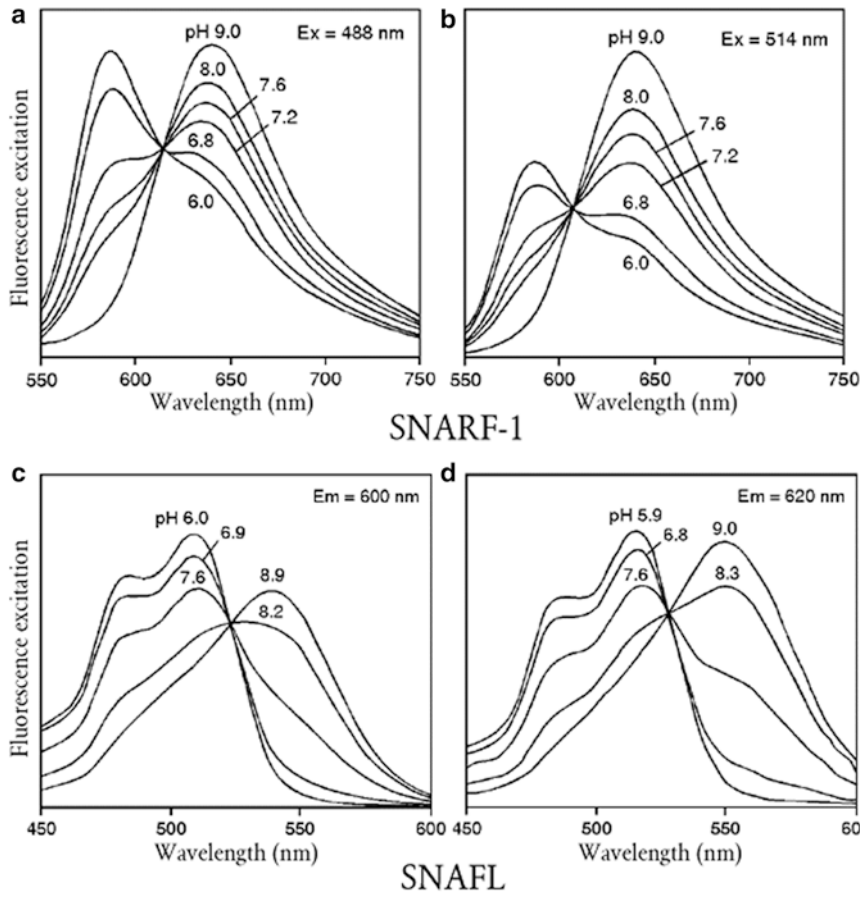

Fig. 5 pH-sensitive ratiometric dyes suitable for confocal microscopy. (**a**) Emission curves of carboxy SNARF-1 from pH 6 to pH 9 with excitation at 488 nm. (**b**) Corresponding curves using 514 nm excitation. (**c**) Excitation curves of carboxy SNAFL-1 from pH 6 to 8.9 measuring emission at 600 nm. (**d**) Excitation curves of carboxy SNAFL-2 measuring emission at 620 nm. Both would be suitable for ratiometric measurement in a confocal system using 488 and 568 nm excitation. Data reproduced from Haughland 1996, by kind permission of Molecular Probes Inc

particular curve we are on, and therefore the ionic concentration present. In practice this is less simple since the signal-to-noise ratio of the image will not be good enough for any reasonable accuracy unless we choose points where large changes can be expected. In general, for a given integration time, a confocal microscope will always give a worse signal/noise ratio than a wide-field CCD camera. During a 1-s exposure acquiring a 512×512 pixel image, each point in the sample will be sampled for 1 s in the wide-field camera, but only for 4 μs in the confocal microscope! This disadvantage is offset by the ability to sample in a particular focal plane so that the measurement is not degraded by interference from cells or free dye in higher or lower planes—*only use a confocal microscope for these measurements if you need this ability.* If not, you will be better off working with a wide-field microscope and CCD camera.

The great advantage of ratiometric measurement is that it is the *ratio* of the intensities at the two wavelengths that defines the ion concentration—the absolute intensity is unimportant. It is therefore unaffected by dye concentration, uneven loading, partitioning among cell components, and bleaching. It *will*, however, be affected by background fluorescence, so care needs to be taken to minimize autofluorescence. Dynamic range is also an issue when dividing one image by another, and 12-bit images are essential for accurate ratiometry. It is important to be sure that even high dye concentrations do not take the intensity at either wavelength to saturation.

In wide-field ratiometric imaging excitation ratioing is often preferred. For calcium measurement the dye of choice is usually Fura-2 [6]. Images are taken using excitation wavelengths of 340 and 380 nm with a 510 nm emission filter, and the ratio is taken between the two images. In the confocal microscope these wavelengths are not available. In confocal microscopy emission ratiometry is possible using either visible or two-photon excitation, and Indo 1, with two-photon excitation at 650–700 nm and detection at 400 nm and 500 nm, is a popular choice for calcium imaging. Excitation ratiometry is (currently) only feasible with single-photon excitation in the visible range of wavelengths.

Sometimes mixtures of dyes are used for emission ratiometric imaging—for example Fura red and fluo-3 to measure calcium concentration. Using 488 nm (argon) excitation, ratio imaging can be accomplished by detecting images at 520 and 650 nm (therefore routine FITC and rhodamine filter sets could be used). Often one dye is inert—does not change with the ion concentration being measured—while the other changes in intensity, but not wavelength. Effectively, therefore, the inert dye acts as a standard. The problem with this approach is that it is difficult to ensure equal loading of the two dyes in all cells of a population. Single dyes are preferable, and more are now being developed with confocal microscopy in mind. However, the discussion of individual dyes is beyond the scope of this chapter.

The fundamental protocol for making an emission ratiometric measurement is to record images at each wavelength (which can normally be taken simultaneously), subtracting the background level (determined previously) and then displaying the ratio of the two images. Confocal microscope manufacturers normally provide software for doing this automatically, though it may be an extra-cost option. It is worth paying for, so that the ratio image as well as the two original images are displayed live, as then one knows immediately if the experiment is working. More sophisticated versions can be calibrated so that they will display graphs of ion concentration against time for multiple points over the image. However, if speed is less of a consideration it is quite possible to make ratiometric measurements without additional software, using commercial image analysis packages or the freeware Image J.

The detection wavelengths will need to be chosen with some care. With a spectral detection system it is straightforward to set optimal channels for each peak, but on a filter-based system there can be problems when using standard filter sets. As an example, Fig. 5 shows how this applies to the pH dye SNARF-1. It will work very effectively with the two-channel filters designed for single-wavelength 488 or 514 nm excitation (argon ion or solid state). It cannot, however, be measured efficiently with filters designed for two-channel detection with dual excitation at 488/568 nm (argon–krypton) or 488/561 nm (solid state), since the fluorescence at 550 nm is very low and the low pH peak at ~580 nm will be blocked by the dichroic since it lies close to the longer excitation wavelength.

Excitation ratioing will require sequential collection of the two images, under software control. On systems where the emission line selection is controlled by an AOTF, the time delay between images will be small—effectively nonexistent if excitation can be switched on a line-by-line basis. On older or simpler systems, though, with filter wheels or shutters, the delay between images may be enough to be noticeable at short timescales. However, in general picking the most effective dye, and building the experiment around it, will usually be the best strategy. The precision of the laser lines (relative to the rather wide-band filters usually used for wide-field emission ratioing) can give a very accurate measurement if they match the characteristics of the indicator. Figure 5 shows an example—carboxy SNAFL-1 will give very effective ratio images from the 488 and 568 nm lines of an argon/krypton laser.

In any ratio imaging accurate calibration is essential if actual numeric output is required. Since both dissociation constants and fluorescent properties may be influenced by the environment inside a cell, this calibration cannot be done in vitro but must be done on the cell system being investigated. The principle is to clamp or buffer the concentration of the ion in question to a known value, or a series of values. EGTA can be used to produce defined calcium ion concentrations, and Nigericin is used to calibrate pH. In general the measured intensity ratios obtained from these known concentrations can be entered into the microscope's ratiometric software so that actual concentrations are shown on the live display.

4.4 Summary

First check that your system is linear in its response—and draw up a calibration curve if it is not. Set gain and black levels to be well clear of overflow and underflow. Then measure an unlabelled sample as well as labeled control and experimental samples. For ratiometric measurements filters and/or laser lines should be chosen to optimize the response and calibration should be done in conditions as close as possible to the experimental ones.

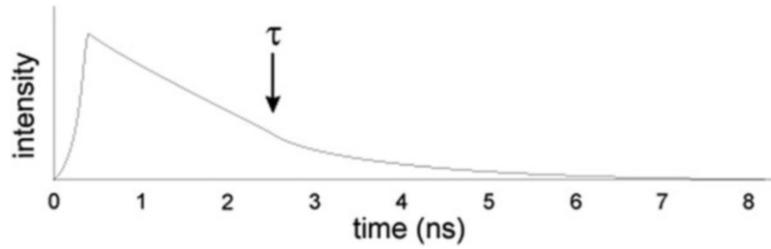

Fig. 6 Typical lifetime curve for a fluorescent pigment. There is a rapid rise followed by a slow, exponential decay. The lifetime τ is taken as the time at which it has decayed to, i.e., (~0.37) of the peak intensity

5 Fluorescence Lifetime, and Resonant Energy Transfer

After a fluorochrome absorbs light, there will be a variable delay before fluorescence is emitted. The electron which was excited by the absorbed photon must lose energy (as heat) to drop down to the lowest vibrational level of the excited state before it can return to the ground state, emitting the fluorescent photon (Kasha's law). There will therefore be an initial delay after excitation, and then fluorescence will commence and decay following first-order kinetics—an exponential decay curve—since only one chemical species is involved (Fig. 6). The rate constant will be different for different molecules, and is usually defined by the fluorescence lifetime τ, the time taken to decay to $1/e$ of the original intensity. (e, the base for natural logarithms, is approximately 2.72.) Common fluorochromes differ in lifetime—eosin has a very short lifetime or around 1.1 ns, with fluorescein at 3.25 ns, while lucifer yellow is much longer, at 7.81 ns.

We can in principle distinguish between fluorochromes by lifetime, even if their emission spectra are identical. Furthermore, we can expect the lifetime to change if anything happens in the chemical environment around the molecule which affects fluorescence. If any other de-excitation mechanism starts to compete with fluorescence we will no longer have first-order kinetics since two or more processes are involved; we will have a curve following second- or third-order kinetics, and there will be a marked reduction in τ. This gives us two potential uses for lifetime measurements—exploration of the chemical environment of the fluorochrome, and multiple labelling even where spectra overlap.

5.1 Practical Lifetime Microscopy

To make use of these possibilities we have to be able to measure the fluorescence lifetime. Two approaches to fluorescence lifetime imaging (FLIM) have been used in practical microscopy. In *frequency domain* systems the excitation is modulated, and the demodulation or the phase shift of the emission is measured to get

a measure of the lifetime. This has found application in wide-field microscopy, using a modulator in front of the mercury lamp or a high-power LED which can be modulated directly, but has not come into use in the confocal field except experimentally.

Time domain measurement, where we measure the rise and decay of fluorescence directly after a pulse of light, is the norm in confocal microscopy, where we deal with each point (pixel) individually. A pulsed laser is required, and the alternatives normally used are either a pulsed diode laser at 405, 440, or 470 nm (single-photon excitation) or the very short pulses of a titanium sapphire laser, which implies multiphoton excitation.

The basic approach is to count photons after each pulse of the laser, and assign each count to a "bin" depending upon its time of arrival. The dwell time on each pixel is of the order of microseconds, whereas fluorescent lifetimes are measured in nanoseconds so that many pulses may be counted at each pixel provided that the pulse repetition rate is fast enough. Most titanium sapphire lasers run at around 80 MHz (80 pulses per microsecond); diode lasers are slower, at around 40 MHz, but this is still more than sufficient. The major difference between current commercial systems is the number of "bins" used. Some (e.g., Becker and Hickl) use many bins (up to 256), for good resolution of the decay curve, at the expense of speed. Getting enough photons in each bin to show a useful curve requires accumulating data for many seconds, even minutes, per frame, but the resulting curve can be analyzed in great detail; one can not only determine τ but also distinguish between single, double or triple exponential decay curves. Many living cells however are too dynamic to allow such precision.

The alternate approach is to use a small number of bins—four, for example, in the Nikon LIMO system. This permits relatively high acquisition speeds at the expense of reduced resolution in the measured curve. With living tissues such a trade-off is often inevitable. Figure 7 illustrates practical lifetime measurement in living cells in the LIMO.

5.2 Non-ratiometric Quantitation Using FLIM

Many indicators vary in fluorescent intensity with changes in ion concentration, but since their wavelength response does not change they cannot be used ratiometrically. In conventional microscopy these dyes (e.g., Calcium Green) can only be used for qualitative imaging. However, lifetime is largely independent of dye concentration, at least at likely concentrations in living cells, but does change with ion concentration. These dyes can therefore be used quantitatively in a FLIM system. Calibration protocols are essentially the same as for ratiometric dyes (Subheading 4.3). This makes a wide range of simple dyes available for quantitative work, using only one excitation wavelength and one detection channel. What is particularly convenient for time-course studies is that it is quite robust to bleaching of the indicator [7].

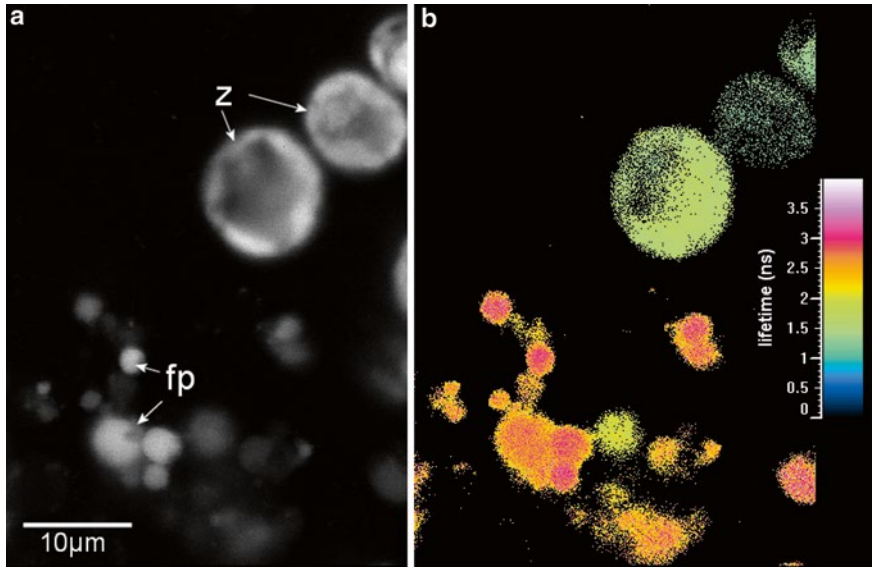

Fig. 7 FLIM imaging of living coral tissue (*Trachyphyllia* sp.). (**a**) Conventional intensity image, showing the fluorescent pigments of the coral (fp) and the symbiotic algae (zooxanthellae, z) which contain chlorophyll. (**b**) Lifetime image showing that the chlorophyll of the algae has a very short lifetime (<2 ns) while the coral pigments have longer lifetimes (2.5–3 ns)

5.3 Fluorescence Resonant Energy Transfer

Fluorescence (or Förster) resonant energy transfer (FRET) is an interaction between the electronic excited states of two dye molecules. Excitation is transferred from a donor molecule to an acceptor molecule without emission of a photon. The emission spectrum of the donor must overlap the excitation spectrum of the acceptor; the extent of this overlap determines the FRET efficiency. There is also a requirement that donor and acceptor transition dipole orientations must be approximately parallel. The electronic interactions are shown as a Jablonski diagram (a "cartoon" of electron energy levels) in Fig. 8.

FRET depends on the inverse *sixth* power of the intermolecular separation, so it falls off extremely rapidly with distance. This makes it useful over distances comparable with the dimensions of biological macromolecules, typically 2–50 nm. When FRET occurs the fluorescence of the donor molecule is quenched and only the acceptor fluoresces, but the excitation maximum is that of the donor. This therefore gives us a powerful tool for measuring the proximity of molecular species, at a level hugely beyond the resolution of any microscope.

The *Förster Radius* R_o is the distance at which energy transfer is 50 % efficient (in other words, where 50 % of excited donors are deactivated by FRET). As an example, for FRET between fluorescein and rhodamine R_o is 5.5 nm, so this is the scale at which interactions between labeled molecules can be probed. No other live

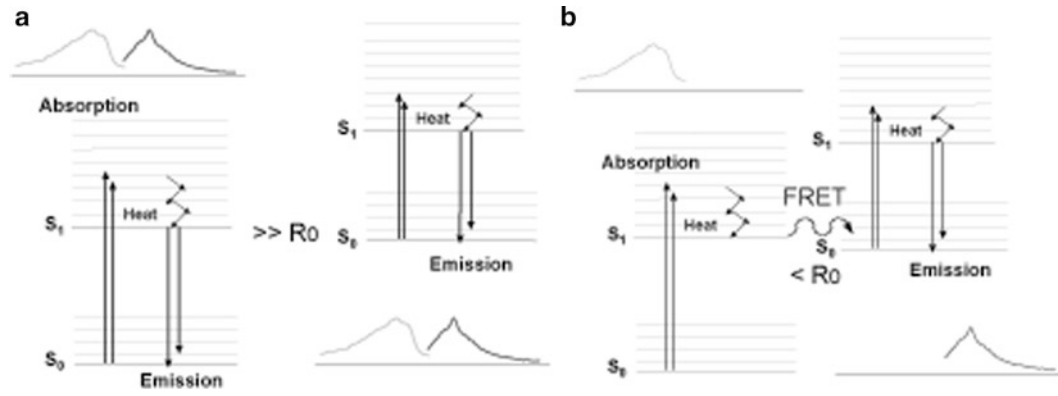

Fig. 8 Jablonski diagram for FRET. (**a**) When two suitable fluorochromes are separated by much more than the Förster Radius R_0, most molecules will absorb and emit independently. (**b**) When they are closer than R_0, the excess energy of the donor electron (in the S_1 state) will pass to the acceptor by FRET; the donor electron returns to the ground state without emitting a photon and the acceptor electron is promoted to the S_1 state without absorbing one. The acceptor then emits a photon on returning to the ground state

cell imaging technique is able to give information at this resolution. However, accurate quantitation is not always easy and there are several different approaches to this. A very comprehensive review is given by Vereb et al. [8] and the major approaches are briefly outlined here.

5.4 Quantifying FRET by FLIM

If FRET is taking place then fluorescence is no longer the only process by which an excited electron can return to the ground state, since energy transfer provides an alternative pathway. This means that in the presence of FRET the fluorescence lifetime τ will be reduced; it will also no longer be a single exponential process since two chemical processes are involved. This makes FLIM an excellent tool for quantifying FRET, and in many cases it will be the method of choice. Figure 9 shows an example of this.

The great advantage of this approach to FRET is that quantification is simple—at least so long as only two FRET participants are involved. The FRET efficiency E is given by

$$E = 1 - \frac{\tau_{da}}{\tau_{d}},$$

where τ_d is the lifetime of the donor on its own and τ_{da} is the lifetime of the donor in the presence of the acceptor.

The main limitation is that the signal must be strong since signal-to-noise ratio will inevitably be limited by the need to sort the number of photons both by wavelength and by time. However, the measurements are clear and unambiguous. Intensity-based approaches to FRET (below) are inherently unable to distinguish between FRET and radiative transfer, where emission from the

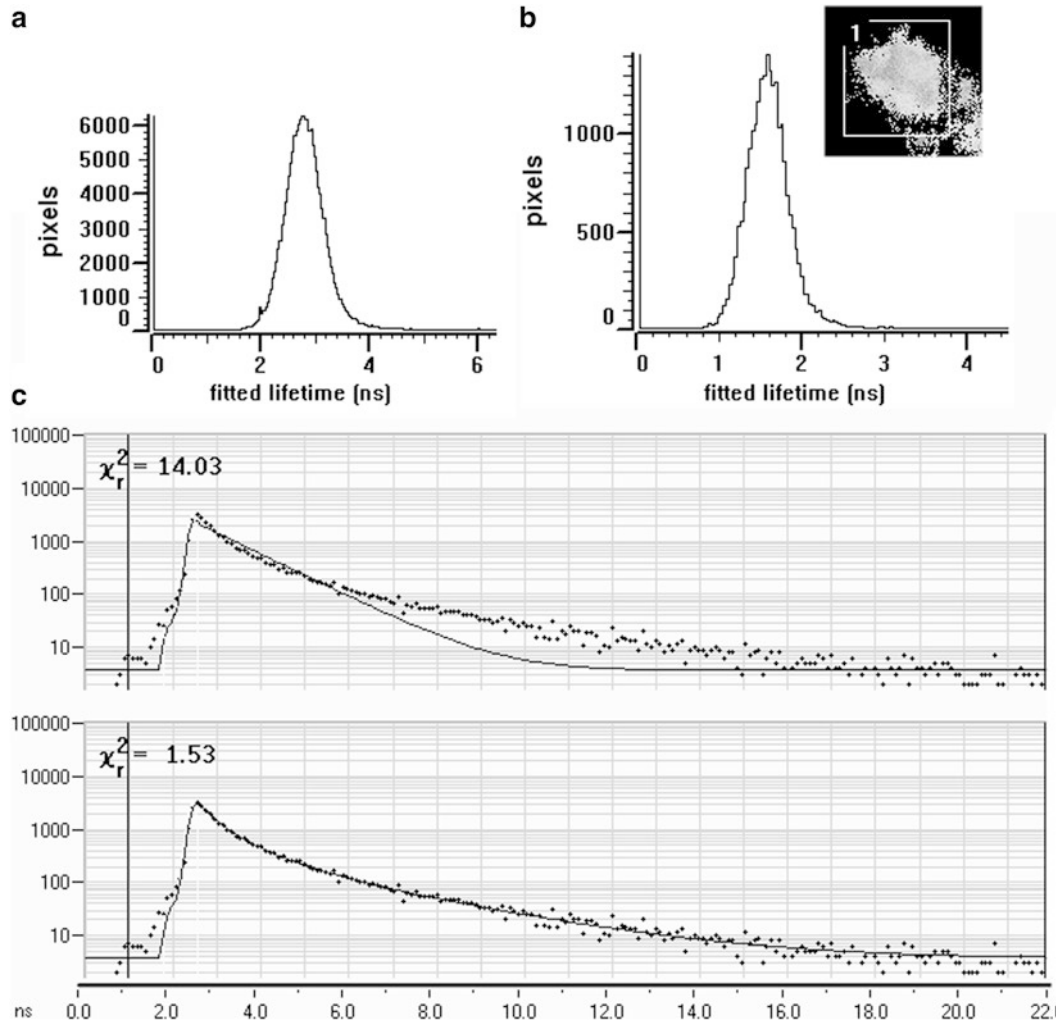

Fig. 9 Reduction in donor lifetime by FRET. (**a**) Lifetime histogram of pure pigment (amil504) from the coral *Acropora millepora*. Modal lifetime is 2.9 ns. (**b**) Lifetime histogram and image of pigment granules in the coral, which contain three pigments. Modal lifetime is 1.56 ns, showing that FRET is taking place. (**c**) Actual decay curve from the coral pigment granule (points); a single exponential decay (*solid line*, *upper trace*) is a very poor match, while a triple exponential decay fits very well (*lower trace*). Excitation 405 nm

donor excites fluorescence from the acceptor. Radiative transfer depends on the inverse square of the distance between the two molecules and therefore is much less sensitive to distance than FRET.

5.5 Other Methods of Quantifying FRET

We can identify and measure the extent of FRET in several other ways:

1. By the increase in brightness of acceptor emission: This is the most obvious criterion and often the one we will have to use, since it will almost always give the best signal-to-noise ratio,

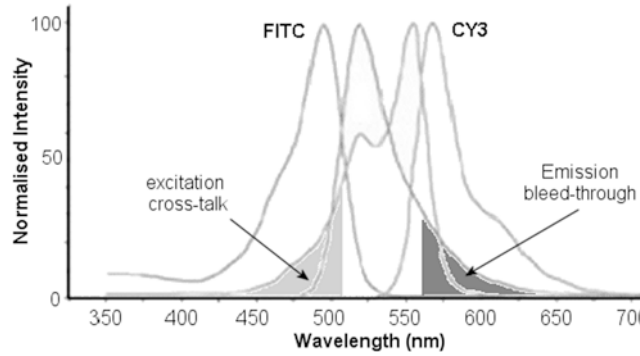

Fig. 10 Corrections which need to be made in intensity-based FRET measurement. The excitation curve of the donor (here FITC) has a substantial overlap (*shaded*) with that of the acceptor (Cy3) so that some of the donor excitation will excite the acceptor directly, without FRET (excitation cross talk). There will also be substantial emission by the donor within the emission spectrum of the acceptor (emission bleed-through, *darker shading*)

and it also does not need any extra hardware on the microscope. However it presents many problems for accurate measurement. Since the excitation and emission spectra of donor and acceptor have to be close there will always be two factors we need to take into account—direct excitation of the acceptor by the donor excitation wavelength (excitation cross talk) and bleed-through—emission from the donor at the wavelengths being measured for the acceptor (Fig. 10).

The rigorous approach to this problem involves collecting a full series of images from control and experimental treatments so that we know the emission of the acceptor when excited at the donor wavelength and the emission of the donor within the collection window used for the acceptor [9]. We therefore need three samples—labeled with donor only, acceptor only, and both donor and acceptor. From each we must collect images (a) with donor excitation, and both donor and acceptor emission, and (b) with acceptor excitation and emission—a total of nine images. While this may seem daunting in fact the two controls (donor alone and acceptor alone) are part of any normal experimental protocol, and the three images of each are routine in any confocal microscope. Software is available (*see* **Note 3**) to automate the corrections and generate an image showing the corrected FRET.

2. By the quenching of emission from the donor: In some experiments, introduction of the acceptor will lead to an immediate loss in fluorescence emission from the donor. This can often be a more accurate indicator since it is free from emission bleed-through and excitation cross-talk problems. As such this will only be useful in dynamic experiments where we start out either without the acceptor present or without FRET.

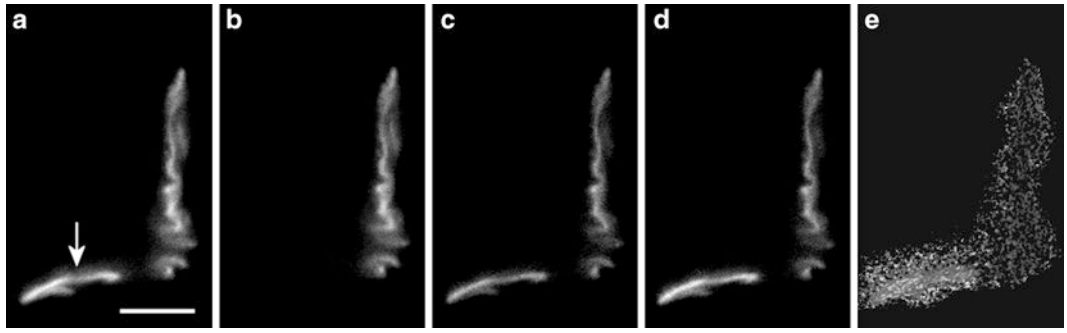

Fig. 11 Labelling of acetylcholine receptor (AChR) using TRITC-alpha-bungarotoxin (donor) and Alexa647-alpha-bungarotoxin (acceptor) in a FRET assay to determine the changes in distance between receptors caused by denervation. The toxin binds to the AChR at the neuromuscular junction (mouse tibialis anterior in this series). (**a**) Acceptor fluorescence, excited at the donor wavelength (543 nm). The endplate (*arrowed*) in the lower part of the image is then selectively bleached at the acceptor excitation wavelength (633 nm). (**b**) Acceptor fluorescence after bleaching of the region containing the endplate. (**c**, **d**) Corresponding donor fluorescence images. The increase in donor fluorescence after acceptor bleaching (**d**) is clear. (**e**) Calculated FRET efficiency from **c** to **d**, on a grey scale where *white* = 50 % efficiency. Scale bar = 5 μm. Images courtesy of Dr. Othon Gervasio

However the same approach can be used "in reverse" for static experiments by bleaching the FRET acceptor. With most FRET pairs, the optimum excitation wavelength for the acceptor will not excite the donor to any significant extent. Therefore an extended exposure to the acceptor excitation will destroy the acceptor and eliminate FRET. The method is then to measure donor emission, then bleach the acceptor, and measure donor emission again. The increase in donor emission is a direct measure of the amount of FRET that was originally present. An example is shown in Fig. 11. This approach is simple and widely used, but does have the problem that other phototoxic effects could occur as a side effect of the bleaching and thus influence the result.

3. Protection from bleaching of donor: Any donor molecules associated in a FRET pair will have an additional pathway for de-excitation and are therefore much less susceptible to bleaching. This is essentially equivalent to measuring lifetime, since the protection from bleaching is directly related to the reduction in τ [10]. So a series of images is taken while the sample bleaches, to which a curve can be fitted and the bleaching lifetime τbl calculated (τbl being the time taken to bleach to $1/e$ of the starting value). This is inversely related to the fluorescence lifetime (shorter lifetime means slower bleaching—longer τbl) and can be used to calculate FRET efficiency E in just the same way as if fluorescence lifetime had been measured, by simply inverting the equation

$$E = 1 - \frac{\tau\mathrm{bl}_{\mathrm{d}}}{\tau\mathrm{bl}_{\mathrm{da}}}.$$

As with lifetime measurement, this method will measure FRET without any interference from radiative transfer. It also requires no special hardware. However the system must be static since nothing must move during the measurement of the bleaching curves. (Fitting a curve to the bleaching progress is better than simply measuring the decay to $1/e$ of the original value since some bleaching is likely to have taken place during focussing and location of the region of interest.) The control to establish the bleaching rate of the donor in the absence of FRET will normally be a separate sample (unless one is lucky enough to have the donor present in two populations, one involved in FRET and the other not). Since many factors can influence bleaching rates this means that several measurements should be made and averaged to establish τbl_d accurately, and laser intensity should be checked at the beginning and end of each experiment.

5.6 Summary

FLIM provides a technique for exploration of the chemical environment of the fluorochrome, and also allows multiple labelling even where spectra overlap. When the hardware is available it is also usually the method of choice for measuring FRET, which can measure molecular interactions in the nanometer range. Without FLIM hardware, either intensity measurements with correction for bleed-through and cross talk or acceptor bleaching are the most popular methods of measuring FRET.

6 Notes

1. It is very simple to make a mirror coverslip for resolution and alignment checks. Get your SEM preparation lab to sputter coat the underside of a #1½ coverslip, and superglue it to a slide. The use of a #1½ coverslip should eliminate any spherical aberration effects with dry lenses—with oil immersion lenses SA should be negligible in any case.
2. 3-D View, by Iain Huxley: A modified version of NIH Image, the freeware image analysis system developed at the National Institute of Health, USA. Available from http://www.physics.usyd.edu.au/physopt
3. CircusSoft PFRET software—http://www.circusoft.com/ based on algorithms developed at the W.M. Keck Center for Biological Imaging at the University of Virginia by a team led by Ammasi Periasamy. It is described in some detail in Chapter 7 of Molecular Imaging: FRET Microscopy and Spectroscopy (Edited by Ammasi Periasamy and Richard N. Day) Oxford University Press, 2005 336 pages ISBN13: 9780195177206.

References

1. Cox GC, Sheppard CJR (2001) Measurement of thin coatings in the confocal microscope. Micron 32:701–705
2. Sheppard CJR, Török P (1997) Effects of specimen refractive index on confocal imaging. J Microsc 185:366–374
3. Cox GC, Sheppard CJR (1998) Appropriate image processing for confocal microscopy. In: Cheng PC, Hwang PP, Wu JL, Wang G, Kim H (eds) Focus on multidimensional microscopy, vol 2. World Scientific Publishing, Singapore, pp 42–54. ISBN ISBN 981-02-3992-0
4. Underwood EE (1970) Quantitative stereology. Addison-Wesley, New York
5. Pawley J (1995) Fundamental limits in confocal microscopy. In: Pawley JB (ed) Handbook of biological confocal microscopy. Plenum Press, New York, pp 19–38
6. Haughland RP (1996) Handbook of fluorescent probes and research chemicals. Molecular Probes Inc., Eugene, OR
7. Agronskaia AV, Tertoolen L, Gerritsen HC (2003) High frame rate fluorescence lifetime imaging. J Phys D: Appl Phys 36:1655–1662
8. Vereb G, Matko J, Szollosi J (2004) Cytometry of fluorescence resonance energy transfer. Methods Cell Biol 75:105–152
9. Elangovan M, Wallrabe H, Chen Y, Day R, Barroso M, Periasamy A (2003) Characterization of one- and two-photon excitation fluorescence resonance energy transfer microscopy. Methods 29:58–73
10. Gadella TWJ Jr, Jovin TM (1995) Oligomerization of epidermal growth factor receptors on A431 cells studied by time-resolved fluorescence imaging microscopy. A stereochemical model for tyrosine kinase receptor activation. J Cell Biol 129:1543–1558

Chapter 15

A Method for Quantifying Blood Flow Distribution Among the Alveoli of the Lung

Robert L. Conhaim, Dennis M. Heisey, and Glen E. Leverson

Abstract

This article describes a method for quantifying blood flow distribution among lung alveoli. Our method is based on analysis of trapping patterns of small diameter (4 μm) fluorescent latex particles infused into lung capillaries. Trapping patterns are imaged using confocal microscopy, and the images are analyzed statistically using SAS subroutines. The resulting plots provide a quantifiable way of assessing interalveolar perfusion distribution in a way that has not previously been possible. Methods for using this technique are described, and the SAS routines are included. This technique can be an important tool for learning how this critical vascular bed performs in health and disease.

Key words Lung, Blood flow, Perfusion, Interalveolar pressure, Microspheres

1 Introduction

Blood is arterialized in the lung because of diffusive exchange of oxygen and carbon dioxide between alveolar gas and capillary blood. This exchange operates effectively because the diffusion distance between the blood and the alveolar gas is only about 0.3 μm and because the combined surface area of the 3×10^8 alveoli in the lung is about 70 m^2 in humans or about one-fourth the size of a tennis court [1].

An important issue in efficient lung operation is the equal distribution of the blood flow to all of the alveoli. How the lung accomplishes this is unknown nor is it known if the capillaries control this perfusion distribution. This subject has received little attention because methods to study it have not previously existed.

To address this, we developed a method that is based on statistical analysis of the distribution of 4 μm diameter latex particles infused into the pulmonary circulation. These particles, which are only slightly larger than red cells, become trapped in alveolar capillaries, and their distribution is therefore an index of the blood flow distribution among the alveoli at the time of infusion. The following

Stephen W. Paddock (ed.), *Confocal Microscopy: Methods and Protocols*, Methods in Molecular Biology, vol. 1075,
DOI 10.1007/978-1-60761-847-8_15,

describes the details of this method, which we use in intact rats or isolated rat lungs to understand how blood flow is distributed among alveoli in health and disease [2–7].

2 Materials

1. 4 μm diameter rhodamine-labeled sulfate microspheres (*FluoSpheres*, Molecular Probes).
2. Bovine serum albumin (Sigma).
3. NaCl, Na_2HPO_4 (anhydrous), $NaH_2PO_4 \cdot 2H_2O$.
4. Laboratory rats fitted with acute or chronic indwelling femoral venous catheters.
5. Infusion pump, rodent ventilator, and a source of compressed air to maintain lung inflation pressure at 5–10 cmH_2O.
6. Confocal fluorescence microscope for imaging rhodamine fluorescence.
7. Personal computer equipped with SAS statistical software (SAS Institute, Cary NC) and NIH Image (National Institutes of Health) or Scion Image (Scion Corp.).

3 Methods

The following methods describe (1) preparation of the latex particles for infusion, (2) imaging the particles within excised, dried lungs, and (3) analysis of particle distributions within the lung.

3.1 Latex Particle Preparation

We infuse 4 μm diameter particles because more than 90 % of them become trapped within lung capillaries [2, 8]. Infusion of 3.6 μm particles results in only about 60 % retention. Thus, the larger particles are better markers of interalveolar perfusion distribution. It is worthwhile to infuse as many particles as possible to improve the resolution of the statistical analysis. However, if too many are infused they become crowded and cannot be imaged as separate particles, which degrades the analysis. We've found that 2×10^8 is a good number to infuse into intact rats or isolated rat lungs. In vasoconstricted lungs, where the particles tend to cluster, 1×10^7 is more appropriate.

We begin preparation of the infusion solution by adding the particle solution supplied by Molecular Probes to 5 ml of 0.5 % bovine albumin solution. For 2×10^8 particles we add 204 μL; for 1×10^7 we add 10 μL. We complete the solution by adding NaCl (0.043 g), Na_2HPO_4 (0.006 g), and $NaH_2PO_4 \cdot 2H_2O$ (0.002 g). The resulting solution consists of albumin-coated latex particles in phosphate buffered saline. The albumin is necessary to prevent the particles from clumping in the presence of the salts.

This solution is infused into the femoral venous catheter of an intact rat or into the pulmonary artery of isolated rat lungs over 1–2 min using an infusion pump. Once the infusion is complete, the lungs are removed and maintained at an inflation pressure of 20–25 cmH_2O for at least 48 h, which causes the lungs to dehydrate. It is important that the lungs are never allowed to collapse after they are removed because the particles could redistribute.

3.2 Imaging the Particles

Air-dried lungs have the consistency of Styrofoam and are easily sliced using a razor blade. We cut four, 2–3 mm thick slices each from the left and right lungs. Three are parallel to the dorsal-ventral plane, and one is in the transverse plane parallel to the hilum [2].

Each of these eight slices are placed one at a time onto the stage of a confocal fluorescence microscope where the particles are imaged using the 4× objective. Any magnification can be used, but low magnification images a larger number of particles which improves the resolution of the subsequent statistical analysis. We excite particle rhodamine fluorescence using the 568 laser line of our Kr/Ar laser and image using the 585 nm emission filter. We routinely set the laser power to 2 %, the gain to 1,250, the offset to −15, and open the aperture fully. This produces clear images of each latex particle in a field of view that measures $3{,}360 \times 3{,}360$ μm in our microscope (BioRad 1024 ES mounted on a Nikon Eclipse TE300).

We open each image file in NIH Image (or Scion Image or Image J) and set the *threshold* (Options) value to 100. We then use "Analyze Particles" to count the total number of particles in the field, with the particle options set to a minimum of 1 and a maximum of 99,9999 pixels. The resulting measurements are then exported (File). Each of the *measurement* files must be opened in Microsoft Word and saved as text (.txt) files. SAS will not recognize the files if this is not done.

3.3 Statistical Analysis of Particle Distributions

We use a SAS routine to analyze the particle distribution in each *measurement* file. The routine begins by subdividing the image into a two-by-two array. It counts the number of particles in each of the four resulting subdivisions and calculates the mean (μ) and variance (σ^2) of the particle count among the four. This process is repeated as the image is further subdivided into 4×4, 8×8, and so on up to 512×512 (9 steps). At each step, the mean and variance of the particle counts in each subdivision is counted. Because the tissue volume encompassed by each image is known ($3{,}360 \times 3{,}360 \times 100$ μm), the tissue volume of each subdivision is also known. The resulting data are displayed with σ^2/μ plotted on a log scale on the vertical axis, and the subdivision volume at each step plotted on the horizontal axis. The resulting graph is known as a *dispersion index* plot [9, 10]. Examples are shown below.

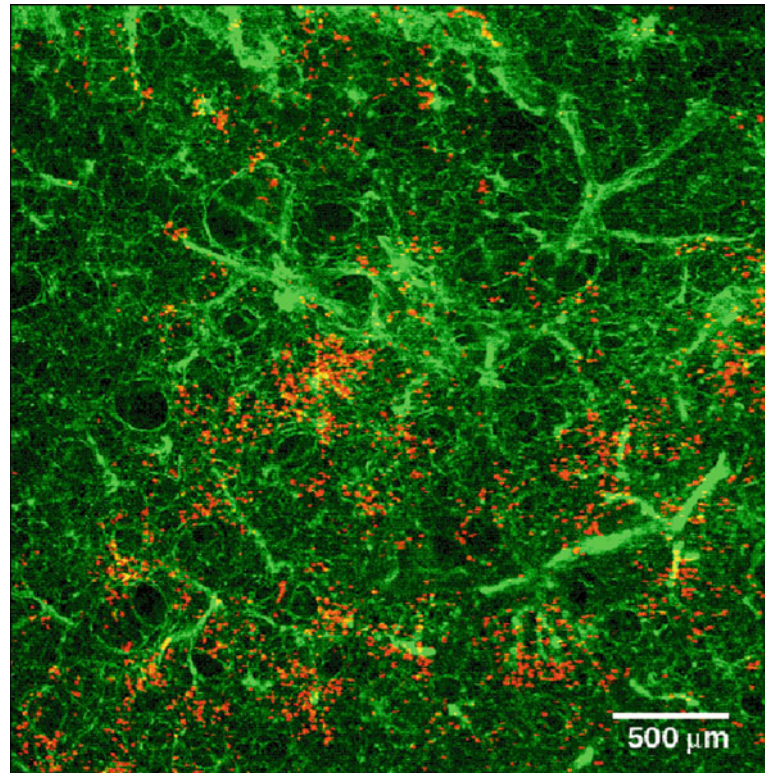

Fig. 1 Confocal fluorescence image showing 4 μm diameter rhodamine-labeled latex particles trapped in the capillary circulation of an isolated rat lung that had been perfused with a thromboxane analog before the particles were infused (1×10^7 particles infused). The thromboxane analog is a potent vasoconstrictor [3]. The image represents a tissue volume of $3{,}360 \times 3{,}360 \times 100$ μm. *red*, particle fluorescence; *green*, tissue autofluorescence

The SAS routine is included in the Appendix at the end of this article (Figs. 1, 2, 3, and 4).

4 Interpretation of Dispersion Index Plots

At a logDI value of zero, the particle distribution is defined as statistically random because $\sigma^2 = \mu$ (i.e., $\sigma^2/\mu = 1$; $\log 1 = 0$) [2, 10]. At logDI values > 0 ($\sigma^2/\mu > 1$), the distribution is defined as clustered, and at logDI values < 0 ($\sigma^2/\mu < 1$) the distribution is lattice-like, as in the distribution of squares on a checker board.

The plots in Fig. 4 suggest that the perfusion distribution in both lungs is random at tissue volumes < 1 alveolus (1×10^0) because the logDI values $= 0$. However, at tissue volumes > 1 alveolus logDI values are greater for the isolated lung, suggesting that

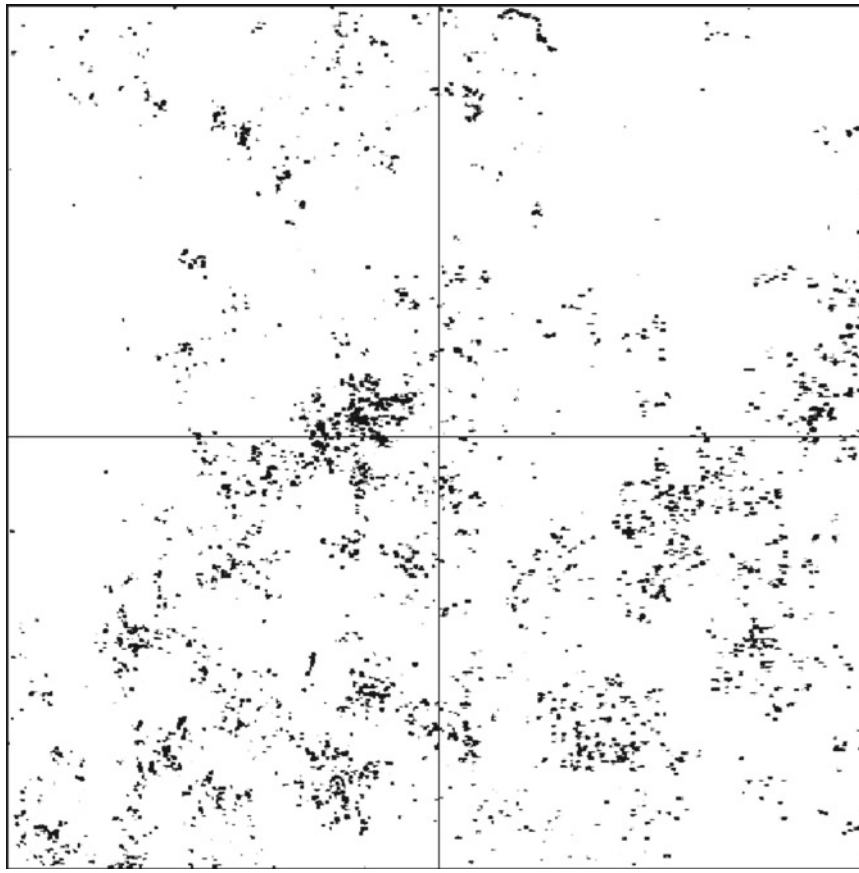

Fig. 2 Confocal image of the latex particles only in Fig. 1. The clustered particle distribution, an effect of the thromboxane vasoconstriction, is obvious. Division of the image into a 2×2 array illustrates the particle distribution analysis method. The number of particles in each subdivision is counted, and the mean (μ) and variance (σ^2) are calculated. This process is continued stepwise as the image is further subdivided into 4×4, 8×8,…512×512 arrays

perfusion distribution in that lung is more clustered than in the lung of the unanesthetized rat. This is consistent with the appearance of the particle images from these lungs and demonstrates how a logDI plot can express these appearances quantitatively.

Note that logDI values for the unanesthetized lung fall slightly below zero at tissue volumes equal to about 1 alveolar diameter (1×10^0). This expresses the particle distribution at the alveolar level where the alveolar distribution itself is lattice-like.

Dispersion index plots provide a quantitative method for describing latex particle distribution patterns in rat lungs and are therefore a useful tool for exploring interalveolar perfusion distribution patterns in experimental conditions.

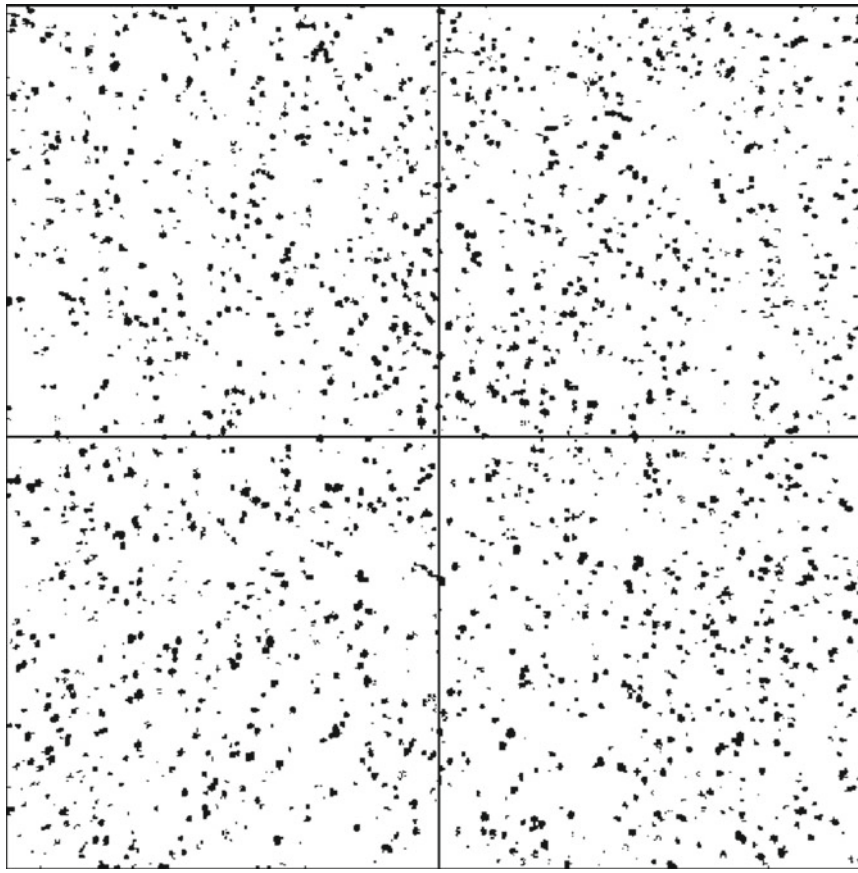

Fig. 3 Confocal image showing 4 μm diameter particles infused into the pulmonary circulation of an unanesthetized, spontaneously breathing rat (2×10^8 particles infused). Note the uniform appearance of the particle distribution in this image compared to that of the thromboxane-perfused lung above (Figs. 1 and 2). Dispersion index analysis of eight images from this lung and eight images from the thromboxane-perfused lung are shown below (Fig. 4)

5 Appendix

To conduct statistical analysis of the *measurement* files, prepare a folder on your computer that contains the following: (1) the *measurement* files saved in .txt format, (2) the SAS statistical analysis program, (3) the SAS plot program, and (4) a text file named *aalung.txt*. Use this file name because the SAS analysis program calls it.

To conduct the statistical analysis, run the statistical analysis program first. This may require 10–20 min for analysis of eight *measurement* files. Next, run the SAS plot program on the output file generated by the SAS statistical analysis program. The plot program should run in only a few seconds. Finally, export the *output* of the plot program to Microsoft Excel.

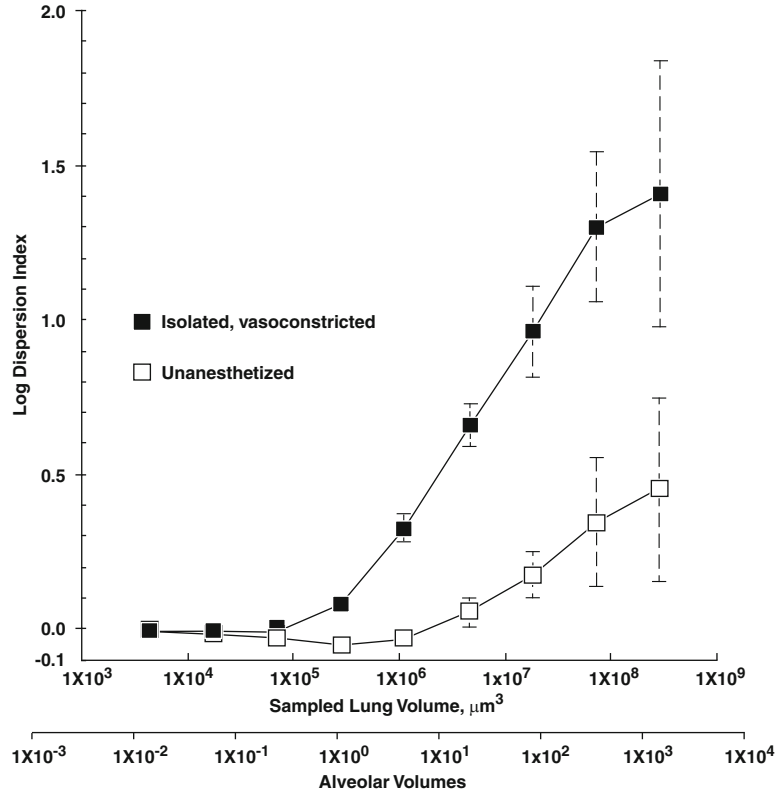

Fig. 4 Dispersion index plot showing particle distribution in a thromboxane-perfused (vasoconstricted) isolated lung and in the lung of an unanesthetized, spontaneously breathing rat. The dispersion index (μ/σ^2) is plotted on the vertical axis (mean ± s.d.; $n = 8$). The tissue volume at each of the nine subdivision steps is shown on the horizontal axis. The 2×2 array has the largest volume and the 512×512 array the smallest. Tissue volume is also expressed in multiples of alveolar volume, which we assume is equal to that of a 75 μm diameter sphere. Interpretation of this plot is described below (4.0 Interpretation of Dispersion Index Plots)

Once in Excel, the DI plots can be prepared. You will be plotting the column labeled *FREQ* on the horizontal axis and the column labeled *Log Dis* on the vertical axis. Before preparing the plot, first sort the values in these two columns based on ascending values in the *FREQ* column. The *FREQ* values are the number of subdivisions in each plotting step: 4 (2×2) up to 262,144 (512×512). You should plot the horizontal axis with the smallest (2×2) value on the right because it represents the largest tissue subdivision.

The SAS Statistical Analysis Program is available from the author.

Acknowledgements

We thank Kal Watson for animal preparation and for preparation of the latex particle infusion solutions. Supported by grants from the Department of Veterans Affairs.

References

1. Weibel ER (1984) The pathway for oxygen. Harvard University Press, Cambridge, MA
2. Conhaim RL et al (2003) Perfusion heterogeneity in rat lungs assessed from the distribution of 4-μm diameter latex particles. J Appl Physiol 94:420–428
3. Conhaim RL et al (2004) Thromboxane receptor analog, U46619, redistributes pulmonary microvascular perfusion in isolated rat lungs. J Appl Physiol 96:245–252
4. Conhaim RL et al (2006) Hemorrhage causes inter-alveolar perfusion mal-distribution in the lungs of anesthetized rats. J Trauma 60: 158–160
5. Conhaim RL et al (2008) Hemorrhage progressively disturbs inter-alveolar perfusion in the lungs of rats. Shock 29:410–416
6. Conhaim RL et al (2008) Acute hypoxia does not alter perfusion distribution among alveoli in unanesthetized rats. Respir Physiol Neurobiol 160:277–283
7. Conhaim RL et al (2008) Bacteremic sepsis disturbs alveolar perfusion distribution in the lungs of rats. Crit Care Med 36:511–517
8. Conhaim RL, Rodenkirch LA (1998) Functional diameters of alveolar microvessels at high lung volume in zone II. J Appl Physiol 85(1):47–52
9. Grieg-Smith P (1952) The use of random and contiguous quadrats in the study of the structure of plant communities. Ann Bot 16: 293–316
10. Diggle P (1983) Statistical analysis of spatial point patterns. Academic, New York

Chapter 16

Imaging Tools for Analysis of the Ureteric Tree in the Developing Mouse Kidney

Luise A. Cullen-McEwen, Richard J. Young, Gabriel Fricout, Dominique Jeulin, Ian S. Harper, Frank Costantini, and John F. Bertram

Abstract

The structure of the ureteric tree in developing mouse and rat kidneys has previously been quantified in two dimensions. While this type of analysis may provide evidence of changes in ureteric growth, these measurements are effectively inaccurate, as the ureteric tree is a three-dimensional (3D) object. Here we describe a method for measuring the ureteric tree in three dimensions. This technique involves (1) culture of the metanephric kidney at embryonic day 12 (mouse) or 14 (rat), (2) whole-mount immunofluorescence to selectively stain ureteric tree epithelium, (3) confocal microscopy to obtain a complete Z series through the ureteric tree, and (4) image analysis algorithms to binarize, skeletonize, and measure individual branch lengths in 3D. This method has been extended to analysis of the same ureteric tree over time (4D). The results obtained provide accurate and precise quantitation of ureteric tree growth in the developing mouse or rat kidney.

Key words Kidney, Confocal, Metanephros, Development, Ureteric tree, Three-dimensional, Measurement, Image processing

1 Introduction

The mammalian kidney (metanephros) develops through a series of inductive molecular interactions between the epithelial ureteric bud and the metanephric mesenchyme. Branching morphogenesis of the ureteric bud results in the formation of the ureteric tree and ultimately the collecting duct system. Simultaneously, the tips of the ureteric tree induce the formation of nephrons, the functional units of the kidney. Since only the tips of the tree have the capability of nephron induction, the efficiency of ureteric branching is a key regulator of nephron endowment in the adult kidney. Moreover, the pattern of ureteric branching morphogenesis is thought to be an important regulator of renal histoarchitecture.

Stephen W. Paddock (ed.), *Confocal Microscopy: Methods and Protocols*, Methods in Molecular Biology, vol. 1075,
DOI 10.1007/978-1-60761-847-8_16,

The molecular regulation of kidney development and ureteric branching morphogenesis has been extensively studied in vitro [1–8]. Whole metanephric organ culture, in which the whole mouse or rat metanephros is explanted just after the ureteric bud has invaded the metanephric mesenchyme and is cultured for up to 7–8 days, is a very powerful and the most widely used in vitro model of metanephric development. Both branching of the ureteric epithelium, and mesenchyme to epithelium conversion forming nephrons, occur in metanephric organ culture. Soluble factors or their inhibitors can be added to the culture medium in order to examine their roles in renal development.

Despite the power of metanephric organ culture as a model for studying the roles of specific molecules in kidney development, there have been relatively few quantitative studies of ureteric branching morphogenesis in vitro. To date, quantitative analysis of ureteric duct growth and branching has been mostly limited to measurements in two dimensions. Although providing some indication of changes in ureteric growth, these measurements are inaccurate in that they do not take into account the third dimension of the growing ureteric tree. We have developed image processing and analysis algorithms which allow us to quantitatively, objectively, and accurately measure ureteric branching morphogenesis in the cultured mouse kidney in 3D. This method has allowed us to detect previously unreported asymmetric growth of the mouse ureteric tree [9]. The method also allows us to measure individual branch lengths as well as the length of specific branch "generations." In addition, this technique allows the development of growth curves, identification of the relationship (if any) between the lengths of adjacent branches, and the development of mathematical models of ureteric growth. This method has been used to examine the normal growth of the mouse ureteric tree in vitro [10]. Our data suggest there is tight regulatory control of ureteric branching which ultimately results in the defined pattern of branching morphogenesis that is unique to the kidney. This technique now also allows the detection of subtle differences in the growth and pattern of branching in the presence of various soluble factors as well as the branching phenotypes in knockout and heterozygous mice [9, 11]. Furthermore, this method is now being used to study the growth of living ureteric trees in vitro, utilizing the fluorescent ureteric trees (Fig. 1) of *Hoxb7*/GFP transgenic mice [12]. Quantitative analysis of a tree on multiple occasions provides a powerful approach to studies of ureteric tree growth rates, generation data, and remodeling under experimental conditions. This chapter describes techniques for quantitative analysis of the ureteric tree in developing mouse kidneys in vitro. Separate protocols are provided for 3D and 4D imaging and analysis.

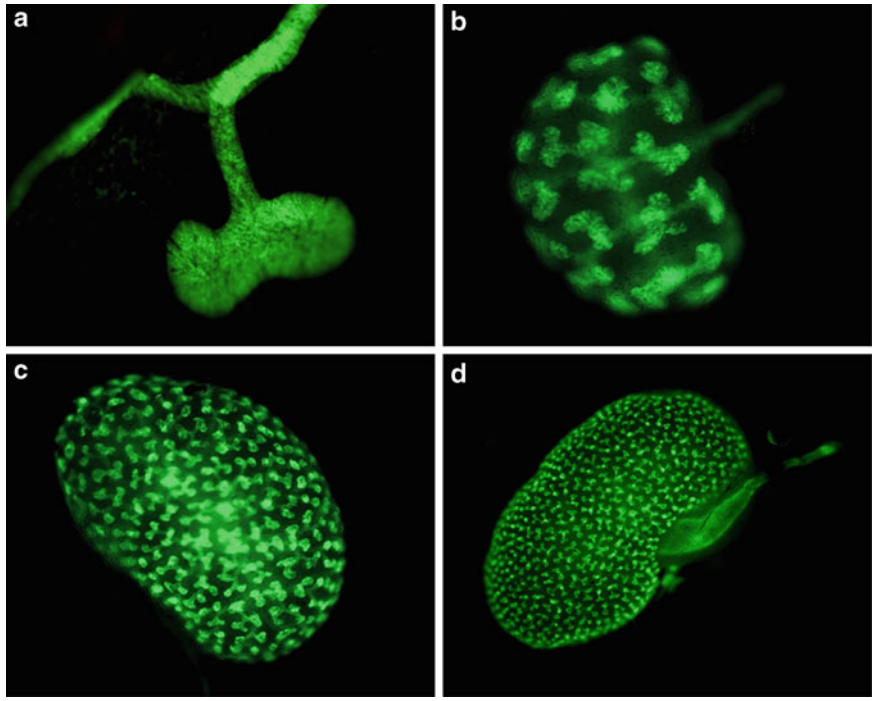

Fig. 1 Photomicrographs of in vivo *Hoxb7/GFP* kidneys at several developmental time points. (**a**) E11.5, (**b**) E13.5, (**c**) E15.5, (**d**) E17.5 (not to scale)

2 Materials

2.1 Metanephric Dissection

1. Fine forceps (Dumostar Biology, straight, superfine point forceps, 110 mm, ProSciTech, Thuringowa Qld Australia).
2. Entomological pins, E179, B3; 0.0076×15 mm (Australian Entomological Supplies, Bangalow, NSW, Australia).
3. Sterile phosphate buffered saline (PBS): dissolve 8 g of NaCl, 0.2 g of KCl, 1.44 g of Na_2PO_4, and 0.24 g of KH_2PO_4 in 800 ml distilled H_2O. Adjust pH to 7.4 with HCl. Adjust volume to 1 L with additional distilled H_2O. Sterilize by autoclaving.
4. 60 mm×15 mm tissue culture dish (Becton Dickinson Labware, NJ, USA) with a layer of Sylgard-silicone elastomer (Dow Corning Corp, MI, USA).

2.2 Metanephric Culture and Fixation

1. Serum-free culture medium (*see* **Note 1**): Dulbecco's Modified Eagle's Medium (DMEM): Ham's F12 liquid medium (Trace Biosciences, Castle Hill, NSW, Australia) supplemented with 5 mg/ml transferrin (Sigma-Aldrich Pty. Ltd., Castle Hill, Australia), 12.9 µl/ml l-glutamine (Trace Biosciences), and 100 µg/ml penicillin/100 U/ml streptomycin (Trace Biosciences).

2. 3.0 μm polycarbonate transfilter membrane insert (Transwell, Corning Costar Corporation, Cambridge, Massachusetts, USA).
   OR
   3.0 μm × 13 mm Poretics polycarbonate membrane filters (GE Osmonics Inc, Minnetonka, MN, USA).
3. 24-well culture plate (Becton Dickinson, Franklin Lakes, New Jersey, USA).
4. 35 mm × 10 mm tissue culture dish (Becton Dickinson, Franklin Lakes, New Jersey, USA).
5. Fixative: ice cold 100 % methanol.
   OR
   4 % paraformaldehyde (PFA) in PBS at 4 °C: dissolve 2 g PFA and 2 NaOH pellets in 50 ml PBS, pH to 7.4 (make up fresh each time).

2.3 Immunolabeling

1. 24-well culture plate.
2. PBS.
3. Blocking solution: 5 % fetal calf serum (FCS) in PBS, make fresh for each use.
4. Antibody diluent: 4.25 g NaCl, 0.2675 g Na_2HPO_4, 0.0975 g $NaH_2PO_4 \cdot 2H_2O$, and 2.5 ml 10 % sodium azide in 250 ml dH_2O, pH to 7.1.
5. Primary antisera: monoclonal mouse anti-Calbindin-D_{28K} (Sigma Chemical Co., St. Louis, Missouri, MO, USA) at 1:200 in antibody diluent. Secondary antisera: Alexa 488 goat anti-mouse IgG (Molecular Probes, Eugene, Oregon, USA) at a dilution of 1:100 in antibody diluent. Both these antibodies can be aliquoted prior to dilution and stored at –20 °C. Once thawed, antibody can be stored at 4 °C for approximately 1 month.
6. Cavity slides (*see* **Note 2**).
7. Mounting medium: Glycerol in PBS with sodium azide (Sigma Diagnostics, St. Louis, Missouri, MO, USA).
8. Cavity slide sealer: clear nail polish.

3 Methods

3.1 3D Analysis of Ureteric Tree Growth

3.1.1 Metanephric Dissection

1. Mice or rats need to be time-mated. The presence of a vaginal plug designates that mating has occurred. Embryonic day 0 (E0) is defined as midnight during the night of mating. Pregnant females are sacrificed by cervical dislocation and embryos removed on E12 (mouse) or E14 (rat).
2. Remove embryos from the embryonic sac, blot to remove excess fluid and weigh (*see* **Note 3**).

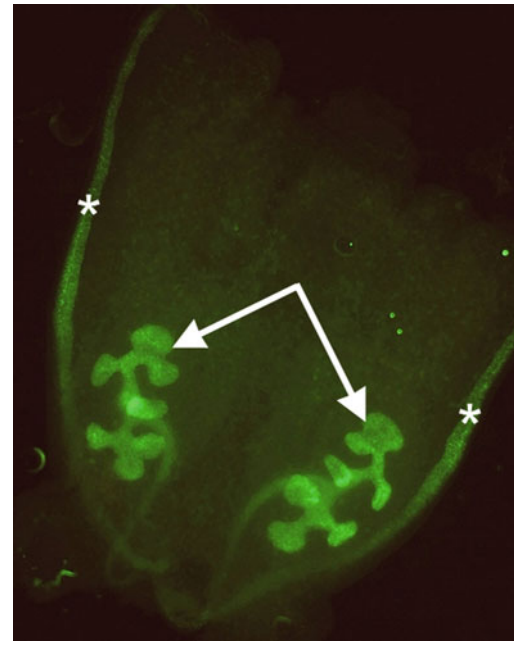

Fig. 2 Urogenital ridge of E12 mouse embryo. *Arrows* metanephroi; *Asterisk* Wolffian ducts

3. Decapitate and pin embryo through first the neck region and then the base of the tail to the layer of Sylgard-silicone elastomer within the Petri dish (*see* **Note 4**).
4. Using fine forceps, remove abdominal contents and discard.
5. Using fine forceps, remove complete urogenital ridge including metanephric kidneys (Fig. 2).
6. Using forceps, pry away metanephric kidneys from urogenital ridge and pipette into sterile serum-free culture medium warmed to 37 °C.

3.1.2 Metanephric Culture and Fixation

1. Wash metanephroi twice in serum-free culture medium warmed to 37 °C and pipette onto 3.0 μm polycarbonate transfilter membrane insert sitting on 350 μl of culture medium/well in a 24-well plate.
   OR
   Pipette onto a 3.0 μm polycarbonate filter membrane floating in a well in a 24 well plate containing ≥350 μl culture media (Fig. 3a).
2. Culture metanephroi for up to 48 h at 37 °C in a humidified incubator with 5 % CO_2 (Fig. 3b, c).
3. At the end of the culture period fix metanephroi in ice cold methanol for a minimum of 15 min at −20 °C (*see* **Notes 5** and **6**).

Fig. 3 Phase contrast photomicrographs of an E12 mouse metanephros in culture. (**a**) day 0, (**b**) Day 1, (**c**) Day 2. Bar = 250 μm

3.1.3 Immunolabeling (Not Required for HOXB7/GFP-Labeled Metanephroi)

1. If using polycarbonate inserts use a scalpel blade to remove the membrane from the bottom of the insert.
2. In a 24-well culture plate, wash whole fixed metanephroi twice in PBS for 5 min each (*see* **Note 7**).
3. Incubate whole metanephroi in blocking solution for 30 min at room temperature to block nonspecific binding.
4. Incubate metanephroi in primary antibody at 1:200 overnight at 4 °C or 2 h at 37 °C (*see* **Note 8**).
5. Wash metanephroi in PBS for 4 × 20 min each to remove excess primary antibody.
6. Incubate metanephroi in secondary antibody at a dilution of 1:100 overnight at 4 °C or 2 h at 37 °C.
7. Wash metanephroi in PBS for 4 × 20 min each to remove excess secondary antibody.
8. Mount whole metanephroi on a cavity slide using mounting medium and seal (*see* **Notes 9** and **10**).

3.1.4 Confocal Microscopy

1. Optically section the whole metanephros, parallel to the polycarbonate membrane filter using a 10× lens (NA = 0.3) on a confocal microscope.
2. Since the 10× lens has a measured axial resolution (FWHM) of about 8 μm, optical sections should be obtained at intervals of 4–5 μm to satisfy the requirements for Nyquest sampling (*see* **Note 11**).
3. The X, Y optical slices, recorded as 8 bit images, have a gray scale range of 256 (0–255) and were typically captured with a resolution of 512 × 512 pixels. These images should be stored in gray scale for further analysis (Fig. 4) (*see* **Note 12**).
4. Obtain a maximum projection image by constructing a maximum intensity projection (MIP) of the complete set of optical sections for use in manual corrections (Fig. 5) (*see* **Note 13**).

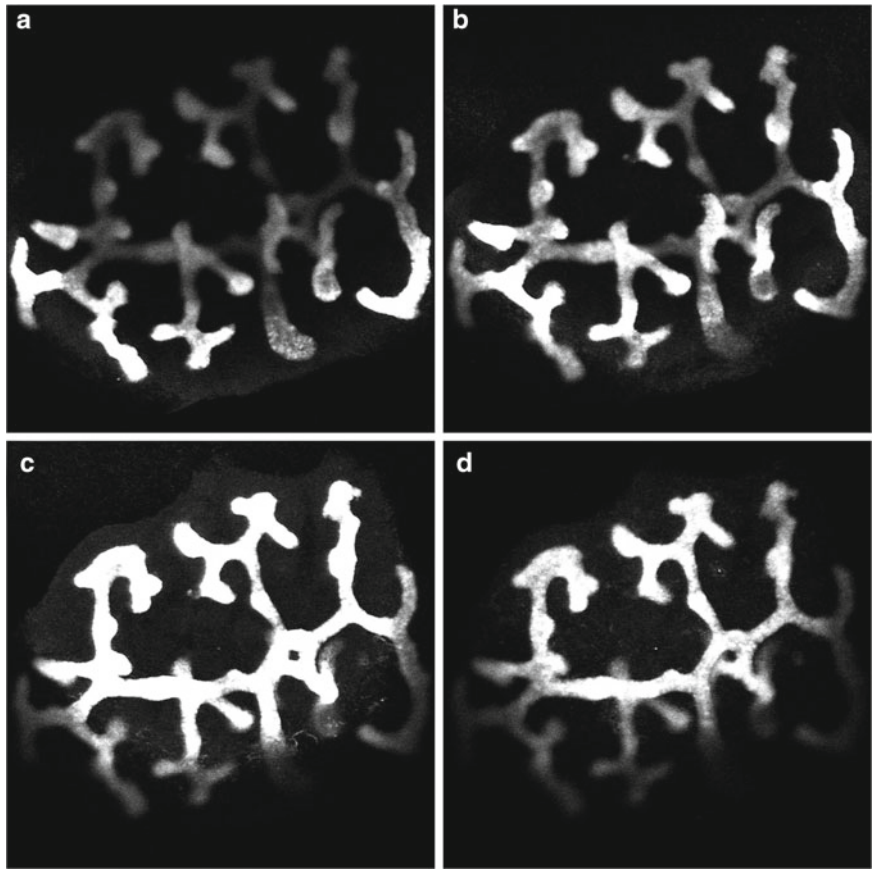

Fig. 4 Confocal optical sections. A Z series of confocal optical sections of an E12 mouse metanephros cultured for 36 h in control media, stained with Calbindin-D_{28k}. Total number of 5 μm sections is 55. (**a**) Section 20 of 55, (**b**) section 25/55, (**c**) section 30/55, (**d**) section 35/55. The two-dimensional optical sections are 8 bit gray-level images typically 512 × 512 pixels

3.2 4D Analysis of Ureteric Tree Growth

4D analysis of ureteric growth using metanephroi from *Hoxb7/GFP* transgenic mice [11] which express green fluorescent protein (GFP) in the ureteric tree provides several advantages over the use of wild-type metanephroi. Firstly, the ureteric tree can be visualized at any time throughout the culture period, as well as during dissection (to aid in easier removal of metanephroi). Secondly, immunostaining of the metanephros is not necessary, and thirdly, *Hoxb7/*GFP metanephroi can be used to analyze ureteric tree growth *in the same metanephros* on multiple occasions, allowing for the determination of branching dynamics, such as rates of growth. Imaging on multiple occasions also enables generation of time-lapse movies of in vitro ureteric tree growth (*see* companion CD for a time-lapse movie of an in vitro kidney imaged every 2 h for 72 h). 4D analysis of a single kidney on multiple occasions requires additional steps and equipment, as now described.

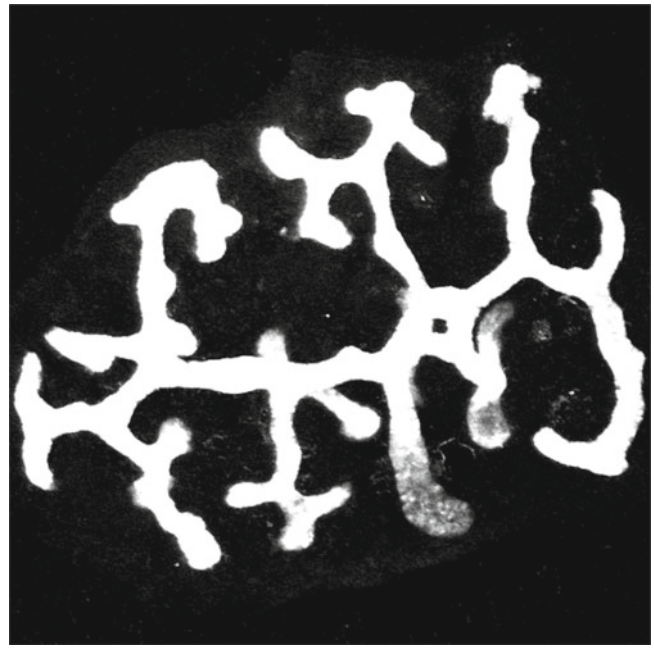

Fig. 5 Overlay of all 55 confocal optical sections

3.2.1 Metanephric Dissection

(As described above).

3.2.2 Metanephric Culture and Fixation

1. Wash metanephroi twice in serum-free culture medium warmed to 37 °C and pipette onto a 3.0 μm polycarbonate filter membrane floating in 7 ml of serum-free culture medium in a 35 mm × 10 mm petri dish.
2. Culture metanephroi on the confocal microscope for up to 48 h in an environmental chamber (micro-incubator). The environmental chamber must be temperature controlled at 37 °C with a continuous low flow of humidified 5 % CO_2 in air mix. The lid of the chamber has a central circular window (40 mm diameter) for the placement of a coverslip (170 μm thickness), through which the *Hoxb7*/GFP metanephroi can be visualized (Fig. 6).
3. Fix metanephroi in 4 % PFA at 4 °C (to maintain GFP) *after* the scanning period if the metanephroi are to be stored and used for other purposes.

3.2.3 Immunolabeling

(Not required as 4D analysis requires use of *Hoxb7*/GFP metanephroi).

3.2.4 Confocal Microscopy

1. At desired time points (e.g., every 6 h), optically section the whole metanephros, parallel to the polycarbonate membrane filter as described above.

Fig. 6 Environmental chamber on the confocal microscope. Chamber design modified with permission from Frank Costantini. *Arrow head* indicates Petri dish containing cultured metanephroi. Metanephroi can be cultured for several days in a humidified temperature-controlled chamber (*arrow*) on the confocal microscope

2. Store images in gray scale for further analysis.
3. Obtain a maximum projection image of the complete set of optical sections for use in manual corrections (Fig. 7).

3.2.5 Image Processing (Images from Both 3D and 4D Are Processed in the Same Way)

The raw images produced by the confocal microscope show various gray scales. To remove the additional information coming from the depth of each optical section, each image is subjected to a series of manipulations.

1. Segmentation (binarization) of the images

   Segmentation is the detection of the contour of an object. The Z series of gray scale images from the confocal microscope are converted from Tagged Image Format (Tif) to Bitmap (Bmp) images by "Irfanview 32" using a batch processing feature (Version 3.07 or later). Once converted, these files are imported into "Micromorph" (Version 1.4) to be binarized. "*Micromorph*" was developed by the Centre de Morphologie Mathématique, Ecole des Mines, Paris, France, in order to process images using morphological tools.

   The main image analysis steps are as follows:

   (a) Thresholding the images
   To threshold each image all pixels on each 2D image are converted to black or white according to a chosen gray scale. The gray scale is chosen by comparing the threshold

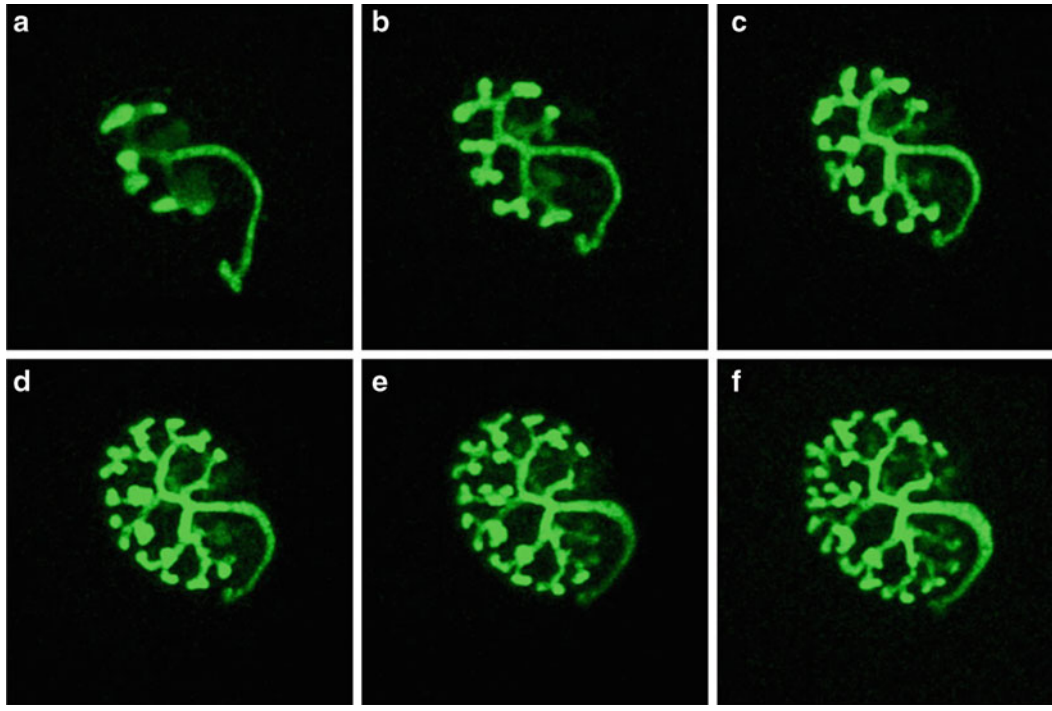

Fig. 7 Maximum projection confocal images of an in vitro *Hoxb7/GFP* kidney growing on the confocal microscope (**a**) time 0 (T0), (**b**) T12, (**c**) T24, (**d**) T36, (**e**) T48, (**f**) T60

image to the original maximum projection image obtained from the confocal microscope. Once an adequate image is obtained with minimum background and maximum information the gray scale is selected. Thresholds can vary from kidney to kidney depending on the quality of the confocal images. The pixels superior to the selected gray scale are converted to white, whereas all those inferior to this level are converted to black pixels.

(b) Producing "maximum" images
Each image is then converted to a "maximum" image which removes the additional information coming from the depth of each section. That is, for each X, Y pixel in 2D the pixel is in focus and therefore at the correct depth (Z) when the pixel is displayed at its maximum intensity. Conversely, the pixel is out of focus when at a gray scale inferior to this maximum. The pixels with the same X, Y coordinates in all frames (Z) are kept if they realize this maximum intensity. All pixels inferior to the maximum are discarded and turned black. Producing "maximum" images results in each pixel only being viewed in the frame(s) where this pixel is a true part of the depth of the tree. This process is conducted for each pixel in the X, Y direction, keeping only those in the Z direction which are at their maximum intensity.

(c) Segmentation algorithm
The maximum images are then binarized. The tree is selected by taking the maximum of the gray scale image (described above), in addition to a threshold of these images where the threshold level is chosen according to the maximum projection of all the images. Markers for the tree are selected by deleting the pixels of all the single maximums (i.e., background pixels). Some of the maximums of the tree are also single pixels and therefore removed during this operation. To detect the background, the algorithm calculates the watershed lines corresponding to the zones of interest of the previously selected sets. The watershed line of the gradient image of the maximum images sampled by these markers segments the object from the background as it calculates the contour of the object. In addition to segmenting the image, a filtering parameter is used to smooth the result, minimizing irregularities in the segmentation.

(d) Interactive correction of the result
Due to the existence of regions within the ureteric tree with less intense immunofluorescence, such as the trunk, the binary images are sometimes discontinuous and require manual (interactive) correction. Prior to skeletonization, interactive corrections to the segmented binary images are made frame by frame. Micromorph allows the binarized image to be superimposed on the maximum projection allowing the binarized images to be corrected when they do not match the maximum image. A function corrects frame by frame the errors in the segmentation. Interactively, using the computer mouse, holes can be filled in and excess areas can be deleted. Thresholds can also be altered for individual frames, and these individual images can then be re-segmented. The binary images are reprocessed with this new information (Fig. 8).

2. Three-dimensional skeletonization
Using the resulting binary images, the second and main part of the algorithm involves construction of a 3D skeleton of the ureteric tree, which is a representation of the original tree using thin lines connected through the center of each branch. The skeletonization algorithm is based on image processing libraries developed at the Centre de Morphologie Mathématique and runs on Xlim 3D as text-based messages in a Linux operating system (Linux 7). This algorithm is described extensively in Fricout et al. [13]. The method to process a skeleton first involves finding pixels centered within the tree and then connecting these pixels by a path centered within the tree. The steps are described below:

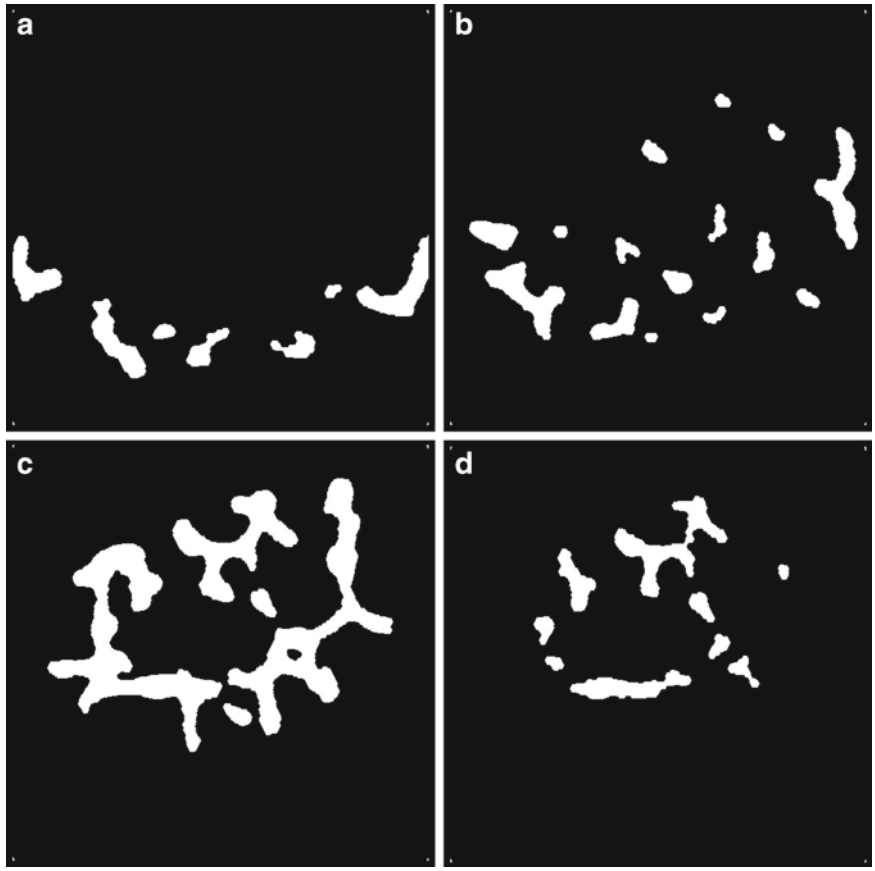

Fig. 8 Binary images of corresponding confocal sections shown in Fig. 4. Following conversion of confocal optical sections to maximum images, each image is binarized. (**a**–**d**) Binary images corresponding to the confocal images in Fig. 4. Calculation of the watershed line and a threshold detects the contour of the object segmenting each individual frame

(a) Calculation of the three-dimensional skeleton
The binary images obtained from "Micromorph" are first incorporated together to produce a single gray-level 3D tree. The skeleton is then produced by finding the extremities of each branch. The extremities of the tree are calculated using the weighted distance from one pixel to each pixel of the tree. The algorithm starts from the root (first pixel at the base of the trunk of the ureteric tree), which is queued with a priority 0. A weight is then attributed to each pixel defined by the distance from the root. The final branches correspond to the maximal distance to the root and are marked white. The pixels are then linked to the root using a path centered within the binary object. Using the weights associated with each pixel, the minimal path is calculated starting from the furthest extremity. This pixel is first linked to the root by selecting its neighbor whose distance to the root is the smallest. This process is iterated

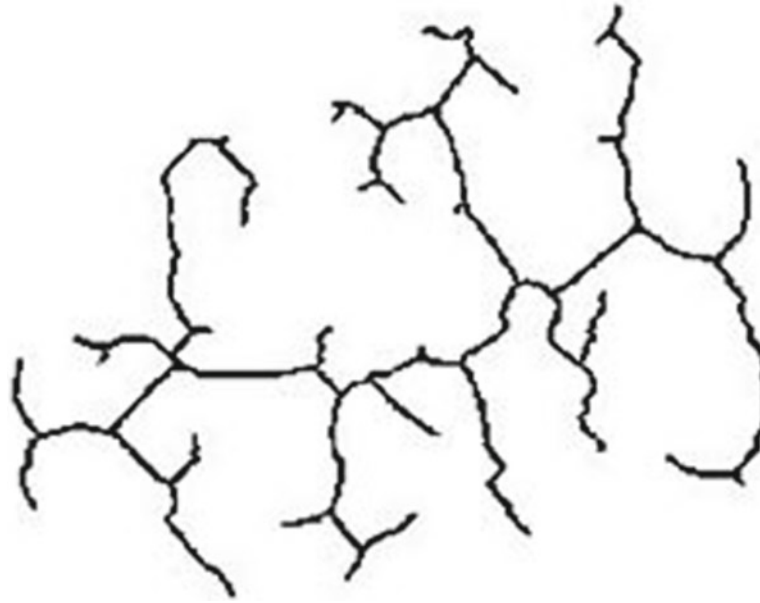

Fig. 9 3D skeleton of E12 mouse metanephros cultured for 36 h

with the neighbors of the point previously selected. The second furthest is then linked to the previously obtained branch, and all the extremity points are iteratively added to obtain the skeleton centered in 3D.

(b) Detecting branch points
The algorithm then labels pixels that are branch points. A pixel is called a branch point if it has three or more neighboring pixels. Usually, these branch points are grouped in connected sets of several voxels termed "branching sets," which are connected by thin lines. The center pixel is labeled a branch point. When there are no longer two neighboring pixels, these branches are labeled terminal branches. Due to the bulbous ending observed in ureteric tree branches, these tend to be two small branches, which are biologically inaccurate. Most of these excess branches are pruned with a final cleaning process where all terminal branches are deleted (Fig. 9).

(c) Measurements
The algorithm produces an information file with each branch point in order of generations stored in an array with the address (in pixels) of the branch arriving at one point and the length of that branch in pixels. This information enables the user to delete or add branches using specific X, Y, and Z pixel locations within the tree if the calculated skeleton does not adequately represent the ureteric tree. Once a skeleton that accurately reflects the ureteric tree of the metanephros has been obtained, the

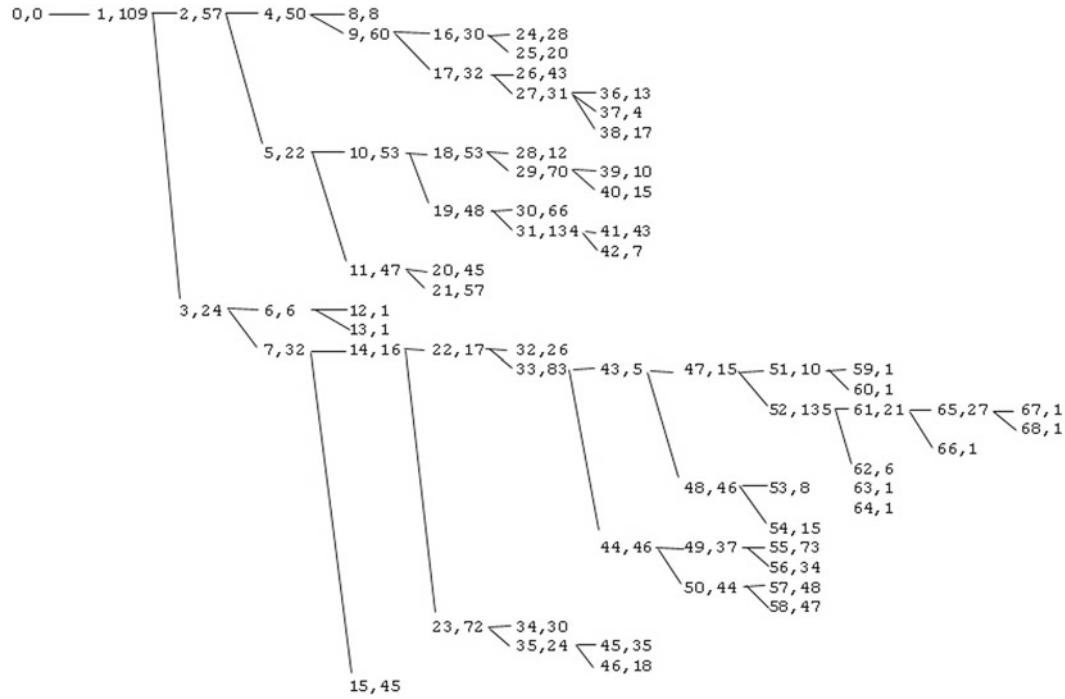

Fig. 10 Text file produced by the algorithm displaying the lengths of individual branches. Each point is identified by the number of the branch point, followed by the length of the branch in pixels, i.e., the branch from point 0 to 1 is 109 pixels in length. The algorithm then converts pixels to micrometers. The total length of the ureteric tree in 3D is 6,314 μm

algorithm converts the skeleton units from pixels to μm. This information provides accurate measurements of individual branch lengths and hence total ureteric length in 3D, as well as identification of branch generations (Fig. 10). Note the length of the ureter should always be discarded from calculations as this length can vary due to the surgical dissection.

3. Four-dimensional skeletonization
   Using the binary images from the same kidney imaged over time skeletons can be constructed using the method described above. Measurements can be made on each of the skeletons constructed to provide branch length increases and branch point generation from the previous time point.

4 Notes

1. Serum-free culture medium is used to avoid the unknown constituents in serum (as well as their concentrations) affecting the results obtained when other secreted proteins are added to the metanephric culture.

2. Cavity slides can be made using standard glass histological slides with 22 mm × 22 mm coverslips adhered to each end, leaving a cavity of approximately 10 mm between them.
3. To decrease variability in metanephric development prior to culture and thereby the final size of cultured metanephroi, restrict embryonic development to a limited range (e.g., embryonic weights of 0.060–0.080 g for mice and 0.130–0.160 for rats).
4. The use of Sylgard-silicone elastomer enables the embryo to be firmly pinned and thereby aids in the removal of metanephroi from the embryo.
5. Immunostaining and confocal scanning is best done with the metanephroi attached to the polycarbonate membrane. The membrane can therefore be used for handling metanephroi and avoids having to remove and potentially damaging metanephroi.
6. If storing metanephroi prior to immunostaining, store at −20 °C in ample 100 % methanol and seal container to prevent evaporation. Fixed metanephroi can be stored for several months.
7. Washes should be done with ample PBS. Washes can be done overnight at 4 °C in PBS, which results in minimal background staining.
8. To conserve 1° and 2° antibody, 200 μl of antibody solution is the minimum volume required to cover the metanephroi in a 24-well plate.
9. Prior to mounting, metanephroi should first be viewed under an epifluorescence microscope to check for optimal immunostaining and adequate washing.
10. Fluorescence can be preserved for several months in sealed slides by storing slides at −20 °C.
11. The thickness of the optical section for a 10× dry lens (NA 0.3) at 530 nm (center of the green light emission) is very approximately 10 μm [from calculations $Z = 1.4n\lambda/(\mathrm{NA})^2 = 8.24$ μm], but measurements using a front surface reflecting mirror yielded a FWHM measurement of $Z = 7.5$ μm. For measurements through a volume in 3D which consists of multiple optical sections, the stage should be driven half (or slightly less than half, as the Nyquest sampling theorem requires a sampling frequency of 2.3), the distance of the optical section thickness. A *Z*-step of 4 μm was thus sufficient to sample the volume.
12. Image resolution of 512 × 512 pixels was more than adequate to resolve the ureteric branches, and indeed for large structures, 256 × 256 may be used. The images should be saved in gray scale for further analysis (Fig. 4), as false color, obtained by applying a color look up table or transformation to RGB, can cause difficulties when images are converted to other formats such as bmp.

13. A note of caution here: projection images such as a maximum intensity projection are generally not suitable for measurements, as the original data is transformed and replaced with selected intensity or height data. We use the MIP images here only for quick inspection, allowing comparison with the original sections and subsequent skeletonized trees.

References

1. Clark AT, Bertram JF (1999) Molecular regulation of nephron endowment. Am J Physiol 276(4Pt2):F485–F497
2. Clark AT, Bertram JF (2000) Advances in renal development. Curr Opin Nephrol Hypertens 9(3):247–251
3. Burrow CR (2000) Regulatory molecules in kidney development. Pediatr Nephrol 14(3): 240–253
4. Kuure S, Vuolteenaho R, Vainio S (2000) Kidney morphogenesis: cellular and molecular regulation. Mech Dev 92(1):31–45
5. Pohl M, Stuart RO, Sakurai H, Nigam SK (2000) Branching morphogenesis during kidney development. Annu Rev Physiol 62: 595–620
6. Davies JA, Fischer CE (2002) Genes and proteins in renal development. Exp Nephrol 10(2): 102–113
7. Bard JB (2002) Growth and death in the developing mammalian kidney: signals, receptors and conversations. Bioessays 24(1):72–82
8. Sakurai H (2003) Molecular mechanism of ureteric bud development. Semin Cell Dev Biol 14:217–224
9. Cain JE, Nion T, Jeulin D, Bertram JF (2005) Exogenous BMP-4 amplifies asymmetric ureteric branching in the developing mouse kidney in vitro. Kidney Int 67:420–431
10. Cullen-McEwen LA, Fricout G, Harper IS, Jeulin D, Bertram JF (2002) Quantitation of 3-dimensional ureteric branching morphogenesis in cultured embryonic mouse kidney. Int J Dev Biol 46(8):1049–1055
11. Cain JE, Bertram JF (2006) Ureteric branching morphogenesis in BMP4 heterozygous mutant mice. J Anat 209:745–755
12. Srinivas S, Goldberg MR, Watanabe T, D'Agati V, al-Awqati Q, Costantini F (1999) Expression of green fluorescent protein in the ureteric bud of transgenic mice: a new tool for the analysis of ureteric bud morphogenesis. Dev Genet 24(3–4):241–251
13. Fricout G, Jeulin D, Cullen McEwen L, Harper IS, Bertram JF (2002) 3-D skeletonization of ureteric trees in developing kidneys. In: Talbot H, Beare R (eds) Mathematical morphology, proceedings of the VIth international symposium-ISMM 2002, Sydney, 3–5 April 2002, CSIRO Publishing, pp 157–164

Chapter 17

Evaluating Confocal Microscopy System Performance

Robert M. Zucker

Abstract

A confocal microscope was evaluated with a series of tests that measure field illumination, lens clarity, laser power, laser stability, dichroic functionality, spectral registration, axial resolution, scanning stability, PMT quality, overall machine stability, and system noise. These tests will help investigators measure various parameters on their confocal microscopes to insure that they are working correctly with the necessary resolution, sensitivity, and precision. Utilization of this proposed testing approach will help eliminate some of the subjectivity currently employed in assessing the CLSM performance.

Key words Confocal microscope, Lasers, Coefficient of variation, Photo multiplier tubes, Field illumination, Axial resolution, Spectral registration, Laser stability, Beads, Microscope lenses, Quality assurance, Quantification, Spectroscopy

1 Introduction

The confocal laser-scanning microscope (CLSM) has enormous potential in many biological fields. When tests are made to evaluate the performance of a CLSM, the usual subjective assessment is accomplished by using a histological test slide to create a "pretty picture." Without the use of functional tests many of the machines may be working at sub optimal performance levels delivering sub-optimum performance and possibly misleading data. In order to replace the subjectivity in evaluating a confocal microscope, tests were derived or perfected that measure field illumination, lens clarity, laser power, laser stability, dichroic functionality, spectral registration, axial resolution, scanning stability, PMT quality, overall machine stability, and system noise. These tests will help serve as a guide for other investigators to ensure that their machines are working correctly to provide data that is accurate with the necessary resolution, sensitivity, and precision. Utilization of this proposed testing approach will help eliminate the subjective nature of assessing the CLSM and may allow different machines to be compared. These tests are essential if one is to make intensity measurements.

Stephen W. Paddock (ed.), *Confocal Microscopy: Methods and Protocols*, Methods in Molecular Biology, vol. 1075,
DOI 10.1007/978-1-60761-847-8_17,

The CLSM has been evaluated by using the following biological test samples: beads, spores, pollens, diatoms, fluorescent plastic slides, fluorescence dye slides, silicone chips, and histological slides from plants or animals [1–14]. In most cases the test sample is of biological origin and is sometimes used in the course of research in the individual's research laboratory. This is a testing procedure recommended by the manufacturers of most CLSM equipment. In the author's opinion, this is too arbitrary a test when applications (i.e., intensity measurements or colocalization studies) other than "pretty pictures" are needed. Unfortunately this technology does not have a single universal standard by which the investigator can evaluate their CLSM. It would be advantageous to have better methods for the investigator to evaluate system performance and image quality.

The CLSM consists of a standard high end microscope with very good objectives, different lasers to excite the sample, fiber optics to deliver the laser light to the stage, acoustical transmission optical filters (AOTF) to regulate the laser light delivered to the stage, barrier filters, dichroics, pinholes to eliminate out of focus emission light, electronic scanning devices (galvanometers), detection devices to measure photons (i.e., PMTs) and various other electronic/optical components. For this system to operate correctly, it is important for it to be properly aligned and to have all the components function correctly. Instrument performance tests that have been devised include the following: laser power, laser stability, field illumination, spectral registration, lateral resolution, axial Z resolution, lens cleanliness, lens functionality, and Z-drive reproducibility [1–13]. This list is not inclusive and additional parameters may be needed to assess whether the CLSM is indeed working properly.

Since a confocal microscope can provide spectacular 3D data of biological structures, there is sometimes a tendency to overlook many of the quality assurance (QA) parameters that may be needed. The CLSM may function at sub-optimum conditions for long periods of time delivering inferior data with the problems being resolved only when the investigator cannot achieve the desired images or there is a hard failure of the equipment necessitating a service personnel visit. Sometimes inferior performance of a CLSM may be attributed to a bad sample preparation of the specimen that is imaged. However if the CLSM is not working correctly, the images and data derived from a confocal microscope may be incorrectly interpreted. Since all the CLSM images are digital and made with sophisticated optical equipment, it is now possible to derive tests that can be used to evaluate many of the machine's components. It is the recommendation that the CLSM microscopes should not be evaluated by deriving a "pretty" image from a histological slide. QA on the CLSM is essential to insure it is performing properly and delivering accurate and reproducible data.

This review attempts to incorporate QA procedures into the operation/maintenance of confocal microscopes to improve the reliability of the machines and the data quality. This review also emphasizes that scientists need to evaluate their CLSM system performance to insure that the machine is working properly. It is their responsibility to insure the machine is functional.

2 Materials

2.1 Confocal Microscope

The majority of data presented in this manuscript was derived on either a Leica TCS-SP1 (Heidelberg, Germany) confocal microscope system. This system contained an argon–krypton laser (Melles Griot, Omnichrome) emitting a 488, 568, and 647 nm lines and a Coherent Enterprise UV laser emitting 351 and 365 nm lines. The system contains an AOTF and the following three dichroics for visible light applications: single dichroic (RSP500); double dichroic (DD); and triple dichroic (TD). These tests derived on a Leica system were shown to be applicable to other point scanning systems that contain different types of lasers, objectives or other hardware configurations. For comparison purposes, similar tests were made on two different Zeiss 510 units containing three lasers [Argon 488 (25 mW); HeNe 543 (1 mW); and HeNe 633 (5 mW)] with a merge module and an AOTF. For additional comparison purposes, similar tests were made on a Leica AOBS unit that contained four lasers UV (Argon 351, 365 Enterprise) [Argon 488 (50 mW); HeNe 543 (1.2 mW); and HeNe 633 (10 mW)] with a merge module and an AOTF.

2.2 Field Illumination: Fluorescent Slides

The field illumination test slides consisted of three fluorescent plastic slides (Delta, Applied Precision Inc, Issaquah, Washington) which had excitation peak wavelengths of 408 nm (blue), 488 nm (orange), and 590 nm (red) and emission peak wavelengths of 440, 519, and 650 nm, respectively. The orange slides (488 nm) were used to test for visible field illumination and alignment. The blue slides (408 nm) were used for UV field illumination and alignment. Field illumination can also be measured using four Fluor-ref slides (Microscopy Education, Springfield, Mass) or four Chroma slides (Chroma, Brattleboro Vermont). These slides work equally well for field illumination tests. Spectral tests were made with the Red Chroma slide. They work well if the surface is clean and free of debris and it may be useful to protect the surface from possible scratches. By sealing a 1.5 cover slip (0.17 mm) with immersion oil or mounting medium (Vectasheild or Prolong) on top of the slide.

2.3 Power Meter

The power meter used to measure light on the microscope stage was a Lasermate Q (Coherent, Auburn, CA) with visible (LN36) and UV detectors (L818). A power meter (1830C) from Newport

Corporation with an SL 818 visible wand detector can also be used for power measurements. A remote control box for the Coherent UV Enterprise laser was used to regulate UV laser power (0163-662-00, Coherent, Santa Clara, CA). On most confocal systems there is a 10× lens: Zeiss uses a 10× Plan Neofluar (NA 0.3) and a Leica has a 10× Plan Fluorotar (NA 0.3) or 10× Plan Apo (NA 0.4). The dry 10× lens was used to take power measurements. The machinist's plans for building the power detector holder are available by e-mailing the author.

2.4 Beads

Various bead types and sizes are useful as test particles to access different aspects of machine functionality. It is useful to have point-spread beads (0.17 μmol Probes) and micron sized particles (0.5–1 μm sized beads, and 4–10 μm beads). The beads having different fluorescent excitation wavelengths were obtained from Spherotech (Libertyville, IL) or Molecular Probes (Eugene, OR). Other manufactures also make suitable beads.

The following Spherotech beads were used: 10-μm Rainbow (EX 365, 488, 568) fluorescent particles (FPS-10057), Yellow beads (5.5 μm FPS-5052, EX 488); UV beads (5.5 μm FPS-5040) EX 365; Blue beads (5.5 μm FPS-5070, EX 647). The 6.2-μm Rainbow beads with three different intensities (FPS-6057-3) were used for early statistical PMT tests. The following PSF Rainbow beads were used: (0.16 μm, FP-02557-2s), (0.5 μm, FP 0857–2), and (1.0 μm FP-0557-2). The polystyrene 10-μm beads (RI = 1.59) were mounted with optical cement (RI = 1.56) on a slide using a 1.5 size cover glass. The Leica immersion oil has a refractive index of 1.518.

The following Molecular Probes beads were used: Tetraspeck beads (T7282 0.5 or 1-μm) EX 365, 488, 568, 647) were used for spectral registration tests and point spread functions (PSF); PSF beads (175 nm P-7220) of different wavelengths were used for acute deconvolution PSF measurements; 15 μm focal check beads (F24634 kit) consisting of orange ring and blue throughout (F7236) for UV and visible colocalization or green, orange, and dark red ring stains (F7235) for visible colocalization of the 488, 543, and 633 laser lines.

Bead slides were made by dropping 3–5 μl of diluted beads onto a slide, allowing the liquid to dry and then covering the spot with Permount, glycerol, water, or oil and sealing it with a #1.5 cover glass. Antifade mounting media from Vector (Vectoshield H-1000) or from Molecular Probes (Slowfade light S-7461) is useful to decrease bleaching.

2.5 Biological Test Slides

FluoCells (F-14780, Molecular Probes, Eugene, OR) were stained with three fluorochomes (Mitotracker Red CMXRos, BODIPY FL phallacidin, DAPI) and used as biological test slides. Additional slides were made in our laboratory with cells grown on cover slips, fixed with Paraformaldehyde, and stained with DAPI for UV excitation or other suitable fluorochromes for visible excitation.

2.6 Axial (Z) Resolution Test

The axial resolution of the CLSM is tested using a single reflecting mirror obtained from Leica or Edmonds Scientific. A 21 mm square (#31008 Edmonds Scientific, Philadelphia, PA) was glued onto a microscope slide and a cover glass (#1.5 Fischer, Pittsburgh, PA) was placed on top of the slide with a drop of immersion oil (Leica Immersion oil, $n = 1.518$) The cover slip is placed firmly onto the mirror to remove all excessive oil. This type of standard test slide can also be obtained from a confocal manufacturer (Leica) or Spherotech (Libertyville, IL).

2.7 Square Sampling

It is important to ascertain whether there was square sampling or rectangular sampling in an image. A computer chip was glued onto a glass slide and used as a test substrate. A commercial product can also be obtained from MicroBrightField (Williston, VT) or Geller MicroScientific (Topsfield, MA) or Richardson Microscopic. A digital TIFF image was obtained using a dry 20× objective and the number of small boxes observed was counted by eye in the vertical and horizontal directions. If there is the same number of boxes per inch in the vertical and horizontal directions, then it can be assumed that the sampling of pixels is square. If they are not equivalent, then the sampling of pixels is rectangular, which is undesirable. This test can also be used for galvanometer stability and proper functioning.

2.8 Software Analysis

The analysis of the images was made on workstations that contained Leica, Zeiss, and Bitplane (Zurich, Switzerland) software packages. If necessary, the TIFF images were imported into Image Pro Plus (Media Cybernetics, Silver Springs MD) or Image J (NIH) for more intensive measurements and analysis. Colocalization software includes Cool Localization and Bitplane software.

2.9 PMT Spectral Evaluation

The PMT spectral response was measured over a large spectral region using an inexpensive PARRIS fluorescence calibration lamp (MIDL) consisting of a defined mixed ion gas (816025, LightForm Inc., Hillsborough, NJ)

3 Methods

3.1 Confocal Microscope Set Up

1. Turn lasers on 15–30 min prior to use for experiments.
2. If there is a variable power control it should be set at sufficient power to eliminate laser noise and when not in use the laser should be in “park” position.
3. Objectives should be cleaned with Sparkle, MEOH or equivalent cleaner prior to use. They must be clean and should be checked often, especially when located in a Core facility. The objectives can be observed with the eyepiece objective, stereo microscope or with the axial resolution test (described below).

4. Lens condenser diaphragm should be totally open.
5. Microscope should be set up for Kohler illumination with the field diaphragm being totally open and the microscope lenses adjusted for parfocality.

3.2 Field Illumination

1. Seal a 0.17 coverslip on the plastic slide (Chroma or Delta) with oil to eliminate potential scratching.
2. The fluorescent slide was placed on the stage and the maximum intensity was found on the surface of the slide. Delta orange slide and the Chroma red slide yielded good excitation and spectral peaks and were thus used for visible or UV excitation. The blue slides were preferentially used for UV excitation.
3. Measure the field illumination at a specific depth in the plastic slide, as the intensity distribution may change from the surface to the interior of the slide. The depth of focus was adjusted between 30–100 μm, dependent on the objective that was used [5× (100 μm); 10× (75 μm); 20× (50 μm); 40× (40 μm); 63× (30 μm); 100× (30 μm)]. Investigators should also be careful not to observe field illumination deep within the plastic slide samples, as it will usually yield a better field illumination pattern than regions closer to the surface due to light scattering.
4. Figure 1 shows data derived from a 20× Plan Apo lens (0.7 NA) zoomed to a factor of 1.2 to illustrate a good visible field illumination (488 nm) pattern and a misaligned UV (365 nm) system yielding bad field illumination pattern. Each laser line must be checked to insure they are aligned properly as they use different dichroics to insure the beams are co localized. In addition, the field illumination of one lens is not necessary identical to the field illumination of the other lenses, necessitating that each lens be checked with the suitable dichroic that will be used in the experiment.

3.3 Power Measurements

3.3.1 Power Meter

1. Connect the suitable UV or visible probe (Coherent probe detectors (UV-L818, Vis-LN36) a power meter (Lasermate/Q, or Field Master, Coherent, Santa Clara, CA) and place it directly on top of the dry 10× objective. A lens holder can also be fabricated in the machine shop and placed on the stage. A different lens design, magnification, or numerical aperture (NA) will affect the laser power transmission and measurement.

   The power meter is adjusted to the specific wavelength (365, 488, 568, or 647 nm) and the maximum power of laser light is read on the digital scale.
2. The CLSM zoom factor is set from 8 to 32 to reduce the beam scan range and to focus the laser light into the “sweet spot” of the detector.

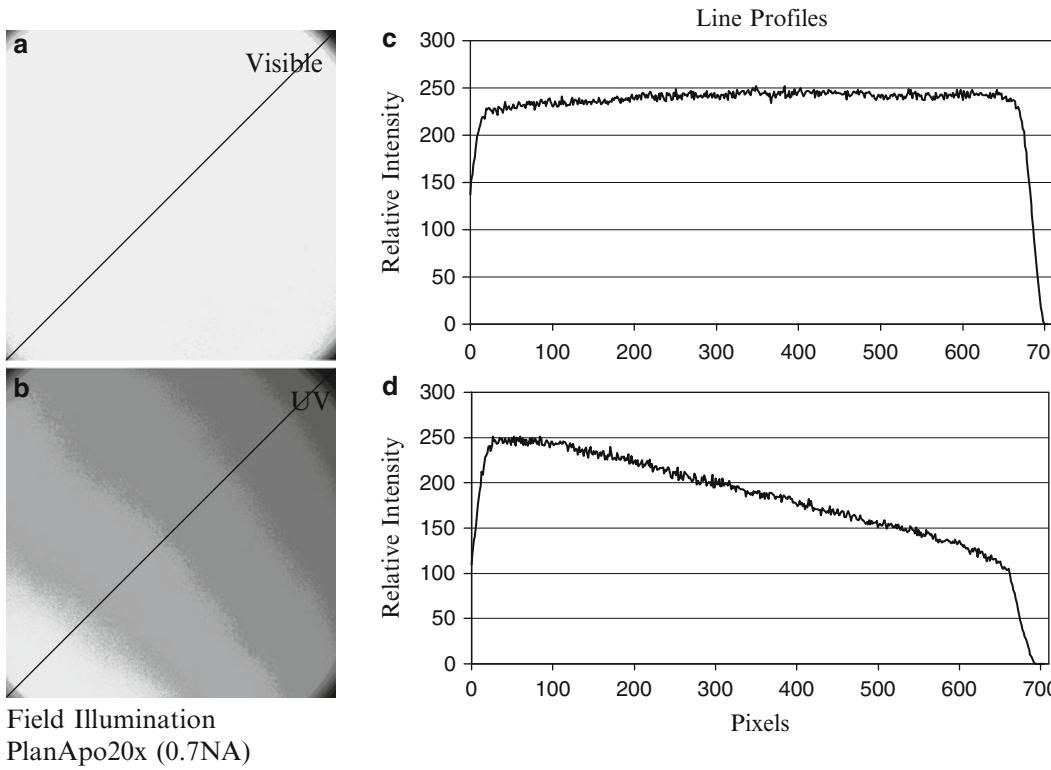

Fig. 1 Field illumination. Field illumination pattern of visible (**a**) and UV (**b**) excitation using a 20× (Plan Apo, NA 0.7) lens. The visible field illumination shows uniform illumination with the brightest intensity being in the center of the objective. The line running diagonally in (**a**) and (**b**) measures the histogram intensity of the field illumination graphically represented in figures (**c**) and (**d**). The variation in intensity from the left to right side of the field is less than 10 % for visible excitation and over 150 % for UV excitation. Acceptable field illumination has brightest intensity in the center of the objective decreasing less than 25 % across the field. The intensity regions were prepared by using Image Pro Plus to divide the GSV into ten equal regions and a median filter was used for additional processing. The non-uniform pattern shown in Fig. 1 with UV illumination clearly illustrates a field illumination problem, which will affect intensity measurements in an image. Although Fig. 1 was obtained with UV optics it represents the type of field illumination that can also occur with visible excitation. This pattern is unacceptable with any CLSM optical system as the maximum intensity should be in the center of the objective and not in a corner

3. The scanner is set at bi-directional-slow speed to reduce the time period that the power meter is reading "0".
4. The maximum digital reading from the power meter was recorded. The power derived from this measurement is dependent on the type magnification and NA of the lens used.
5. Each lens will have a unique set of values, which is dependent on objective's NA and other transmission factors. The power meter diode located in the machine was not reliable and could only be used as a crude relative estimate of the laser's functioning. This internal power meter may change in the future with better-designed systems.

3.3.2 UV Power Test

The test was carried out in a similar manner to that described for the visible power measurement except the power meter was set for 365 nm and the UV detector (L-818) was attached to the power meter. A Coherent UV, 60-mW, Enterprise laser delivered normal power output at the laser head (over 40 mW of laser power), but only about 500-uwatt maximum power through a Plan Fluor 10× (0.3 NA). When our system had insufficient output under these conditions (approximately 500 uwatt through a 10× Leica (0.3 NA) lens) we also had insufficient light for many UV experiments using higher magnification objectives (40×, 63×, and 100×). Power throughput is a reflection of both laser status and system alignment problems

3.3.3 Bead or Histological Power Meter

If a power meter is not available, the crude power of the system can be also be assessed by recording the PMT voltage necessary to acquire an image at almost saturation values by using standard histological samples like the FluorCells slide (F-14780, Molecular Probes, Eugene, OR), beads like the 10-μm Spherotech beads (FPS-10057-100) or fluorescent plastic slides. The light throughput in the system can be determined by setting the laser at maximum values and recording the specific PMT voltage in which saturation of the bead occurs. If conditions are identical between machines, this PMT value can be used as a reference value to compare CLSM units and to establish their acceptable performance levels. Leica technicians routinely use a 40× lens to measure the fluorescence saturation of a histological stained plant sample (Convalaria). If the plant sample saturates in the PMT range between 600 and 700 units in PMT 1 the system is passed as having adequate power by confocal technicians.

3.4 Axial (Z) Resolution

3.4.1 Axial (Z) Resolution (Mirror)

The axial resolution test is considered the "gold standard" of resolution in confocal microscopy [1, 2, 5, 11, 14]. Although it is not the only criteria for a good image, the axial resolution of the system should be maximized to yield a minimal axial Z-Resolution value with a symmetrical histogram and minimal spherical smaller diffraction peaks (Fig. 2)

1. Place the mirror on the stage and use a high NA oil lens (63× or 100×).
2. Set the microscope up in reflecting mode using a RT 70/30 dichroic.
3. Fully open up lens condenser so lens is operating at highest NA.
4. Using XY scanning mode one should find the reflected surface of the mirror keeping the pinhole aperture open for good light transmission. This will be the brightest intensity. Zoom should be 1.

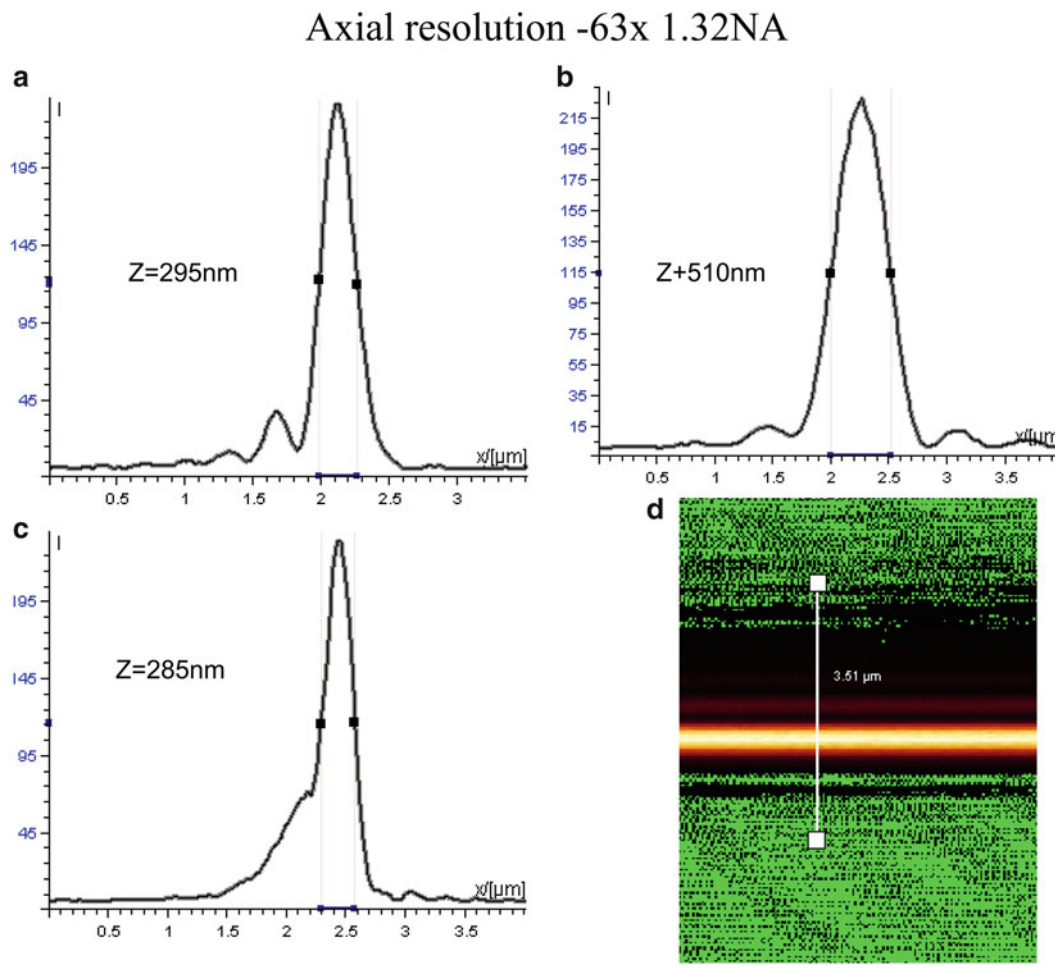

Fig. 2 Axial resolution. The axial resolution was made with two 63× lenses (NA 1.32) at different times on the same Leica TCS-SP1 confocal system. The peak intensity of the histogram is approximately 235 and the half-maximum intensity is at 117. One lens gave an excellent Full-Width Half-Maximum (FWHM) of 285 nm (**a**) while the other lens yielded a bad value of 510 nm (**b**). The system was aligned properly in both cases. The axial resolution of a Plan APO 63× (1.32 NA, 285 nm) showing a symmetrical major peak and a diffraction pattern consisting of smaller peaks and valleys (**a**). This pattern is suggestive of an excellent quality lens A. By accident, a dirty lens with dried oil was measured and it also was found to have a larger FWHM (**c**). However the pattern of this dirty lens showed a peak with a shoulder suggestive of spherical aberrations which is not desirable. It is important the FWHM be as low as possible and the histogram pattern look like (**a**) and not (**c**). Lens B shows a distribution with the collar partially closed which increases the FWHM. System with higher FWHM will perform less effectively. The lens with the lower FWHM is desirable for good biological resolution

5. Switch to XZ scanning mode.
6. Find the reflecting line and adjust it so it is located in the middle of the field.
7. One may adjust the offset so there is a little background. This will reduce the axial value by about 7 nm but it will allow the diffraction pattern to be better observed.

8. Adjust the Zoom to approximately10× and reduce the pinhole to minimum size values (20 μm on a Leica SP and 10 μm on a Zeiss 510).
9. The reflected image is then obtained and the intensity histogram line profile across the image to determine the full-width half-maximum (FWHM) distance.
10. The maximum intensity of the peak is determined and then the half-maximum intensity value of the histogram is obtained. This value is the axial resolution of the system with the specific lens.
11. The specification for axial registration in a Leica TCS-SP system using 100× NA 1.4 is below 350 nm. A Leica 63× (NA = 1.32) has yielded values of 310 nm although a value of 400 nm is acceptable. There are no other lens specifications using a confocal microscope.
12. The histogram data can be observed graphically or it can be transferred into Excel to measure the peak and the half-maximum values.
13. The pattern of axial resolution curve is also very important. An acceptable pattern has a symmetrical large peak with a low valley and smaller peaks to left of it (Fig. 2a). If the valley is not low then it yields an asymmetrical histogram suggestive of increased spherical aberrations (Fig. 2c)
14. These axial registration values will change dependent on lens quality, cleanliness of the lens and system alignment. A dirty lens will yield and asymmetrical pattern (Fig. 2c) and a lens with a partially opened condenser (Fig. 2b) will yield a lower NA and thus will show a wider histogram distribution (Fig. 2b, c).

    Wider histograms and higher FWHM are suggestive of a system that is not performing well due to alignment problems, lens NA or lens cleanliness.

3.4.2 Axial (Z) Registration (Beads)

Small beads (0.5–1.0 μm) from Molecular probes (Tetraspec, T7284) or Spherotech (Rainbow, FP–0857-2) are first located in the XY direction and then scanned in the XZ direction. The power is adjusted for saturation and then they are zoomed approximately 8× and averaged 4×. The size of the bead in the horizontal is compared to the vertical size. The difference between the two numbers will yield the axial resolution of the lens. This method is slightly more subjective than the gold standard axial resolution mirror test but it does yield similar values. For unknown reasons, the bead derived axial values may be better or worse than the mirror tests.

3.5 Square Pixels and Phase Alignment and Galvanometer Check

The pixel size and symmetry in XY directional field scanning can be checked by using a computer chip attached to a glass slide or a slide obtained from Microbright, Geller MicroScientific or Richardson scientific.

1. The confocal should be set up in reflective mode (RT 70/30) using a 10× or 20× dry lens.
2. The slider should be placed over the excitation line and the PMT should be adjusted.
3. The small boxes or reticule lines in the vertical and horizontal direction should be compared by either counting them or by a measuring a standard line across them.
4. This test insures that the scanning in the X and Y directions yields a perfect square and the information will be registered correctly. If there is the same number of boxes per inch in the vertical and horizontal directions, then it can be assumed that the sampling of pixels is a square. If they are not equivalent then the sampling of pixels will be rectangular, which is not desired.
5. This test can be used to assure that alignment exists in bi-directional scanning.

3.5.1 Galvanometer Check

1. Set the system up in reflecting mode with the PMT detector positioned over the 488 excitation line.
2. Acquire only one scan and then observe the grid pattern (i.e., Microbright).
3. Acquire 25 sequential scans each separated by only a few seconds. Average the 25 scans and get a maximum projection.
4. Compare the width of the grid lines with one scan and 25 scans. They should be identical but if there is a widening of these lines with the 25 scans, it suggests the system has a faulty galvanometer (Fig. 3).
5. This test can also be shown visually by comparing sequential scans. They should be identical with no widening of the lines.
6. Observe the grid pattern. It should be square but occasionally improper scanning with the galvanometer will cause the vertical lines to be irregular and thus widen the lines shown in Fig.3a vs. Fig. 3b.

3.6 Spectral Registration (Lenses and Lasers Lines Using Small Beads, Mirror, and Focal Check Beads)

The 1 μm multiple wavelength fluorescent beads (Tetraspec, T7284 Molecular Probes, or Rainbow beads, FP–0857-2 Spherotech) were used to monitor the visible spectral registration of the following lenses: (100× Plan APO, NA 1.4; 63× Plan APO, NA 1.2; 63× Plan APO, NA 1.32, Plan Fluor 40×, NA 1.0).The bead could also be used to measure the registration between multiple laser lines (UV and 568 nm).

3.6.1 Spectral Registration of Laser Lines with 1 μm Beads (UV and Visible)

1. The bead was located at low zoom values in XY and the gain (slightly saturated as bleaching will occur) and offset were adjusted to their respective optimum image quality levels.
2. An XZ scan was obtained at the proper zoom magnification (4–8×) to observe the bead. Care was made to make adjustments

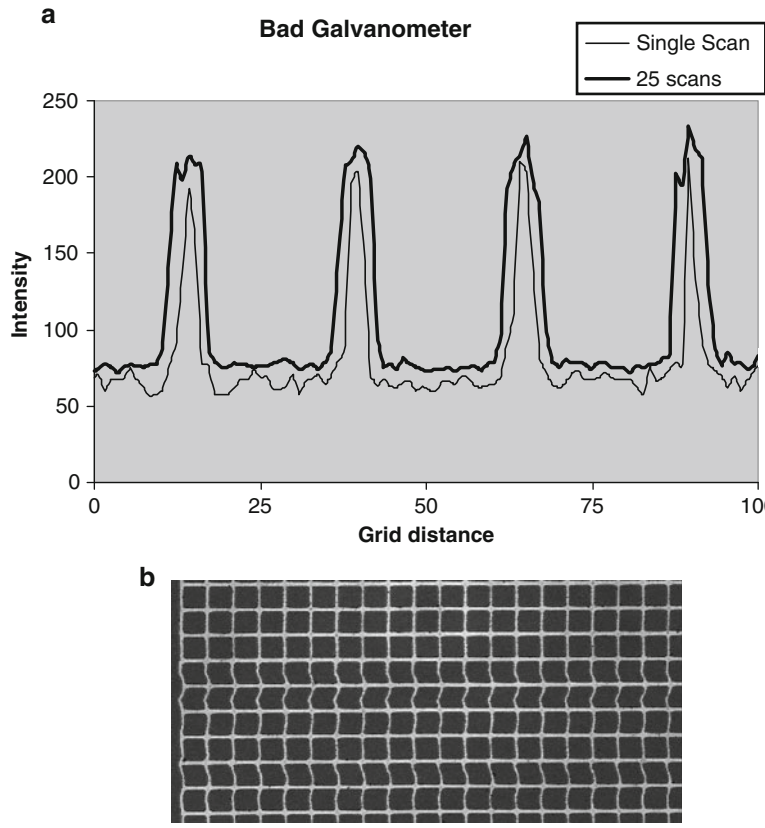

Fig. 3 A MicroBrightField slide contains a rectilinear grid that can be used to detect if the field being scanned is actually square and not oblong. Using reflection mode, the detector PMT placed directly over the laser line and a grid pattern is observed. As shown in (**b**) (*insert of partial grid*) the boxes in the vertical and horizontal direction should be equivalent and straight. A malfunctioning galvanometer is shown by rectangular irregular boxes, jagged edges in the scan or irregular vertical lines. If a horizontal line is drawn over a few of the squares in (**a**), the width of it should be the same with one image as it is with 25 images that are sequentially acquired with a time delay of approximately 2 s between images. (**a**) shows a very narrow distribution which is widened after 25 sequential images are acquired. Widening of the vertical lines will indicate a badly functioning galvanometer. Tests should be run with a zoom setting of 1 and a dry 20× lens. Irregular vertical lines showing jagged edges or bends as shown in (**b**) will also indicate problems with the galvanometers

at the lower power levels to reduce possible bleaching effects and zoom values.

3. By balancing laser light intensity with the Acoustical Optical Transmission Filter (AOTF), the fluorescence emission cross talk between the detection channels was minimized. If too much crossover exists the test will be invalidated. To check for cross talk, one laser light line is closed with the AOTF and the signal

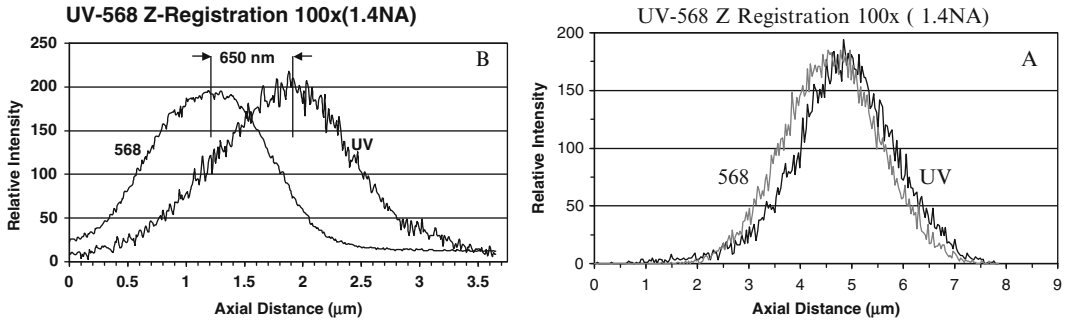

Fig. 4 (**a**, **b**) Spectral registration (UV and Visible). The XZ spectral colocalization of this UV (365 nm) and visible wavelength (568 nm) was evaluated with a 100× Plan Apo NA 1.4 lens using a 1 μm multiple wavelength fluorescent bead (Tetra Spec T7284 Molecular Probes). An aligned system has a full-width half-maximum (FWHM) of less than 210 nm (**a**) while a misaligned system has a FWHM difference of 650 nm (**b**). The bead was imaged using XZ scans with a 24× zoom, a slow scanning rate, and averaged eight times. The 568 line was chosen instead of the 488 line to minimize the crossover between the visible and UV wavelengths

is observed in the other channels with the PMT voltage setting that is necessary to acquire the proper signal. It will be necessary to decrease the laser power with the AOTF and increase the PMT voltage which will help to eliminate cross talk.

4. The bead was imaged (XY and XZ scans) with an 8–24× zoom, a slow to medium scanning rate, and frame averaged 4–8 times at two different times. The registration of fluorescence images derived from beads using the 365 nm UV laser wavelength and the 568 nm visible laser wavelength in an aligned system was almost superimposable (Fig. 4a). However at a later time, in a misaligned system, the XZ registration between the 365 nm UV line and the 568 nm visible line was not super imposable (Fig. 4b). The misaligned had a difference between the peaks of 650 nm while an acceptable difference between the two emission peaks was 210 nm. This test is critical for colocalization studies. The 568 nm line was chosen instead of the 488 line to minimize possible bead crossover fluorescence between the visible and UV wavelengths.

3.6.2 Spectral Registration of Laser Lines with Reflective Mirror

This spectral registration test demonstrates the CLSM ability to colocalize different wavelengths of fluorescence in the same plane. To evaluate the spectral registration of the 488, 568, and 647 nm lines, a front surface, single reflective mirror (Fig. 4) was used to check visible spectral registration in a Leica TCS-SP system, in a similar manner to what was described in Fig. 2 for axial Z registration.

1. In the Leica SP system, a 10 nm refection bandwidth is put over each excitation wavelength and the reflection can be measured sequentially with one PMT or simultaneously with three PMTs. This is similar to axial resolution test using

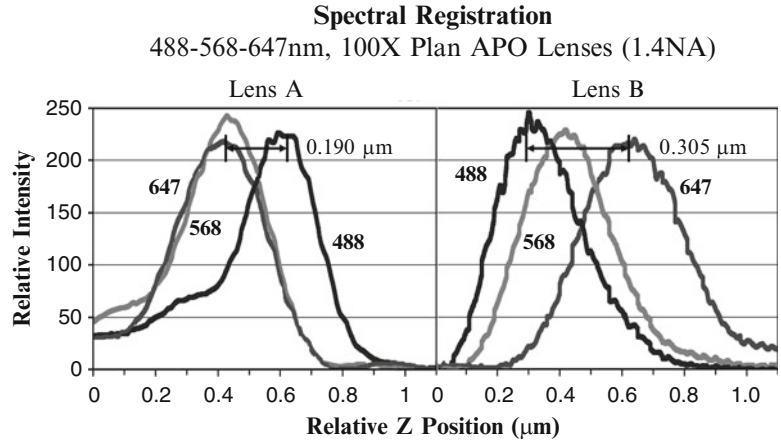

Fig. 5 Lens spectral registration (visible). The visible spectral registration of a 100× Plan Apo NA 1.4 objective was evaluated using a front surface, single reflection mirror with the same lens at different times. A 10 nm slit is put over each wavelength and the reflection of each line was measured sequentially. The AOTF and PMT intensity was adjusted so the maximum intensity of each line was 250 GSV. Lens B was sent back to the factory, as it did not meet the following: (1) spectral registration for UV (365) and visible (568); (2) spectral registration for the three visible lines; and (3) axial resolution specifications. The refurbished Lens A showed excellent registration between the three visible lines with the difference being less than 220 μm. Refurbished Lens A also had an axial registration below 350 nm. This single reflection mirror test will yield slightly better spectral registration than 1 μm bead data for the 647-excitation line, as the fluorescence emission occurs in the far-red range (>660 nm) and many lenses have difficulty colocalizing this far red emitted light with the fluorescence emitted from the 488 and 568 wavelength excitation

reflection mode and XZ scanning which can be acquired sequentially or simultaneously for the three laser lines.

2. By tweaking the AOTF and PMT voltage adjustments, the reflected light is adjusted so the maximum peak is close to 255 but does not exceed it. The intensity of each reflected line was adjusted for a maximum intensity of the image was approximately 250 GSV.
3. The images representing three laser lines (i.e., 488, 568, 647) are displayed as an overlay and a line is drawn through the composite image. The overlapping histograms will represent three laser lines and will have a distribution representing the spectral registration of optical system with an argon–krypton laser to distribution represents the lens quality (Fig. 5).
4. With the multilaser system the distribution represents the composite of lens spectral properties and the laser alignment. Studying multiple magnification lenses should allow one to determine if lens quality or system alignment is correct.

3.6.3 Spectral Registration of Laser Lines with Beads

1. A 1-μm bead can be used to test visible wavelengths for colocalization in a similar manner to that described for colocalizing UV and visible light. Using the bead test, it is necessary to

reduce the laser light to reduce bead bleaching and then adjust the laser light with the AOTF and PMT voltage so fluorescence cross talk between the different laser lines emitted wavelengths is minimized. It is also useful to suspend the beads in antifade to reduce bleaching for this test, as they will be zoomed at high magnification, which increases bleaching (Fig. 4).

3.6.4 Spectral Registration of Laser Lines with Focal Check Beads (UV and Visible Lines)

Molecular Probes produces a series of beads (Focal Check) that can be used to assess the different visible wavelengths from multiple lasers in a confocal system. These beads have different fluorescent excitation rings and core colors that can be used to assess colocalization of laser light from multiple lasers.

1. To examine the UV (365) and visible lines (568) in a Leica TCS-SP1 confocal system that had an argon–krypton laser emitting three lines and a UV Enterprise laser. A 15-μm bead with UV blue interior and orange fluorescence ring exterior (F7236, Molecular Probes) was used to show that the UV and 568 lines were aligned (Fig. 4). In a similar manner, the F7237 bead consists of a UV blue core and a green ring and this can be used to show colocalization of the 488 and 365 laser lines. This bead may have slightly more cross talk than the blue core with a red ring (F7236). The laser power and AOTF should be adjusted to reduce cross talk between the emitted fluorescence. Any deviation between the concentric localization of the rings or the maximum diameter of the rings and core bead size suggests misalignment.
2. In the newer confocal systems that have three lasers and a merge module, it is recommended to test for colocalization with focal check beads (F7235) that has three rings representing green, orange, and red or a focal check bead (F7239) that has a red ring and a green core. This test is similar to that described above for UV and 568 excitation with the F7236 bead. Using three separate visible laser excitation the bead should reveal concentric fluorescent rings that have maximum values in the same focal plane with either a XY or XZ scan. Variations will indicate a system out of alignment and lacking colocalization.
3. Individual pinholes in a Zeiss system may have to be realigned monthly. This test can indicate if the pinhole needs adjustments and if the system is meeting the colocalization test.
4. Smaller focal check beads should yield more accuracy.

3.7 Lens Spectral Registration

Different lenses were tested by the axial resolution single reflective mirror test described above. Figure 5 represents a 100× lens measured over a time period of approximately 6 months on the same CLSM system. On testing Lens B problems in axial resolution and spectral registration existed. The separation between the 488 and

647 nm line was 305 nm in lens B and the axial registration was 410 nm (Acceptable was 350 nm). This lens (B) was returned to the factory to correct this spectral registration problem in visible, and a spectral registration problem between UV and visible. After factory repair, lens A showed perfect colocalization between the 488 and 647 nm lines and acceptable registration between the 488, 647, and 568 lines. The UV and 568 nm (Fig. 5a) also showed acceptable registration after repair.

Depending on the laser configuration, this test can be revealing characteristic of the lens spectral registration or system alignment. In an argon–krypton laser system since all three lines are derived simultaneously, the test will reveal the lens characteristics. If a three laser system with a merge module is used it will reveal the combination of both lens characteristics and laser alignment. It is useful to make this test with more than one objective, as it will be rare that a system will contain multiple lenses with axial and spectral registration problems

3.8 Dichroic Functionality

The dichroics reflect good light and eliminate unwanted light. It is important that the most light be reflected to allow the system to operate efficiently.

1. An API fluorescent plastic slide (orange) or Chroma Red slide was placed on the stage using either 488 or 568 excitation light. After the dichroic was switched into position, the PMT was kept constant and the mean GSV (Gray Scale Value) of a region of interest (ROI) in the image was determined for each acquisition condition. The values for the three dichroics can be compared to determine which one has the highest reflectivity (Table 2).
2. The maximum values are normalized to 1 and the other values are reported as a percentage of the maximum GSV. It is important to use a bandpass or barrier filter to collect the desired light. Light at different regions of the spectra may have unique information and it is sometimes advisable to use a narrower bandpass with higher reflection to get the desired fluorescent information.

3.9 Laser Stability

3.9.1 Laser Stability (Visible, Long-Term Hours)

Laser stability measurements were made over hours to evaluate the possible fluctuations in power [1, 2, 5, 14]. The laser power fluctuations were initially measured both in PMT 1 (blue light sensitive, low noise, R6857) and in the transmission detector using a fluorescent plastic slide with very low laser power that was reduced with either neutral density filters or with the AOTF adjustments. The transmission optical system without a slide showed similar results to PMT 1 with fluorescent plastic slides and this was the desired optical system to perform this test if it exists on the system as it eliminated any possibility of bleaching, laser interaction with the

substrate, and possible stage drift. Fluorescent colored slides, reflecting mirrors and beads have been used to demonstrate power stability but they are not as reliable as the transmission detector to evaluate power stability problems.

1. To measure laser stability using the transmission optical system, the microscope is first aligned for Kohler illumination using a histological slide, which is then removed from the optical path.
2. The laser power is adjusted by a combination of laser power and AOTF adjustment of the laser line power. It is desirable to adjust the AOTF so the transmission detector voltage remains constant for all three wavelengths. Adjust the AOTF for 647(or 633) first and then 568 (or 543) and finally 488.
3. The image intensity is measured using the one transmission detector for the three wavelengths of the argon–krypton laser by sequentially measuring the laser light with the 488, 568, and 647 wavelengths. The test can be made with a three laser system substituting either the 543 or 561 laser lines or the 633 laser line for the 568 and 647, respectively. Only two lines are shown in Fig. 6 for clarity.
4. The test usually takes a few hundred scans separated by 10–30 s over a period of 2 h.
5. The intensity of the same large ROI of the three fields is averaged and plotted over time for the three wavelengths. The goal of this test is to have a straight line with no variations in power to insure accuracy in the intensity measurements. It is not necessary to save the images in the scan but it is useful to save the data measurements in an Excel file, text file, or equivalent.
6. Illustration of laser power: The type of laser power stability data that can be achieved with this test is represented in Fig. 6a, b. There is periodic noise in the laser system that exceeds both the manufactures (Ominichrome) laser stability fluctuations specifications of less that 0.5 % over a 2-h time period. The 488 and 568 lines have a periodic cycle and stability are never achieved (Fig. 6a). This is not a typical pattern as expected for argon –krypton laser and indicates there is instability in the system, which will affect intensity measurements.
7. A Chroma red slide is placed in the light path and images are taken sequentially for 3 h at an interval of 30–60 s (Fig. 6b). Care is taken to reduce the laser power by the AOTF and the neutral density filters to reduce possible bleaching of the slide. Figure 6b shows wide fluctuations with the 568 visible line while the UV is relatively stable. The source of noise has not been indentified, but it is believed to be derived from the AOTF, as the light entering the AOTF has less than 1 % power fluctuations while after the AOTF the fluctuations are over

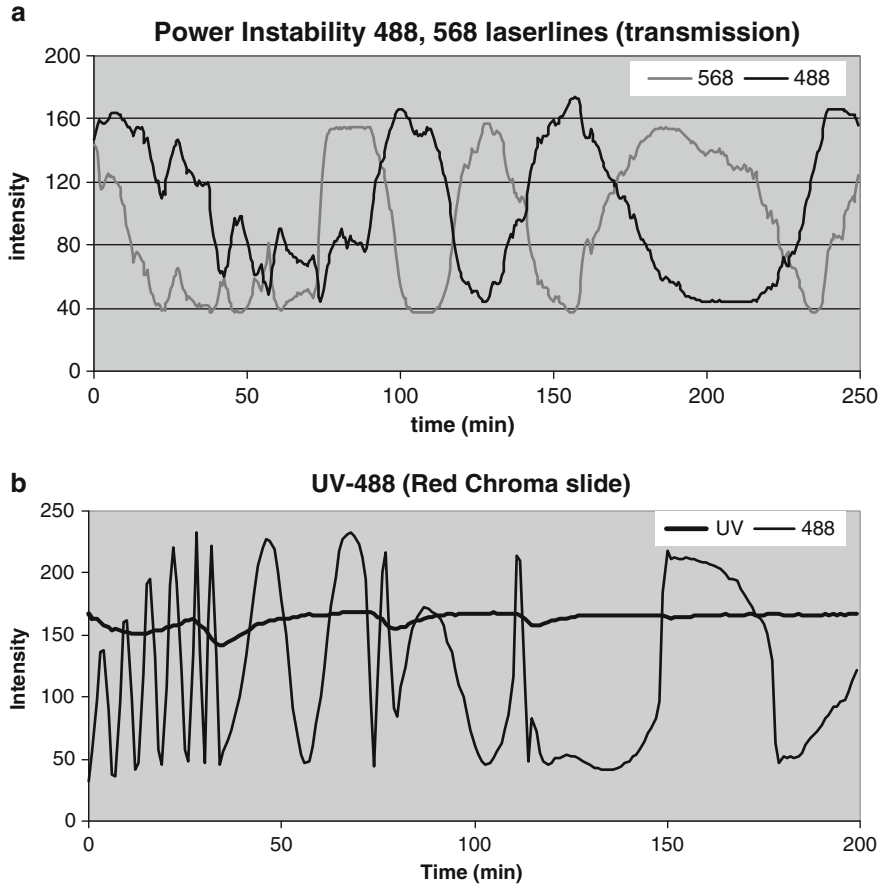

Fig. 6 (**a**) Laser power fluctuations. The periodic change in laser power was measured using transmitted interference optics without a slide in the optical path. The two lines show a visible system delivering 488 and 568 power fluctuations. The 488 and 568 lines are cycling periodically. These variations in this power intensity occur over hours and never seem to stabilize. To measure laser stability over time the PMT was kept constant and the laser power of the three lines was adjusted with the AOTF (only two laser lines are shown for clarity). Next, over 200 measurements were sequentially acquired every 30 s. After the test was complete, the intensity of a large ROI was evaluated and plotted over time. The laser power instability may be due to either laser light entering a fiber with an incorrect laser polarization, thermal instability in the AOTF or a badly aligned system. The reason for the source of power instability is not known. It can vary from as little as 10 % to as high as 400 %. (**b**) Laser power fluctuations. A red fluorescent Chroma slide was placed on the stage and it was sequentially excited with the 365(UV) and 568 laser lines. Two hundred acquisitions were made every minute for 3.3 h using a bandpass of 500–650 nm for emission. To reduce possible bleaching the laser power was reduced to minimum values using neural density filters (UV) and the AOTF (568 line). The red Chroma slide has the possibility of bleaching and possible stage drift. The data shows a "cold" system showing poser foliations. These fluctuations in visible continued after the system was warm while the UV system became very stable. The contrast between the two lines suggests that the AOTF may be introducing errors

10 % and in this case the peak-to-peak variation is 400 % (40–160 GSV). The goal of this test is to achieve a flat stable line as illustrated with the UV light. Proper heat dissipation may also be attributed to laser instability.

3.9.2 Laser Stability (UV, Long Term)

The Coherent Enterprise laser delivers less than 1 % peak-to-peak noise and is considered very quiet and stable laser. The Coherent laser was tested in a similar manner to that described for visible lasers using the transmitted optical system or the PMT system with blue colored fluorescent plastic slides and very low laser power. A relatively stable line showing minimal fluctuations should be obtained (Fig. 7a) The temperature of the cooling system must be regulated properly or power fluctuations will occur (Fig. 7b, c). One source of power stability appears to be the way laser is cooled and how the laser heat is dissipated. This was illustrated with our Coherent Enterprise UV laser that was connected to a Coherent LP 20 water–water exchange cooler. This cooler should be set at least 10 °C above the circulating cooling water of the building and it should be set above the ambient temperature of the room. Improper set points for the LP 20 cooler resulted in temperature regulation problems of the circulating cooling water in the laser which in turn resulted in the improper regulation of the laser power (Fig. 7b).

3.9.3 Fiber Optic Stability and Polarization

The fiber optics may influence artifacts due to deterioration with time or improper polarization alignment. Fiber optical problems

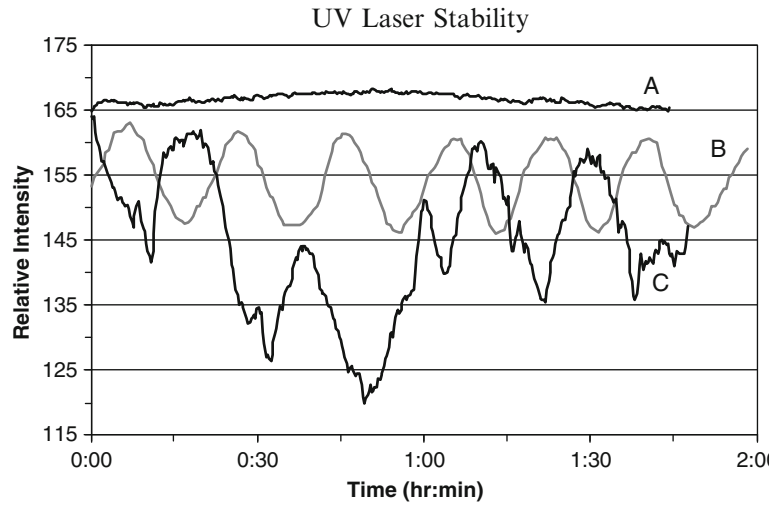

Fig. 7 Laser stability of a coherent enterprise UV laser. The Coherent Enterprise UV laser delivers less than 1 % peak-to-peak noise. The laser was connected to an LP 20 water–water cooler, which should be set at least 10 °C above the cooling water of the building. It should also be set above the ambient temperature of the room. Improper set points for laser cooling resulted in bad thermal regulation of the laser B. Improper fiber alignment resulted in additional laser intensity variations C. The elimination of the temperature and polarization issues resulted in proper laser stability (A, 3 % power variation over time) The test was conducted by measuring the laser power stability in PMT 1 using a fluorescent plastic slide. Neutral density filters were used to reduce the power and thus minimize slide bleaching. The transmission detector optics gave similar results to the UV fluorescent plastic slide and was also used to measure UV laser stability

will attenuate the laser power and necessitate using higher laser power or higher PMT settings in the operation of the CLSM.

1. One test procedure recommended by one manufacturer to insure that polarization is correct after the alignment procedures is to wiggle the fiber optic and see if the image returns to the same intensity values suggesting the polarization are correct. This is a fairly crude test, but it will demonstrate whether the system fiber optic needs further polarization alignment. Better procedures are being tested by the manufactures to eliminate this polarization alignment problem.
2. Laser stability tests over time may be related to laser polarization and fiber optics problems.

3.9.4 Laser Power Stability (Short Term, Seconds)

Laser stability and system noise while scanning are measured using the transmission optical system. The goal of this test is to have a straight line with no variations in power. If power fluctuation exists they can be averaged to increase image quality. Averaging will reduce the CV and system noise.

1. The microscope is first aligned for Kohler illumination with a histological slide, which is then removed from the optical path.
2. The laser power is measured with a power meter on the stage as previously described. This is a step that is necessary if the data is to be compared between machines and over time.
3. The image intensity is measured using the transmission detector for the three wavelengths of the argon–krypton laser by sequentially measuring the laser light with the 488, 568, and 647 nm wavelengths with the power being adjusted by the AOTF transmission control so the transmission detector voltage remains constant for all three wavelengths. In contrast to the long-term stability test, the short-term test uses only one scan for each wavelength.
4. The intensity of part of a single line scan is averaged and the mean, standard deviation and CV are determined (Fig. 8).
5. If transmission optics is unavailable on the system this test can also be done with fluorescent plastic using very low laser power to reduce bleaching.

3.10 Spectral Scanning: PMT Comparison and Light Form Lamp

The spectral accuracy on confocal microscopes was measured on the Leica SP, Zeiss 510 Meta, and the Olympus FV 1000 spectral systems using a Lightform lamp positioned on the stage [4]. The test has the ability to demonstrate proper spectral representation of defined wavelengths of light in addition to determining misalignment of the system and possible stray light occurring within the system.

1. On the Leica system, this feature allows for a sequential scan across the range of 400–800 nm in units as small as 5 nm.

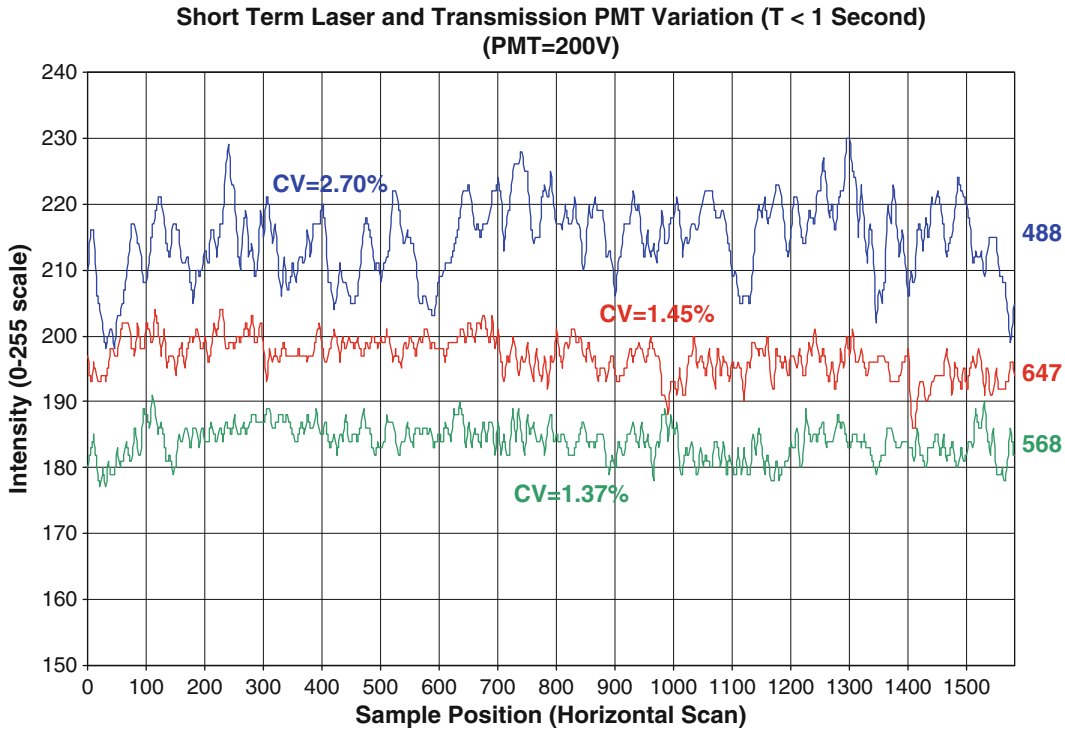

Fig. 8 Laser noise (short time). The Transmission PMT was set to a constant value and the intensity of the laser lines was adjusted with the AOTF to bring the intensity to approximately the same point for graphic representation. The various intensities on one line in one scan were made and it demonstrated that the 488(CV = 2.70), 568(CV = 1.45), and 647(CV = 1.37) had variations in intensity at very low PMT settings. The blue line (488) was twice as noisy as the green (568) or red (647) lines. Higher PMT values will increase the CV and should be averaged to eliminate this noise (Color figure online)

The test used an inexpensive defined mixed ion light source, (LightForm Inc, Hillsborough NJ) to measure spectral response of a PMT across a large spectral region.

2. If necessary, the microscope slide holder was removed and the light source position on the stage. A spectral scan consisting of 50 increments of 5 nm each was made between 400 and 650 nm using a 10× (0.4 NA) Plan Apo lens without averaging at an airy disk of 1 (Pinhole size 79 μm). A 20× air lens is also acceptable for this test. The efficiency of the light collection system was low which necessitated that a large PMT voltage setting be used. Opening the pinhole will change the observable pattern as the peaks will widen [4].
3. The intensity of each 5 nm scan was calculated as the mean from a large ROI and the data were displayed as an intensity graph between the 400 and 650 nm range (Fig. 9).
4. To detect spectral accuracy above 650 nm the PMT scan was repeated for the three PMTs and between the 650 and 800 nm

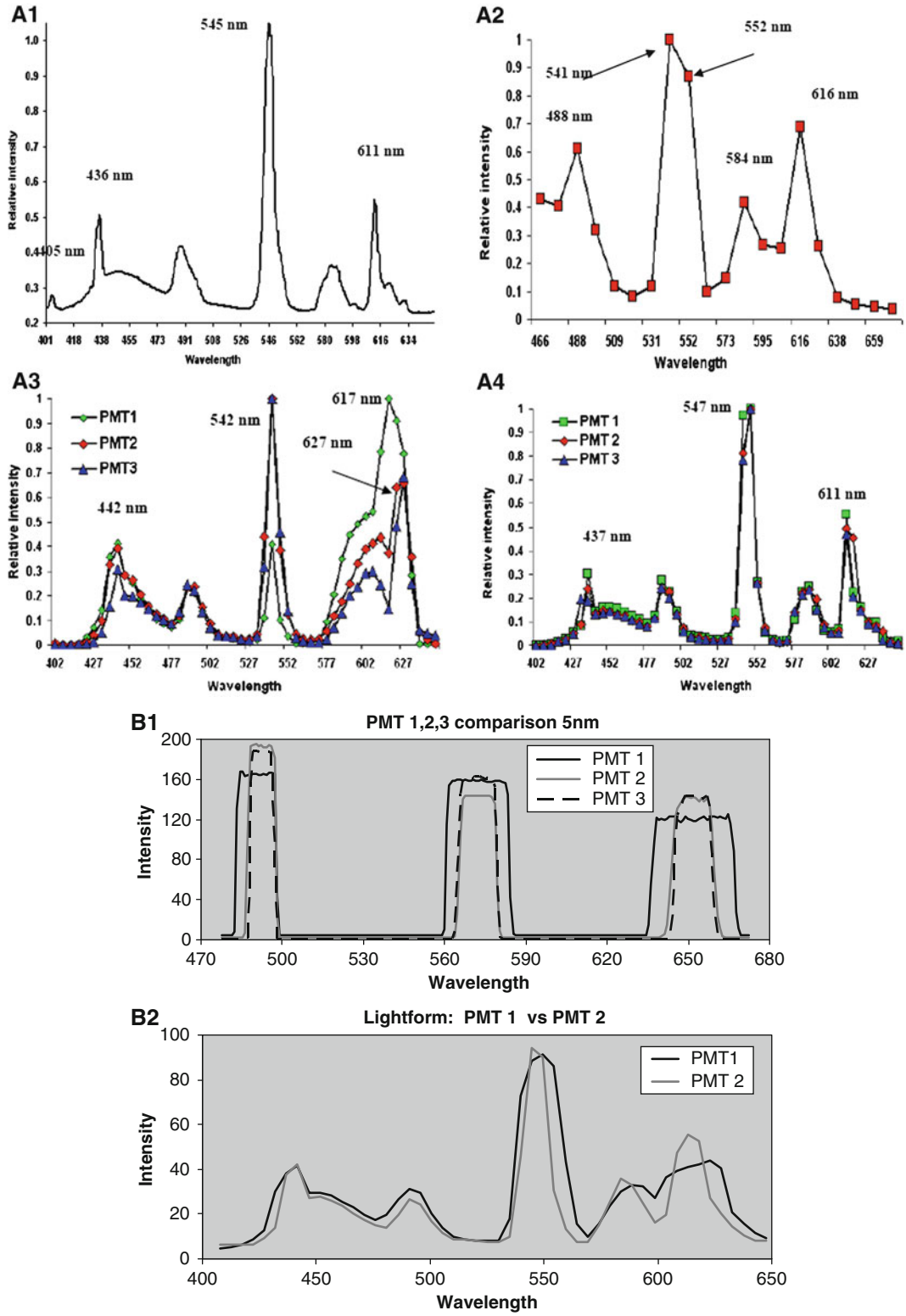

Fig. 9 Spectral scanning. The performance of an Olympus FV 1000 (**a**) Zeiss 510 and Leica AOBS confocal microscope was measured using their spectral scan functions and the light source (LightForm Inc, Hillsborough, NJ)

regions using MP 760 nm fluorescent beads and 647(633) excitation.

5. A similar test can be made on a Zeiss 510 Meta using a fixed bin range of 10.7 nm. To cover the range of 462–650 nm it is necessary to scan twice. If necessary, the pinhole can be opened to let in more light but this can widen the peaks and change the observable pattern.
6. A similar test has been made using a new Olympus FV 1000 using 2 nm separation on a demo machine.

3.10.1 Spectral Scanning: Mirror

In a similar manner to the axial resolution test, a mirror is put on the stage and the system is set up for reflection and XZ scanning using the 70/30 dichroic. Either a 20× dry or a 63× oil lens can be used. A lambda scan is made to observe the position of the laser lines (Fig. 9b) The pattern suggests the allowable bandpass region which cannot be used which is not reflected laser light. A system with narrow reflection laser lines suggest a properly functioning system while wider reflection lines suggest a system with internal reflections and one that may be miscalibrated. Such a system may not be properly functioning for accurate data acquisitions. The data shows that PMT 1 is unstable with broader distributions while PMT 2, 3 are identical with a narrower distribution. Usually we get the following values for reflected lines from a properly calibrated SP1 system. 5 nm (488), 8 nm (568), and 13 nm (647).

Fig. 9 (continued) that was positioned on the stage in place of the laser light (**A**). The minimal band pass obtainable was used for each microscope; 2 nm for the Olympus (A1), 5 nm for the Leica (A3) and 10.7 nm for the Zeiss (A3). The smaller band pass is responsible in part for the increased resolution observed with the Olympus microscope. Note the increased resolution of peaks and features in the Olympus curve. In the Leica AOBS system the PMT performance was measured across the 400–650 nm spectral ranges using the Leica spectral scan feature at two different time periods. In panel (A3) note that the three PMTs are yielding three different spectra while in panel (A4) the patterns are identical. The machine represented in panel (A3) was out of spectral alignment and it was corrected by a service technician shown in panel (A4). (**b**) spectral scanning. The performance of the Leica SP system was measured by scanning the three laser lines over a mirror in reflection mode using a 20× lens with 5 nm steps over a range of 200 nm using PMT 1, PMT 2, and PMT 3 (B1). The performance was compared with the LightForm lamp under the same conditions using 5 nm steps over a range between 400 and 650 nm. PMT 3 is not shown for clarity. At the time of analysis, continual prior use of PMT 1 in lambda scanning mode was believed to overheat the lambda scan control board which resulted in problems in the proper representation of spectra. PMT 2 and PMT 3 have narrower patterns than PMT 1. The lambda scan using the mirror showed that all three laser lines were letting in more light around the laser excitation lines, i.e., PMT 1 demonstrated 15 (488), 24(568), and 32 (647 nm) nm around the three laser lines while PMT 3 showed 9 (488), 14(568), and 16 (488) nm around the same laser excitation lines (B1). The smaller the number the more calibrated and accurate the system appears to be. A smaller number also allows one to detect emission closer to the laser line. More importantly it appears that when the reflected lines are greater there are extra reflections that are occurring within the system. The pattern of the MIDL lamp also showed a widening of the spectral peaks and a shift of the spectrum to higher wavelengths which correlated with the mirror data (B2)

Proper calibration of the system by a manufacturer's technician will decrease the width of the reflected laser light. The SP2 and AOBS have narrower reflected laser lines than the SP1 and this yield supposedly better performance. This data shows that confocal systems can become unstable yielding different data from the same system using different PMTs.

3.11 Coefficient of Variation Principle to Determine Sensitivity, PMT Function and System Comparisons

3.11.1 CV Principle for Sensitivity Tests, PMT Tests and System Comparisons

One of the major elements of a bad image in a confocal system is related to using the PMT at high voltage values. This can be the result of insufficient sample staining, a misaligned system, a failing hardware component or attenuation of light through a fiber optic. If the unit could be operated at lower PMT values then the image quality would be improved and the PMT noise decreased. The noise present in the system can be evaluated using a large 10-μm bead (Spherotech) or a fluorescent substrate slide (Delta or Chroma). If a clean fluorescent substrate slide is used it should be measured at a specific depth or at the surface so the intensity is reproducible. The coefficient of variation (CV) is defined as the standard deviation (σ) of the population of beads or pixels expressed as a proportion or percentage of the mean (μ).

1. The 10-μm bead consists of nearly uniform size and intensity (CV = 5 % by flow cytometry) is zoomed 4× to increase the number of pixels contained in the ROI with either a 100× objective (Plan Apo NA 1.4) or a 63× (water 1.2 NA or oil 1.32 NA) lens. The bead is located in the center of the field and the image of the bead is obtained at the center cross section of the bead which relates to its maximum diameter. This large bead suspended in an antifade solution permitted repeated measurements with minimal bleaching of the bead sample.
2. A fixed ROI was determined in the bead image that consisted of approximately half of the bead's area. This test can also be done with a fluorescent plastic slide (Chroma or Delta)
3. The mean and standard deviation of the pixel intensities in the ROI of the bead or Fluorescence slide were determined to yield the CV using either the manufactures software of Image J.
4. It is important to maintain the machine variables (pinhole size-Airy Disk, PMT voltage, averaging, etc.) at reproducible values for these studies. The laser power was set at a constant value that allowed the mean intensity level of the bead to be approximately 150 (out of 255) for each PMT setting.
5. Figure 10 illustrates the pixel distribution of a 10 μm bead that was measured with a PMT voltage setting of 400 and 600 and a zoom of 4× and an airy disk of 1. These two bead images were obtained in the following manner: the mean intensity value in the ROI within the bead was set at channel # 150 by adjusting the AOTF manipulation instead of actually lowering/raising the laser power. The higher PMT voltage yielded a broader

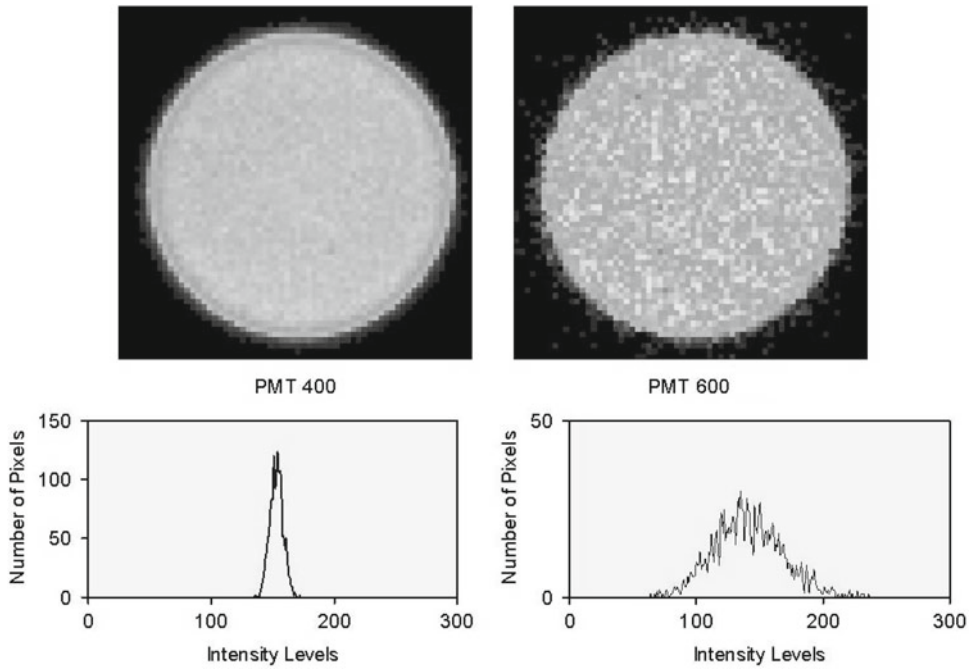

Fig. 10 Bead pixel variations. TIFF images of a 10-μm Spherotech bead were obtained with two different PMT settings (PMT = 400, PMT = 600) with a zoom of 4 and no frame averaging using a 100× Plan Apo lens (1.4 NA). A ROI was drawn in the interior of the bead and the histogram of the population of pixel intensities is displayed in the bottom panels. The mean pixel intensity in both images was approximately 150 intensity levels and was obtained by keeping the PMT at 400 or 600 and adjusting the laser power with the AOTF. The coefficient of variation (CV) is defined as the standard deviation (σ) of the fluorescent intensity of a population of beads or pixels expressed as a proportion or percentage of the mean (μ) intensity (CV = σ/μ). The noise at a specific setting can be reduced if frame averaging is increased. The averaging decreases the pixel variation, which lowers the SD and decreases the CV. Theoretically by averaging the image "*n*" times the CV and SD are decreased by the square root of "*n*"

histogram, which translated into more pixel intensity variations. Since the CV (σ)/(μ) is defined as the standard deviation (σ) divided by the mean (μ), one can compare the quality of images using this technique. As the quality (less bead noise) of the images increases, the CV of the population of pixel intensities within the bead decreases. To compare image quality between different confocal microscopes, it is critical that as many variables as possible be kept constant [1, 2, 5, 6].

3.11.2 PMT Function

The PMT is the detecting system and there exists different quality PMT of the same type in a confocal system. This CV bead test method can be used to access the operation and quality of the PMTs in the confocal system. The use of the Leica SP system easily allowed for switching of PMTs and pairing them with different excitation wavelengths. In effect, any PMT could be used in conjunction with any of the four-excitation wavelengths. Although the PMT position will affect the CV, it is not considered to be a major factor in image

quality. All the PMTs were considered equivalent in setting up the machine. PMT 1 and PMT 3 contain an additional mirror in their light path that measures the light reflected from slider 2 while PMT 2 collects the light directly after it leaves the prism and goes through a focusing lens.

1. The system was set up with a triple dichroic (TD) using 488, 568, and 647 nm wavelength excitation.
2. The three PMTs were adjusted to allow the mean pixel intensities to be at approximately channel 150.
3. The relative intensities were measured with the three PMTs using software for all experimental conditions (Table 3). Lower CVs will translate into better image quality and will require less frame averaging to produce the equivalent image quality. This is a test that is useful to determine system quality and identify a possible problem in PMT performance prior to a hard failure. The test can be done with dichroics and barrier filters to assess the efficiency of each filter in the light path. It is important to define the band pass region that is being evaluated, as dichroics will eliminate specific regions in the transmission. It is possible to use this approach to evaluate the PMTs on systems (Biorad, Zeiss, Olympus, and Nikon) that contain dichroics and band-pass filters system.

3.11.3 Biological Samples

Biological samples are often used as a reference to subjectively compare system performance. This is a valuable subjective technique if one knows how to interpret the image. The CV technique developed on beads was applied to biological specimens (MP Fluo cells, chicken cells stained with AO to observe if the same relationship between PMT voltage and averaging described on beads are maintained on biological cells. Fluo cells (F-14780, Molecular Probes) were excited with a 568 nm laser line and detected with a 580–630 band pass filter in PMT 2.

1. The difference in image quality illustrated by averaging 1, 4, or 32 times at two different PMT settings (552 or 799) is shown in Fig. 11. The images B–F are zoomed 4× using Image Pro Plus to clearly illustrate the individual pixels. The CVs of a selected ROI in the nucleus varied with the number of frames averaged and the PMT voltage. The best image quality (low CV) consisted of either low PMT voltages (B, C) with minimal amounts of frame averaging or high PMT voltages that were frame averaged 32 times. (F). High PMT settings (D, E) with minimal amounts of frame averaging (1 or 4) demonstrated high CVs and poor image quality. In all cases, the increase in averaging resulted in a decrease in the CV and a corresponding increase in image quality. In contrast, raising the PMT voltages increased the CV and decreased image quality.

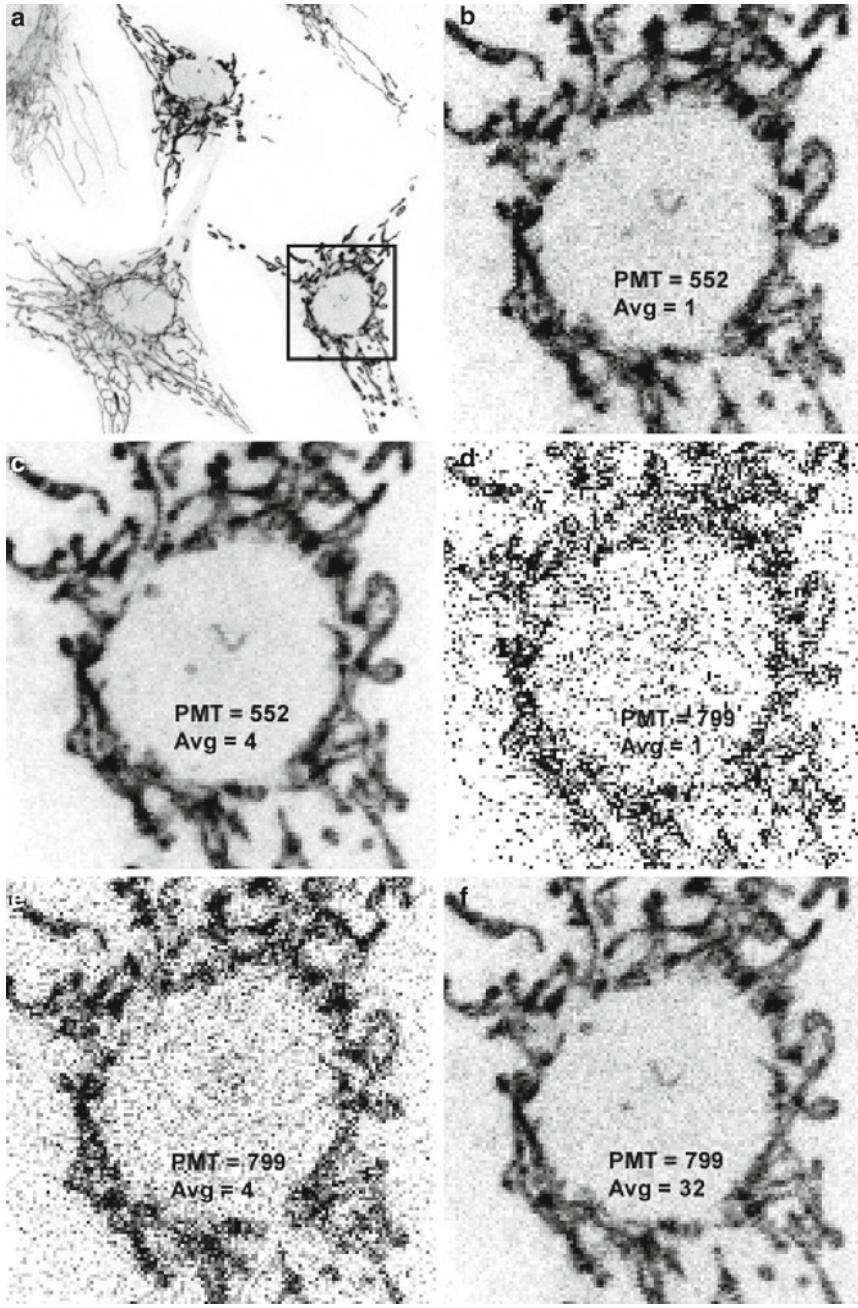

Fig. 11 PMT and averaging of cells. Fluo cells (F-14780, Molecular Probes) were excited with a 568-laser line and detected with a 580–630 band pass in PMT 2. Averaging 1 measured the resolution, 4 or 32 times at two PMT settings (552 or 799). Figure 11a shows the distribution of three cells at normal magnification while Figs. 11b–f shows one cell located in the *box* in Fig. 11a that was zoomed 4× with Image Pro Plus. The settings in the different panels were the following: (**a**) control (PMT = 552, AV = 1); (**b**) (PMT552, AV = 1), (**c**) (PMT = 552, AV = 4), (**d**) (PMT = 799 AV = 1), (**e**) (PMT = 799, AV = 4), and (**f**) (PMT = 799, AV = 32). Note the difference pixel variations in the six panels of the same cell acquired at different PMT/Averaging settings. The CVs of an ROI in the nucleus of the various panels were the following: (**b**)–49 %, (**c**)–40 %, (**d**)–212 %, (**e**)–109 %, and (**f**)–49 %. This figure of a biological cell demonstrates a similar relationship between PMT values and averaging as shown in Fig. 10 for beads

2. The higher PMT settings necessitated the use of greater frame averaging to increase image quality.
3. Comparison of biological samples between machines or over time can be made if the laser power is first measured and recorded and then the image is obtained at fixed settings. This is a subjective test that is influenced by many factors.

3.11.4 Confocal Sensitivity

The sensitivity of a confocal microscope is an important parameter to determine as its value influences the acquisition settings of the PMT voltage, laser power, and frame averaging that are used to acquire images. The values derived will relate to alignment, equipment functionality, and general performance of the CLSM. This test can be made with a 10 μm bead, a fluorescent slide, a fixed green diode light source, or other objects emitting a constant light source.

1. The test particle described was a 10-μm Spherotech bead but a similar test can be made with other objects described above. The measurements were made using a 100× Plan Apo objective (1.4 NA) with a zoom factor of 4 with 488 nm excitation in two different confocal microscopes with unique configurations: a Leica TCS-SP1 containing one argon–krypton laser emitting three laser lines and a Zeiss 510 system that contains three individual lasers with a merge module (Table 4). Chroma slides can also be used in place of the 10 μm bead.
2. The laser power in both systems was measured on the stage using a 10× (0.3 NA) objective and a power meter detector secured on the stage. It is essential that the acquisitions parameters be as equivalent as possible when trying to compare machines from the same or different manufacture. Since there are considerable differences between the designs of different machines, extreme care must be made when interpreting the results of data obtained from different manufacturer's machines.
3. The variables that must be considered included specific wavelength, laser type, objective lens, optical components, pinhole size, scan speed, zoom, and pixel size. Other variables not mentioned may also affect the measurement.
4. It should be emphasized again that it is extremely difficult to compare different manufacturers machines due to the number of variables that must be kept constant and conclusions drawn from this head to head test can only be made if all the variables are nearly equivalent.
5. To illustrate the test, we used a Leica machine that has one noisy Omnichrome argon krypton laser emitting three laser lines and a new Zeiss 510 CLSM containing three relatively quite lasers. It would be expected that by using different lasers, the tests would reveal different sensitivity values (Table 4). The sensitivity of two machines was made by maintaining the

laser power at a constant value of 1 mW for 488 wavelengths and 0.2 mW for 568/543 wavelengths. The data from this test revealed that 1 mW of 488 power measured on the scan head yielded a CV value of 4 % with a Leica TCS-SP1 and a CV value of 1.3 % with a Zeiss 510. Comparable power readings on both systems showed the CV to be almost three times lower with the 488 and 568 lines with the Zeiss 510 system as with the Leica TCS-SP system containing an Omnichrome argon–krypton laser. The significance of a higher CV value means that the samples will have to be frame averaged to increase the image quality. These CV values will change if the laser power and PMT values are changed. The quality of lasers will also affect the CV values as shown by the data in this test. Increasing the laser power to a maximum value resulted in the CV being lowered with both the Zeiss 510 and Leica TCS-SP1 systems. However it is not recommended to operate some lasers at maximum power due to sample bleaching considerations and laser lifetime considerations.

6. This CV sensitivity data may be considered an initial reference point that can be used by other investigators to compare their CLSM performance with similar machines. It seems to be possible with this approach that the sensitivity of systems in different laboratories can be compared. Due to the number of variables that must be kept constant, extreme care must be made when interpreting this test in the comparison of different manufactures machines. However there is no reason why similar machines from the same manufacture cannot be compared if they are run under nearly identical conditions.
7. A similar approach could be used with a laser diode (Luxor) emitting a fixed power output. This light is simply positioned on the stage and the PMT adjusted for maximum intensity. Similar machines can be compared in this fashion.

4 Notes

Image quality is an important parameter in the evaluation of a confocal microscope performance. Unfortunately, image quality is too often used as the "gold standard" to evaluate confocal microscope functionality and performance. Variables that affect image quality should be assessed to insure the system is delivering its optimum performance. In the cases in which intensity measurements are required, it is essential that the machine be stable to deliver reproducible data. A series of tests were either adapted from the literature or devised in our laboratory to measure the system performance of the confocal microscope [1–14]. These tests include the following: laser power measured at the stage, field illumination, laser stability,

dichroic performance, PMT performance, system linearity, axial resolution, spectral registration, sensitivity, and lens quality. This list is not inclusive but represents what can be tested and interpreted to insure the machine is operating properly. Hopefully other tests will be added to this list in the future.

4.1 Field Illumination

1. Field illumination is one of the easiest and most important tests to make on a confocal microscope. Many CLSM units in the field that have been checked for field illumination using a plastic fluorescent slide (Applied Precision (API) or Chroma) have demonstrated unacceptable field illumination patterns.
2. The plastic slides (Applied Precision or Chroma) were found to be the most consistent sample to test field illumination. From Applied Precision, we use the blue slide for UV excitation and the orange slide for 488 and 568 nm excitation. The API red slide was found to bleach rapidly with 568 excitation and therefore it is preferable to use the orange slide for this wavelength. The Chroma red slide was chosen for the UV, 488, or 543/568 excitation. The green slide can also be used for 488 excitation.
3. Field illumination should be relatively uniform with the maximum intensity being in the center of the objective and decreasing less than 25 % across the field according to one manufacturer. The light should come into the center of the objective and it should decrease in all directions in a similar manner. Although this is logical there is no specification on this parameter.
4. One should not assume that field illumination is proper on confocal systems without testing it. Most confocal alignment procedures are made using high magnification objectives (i.e., 40×). In the author's experience, this does not always translate into good performance with all the objectives on the microscope. Characteristics of the objective, including its magnification may affect its field illumination. All objectives must be tested to insure proper field illumination.
5. This test should be made with all objectives and all wavelengths of visible and UV light to insure the machine is delivering proper field illumination.
6. Initially, the surface of the slide is determined as it is the region that emits the most intense fluorescence in the "Z" axial direction.
7. It is important to measure the field illumination at a specific depth in the plastic slide, as the intensity distribution may change from the surface to the interior of the slide. Investigators should also be careful not to observe illumination fields deep within the plastic slide samples as it will usually yield a better field illumination than regions closer to the surface due to

various optical distortion factors [12]. It is also important that the plastic slide be placed on a firm surface to eliminate any possibility of substrate flex.

8. Although it has been proposed to use this fluorescent slide to take daily measurements for system stability, the factor of reproducible depth in addition to instability of laser power makes this application questionable and we have not been successful in developing this test. Power fluctuations appear to make this not a suitable test.
9. The illumination intensity across the observation field can be measured with different types of test specimens in order to insure that homogeneous field illumination exists. The following test substrates have been used: concentrated fluorescent dye suspended in a hanging drop well slide, small concentrated fluorescent beads (1–3 μm) or large concentrated fluorescent beads (10 μm) (Spherotech), fluorescent specimens, uranyl glass slides, Altuglas, or plastic fluorescent slides (Applied Precision, Chroma), a piece of tissue paper stained with fluorescent dye or fluorescent dye solution [Fluorescein (F-7505) or Rhodamine B (R-6626) Sigma St Louis, MO)] and mixed with immersion oil (Leica Immersion oil, $n = 1.518$) [1, 2, 5, 6]. A histological sample derived from plant or animal has been used by investigators and service field engineers [1, 5, 11].
10. Some criticisms of these tests are as follows. Uranyl glass has previously been used to check field illumination, but it is currently difficult to obtain and we have observed that plastic slides have higher fluorescent efficiency than the uranyl glass at all wavelengths. A field of small or large beads on a slide (Spherotech) can be used but it is essential that all of these beads are located at the same plane or the image will be inaccurate. In order to eliminate this potential error, a stack of images can be obtained from the beads followed by a maximum projection of the stack to obtain an image of bead that represents field intensity. However, the downside of this method is that it is very time consuming. Solutions of fluorescence fluid are instable and shift with time and temperature and bleaching. Histological sample derived from plant or animal can also be used to measure field illumination and these are usually the choice of service field engineers. Although the histological samples will show the illumination pattern indicating proper or uneven illumination, in our experience histological samples are not sensitive enough to properly measure field illumination. It usually will yield a sense of false security for the investigator. Fluorescence plastic is a superior test substrate. If there is a discrepancy between the plastic substrate test slide and other test slides in measuring field illumination it may be due to a greater sensitivity in the plastic substrate.

11. In our system, the three visible wavelengths of light are derived from one Omnichrome argon–krypton laser that allows us to test the field of illumination at one wavelength (488 nm) and assume it is equivalent to testing field illumination with the other wavelengths. Since the UV line is derived from a different laser (Enterprise, Coherent), it is essential to check all objectives for proper field illumination at the 365 nm excitation in addition to the visible 488 nm excitation.
12. Newer designed confocal systems use three individual lasers with merge modules, requiring that all laser wavelengths have correctly aligned beams emitted from the merge modules. In these systems, each of the three lines has to be individually tested. One laser line may be perfectly aligned yielding acceptable field illumination while the other laser lines may be misaligned yielding intensity values in which the brightest region is not in the center of the field as illustrated in Fig. 1 with UV illumination.

4.2 Objectives

1. The lenses are the engines that drive this technology and their selection is very critical for optimum performance. Some of the factors to consider are the following: high NA relative to the specific magnification, flat field objectives, long working distance (WD) relative to NA, good fluorescence transmission, and good achromatic correction at desired wavelengths [1, 5, 8, 16, 17].
2. Currently microscope manufactures make lenses that go though extra tight QA procedures and have been classified as confocal objectives. These should be bought, as they are believed to be of a higher quality than ordinary microscope objectives.
3. As a general rule one should use the smallest magnification and the largest NA lens to acquire images [17]. These lenses offer a larger field of view and better light transmission.
4. The choice of a good fluorescent transmission lens is sometimes chosen over Plan Apo and spectral precision.
5. If a fluorescence bull's eye pattern exists it is necessary to increase zoom to even out the fields. Increasing zoom also increases the magnification and bleaching rate of the sample.
6. Although it is critical to reject out of focus light for confocality, it is also necessary to have sufficient laser light entering the system and lenses should be chosen that have good fluorescent transmission characteristics. Opening the pinhole can increase transmission but this should be done only if insufficient light is present as this parameter decreases the confocality of the system in both the lateral and axial directions.
7. In order to eliminate field illumination problems the system should be aligned correctly with the brightest light being focused into the center of the field and decreasing less that 25 % in all directions equally from the center with most lenses.

4.2.1 Dirty Objecties

Not all problems with the field illumination test are the result of bad alignment, lens design/quality or incompatibility of a lens with specific wavelengths of light.

1. A dirty lens will yield bad field illumination, bad resolution and bad axial resolution. If a lens is dirty or covered with dried oil then it would yield a non-uniform field illumination pattern [1, 5]. In one example the intensity of the field from a 20× (NA 0.6) dirty lens varied by as much as 70 % with the maximum intensity being off center on the right side of the image. After cleaning the lens to remove oil and other particles, an acceptable illumination pattern was obtained with the maximum intensity being located in the center of the image and decreasing in intensity by less than 10 % from the center maximum [1, 5].
2. A dirty lens will also affect the axial resolution of the system as shown by the non symmetrical pattern observed with axial resolution mirror test. A dirty lens may increase the spherical aberrations. It is strongly recommended that lens be checked for cleanliness prior to experimentation, especially in a core confocal facility.

4.3 System Evaluation by Power Meter Measurements

4.3.1 Visible Power Meter Measurements

Knowing specifications of laser power output on a stage is a critical parameter to assess system performance. This power test appears to be one of the most useful tests because it quickly evaluates both the system alignment and performance. For the adequate operation of a CLSM, a sufficient laser power must excite the specimen. If a system is misaligned or functioning sub optimally it can be assessed measuring the laser power. The power test can indicate if the system is aligned properly up to the plane of excitation on the stage or if the machine has a defective component (i.e., a dying laser, or a defective fiber). It should be emphasized that this test is performed at the microscope stage prior to the light reflecting the dichroics for a second time and penetrating through the emission pinhole and the emission barrier filters or prisms (if they exists in the system) and into the PMT. In our experience, without sufficient power throughput in the system, the voltages will have to be increased to high values to visualize fluorescence derived from specimens, which will introduce PMT noise. In addition the cause of the decreased laser power may result in other problems, i.e., laser instability, loss of axial resolution, increased laser noise, and increased PMT noise.

The laser power measurements are listed in Table 1 and are useful to illustrate the maximum power that can be obtained from a CLSM having these different laser configurations. These measurements serve as a valuable reference for an individual lab to QA their system over time and as a comparison with other similar CLSM for adequate performance. In a three-laser system, it appears

Table 1
Comparison of relative power on microscope stage

Maximum power comparison (mW)			
	Leica SP1	Leica SP2	Zeiss 510
Laser	Ar–Krypton	(3-laser)	(3-laser)
488 nm	1.1	4.5	3.13
543–568 nm	1.45	0.22	0.26
633–647 nm	1.6	2.8	1.21

The maximum power was measured in milliwatt with a LN 36 detector and a Coherent Lasermate power meter adjusted to the specific excitation wavelengths. The power was measured on the stage of a Zeiss 510, a Leica SP2, and a Leica SP1 system. This test can be used to determine if the system has acceptable laser power by measuring the power on the microscope stage

there are sufficient power with the 633 and 488 lasers, but since the maximum power of the 543 laser is so low and the attenuation of the 543 laser is so great, at least 0.2 mW of power are necessary from the 1.2 mW HeNe 543 laser so there is sufficient light to excite the samples. If the system is not aligned properly, the laser output will be decreased. With insufficient power, the PMTs will need to be operated at high voltage settings, which increases the system noise and produces unacceptable images. Less power throughput in the confocal system suggests a problematic laser, a fiber polarization problem, or just a badly aligned system. The maximum laser power is dependent on the laser, optical configuration, and the specific objective used. Using a 10× objective (NA = 0.3) it is desirable to have at least 1 mW of power on the microscope stage for each laser line derived from a 75 mW Omnichrome 643 argon–krypton laser. Other confocal systems with different laser configurations will naturally have different power values as indicated in Table 1.

It is important to measure the power output to evaluate system performance for all three lines after installation to make sure the system is aligned properly and the laser functioning correctly. These power values will not only serve as a reference to ensure the system is performing properly but can be useful to notify the confocal manufacturer of deviations from acceptable values that will mean either laser failure or misalignment. A new Omnichrome 75 mW argon–krypton mixed gas laser delivered the following power outputs: 488 nm, 1.1 mW; 568 nm, 2.68 mW; 647 nm, 1.60 mW. After time and proper laser alignment, almost 3 mW for each line have been achieved in this system. However on another day the maximum power with a Leica TCS-SP1 system using a Plan 10× Fluor (NA 0.3) was the following: 488 (1.1 mW), 568 (1.45 mW), and 647 (1.65 mW). Similarly the maximum

power measured on installation with a Leica SP2 system using a Plan 10× Fluor (NA 0.3) was the following: 4.6 mW (TD, 488 nm), 6.5 mW (DD, 514 nm), 0.22 mW (TD 543 nm), and 2.8 mW (TD 633 nm). The values on the same machine taken a few months later were the following: 2.87 mW (TD, 488 nm), 3.9 mW (DD, 514 nm), 0.093 mW (TD 543 nm), and 1.45 mW (TD 633 nm). The reason for the fluctuations is unknown but it appears they may be attributed to fiber polarization problems.

4.3.2 UV Power Test

One of the major problems that occur with UV confocal systems is that there is an insufficient UV power output. The UV power transmission can be decreased from a number of factors, which include: misalignment, aging fiber optic, polarization mismatch between fiber and laser, unfocused collimator lens and dying laser. This measurement of UV power helps access the system performance and determines if adequate UV power is being transmitted through the system and if the fiber is in a good condition. Although it is recommended to take the measurements at the back objective aperture region to eliminate the characteristics of the lens from influencing the test, we were not able to mount our detector probes on the objective or the stage.

1. An objective designed with good UV transmission characteristics should be used to increase the power throughput. Attenuation of the laser light through the low power optics of the system will still occur and the power values obtained are relative values that are highly dependent on the specific type of objectives used. Since our laser power detector does not work with higher power optics (40, 63, 100×) due to optical limitations of the stage, it is useful to use a histological test slide sample, fluorescence slides or bead sample to assess relative UV power with these higher power lenses. For instance by using maximum UV laser power, it was found that the 10 μm Spherotech bead saturates PMT 1 (low noise PMT) at a setting of 650 using a 100× Plan Apo lens (NA 1.4).
2. Leica technicians routinely use a 40× lens to measure the fluorescence saturation of a histological plant sample. If it saturates in the PMT range between 600 and 700 units in PMT 1 the system is passed as having adequate power. In our opinion, this test is very crude and subjective due to the acceptability of such a large range of PMT amplification values, the variations in staining between different plant samples, variations in PMT characteristics and the logarithmic relationship between PMT and intensity [1, 5]. It does however; yield a rough estimate to determine if there is sufficient laser power in the CLSM. It would be useful to measure these values on a user histological test slide or bead when the machine is first installed and deemed working acceptably by the manufacturer's service and sales representative.

4.4 Laser Adjustments

Argon, UV, and argon–krypton lasers need to be aligned and adjusted on a regular basis as they occasionally go out of alignment. The investigator can easily measure laser power over time using a power meter positioning on the stage (Table 1). The investigator usually will not notice a problem with laser power or alignment, but will continually have to increase the laser power to compensate for the reduced system laser power. This use of increased laser power will not only shorten the life of the laser but will not correct the CLSM system problems that are indicated by reduced power. Failing lasers or bad optical alignments will result in the reduction of laser power necessitating an increase in PMT voltages to compensate for lack of laser light intensity. If minor adjustments are made to the mirrors with the horizontal and vertical knobs located on the back of these lasers, the laser power can be increased. If done, remember to turn only one knob at a time in the adjustment or you may lose the laser line. These visible lasers are usually enclosed in a box with the rear knobs being inaccessible for adjustment by the investigator. In fact, most confocal manufactures do not allow the user to adjust these controls, as it is the responsibility of the manufacturer on a service contract to insure that the lasers and system are functioning properly.

4.5 Axial (Z) Resolution: Mirror

The axial resolution test is considered the "gold standard" of resolution in confocal microscopy [1, 4–6]. The axial resolution test using a 100× Plan APO (1.4 NA) objective has yielded a value less that 350 nm on a Leica SP1 system. It should be emphasized that this is the only performance specification in 2004 that a company has said it will guaranteed on a confocal microscope. Normally in a functioning system, values between 280 and 350 nm with a 100× (1.4 NA lens) were obtained. A 63× Plan Apo (1.32 NA) lens should meet the specification of below 350 nm, although Leica does not currently guarantee this value on a TCS-SP system. We have achieved values between 295 and 315 nm with a clean lens on a Leica SP1 system. It is also important that the pattern of the axial resolution be symmetrical with suitable diffraction regions (peaks and valleys) to the left of the major peak (Fig. 3a). The cleanliness (Fig. 3b) of the lens and the numerical aperture of the lens (Fig. 3c) will be indicated by this test. The values and patterns obtained will relate to the quality of the biological image and that is why it is called the "gold standard."

4.6 Square Pixels and Galvanometer Check

Measurements of objects will be inaccurate if the XY scanning does not yield a perfect square. This value should stay constant, but it must be checked and adjusted especially if a galvanometer is replaced. The phase adjustment in bi-directional scanning can also be checked and adjusted by this test. A lack of adequate phase alignment will result in a decrease in resolution by mismatching the scans in the left direction from those in the right (opposite) direction. In cases that require the highest resolution image, unidirectional scanning

should be made knowing that it will take twice as long to acquire the image. This test for the galvanometer reliability is a key test to insure the system is functioning for maximum image resolution. Images will be less sharp if this component is working incorrectly.

4.7 Spectral Registration (UV and Visible)

The 1 μm multiple wavelength fluorescent beads (Tetraspec, T7284 Molecular Probes, or Rainbow beads, Spherotech) were used to monitor the UV and visible colocalization.

1. The registration of bead fluorescence images between the 365 UV wavelengths and the 568 visible wavelengths in an aligned system was almost super imposable (Fig. 4a) while in a misaligned system (Fig. 4b) the difference between the peaks was 650 nm (acceptable difference is only 210 nm). The 568 nm line was chosen instead of the 488 nm line to minimize the crossover fluorescence between the visible and UV wavelengths. If the wavelengths are not aligned then co localization and FRET studies cannot be effectively made on the machine.
2. It appears for an unknown reason that if there is proper spectral registration between UV and visible wavelengths, then the UV field illumination may not be uniform and vice versa. Both field illumination and spectral registration parameters must be checked.
3. In addition, the confocal machines have separate collimator lenses that are used to align the UV light for different magnification lenses. It appears to be very difficult to get all the objectives to show proper spectral registration between UV and visible wavelengths.
4. The spectral registration of the 365, 488, 568, and 647 nm lines can be made with either a small (0.5 or 1.0 μm multicolored bead), or a front surface, single reflective mirror (Fig. 5). The spectral registration with the mirror on a Leica system is a superior test to the bead as the laser light can be measured sequentially or simultaneously to eliminate any cross talk between adjacent emission wavelengths. In addition, no bleaching occurs at high zoom magnifications with the mirror.
5. This mirror test is more accurate than the bead tests, but the data obtained skews the results slightly towards better values as in normal operating conditions. The emission from either specimens or beads are normally recorded at least 10–40 nm above the excitation wavelengths and not at the excitation wavelength. Many lenses have difficulty in colocalizing far-red fluorescence with the blue and green fluorescence so measuring the emission at 647 ± 10 nm will yield better resolution than measuring the emission at 660–700 nm.
6. With new confocal systems that contain three individual visible lasers, the spectral registration test is measuring both the lens spectral registration and the laser spectral registration. It would be useful to measure a few different objectives to determine if

the spectral registration of the lasers is correct or a pattern of misalignment occurs. It is highly unlikely that different lenses will show the same spectral mismatch and thus the pattern observed should indicate if there are potential problems with either the lasers or with the objectives.

7. Molecular Probes produces a series of different sized beads (Focal Check 1, 6, 15 μm) with different fluorescent rings and core bodies to assess colocalization from multiple lasers. This data should reveal if the laser lines are aligned correctly. The smaller bead should be more sensitive but slightly harder to use.

4.8 Laser Power Stability

4.8.1 Visible Laser Power Stability

1. Laser stability measurements should be made on the CLSM for the investigator to have confidence that the CLSM is not introducing artifacts in experiments requiring intensity measurements or time dependent physiological experiments. In our system there was periodic noise in the laser power tested by the transmitted light detectors that exceeds the manufacturers specifications (Ominichrome) of laser stability fluctuations of less that 0.5 % over a 2-h time period. The 488 and 568 lines have a periodic cycle that is directly opposite the 647 line (Fig. 6). Argon lasers and helium neon lasers (543 or 633) are considerably quieter than the argon krypton laser and are preferable. However it is believed that the noise is being derived from the system and not the laser.

   Power stability in a CLSM can be influenced by many factors, which include the lasers, PMTs, electronics, electronic component failure, fiber optics transmission, fiber optical polarizations incompatibility, AOTF thermal regulation, thermal heat dissipation, laser polarization mismatch, optical components, and galvanometers. One of the most likely causes are laser polarization, which may be mismatched with the polarization of the fiber. The data obtained from this power stability test alerts the investigator to possible errors that may exist in the acquisition of intensity measurements in biological and physiological experiments [1, 5, 6, 14]. Similar lasers used in flow cytometry or confocal microscopy equipment should be stable with low peak-to-peak noise and minimal power fluctuations over hours. However the same lasers in confocal systems generate lager fluctuations over time. The reason for such high variations in CLSM systems is unknown.

2. In a confocal microscope, there are different ways to measure power stability over time (hours). These include the following: (1) manufacturers installed pin diodes, (2) laser meters on the microscope stage connected to a readout device, (3) fluorescent emission intensity from a plastic slide detected by a PMT, and (4) transmission optical system detection. The pin diode test was not stable and should only be used as a subjective assessment of power. In our experience, the most reliable

method to measure the laser power stability consisted of using the transmission optics of the CLSM without a fluorescence slide in the optical path.

3. If transmission optics is not present, a fluorescent colored slide can be used, but extreme care must be made to reduce the laser power with an AOTF to reduce possible interaction of the laser beam on the sample. Sometimes the output fluorescence intensity may increase due to repetitive additive excitation or decrease due to bleaching.
4. In summary, many components in a confocal system can introduce power fluctuations. Fluctuations over an hour will affect intensity measurements. However, short term line fluctuations (Fig. 8) in an individual scan must be averaged to increase image quality. Naturally, the more fluctuations that exists the more averaging that will be necessary to achieve adequate image quality (Figs. 10 and 11). Averaging will reduce the CV and system noise and improve image quality. Averaging may also bleach the sample.

4.8.2 Laser Power Stability (UV)

In contrast to the Melles Girot Argon–Krypton laser (3–5 % peak-to-peak noise), the Coherent Enterprise laser delivers less than 1 % peak-to-peak noise and is considered as a very quiet and stable laser. The argon air-cooled lasers, HeNe lasers, and Spectrophysics argon–krypton laser are all rated at less than 1 % peak-to-peak noise. However, even with the Coherent UV Enterprise laser or a HeNe laser (543 nm), periodic noise and large power fluctuations were observed.

1. One source of power stability appears to be connected to the way the laser is cooled and how the laser heat that is generated is dissipated. This was illustrated with our Coherent Enterprise UV laser that was connected to a Coherent LP 20 water–water exchange cooler. This cooler should be set at least 10 °C above the circulating cooling water of the building and it should be set above the ambient temperature of the room. Improper set points for the LP 20 cooler resulted in temperature regulation problems of the circulating cooling water in the laser which in turn resulted in the improper regulation of the laser power (Fig. 7b). In addition, problems with proper fiber alignment also appeared to occur with the UV system resulting in power fluctuations (Fig. 7c). The elimination of these temperature and polarization issues resulted in proper laser cooling and laser stability (Fig. 9a, <3 % noise). The water exchanger appear to have better thermal regulation than the nosier air–air (LP5) exchanges but as illustrated in Fig. 9, the water exchanger adjustments must be set properly or power instability can occur.
2. In summary, the laser power instability may be attributed to the following possible factors: power supply, AOTF thermal

regulation, improper thermal heat dissipation, and electronic component failure or fiber optical polarizations incompatibility. The definitive source of laser power fluctuations has not been identified at this time.

4.8.3 Laser Configurations (Fiber Optic Polarization)

The new systems from Leica, Zeiss, Nikon, Olympus, and Biorad all have merge modules and individual lasers. The merge module design allows for the incorporation of multiple lasers in a confocal microscope. One major problem with the design of the current version of confocal microscopes that use merge modules is that the laser lines are directed into the scan head with fiber optics. This is in contrast to the older versions of confocal which used direct coupling with only dichroics to deliver the light to the microscope's scan head. The use of the fiber optics makes it critical to align the polarization in the fiber optic with that of the laser's polarization value [1]. Failure to do this may result in laser power instability in the CLSM system. The fiber optics also deteriorates with time, which will attenuate the laser power and necessitate running the machine with higher laser power or higher PMT settings and may influence the fiber optic polarization.

1. One test procedure to insure that polarization is correct after the alignment procedures is to wiggle the fiber optic and see if the image returns to the same intensity suggesting the polarization is correct. This is a fairly crude test but it will demonstrate whether the system needs further alignment. Confocal microscope manufacturers are supposedly devising more reliable tests to check for polarization and insure laser power stability exists in the CLSM.

4.8.4 Heat Dissipation

The dissipation of heat is a very important variable to consider in measuring laser stability. Improper heat dissipation with the air-cooled lasers will result in laser power fluctuations. In our case we have observed fluctuations with an argon–krypton air-cooled laser that (1) had a restrictor in the exhaust line and (2) used a smaller exhaust duct (4″ instead of 5″) to remove heat. In both cases the heat was not dissipated correctly and the laser power in the CLSM fluctuated above 20 %. Removal of these problems reduced the laser stability to fewer than 5 %.

1. All lasers have to dissipate heat properly and their thermo regulators must be set correctly or the power to the lasers will fluctuate as illustrated using the Coherent Enterprise laser in Fig. 7.
2. Try to attach an inexpensive indoor–outdoor thermometer in the exhaust system to determine laser exhaust temperature and room temperature.
3. Electronic bards may generate heat making the system unstable. This effect should be monitored.

4.8.5 AOTF

The AOTF may also be introducing power fluctuations in the CLSM system by improper thermal regulation. The AOTF is a birefringence crystal capable of rapid and precise wavelength selection. Earlier CLSM systems used dichroics, barrier filters, and neutral density filters to regulate the proper intensity of laser light that illuminates the samples and did not use the AOTF. However the AOTF is enormously useful in operating a confocal microscope as wavelength selection can be very easily and accurately controlled. It is also used to control the power that illuminates a sample, which effectively acts to reduce the cross talk between detectors. The original AOTF that was installed in older CLSM models were not temperature regulated and may have introduced some power instability in confocal microscope systems. The AOTF is designed to select wavelengths of light and there maybe some function in power intensity as the light leaves this part. Most lasers have long term stability under 1 % but after leaving the AOTF the light seems to have long term variation in excess of 10 %. This problem is very disturbing to investigators expecting to make comparative intensity measurements on biological samples. It is hard to set up the upper and lower limits when the power is fluctuating and the sample exposure is long.

4.9 Reference Standards

In flow cytometry, alignment beads, linearity beads, and chicken red blood cells (CRBC) are used to ensure that the machine is functioning properly [18–21]. It would be useful if a suitable bead or fluorescence slide test sample were used for a similar assessment on the CLSM. Fluorescent colored plastic slides can be used as a reference standard, however, the issue of the depth that the measurement is taken and possible surface irregularities will both affect the measurements. If these two variables are controlled the plastic slide can be effectively used as a reference standard. Beads and a histological slide can also be used using the PMT as a crude power meter. For unknown reasons it does not seem possible to use a fluorescence slide or beads as a reference standard to measure the daily system functionality of a confocal microscope.

4.9.1 Standard Bead and Fluorescent Plastic Slide Tests

4.9.2 Biological Test Slides

A biological sample is a very subjective method of addressing total system performance. It is important to have a reliable sample that can be used to test the machine performance and image quality. The most useful histological test slide in our laboratory was a FluoCells slide (Molecular Probes, F-14780) stained with three fluorchromes. This slide allows for proper evaluation of resolution, cross talk between detector channels and observation of the emission from multiple excitation wavelengths (UV, 488 and 568). The resolution of biological structures of mitochondria (Mitotracker red), nucleus (DAPI), and tubules (Alexa 488) can be assessed with the slide. The pollen or diatom slides (Carolina Biological) has also been used to demonstrate fine

structure at various magnifications with different excitation wavelengths. Leica service engineers use a fluorescent plant tissue that can be excited using all the wavelengths. The histological plant test sample has been used for a combination of power output, field illumination, resolution, and overall assessment of the machine. Most sales and service personnel use their favorite histological slide as their gold standard to determine if the system is functioning properly. Although a trained confocal person can evaluate many parameters on a confocal microscope with a histological slide, these observations are subjective and the machine performance should not be totally based on this type of sample as a performance standard. A subjective test can always be challenged for its reliability.

4.10 PMTs

PMT is the detection unit of a confocal microscope and its quality and function is extremely important to a confocal microscope [21]. The sensitivity and the ability to detect across the spectra should be considered in choosing a PMT.

1. Not all PMTs contained in a confocal system are equal. Therefore the PMTs should be checked to determine if the unit in the confocal microscope has good sensitivity and good spectral response across the entire spectrum that it is used. The bead tests describe a procedure that can be used to measure PMT sensitivity. The PMT should have a large dynamic range, be linear, and show good sensitivity in the wavelengths measured [10, 22] Often the confocal user will set the PMT at high voltages to observe an image and be unaware how this setting influences image quality. Operating a system with high PMT values will generate a poor image quality due to reduced signal and excessive noise. This noise will have to be eliminated by averaging to yield a good image. Frame averaging or high laser power both will increase image quality (by decreasing PMT voltage used), but bleaching usually occurs by repeated scans over the same sample or with high laser power. It would be useful to have the best PMT with the least noise and greatest dynamic range installed in the machine.
2. There are two types of PMTs used in the Leica system: PMT 1 is considered low noise (R6357) and PMT 2 and 3 (R6358) have high efficiency and sensitivity in the far-red wavelength regions. Zeiss has only low noise (R6357) PMTs in their systems in addition to the multichannel Meta detector. In our opinion it is critical to use the best-quality PMT with the lower noise and best sensitivity. In our opinion the R6357is superior to the R6358 in confocal systems and should be requested at purchasing. Other confocal spectral tests have shown that some Leica system has problems detecting in the far-red range (720–850 nm), which negates the use of the far-red R6358 PMT.

4.11 Spectral Scanning-PMT Comparisons

A useful test is to determine the functionality of the PMT in the confocal machine and to determine that the machine is detecting proper spectra [3–7].

1. This can be easily achieved using the Lightform lamp and to less of a degree with halogen light and bandpass filters or laser light and fluorescent slides
2. The PMT performance was measured on the Leica SP1, SP2 and AOBS, the Zeiss 510 Meta and the Olympus FV 1000.
3. In a Leica system, a sequential scan can be made across the range of 400–800 nm in units as small as 5 nm. A spectral scan of images consisting of 50 increments of 5 nm each was made without averaging between 400 and 650 nm using 10× (0.4 NA) Plan Apo lenses with an airy disk of 1. The light efficiency of the LightForm lamp in a Leica SP1 was low necessitating that a large PMT voltage setting be used. It is essential to use a reflecting mirror and not a dichroic to measure the spectral scans so no attenuation of light will be introduced across the spectral range. There are two types of PMTs used in the Leica system: PMT 1 is considered low noise (R6357) and PMT 2 and 3 (R6358) have high efficiency and sensitivity in the far-red wavelength regions. In our Leica SP system, PMT 2 has direct path to the detector while PMT 1, 3 needs to be reflected off an additional mirror prior to entering the detector. PMT 2 was also superior to PMT 1, 3 for spectral imaging experiments. The test apparently shows not only the accurate representation of specific spectral bands but using CV concept it appears that the total functionality of the system can be determined. The tightest peaks with the largest valleys define the PMT with the best spectral response and determined which PMT should be used for spectral scanning (Fig. 9). In addition stray light and misalignment of the system appears to be able to be determined with this test.
4. Instability may occur in a confocal system. This manifests itself by the beams not being registered correctly and reflections being observed in the PMT detectors in spectral regions where they did not occur precisely. This could be manifested by turning down the PMTs to acquire an unsaturated image and the observed of diffraction patterns in the image. Unstable system is very detrimental to good scientific.

4.11.1 AOTF and Spectrophotometer Sliders and Functional Wavelengths

The functioning of the AOTF and spectrophotometer sliders may be checked by the following two procedures. Set the machine up in reflection mode similar to doing the axial Z resolution test. Positioning the 5 nm sliders over the individual laser lines indicates the approximate relative position of the laser line. By moving the 5 nm slider above or below the laser line the laser light should eventually be attenuated. The laser light should be reflected from

regions 2–3 nm below and above the desired laser line of choice. If light is being reflected below or above the laser line being checked, it suggests that the sliders or AOTF may not be selecting the correct lines. Occasionally we have observed the system reflecting quite a bit of light above or below the laser line indicating an unstable system.

The test can also be made by doing a lambda scan across the laser lines and then measuring the width of reflected light. We found in our Leica SP1 system that the 488 reflections were usually 5 nm, the 568 was 8 nm, and the 647 was 13 nm. Newer confocal systems should have better construction and will show less channels being occupied with reflecting laser light.

The LightForm lamp can also be put on the stage and the pattern will reflect how the sliders are working. Patterns with tight peaks located at the correct wavelengths that have small CVs and large valleys in their proper positions should indicate that the slider is functioning properly and the system is calibrated correctly. Patterns with choppy curves or cutoffs at the high or low spectra can indicate optical problems which include a malfunction slider, misaligned PMT, stray light, or other alignment problems.

A mirror can also be put on the stage and the reflections of laser lines into the PMTs will give indications of what constitutes a properly calibrated system. Data shown in Fig. 9 shows indications of an unstable (Fig. 9b) and uncalibrated system (Fig. 9a)

4.12 Interference Contrast and Confocal

Interference contrast is very useful parameter in microscopy and it can be combined with fluorescence. However since the microscope system was designed for light to traverse through two interferences filters when this optical system is applied to a confocal microcopy there is distortion in the fluorescence signals. The fluorescent light traverses the interference contrast filter, excites the sample and then the emitted fluorescence travels back down through the same interference contrast filter and back through the scan head. The resulting image shows a duplication of very small particles (0.17 μm, PSF beads) and a distortion of larger particles. PSF beads show two spots and 0.5 beads show an egg instead of a round image. The same distortion that is observed on beads will occur on biological structures in cells. The result is spots and point sources of fluorescence will become blurred when using interference optics simultaneously with fluorescence. For optimum resolution of fluorescence data it is recommended that the interference filters be removed when acquiring images (Fig. 12).

4.13 Image Size

A sample should be adjusted using medium speed. A slower scan speed is equivalent to averaging more as the laser spends a longer time on each pixel. Larger sized images 1024×1024 or 2048×2048 give only slightly better detail than 512×512 but allow for extra zooming, which could be useful in visualization of structures. Compared to the 512 images the 1024 images are 4× larger and

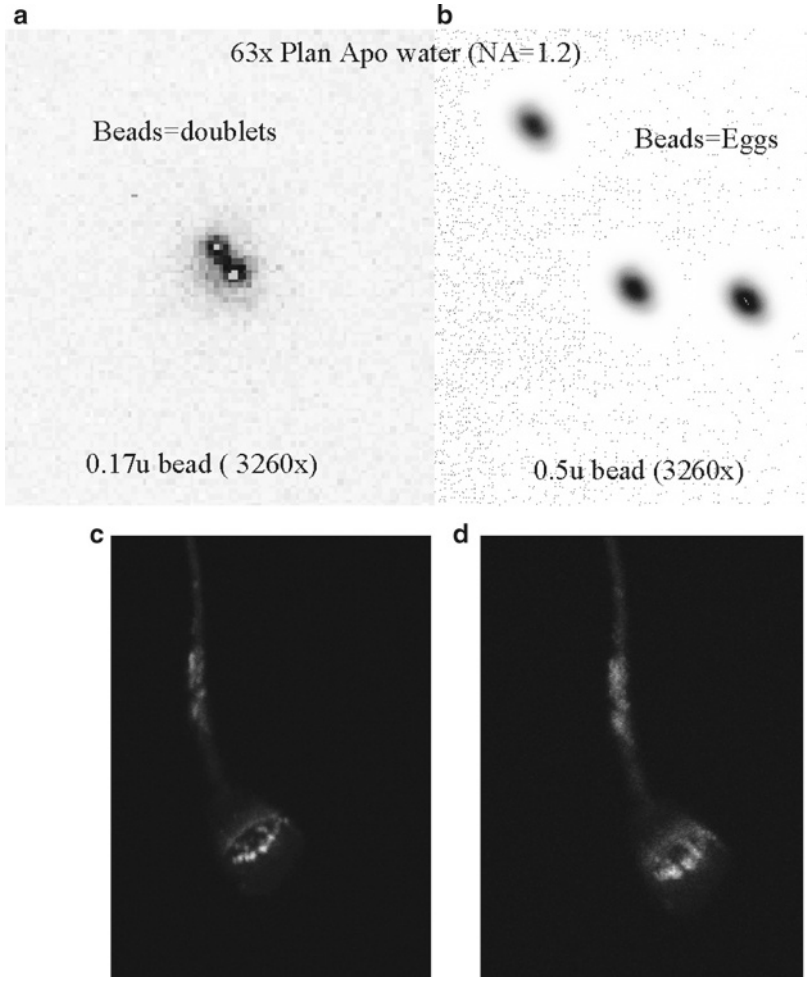

Fig. 12 Incompatibility of interference and CLSM. The Normarski interference contrast light path consists of an analyzer and a polarizer and two interference filters. In acquiring an interference image simultaneously with a fluorescent image, the interference filters interferes with the fluorescent image resulting in doublets using PSF beads [(**a**), 0.17 μm] and egg shape objects with 0.5 μm beads (**b**). All objectives show aberrations with the interference contrast transmission optics in place and it is assumed that the same aberrations will occur with biological structures. Fluorescence of sperm stained with specific antibodies showed more clarity in a system without the Normarski optics [(**c**) vs. (**d**)]

the 2048 images are 16× larger. They will take 4× and 16× respectively longer to acquire, and it will need 4× and 16× more image space to store the data. Most of our routine work in our laboratory is accomplished at 512 × 512 resolutions [23]. Reducing the image size will allow one to take images in less time which may be useful for live cell experiments.

4.14 General Confocal Principle

Generally as the PMT is used at higher values, the sample needs to be averaged more to reduce the noise in the image. How much averaging is done is dependent on the amount of bleaching in the sample and the amount of time available to average. The more averaging the

better the image but there are limiting returns after a few averaged scans due to factors of bleaching affecting image quality. We have found that averaging between three and six times depending on PMT value yields good images. There high numbers maybe due in part to galvanometer problems. Figure 10 shows the relationship between CV averaging and PMT value. In certain cases, the pinhole size may need to be increased to lower the PMT voltage and decrease the noise. This will sacrifice some confocality in the lateral and axial direction of the system.

Similar to beads, biological test samples (FluoCells, F-14780 Molecular Probes, AO stained Chicken Red Blood cells) show a relationship between frame averaging and PMT voltage. The higher the voltage the more averaging that is necessary to produce a desirable image. Since the relationship between PMT and CV (image quality) is logarithmic, very small changes PMT values can indicate major changes in system performance [1, 5]. In the author's opinion, the use of an acceptable range of hundreds of PMT units is for too large to effectively access instrument performance. [1, 2, 5, 6].

4.15 Good Images: Take Home Lessons

In order to obtain a good confocal image, it is necessary to balance laser power, PMT voltage, and frame averaging and pinhole aperture size, scan speed, and zoom magnification [1–6]. For a novice user, it may be difficult to know how to balance these factors to produce an ideal image. Although all of these factors affect image quality, we have found that the zoom greatly bleaches samples and high PMT settings will introduce excessive noise that can only be eliminated through averaging which in turn can also bleach the sample. The zoom increases the bleaching by the square of the zoom. If possible, magnification should be obtained with objectives and not with the zoom magnification [14]. The PMT values should be kept as low as possible, even if one has to increase the pinhole diameter, decrease the scan speed and increase the laser power. Although the pinhole diameter determines the confocality of the system and should ideally be set at the size of the first Airy disk, the pinhole diameter can be increased, if insufficient fluorescent laser light is emitted from the sample making the visualization of the image very noisy. However, increase in the pinhole size will decrease the lateral and axial resolution of the system. In a filter system, the detection band pass barrier filter can also be replaced with a Schott long pass filter to increase the amount of detected light or in a Leica spectrometer system (TCS-SP) the slit can be adjusted to wider values. A slow scan speed can be used, which increases the time the laser beam resides on each pixel. These acquisition factors should be regarded as starting points for using the CLSM and not as an absolute rule, as every sample may have unique qualities that must be considered prior to imaging.

The aim of acquiring of good image is to lower the CV of the image. The challenge for the investigator is to create this image using a standard pinhole (airy disk = 1, eliminates light) without

bleaching the sample and without using excessive laser power or long exposure times. At a given PMT setting, increased frame averaging produces a greater reduction of CV (decreased noise). The use of lower PMT settings allows for less averaging due to the decrease in noise in the system ([1, 3], Figs. 10 and 11). Antifade compounds are useful to reduce the bleaching allowing for increased averaging with fixed samples. Another way to reduce bleaching is to reduce the size of the sample image field (e.g., from 512 × 512 to 128 × 128) acquired. This will result in shorter exposure times with less bleaching while keeping the PMT and laser power settings constant. However this also results in a smaller sample size and less resolution. For histological timed experiments, the loss of minor details due to decreased resolution is not a significant issue, but for biological samples structural details are very important and good images should be taken at pixel values of 512 × 512 or higher.

In summary in order to visualize any fluorescent specimen, a sufficient amount of light has to be delivered onto the sample located on the stage to excite it and then the emitted fluorescence light has to reach the PMT detector. If the sample cannot be adequately visualized, then it will be necessary to either increase the PMT voltage. Increase the laser intensity, or increase the pinhole size. As the PMT voltage is increased, the image noise also increases. At higher PMT settings, it is necessary to use more frame averaging in order to reduce the noise in the image. This leads to longer exposure times and possible sample bleaching.

4.16 CV Principle

We have applied the principle of CV of a population of beads to evaluate confocal system noise, image quality, and system performance. Instead of using thousands of beads to produce a fluorescent histogram, this novel technique uses thousands of pixels from a single bead to generate a population distribution. From these pixel intensity values, the population means and standard deviation, and thus the CV, can be determined. The CV that we are measuring in a confocal microscope is actually the variation of pixel intensity within the bead, as opposed to flow cytometer where the variation of intensity is among a population of beads. The 10 μm bead appeared to be the correct size using an Airy disk of 1 as the image that was captured contained relatively homogenous pixels throughout the bead area using two different microscope systems (Zeiss 510 and Leica TCS-SP1). The region of interest (ROI) inside the bead was of sufficient size to allow a uniform ROI to be defined within it. It was helpful to zoom the bead four times to increase the quantity of pixels contained within the ROI. Repeated sampling of the same bead resulted in minimal bleaching and the CV did not change significantly during subsequent scans.

There are numerous factors, which affect the CV measurement. These include the fluorescence of the bead at the emission and excitation wavelength, optical components and efficiency of the system, maximum system laser power obtainable, and functionality

of optical components in the system and electronic components (PMTs). In addition, many acquisition parameters such as scan speed; pinhole setting and objectives will affect the CV value. When all of these factors are considered the CV will essentially be a measure of the system's relative sensitivity. Lower CVs will translate into better image quality with less image averaging and less bleaching. It is important to maintain the machine variables (pinhole size, PMT voltage, averaging, etc.) at reproducible values for all studies. The laser power was set at a constant value that allowed the mean intensity level of the bead to be approximately 150 (out of 255) for each PMT setting. Since PMTs will deteriorate with time, it is important to measure the initial CV (bead) and then to periodically measure how the CV (image quality) changes over time as a reference point for possible replacement (Table 3).

Although the CV Spherotech bead (or Fluorescent slide) noise test may be useful to evaluate the reproducibility of the system over weeks and months, its applicability in our laboratory was found to be limited as a daily/monthly test. The laser power and stability in the CLSM system were extremely variable for unknown reasons. Perhaps this can be attributed to the quality of the argon–krypton laser alignment instability, variable temperature dissipation, or the AOTF temperature instability.

4.16.1 CV Test Interpretation

The relationship between the PMT and calculated CV is the following: as the PMT voltage is raised, the distribution of the pixels in the bead increases resulting in an increased CV. At higher PMT settings, it is necessary to frame average more to reduce the CV and increase image quality. The same relationship exists in biological samples.

The CV value gives the reference of each PMT relative to each other and suggests which one should be used for optimum performance. In a Leica system this information is useful to evaluate the PMTs and thus determine the best PMT that should be used to acquire signal at the lowest voltage settings and possibly how much averaging will be necessary to achieve a desired image quality [1–3]. By using the most efficient PMT, the image CV is decreased as lower the PMT values are used. An increase in CV values may imply that there is a decrease in laser power after the stage measurement from misalignment resulting in higher PMT values. This CV test on beads can detect a noisy laser. With the argon krypton laser, fast scans actually yielded less noise than slower scans, which was interpreted, as when the pixel dwell time was longer the laser fluctuations were more detectable.

4.16.2 Sensitivity Tests

It is possible to compare similar and different systems using this CV test. This is accomplished by first measuring a specific fixed power value on the stage, keeping all staining parameters constant and then measuring the noise of one single scan line. The amount

of fluctuations that occur in a line scan at a specific power measured on the stage will indicate the instability of the system that will need to be addressed to produce a good image. The more line fluctuations that occur during scanning, the more averaging that will have to be used to create a desirable image.

The sensitivity of any fluorescence optical system depends on the intensity of the light source, the efficiency of the optical system and the quality of the detection system [1, 2, 7, 18, 19]. For confocal microscopes specifically, the sensitivity comprises variables that include, PMT noise, laser noise, alignment, and system efficiency. It would be extremely useful if there were a test that could assess sensitivity in this optical equipment. We believe that we have developed a fluorescent CV test that can be used to measure sensitivity over time, so an assessment can be made on how the machine is performing over time. The test can also be used to compare the sensitivity of two machines from one manufacturer or compare the machines from different manufactures with regard to sensitivity and performance. Extreme care must be made to insure all variables are equivalent when undertaking this exercise. We have shown that the CV bead test confirms principles of noise reduction by averaging sequential frames. The noise is reduced inversely as the square root of the number of frames averaged [1, 2, 5, 23, 24].

The voltage setting of the PMT was the primary determinant of image quality and bead noise. An increase in PMT voltage values was always accompanied by an increase in image noise and pixel CV distributions. For example, at maximum laser power, the best CV on a Leica TCS-SP1 with UV excitation that was obtainable using a 10-μm Spherotech bead was 19 % while the best CV obtainable for a 488 nm excitation was 3.8 % and a 568 nm excitation was 2.5 %. Explanations for the difference in CV between the three excitation wavelengths include the following: (1) the bead may not be excited as well in UV as the visible system, (2) the optical system may be more efficient and less attenuated with visible excitation compared to UV excitation, or (3) there is insufficient UV laser power necessitating the increase of the PMT value to observe the bead at channel 150 (pixel mean). These percentages are invaluable to determine the sensitivity of our TCS-SP and compare its sensitivity to other CLSMs. The values will represent how well the system is aligned and how well each system is functioning regarding this sensitivity parameter. These values are dependent on the maximum power throughput in a system. This test can be used to access the sensitivity of an individual machine and if the acquisition variables are rigorously controlled possibly measure the sensitivity between different machines.

The comparison of the CV from an argon–krypton laser system (Leica TCS-SP1) and air cooled argon/HeNe system (Zeiss 510) and Leica AOBS system at the same mW ranges were made and it was determined that the system with individual lasers was

functioning better than the system with only a single Omnichrome argon–krypton laser emitting three wavelengths. To compare the sensitivity of CLSM system lasers, one can measure a defined milliwatt power on the stage and then conduct the bead noise test as described previously. Since the power on the stage is the same under different systems and configurations, the CV should be an indicator of system sensitivity that includes efficiency, laser noise, and PMT detector quality. Using this test we found that 1 mW of power yielded a CV of 4 % on a Leica TCS-SP and 1.3 % on a Zeiss 510 system. With the 568 line using 0.2 mW of power yielded 4 % on a Leica TCS-SP system and 2 % on a Zeiss 510 system. This test reveals as expected that the noisy argon–krypton laser yield a higher CV than the quieter three individual laser systems.

It should be emphasized that reducing the light to increase confocality will also decease the sensitivity of the system as less photons hit the PMT necessitating that the PMT voltage will need to be raised. It is important to do these tests at a uniform pinhole setting of one airy disk and keeping all other variables equivalent.

This test is important not only to detect defective lasers and system alignment problems but also to set some rational basis to determine how much averaging will be necessary to remove the noise from an image

4.17 Purchase Considerations

The purchase of a new confocal machine is a very difficult and complex decision [25]. Too often it is decided on subjective criteria, such as whether a specific machine can observe a phenomenon on a slide or generate a "pretty picture" during the demo. The pretty picture may be primarily determined by lens characteristics or the functionality of the demo unit. It is critical when comparing machines from different manufacturers that they are set up in a similar fashion. The laser power, objectives, scans speed, illumination and detection pinhole size, and other hardware components are factors that affect image quality. Other critical factors entering into the buying decision should include service and company support after the machine is delivered. QA issues, organizational and service issues should not be overlooked in choosing which manufacturer's machine to buy, as the buyer will have a long-lasting relationship with the vendor and it should be based on trust and knowledge that the machine is operating at its top performance levels. The ability of a manufacturer to guarantee specifications on their machine and address the issues of QA would rate very high on the list of criteria for choosing which CLSM machine to buy. It does the investigator little good if he/she has the best-designed machine that does not perform to those high-advertised standards in his/her laboratory.

Microscopes connected to confocal scanning apparatus can also be combined with digital cameras if a suitable port exists. The confocal microscope contains great objectives and the microscope should be ordered with a 100 mW bulb light housing

instead of 50 mW housing so the microscope can be used also for conventional fluorescence applications. These should have the largest NA and greatest working distance possible. Confocal units are sometimes ordered with lower quality objectives due to budgetary constraints. This is one of the biggest mistakes in operating a confocal microscope facility. The lenses are the engines that drive this technology and they should always be the best quality available. Very high quality confocal grade objectives consisting of dry, water, multi-immersion, and oil should be ordered

4.18 Summary

We have described the following tests to measure system performance in a CLSM: field illumination for individual lenses, laser power indicators, dichroic efficiency, chromatic lens aberration, axial resolution, spherical registration, bead noise, PMT performance, sensitivity, laser stability, and noise analysis [1, 5]. The work of the field engineer also has to be checked carefully as the field engineer may not be able to accomplish all of these tests during an installation or a preventative maintenance visit. Many sales and service representatives may have different levels of machine understanding and without specifications provided by the manufactures, the level of a correctly aligned and functional machine is open to question and debate. Unfortunately, even sales/service representatives from confocal companies can make mistakes in judgment of what constitutes a correctly aligned machine, thus it becomes necessary to use these tests to insure the machines are working correctly in the scientist's laboratories. Unfortunately the CLSM may function at sub-optimum conditions during their operation and problems are resolved only when the investigator cannot achieve the desired images or there is a hard failure of the system necessitating a service personnel visit [6]. It is the responsibility of the core director in each lab to insure the machine is working at acceptable levels of performance. This summary will help identify some of the tests to use and some of the parameters to investigate. With a proper functioning system great images of thick tissues can be achieved [26, 27].

Acknowledgments

We wish to thank Jeff Wang of Spherotech for providing us a 10-μm bead that was uniform in size and fluorescence intensity and did not readily bleach with repeated samplings. Thanks to Gary Klinefelter for providing the sperm sample for comparisons of confocal with Normarski optics. We wish to specially thank Jeremy vLerner for providing us the light source to properly evaluate spectra in a confocal microscope. Figures 1, 4, 5, 7,and 11 and Tables 1, 2, 3, and 4 have been previously published in Cytometry and the journal has allowed these figures to be reproduced in this book chapter.

Table 2
Comparison of relative dichroic reflectance

Wavelength	Dichroic	10× (0.3 NA)	63× (1.2 NA)
488	SD	0.95	0.97
	DD	1.00	1.00
	TD	0.84	0.80
568	SD	0.05	0.06
	DD	0.62	0.72
	TD	1.00	1.00

The relative laser power was measured with the 488 and 568 wavelengths using six different magnification objectives and three dichroics. The 10× and 63× data is shown for clarity. The table demonstrates the relative reflectivity of the dichroics in the system. The test was accomplished by measuring the intensity in a ROI of an image using either 488 or 568 excitation light, a fluorescent plastic slide, one of three specific dichroic and maintaining the PMT at a constant voltage. A ROI of the image yielded the mean value for each acquisition condition (wavelength, objective, and dichroic). The GSV of the highest value image is diveded into the other images to yield a ratio that is expressed in the table as a fraction. The value of 1.00 is the maximum reflection. The dichroic with the maximum reflection should be used when only one fluorochrome is required. Unexpectedly, the double dichroic (DD) yielded the best reflectivity with 488 nm wavelength light with most lenses and the triple dichroic (TD) yielded the best reflectively with the 568 wavelength light (30 % more light reflected than the DD) with most objectives. This table can be used to choose the dichroic that should be used with each excitation wavelength for optimized reflection

Table 3
PMT comparison and noise

PMT comparison					
Excitation	**Emission**	**PMT #**	**PMT voltage**	**CV (%)**	**Relative CV**
488 nm	505–555 nm	1	474	6.06	100
		2	428	6.58	108.65
		3	425	6.23	102.86
	555–600 nm	1	471	6.02	100
		2	432	7.00	116.25
		3	421	6.46	107.17
568 nm	580–630 nm	1	439	4.00	100
		2	411	4.88	122
		3	393	4.49	112.11
647 nm	665–765 nm	1	802	20.30	100
		2	732	22.70	111.68
		3	675	20.30	100.12

The noise of the system was evaluated using a 10 μm bead (Spherotech) and a 100× Plan Apo (1.4 NA) objective. The intensity of a 10 μm bead was determined at a constant laser power, a zoom of 4 and no averaging using various PMT settings. The emitted light was measured in each of three PMTs. The pixels in each ROI were set to a mean of approximately 150 and the SD of pixel distribution was measured to determine the CV. The CV of the pixel intensity within the bead was measured at each PMT setting. PMT 1 is low noise blue sensitive while PMT 2,3 are far-red sensitive. The quality and the performance of each PMT can be measured with this test

Table 4
CLSM sensitivity

Relationship between laser power and CV			
Laser type	**Wavelength (nm)**	**Power (mw)**	**CV–Bead % (SD/mean)**
(A, fixed power comparison)			
Argon Krypton (75 mW, Leica)	488 568	1 0.2	4 4.6
Argon 25 mW (Zeiss)	488	1	1.3
HeNe 1 mW (Zeiss)	543	0.2	1.9
(B, maximum power comparison)			
Argon Krypton (75 mW, Leica)	488 568	1.1 1.45	3.8 2.6
Argon 25 mW	488	3.2	1
HeNe 1 mW	543	0.23	1.9

The sensitivity from a Leica TCS-SP1 containing one noisy argon–krypton laser emitting three laser lines and a Zeiss 510 containing three individual quite lasers and a merge module are represented. The CVs were obtained from a 10-μm bead using a 100× Plan Apo objective (1.4 NA). The laser power was derived by using a 10× (0.3 NA) objective and a power meter situated on the stage. By setting the power to a fixed value of 1 mW of 488 nm laser light or 0.2 mW laser light on the stage, the sensitivity of two machines was measured (A, fixed power comparison). The CV of the bead was to be almost three times lower with the 488 nm and 568 nm laser lines using the Zeiss 510 system compared to the Leica TCS-SP1 system. By increasing the lasers to their maximum power the CV values were decreased (B, maximum power comparison). This test illustrates that different systems having different laser configurations can yield different sensitivity values using this test

References

1. Zucker RM, Price OT (2001) Evaluation of confocal system performance. Cytometry 44: 273–294
2. Zucker RM, Price OT (2001) Statistical evaluation of confocal microscopy images. Cytometry 44:295–308
3. Zucker RM, Lerner J (2005) Wavelength and alignment tests for confocal imaging systems. Microsc Res Tech 68(5):307–319
4. Lerner JL, Zucker RM (2004) Calibration and validation of spectroscopic imaging. Cytometry 62A:8–34
5. Zucker RM (2006) Confocal slide based system: performance. Cytometry 69A:659–676
6. Zucker RM (2006) Confocal microscopy slide based systems: instability. Cytometry 69A: 677–690
7. Zucker RM, Rigby P, Clements I, Salmon W, Chua P (2007) Reliability of confocal spectral imaging systems: use of multispectral beads. Cytometry V71A:174–189
8. Centroze V, Pawley J (1998) Practical laser scanning confocal light microscopy: obtaining optimum performance from your instrument. In: Celis J (ed) Cell biology, vol 3, 2nd edn. Academic, New York, pp 149–169
9. Sheppard CJR, Shotton DM (1997) Confocal laser scanning microscopy. Bios Scientific, New York
10. Marjlof L, Forsgren PO (1993) Accurate imaging in confocal microscopy. In: Matsumato B (ed) Methods of cell biology. Academic, San Diego, CA, pp 79–95
11. Carter D (1999) Practical considerations for collecting confocal images. Methods Mol Biol 122:35–57
12. Pawley J (1995) Fundamental limits in confocal microscopy (chapter 2). In: Pawley J (ed)

Handbook of biological confocal microscopy, 2nd edn. Plenum, New York, pp 19–36

13. Pawley J (2000) The 39 steps: a cautionary tale of quantitative 3-D fluorescence microscopy. Biotechniques 28(5):884–886
14. Cogswell CJ, Larkin KG (1995) The specimen illumination path and its effect on image quality (chapter 8). In: Pawley J (ed) Handbook of biological confocal microscopy, 2nd edn. Plenum, New York, pp 127–137
15. Czader M, Liljeborg A, Auer G, Porwit A (1996) Confocal 3-dimensional DNA image cytometry in thick tissue sections. Cytometry 25(3):246–253
16. Zucker RM, Chua M. Evaluation and purchase of confocal microscopes: numerous factors to consider. Curr Protoc Cytom. 2010 Oct; Chapter 2:Unit2.16
17. Piston DW (1998) Choosing objective lenses: the importance of numerical aperture and magnification in digital optical microscopy. Biol Bull 195(1):1–4
18. Shapiro H (1995) Practical flow cytometry, 3rd edn. New York, Wiley Liss
19. Watson JV (1991) Introduction to flow cytometry. Cambridge University Press, Cambridge, England
20. Muirhead K (1993) Quality control for clinical flow cytometry. In: Bauer KD, Duque RE, Shankey TV (eds) Clinical flow cytometry principles and applications. Williams & Wilkins, Baltimore, MD
21. Art J (1995) Photon detectors for confocal microscopy (chapter 12). In: Pawley J (ed) Handbook of biological confocal microscopy, 2nd edn. Plenum, New York, pp 183–195
22. Pawley JB (1994) Sources of noise in three dimensional microscope data sets in three dimensional confocal microscopy: volume investigations of biological specimens. Academic, New York
23. Russ JC (1998) Image processing handbook, 3rd edn. Boca Raton, FL, CRC
24. Cardullo RA, Alm EJ (1998) Introduction to image processing. Methods Cell Biol 56:99–115
25. Steyger P (1999) Assessing confocal microscopy systems for purchase. Methods 18(4):435–446
26. Zucker RM (2006) Technical note: whole insects and mammalian embryo imaging with confocal microscopy: morphology and apoptosis. Cytometry 69A:1143–1152
27. Zucker RM, Jeffay SC (2006) Confocal laser scanning microscopy of whole mouse ovaries: excellent morphology with apoptosis detection and spectroscopy. Cytometry 2006(69A):930–939

INDEX

Stephen W. Paddock (ed.), *Confocal Microscopy: Methods and Protocols*, Methods in Molecular Biology, vol. 1075,
DOI 10.1007/978-1-60761-847-8, © Springer Science+Business Media New York 2014

D

E

F

G

H

I

K

L

M

N

O

P

Q

R

S

T

U

V

W

X

Y

Z